

***Supramolecular metal-organic frameworks: joining porosity
and magnetic properties into functional materials***

Rubén Pérez Aguirre

Tesis Doctoral

(c) 2021 Rubén Pérez Aguirre

eman ta zabal zazu



Universidad
del País Vasco

Euskal Herriko
Unibertsitatea

Realizar una Tesis Doctoral es como escalar una montaña enorme: la tarea comienza de manera sencilla, con la confianza y la inocencia de aquel que todavía no sabe lo que le espera. A medida que asciendes empiezas a enfrentarte a los primeros problemas, pero no te desanimas y sigues escalando, dispuesta a enfrentarte a cualquier adversidad con tal de superarla. La última parte, el llegar a la cumbre, es lo más difícil, sientes que tu voluntad flaquea y empiezas a necesitar la ayuda de los demás, gente a la cual apoyarte para poder coronar la cima. Y después de todo el sufrimiento, penurias, alegría y disfrute de la tarea que te encomendaste superar hace cinco años, por fin te encuentras en la cumbre. Es en ese momento, cuando miras a tu alrededor maravillándote con las vistas de aquello que has conquistado y piensas “Ha merecido la pena”. Pero claro, como anteriormente he mencionado no todo fue un camino de rosas y he tenido la suerte de tener una gran cantidad de personas que me han ayudado en todo este periplo así que, aquí estoy, dispuesto a plasmar con palabras la gratitud que siento por aquellos que me ayudaron.

En primer lugar comenzaré con mis directores de tesis, el Dr. Garikoitz Beobide Pacheco del Departamento de Química Inorgánica de la Facultad de Ciencia y Tecnología de la Universidad del País Vasco, gran investigador que me ha hecho siempre mantenerme con los pies en la tierra y el Dr. Imanol de Pedro del Valle, del Departamento de Ciencias de la Tierra y Física de la Materia Condensada de la Facultad de Ciencias de la Universidad de Cantabria que me ha enseñado que la distancia no es excusa para involucrarse por algo y siempre me ha obligado a sacar el 110%. La ayuda de ambos ha sido inestimable. Han sabido guiarme y enseñarme de la mejor manera que han podido, tantos en las situaciones malas como en las buenas. Han sido muy pacientes conmigo y me han animado a ser no solo mejor investigador, sino también mejor persona.

De la misma manera tengo que agradecer al Dr. Oscar Castillo García. Si bien no ha sido oficialmente mi director de tesis, se ha comportado como si lo fuera. La verdad es que he conocido a pocas personas como él, con la inteligencia y sabiduría característica de alguien de su titulación pero también con la capacidad de ver las cosas desde otra perspectiva y ser capaz de ver potenciales ocultos donde otros no veían nada. Ha sido una pieza fundamental en el desarrollo de este capítulo de mi vida, dándome buenos consejos que he sabido llevar tanto al terreno profesional como personal y alegrías junto con su mujer, Sonia. Sinceramente, no creo que me olvide nunca la travesía que hicimos a Sevilla, mi primer viaje a un congreso. Estaba hecho un flan de nervios pensando que la liaría en algún momento, pero tanto Oscar como Sonia transformaron esos sentimientos negativos en un sincero disfrute que hace que me salga una sonrisa cada vez que me acuerdo.

También me gustaría agradecer a los demás compañeros del Departamento de Química Inorgánica. A los doctores Sonia Pérez y Javier Cepeda la pareja de investigadores que me amenizaron muchos días y que estuvieron tan pendientes de mí y me facilitaron la integración en el equipo. A la Dra. Mónica Lanchas, mi madre allí en el laboratorio, que me enseñaba con mano firme pero cariñosa en mis etapas más rebeldes en el laboratorio. A Dani, que ahora ha iniciado sus primeros pasos en la paternidad en Logroño junto con su mujer y su hija y que espero que disfrute y que sepa que, a pesar de no vernos tanto, seguirá siendo un gran amigo. Como no olvidarme del Dr. Antonio Luque con el que inicié mis primeros pasos en el sector y claro está, a mis compañeros de laboratorio, tanto los que siguen como los que se fueron, con los que me tiraba horas y horas trabajando.

Deseo agradecer a los Servicios Generales de Investigación (SGIker) de la Universidad del País Vasco por su apoyo técnico y humano. En particular a Javier Sangüesa, Leire San Felices, Iñaki Orue, María Belén Sánchez y Aitor Larrañaga por toda su ayuda.

También quisiera agradecer al Dr. Victor Sans Sangorrin, del centro *Glaxo Smith Kline Carbon Neutral Laboratory for Sustainable Chemistry* de la Universidad de Nottingham (Reino Unido) y a todo su grupo de investigación, por su cálida bienvenida y por los buenos ratos que nos pasábamos tomando cervezas los viernes después de una dura y gratificante semana de trabajo. De todos ellos voy a hacer una mención especial a los doctores Israel Cano y Carmen Martin, con quienes compartí la mayor parte del tiempo en la estancia, haciéndome sentir como en casa. Espero que les vaya todo genial ahora que volvieron a España y que sigan compartiendo unos felices años junto a su hijo Aitor.

Pero no solo he tenido gente a mí alrededor en el terreno profesional. Por tanto, quiero agradecerles su apoyo en esta odisea a todas esas personas de mi círculo más estrecho, aunque sé que ninguno va a tocar mi tesis ni con un palo después de todas las maldiciones que me han oído echar por la boca. Para empezar me gustaría darles las gracias a los compañeros de karate, que supieron templar mi carácter y se llevaron todos los golpes cuando iba tenso a entrenar. Luego, a mi cuadrilla de toda la vida, que consiguieron sacarme de casa cuando estaba más huraño y me hacían evadirme y reír a carcajadas. De entre todos ellos Adrian Casado y Susana Retes tuvieron un papel principal, ya que estuvieron muy pendientes de mí, preguntándome cada poco que tal iba, sobre todo en la redacción de la tesis, y supieron arrojar un poco de luz en los días más nubosos. Adrian, con el que he caminado lo incaminable y me supo enseñar como el camino pedregoso no es sino algo necesario para finalizar la meta.

A Susana, que se preocupaba muchísimo por mí, dándome un enfoque distinto al que estaba acostumbrado y con la que siempre he disfrutado de esos desayunos con tortilla.

A mis familiares, sobre todo a mi hermana Sandra. Qué paciencia tenía conmigo con el inglés. La verdad, si no hubiese sido por ella no tendría ni el nivel que tengo ahora, ni parte de la pasión por la lectura. Chocaremos muchísimas veces, pero siempre la querré tal y como es.

Y por supuesto, la piedra angular en todo esto, mi pareja Alazne. No sé ni por dónde empezar a agradecerle y sigo pensando que debería de convalidarla al menos la carrera de Química después de todas las penurias que le he hecho pasar. Ha estado allí en mis peores momentos, aupándome y haciéndome seguir adelante. Ha estado ahí en mis mejores momentos, compartiendo las alegrías de mi vida, que siempre giraban en torno a ella. Podría rellenar otra tesis solo con las palabras de agradecimiento que la profeso y me estaría quedando corto. Ha sido mi todo, la parte Ying de mi Yang y la chispa de vida que me ha permitido vislumbrar el final, la cumbre de esta montaña que he conquistado. Gracias por estar ahí. Te amo.

A mi familia

A mis amigos

A Alazne

INDEX

CHAPTER 1: INTRODUCTION	1
1.1. CRYSTAL ENGINEERING: BRIEF HISTORY AND GENERALITIES	3
1.2. METAL-ORGANIC FRAMEWORKS	4
1.3. SUPRAMOLECULAR METAL-ORGANIC FRAMEWORKS	11
1.3.1. Generalities	11
1.3.2. Supramolecular engineering	13
1.3.3. Design principle of supramolecular metal-organic frameworks.	15
1.3.4. Biomolecules as ligands in SMOF	16
1.4. SYNTHETIC METHODS.....	23
1.5. APPLICATIONS OF POROUS METAL-ORGANIC MATERIALS	26
1.5.1. Sorption and storage	27
1.5.2. Drug delivery and medical applications.....	28
1.5.3. Catalytic activity	29
1.6. OBJECTIVES	31
CHAPTER 2: 2-HYDROXYQUINOLINE-4-CARBOXYLIC ACID BASED SMOFS	34
2.1. INTRODUCTION	36
2.2. SYNTHESIS AND CHEMICAL CHARACTERIZATION	42
2.2.1. Synthesis	42
2.2.2. Infrared spectroscopy	45
2.2.3. Thermal analysis	48
2.3. RESULTS AND DISCUSSION	51
2.3.1. Crystallographic analysis.....	51
2.3.2. Structural description	54
2.3.3. Magnetic properties.	78
CHAPTER 3: HOMOMETALLIC ADENINE NUCLEOBASE BASED SMOFS	87
3.1. INTRODUCTION	89
3.2. SYNTHESIS AND CHEMICAL CHARACTERIZATION	92
3.2.1 Synthesis	92
3.2.2. Infrared spectroscopy.....	95
3.2.3. Thermal analysis	99
3.3. RESULTS AND DISCUSSION	102
3.3.1. Crystallographic analysis.....	102
3.3.2. Structural description	105
3.3.3. Magnetic properties.	142

3.3.4. Specific heat.....	147
CHAPTER 4: HETEROMETALLIC ADENINE NUCLEOBASE BASED SMOFS	152
4.1. INTRODUCTION	154
4.2. SYNTHESIS AND CHEMICAL CHARACTERISATION.....	157
4.2.1. Synthesis	157
4.2.2. Infrared spectroscopy	160
4.2.3. Thermal analysis	163
4.3. RESULTS AND DISCUSSION	166
4.3.1. Crystallographic analysis.....	166
4.3.2. Structural description	170
4.3.3. Magnetic properties.	192
4.3.4. Magnetic sustentation experiments.....	200
CHAPTER 5: APPLICATION ON THE DRUG CAPTURE AND MAGNETIC SENSING	207
5.1. INTRODUCTION	209
5.2. DRUG ACTIVE-CAPTURE EXPERIMENTS.....	209
5.3. ELECTROMAGNET SUSTENTATION EXPERIMENT ON DRUG LOADED Cu_6CrAD SAMPLES	227
CONCLUSIONS	231
6.1. CONCLUSIONS.....	233
REFERENCES	237
7.1. INTRODUCTION	238
7.2. REFERENCES.....	238
APPENDICES	252
A.1. CHEMICALS	254
A.2. INSTRUMENTAL TECHNIQUES	255
A.2.1. Infrared spectroscopy.....	255
A.2.2. Thermal analysis.....	255
A.2.3. Elemental analyses	255
A.2.4. Single-crystal X-ray diffraction	256
A.2.5. X-ray powder diffraction.....	257
A.2.6. X-Ray Photoelectron Spectroscopy	258
A.3. THERMAL ELLIPSOID PLOT REPRESENTATIONS	258
A.3.1. Chapter 2	259
A.3.2. Chapter 3	262
A.3.3. Chapter 4	265
A.4. XPS ANALYSIS.....	267

A.5. MAGNETIC FITTING MODELS.....	269
A.6. MAGNETIZATION CURVES OF COMPOUNDS OF CHAPTER 3.....	272
A.7. PUBLICATIONS ARISING FROM THIS WORK.....	273

Chapter 1: Introduction

1.1. Crystal engineering: brief history and generalities

1.2. Metal-organic frameworks

1.3. Supramolecular metal-organic frameworks

1.4. Synthetic methods

1.5. Applications of porous metal-organic materials

1.6. Objective

1.1. CRYSTAL ENGINEERING: BRIEF HISTORY AND GENERALITIES

The cornerstone for technological proliferation has always been the synthesis of new materials. However, in the beginning it was considered an art rather than a science. This was mainly due to the fact that most of the new synthesized compounds were obtained by serendipity and using methods not considered very scientific such as "mix and wait". This methodology was used with good results in the 20th century, but nowadays the increasing requirement of materials with specific functions demands *ad hoc* design of new material.^[1]

One of the first major changes in the rational design of materials was the use of rigid and well-defined building blocks. In this way, one of the main problems, i.e. the lack of control in the synthesis, was solved, in such a way that the building blocks would maintain their structural integrity throughout the construction process, smoothing over the synthesis of the targeted product.^[2] Note dispensing with such building blocks leads to a poor correlation between the reactants and the targeted products. This breakthrough in materials science was boosted by crystalline engineering, a field that covers computational studies of interactions and their role in determining crystal packing, molecular and supramolecular synthesis, and also, by a wide variety of techniques to establish and quantify properties of the obtained materials. In this way, it is possible to direct the synthetic methods towards a specific compound that is able to fulfil the functional requirements of a desired application, that is, carrying out a rational design of a functional molecular solid.^[3]

An outstanding area within the field of crystal engineering is the reticular synthesis (named by O. Yaghi).^[4] Reticular synthesis is distinguished from supramolecular assembly,^[5] because in the former, building blocks are linked by strong bonds throughout the crystal, while in the second the assembling is conducted by weaker non-covalent interactions.

The correlation between shape, symmetry and intermolecular forces is key to the successful design of crystalline architectures.^[6] To carry out a crystalline design in molecular materials, without the presence of coordination bonds, the concepts of tectons and synthons are used. Tectons are molecular entities that assemble into aggregates by synthons

¹ (a) Stein, A.; Keller, S. W.; Mallouk, T. E. *Science*, **1993**, *259*, 1558–1563. (b) Yaghi, O. M.; O’Keeffe, M.; Kanatzidis, M. G. *J. Solid State Chem.*, **2000**, *152*, 1–2.

² (a) Yaghi, O. M.; Li, H.; Davis, C.; Richardson, D.; Groy, T. L. *Acc. Chem. Res.*, **1998**, *31*, 474–484. (b) Eddaoudi, M.; Moler, D.; Li, H.; Chen, B.; Reineke, T.; O’Keeffe, M.; Yaghi, O. M. *Acc. Chem. Res.*, **2001**, *34*, 319–330.

³ (a) Braga, D.; Grepioni, F.; Orpen, A. *Crystal engineering: From molecules and crystals to materials*; Kluwer Academic Publishers: Boston, **1999**. (b) Braga, D.; Brammer, L.; Champness, N.R. *CrystEngComm* **2005**, *7*, 1.

⁴ (a) Yaghi, O. M.; O’Keeffe, M.; Ockwig, N. W.; Chae, H. K.; Eddaoudi, M.; Kim, J. *Nature*, **2003**, *423*, 705. (b) Ohrstrom, L.; Larsson, K. *Molecular Based Materials: The Structural Network Approach*; Elsevier: Amsterdam, **2005**.

⁵ Lehn, J. M. *Chem. Scr.*, **1988**, *28*, 237–262.

⁶ (a) Desiraju. G. R. *Angew. Chem .Int. Ed.* **1995**, *34*. 2311-2327. (b) Stang, P.J.; Olenyuk, B. *Acc. Chem. Res.*, **1997**, *30*,502–518.

(combinations of functional groups or molecules that are usually linked by the same type of non-covalent interactions), giving rise to a supramolecular structure with controlled geometries.

The crystal engineering of metal-organic systems can be divided into two main lines:

(a) Crystals formed by extended structures (coordination polymers) that are propagated by coordination bonds between the metal and the ligand.

(b) Crystals formed by molecular building blocks (neutral or ionic) that are joined by non-covalent interactions.

Coordination polymers, including metal-organic frameworks (MOF), belong to the first case as their framework and crystal design is based on coordination bonds. The second case includes organic molecular structures and coordination compounds consisting of discrete complex entities, among others, since building blocks are assembled by intermolecular interactions. Supramolecular metal-organic frameworks (SMOF), subject of the current PhD Thesis, belong to the latter class as they consist of discrete complex entities (see section 1.3).

1.2. METAL-ORGANIC FRAMEWORKS

MOFs or formerly called coordination polymers (CP) are compounds that became known in the mid-20th century^[7] although they did not arouse any special interest until decades later. The seminal papers published by the teams of Robson^[8], Kitagawa^[9], Yaghi^[10], Lee and Moore^[11] and Férey^[12], can be considered the first works that identified the outstanding potential of this novel family of porous solids. Due to the increment in works related to metal-organic compounds, the terminology referring to MOFs expanded, using different names to refer the same types of coordination polymers (1D, 2D, 3D), regardless of whether they are compact or open structures.^[13] Therefore, observing the great boom that the area of MOFs was experiencing, in order to clarify the unceasing increase of ambiguous terms, the IUPAC recommended the following definitions:

⁷ (a) Kinoshita, Y.; Matsubara, I.; Higuchi, T.; Saito, Y. *Bull. Chem. Soc. Jpn.* **1959**, *32*, 1221–1226. (b) Berlin, A.A.; Matveeva, N.G. *Russ. Chem. Rev.* **1960**, *29*, 119–128. (c) Block, B.P.; Roth, E.S.; Schaumann, C.W.; Simkin, J.; Rose, S.H. *J. Am. Chem. Soc.* **1962**, *84*, 3200–3201. (d) Knobloch, F.W.; Rauscher, W.H. *J. Polym. Sci.* **1959**, *38*, 261–262. (e) Kubo, M.; Kishita, M.; Kuroda, Y. *J. Polym. Sci.* **1960**, *48*, 467–471. (f) Tomic, E.A. *J. Appl. Polym. Sci.*, **1965**, *9*, 3745–3752.

⁸ (a) Batten, S.R.; Hoskins, B.F.; Robson, R. *J. Am. Chem. Soc.*, **1995**, *117*, 5385–5386. (b) Hoskins, B.F.; Robson, R. *J. Am. Chem. Soc.*, **1990**, *112*, 1546–1554.

⁹ (a) Kitagawa, S.; Kawata, S.; Nozaka, Y.; Munakata, M. *J. Chem. Soc. Dalton Trans.*, **1993**, *9*, 1399–1404. (b) S. Kitagawa, S. Matsuyama, M. Munakata, T. Emori, *J. Chem. Soc. Dalton Trans.* **1991**, *11*, 2869–2874.

¹⁰ Yaghi, O.M.; Li, H.L. *J. Am. Chem. Soc.*, **1995**, *117*, 10401–10402.

¹¹ Gardner, G.B.; Venkataramani, D.; Moore, J.S.; Lee, S. *Nature*, **1994**, *374*, 792–795.

¹² Riou, D.; Férey, G. *J. Mater. Chem.*, **1998**, *8*, 2733–2735.

¹³ Rowsell, J. L.C.; Yaghi, O. M. *Micropor. Mesopor. Mat.* **2004**, *73*, 3.

Coordination compound: any compound that contains a coordination entity being an ion or a neutral molecule, which is composed by a metallic central atom attached to a group of atoms, called ligands.

Coordination Polymers (CP): a coordination compound that spans in 1, 2, or 3 dimensions through coordination links.

Metal-Organic Framework (MOF): a coordinating polymer (or alternatively a coordination network) with an open framework that has potentially accessible holes.

MOFs are crystalline compounds consisting of both inorganic and organic units. The inorganic units are the metal ions or clusters, which can be termed as nodes. Its geometry is determined by the coordination number, coordination geometry of the metal ions, and the nature of the functional groups. The organic units act as a linkers, connecting the nodes by coordination bonds of moderate strength.^[14]

In fact, the high existing knowledge about these components allows to carry out a rational design in order to obtain a material with specific properties. Moreover, the correct selection of the metal ion, the ligands and the way in which both can be coordinated are of vital importance, allowing a reticular design of the coordination compounds and, therefore, of their physical and chemical properties. Figure 1.1 shows the most common coordination numbers for each metal ion while Figure 1.2 displays some examples of organic ligands and their usual coordination mode in the building up of coordination polymers.

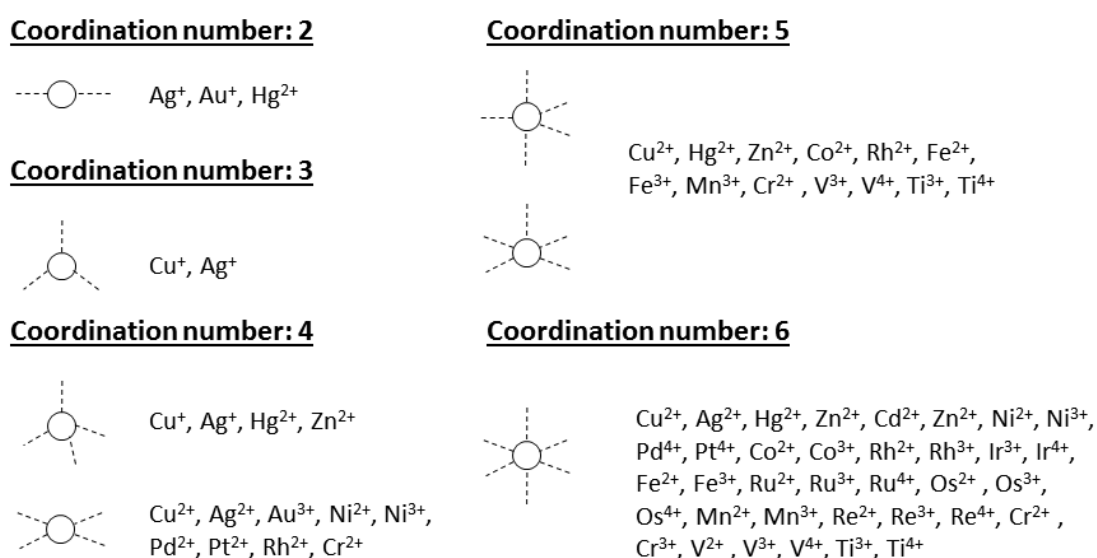


Figure 1.1. Most common coordination numbers and coordination geometries for each metal ion.

¹⁴ (a) Batten, S.R.; Champness, N.R.; Chen, X.M.; Garcia-Martinez, J.; Kitagawa, S.; Ohrstrom, L.; O'Keeffe, M.; Suh, M.P.; Reedijk, J. *Pure Appl. Chem.*, **2013**, *85*, 1715–1724. (b) Batten, S.R.; Champness, N.R.; Chen, X.M.; Garcia-Martinez, J.; Kitagawa, S.; Ohrstrom, L.; O'Keeffe, M.; Suh, M.P.; Reedijk, J. *CrystEngComm*, **2012**, *14*, 3001–3004.

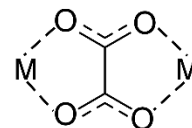
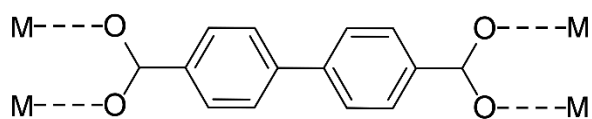
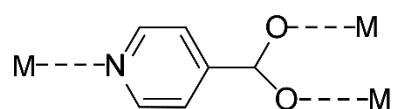
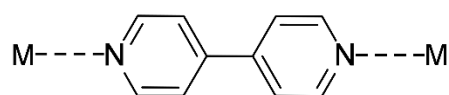
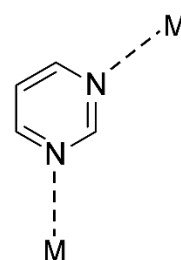
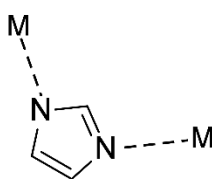
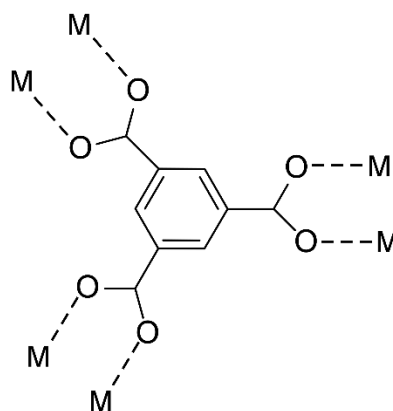
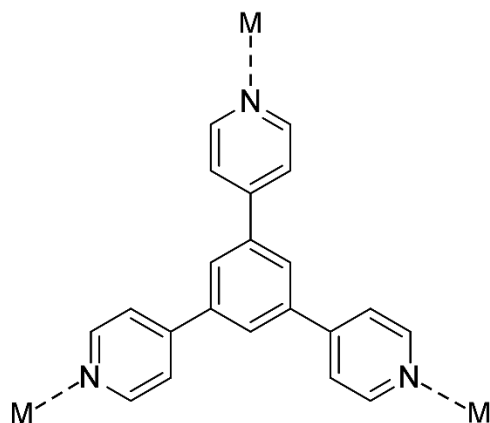
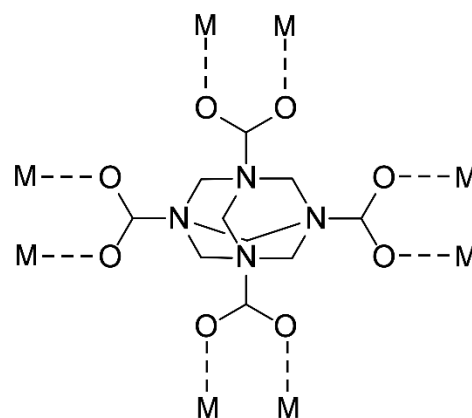
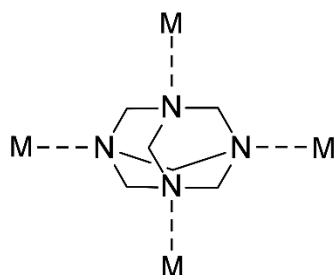
Linear linkers**Angular linkers****Trigonal linkers****Tetrahedral linkers**

Figure 1.2. Examples of different organic linkers used in crystal engineering.

The self-assembly process between metal nodes and organic linkers is led by the formation of coordination bonds as well as by hydrogen bonds and van der Waals interactions between non-metallic components. Therefore, the variation of the coordination geometries of the metal ions and functional groups of the ligands, leads to a wide structural diversity ranging from discrete entities to extended systems (1D, 2D, 3D) (Figures 1.3 and 1.4).

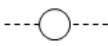

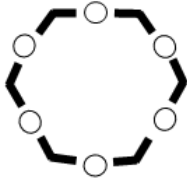




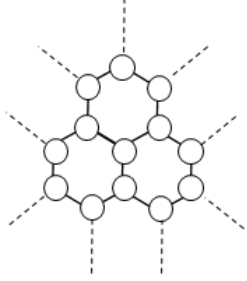
Metallic node	Ligand/linker	Structure	Dimensionality
 Linear	 Angular	 Hexagonal ring	0D
	 Linear	 Linear	1D
 Trigonal	 Linear	 Honey comb	2D

Figure 1.3. Different structures obtained by node-linker combinations.



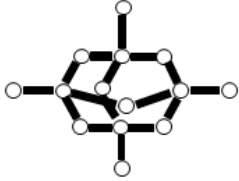
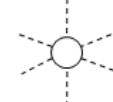

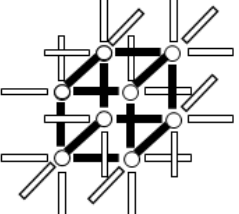
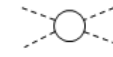

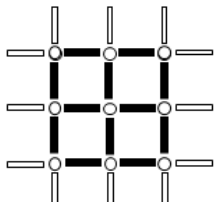
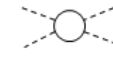

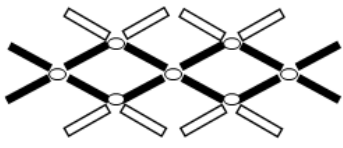
Metallic node	Ligand/Linker	Structure	Dimensionality
 Tetrahedral	 Linear	 Tridimensional diamond type	3D
 Octahedral	 Linear	 Simple cubic	3D
 Square planar	 Linear	 Square planar	2D
 Square planar	 Square planar	 Braid	2D

Figure 1.4. Different structures obtained by node-linker combinations (cont.).

In principle, a bridging ligand (ditopic, tritopic, tetratopic, or multitopic linkers) reacts with a metal ion with more than one vacant or labile site. Depending on the ligand features and on the coordination number/geometry of the metal ion and synthesis conditions, infinite-extended polymeric or discrete oligomeric structures can arise. Furthermore, to control the dimensionality of the coordination entity, auxiliary ligands can also be used to block some positions of the coordination sphere, imposing geometries of the metallic centre that hinder the growth of high dimensionality network or at least, partially reduce it (Figure 1.5).

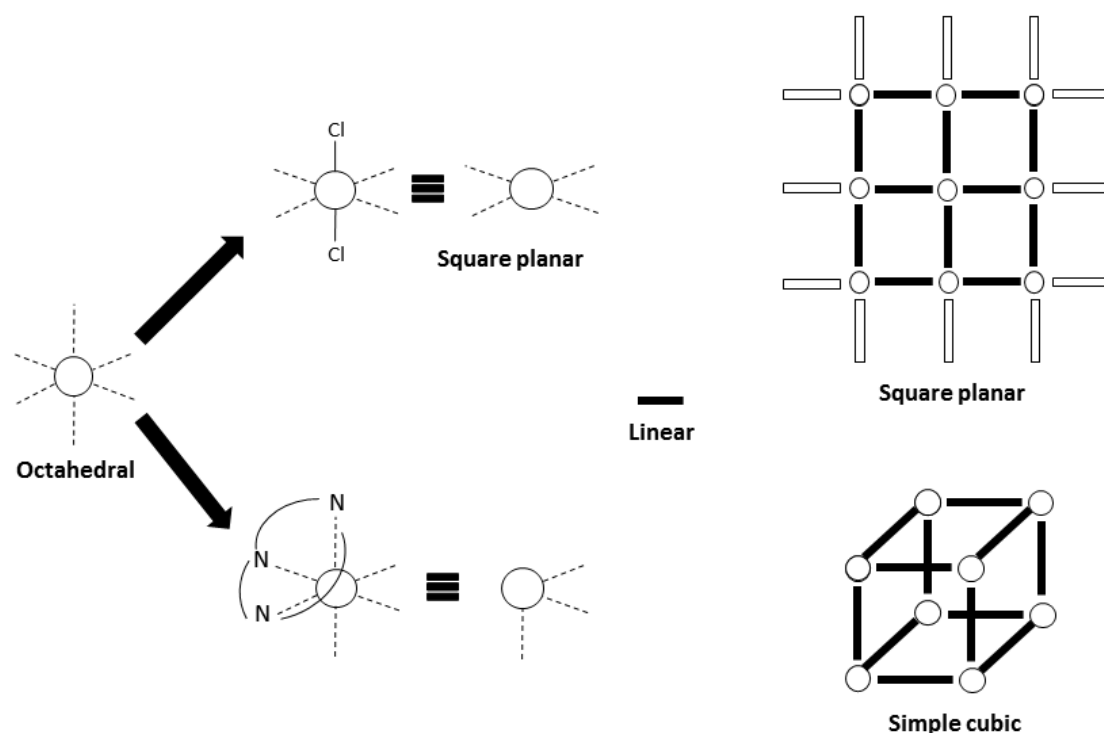
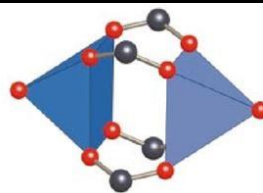
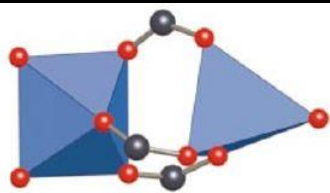
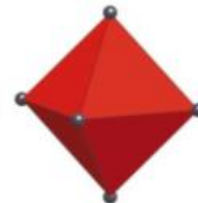
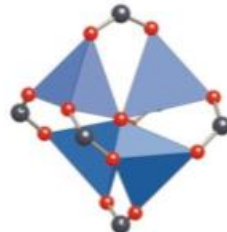
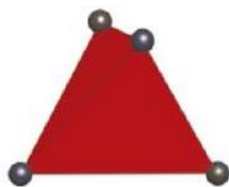
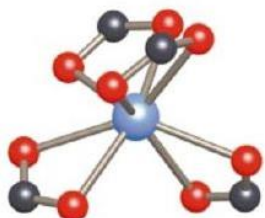
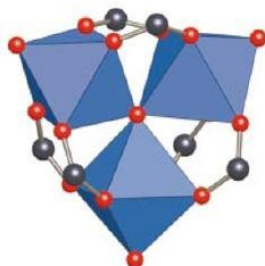


Figure 1.5. Examples of how auxiliary ligands can direct the topology and dimensionality of the coordination entity.

Sometimes is nearly impossible the design of complex structures just by the connection between metallic ions and organic linkers so the use of secondary building units (SBUs) takes a great relevance. SBUs are formed not only by the metals that make up the cluster but also by the functional groups that give cohesion to it. In this way, a variety of SBU geometries with different number of points of connection have been observed in MOF structures, such as octahedron (six points), trigonal prism (six points), square paddle-wheel (four points), and triangle (three points) (Figure 1.6).

INORGANIC UNITS

**Triangle****Paddle-Wheel****Tetrahedron****Octahedron****Trigonal Prism**

ORGANIC UNITS

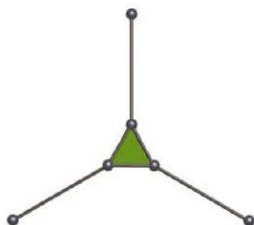
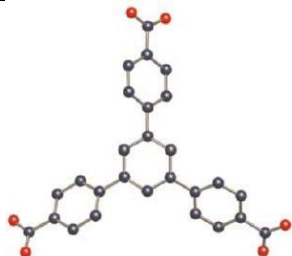
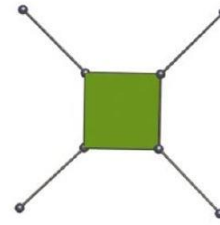
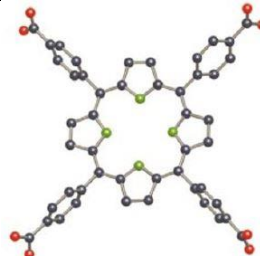
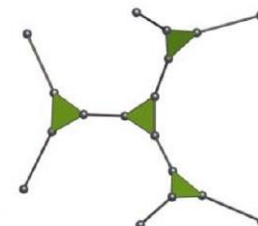
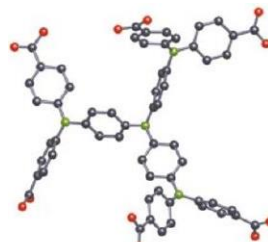
**Trigonal****Square planar****Tetrahedral****Trigonal**

Figure 1.6. Examples of SBUs. C, N and O atoms are shown in black, green and red respectively. The polyhedra in inorganic units are shown in blue while polyhedron defined by carboxylate carbon atoms (SBUs) are red. In organic units the polyhedra are shown in green.

1.3. SUPRAMOLECULAR METAL-ORGANIC FRAMEWORKS

1.3.1. Generalities

Considering the great potential of MOFs, some time ago it was decided to explore a related type of material, in which the coordination bonds are replaced with supramolecular interactions as linkers to yield SMOFs that would also contain potential voids (Figure 1.7).

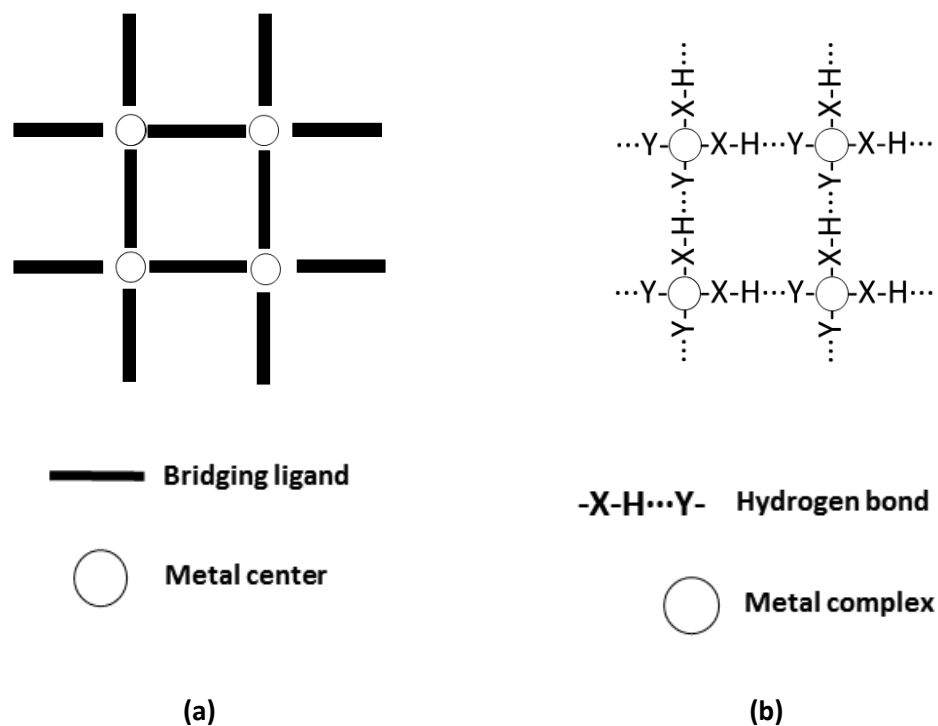


Figure 1.7. Similarity between (a) coordination bonds and (b) hydrogen bonding interactions as structure directing agents.

Related to this, the area of supramolecular chemistry^[15] has experienced a rapid growth over the past decades.^[16] As previously stated, the supramolecular term includes a variety of non-covalent intermolecular interactions, such as, van der Waals forces, π - π interactions, and other weak interactions. Despite these type of interactions are not individually as strong as covalent interactions, they have demonstrated to be highly valuable in the design of large entities called supramolecules,^[17] being hydrogen bonding the most predominant. Speaking about these last interactions, during decades, the concept of hydrogen bonding has evolved through numerous discussions. As a result, there were several

¹⁵ (a) Lehn, J. M. *Angew. Chem., Int. Ed.*, **1990**, *29*, 1304–1319. (b) Menger, F. M. *Proc. Natl. Acad. Sci. U. S. A.*, **2002**, *99*, 4818–4822.

¹⁶ (a) Prins, L. J.; Huskens, J.; de Jong, F.; Timmerman, P.; Reinhoudt, D. N. *Nature*, **1999**, *398*, 498–502. (b) Scherman, O. A. *Nat. Chem.*, **2009**, *1*, 524–525. (c) Aida, T.; Meijer, E. W.; Stupp, S. I. *Science*, **2012**, *335*, 813–817. (d) C. Hansell, *Nat. Chem.*, **2014**, *6*, 459.

¹⁷ Lehn, J. M. *Supramolecular Chemistry: Concepts and Perspectives*, Wiley VCH, **1995**.

definitions^[18] until 2011, when the IUPAC published a definitive description of the hydrogen bond describing it as “an attractive interaction between a hydrogen atom from a molecule or a molecular fragment X–H [the hydrogen-bond donor] in which X is more electronegative than H, and an atom or a group of atoms [the hydrogen-bond acceptor] in the same or a different molecule, in which there is evidence of bond formation”.^[19]

Although, there are clear structural analogies between SMOFs and MOFs, a crystal structure predominantly grown through only supramolecular interactions has different properties from that sustained solely by coordination bonds. In this regard, as above mentioned, the strength of supramolecular interactions is generally weak and due to ability of molecular solvents to form this type of interactions, many supramolecular networks depend on solvent guests. Therefore, the solvent removal, can promote the collapse of the supramolecular networks. In fact, despite the large number of porous supramolecular structures reported, only a few of them correspond to compounds with permanent porosity (Figure 1.8).^[20] Nonetheless this apparent disadvantage, provides the ability to regenerate at room temperature the structure through dissolution and recrystallization, which is unique feature for molecular porous materials (including SMOFs), in contrast to other porous materials based on covalent or coordination bonds (Figure 1.9).^[21]

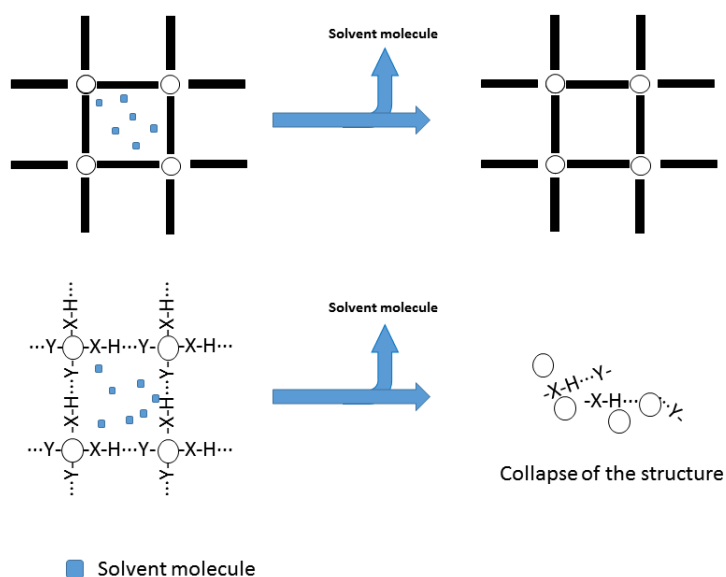


Figure 1.8. Representation of the solvent evacuation from a MOF (upper scheme) and SMOF (lower scheme). The figure aims to depict the most common cases for each type of compound.

¹⁸ Gilli, G.; Gilli, P. Oxford University Press: Oxford, **2009**.

¹⁹ Arunan, E.; Desiraju, G. R.; Klein, R. A.; Sadlej, J.; Scheiner, S.; Alkorta, I.; Clary, D. C.; Crabtree, R. H.; Dannenberg, J. J.; Hobza, P.; Kjaergaard, H. G.; Legon, A. C.; Mennucci, B.; Nesbitt, D. J. Definition of the Hydrogen Bond (IUPAC Recommendations **2011**). *Pure Appl. Chem.* **2011**, *83*, 1637–1641.

²⁰ Cooper, A. I. *Angew. Chem., Int. Ed.*, **2012**, *51*, 7892.

²¹ (a) Mastalerz, M.; Oppel, I. M. *Angew. Chem., Int. Ed.*, **2012**, *51*, 5252. (b) Liu, Y.; Hu, C.; Comotti, A.; Ward, M. D. *Science*, **2011**, *333*, 436.

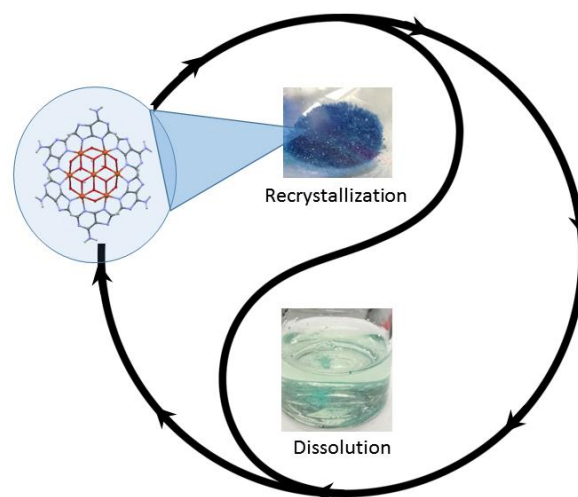


Figure 1.9. Regeneration ability of SMOFs through dissolution-recrystallization process.

1.3.2. Supramolecular engineering

As above mentioned, hydrogen-bonding is the most predominant interactions used to build up pre-designed supramolecules, due to both its directionality and its relative strength compared to other non-covalent forces. It must be taken into account that, in terms of energy, the bond strength of supramolecular interactions is not as strong as covalent interactions but the former is often decisive in the resulting crystal structure. In fact, computational calculations overall bond energies do not present a significant difference between the two interactions in orders of magnitude.^[22] However, that depends on the type of hydrogen bonding that is used to form the supramolecular synthon. The energy of hydrogen bonds ranges from 0.2 to 40 kcal mol⁻¹. This wide energy range is due to several weak forces, such as, the polarization, electrostatic, dispersion, charge transfer and exchange-repulsion forces that depend on the atoms that are taking part in the hydrogen bonding. Thus, hydrogen bonds can be classified in three types, based on their bond energies: weak, moderate, and strong.^[23]

- **Weak hydrogen bond (<4 kcal mol⁻¹):** dominated by electrostatic and dispersive forces.
- **Moderate hydrogen bond (4–15 kcal mol⁻¹):** dominated only by electrostatic forces.
- **Strong hydrogen bond (15–40 kcal mol⁻¹):** strongly covalent in nature.

In contrast to this classification, Desiraju provides a slightly different organization based on the strength (Figure 1.10).^[24]

²² Gavezzotti, A., *New J. Chem.*, **2016**, *40*, 6848–6853.

²³ Jeffrey, G. A. *An Introduction to Hydrogen Bonding*; Oxford University Press: Oxford, **1997**.

²⁴ Desiraju, G. R. *Acc. Chem. Res.* **2002**, *35*, 565–573.

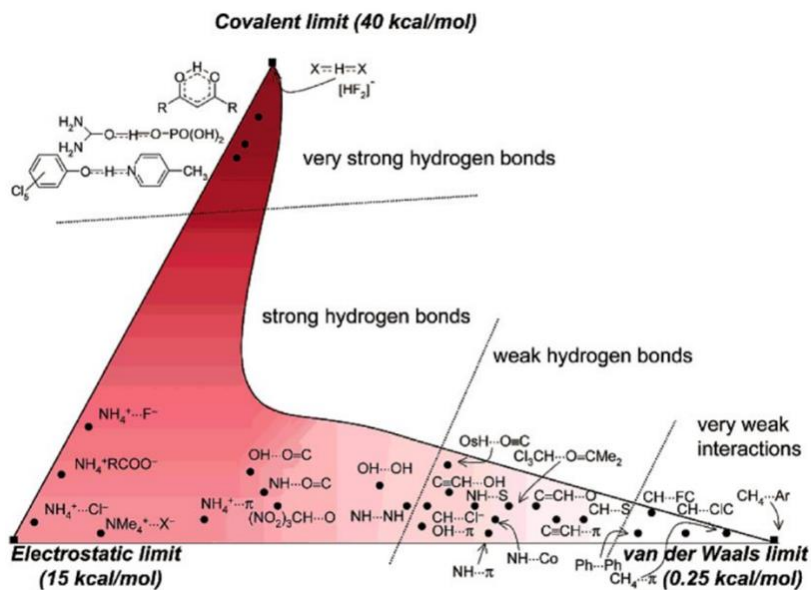


Figure 1.10. Energies of a wide range of chemically diverse hydrogen bonds (darker coloured areas indicate higher bond energies).

Numerous studies in the late of 20th century by Etter,^[25] Desiraju^[26] and others stated that hydrogen bonds are able to connect molecules by well-defined structural units. Desiraju termed these structural fragments as supramolecular synthons (Figure 1.11).^[6]

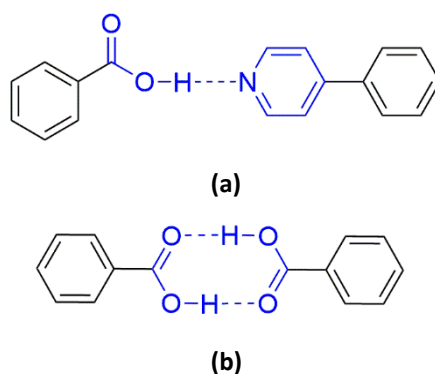


Figure 1.11. Supramolecular hetero- (a) and homosynthons (b), coloured in blue, formed by two compatible molecular functional groups

Since in the area of molecular crystals, supramolecular synthons are the basic building, the selection of the synthon is the key to tune the features of the supramolecular aggregate. Figure 1.12 lists some examples of supramolecular synthons.

²⁵ (a) Panunto, T. W.; Urbanczyk-Lipkowska, Z.; Johnson, R.; Etter, M. C. *J. Am. Chem. Soc.* **1987**, *109*, 7786–7797. (b) Etter, M. C. *J. Phys. Chem.* **1991**, *95*, 4601–4610. (c) Etter, M. C.; Urbanczyk-Lipkowska, Z.; Zia-Ebrahimi, M.; Panunto, T. W. *J. Am. Chem. Soc.* **1990**, *112*, 8415–8426. (d) Etter, M. C. *Acc. Chem. Res.* **1990**, *23*, 120–126.

²⁶ (a) Desiraju, G. D. *Crystal Engineering: The Design of Organic Solids*; Elsevier: New York, **1989**. (b) Desiraju, G. R. *Prog. Solid State Chem.* **1987**, *17*, 295–353.

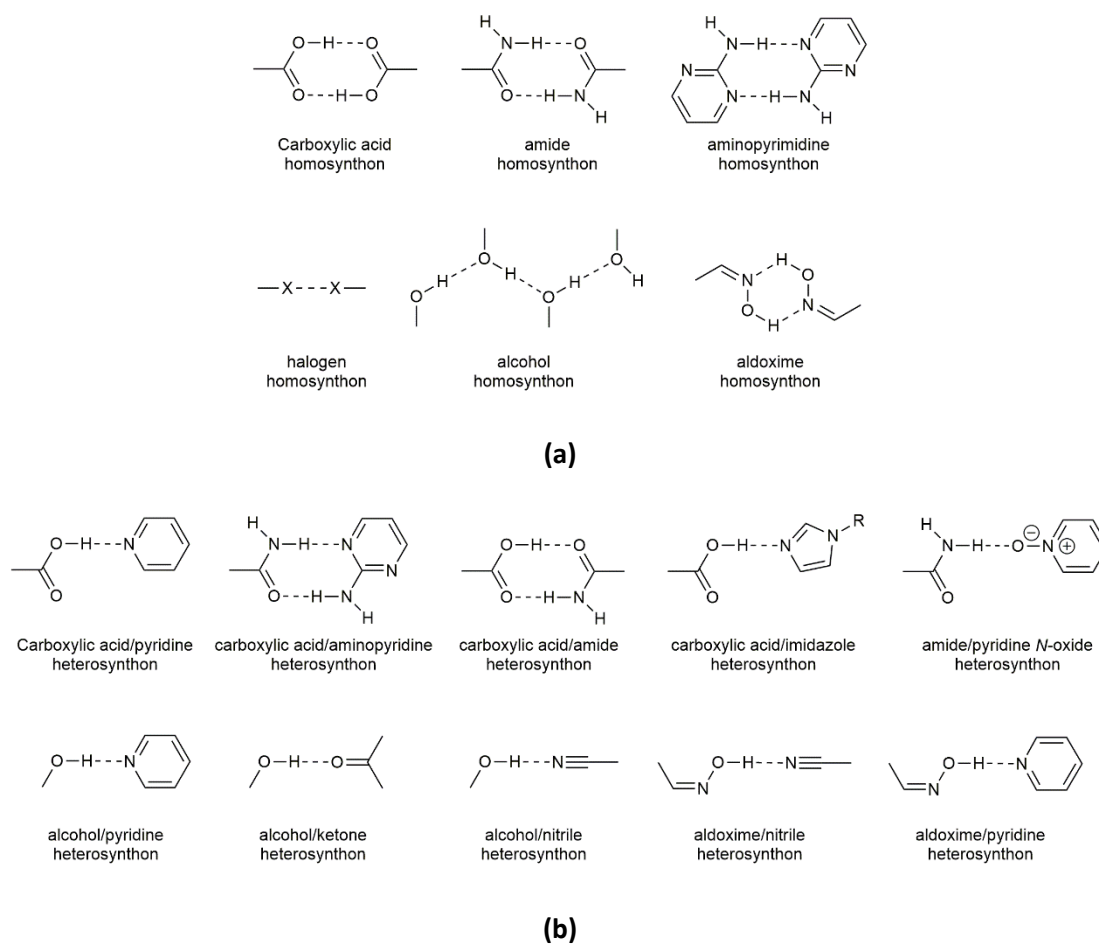


Figure 1.12. Examples of supramolecular synthons divided in (a) homosynthons and (b) heterosynthons.

1.3.3. Design principles of supramolecular metal-organic frameworks.

The design of a supramolecular metal-organic framework must be based on the following key factors in order to obtain a 3D crystal building that contains potentially accessible voids and that is sustained by hydrogen bonds, among other supramolecular interactions, as connectors:

1. Rigid building units.
2. Rigid synthons connecting this building units.
3. Non-coplanarity of functional groups involved in the synthons.

Although supramolecular engineering presents a wide variety of ways in which the previously proposed guidelines can be completed, the following will be taken as the cornerstone: the stiffness of the synthesized structures is obtained due to the use of non-flexible ligands, which in turn have functional groups capable of forming complementary hydrogen bonds in more than one position. In this way, a perfect building block is obtained for the formation of a rigid and stable supramolecular compound. Although with these guidelines, the formation of a supramolecular compound would be allowed, the self-imposed requirement

of obtaining three-dimensional structures requires the use of at least three non-coplanar synthons.

1.3.4. Biomolecules as ligands in SMOF

For biological or environmentally compatible applications, ligands that meet other requirements in addition to those mentioned above are required. For applications where organisms will be in contact (such as the release of drugs into living bodies), the generated SMOF must be non-toxic. In this sense, biomolecules are ideal candidates to act as construction units in the formation of metal-biomolecule framework (MBioFs).^[27] MBioFs are defined as MOFs built by at least one biomolecule that acts as organic linker. While the time studying BioMOF (10 years) is significantly shorter than other types of compounds, they have attracted great attention due to their rich supramolecular chemistry, that endorse them molecular recognition capability and unique biomimetic properties. Nonetheless, the use of biomolecules can also imply significant disadvantages. For instance, symmetry defects that cause difficulties synthesizing ordered crystalline materials are characteristic of this type of compound. Furthermore, due to the flexibility of some of the biomolecules and their labile metal-ligand coordination, biomolecular ligands can lead to interpenetration and unfavourable geometries or stoichiometries, resulting in non-porous structures. These disadvantages hinder the development of new BioMOFs. For all this, the correct selection of biomolecules and metal centres has a considerable nuance in this type of supramolecular chemistry.

The use of nucleobases is a very promising area in the synthesis of SMOFs due to their ability to allow the formation of rigid structures that fulfil the aforementioned requirements based on their multiple possible coordination modes and a series of well suited functional groups to establish rigid synthons. Regarding the potential synthons, note that the pyrimidine and purine rings of nucleobases are capable to assemble neighbouring nucleobases by π - π interactions. Furthermore, they display several hydrogen bonding donor and acceptor groups capable of participate simultaneously in the formation of hydrogen bonds not only with other ligands but also with themselves by complementary base pairing interactions.

Natural nucleobases, divided in two groups (purines: adenine, guanine and pyrimidines: thymine, cytosine and uracil) are the keystone of the basic life, being the primal structure of the DNA and RNA double helices (Figure 1.13).

²⁷ (a) Imaz, I.; Rubio-Martínez, M.; An, J.; Solé-Font, I.; Rosi, N. L.; Maspoch, D. *Chem. Commun.* **2011**, 47, 7287–7302. (b) Rabone, J.; Yue, Y. F.; Chong, S. Y.; Stylianou, K. C.; Bacsa, J.; Bradshaw, D.; Darling, G. R.; Berry, N. G.; Khimyak, Y. Z.; Ganin, A. Y.; Wiper, P.; Claridge, J. B.; Rosseinsky, M. J. *Science*, **2010**, 329, 1053–1057. (c) Rojas, S.; Devic, T.; Horcajada, P. *J. Mater. Chem. B*, **2017**, 5, 2560–2573. (d) Giménez-Marqués, M.; Hidalgo, T.; Serre, C.; Horcajada, P., *Coord. Chem. Rev.*, **2016**, 307, 342–360. (e) Beobide, G.; Castillo, O.; Cepeda, J.; Luque, A.; Pérez-Yañez, S.; Roman, P.; Thomas-Gipson, J. *Coord. Chem. Rev.*, **2013**, 257, 2716–2736.

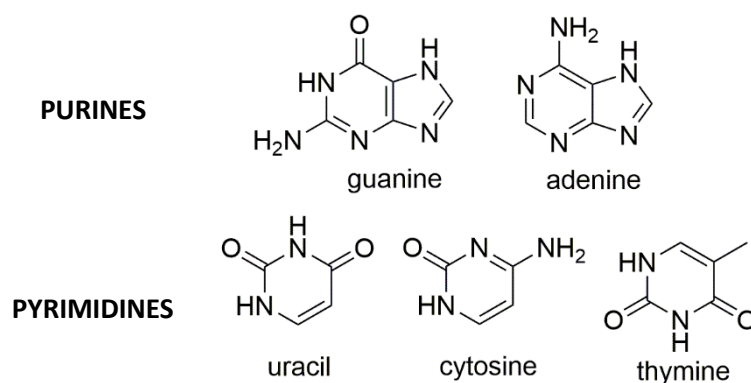


Figure 1.13. Structure of the nucleobases.

According to canonical base pairing interactions, (1) adenine binds to thymine or uracil by means of two hydrogen bonds, in DNA and RNA, respectively, and (2) guanine, in contrast, establishes three hydrogen bonds with cytosine. The large number of available heteroatoms in these biomolecules, allows them to act as multidentate organic ligands, in addition to being able to form a wide network of hydrogen bonding, which make them suitable ligands for the construction of coordination compounds.^[28] Due to their great role as ligands in the construction of biomimetic compounds,^[29] their use in the construction of porous materials is not surprising.^[30] In this way, the purine type nucleobases are considered the most suitable within the nucleobases due to their greater number of coordination atoms since they have two aromatic rings. Between the purine nucleobases, the adenine is the most used because of its solubility and coordination capability.^[31] In contrast, the low solubility and inappropriate geometric arrangement of the hydrogen bond donor atoms of guanine limits greatly its use as ligand.

Adenine or 6-aminopurine has five nitrogen atoms (four endocyclic and the exocyclic nitrogen N6) in the following order of basicity: $N9 > N1 > N7 > N3 > N6$,^[32] which gives it great versatility as ligand. In fact, sixteen different coordination modes have been found where adenine coordinates to one or more metal centres (Figure 1.14).

²⁸ (a) Hadjiliadis, N; Sletten, E. *Metal Complex-DNA Interactions*; John Wiley & Sons: Chichester, **2009**. (b) Lippert, B. *Coord. Chem. Rev.* **2000**, *200-202*, 487.

²⁹ Verma, S.; Mishra, A. K.; Kumar, J. *Acc. Chem. Res.* **2010**, *43*, 79–91.

³⁰ García-Teran, J. P.; Castillo, O.; Luque, A.; García-Couceiro, U.; Roman, P.; Lezama, L. *Inorg. Chem.* **2004**, *43*, 4549.

³¹ (a) Amo-Ochoa, P.; Zamora, F., *Chem. Soc. Rev.*, **2005**, *34*, 9–21. (b) Verma, S.; Mishra, A.K.; Kumar, J., *Acc. Chem. Res.*, **2009**, *43*, 79–91.

³² de Meester, P.; Skapski, A. C. *J. Chem. Soc., Dalton Trans.* **1973**, 424.

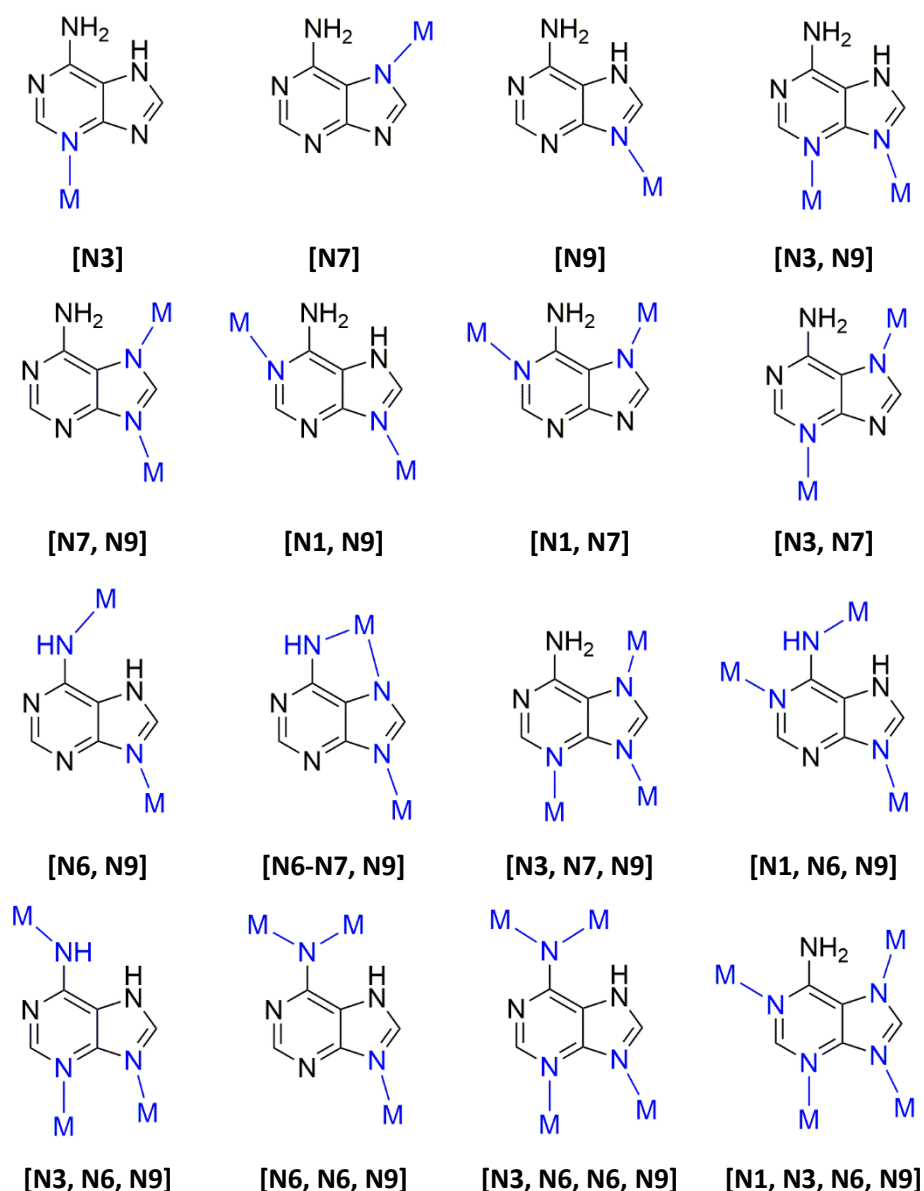


Figure 1.14. Coordination modes of the adenine ligand.

As observed in the previous figure, the adenine can act as a simple monodentate ligand through the N3, N7 and N9 sites.^[33] It can also act as a bidentate ligand with a great variety of combinations such as [N3, N9], [N7, N9], [N1, N9], [N1, N7], [N3, N7] and [N6, N9].^[34] Moreover, as a tridentate ligand [N1, N6, N9], [N3, N6, N9], [N6, N6, N9], [N3, N7, N9] and [N6-N7, N9] can appear with a wide variety of coordination modes being the exocyclic amine capable of coordinating up to two different metal centres.^[35] Finally, even though is not very

³³ (a) Pérez-Yañez, S.; Castillo, O.; Cepeda, J.; García-Terán, J.P.; Luque, A.; Román, P. *Inorg. Chem. Acta*, **2011**, *365*, 211–219. (c) García-Terán, J.P.; Castillo, O.; Luque, A.; García-Couceiro, U.; Beobide, G.; Román, P. *Dalton Transactions*, **2006**, 902–911.

³⁴ (a) Stylianou, K.C.; Warren, J.E.; Chong, S.Y.; Rabone, J.; Basca, J.; Bradshaw, D.; Rosseinsky, M.J. *Chem. Comm.*, **2011**, *47*, 3389–3391. (b) Wang, F.; Tan, Y.-X.; Yang, H.; Zhang, H.-X.; Kang, Y.; Zhang, J., *Chem. Comm.*, **2011**, *47*, 5828–5830. (c) Paul, A.K.; Sanyal, U.; Natarajan, S., *Crystal Growth & Desing*, **2010**, *10*, 4161–4175. An, J.; Geib, S.J.; Rosi, N.L. *J. Am. Chem. Soc.*, **2010**, *132*, 38–39.

³⁵ (a) Li, T.; Chen, D.-L.; Sullivan, J.E.; Kozłowski, M.T.; Johnson, J.K.; Rosi, N.L. *Chemical Science*, **2013**, *4*, 1746–1755. (b) Pérez-Yañez, S.; Beobide, G.; Castillo, O.; Cepeda, J.; García-Terán, J.P.; Luque, A.; Aguayo, A.T.; A.; Román, P. *Inorg. Chem.*, **2011**, *50*,

usual, it can also coordinate with four metal centres.^[36] Note that although there are a lot of examples of compounds containing adenine as ligand, herein we have just included some referential works. Of all these coordination modes, the [N3,N9] is the most interesting one, because of its close resemblance to the coordination mode of a carboxylate group, replacing the two oxygen atoms with the nucleobase nitrogens.

All these features, make adenine one of the more valuable ligand in the design and construction of SMOFs.^[37] In fact, most of the reported SMOFs are built with this ligand. An example is provided by the recurrent paddle-wheel shaped dinuclear complex. This ligand in combination with several transition metal ions, under suitable synthesis conditions, can provide porous supramolecular compounds (Figure 1.15).

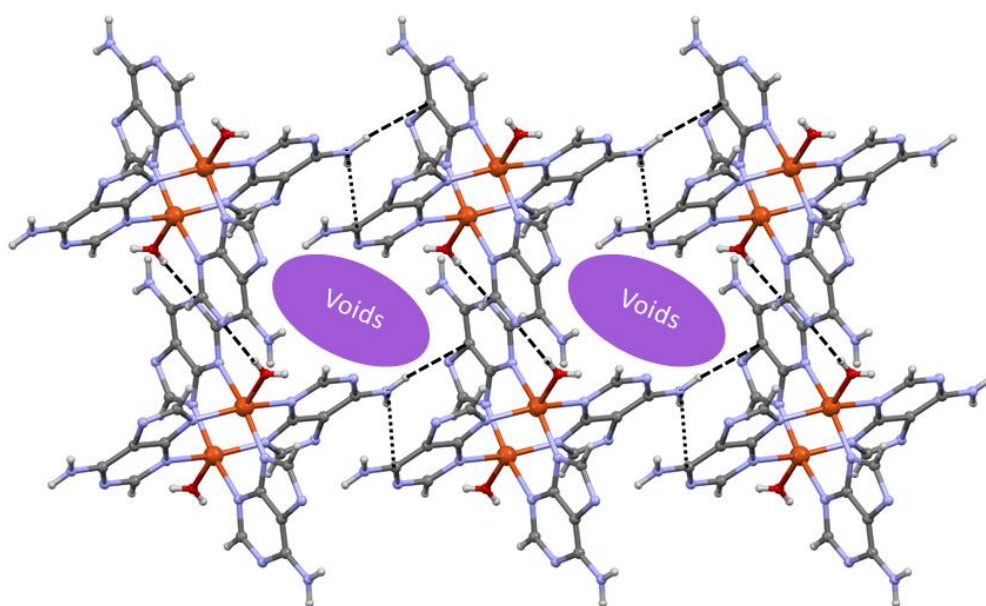


Figure 1.15. View of the crystal packing of the $[\text{Cu}_2(\text{C}_5\text{H}_4\text{N}_5)_4(\text{H}_2\text{O})_2] \cdot 4\text{H}_2\text{O}$ paddle-wheel structure showing the supramolecular interactions.^[38]

Another example that fulfils the requirements to be SMOF is a Zn(II) based compound $[\text{Zn}_6(\mu\text{-ade-}\kappa\text{N7}:\kappa\text{N9})_6(\text{pyridine})_6(\text{dimethylcarbamate})_6] \cdot 10.5\text{DMF}$, which is composed by zinc-adeninate hexanuclear entities capable of forming rigid entities, allowing to meet the first requirement. The supramolecular scheme of this compound occurs through the Watson-Crick faces of the adeninatos, where hydrogen bonding interactions allow to connect each hexamer ring to the neighbouring ones in order to form a three-dimensional supramolecular network

5330–5332. (c) Pérez-Yañez, S.; Beobide, G.; Castillo, O.; Cepeda, J.; Luque, A.; Román, P. *Crystal Growth & Desing.*, **2012**, *12*, 3324–3334.

³⁶ (a) Yang, E.-C.; Zhao, H.-K. Feng, Y.; Zhao, X.J. *Inorg. Chem.*, **2009**, *48*, 3511–3513. (b) An, J.; Farha, O.K.; Hupp, J.T.; Pohl, E.; Yeh, J.I.; Rosi, N.L., *Nat. Comm.*, **2012**, *3*, 604.

³⁷ Beobide, G.; Castillo, O.; Luque, A.; Pérez-Yañez, *Cryst. Eng. Comm.* **2015**, *17*, 3051-3059.

³⁸ Gonzalez-Perez, J.M.; Alarcon-Payer, C.; Castineiras, A.; Pivetta, T.; Lezama, L.; Choquesillo-Lazarte, D.; Crisponi, G.; Niclos-Gutierrez, J. *Inorg. Chem.*, **2006**, *45*, 877.

(Figure 1.16). The channels in this network are obtained through the voids generated by each individual hexameric unit, which are ordered in the same dimension. However, their entry is obstructed by the presence of the pyridine molecule so it is necessary to partially remove it in order to use the compound for gas adsorption. In this way, this compound will be able to adsorb gaseous molecules although with fairly low results. In the case of N_2 the adsorption is negligible while in the case of H_2 and CO_2 the results obtained are 1% of mass and 3.5 mmol/g respectively.^[39]

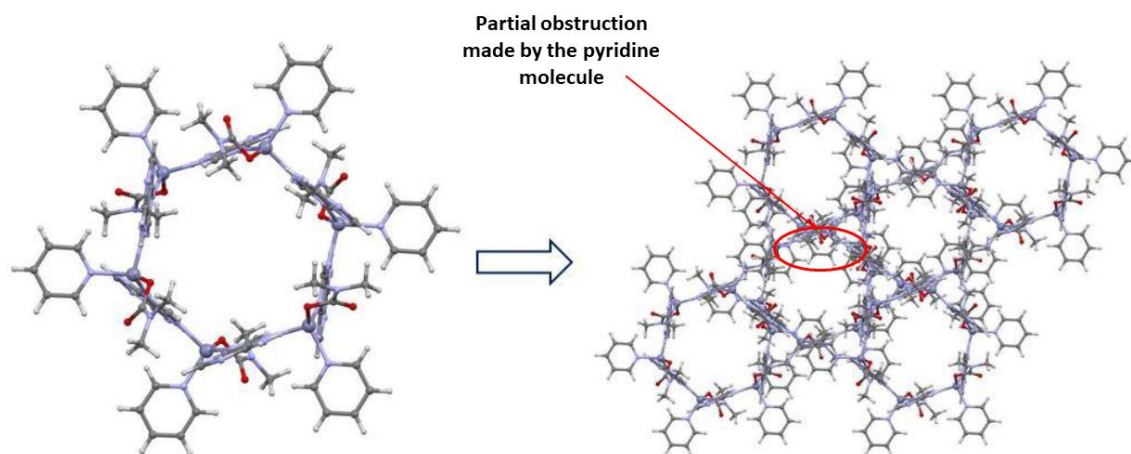


Figure 1.16. Hexanuclear ring and 3D supramolecular network of $[Zn_6(\mu\text{-ade-}\kappa N7:\kappa N9)_6(\text{pyridine})_6(\text{dimethylcarbamate})_6]\cdot 10.5\text{DMF}$ entity.^[39]

Following the line of SMOFs with permanent porosity (i.e. capable of adsorbing gases), we can stand out the family of compounds based on $[Cu_2(\mu\text{-Hade-}\kappa N3:\kappa N9)_4Cl_2]^{2+}$ building unit. In these compounds, the nucleobases are tightly anchored to the metal centres by two donor positions at the same time (N3 and N9 sites), imposing a rigid building unit. The metal coordination geometry imposes a rigid geometrical restraint among the nucleobases providing a set of non-coplanar synthons that otherwise would be difficult to achieve. As many hydrogen donor/acceptor positions of the nucleobase remain free, these discrete entities are able to self-assemble among them by means of complementary double hydrogen bonds (rigid synthons) prompting the growth of extended supramolecular solids in which great channels are present. In these compounds, the presence of the anion (Cl^- or Br^-) causes a non-coplanar orientation of the dimeric entities to allow obtaining three-dimensional supramolecular structures (Figure 1.17). However, the use of neutral adenines implies the presence of chloride/bromide counterions to balance the charge, reducing the accessible volume in the crystal structure. However, this apparent disadvantage in reducing the accessible volume allows this compound to be highlighted as a material that selectively adsorbs gases, that is, it

³⁹ An, J.; Fiorella, R.P.; Geib, S.J.; Rosi, N.L., *JACS*. **2009**, *131*, 8401–8403.

allows the passage of CO₂ molecules while preventing the entry of others such as N₂, H₂ or CH₄ causing a great interest as a selective adsorption material.^[40]

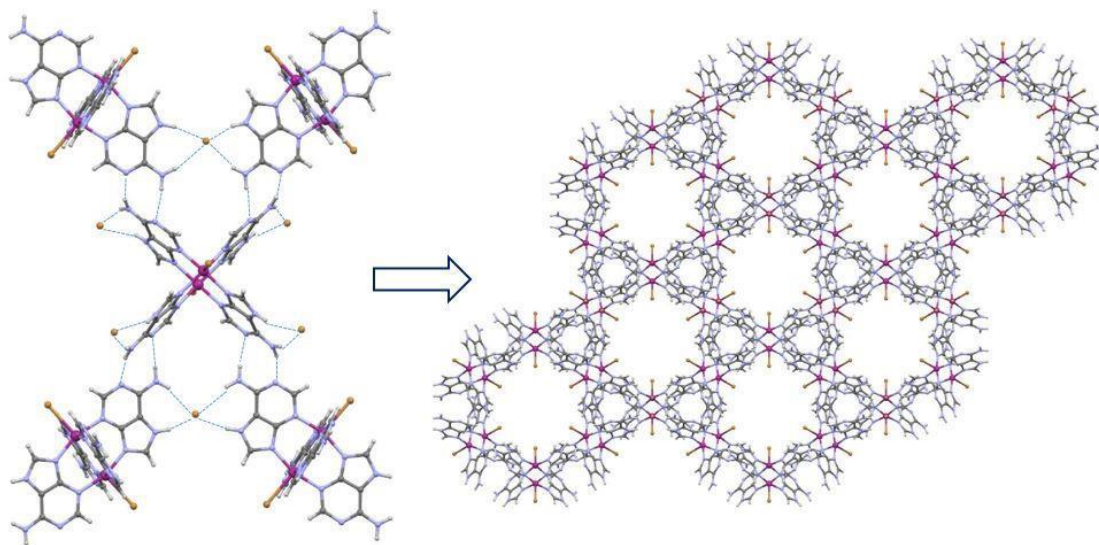


Figure 1.17. Supramolecular 3D structure made by $[\text{Cu}_2(\mu\text{-Hade-}\kappa\text{N3:}\kappa\text{N9})_4\text{Cl}_2]^{2+}$ entities.^[40]

In both cases, the requirements necessary to form the desired porous SMOF compounds have been met. In the following case, examples of supramolecular compounds will be given that do not meet all the requirements and, therefore, do not allow obtaining porous structures.

The first case belongs to the $[\text{Co}_3(\mu\text{-Hade})_2(\mu\text{-Cl})_4\text{Cl}_2(\text{H}_2\text{O})_4]\cdot 2\text{H}_2\text{O}$ compound where the linkage of the metal centres occurs through the bridges generated from four chloride ions and two adenines. Although the coordination mode through the N3 and N9 atoms of adenine guarantees that the Watson-Crick face of adenines are free, in such a way that they can form a hydrogen bonding scheme analogously to the previous compounds, the water molecules interact with the N1 atom of the purine base. As a consequence, a one-dimensional chain is formed through the chloride ions and the water molecules instead of a three-dimensional structure (Figure 1.18). As the water molecules present in the compound (due to its participation as a solvent in the synthesis) have prevented the formation of the desired three-dimensional structure, it would be expected that a synthesis in the absence of solvent could provide the desired structure.

⁴⁰ Thomas-Gipson, J.; Beobide, G.; Castillo, O.; Fröba, M.; Hoffmann, F.; Luque, A.; Pérez-Yáñez, S.; Román, P., *Cryst. Growth Des.* **2014**, *14*, 4019-4029.

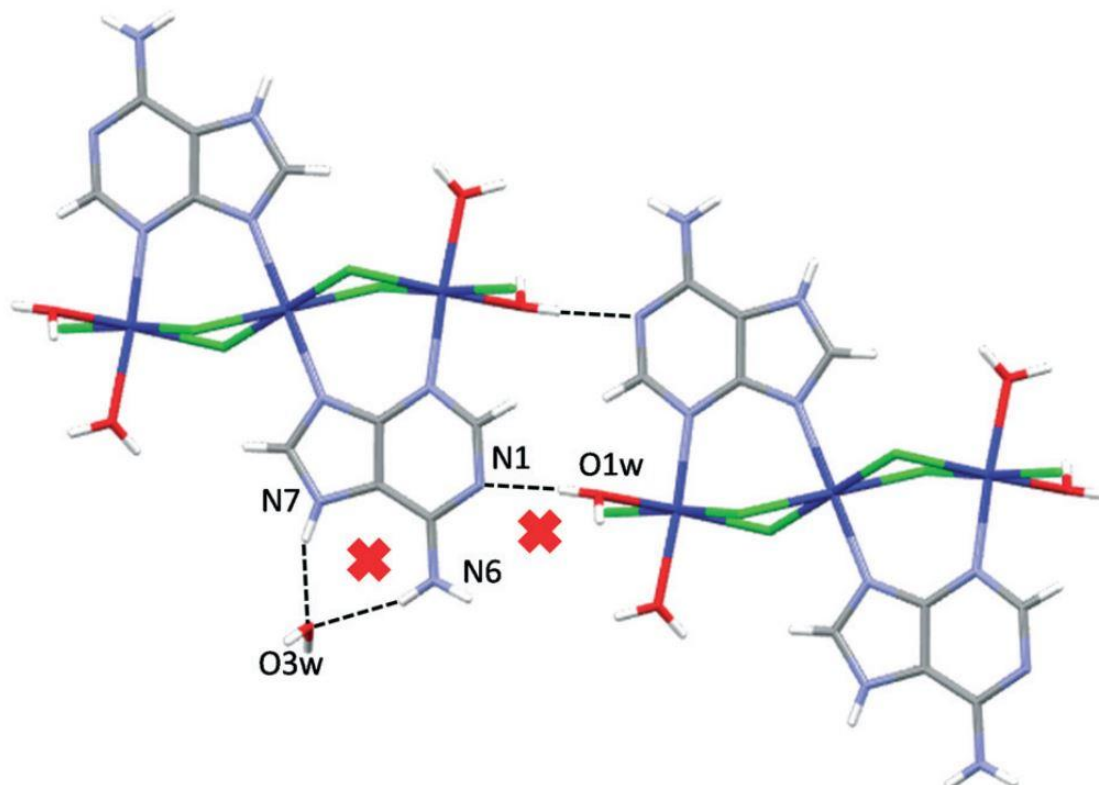


Figure 1.18. Hindrance in the formation of supramolecular bond between adenines due to the presence of water molecules.^[41]

The last example is given by the compound $[\text{Co}_3(6\text{-Clpur})_2(\text{H}_2\text{O})_4]\cdot 4\text{H}_2\text{O}$. In this case the Co(II) metal centres are linked through the N9 positions of two 6-chloropurine and four water molecules. As a result, a rigid structure is obtained due to the intramolecular hydrogen bonding scheme that occur between the N3 atom of 6-chloropurine and the adjacent water molecules (Figure 1.19). Due to the deprotonation of 6-chloropurine, interactions between neighbouring 6-chloropurine molecules only happen through π - π stacking. For all this, the compound does not present any porosity.

⁴¹ Thomas-Gipson, J.; Beobide, G.; Castillo, O.; Luque, A.; Pascual-Colino, J.; Pérez-Yáñez, S.; Román, P., *CrystEngComm* **2018**, *20*, 2528-2539.

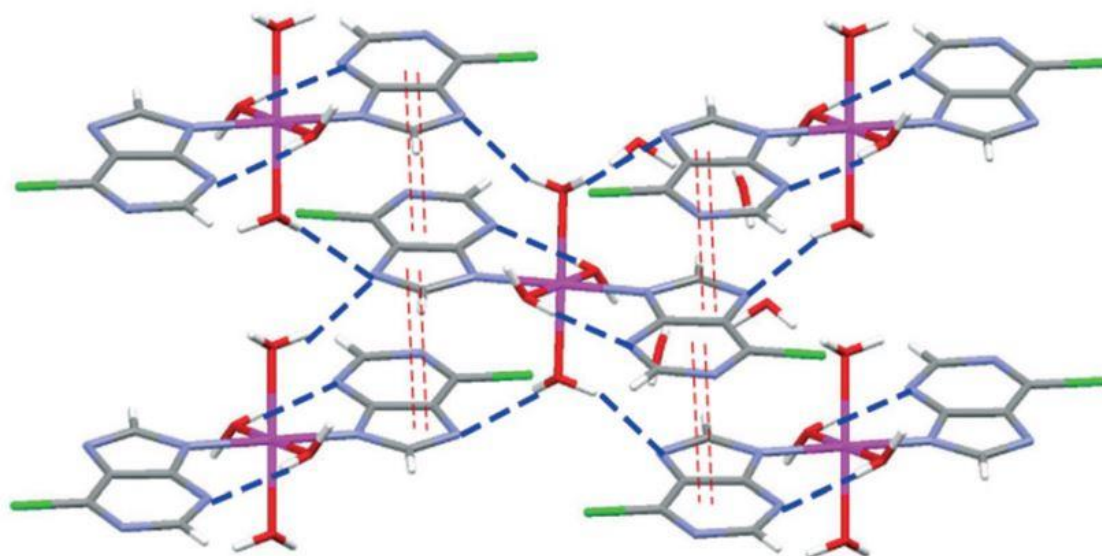


Figure 1.19. Hydrogen bonding (blue dot lines) and π - π stacking (red dot lines) interactions between entities.^[41]

1.4. SYNTHETIC METHODS

Another point to consider is the synthesis conditions, since they can influence significantly in the final product obtained. The choice of solvents, mixtures or even the absence of them, as well as the control of the pH, the temperature, humidity and pressure are factors to consider. The selection and variation of these factors is of special interest allowing to obtain different crystalline structures generated from the same building blocks. Next, the most commonly used synthesis methods to obtain new metal-organic compounds are briefly detailed.^[42]

- **Solvent evaporation method.** In order to successfully obtain crystals of new compounds, previously, certain requirements must be met. Firstly, the concentration of the obtained product must be high enough to reach saturation. Likewise, special care must be taken in the cooling process, due to the possible crystallization of sub-products, obtained in the synthetic process. In fact, the constants of solubility for each product play a fundamental role, since the continuous evaporation of the solvent can cause by-products that were dissolved to crystallize, reaching saturation values (Figure 1.20).

⁴² Hermann, W.A. Synthetic Methods of Organometallic and Inorganic Chemistry, Georg Thieme Verlag Stuttgart, New York 1977.

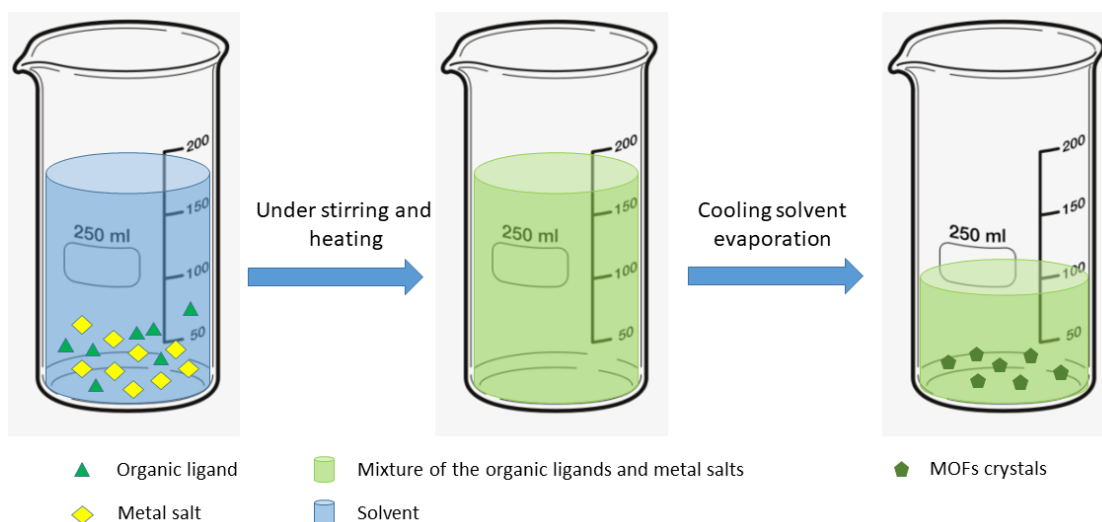


Figure 1.20. Schematic representation of the synthetic method.

- Diffusion method.** This method is based on the slow interaction of the species in solution due to a physical barrier and can be divided into two depending on the barrier that separates the species. In the first one, the barrier is a solvent liquid layer that separates the metal salt in a solvent and another containing the organic linker. They must have different densities, being the solvent layer the one that must be in the middle of the other two. In this way, the organic ligand containing solvent slowly diffuses into the separate layer and crystal growth occurs at the interface (Figure 1.21a). The second one, involves a physical barrier that slows the diffusion of reactants (Figure 1.21b). The diffusion method is preferred to obtain single crystals suitable for X-ray diffraction analysis instead of powder products, especially if the products are poorly soluble.

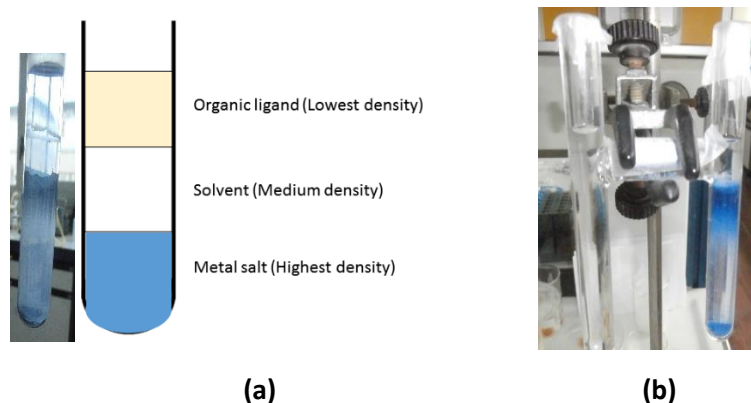


Figure 1.21. Schematic representation of two diffusion methods.

- Hydro(solvo)thermal method.** This method exploits the self-assembly of products from soluble precursors.^[43] It was originally used for the synthesis of zeolites, but it has been adapted to the synthesis of MOFs. In contrast with the previous synthetic methods, the temperature range is significantly higher, with values that oscillate between 80–260 °C. The entropic effect of high temperatures favours a greater connectivity between the metal centres, giving access to new 3D MOFs structures. In these conditions, the properties of the solvent vary (reduction of the viscosity, modification of its dissociation constant, ...) increasing the solubility of the reagents, which allows the use of a large number of both organic and inorganic precursors. The reagents, that previously are homogenized, are added inside a closed reactor (autoclave) under autogenous pressure (Figure 1.22). The type of product that can be obtained is mainly influenced by onset temperature and the rate of cooling speed at the end of the reaction.

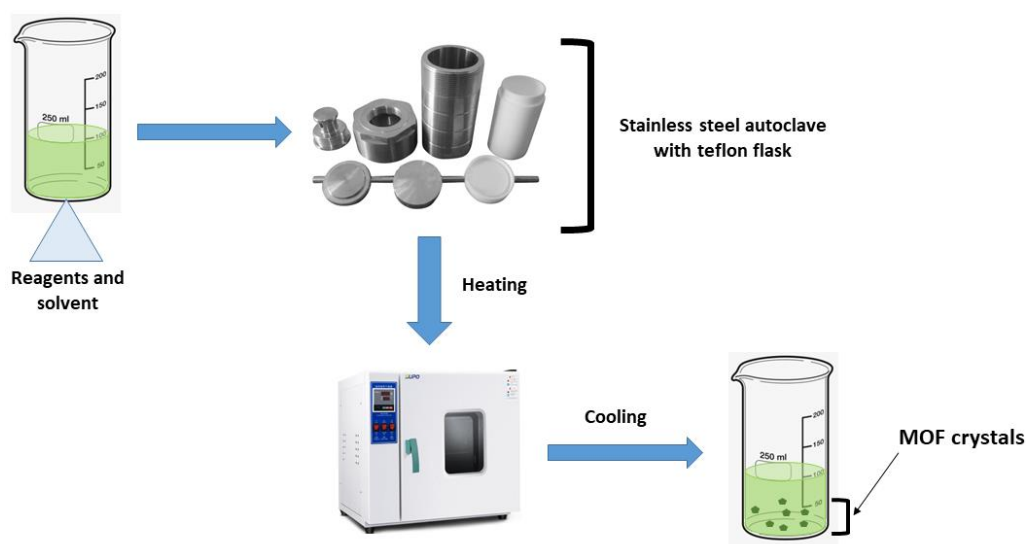


Figure 1.22. Representation of the synthetic route in a solvothermal procedure.

- Microwave reaction and ultrasonic methods.** These are not often used, for the preparation of single-crystals of MOFs, but are an invaluable technique to perform high-speed synthesis. It is also a good method to control the size and the shape of the resulting particles. In contrast to solvothermal synthesis, where heating the reactor with the mixture of reagents occurs by convection and conduction from the outside of the reactor to its interior, in microwave synthesis it is due to the interaction of the

⁴³ (a) Tian, Y.-Q.; Zhao, Y.-M.; Chen, Z.-X.; Zhang, G.-N.; Weng, L.-H.; Zhao, D.-Y. *Chem. Eur. J.*, **2007**, *13*, 4146. (b) Meek, S. T.; Greathouse, J. A.; Allendorf, M. D. *Adv. Mat.*, **2011**, *23*, 249. (c) Schlesinger, M.; Schulze, S.; Hietschold, M.; Mehring, M. *Micropor. Mesopor. Mater.*, **2010**, *132*, 121. (d) Zubietta, J.: *Comprehensive Coordination Chemistry II*, Elsevier Ltd, **2004**, *1*, 697.

electric field of microwave radiation with the dipole moment of the molecules in the reaction medium, producing a heating from the inside to the outside (Figure 1.23).^[44]

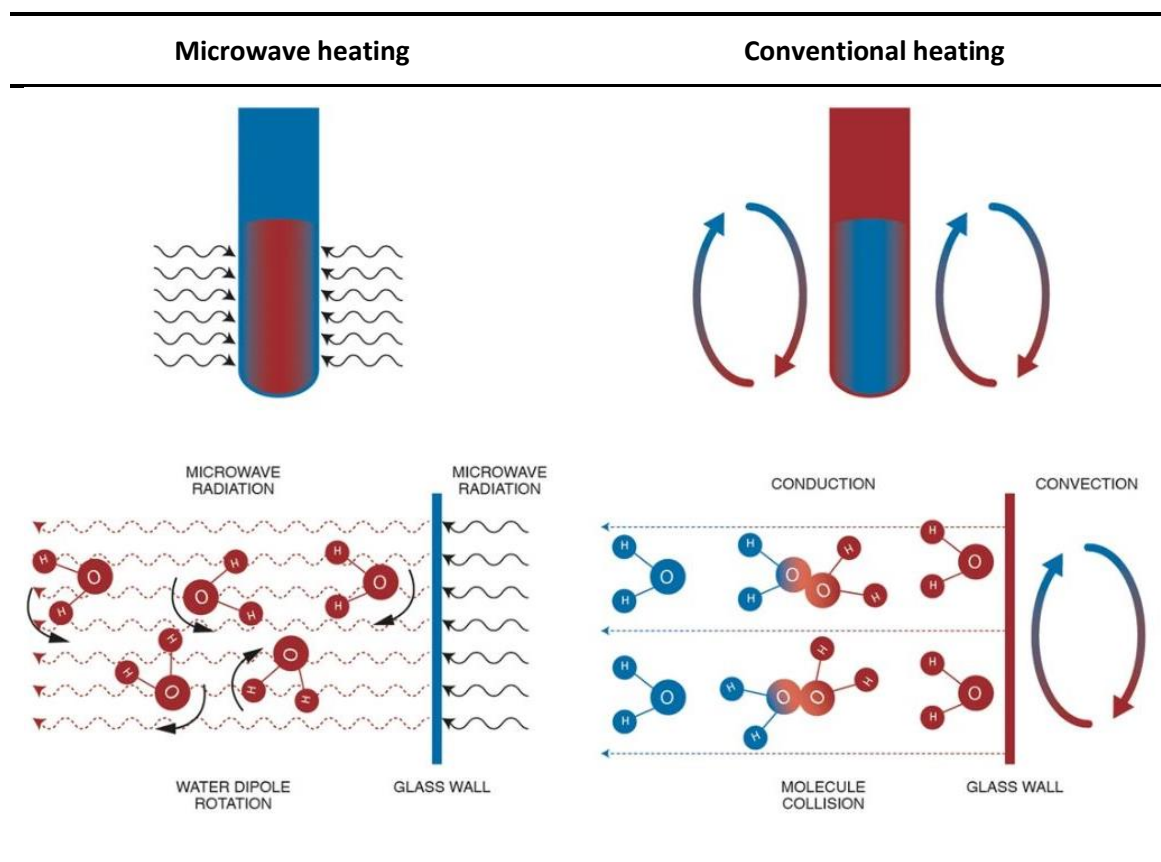


Figure 1.23. Differences between heating using a microwave and a conventional oven.^[45]

1.5. APPLICATIONS OF POROUS METAL-ORGANIC MATERIALS

Synthesis conditions in porous compounds significantly influence the applicative properties of the products obtained. Although the type of ligand, the metal and the coordination mode are very important variables to consider, the porous nature is the cornerstone in order to model its properties. In fact, their high and permanent porosity levels are one of the most important characteristics of metal-organic networks, being also noteworthy for their low density and high surface value.^[46] Next, some of the most widely-known applications of this type of compounds are going to be detailed.^[47]

In addition, the progress that has involved the use of these easily tunable materials for industrial purposes has led to the development of new chemical methodologies to

⁴⁴ (a) Amo-Ochoa, P.; Givaja, G.; Sanz Miguel, P. J.; Castillo, O.; Zamora, F. *Inorg. Chem. Comm.*, **2007**, *10*, 921–924. (b) Thi Dang, Y.; Trung Hoang, H.; Cao Dong, H.; Thi Bui, K.-B.; Ho Thuy Nguyen, L.; Bach Phan, T.; Kawazoe, Y.; Le Hoang Doan, T. *Micr. Meso. Mat.*, **2020**, *298*, 110064. (c) Wu, X.; Bao, Z.; Yuan, B.; Wang, J.; Sun, Y.; Luo, H.; Deng, S. *Micr. Meso. Mat.*, **2013**, *180*, 114–122.

⁴⁵ Sweygens, N.; Alewaters, N.; Dewil, R.; Appels, L., *Scientific Reports*, **2018**, *8*, 7719.

⁴⁶ Furukawa, H.; Ko, N.; Go, Y.B.; Aratani, N.; Choi, S.B.; Choi, F.; Yazaydin, A.; Snurr, R.Q.; O’Keeffe, M.; Kim, J.; Yaghi, O.M. *Science*, **2010**, *329*, 424–428.

⁴⁷ Phan, A.; Czaja, A. U.; Gándara, F.; Knobler, C. B.; Yaghi, O. M. *Inorganic Chemistry*, **2011**, *50*, 7388–7390

functionalize their internal areas,^[48] to generate new flexible porous materials (also known as breathing),^[49] and to obtain them in shape thin-film^[50] or as nanoparticles.^[51] Additionally, simple synthetic methods have been developed to scale the production of these compounds to industrial quantities, helping their applications to be extended.^[52] Table 1.1 shows referential examples of MOFs and their applications.

1.5.1. Sorption and storage

It has been decided to combine the sorption and storage properties because they are usually overlapping processes that take place in many MOFs. The term of sorption is given when the porous compound is able to occlude within its channels, in a satisfactory manner, several molecules. At this point, this sorption process can be divided into two depending on the state of aggregation of the compound that are being added. It is called absorption when the compounds are in liquid phase, usually solvents, and adsorption when gas-phase molecules are trapped in the pores. Molecules in gas phase tend to be in greater demand, because they are released as a by-product in many industrial chemical reactions (CO₂, SO₂, NO_x...) as well as in the use of cleaner fuels (H₂, CH₄), encouraging green chemistry and reducing pollution (Figure 1.24).^[53]

The chemical storage systems have either low storage capacity or need high temperature to release the adsorbed gas molecule. In physical adsorption, molecules are adsorbed inside the micropores of porous materials. The basic advantage of physical adsorption is its reversibility and fast kinetics of sorption compared to chemical adsorption, but it has also disadvantages as the very low adsorption enthalpy, resulting in high storage capacity only at very low temperatures. In fact, MOFs have shown quite high storage capacity for hydrogen through physical adsorption.^[54]

⁴⁸ Wang, Z.; Cohen, S. M. *Chem. Soc. Rev.* **2009**, *38*, 1315.

⁴⁹ Férey, G.; Serre, C. *Chem. Soc. Rev.* **2009**, *38*, 1380.

⁵⁰ Zacher, D.; Shekhah, O.; Wöll, C.; Fischer, R. A. *Chem. Soc. Rev.* **2009**, *38*, 1418.

⁵¹ Spokoyny, A. M.; Kim, D.; Sumrein, A.; Mirkin, C. A. *Chem. Soc. Rev.* **2009**, *38*, 1218–1227.

⁵² Czaja, A. U.; Trukhan, N.; Müller, U., *Chem. Soc. Rev.* **2009**, *38*, 1284.

⁵³ (a) Panella, B.; Hirscher, M.; Pütter, H.; Müller, U. *Adv. Funct. Mater.* **2006**, *16*, 520–524. (b) Saha, D.; Wei, Z.; Deng, S.; *Int. J. Hydr. En.* **2008**, *33*, 7479–7488. (c) Chowdhury, P.; Mekala, S.; Dreisbach, F.; Gumma, S. *Micr. and Mes. Mat.* **2012**, *152*, 246–252. (d) Bao, Z.; Alnemrat, S.; Yu, L.; Vasiliev, I.; Ren, Q.; Lu, X.; Deng, S. *J. Col. Int. Sci.*, **2011**, *357*, 504–509. (e) Moellera, J.; Moellera, A.; Dreisbach, F.; Glaeser, R.; Staudt, R. *Micr. and Mes. Mat.* **2011**, *138*, 140–148.

⁵⁴ Kaneko, K.; Rodríguez-Reinoso, F. *Nanoporous Materials for Gas Storage*, Singapore : Springer, **2019**.

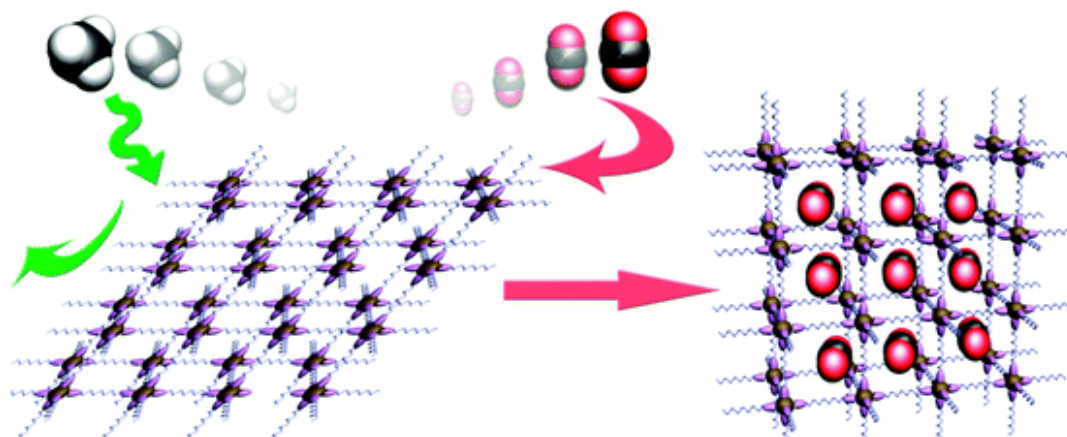


Figure 1.24. Schematic illustration of selective gas adsorption in a flexible MOF.^[55]

1.5.2. Drug delivery and medical applications

A great challenge in the medical field was finding a non-toxic material that allows a proper storage and subsequent release of drugs. Because of their ability to adjust and functionalize pore size, MOFs have been shown to be useful in the field of biomedicine (Figure 1.25). The large surface area and pore sizes of these materials guide the therapeutic pathway of many drugs,^[56] becoming particularly applicable as a protection and supply in molecular therapies, biocatalysis, virus and cell manipulation and biopharmaceuticals. Not all the MOFs fulfil the prerequisites to be a drug deliver: the particle size of their porous must be nanometric, and it cannot be toxic.^[57] Good examples are mesoporous MIL-100 and MIL-101 MOFs from Horcajada et al., storing and releasing many drugs such as ibuprofen.^[58]

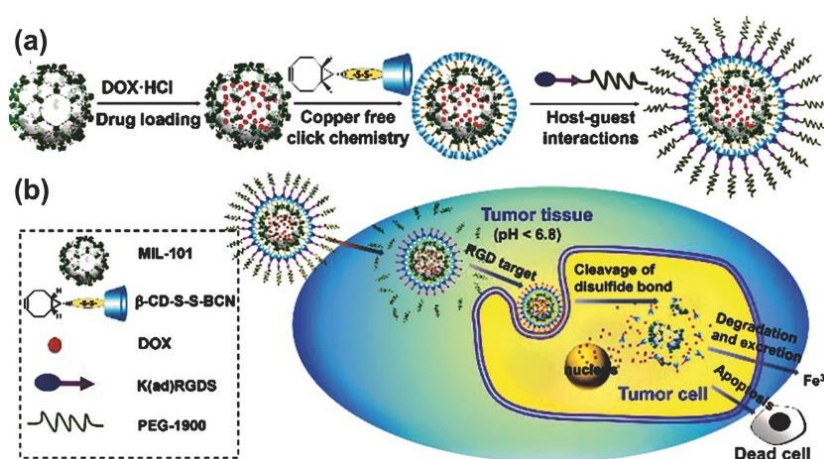


Figure 1.25. Drug delivery scheme of MIL-101.^[59]

⁵⁵ Li, J.-R.; Kuppler, R. J.; Zhou, H.-C. *Chem. Soc. Rev.*, **2009**, *38*, 1477–1504.

⁵⁶ Jiao, L.; Joanne, S.; Skinner, W.; Wang, Z.; Jiang, H.-L. *Materials Today*, **2019**, *27*, 43–68.

⁵⁷ Lanchas, M. (2015). "Métodos no convencionales para la preparación de polímeros de coordinación porosos. Una aproximación económica, medioambientalmente amigable y escalable", D. Tesis, UPV-EHU, Leioa (España).

⁵⁸ Horcajada, P.; Serre, C.; Vallet-Reg, M.; Sebban, M.; Taulelle, F.; Frey, G. *Angew. Chem. Int. Ed.* **2006**, *45*, 5974–5978.

⁵⁹ Wang, X.G.; Dong, Z.Y.; Cheng, H.; Wan, S.S.; Chen, W.H.; Zou, M.Z.; Huo, J.W.; Deng, H.X.; Zhang, X.Z. *Nanoscale*, **2015**, *7*, 16061.

1.5.3. Catalytic activity

MOFs have been widely used as a catalyst, to carry out both organic and inorganic reactions. In fact, this activity was one of the first proposed applications for metal-organic networks, and also has been demonstrated with a plethora of examples.^[60] The pore sizes of MOFs are suitable for acting as hosts for small molecules and for chemical reactions. In addition, due to their orderly and well-defined pore structure, they can be used for encapsulating metal nanoparticles or binding catalyst molecules.^[61]

One of the most typical catalytic activity in these porous materials was the solid base heterogeneous catalysts^[62], which has attracted a great deal of attention for the advantages that they can accomplish in comparison with the homogeneous analogues. Firstly, solid bases are less corrosive. Moreover, it is much easier the separation between the catalysts and the products, allowing to be reused.^[63] As a result, these solid bases are economically and ecologically helpful dealing a strong impact in green chemistry. Its importance has been effectively demonstrated in Knoevenagel^[64], aldol condensation^[65], Michael addition^[66] and esterification reactions^[67], among others.

⁶⁰ Valtchev, V.; Mintova, S.; Tsapatsis, M. *Ordered Porous Solids, Recent Advances and Prospects*, Elsevier Science, **2009**.

⁶¹ Saha, D.; Sen, R.; Maity, T.; Koner, S. *Langmuir*, **2013**, *29*, 3140–3151.

⁶² (a) Niebing, S.; Janiak, C. *Molecular Catalysis*, **2019**, *467*, 70–77. (b) Zhao, S.-N.; Song, X.-Z.; Song, S.-Y.; Zhang, H.-j. *Coord. Chem. Rev.* **2017**, *337*, 80–96. (c) Ren, Y.-w.; Liang, J.-x.; Lu, J.-x.; Cai, B.-w.; Shi, D.-b.; Qi, C.-r. Jiang, H.-f.; Chen, J.; Zheng, D. *Eur. J. Inorg. Chem.* **2011**, *28*, 4369–4376.

⁶³ (a) Valvekens, P.; Vermoortele, F.; Vos, D. D. *Catal. Sci. Technol.* **2013**, *3*, 1435–1445. (b) Larrea, E. S.; Fernández de Luis, R.; Orive, J.; Iglesias, M.; Arriortua, M. I. *Eur. J. Inorg. Chem.* **2015**, *10*, 4699–4707.

⁶⁴ Valvekens, P.; Vandichel, M.; Waroquier, M.; Van Speybroeck, V.; De Vosa, D. *Journal of Catalysis*, **2014**, *317*, 1–10.

⁶⁵ Kikhtyanin, O.; Kubička, D.; Čejka, J. *Catalysis Today*, **2015**, *243*, 158–162.

⁶⁶ Zhu, L.; Liu, X.-Q.; Jiang, H.-L.; Sun, L.-B. *Chem. Rev.* **2017**, *117*, 8129–8176.

⁶⁷ Xu, Z.; Zhao, G.; Ullah, L.; Wang, M.; Wang, A.; Zhang, Y.; Zhang, S. *RSC Adv.*, **2018**, *8*, 10009–10016.

Table 1.1. Some examples of MOFs and their applications.

Application	MOF	Metal	Ligand
Adsorption			
Adsorption of CO ₂ over N ₂ ^[68]	Mn ₃ (HCOO) ₆ ·nDEF	Mn	Formic acid
Ar and CH ₄ sorption ^[69]	[Cu(trans-fum)]	Cu	Fum: Fumaric acid
Reversible H ₂ O sorption/desorption ^[70]	[Ni ₇ (suc) ₆ (OH) ₂ (H ₂ O) ₂ ·2H ₂ O	Ni	Suc: Succinic acid
Highly selective adsorption of CO ₂ ^[71]	CD-MOF-2	Rb	γ-CD
Adsorption ^[72]	CD-MOF-1, CD-MOF-2 and CD-MOF-3	K, Rb and Cs	γ-CD
Storage			
Methane storage ^[73]	MOF-5 Zn ₄ (1,4-bdc) ₃	Zn	Bdc
Adsorption and storage ^[74]	HKUST (Hong Kong University of Science and Technology)-1 Cu ₂ (H ₂ O) ₂ (CO ₂) ₄	Cu	H ₃ btc
Medical applications			
Drug delivery ^[58]	MIL-101 [Cr ₃ O(OH,F,H ₂ O) ₃ (1,4-bdc) ₃ and MIL-100	Cr	1,4-benzenedicarboxylate moieties (bdc) or H ₃ btc
Antibacterial ^[75]	Cu-BTC(MOF-199)	Cu	H ₃ btc
Cation drugs and lanthanide exchange capabilities ^[76]	Zn ₈ (Ade) ₄ (bpdc) ₆ O·2 Me ₂ NH ₂ ·8 DMF·11H ₂ O	Zn	Adenine and bpdc: biphenyldicarboxylate
Therapeutic agent ^[77]	BioMIL-1	Fe	Nicotinic acid (vitamin B3)
Drug storage/release or immobilization and organization of large biomolecules ^[76]	Bio-MOF-100	Zn	Adenine
Catalytic activity			
Heterogeneous asymmetric catalysts for the methanolysis of rac-propylene oxide ^[78]	Ni ₂ (L-Asp) ₂ (4,4'-bipy)·(HCl)1.8(MeOH)	Ni	L-Asp and 4,4'-bipy
	Cu ₂ (L-Asp) ₂ (bpe)·(HCl) ₂ ·(H ₂ O) ₂	Cu	L-Asp and bpe: 1,2-bis(4-pyridyl)ethane

⁶⁸ Dybtsev, DN; Chun, H; Yoon, SH; Kim, D; Kim, K., *J. Am. Chem. Soc.* **2004**, *126*, 32–33.

⁶⁹ Seki, K; Takamizawa, S; Mori, W. *Chem. Lett.* **2001**, *30*, 122–123.

⁷⁰ Forster, PM; Cheetham, AK. *Angew. Chem.*, **2002**, *41*, 457–459.

⁷¹ Gassensmith, JJ.; Furukawa, H.; Smaldone, RA.; Forgan, SS.; Botros, YY.; Yaghi, OM.; Stoddart, JF. *J. Am. Chem. Soc.* **2011**, *133*, 15312–15315.

⁷² Forgan, RS.; Smaldone, RA.; Gassensmith, JJ.; Furukawa, H.; Cordes, DB.; Li, Q.; Wilmer, CE.; Botros, YY.; Snurr, RQ.; Slawin, AMZ.; Stoddart, JF. *J. Am. Chem. Soc.* **2012**, *134*, 406–417.

⁷³ (a) Li, H; Eddaoudi, M; O'Keeffe, M.; Yaghi, O. M. *Nature*, **1999**, *402*, 276–279. (b) Eddaoudi, M; Kim, J; Rosi, N; Vodak, D; Wachter, J; O'Keeffe, M; Yaghi, O. M. *Science*, **2002**, *295*, 469–472.

⁷⁴ Rowsell, JLC.; Yaghi, OM. *J. Am. Chem. Soc.* **2006**, *128*, 1304–1315.

⁷⁵ Rodriguez, HS.; Hinestroza, JP.; Ochoa-Puentes, C.; Sierra, CA.; Soto, CY. *J. Appl. Polym. Sci.* **2014**, *131*, 40815.

⁷⁶ An, J.; Geib, SJ.; Rosi, NL. *J. Am. Chem. Soc.* **2009**, *131*, 8376–8377.

⁷⁷ Miller, SR.; Hertaux, D.; Baati, T.; Horcajada, P.; Greneche, JM.; Serre, C. *Chem. Commun.* **2010**, *46*, 4526–4528.

⁷⁸ Ingleson, MJ.; Barrio, JP.; Bacsa, J.; Dickinson, C.; Park, H.; Rosseinsky, MJ. *Chem. Commun.* **2008**, *11*, 1287–1289.

1.6. OBJECTIVES

Keeping in mind the crystal design principles described in section 1.3.3., the main goal of the current PhD thesis is to develop new supramolecular metal-organic materials, built up from discrete molecular building blocks which are based on ligands suited with functional groups that can lead the self-assembly process by means of the establishment of robust synthons. Implicit in this major goal, the performed research aims to deeply analyse the obtained crystal structures in order to understand how the features of the synthesised molecular building blocks govern the crystal packing and porosity of the obtained compounds.

Furthermore, the performed research work aims also to design molecular building blocks with tunable magnetic behaviour, with the capacity to self-assemble into a multifunctional material that brings together porosity with relevant magnetic properties.

As a last objective, the current research work pursues to explore the application of the developed SMOFs. This is an important point, since although the applications of MOF have been widely explored, the studies performed on SMOF are scarce and circumscribed to gas sorption experiments, trapping of certain chemical species and luminescent properties. Thus, the discovery of novel and promising application for SMOFs, could boost the interest from the scientific community in this kind of materials.

Regarding the units comprising the molecular building blocks, we have selected copper(II) ion as metal centre, due to the plasticity of its coordination sphere, to its intermediate Pearson hardness that makes it suitable for common N and O donor atoms, and straightforward modelling of the magnetic properties of its compounds. Nonetheless, the aimed modulation of the magnetic properties will conduct us to incorporate other transition metals (M) in order to achieve heterometallic Cu/M building blocks (M: Cr(III), Mn(III), Co(II), Ni(II), Zn(II)).

As ligands, we have selected 2-hydroxyquinoline-4-carboxylate and adenine due to their potential capability to yield, upon the coordination to a transition metal ion, molecular building blocks that can fulfil the three criteria required to self-assemble as a SMOF (Figure 1.26).

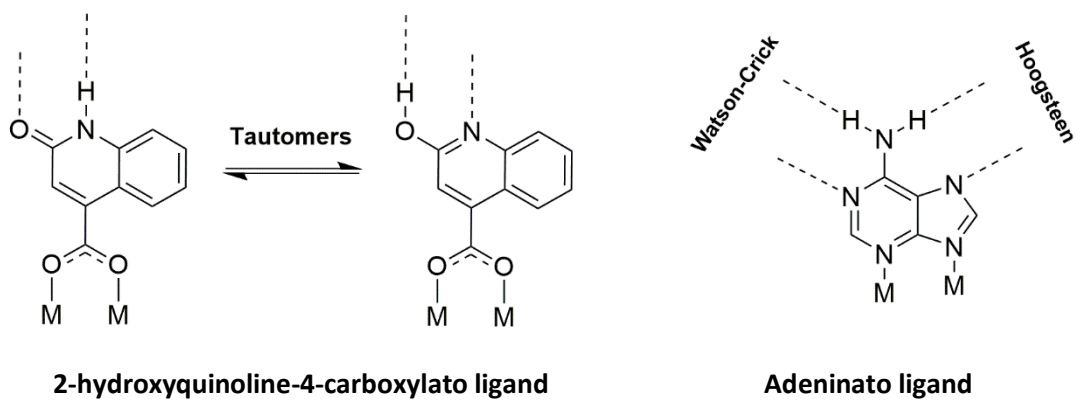


Figure 1.26. Representation of the selected ligands showing a coordination mode that would provide a rigid molecular building block, suited with predictable and rigid synthons.

Chapter 2: 2-Hydroxyquinoline-4-carboxylic acid based SMOFs

2.1. Introduction

2.2. Synthesis and chemical characterization

2.3. Results and discussion

2.1. INTRODUCTION

This chapter assesses the capability of 2-hydroxyquinoline-4-carboxylate (HQ) ligand to generate supramolecular metal-organic frameworks. In this respect, this section rationalises the criteria in which is based the selection of the ligand and summarises some of the most representative published research works that have dealt with metal-HQ complexes.

Neutral or monoanionic HQ ligand presents a tautomeric equilibrium between its quinoline and quinolinone forms (Figure 2.1).^[79] In any case, as it is described below both tautomers are expected to behave analogously in terms of crystal design.

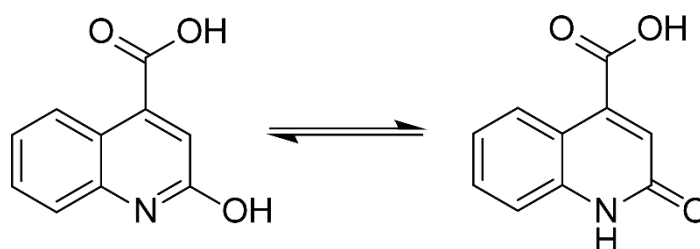


Figure 2.1. The tautomers of the HQ ligand in its neutral form.

As mentioned in the introductory chapter, the assembling of discrete or low dimensionality metal-organic complexes by means of non-covalent interactions (hydrogen bonds and π - π interactions) has demonstrated to be well-suited tool in the crystal engineering of supramolecular metal-organic framework (SMOF). The success of such goal relies on the fulfilment of a series of prerequisites: (a) the use of rigid building blocks, (b) the formation of rigid synthons in a predictable manner between the building blocks and (c) the presence of a minimum set of synthons contained in non-parallel planes that ensures the growth in three dimensions.^[80]

Keeping in mind the aforementioned, 2-hydroxyquinoline-4-carboxylate has been chosen as ligand for its envisaged suitability to yield molecular building blocks that fulfil all the three criteria. Firstly, HQ ligand presents several possible modes of coordination (Figure 2.2), among which B (carboxylate chelation), C (carboxylate *syn-syn* bridging), E and F can provide stiff building blocks, in which the double N-H \cdots O=C synthon (see below) would be potentially enable. However, the most recurrent coordination mode, i.e. A-coordination mode, binds to the metal through a single coordination bond through which the rotation of the HQ ligand

⁷⁹ (a) Bernstein *J. Phys. Chem.* **1987**, *91*, 27, 6610-6614. (b) Tokay, N.; Ögretir, C. *J. Mol. Struct. (Theochem)*. **2002**, *594*, 185-197. (c) Bu, Lintao; E. Himmel, M; R. Nimlos, M. *ACS Symposium Series*, **2010**, *1052*, 99-117.

⁸⁰ Thomas-Gipson, J.; Pérez-Aguirre, R.; Beobide, G.; Castillo, O.; Luque, A.; Pérez-Yáñez, S.; Román, P. *Cryst. Growth Des.* **2015**, *15*, 975-983.

would be permitted and therefore, the resulting building blocks would not fulfil the first criterion.

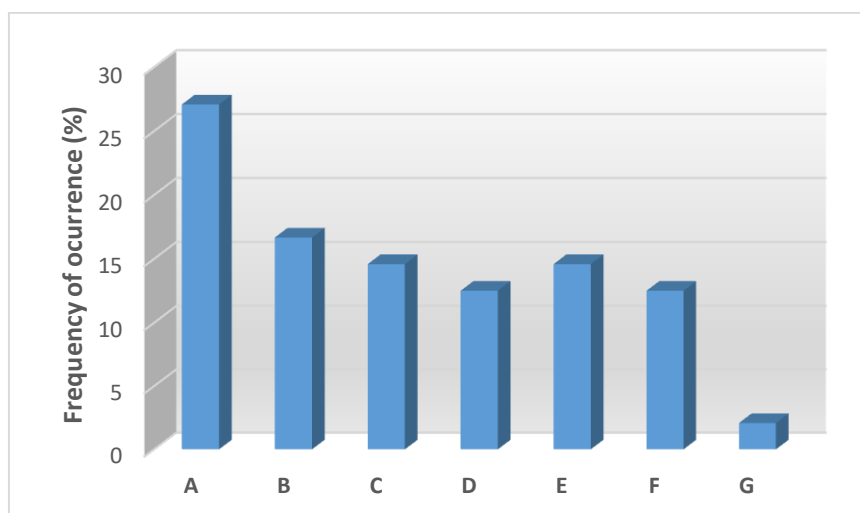
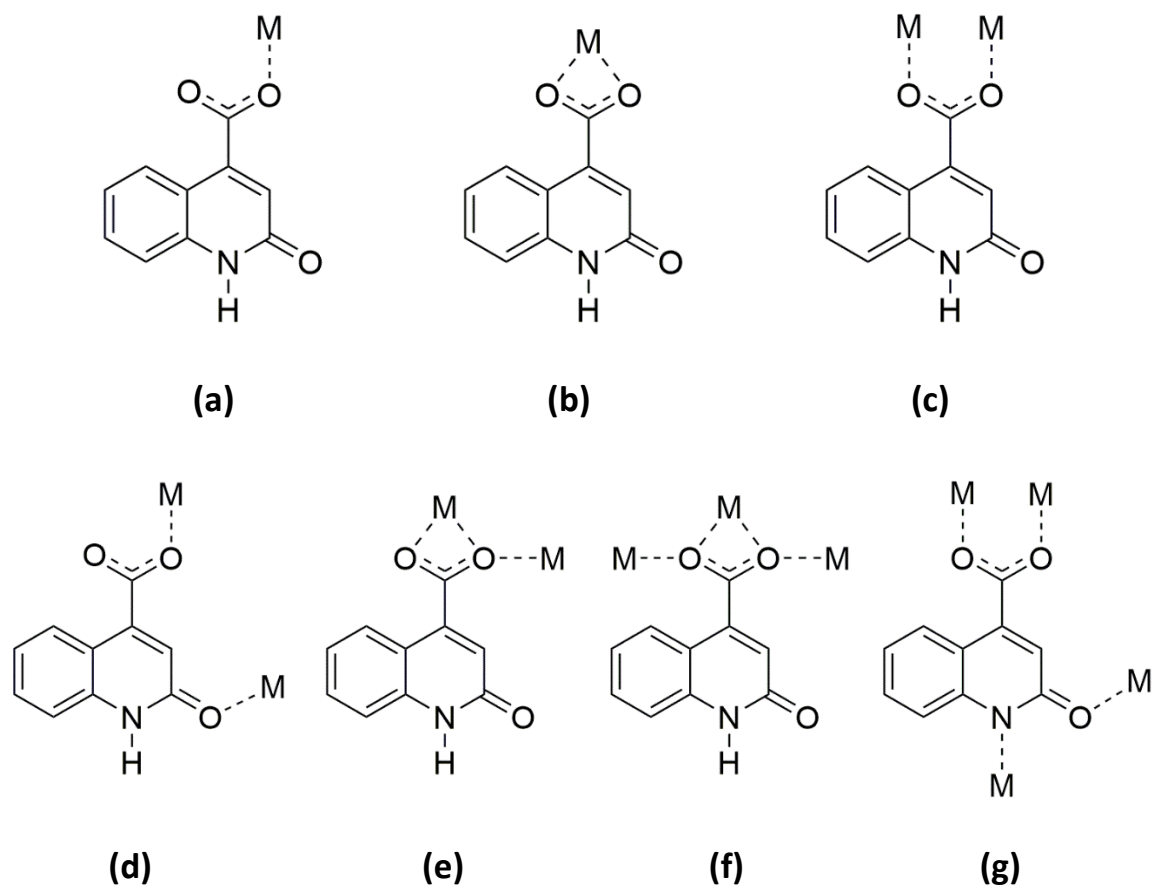


Figure 2.2. Coordination modes of HQ ligand and frequency of occurrence of each coordination mode subtracted from a search in CSD (*Cambridge Structural Databases*).^[81] The search has considered the two tautomeric forms of Figure 2.1.

⁸¹ (a) Cambridge Structural Database (CSD). Version 5.41 (2019). (b) Groom, C. R.; Bruno, I. J.; Lightfoot, M. P.; Ward, S. C. *Acta Cryst.* **2016**, 72, 171-179.

Secondly, the disposition of the endocyclic N-atom and OH group (or alternatively, C=O and N-H ensemble in its quinolinone tautomer) is suitable to guide a self-assembly process by means of complementary hydrogen bonding (i.e. a rigid and predictable synthon) (Figure 2.3).

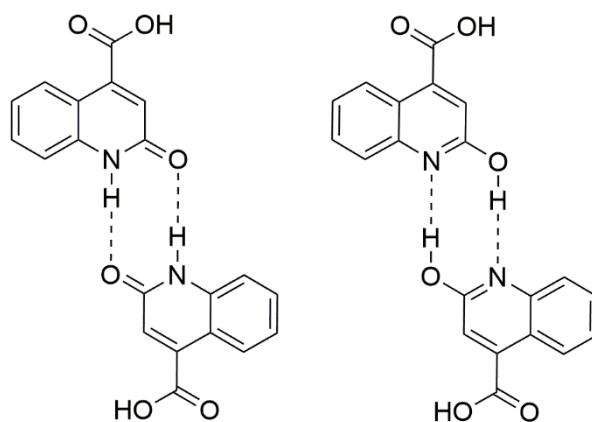


Figure 2.3. Complementary hydrogen bonding scheme between neutral HQ tautomers.

Last but not less, the ionic charge of the carboxylate form (2-hydroxyquinoline-4-carboxylate) implies the coordination of at least two HQ molecules per M(II) centre, which might be helpful to generate a building block capable of establishing synthons that provide non-parallel supramolecular growing vectors. In this sense, note that the use of charge neutral bulky co-ligands can make more favourable to afford non-parallel synthons. Alternatively, the increase of the charge of the metal centre could make also even more favourable the fulfilment of the third criteria, since to afford a charge neutral complex entity; more than two HQ ligands per metal centre would be required. Nonetheless, as the carboxylate *syn-syn* bridging mode is the preferred mode, it seems feasible the formation of paddle-wheel type M(II)-dinuclear complexes,^[82] in such a way, that to balance the charge, each dinuclear complex should incorporate four monoanionic HQ bridges. Consequently, the proposed building block would fulfil simultaneously the above-mentioned three criteria. Figure 2.4 shows the plausible paddle-wheel shaped Cu(II)-dinuclear entities of formula $[\text{Cu}_2(\text{HQ})_4]$ for each HQ tautomer, indicating the sites through which the supramolecular self-assembly process is expected to occur.

⁸² (a) Van Niekerk, J. N.; Schoening, F. R. L. *Acta Crystallogr.* **1953**, *6*, 227. (b) Rap, V. M.; Manohar, H. *Inorg. Chim. Acta* **1979**, *34*, L213. (c) Yamanaka, M.; Uekusa, H.; Ohba, S.; Saito, Y.; Iwata, S.; Kato, M.; Tokii, T.; Muto, Y.; Steward, O. W. *Acta Crystallogr.* **1991**, *B47*, 344. (d) Werner, U.; Christina, S.; Matthias, V.; Marcus, L.; Friedhelm, R.; Jutta, K. Z. *Anorg. Allg. Chem.* **2015**, *641*, 253–260.

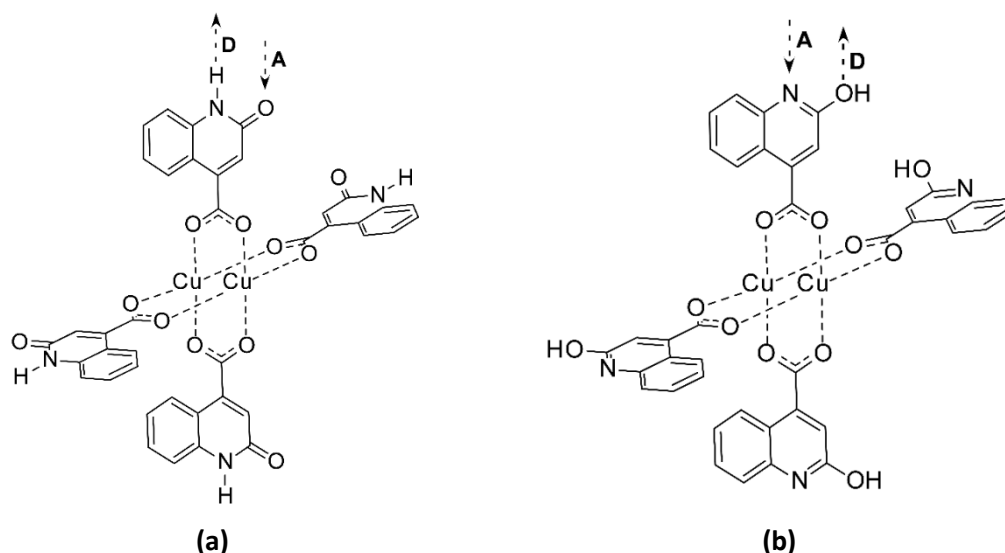


Figure 2.4. Plausible paddle-wheel shaped Cu(II)-dinuclear entities for the two tautomers of HQ ligand (D: hydrogen bond donor site; A: hydrogen bond acceptor site). Note, that the relative position of the HQ ligands is inverted between the neighbouring ones, while it is equivalent between the opposed ones. This kind of configuration is called up-down-up-down (UDUD). Other, possibilities are UUDD and UUUU. The type of configuration of course, will determine the resulting topology of the supramolecular network.

A detailed analysis of the 19 metal-organic crystal structures containing HQ ligand published up date in the CDS,^[82] reveals that ten of them are built of discrete metal/HQ complexes, including mononuclear and dinuclear species (Figure 2.5). The mononuclear Ni(II) entity^[84] does not meet the first criteria, since it allows the rotation along the single metal-HQ coordination bond and as a result, it does not render what we could consider a SMOF. Both reported Ga(III) complexes, $[\text{Ga}_2(\text{HQ})_2(\text{CH}(\text{SiMe}_3)_2)_4] \cdot 2\text{THF}$ and $[\text{Ga}_4(\text{HQ})_4(\text{CH}(\text{SiMe}_3)_2)_4] \cdot 6\text{THF}$, can be regarded as rigid building blocks; the former complex meets the second criteria but not third one, while the second one meets all the three criteria required to afford a SMOF. However, the selected synthesis solvent (H_2O) is a strong hydrogen bonding acceptor and acts as disruptor of the HQ pairing interactions, inhibiting the self-assembly of the complexes. Contrarily, $[\text{M}_2(\text{HQ})_6(\text{H}_2\text{O})_4] \cdot 8\text{H}_2\text{O}$ (M(III): La, Ce, Pr, and Eu) and $[\text{M}_2(\text{HQ})_6(\text{H}_2\text{O})_2(\text{DMF})_2] \cdot 2\text{H}_2\text{O}$ (M(III): Eu, Dy and Ho) fulfill the three criteria simultaneously and, as expected, the self-assembly of the complex units weaves a 3D porous supramolecular architecture with 1D channels (Figure 2.6) in which crystallization water molecules are hosted (porosity: 3.0–19.1%). This was not reflected by the authors in the original manuscript, which was mainly focus on the luminescence properties of the compounds. The remaining nine structures have polymeric frameworks (1D and 3D) and therefore, they have been disregarded from this preliminar analysis.

In any case, none of the reported structures fits to our above envisaged paddle-wheel type structure, but we must note that the published examples are relatively scarce and most of them are built up with unsuitable metal centres (i.e. higher coordination number and/or ionic charge: lanthanide(III), cadmium(II) and gallium(III)). So that herein we have selected Cu(II) as metal centre due to (a) its relation with the research work developed in the next chapters and (b) its trend to form paddle-wheel type entities.

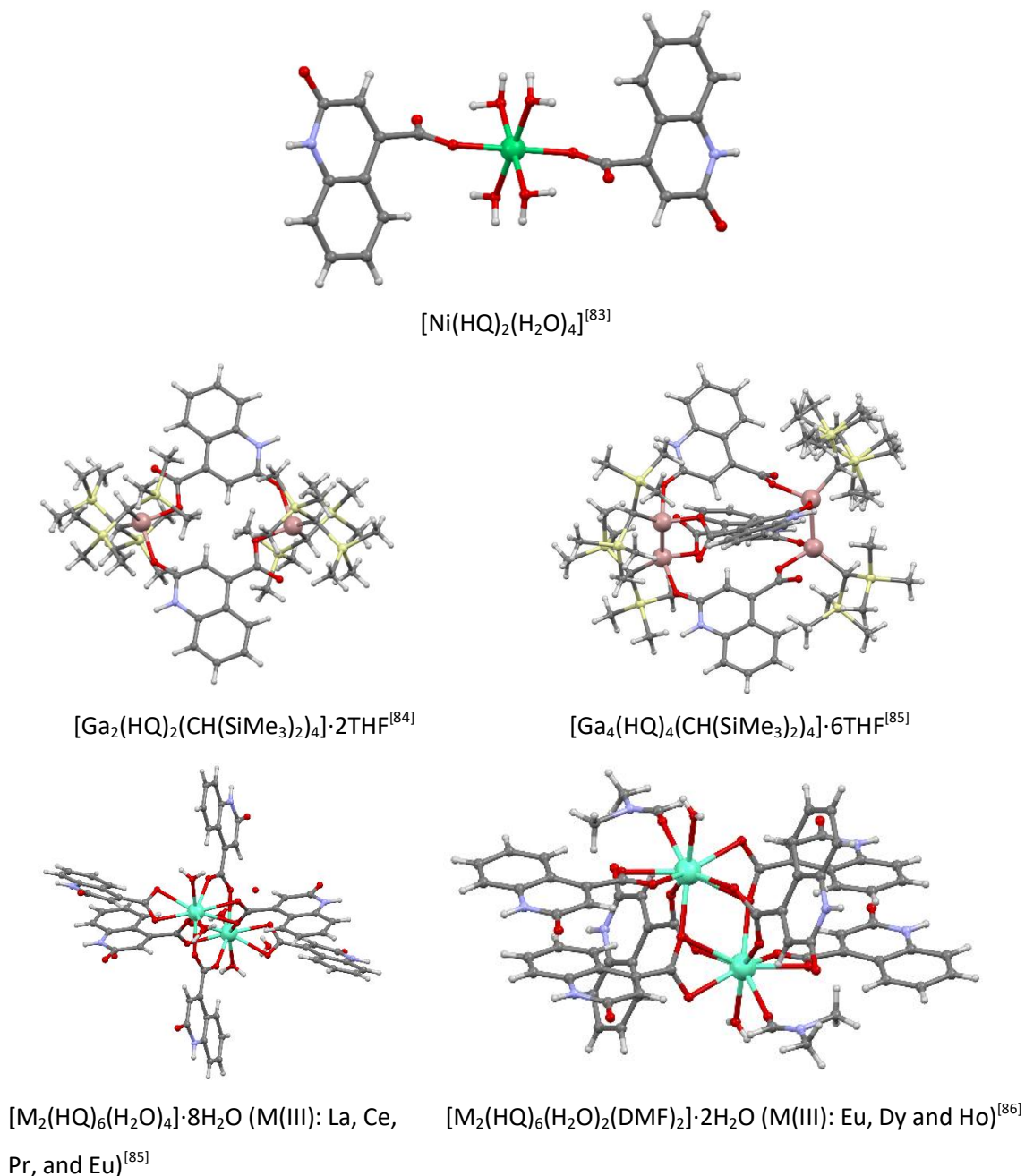


Figure 2.5. Examples of compounds with HQ and BPA and the coordination modes of HQ.

⁸³ Yuan, G.; Qin, J.-S.; Su Z.-M.; Shao, K.-Z.; Fu, Y.-M. *Acta Cryst.* **2008**, *64*, m389-390.

⁸⁴ Uhl, W.; Stefaniak, C.; Vo, M.; Layh, M.; Rogel, F.; Kosters, J. Z. *Anorg. Allg. Chem.* **2015**, *641*, 253.

⁸⁵ Rui, F.; Fei-Long, J.; Ming-Yan, W.; Lian, C.; Chun-Feng, Y.; Mao-Chun, H.; *Cryst. Growth Des.* **2010**, *10*, 2306–2313.

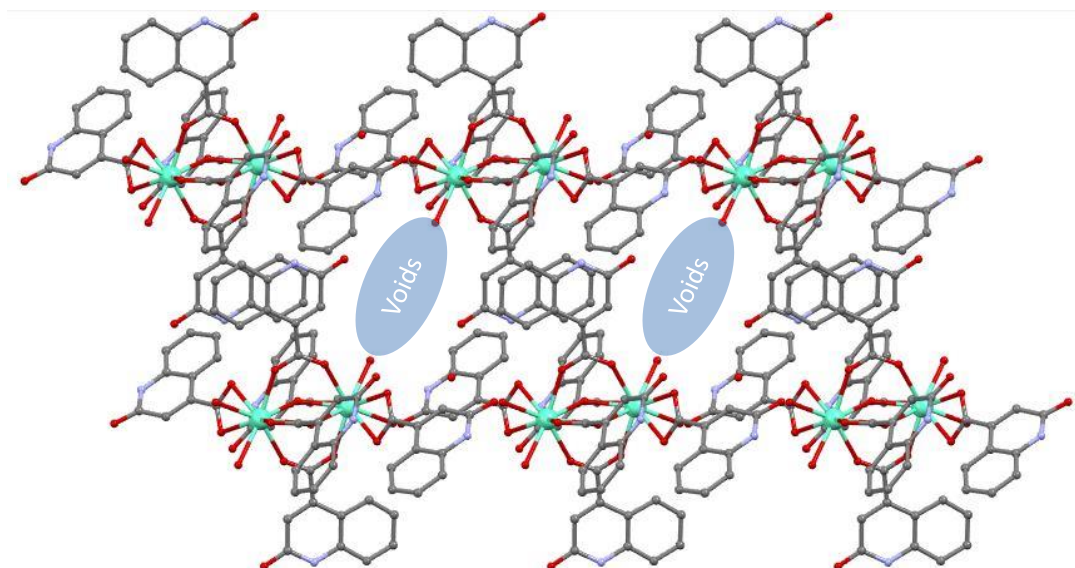


Figure 2.6. View of the crystal packing in $[M_2(HQ)_6(H_2O)_4] \cdot 8H_2O$ (M(III): La, Ce, Pr, and Eu).^[86] Hydrogen atoms have been omitted for clarity.

Keeping in mind the described analysis, several synthetic conditions were explored with the aim of obtaining metal/HQ complexes that fulfil the requirements to assemble into a SMOF. Precisely, the effect of the synthesis temperature and use of bulky co-ligands were assessed. Room temperature syntheses, provided dinuclear complexes (codes: 0D-CuHQMEOH, 0D-CuHQAQ) with μ -HQ- $\kappa O_{\text{carboxylate}}:\kappa O_{\text{carboxylate}}$ bridging mode for the HQ ligand, but not with the pursued carboxylate *syn-syn* bridging mode. In both cases, the observed dinuclear building block is rigid, but the synthons implying the N-H/O groups of the HQ (Figure 2.3) are parallel. Thus, in a third trial, we included pyridine (PY) and 4,4'-bipyridinethane (BPA) as bulky co-ligands with the aim of **(a)** favouring the occurrence of non-parallel synthons (PY and BPA) and **(b)** providing an alternative growing vector (the cross-linking of complex entities through BPA) that could make more probable the formation of a robust and porous 3D structure sustained by a combination of complementary synthons and bridging ligands. However, steric hindrance of pyridine led to a change into the bridging mode of the HQ ligand (μ -HQ- $\kappa O_{\text{carboxylate}}:\kappa O_{\text{carbonyl}}$) and rendered a dinuclear entity (0D-CuHQPY) in which the aforementioned synthons are still parallel, ruling out again the formation of a 3D open supramolecular framework sustained by robust and predictable synthons. Similarly to pyridine, the coordination of the BPA ligand alters the coordination mode of the HQ ligands to μ -HQ- $\kappa O_{\text{carboxylate}}:\kappa O'_{\text{carboxylate}}$, rendering a 2D coordination network in which HQ pairing interactions only take place within the polymeric layers.

Coming back to compounds 0D-CuHQMEOH and 0D-CuHQAQ, since each copper atom of the dinuclear entities exhibits two coordinated solvent molecules, the accomplishment of

targeted paddle-wheel structure should be entropically favoured at higher synthesis temperatures. Accordingly, upon a mild increase of the synthesis temperature (358 K), Cu(II) and HQ assembled as the paddle-wheel structure depicted in Figure 2.4a. As predicted, the obtained complex (1D-CuHQ) fulfils all the three criteria and the self-assembling by means of the complementary hydrogen bonding between HQ ligands weaves an open 3D supramolecular-framework (**lvt**-type topology). In any case, the overall structure is doubly interpenetrated, in such a way, that the dinuclear entities of the two coexisting supramolecular **lvt**-type networks are successively assembled by means of an elongated coordination bond that implies the free apical position of the paddle-wheel entity. Thus, the crystal structure could be alternatively described as a 1D coordination polymer crosslinked by complementary hydrogen bonding of HQ groups. At higher synthesis-temperature (433 K), unexpectedly, HQ ligand exhibits a cycloaddition process to yield cyclobutadiquinoline (CBDQ) ligand. The resulting compound (0D-CuCBDQ) is built from paddle-wheel shaped dinuclear entities analogous to that of 1D-CuHQ and again, the self-assembling through HQ pairing interactions (Figure 2.4) yields a **dia**-type porous network, being in this case triply interpenetrated. Contrarily to 1D-CuHQ, in 0D-CuCBDQ, the steric-hindrance imposed by the cycloaddition of HQ (i.e. CBDQ), hinders the assembling of neighbouring paddle-wheel complexes through their apical positions and as a result, the crystal structure is solely sustained by means of supramolecular interactions.

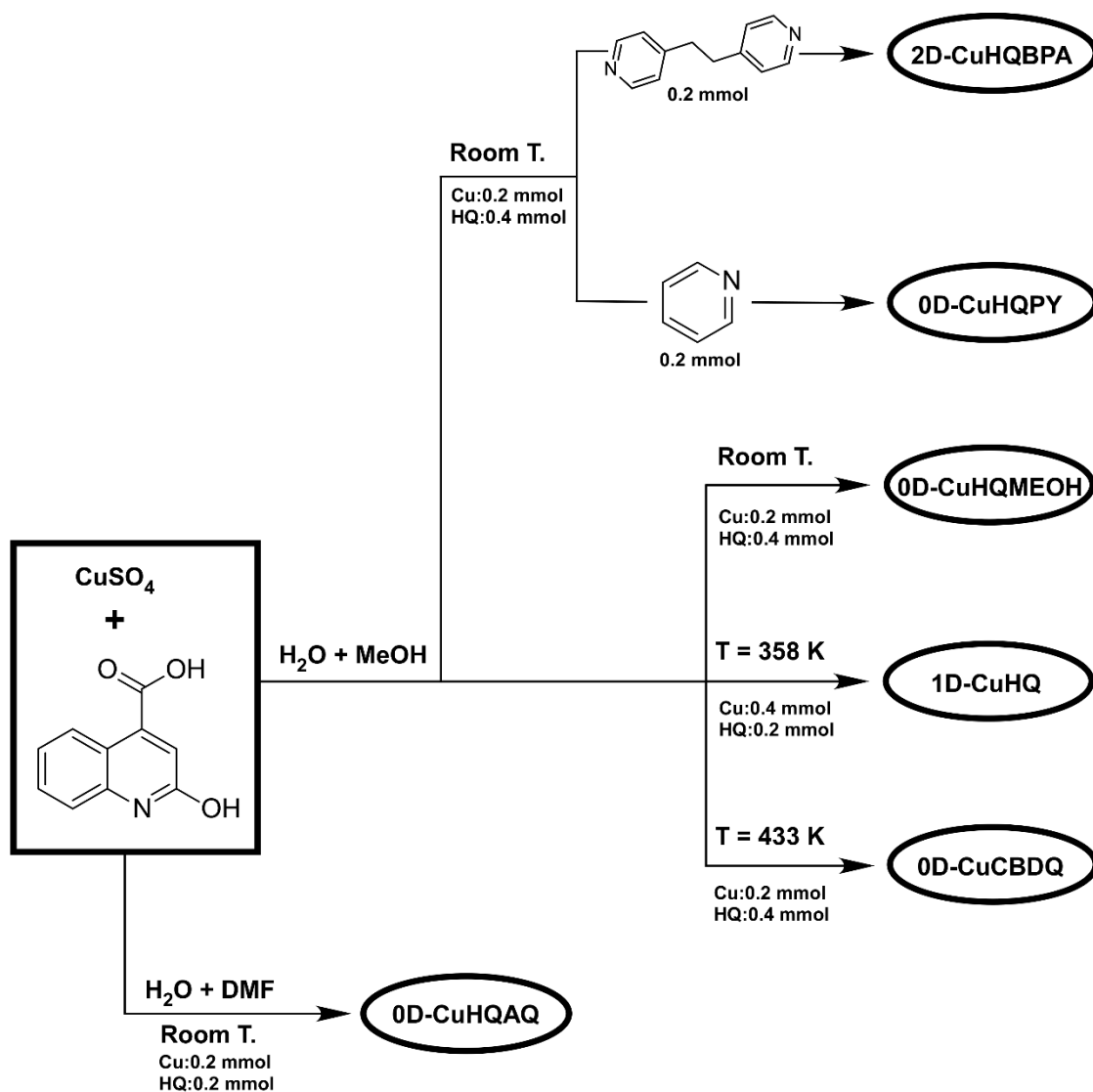
2.2. SYNTHESIS AND CHEMICAL CHARACTERIZATION

2.2.1. Synthesis

The six compounds synthesized and characterized in this chapter are listed in Table 2.1. In all compounds, suitable single-crystals have been obtained to carry out their structural characterization by X-ray diffraction. Figure 2.7 shows a scheme that depicts the synthetic procedures used in this chapter.

Table 2.1. Formula and code of the compounds synthesized with Cu(II) and HQ.

Compound	Code
$[\text{Cu}_2(\mu\text{-HQ}\text{-}\kappa\text{O}_{\text{carboxylate}}:\kappa\text{O}_{\text{carboxylate}})_2(\text{HQ}\text{-}\kappa\text{O}_{\text{carboxylate}})_2(\text{H}_2\text{O})_2(\text{CH}_3\text{OH})_2]\cdot 4\text{H}_2\text{O}\cdot\text{CH}_3\text{OH}$	0D-CuHQMEOH
$[\text{Cu}_2(\mu\text{-HQ}\text{-}\kappa\text{O}_{\text{carboxylate}}:\kappa\text{O}_{\text{carboxylate}})_2(\text{HQ}\text{-}\kappa\text{O}_{\text{carboxylate}})_2(\text{H}_2\text{O})_4]\cdot 4\text{H}_2\text{O}\cdot 2\text{DMF}$	0D-CuHQAQ
$[\text{Cu}_2(\mu\text{-HQ}\text{-}\kappa\text{O}_{\text{carboxylate}}:\kappa\text{O}_{\text{carbonyl}})_2(\text{HQ}\text{-}\kappa\text{O}_{\text{carboxylate}})_2(\text{H}_2\text{O})_2(\text{PY})_2]$	0D-CuHQPY
$[\text{Cu}_2(\mu\text{-HQ}\text{-}\kappa\text{O}_{\text{carboxylate}}:\kappa\text{O}'_{\text{carboxylate}})_4(\mu\text{-BPA}\text{-}\kappa\text{N}:\kappa\text{N}')]_n$	2D-CuHQBPA
$[\text{Cu}_2(\mu\text{-HQ}\text{-}\kappa\text{O}_{\text{carboxylate}}:\kappa\text{O}'_{\text{carboxylate}})_2(\mu_3\text{-HQ}\text{-}\kappa\text{O}_{\text{carboxylate}}:\kappa\text{O}'_{\text{carboxylate}}:\kappa\text{O}_{\text{carbonyl}})_2]_n$	1D-CuHQ
$[\text{Cu}_2(\mu\text{-CBDQ}\text{-}\kappa\text{O}_{\text{carboxylate}}:\kappa\text{O}'_{\text{carboxylate}})_4(\text{H}_2\text{O})_2]\cdot x(\text{solvent})$	0D-CuCBDQ

**Figure 2.7.** Synthesis scheme for the compounds of chapter 2.

2.2.1.1. Synthesis of compound OD-CuHQMEOH

10 mL of an aqueous solution of copper(II) sulfate (0.2 mmol, 0.050 g) were added over 10 mL of a methanol solution of 2-hydroxyquinoline-4-carboxylic acid (0.4 mmol, 0.076 g), under continuous stirring at 80 °C to facilitate the dissolution of HQ. The resulting greenish solution is cooled down to room temperature and stored in a crystallizer. Compound OD-CuHQMEOH crystallized several hours later as poor quality crystals. Single-crystals suitable for X-ray diffraction were obtained by placing the reaction mixture in a closed vial at 60 °C in an oven during 24 h. The crystals were filtered off, washing them with DMF to dissolve the unreacted 2-hydroxyquinoline-4-carboxylic acid that began to precipitate as soon as the temperature decreased. Yield: 70–75% (based on metal).

2.2.1.2. Synthesis of compound OD-CuHQAQ

10 mL of an aqueous solution of copper(II) sulfate (0.2 mmol, 0.050 g) were added over a 10 mL solution of DMF containing 2-hydroxyquinoline-4-carboxylic acid (0.2 mmol, 0.038 g). The reaction mixture was stirred for few minutes. OD-CuHQAQ precipitated as blue coloured poor quality crystals. Single-crystal X-ray diffraction quality specimens (dark-blue coloured with square prism habit) were obtained by placing in a closed vial the above described reaction mixture and heating it at 60 °C during 24 h. They were filtered off and washed with DMF. Yield: 35–45%.

2.2.1.3. Synthesis of compound OD-CuHQPY

5 mL of an aqueous solution of copper(II) sulfate (0.2 mmol, 0.050 g) were added over 5 mL of a methanol solution of 2-hydroxyquinoline-4-carboxylic acid (0.4 mmol, 0.076 g), under continuous stirring at 80 °C. Pyridine (0.2 mmol, 32.2 μ L) was added drop by drop and the final mixture was allowed to stand at room temperature. Again, several hours later small-sized poor quality crystals were obtained. Similarly, to previous cases, good quality square prismatic blue single-crystals were obtained by subjecting the reaction mixture to 85 °C in a closed vial. Yield 65%.

2.2.1.4. Synthesis of compound 2D-CuHQBPA

The synthesis process of 2D-CuHQBPA was similar to that of OD-CuHQPY, but adding BPA (0.2 mmol, 0.050 g; in 5 mL of methanol) instead of pyridine. The reaction mixture was placed in a sealed vial and heated up to 85 °C in an oven during 24 h. Thereafter, blue coloured prismatic crystals were filtered off and thoroughly washed with methanol. Yield 40%.

2.2.1.5. Synthesis of compound 1D-CuHQ

Copper(II) sulfate (0.4 mmol, 0.100 g) and 2-hydroxyquinoline-4-carboxylic acid (0.2 mmol, 0.038 g) were placed in a sealed vial containing 5 mL of H₂O and 5 mL of MeOH. The reaction mixture was left in an oven at 85 °C for 24 hours. Thereafter, dark green needle-shaped crystals were collected and filtered off, washing them with methanol. Yield: 17%.

2.2.1.6. Synthesis of compound 0D-CuCBDQ

A mixture of 2-hydroxyquinoline-4-carboxylic acid (0.4 mmol, 0.076 g) and copper(II) sulfate (0.2 mmol, 0.050 g), was placed in 20 mL of an aquo-methanolic solution (1:1 V/V) and stirred at 80 °C during ten minutes. The obtained solution was transferred to a sealed vial and heated up to 160 °C during 24 h. After cooling down the vial, light green plate-like crystals were obtained. Only few crystals of 0D-CuCBDQ were yielded, so its characterization was limited to the structural analysis performed upon single-crystal X-ray diffraction data. Yield: not determined.

2.2.2. Infrared spectroscopy

Infrared spectroscopy with attenuated total reflection (ATR-FTIR) has been used to qualitatively identify molecular species comprising the herein synthesized compounds. Figure 2.8 and Figure 2.9 show collected spectra, while the assignment of the most relevant bands,^[86] the relative intensity and the wavenumber are shown in Table 2.2. Note that all spectra lack of the carbonyl $\nu(\text{C}=\text{O})$ vibration mode located at *ca.* 1750 cm⁻¹ for –COOH groups and, contrarily, present the antisymmetric $\nu_{\text{as}}(\text{OCO})$ vibration mode of carboxylate groups at *ca.* 1650 cm⁻¹. Both observations point to the deprotonation of carboxylic groups and their subsequent coordination to the metal centres.

⁸⁶ (a) Nakamoto, K. *Infrared and Raman spectra of inorganic and coordination compounds*; John Wiley & Sons: New York, 1997. (b) Ghose, R. *Synth. React. Inorg. Met. Org. Chem.* 1992, 22, 379. (c) Ghose, R. *Inorg. Chim. Acta* 1989, 156, 303.

Table 2.2. Infrared spectra bands (cm^{-1}) of the neutral HQ ligand and the compounds of chapter 2. ^[a]

HQ	0D-CuHQMEOH	0D-CuHQQAQ	0D-CUHQPY	1D-CuHQ	2D-CUHQBPA	Assignment ^[b]
3006s	over	over	over	over	over	$\nu(\text{C-H})$
1716	-	-	-	-	-	$\nu(\text{C=O})_c$ ^[c]
1650vs	1651s	1650s	1658s	1651s	1655vs	$\nu_{\text{as}}(\text{COO}) + \nu(\text{C=O})_r$ ^[c]
1612vs	1612vs	1613vs	1619vs	1613vs	1610vs	$\delta(\text{NH}) + \nu(\text{CC})$
1545s	1536m	1539m	1549s	1535m	1543s	$\nu(\text{CC})$
1433s	1436m	1430m	1436m	1436m	1430s	$\nu(\text{CC}) + \delta(\text{NH}) + \delta(\text{CH})$
1383m	1378s	1368s	1358 vs	1377s	1360 vs	$\delta(\text{NH}) + \delta(\text{CH})$
1320w	1329w	1329m	1319vw	1330w	1326m	$\nu(\text{C-O}) + \delta(\text{NH}) + \delta(\text{OH})$
1279vs	1265s	1265s	1268s	1265s	1267s	$\delta(\text{NH}) + \delta(\text{CH})$
1258vs	1241w	1257m	1251w	1241w	1243vw	$\nu(\text{CN}) + \delta(\text{CH})$
1229vs	1223vw	1233vw	1218s	1224vw	1225w	$\nu(\text{CC}) + \delta(\text{CH})$
1154m	1158s	1158s	1165m	1158s	1157m	$\delta(\text{CH}) + \delta(\text{OH})$
1137w	1134s	1135w	1137w	1135s	1137m	$\delta(\text{CH}) + \nu(\text{C-OH})$
1041vw	1044w	1040vw	1038w	1044w	1033m	$\delta(\text{CH}) + \nu(\text{CC}) + \gamma(\text{CH})$
1004w	988w	985vw	979w	988w	981w	$\omega(\text{C-C})_{\text{ring breathing}}$
937m	951vs	943vw	937w	950vs	945vw	$\gamma(\text{CH}) + \nu(\text{NH})$
880s	882s	881s	881s	880s	876m	$\nu(\text{NH}) + \nu(\text{C=O})_r$
853s	862m	861m	854m	862m	838m	$\nu(\text{NC}) + \nu(\text{CH}) + \nu(\text{C-C-O})$
773m	768m	765m	770w	766m	775w	$\gamma(\text{CH}) + \nu(\text{COOH})$
759s	755s	744vs	760m	755s	761m	$\gamma_{\text{ring}} + \nu(\text{CO})_c$
711s	709m	696m	697vs	708m	698s	$\gamma_{\text{ring}} + \nu(\text{NH}) + \nu(\text{CH})$
654vs	650vs	663s	647m	650vs	648s	$\nu(\text{NH}) + \nu(\text{OH})$

^[a] vs = very strong, s = strong, m = medium, over = overlapped, w = weak, vw = very weak. ^[b] ν = tension vibrations, δ = deformation vibrations, τ = torsion, γ = plane vibration, ω = ring breathing. ^[c] tension vibration of c = carboxylate group, r = carbonyl group of ring.

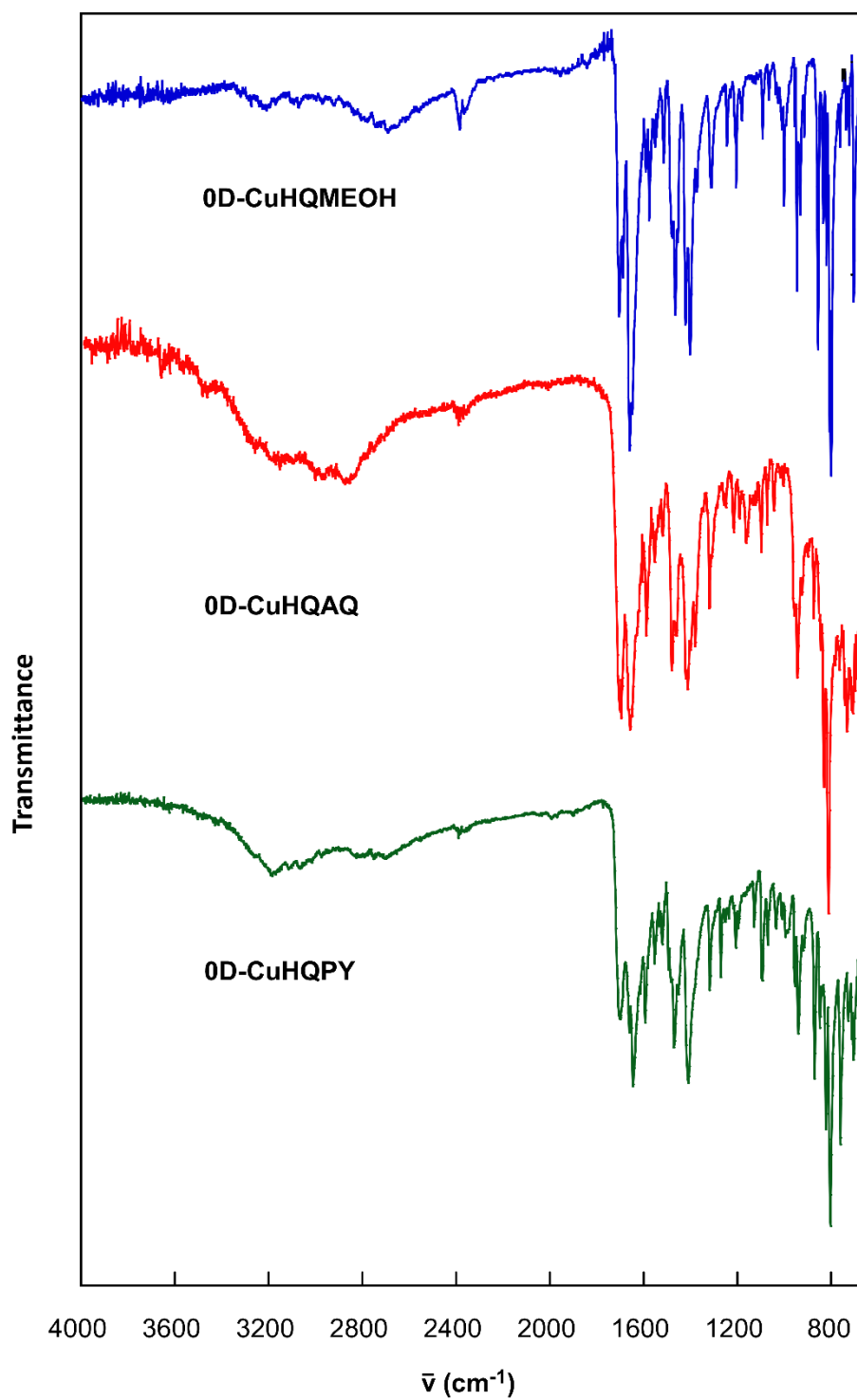


Figure 2.8. Infrared spectra of compounds 0D-CuHQMEOH (blue), 0D-CuHQAQ (red) and 0D-CuHQPY (green).

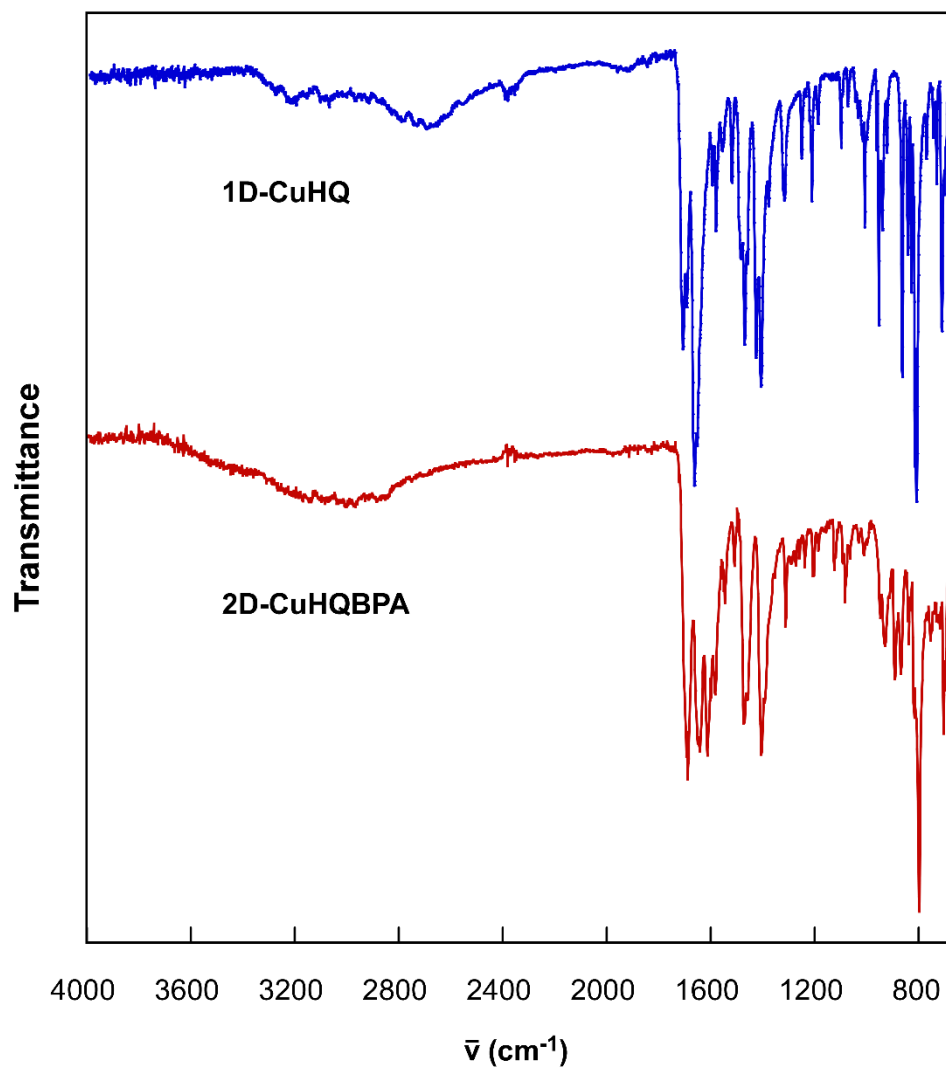


Figure 2.9. Infrared spectra of compounds 1D-CuHQ (blue) and 2D-CuHQBPA (red).

2.2.3. Thermal analysis

The results of the thermogravimetric analyses (TGA) and the thermal differential analyses are plotted in Figure 2.10, while the processes occurring in each degradation stage are gathered in Table 2.3. Note that all experimental mass losses fit fairly well with those expected from the chemical formula of the compounds. All the measurements were run using synthetic air (79% N₂, 21% O₂) as atmosphere.

2-Hydroxyquinoline-4-carboxylic acid based SMOFs

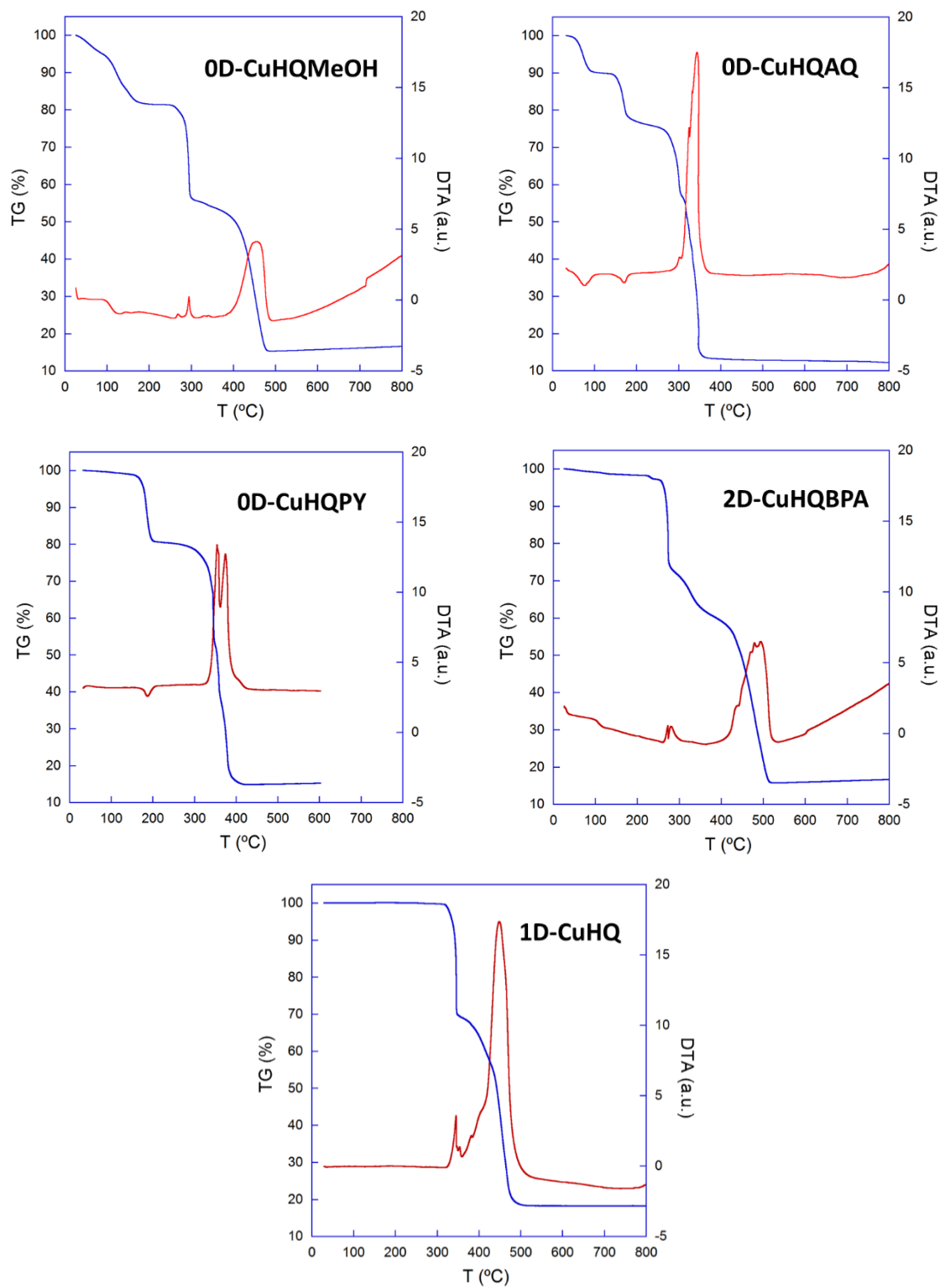


Figure 2.10. Thermogravimetric measurements performed upon representative samples.

Table 2.3. Thermoanalytic data for compounds of Chapter 2.^[a]

Step	T _i	T _f	T _{peak}	ΔH	Δm(%)	ΣΔm(%)	ΣΔm _{theo} (%)
OD-CuHQMEOH							
1	30	165	125	Endo	18.1	18.1	18.8 (-6H ₂ O -3CH ₃ OH)
2	250	310	295	Exo	26.5	44.6	45.5 [Cu ₂ (C ₁₀ H ₆ NO ₃) ₂ (C ₂ O ₄)]
3	365	490	455	Exo	66.8	84.9	85.3 (2CuO)
OD-CuHQAQ							
1	30	100	75	Endo	10.0	10.0	9.2 (-6H ₂ O)
2	100	215	170	Endo	14.5	24.7	24.7 (-2H ₂ O -2C ₃ H ₇ NO)
3	250	385	345	Exo	62.4	87.1	86.4 (2CuO)
OD-CuHQPY							
1	150	210	190	Endo	19.5	19.5	18.1 (-2H ₂ O -2C ₅ H ₅ N)
2	260	355	355	Exo	26.1	45.6	44.9 [Cu ₂ (HQ) ₂ (C ₂ O ₄)]
3	230	425	375	Exo	65.8	85.3	85.2 (2CuO)
2D-CuHQBPA							
1	220	280	275	Exo	26.7	26.7	27.1 [Cu ₂ (HQ) ₂ (C ₂ O ₄)(BPA)]
2	280	520	--	Exo	56.7	83.4	85.0 (2CuO)
1D-CuHQ							
1	315	350	345	Exo	30.4	30.4	32.8 [Cu ₂ (HQ) ₂ (C ₂ O ₄)]
2		515	450	Exo		81.8	81.9 (2CuO)

^[a]T_i = initial temperature; T_f = final temperature; T_{peak} = peak temperature ATD; Δm(%) = mass loss percentage in each step; ΔH = type of process according to DTA; ΣΔm(%) = cumulative mass loss after each step; ΣΔm_{theo}(%) = cumulative loss mass theoretically calculated from the crystallographic formula.

Compounds OD-CuHQMEOH, OD-CuHQAQ and OD-CuHQPY decompose similarly by releasing in a single step or successive steps the co-crystallized solvent molecules and/or coordinated co-ligands. This first decomposition stage finishes at a temperature close to 200 °C and the resulting desolvated Cu/HQ entity remains stable up to ca. 290 °C. At this temperature, the organic constituent decomposes in two overlapped exothermic processes, a first in which two of the four HQ ligands decompose to lead [Cu₂(C₁₀H₆NO₃)₂(C₂O₄)] than almost

immediately decompose further to yield CuO as the final product. The identification of the final product was performed by PXRD analysis.

Note that as compounds 1D-CuHQ and 2D-CuHQBPA lack co-crystallized solvent molecules or co-ligands, they remain stable up to *ca.* 290 °C, after which decompose following a similar two-step decomposition pattern to that aforementioned.

2.3. RESULTS AND DISCUSSION

2.3.1. Crystallographic analysis

The crystallographic data and details of the refinement parameters of each compound have been gathered in Table 2.4 and Table 2.5. All non-hydrogen atoms were refined anisotropically, except those corresponding to disordered entities. The hydrogen atoms belonging to organic entities have been geometrically fixed and refined according to a riding model with an isotropic thermal parameter linked to the atom to which they are attached (120 %). In most of the cases, the hydrogen atoms of the coordination and the crystallization water molecules have been located in the difference Fourier map, while in the remaining cases the routine CALC-OH^[87] implemented in WinGX interface has been employed. The refinement of water hydrogen atoms has been performed using an isotropic thermal parameter of 150 % regarding their parent atom.

In the case of 0D-CuHQMEOH, after fixing all the atoms comprising the metal complex, the analysis of the computed electron density map revealed three Q peaks whose intensity ratio (1:0.5:0.5 for Q1, Q2 and Q3) and distances (Q1...Q2: 1.46 Å and Q1...Q3: 2.6 Å) led us to model them as two site-sharing group of atoms with an occupation factor 0.5 for each one (group 1: O3w and O4w modelled from Q1 and Q3, and group 2: methanol molecule modelled from Q1 and Q2). The resulting refinement was stable upon the application of DFIX restrains and isotropic displacement parameters, and it rendered a coherent hydrogen bonding scheme.

0D-CuHQAQ was refined as a two component twin with a batch scale factor (BASF) parameter of 0.318 and where the second component is rotated by a binary axis (i.e. 180 °) around [1 0 0] direction. Regarding 2D-CuHQBPA, the initial resolution showed anomalous elongated ellipsoids for a series of atoms of one of the crystallographically independent quinolones (C19, C110, O12). The elongation of the ellipsoids suggested a disorder of the double ring of the ligand into two positions (quinolone-1A and quinolone-1B) that swing along the C17–C14...N11 axis (implying a fixed carboxylate group). The occupation factor was refined

⁸⁷ Nardelli M., *J. Appl. Crystallogr.* **1999**, *32*, 563-571.

leading to a ratio of 0.52:0.48 for each part. All the non-hydrogen atoms of the disordered HQ counterparts were also refined anisotropically.

1D-CuHQ shows two isolated voids each of ca. 180 \AA^3 per unit cell. However, the analysis by means of the SQUEEZE routine of PLATON^[88] renders two electrons per void, implying that they are essentially empty. This crystallographic analysis is consistent with the assessment of TGA results. Contrarily, in compound 0D-CuCBDQ, after locating all the atoms comprising the metal complex, the crystal structure presents four isolated void per unit cell, each one of 368 \AA^3 and 85 electrons, which would imply 32–36 H_2O molecules per unit cell or 8–9 molecules per formula (or void). Unfortunately, we could not collate this result with TGA data as there was not enough sample.

⁸⁸ Spek, A. L. *Acta Crystallogr.* **2009**, *D56*, 148.

Table 2.4. Crystallographic data and refinement details of compounds OD-CuHQMEOH, OD-CuHQAQ and OD-CUHQPYPY.

	OD-CuHQMEOH	OD-CuHQAQ	OD-CUHQPYPY
Formula	C ₄₃ H ₄₈ Cu ₂ N ₄ O ₂₁	C ₄₆ H ₅₄ Cu ₂ N ₆ O ₂₂	C ₅₀ H ₃₈ Cu ₂ N ₆ O ₁₄
M (g mol ⁻¹)	1084	1170	1074
Cryst. Syst.	Triclinic	Triclinic	Triclinic
Space group	<i>P</i> $\bar{1}$	<i>P</i> $\bar{1}$	<i>P</i> $\bar{1}$
<i>a</i> (Å)	7.0532(4)	7.0221(14)	9.0948(12)
<i>b</i> (Å)	10.8576(7)	11.4720(3)	10.7660(3)
<i>c</i> (Å)	15.9938(8)	16.0600(2)	12.2521(15)
α (°)	103.263(5)	90.9010(15)	95.515(15)
β (°)	98.947(4)	100.3870(15)	100.8960(11)
γ (°)	103.078(5)	107.0950(19)	92.4360(16)
V (Å ³)	1133.1(1)	1213.1(4)	1170.3(4)
Z	1	1	1
ρ_{calcd} (g·cm ⁻³)	1.588	1.602	1.524
Color	Green	Blue	Light blue
F(000)	560	606	550
μ (cm ⁻¹)	1.934	1.882	1.773
θ range (°)	2.909–76.353	4.042–75.161	4.134–75.876
hkl range	–8 ≤ h ≤ 8; –13 ≤ k ≤ 12; –18 ≤ l ≤ 20	–8 ≤ h ≤ 7; –14 ≤ k ≤ 14; –19 ≤ l ≤ 19	–11 ≤ h ≤ 10; –11 ≤ k ≤ 13; –14 ≤ l ≤ 15
Meas./indep. refl.	8452/4626	12468/7573	9742/4757
R eqv.	0.0493	0.1222	0.0827
Obs. Refl. [<i>I</i> > 2σ(<i>I</i>)]	3611	3817	2674
R, R _w [<i>a</i> , <i>b</i>]	0.0565/0.1448	0.1077/0.2788	0.0756/0.2006
R, R _w (all)	0.0747/0.1608	0.1752/0.3374	0.1336/0.2480
Gof(S)[<i>c</i>]	1.029	1.021	1.011
Parameters	350	345	326
Weighting sch.[<i>d</i>]	Shelxl	Shelxl	Shelxl
Max./min. Δρ (e Å ⁻³)	1.728/-0.608	1.179/-1.486	1.253/-1.184
Diffractometer	SuperNova	SuperNova	SuperNova
λ (Å)	1.54184	1.54184	1.54184
Temperature (K)	100(2)	100(2)	100(2)

[a] $S = [\sum w(F_o^2 - F_c^2)^2 / (N_{\text{obs}} - N_{\text{param}})]^{1/2}$ [b] $R_1 = \sum ||F_o| - |F_c|| / \sum |F_o|$ [c] $wR_2 = [\sum w(F_o^2 - F_c^2)^2 / \sum wF_o^2]^{1/2}$; $w = 1/[\sigma^2(F_o^2) + (aP)^2 + bP]$ where $P = (\max(F_o^2, 0) + 2F_c^2)/3$. a) OD-CuHQMEOH (0.0873), OD-CuHQAQ (0.2000) and OD-CUHQPYPY (0.1324). b) OD-CuHQMEOH (0.221).

Table 2.5. Crystallographic data and refinement details of compounds of 2D-CUHQBPA, 0D-CuBCDQ and 1D-CuHQ.

	2D-CUHQBPA	1D-CuHQ	0D-CuBCDQ
Formula	C ₅₂ H ₃₆ Cu ₂ N ₆ O ₁₂	C ₄₀ H ₂₄ Cu ₂ N ₄ O ₁₂	C ₈₀ H ₅₆ Cu ₂ N ₈ O ₂₆
M (g mol ⁻¹)	1064	880	1672
Cryst. Syst.	Monoclinic	Tetragonal	Tetragonal
Space group	<i>P2₁/n</i>	<i>P4₂/n</i>	<i>I4₁/a</i>
<i>a</i> (Å)	12.7028(7)	21.1781(1)	25.9460(7)
<i>b</i> (Å)	6.8477(4)	21.1781(1)	25.9460(7)
<i>c</i> (Å)	24.5923(12)	8.1870(1)	11.7125(9)
α (°)	90	90	90
β (°)	100.8170(5)	90	90
γ (°)	90	90	90
<i>V</i> (Å ³)	2101.2(2)	3671.9(6)	7884.8(7)
<i>Z</i>	2	4	4
ρ_{calcd} (g·cm ⁻³)	1.675	1.591	1.409
Color	Green	Green	Light green
F(000)	1080	1784	3432
μ (cm ⁻¹)	1.093	2.058	0.625
θ range (°)	1.691–27.364	5.794–74.429	1.570–28.287
<i>hkl</i> range	–15 ≤ <i>h</i> ≤ 16; –7 ≤ <i>k</i> ≤ 8; –26 ≤ <i>l</i> ≤ 30	–25 ≤ <i>h</i> ≤ 26; –26 ≤ <i>k</i> ≤ 18; –9 ≤ <i>l</i> ≤ 10	–26 ≤ <i>h</i> ≤ 34; –34 ≤ <i>k</i> ≤ 33; –13 ≤ <i>l</i> ≤ 15
Meas./indep. refl.	8270/4206	29289/3721	29166/4630
R eqv.	0.1027	0.0452	0.0645
Obs. Refl. [<i>I</i> > 2 σ (<i>I</i>)]	2281	3355	3665
R, R _w [<i>a</i> , <i>b</i>]	0.0808/0.1269	0.0260/0.0687	0.0516/0.1314
R, R _w (all)	0.1607/0.1622	0.0297/0.0711	0.0679/0.1428
Gof(S)[<i>c</i>]	0.999	1.055	1.083
Parameters	359	262	266
Weighting sch.[<i>d</i>]	Shelxl	Shelxl	Shelxl
Max./min. $\Delta\rho$ (e Å ⁻³)	0.759/-0.626	0.309/-0.409	0.772/-0.552
Diffractometer	SuperNova	SuperNova	SuperNova
λ (Å)	0.71073	1.54184	1.54184
Temperature (K)	100(2)	100(2)	100(2)

[a] $S = [\sum w(F_o^2 - F_c^2)^2 / (N_{\text{obs}} - N_{\text{param}})]^{1/2}$ [b] $R_1 = \sum ||F_o| - |F_c|| / \sum |F_o|$ [c] $wR_2 = [\sum w(F_o^2 - F_c^2)^2 / \sum wF_o^{2+1/2}]^{1/2}$; $w = 1/[\sigma^2(F_o^2) + (aP)^2 + bP]$ where $P = (\max(F_o^2, 0) + 2F_c^2)/3$. a) 2D-CUHQBPA (0.0206), 1D-CuHQ (0.0384) and 0D-CuBCDQ (0.0646). b) 1D-CuHQ (1.3341) and 0D-CuBCDQ (20.0495).

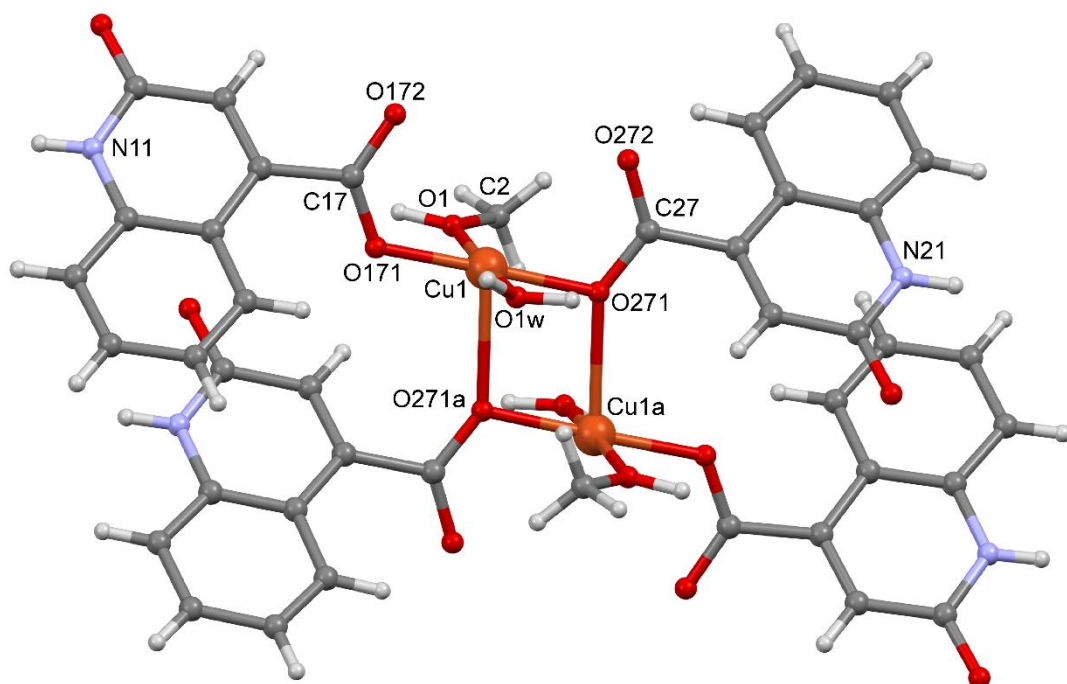
2.3.2. Structural description

2.3.2.1. Structural description of compounds 0D-CuHQMEOH, 0D-CuHQAQ and 0D-CuHQPYP.

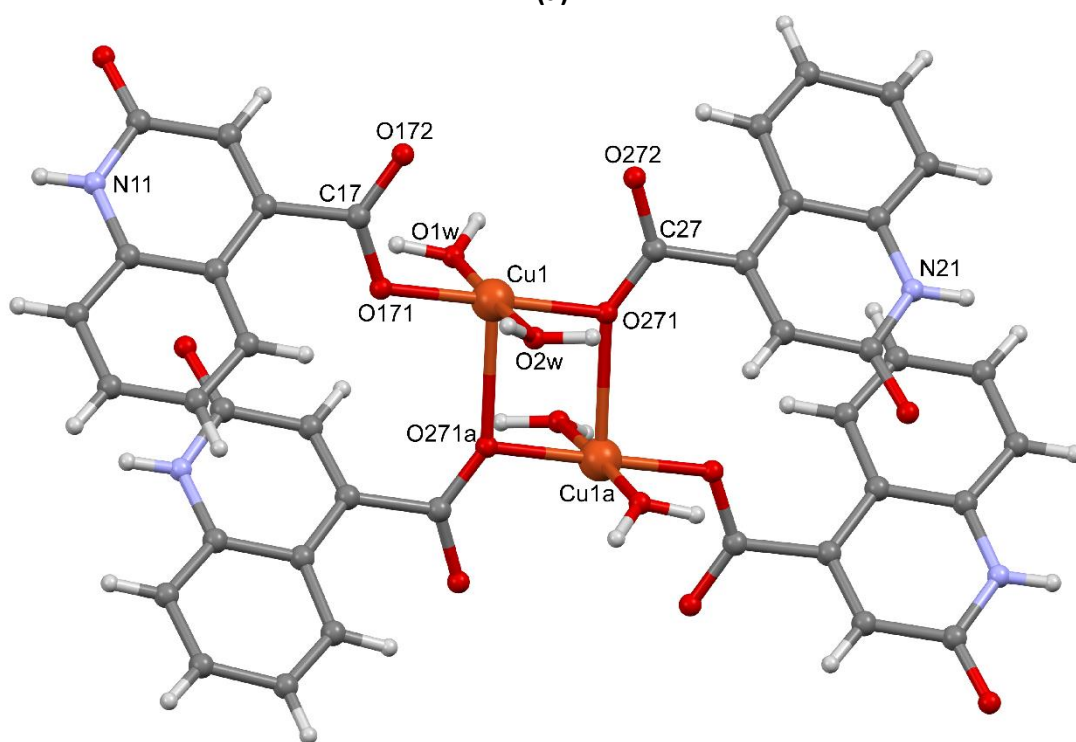
The crystal structures of herein described compounds consist of dinuclear entities (Figure 2.11, Figure 2.12 and Table 2.6) built by the assembling of [Cu(HQ- κ O_{carboxylate})₂(H₂O)(L)] mononuclear entities (L = MeOH, H₂O or pyridine in compounds 0D-CuHQMEOH, 0D-CuHQAQ and 0D-CuHQPYP, respectively). In compounds 0D-CuHQMEOH and 0D-CuHQAQ the assembling between the monomeric entities takes place by means of the coordinated O_{carboxylate} atom

setting a double μ -HQ- $\kappa O:\kappa O$ bridge. Whereas in compound OD-CuHQPY the steric hindrance imposed by the pyridine molecule precludes the aforementioned assembling and, as a consequence, the monomers are linked together through the carbonyl O atom of one each HQ ligands to form a double μ -HQ- $\kappa O:\kappa O'$ bridge. Note that μ -HQ- $\kappa O:\kappa O$ coordination mode of HQ bridge sets markedly shorter intradimeric Cu \cdots Cu distances (3.44 and 3.39 Å for OD-CuHQMEOH and OD-CuHQAQ, respectively) than that corresponding to μ -HQ- $\kappa O:\kappa O'$ mode (7.25 Å for OD-CuHQPY).

In all cases, the coordination polyhedron around the Cu(II) atoms resembles a distorted square pyramid, in which the basal plane is defined by the four donor atoms of the monomeric sub-unit (with short bond distances: 1.92–2.01 Å), while the apical position is occupied by the bridging O_{carboxylate} atom of an upper monomer influenced by the Jahn-Teller elongation (Cu–O_{carboxylate} bond distances: 2.31–2.45 Å). In contrast to the neutral HQ and the free HQ anion where the carboxylate group is in the same plane as the rest of the molecule, the carboxylate groups of these Cu(II) complexes are twisted respect to the fused aromatic rings by 45.5–47.5°. Such distortion from the planarity of the HQ can be ascribed to the steric hindrance occurring upon the approach of two monomeric sub-units during the assembling process. It deserves to note that the pyridine molecule establishes an intramolecular hydrogen bonding with the non-coordinated carboxylate O-atom of the terminal HQ ligand (C32–H32 \cdots O172; see Table 2.10).



(a)



(b)

Figure 2.11. Dimeric entities of compounds 0D-CuHQMEOH (a) and 0D-CuHQAQ (b).

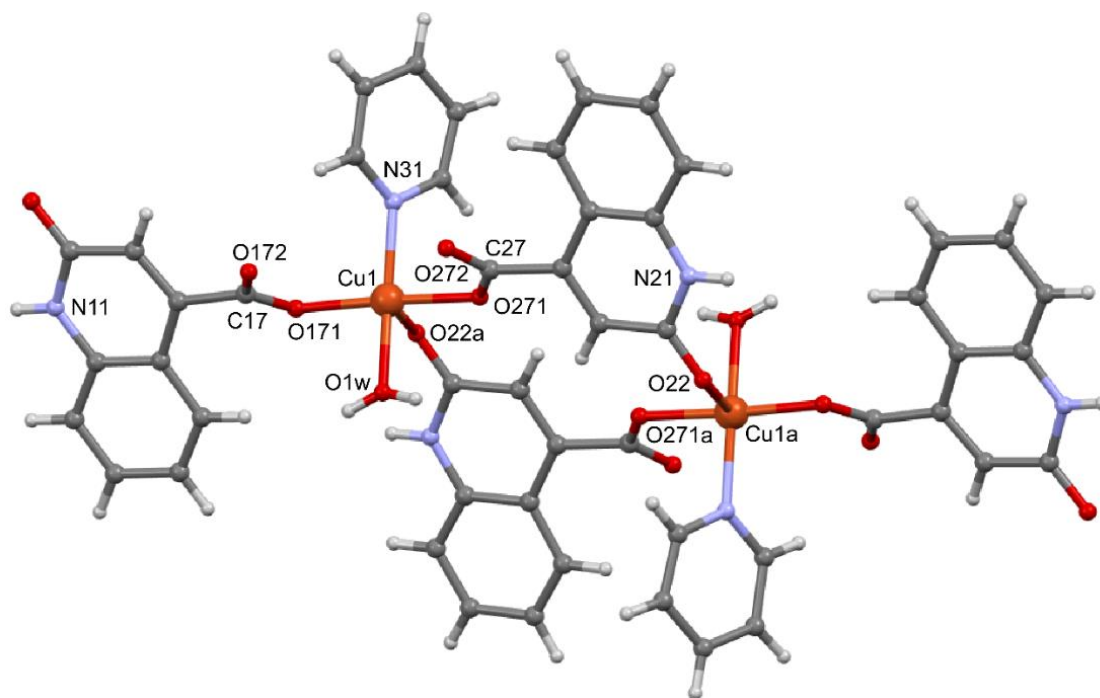


Figure 2.12. Dimeric entity of compound OD-CuHQPY.

Table 2.6. Coordination bond distances (Å) of compounds OD-CuHQMEOH, OD-CuHQAQ and OD-CuHQPY.¹

OD-CuHQMEOH			
Cu1–O171	1.958(2)	Cu1–O1	1.960(3)
Cu1–O271	1.926(2)	Cu1–O1W	1.952(3)
Cu1–O271a	2.395(2)	Cu1…Cu1a	3.441(9)
OD-CuHQAQ			
Cu1–O171	1.936(6)	Cu1–OW1	1.923(8)
Cu1–O271	1.958(6)	Cu1–OW2	1.958(8)
Cu1–O271a	2.447(4)	Cu1…Cu1a	3.393(4)
OD-CuHQPY			
Cu1–O171	1.936(4)	Cu1–O22a	2.308(4)
Cu1–O271	1.941(4)	Cu1–O1W	2.011(5)
Cu1–N31	2.012(7)	Cu1…Cu1a	7.255(2)

¹ Symmetry-codes: OD-CuHQMEOH, (a): $-x+2, -y+1, -z+2$; OD-CuHQAQ, (a): $-x+1, -y, -z+2$; OD-CuHQPY, (a): $-x+1, -y, -z+1$.

In spite of the structural and chemical dissimilarities of the metal complexes all of them give rise to similar crystal packing. Precisely, each dinuclear entity is linked to a neighbouring one through the double $\text{N-H}\cdots\text{O}_{\text{carbonyl}}$ hydrogen bonding pairing between the HQ ligands, leading to 1D supramolecular chain. These chains are crosslinked by means of the hydrogen bonding interactions established between a coordinated water molecule (O1w) and the non-coordinated carboxylate oxygen atoms, yielding a square grid-like (sql) supramolecular layer (Figure 2.13).

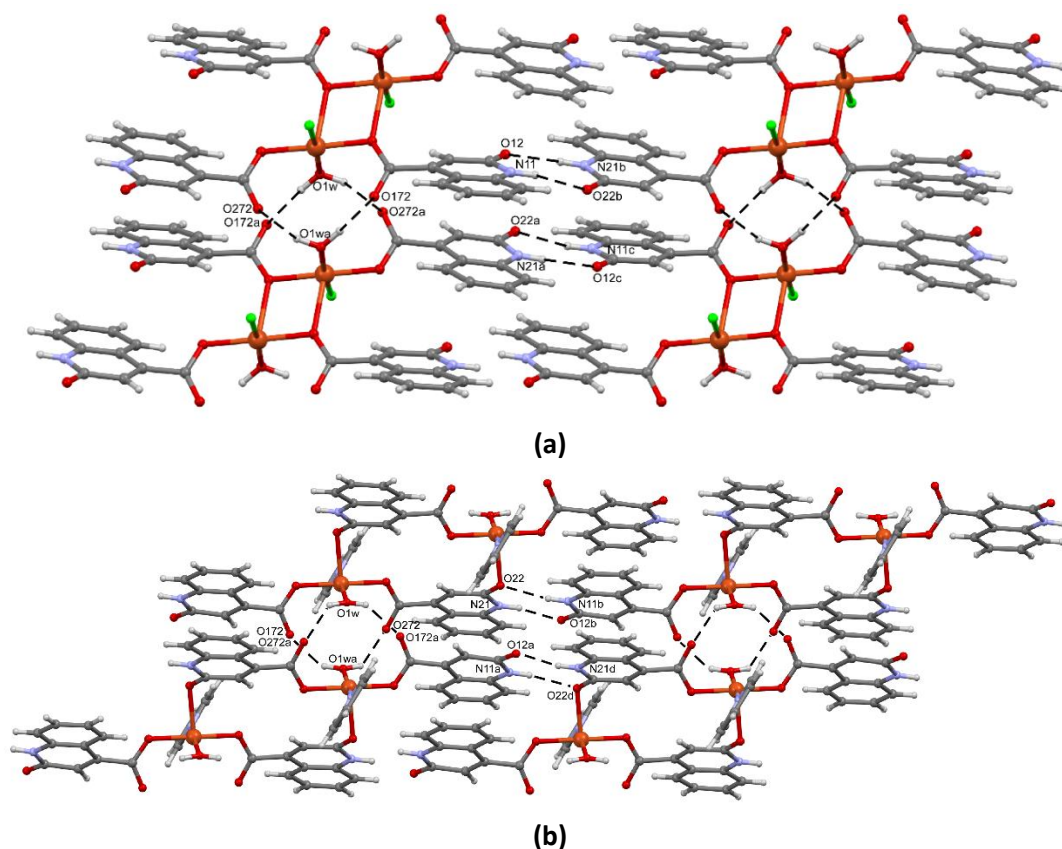


Figure 2.13. Supramolecular interactions between neighbouring dimeric entities in compounds 0D-CuHQMEOH and 0D-CuHQAQ (a) (the green atoms depict the coordinated methanol or water molecule) and in compound 0D-CuHQPY (b).

These layers pile up one above each other generating one-dimensional (diameter: *ca.* 3.50 and 5.10 Å) channels that account for the 18.4 and 26.4 % of the unit cell volume in compounds 0D-CuHQMEOH and 0D-CuHQAQ, respectively (Figures 2.14a and 2.14b). The channels are occupied by solvent molecules: water and methanol in compound 0D-CuHQMEOH and water and DMF in compound 0D-CuHQAQ. Compound 0D-CuHQPY (Figure 2.14c), in contrast, exhibits isolated voids (diameter: *ca.* 3.10 Å) that remain unoccupied, probably due to their hydrophobic nature (i.e. no hydrogen bonding or acceptor groups lie on the pore wall). Table 2.7 and Figure 2.15 show the porosity features and pore size distribution of all of them.

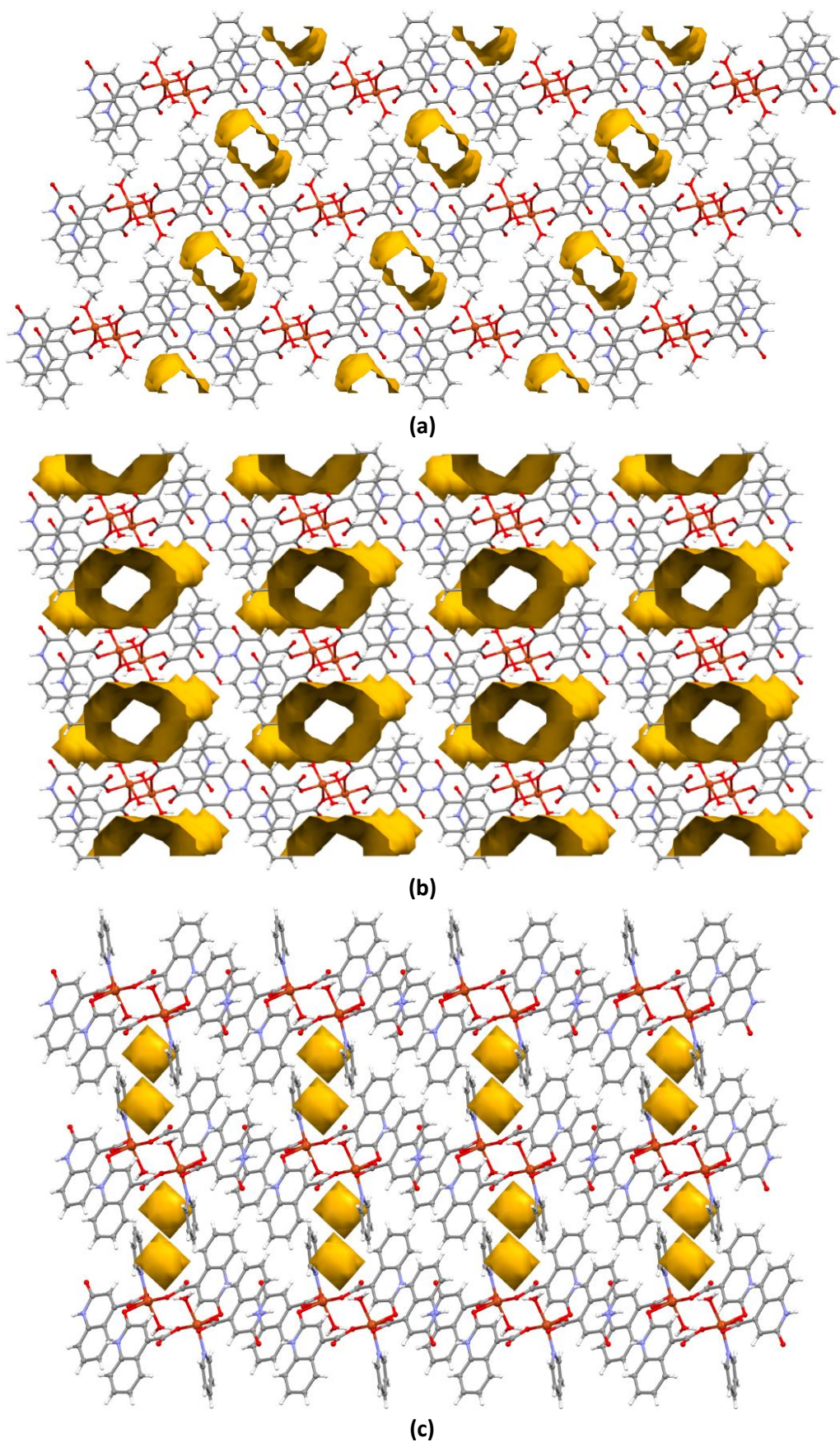


Figure 2.14. Crystal packing of compounds 0D-CUHQMEOH (a), 0D-CUHQAQ (b) and 0D-CUHQPY (c) showing the voids in yellow.

Table 2.7. Porosity features of compounds 0D-CUHQAQ, 0D-CUHQMEOH and 0D-CUHQPY.¹

Sample	$V_{\text{pore}(\text{cell})}$ (\AA^3)	$V_{\text{pore}(\text{sp})}$ ($\text{cm}^3 \cdot \text{g}^{-1}$)	Porosity (%)	D_{lim} (\AA)	D_{max} (\AA)	Dim.
0D-CUHQMEOH	209.0	0.128	18.4	3.10	3.5	1D
0D-CUHQAQ	321.0	0.203	26.5	4.00	5.1	1D
0D-CUHQPY	73.0	0.041	6.2	--	3.1	0D

¹: $V_{\text{pore}(\text{cell})}$ and $V_{\text{pore}(\text{sp})}$ stand for pore volume per unit cell and specific pore volume, respectively. D_{lim} and D_{max} correspond to limiting and maximum pore diameters. Dim. stands for dimensionality of the pore system.

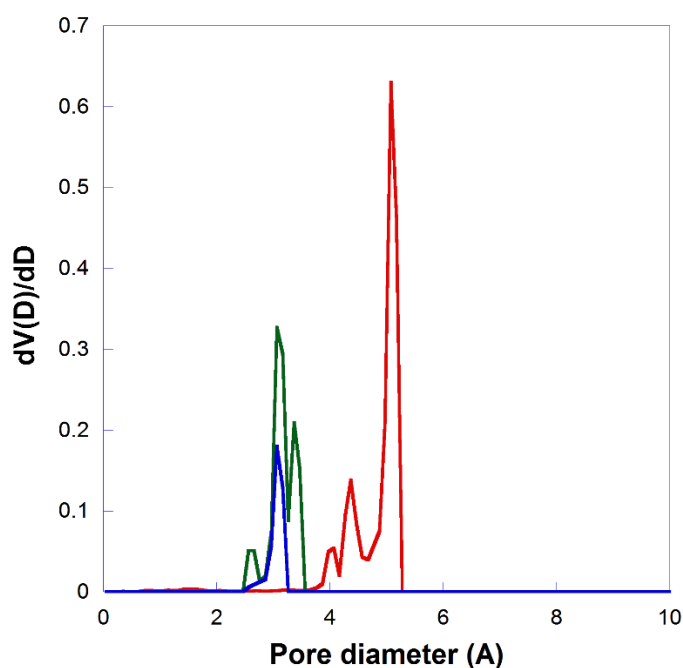


Figure 2.15. Pore size distribution in compounds 0D-CUHQMEOH (green), 0D-CUHQAQ (red), and 0D-CUHQPY (blue).

In the case of compound 0D-CUHQMEOH, neighbouring layers interact through a direct hydrogen bond between an aromatic H-atom and a non-coordinated carboxylate O-atom (C111–H111...O172) (Figure 2.16a). The adhesion between layers is further reinforced by means of the hydrogen bonding network implying the crystallization solvent molecules and the donor/acceptor groups of complexes of neighbouring layers. In compound 0D-CUHQAQ, the interlayer space is somewhat greater and all meaningful interactions between supramolecular layers take place via crystallization solvent molecules hosted in the pores (Figure 2.16b). On the other hand, in compound 0D-CuHQPY neighbouring layers are connected through a hydrogen bonding occurring between an aromatic H-atom and a non-coordinated carboxylate O-atom (C29–H29...O12) and through a CH/ π interaction between an aromatic H-atom of PY and the π -system of one HQ (C35–H35...C210: 3.686 \AA and 159.85°) (Figure 2.17). Tables 2.8,

2.9 and 2.10 gather representative parameters of the non-covalent interactions of the herein described compounds.

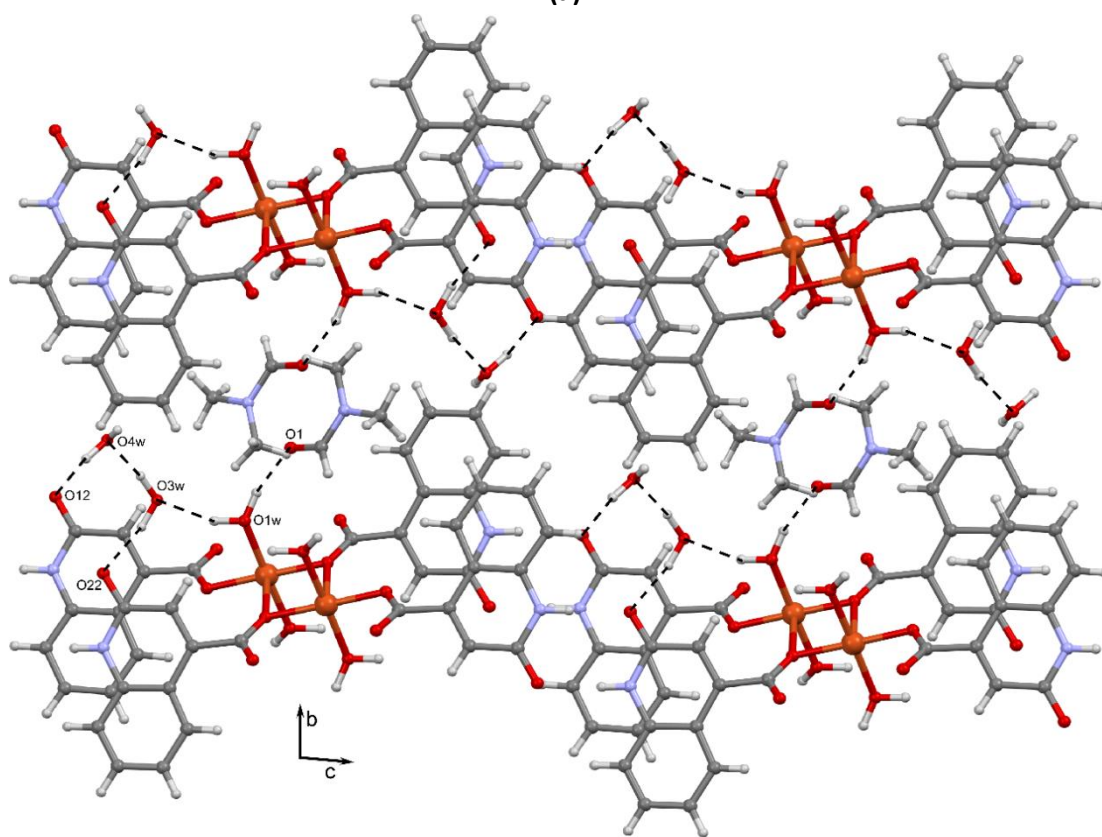
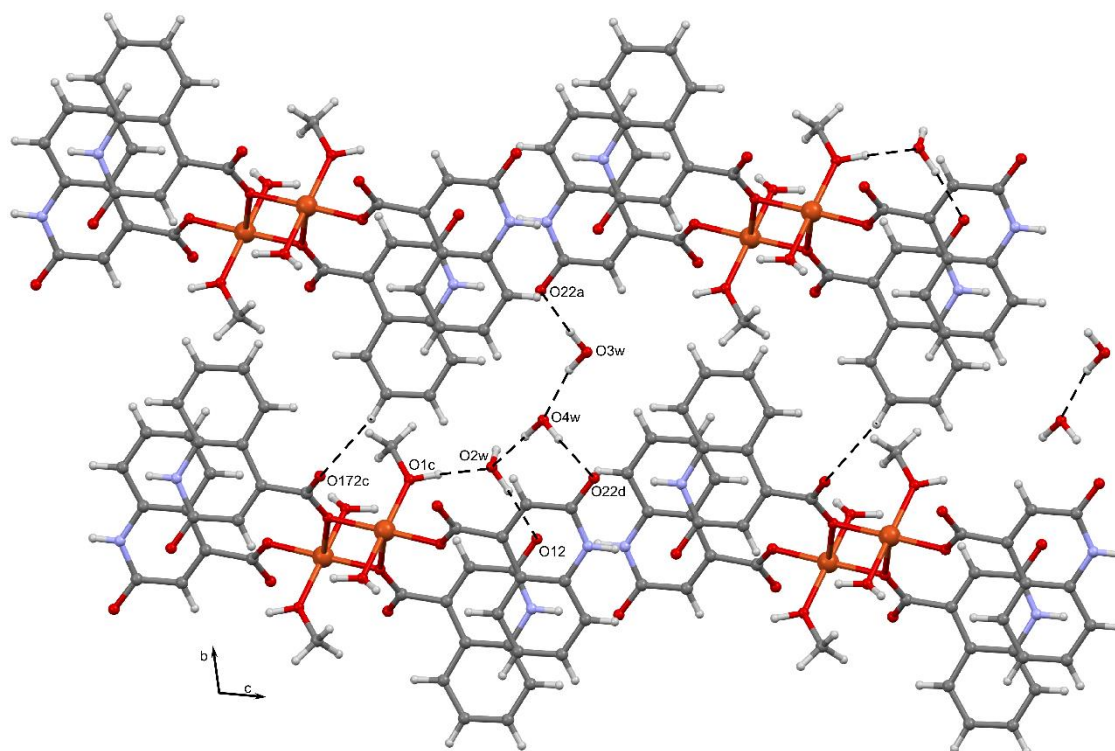


Figure 2.16. View of the crystal packing representing the non-covalent interactions between supramolecular in compounds 0D-CuHQMEOH (a), 0D-CuHQAQ (b).

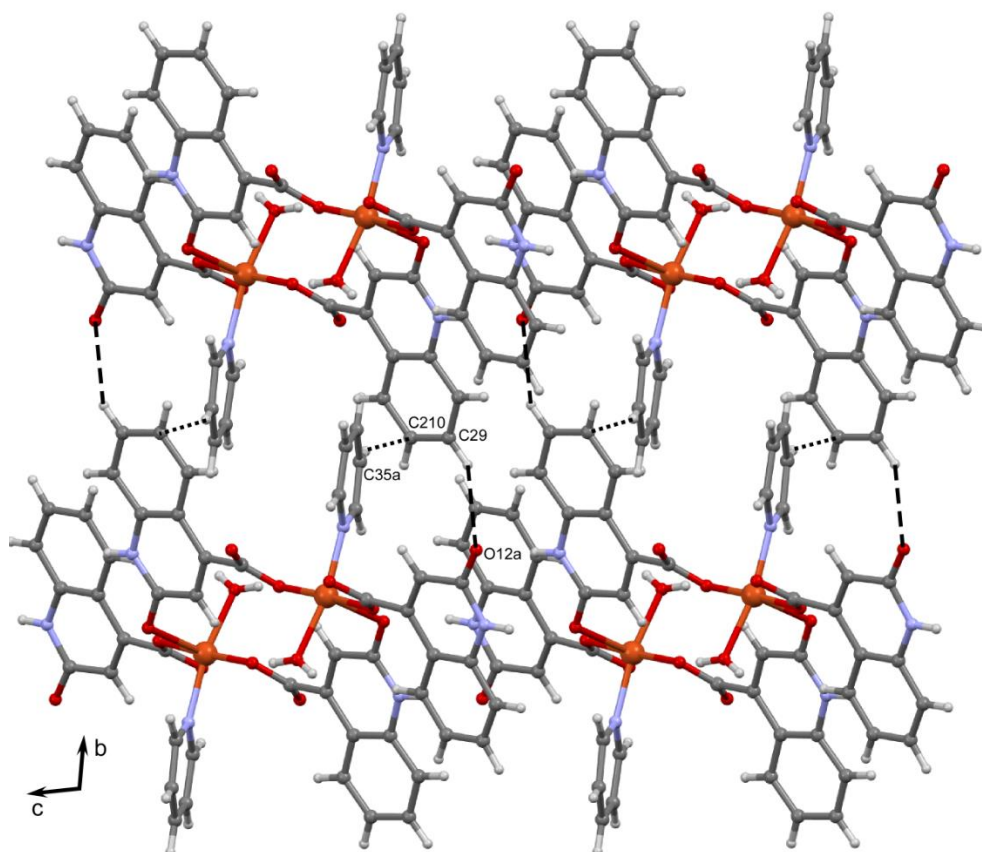


Figure 2.17. View of the crystal packing representing the non-covalent interactions between supramolecular in compound OD-CuHQPY.

Table 2.8. Hydrogen-bonding parameters (Å, °) of compound 0D-CuHQMEOH.¹

D–H...A	H...A	D...A	D–H...A
O1–H1...O2w	1.72	2.643(6)	177
O3w–H3w...O22a	1.92	2.822(1)	164
O2w–H2w2...O12b	1.88	2.789(2)	165
O2w–H2w1...O3wc	2.06	2.894(1)	151
O1w–H1w1...O272d	1.75	2.632(5)	162
O1w–H1w2...O172d	1.76	2.678(5)	172
O4w–H4w1...O2we	1.90	2.849(6)	176
O4w–H4w2...O22e	2.12	3.076(6)	177
N11–H11...O22f	1.93	2.777(7)	171
N21–H21...O12g	1.96	2.818(4)	178
C2–H2B...O1wb	2.36	3.266(5)	157
C23–H23...O4wh	2.60	3.043(8)	110
C110–H110...O172i	2.50	3.422(6)	169

¹: Symmetry-codes: (a) 2–x, 1–y, 1–z; (b) –x, 1–y, –z; (c) 1–x, 1–y, 1–z; (d) 1–x, 1–y, –z; (e) x, –1+y,z; (f) –1+x, y, –1+z; (g) 1+x, y, –1+z; (h) x, 1+y, z; (i) 1–x, 2–y, –z.

Table 2.9. Hydrogen-bonding parameters (Å, °) of compound 0D-CuHQAQ.¹

D–H···A	H···A	D···A	D–H···A
N21–H21···O12a	1.96	2.811(10)	171
O1w–H1W1···O1b	1.71	2.612(12)	165
O1w–H2W1···O3wd	1.87	2.702(9)	148
O2w–H2W2···O172c	1.80	2.682(9)	160
O2w–H1W2···O272c	1.70	2.638(10)	171
O3w–H1W3···O22d	1.83	2.749(10)	168
O3w–H2W3···O4wd	1.95	2.854(12)	160
O4w–H1W4···O12e	1.84	2.742(12)	162
N11–H11···O22f	1.90	2.758(10)	178
C2–H2A···O172d	2.54	3.350(2)	142
C210–H210···O3wb	2.49	3.272(14)	141

¹: Symmetry-codes: (a) $-1+x, y, -1+z$; (b) $1-x, -y, 1-z$; (c) $2-x, 1-y, 1-z$; (d) $1-x, 1-y, 1-z$; (e) $-1+x, y, z$; (f) $1+x, y, 1+z$.

Table 2.10. Hydrogen-bonding parameters (Å, °) of compound OD-CuHQPY.¹

D–H···A	H···A	D···A	D–H···A
O1w–H1W1···O272a	2.04	2.708(5)	137
O1w–H2W1···O172a	2.01	2.734(9)	146
N11–H11···O22b	2.13	2.976(7)	167
N21–H21···O12b	1.88	2.734(8)	170
C23–H23···O271	2.47	3.094(10)	124
C29–H29···O12c	2.57	3.403(5)	149
C32–H32···O172	2.56	3.345(6)	142
C111–H111···O171	2.46	2.999(8)	117
C211–H211···O272d	2.51	3.006(1)	114

¹: Symmetry-codes: (a) $-x, -y, 1-z$; (b) $-x, -y, 2-z$; (c) $1+x, 1+y, z$; (d) $1-x, 1-y, 1-z$.

2.3.2.2. Structural description of compound 2D-CuHQBPA.

The crystal structure of compound 2D-CuHQBPA consists of a two dimensional coordination framework of formula $[\text{Cu}_2(\mu\text{-HQ-}\kappa\text{O}_{\text{carboxylate}}:\kappa\text{O}'_{\text{carboxylate}})_4(\mu\text{-bpa-}\kappa\text{N}:\kappa\text{N}')]_n$ in which the asymmetric unit is comprised by a Cu(II) atom, two bridging HQ ligands and half bridging BPA ligand (Figure 2.18). As in previous cases, the NO_4 donor set fits to a distorted square pyramid polyhedron where the coordination bond implying the apical atom (O272a) is substantially longer than those corresponding the basal plane atoms (N31, O171, O271, O172a) (see Table 2.11).

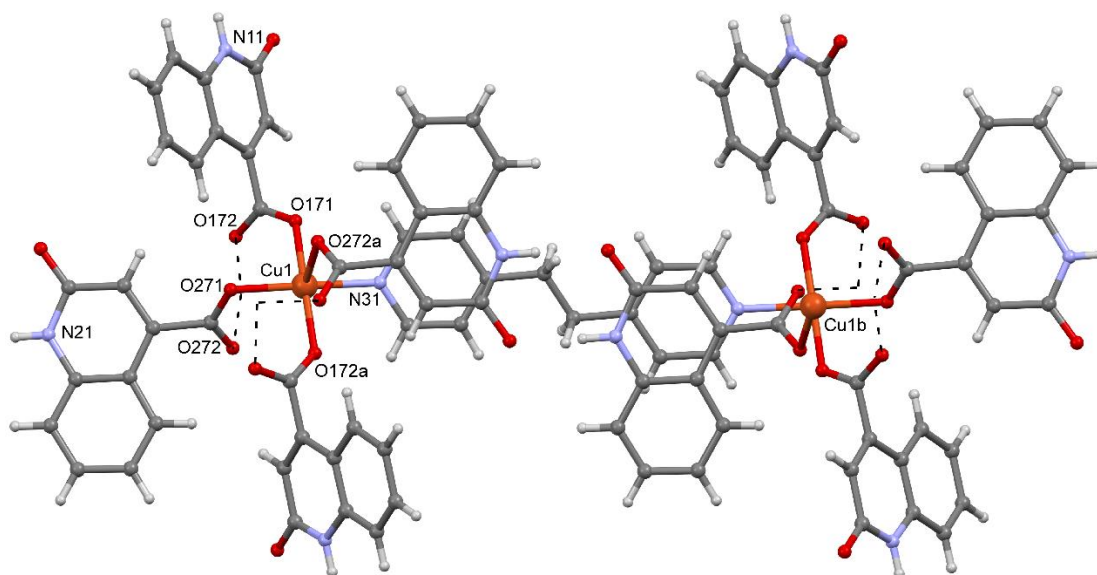


Figure 2.18. Depiction of the asymmetric unit of compound 2D-CuHQBPA. For clarity, the disordered counterpart of HQ-1 (see section 2.3.1) has been omitted in all the graphic representations of the current section.

Table 2.11. Coordination bond distances (Å) of compound 2D-CuHQBPA.¹

2D-CuHQBPA			
Cu1–O271	1.952(4)	Cu1–N31	2.000(5)
Cu1–O171	1.964(4)	Cu1–O272a	2.369(4)
Cu1–O172a	1.981(4)		

¹: Symmetry-codes: (a) $-x+1/2, y-1/2, -z+3/2$.

With regard to the molecular structure of the polymeric framework, subsequent Cu(II) atoms are assembled by double μ -HQ- $\kappa O_{\text{carboxylate}}:\kappa O'_{\text{carboxylate}}$ bridges into one-dimensional chains running along the [0 1 0] crystallographic direction (Figure 2.19). These chains are cross-linked by means of BPA bridges to yield a two-dimensional coordination network with a brick-wall type topology (point symbol: (6, 3)) (Figures 2.20a and 2.20b). It must be emphasized that, despite both symmetrically independent HQ ligands coordinate through equivalent donor atoms, HQ-1 and HQ-2 exhibit *syn-syn* and *syn-anti* bridging modes, respectively. This feature is of particular interest in the magnetic properties of complexes based on μ -carboxylate- $\kappa O:\kappa O'$ bridges, as the nature and magnitude of the magnetic exchange is tightly related to the *syn-syn*, *syn-anti* and *anti-anti* coordination modes. Therefore, it is further discussed in section 2.3.3 when describing the magnetic properties of compound 2D-CuHQBPA.

The 2D molecular structure is further stabilized by the recurrent pairing interaction (N21–H21...O22) between faced HQ-2 ligands of neighbouring chains (see inset graphic in Figure 2.21 and Table 2.12). Contrarily, HQ-1 is exposed outwards the coordination framework layers and it contributes to supramolecular self-assembling of the polymeric complexes (see below).

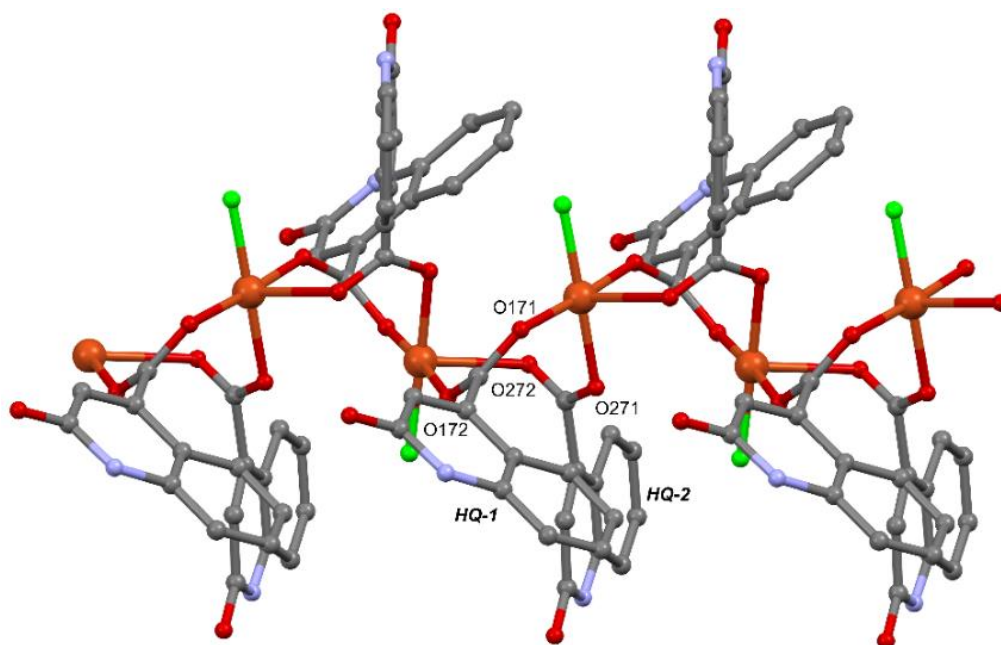
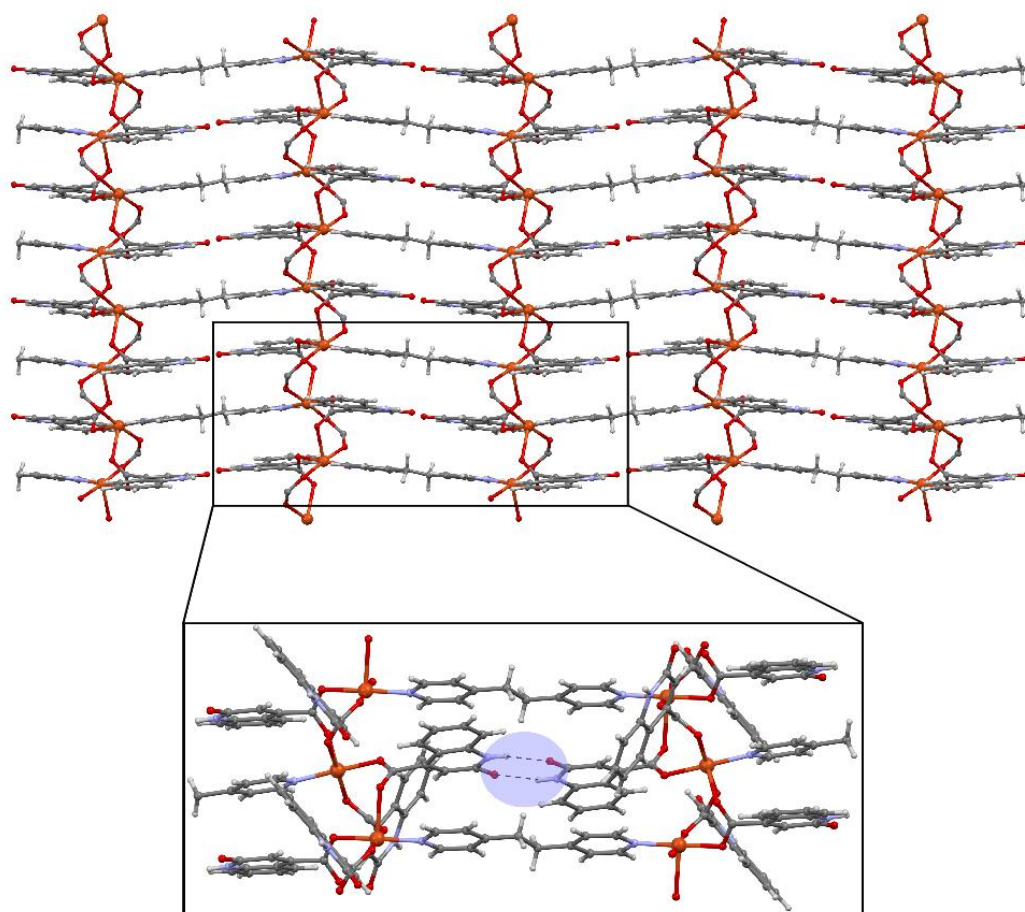
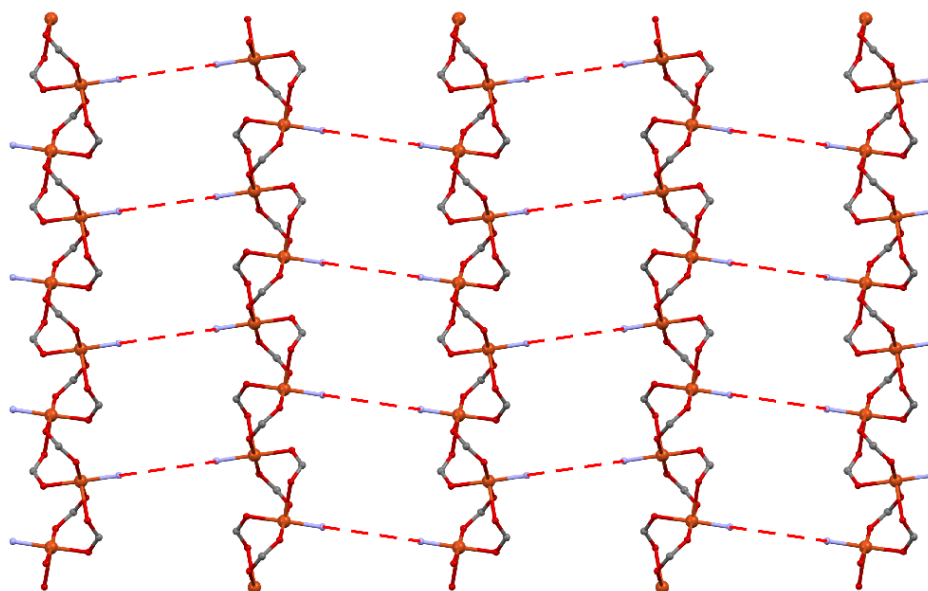


Figure 2.19. Fragment of the 1D chain built from Cu(II) and double μ -HQ- $\kappa O_{\text{carboxylate}}:\kappa O'_{\text{carboxylate}}$ bridges. For clarity, H atoms were omitted and BPA ligand was depicted by green atoms.



(a)



(b)

Figure 2.20. (a) View of the 2D coordination network through $[1\ 0\ 1]$ crystallographic direction. The inset graphic shows an enhanced area highlighting the complementary hydrogen bonding interactions between faced HQ-2 ligands (the fragment has been slightly rotated in order to observe more clearly the hydrogen bonding interaction). (b) Simplified representation of the 2D coordination network to enlighten brick-wall type topology (only Cu(II) atoms and donor groups of the bridging ligands were retained).

The 2D polymer layers pile up, in a staggered manner, along the [1 0 1] crystallographic direction (Figure 2.22). The resulting packing is compact and voids were not detected using a molecular probe of 1.2 Å. Neighbouring layers interact by means of the hydrogen bonding taking places between HQ-1 and HQ-2 ligands (N11–H11...O22). Furthermore, couples of HQ-1 ligands of upper and lower layers interact through face-to-face π - π contacts implying their phenyl group rings (centroid...centroid distance: 3.29 Å; centroid to plane distance: 3.05 Å; lateral displacement: 1.25 Å; plane tilting: 0.00 °; shortest C...C distance range: 3.05–3.31 Å).

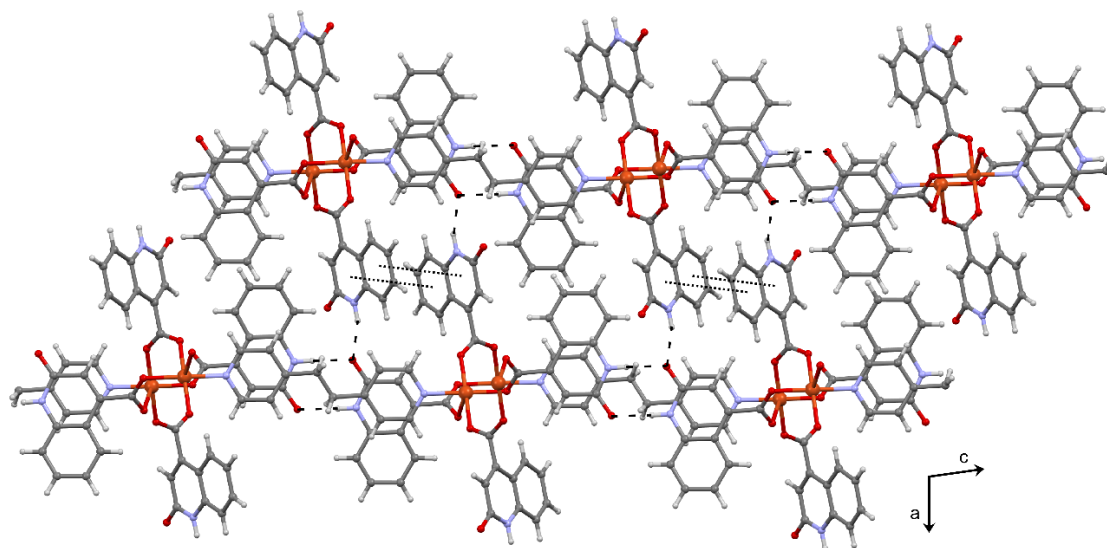


Figure 2.21. Crystal packing view of compound 2D-CuHQBPAA showing the HQ-1 mediated inter-layer interaction set (dashed and dotted lines stand for hydrogen bonding and π - π stacking respectively).

Table 2.12. Hydrogen bonding parameters (Å, °) in compound 2D-CuHQBPAA.¹

D–H...A	H...A	D...A	D–H...A
N11b–H11b...O22	2.17	2.921(3)	145
N21–H21...O22a	1.96	2.871(3)	171
C111–H111...O271	2.59	3.505(9)	169
N18b–H18b...O22	2.50	3.200(2)	132
C32–H32...O171	2.54	2.990(5)	110
C36–H36...O172c	2.40	2.853(3)	110
C211–H211...O272	2.59	3.116(6)	116

¹: Symmetry-codes: (a) 2–x, –y, –z; (b) 1–x, –y, –z; (c) 3/2–x, 1/2+y, 1/2–z.

2.3.2.3. Structural description of compound 1D-CuHQ.

Compound 1D-CuHQ is built up with the $[\text{Cu}_2(\mu\text{-HQ-}\kappa\text{O}_{\text{carboxylate}}:\kappa\text{O}'_{\text{carboxylate}})_4]$ paddle wheel entities envisaged in Figure 2.4 of the introductory section, however, unexpectedly these dinuclear entities self-assemble into a 1D-chain through an elongated coordination bond implying the coordinative unsaturated apical position and the carbonyl oxygen atom of a neighbouring dinuclear complex (Figure 2.22). As a result, while two of the HQ ligands (HQ-1) present the expected $\mu_2\text{-}\kappa\text{O}_{\text{carboxylate}}:\kappa\text{O}'_{\text{carboxylate}}$ coordination mode for a carboxylate bridge in a paddle-wheel type structure, the two remaining ones (HQ-2) behave as tridentate ligand ($\mu_3\text{-HQ-}\kappa\text{O}_{\text{carboxylate}}:\kappa\text{O}'_{\text{carboxylate}}:\kappa\text{O}_{\text{carbonyl}}$) linking to a third metal atom (that of a neighbouring dimer) through their carbonyl oxygen atom (O22). The coordination polyhedron around the copper atoms adopts a distorted square pyramid geometry, where the basal positions are occupied by the oxygen atoms of four carboxylate groups (with short bond distances: 1.96–1.97 Å) and the apical position is occupied by the oxygen atom of the carbonyl group (Cu1–O22: 2.14 Å). Table 2.13 shows the coordination bond lengths and angles around Cu(II) centres. The intradimeric Cu...Cu distances are as short as 2.63 Å, while the shortest interdimeric ones extend to 7.05 Å. As discussed in section 2.3.2, the latter feature will let us to model the magnetic behaviour of 1D-CuHQ as dinuclear entities.

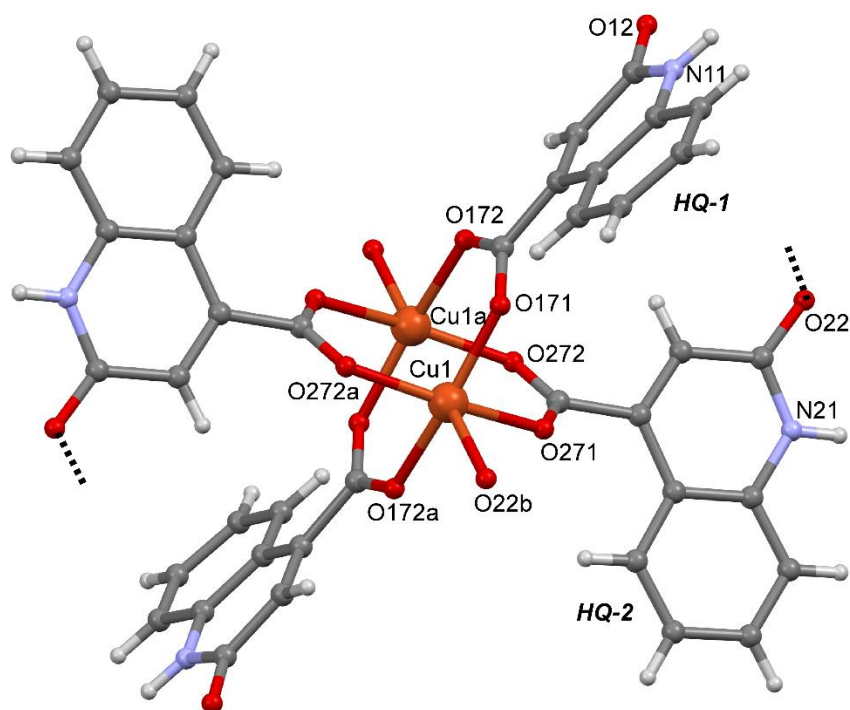


Figure 2.22. Dinuclear entity of compound 1D-CuHQ showing the labelling scheme. The HQ ligands adopt an UDD configuration (see legend of Figure 2.4).

Table 2.13. Coordination bond distances (Å) of compound 1D-CuHQ.

1D-CuHQ			
Cu1–O171	1.963(1)	Cu1–O272a	1.973(1)
Cu1–O172a	1.960(1)	Cu1–O22b	2.138(1)
Cu1–O271	1.970(1)	Cu1...Cu1a	2.633(4)

¹: Symmetry-codes: (a) $-x+1, -y+1, -z$; (b) $x, y, 1+z$.

Figure 2.23a shows a fragment of the polymeric chain which run along the [0 0 1] crystallographic direction. Despite the polymerization of the dinuclear entities, the supramolecular structure is governed by a similar synthon scheme to that predicted for the paddle-wheel shaped Cu/HQ complex (Figure 2.4). Precisely, each $[\text{Cu}_2(\mu\text{-HQ-}\kappa\text{O}_{\text{carboxylate}}:\kappa\text{O}'_{\text{carboxylate}})_4]$ subunit binds to another four subunits of neighbouring 1D-chains by means of the N–H...O pairing interactions of the HQ ligands (Figure 2.23b and Table 2.14). In fact, when considering the paddle-wheel entity as a node and the pairing interactions (N21–21...O6 /N11–H11...O1) among the HQ ligands as connectors, the overall three-dimensional network can be described topologically^[89] as a doubly interpenetrated 4-connected uninodal net with **lvt** topology (point symbol: $(4^2.8^4)$). Thus, the crystal structure could also be alternatively described as doubly interpenetrated porous **lvt**-type hydrogen-bonded networks, in which the paddle-wheel entities of the two coexisting supramolecular networks are successively assembled by means of an elongated coordination bond that implies the free apical position. The latter result can be regarded as a validation of the working hypothesis stated in the goals of this chapter. Furthermore, the HQ pairing interaction must be considered as a governing factor in the crystal packing, not necessarily being subordinated to the polymerization occurring through the elongated coordination bonds. In fact, when considering the amount of hydrogen bonds and coordination bonds that each dinuclear complex establishes (4 hydrogen-bond pairing interactions and 4 elongated coordination bonds) and their mean bond energies (hydrogen-bond pairing: -52 kJ/mol an equivalent N–H...O taking place in uracil ensembles^[90]; elongated-coordination bond: from -98 to -114 kJ/mol for equivalent Cu...O interactions taking place with the apical position of $[\text{Cu}_2(\text{COO})_4]$ paddle-wheel entity, it becomes clear that both growing vectors do not differ greatly in magnitude (4

⁸⁹ (a) TOPOS Main Page. <http://www.topos.ssu.samara.ru> (accessed Jan. 2015). (b) O'Keeffe, M.; Yaghi, O. M. *Chem. Rev.* **2012**, *112*, 675.

⁹⁰ (a) Hobza, P.; Jurečka, P.; Šponer, J.; *J. Am. Chem. Soc.* **2004**, *126*, 10142–10151. (b) Heine, T.; Mavrandonakis, A.; Supronowicz, B.; *J. Phys. Chem. C.* **2015**, *119*, 3024–3032.

hydrogen-bond pairing: -208 kJ/mol; 4 elongated-coordination bond: -392 to -456 kJ/mol). Nonetheless, further evidence provided by computed bond-energies on the current system will be desirable to support the aforementioned statement. To end up, it must be mentioned that in spite of the interpenetration, crystal packing exhibits isolated voids of *ca.* 180 \AA^3 that account for the 10 % of the total pore volume (Figure 2.24).

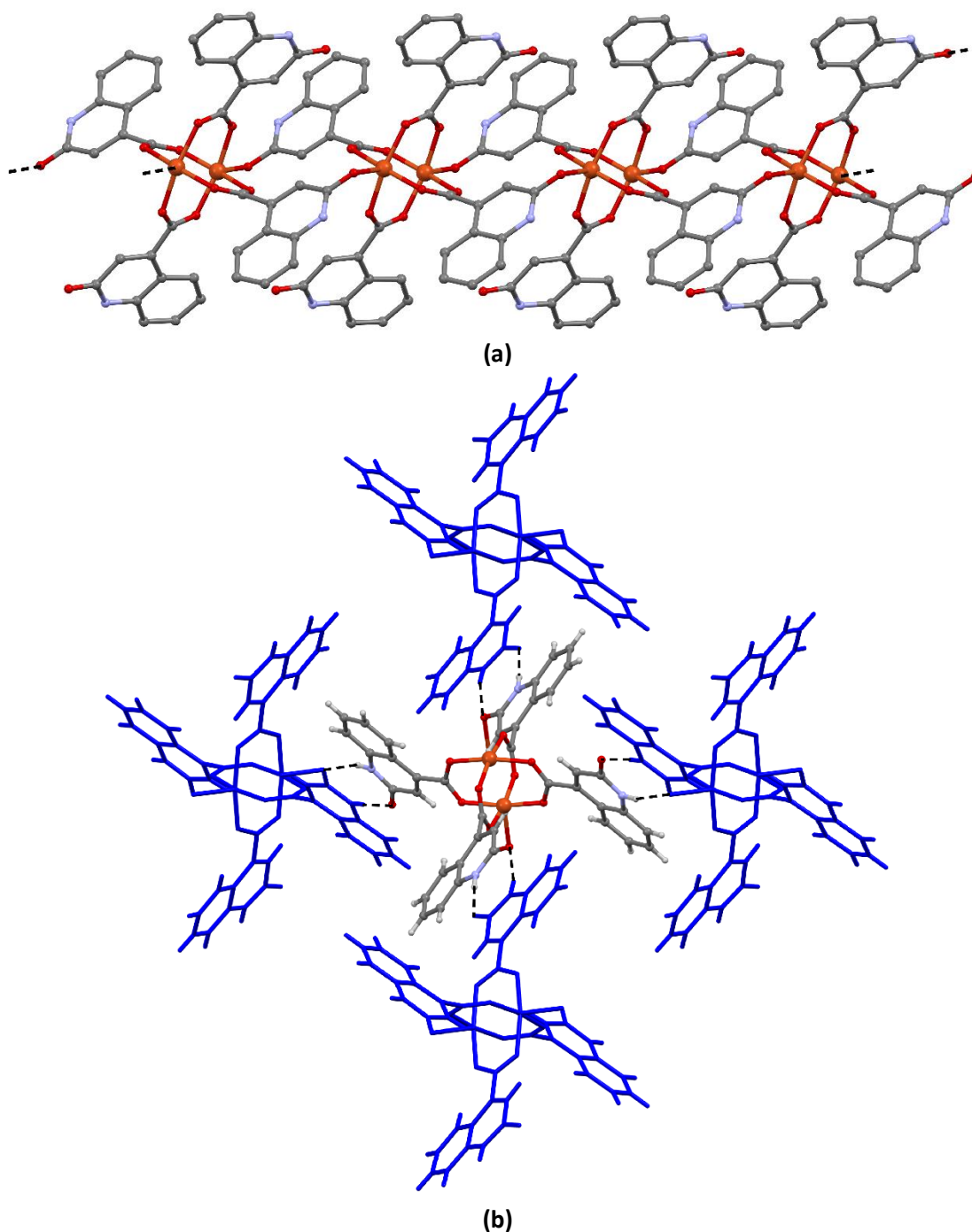
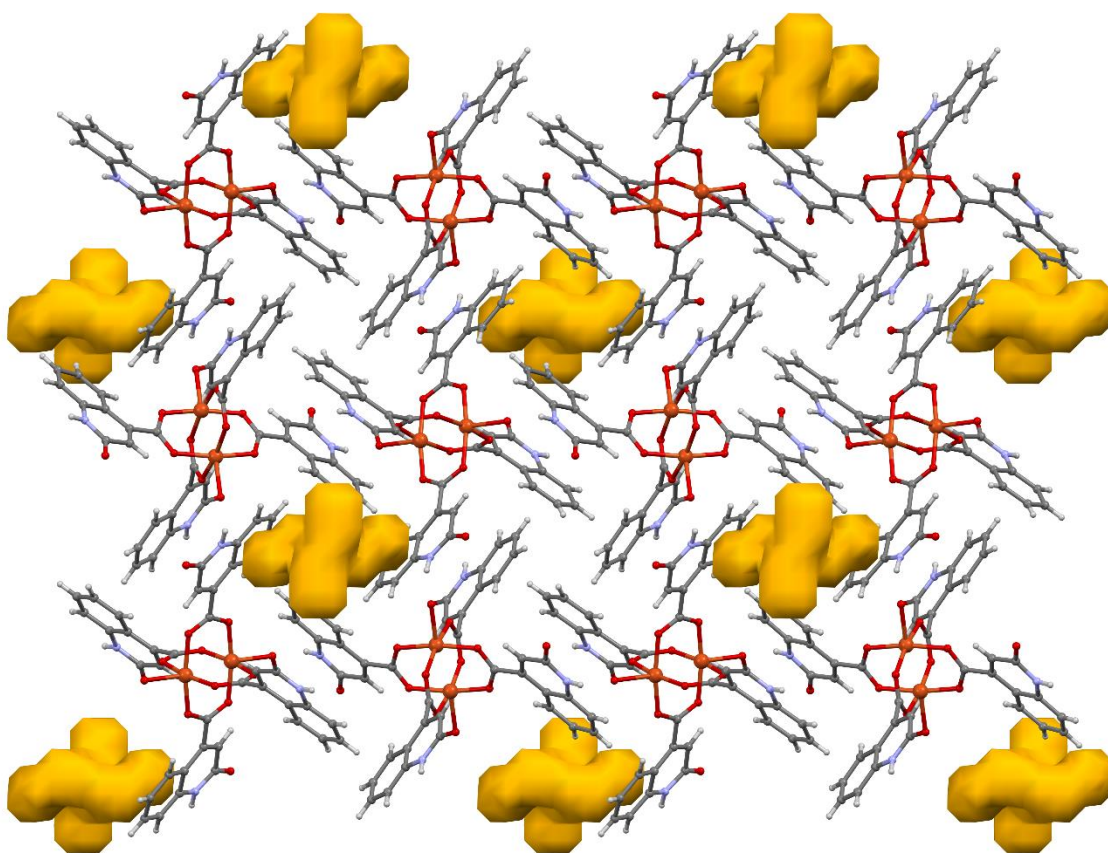


Figure 2.23. (a) Fragment of 1D polymeric chain of compound 1D-CuHQ. (b) HQ pairing interactions occurring between neighbouring paddle-wheel entities.

Table 2.14. Hydrogen-bonding parameters (Å, °) of compound 1D-CuHQ.¹

D–H···A	H···A	D···A	D–H···A
N11–H11···O22a	2.23	3.066(17)	164
N21–H21···O12b	1.84	2.691(18)	172
C18–H18···O171c	2.58	3.428(2)	151

¹: Symmetry-codes: (a) 1+x, y, 2-z; (b) x, 1+y, 2-z; (c) 1+x, y, 1-z.

**Figure 2.24.** Crystal packing of compound 1D-CuHQ showing the voids in yellow.

2.3.2.4. Structural description of compounds 0D-CuCBDQ.

The crystal structure of compound 0D-CuCBDQ is comprised of paddle-wheel shaped entities with formula $[\text{Cu}_2(\mu\text{-CBDQ-}kO_{\text{carboxylate}}:kO'_{\text{carboxylate}})_4(\text{H}_2\text{O})_2]$. Figure 2.25a shows a view of the complex structure with the numbering scheme, while Table 2.15 gathers the coordination bond distances. The coordination polyhedron of each Cu(II) resembles a distorted square pyramid in which the basal plane is completed by four carboxylate oxygen atoms of the CBDQ

ligands (distances of 1.92–2.03 Å) and the apical position is occupied by a water molecule with somewhat longer bond distance (*ca.* 2.10 Å). Contrarily to 1D-CuHQ, in compound 0D-CuCBDQ, the steric hindrance exerted by the bulkier CBDQ ligands hinders the self-assembling among neighbouring dinuclear entities into an analogous polymeric chain, and thus, the coordinative unsaturated sites of the paddle-wheel complex are occupied by two water molecules. The $\mu\text{-K}O_{\text{carboxylate}}:\text{K}O'_{\text{carboxylate}}$ coordination mode of the carboxylate groups leads to intradimeric Cu...Cu distance (2.66 Å) comparable to that found in 1D-CuHQ (2.63 Å), but markedly shorter than those observed in the dinuclear entities of section 2.3.2.1 (0D-CuHQMEOH, 0D-CuHQAQ and 0D-CuHQPY).

As mentioned in the introductory section of the current chapter, the high temperatures employed in the synthesis conditions of this compound caused the cycloaddition of the HQ ligands rendering CBDQ. This cycloaddition changes the hybridization of the third and fourth C-atoms (CX3 and CX4; X = 1 or 2) of the two cycloadded HQ ligands to sp^3 (Figure 2.25b) breaking the planarity of one of the rings. Besides, the cycloaddition of the ligand causes the torsion of the carboxylate groups (torsion angles: 104.13–114.35 ° and 109.70–119.55 ° for coordinated carboxylate and free carboxylate, respectively) to be much greater than in the above compounds, due to the tetrahedral geometry adopted by the CX4 atoms and to the resulting unrestrained rotation trough the $C_{X4}-C_{\text{carboxylate}}$ axis. Note that only one of the two carboxylate groups is implied in the coordination bonding, while the second one remains protonated.

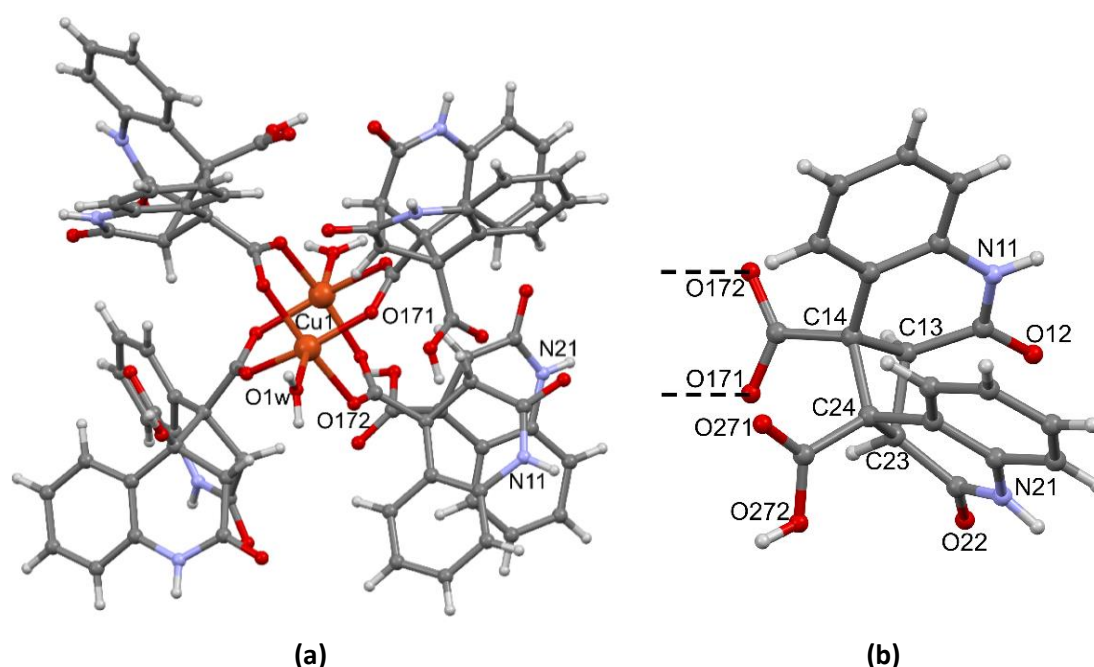


Figure 2.25. Dimeric entity (UUDU configuration) of compound 0D-CuCBDQ (a) and the CBDQ ligand resulting from the cycloaddition of two HQ molecules (b).

Table 2.15. Coordination bond distances (Å) of compound 0D-CuCBDQ.¹

0D-CuCBDQ			
Cu1–O171	1.916(1)	Cu1–O172c	2.032(1)
Cu1–O171a	1.916(1)	Cu1–O1w	2.102(3)
Cu1–O172b	2.032(1)	Cu1...Cu1b	2.659(9)

¹: Symmetry-codes: (a) $-x+1, -y+1/2, z$; (b) $-x+5/4, y-7/4, -z-9/4$; (c) $x-5/4, -y-1/4, -z-9/4$.

With regard to the crystal packing, it must be considered that despite of the unexpected cycloaddition the resulting paddle-wheel shaped Cu/CDBQ complex fulfils the aforementioned three criteria to yield a SMOF. Accordingly, the complex units are rigid molecular building blocks (1st criteria) that self-assemble by means of rigid and predictable synthons (2nd criteria) consisting of the complementary hydrogen bonding between N–H/C=O groups (as foreseen in Figure 2.3). Furthermore, the high number and disposition of the synthons ensures the three-dimensional growth of the supramolecular network (3rd criteria). In fact, considering the paddle-wheel entity as a node and the pairing interaction (N21–H21...O22; Table 2.16) among the CDBQ ligands as connectors, the overall three-dimensional network can be described topologically^[91] as a 4-connected unimodal net with diamond (**dia**) topology with a net point symbol (6⁶). Note that the growth of the supramolecular building by means of the complementary N–H/C=O hydrogen bonding implies only the non-coordinated HQ fragment of the CDBQ (Figure 2.25).

At this point, it becomes clear that the relative disposition of the HQ (or cycloaddition HQ) ligands within the paddle-wheel structure (see legend of Figure 2.4), determines the resulting topology of the supramolecular porous network, in such a way that the UDD configuration of 1D-CuHQ yield **lvt**-type network, while the UDUD configuration of 0D-CuCBDQ renders a **dia**-type network.

The **dia**-type framework of 0D-CuCBDQ is, as expected, highly porous (Figure 2.26a). However, the remaining porosity (72.9 %) is wide enough to allow the interpenetration of two more equivalent networks, giving rise to a triply interpenetrated diamond-like supramolecular network (Figure 2.26b). In spite of it, the overall crystal structure presents isolated voids of 365 Å³ that account for the 18.8 % of the total cell volume (Figure 2.27).

⁹¹ Blatov, V. A.: Multipurpose crystallochemical analysis with the program package TOPOS. *IuCr CompComm. Newsl.* **2006**, 7, 4–38.

It deserves to note, that neighbouring supramolecular networks interact by means of the single hydrogen bonding (N11–H11...O271; Table 2.16) occurring between the N–H group of a coordinated HQ fragment (HQ-1) and the carboxylate C=O group of the non-coordinated fragment (HQ-2). The remaining hydrogen bonding donor/acceptor groups are pointing towards the voids, which presumably enable to interact with the solvent molecules that could not be crystallographically located.

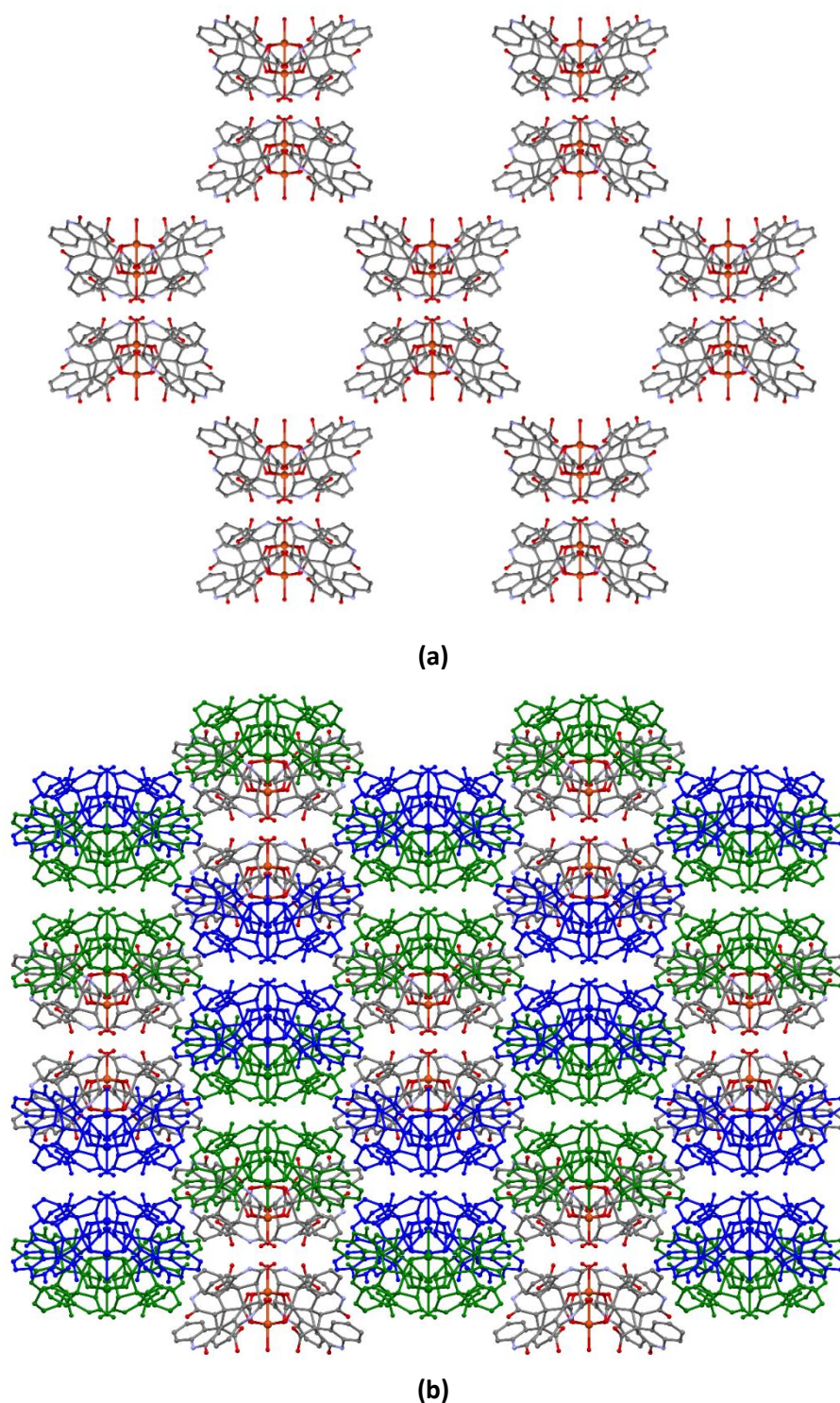


Figure 2.26. Crystal packing of compound OD-CuCBDQ showing the different single *dia*-like supramolecular network (a) and the triply interpenetrated structure (b). For clarity, hydrogen atoms have been omitted and complex entities belonging to the second and third networks have been coloured in blue and green, respectively.

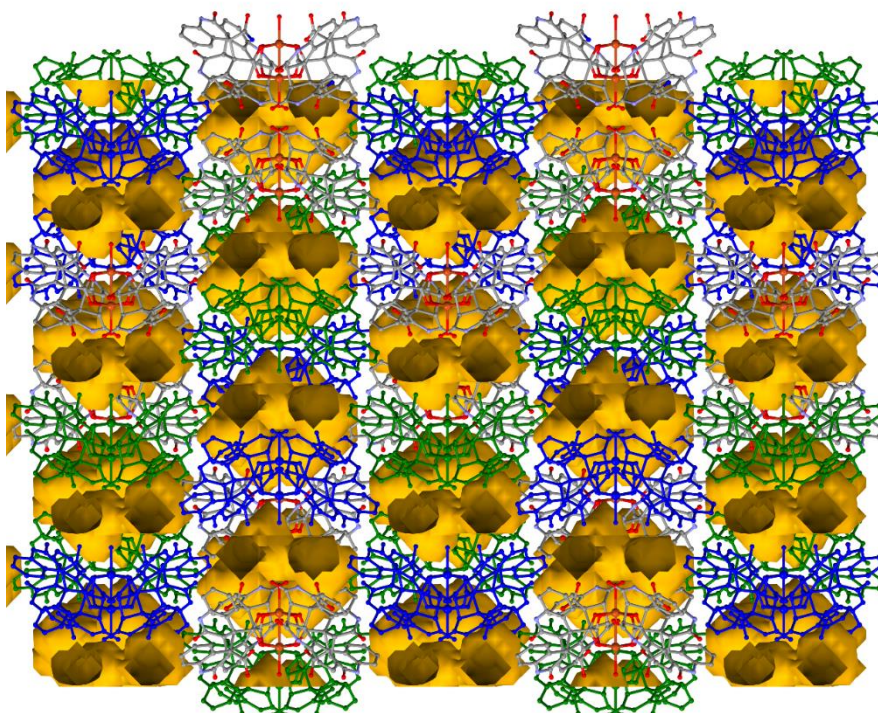


Figure 2.27. Crystal packing of compound 0D-CuCBDQ showing the voids in yellow.

Table 2.16. Hydrogen-bonding parameters (\AA , $^\circ$) of the non-covalent interactions in compound 0D-CuCBDQ.

D–H \cdots A	H \cdots A	D \cdots A	D–H \cdots A
N11–H11 \cdots O271a	2.08	2.887(3)	156
N21–H21 \cdots O22b	2.02	2.871(3)	171

¹: Symmetry-codes: (a) $-1/4+x, 1/4-y, -1/4+z$; (b) $-x, -y, 2-z$.

2.3.3. Magnetic properties.

According to the thermal evolution of the plots of the molar magnetic susceptibility (χ_m) and the $\chi_m T$ product (Figure 2.28 and 2.29), all the compounds described in this chapter exhibit an antiferromagnetic behaviour. χ_m curves of 0D-CuHQMEOH, 0D-CuHQAQ and 0D-CuHQPY display rounded maximums around 4.4, 4.4 and 7.8 K, respectively. The fitting of the χ_m^{-1} to the Curie-Weiss law provides Neel temperatures (T_N) of 2.44, 2.49 and 4.01 K, respectively. In compound 2D-CuHQBPA χ_m increases as the temperature decreases from room temperature and reaches a rounded maximum at approximately 40 K. Below 20 K, a new increase in the magnetic signal appears, attributable to the presence of paramagnetic impurities. In compound 1D-CuHQ, the magnetic susceptibility decreases continuously from room temperature until a null value at temperatures close to 50 K, which is indicative of a

stronger antiferromagnetic coupling probably coming from the intradimeric subunit interactions ($\text{Cu}\cdots\text{Cu}$: 2.633 Å) as the coordination mode bridging these dimeric subunits is longer ($\text{Cu}\cdots\text{Cu}$: 7.054 Å) and involves the elongated apical copper(II) position. The increase observed upon further cooling can be again attributed to the presence of paramagnetic impurities.

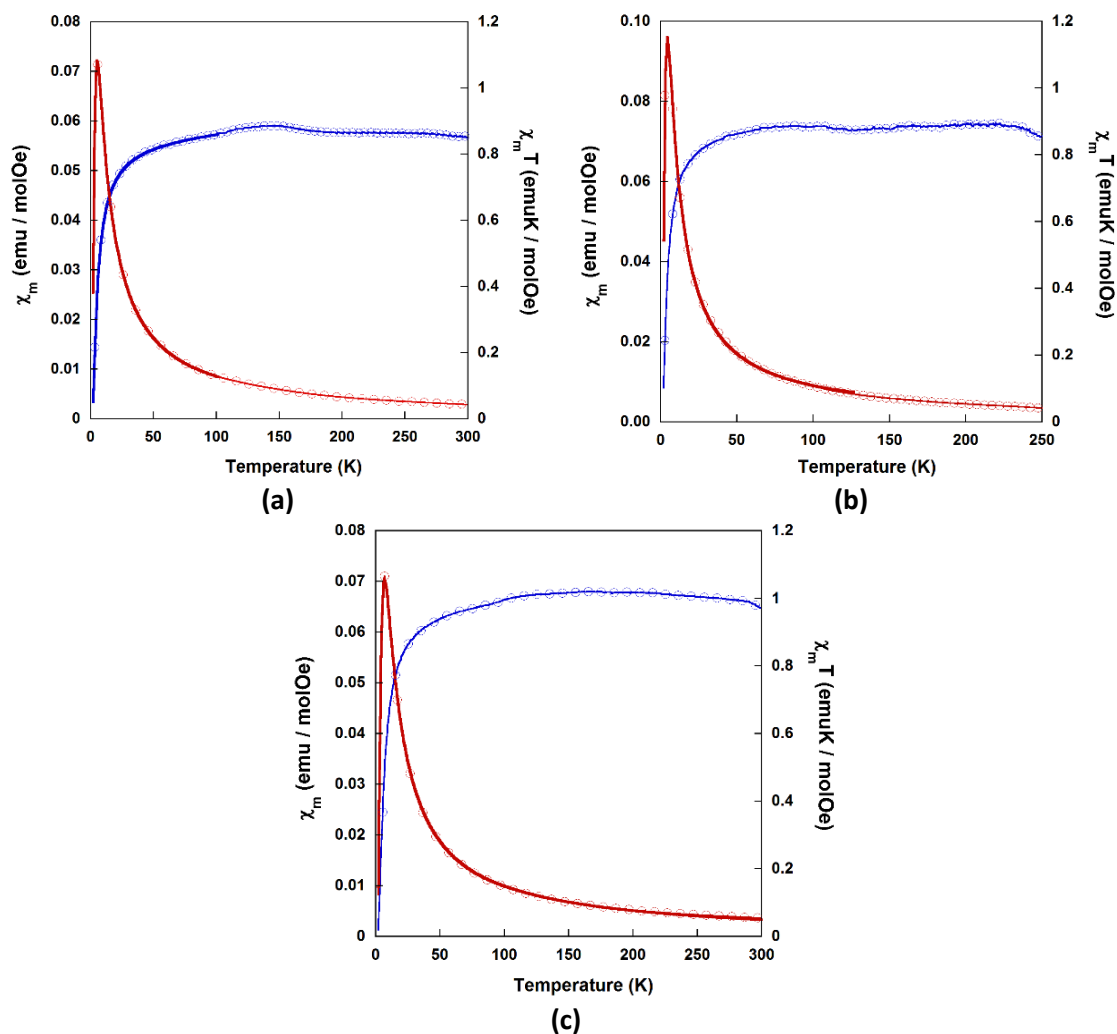


Figure 2.28. Thermal evolution of the molar magnetic susceptibility (χ_m) and the $\chi_m T$ product in compounds 0D-CuHQMEOH (a), 0D-CuHQAQ (b) and 0D-CuHQPY (c). Experimental χ_m value is represented by red circles, while the fitting to the magnetic data is depicted by a continuous line.

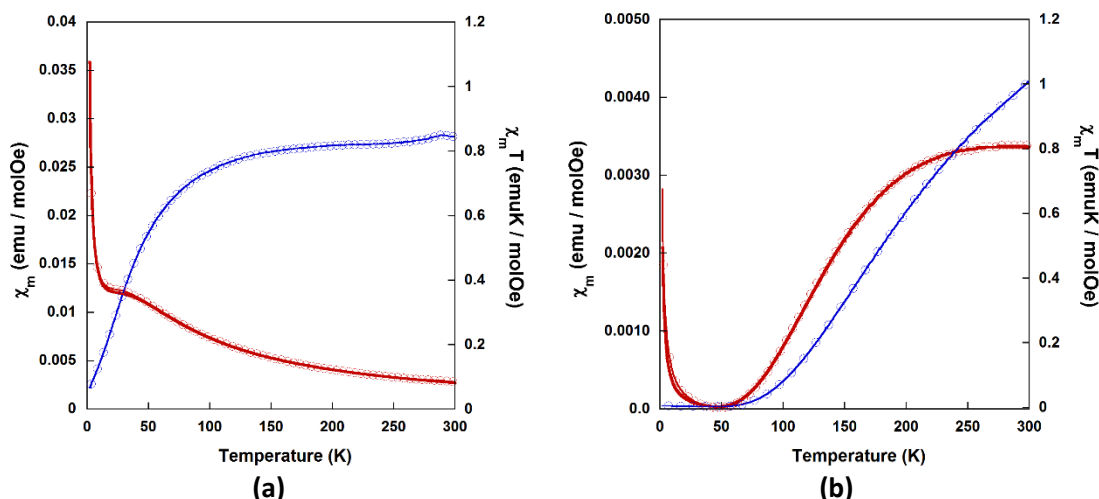


Figure 2.29. Thermal evolution of the molar magnetic susceptibility (χ_m) and the $\chi_m T$ product in compounds 2D-CuHQBPA (a) and 1D-CuHQ (b). Experimental χ_m value is represented by red circles, respectively, while the fitting to the magnetic data is depicted by a continuous line.

In compounds 0D-CuHQMEOH, 0D-CuHQAQ, 0D-CuHQPY and 2D-CuHQBPA, the product $\chi_m T$ at room temperature (RT) corresponds to the expected value for two magnetically isolated copper atoms ($S = 1/2$, $g = 2.1$, $\chi_m T(\text{expected}) = 0.840 \text{ cm}^3 \text{ mol}^{-1} \text{ K}$). The value of the $\chi_m T$ product remains almost unchanged until it reaches temperatures below 50 K, where it suffers a significant drop typical of the antiferromagnetic coupling. Contrarily, in compound 1D-CuHQ, $\chi_m T$ value at RT, is significantly below of the expected value and it continuously decreases upon cooling. This issue is indicative of the presence of stronger antiferromagnetic exchange interactions.^[92-93]

Compounds 0D-CuHQMEOH, 0D-CuHQAQ, 0D-CuHQPY and 1D-CuHQ can be considered as magnetically isolated dinuclear entities and thus, the magnetic data have been adjusted to the Bleaney-Bowers^[94] equation for copper(II) dimers ($H = -JS_1S_2$; $S = 1/2$), modified to include the presence of impurities. In compound 2D-CuHQBPA, despite of being a bidimensional coordination polymer, the magnetic coupling through $\mu\text{-bpa-}\kappa N:\kappa N'$ bridge (Cu...Cu: 13.405 Å) its longer and it can be disregarded with respect to the shorter double $\mu\text{-HQ-}\kappa O_{\text{carboxylate}}:\kappa O'_{\text{carboxylate}}$ bridge Cu...Cu: 3.783 Å. Therefore, the fitting of its magnetic data has been performed using the numerical expression obtained for an antiferromagnetic chain

⁹² Gutiérrez, L.; Alzuet, G.; Borrás, J.; Castiñeiras, A.; Rodríguez-Forteza, A.; Ruiz, E. *Inorg. Chem.* **2001**, *40*, 3089–3096.

⁹³ (a) Rodríguez-Forteza, A. Alemany, P.; Alvarez, S.; Ruiz, E. *Chem. Eur. J.* **2001**, *7*, 627. (b) Youngme, S.; Cheansirisomboon, A.; Danvirutai, C.; Pakawatchai, C.; Chaichit, N.; Engkagul, C.; A. van Albada, G.; Sanchez-Costa, J.; Reedijk, J. *Polyhedron* **2008**, *27*, 1875. (c) Fontanet, M.; Popescu, A-R.; Fontrodona, X.; Rodríguez, M.; Romero, I.; Teixidor, F.; Viñas, C.; Aliaga-Alcalde, N.; Ruiz, E. *Chem. Eur. J.* **2011**, *17*, 13217. (d) Cejudo, R.; Alzuet, G.; Borrás, J.; Liu-González, M.; Sanz-Ruiz, F. *Polyhedron* **2002**, *21*, 1057.

⁹⁴ Bleaney, B.; Bowers, K. D. *Proc. R. Soc. London Ser. A.* **1952**, *214*, 451.

from the Hamiltonian $H = -J\sum_i S_i S_{i+1}$ with $S = \frac{1}{2}$.^[95] The data obtained from the fittings are shown in Table 2.17.

Table 2.17. Magnetic data of all compounds.

	$\chi_m T$ (cm ³ mol ⁻¹ K) ^[a]	J (cm ⁻¹) ^[b]	g	ρ (%) ^[c]
0D-CuHQMEOH	0.848	-4.86	2.14	0.0
0D-CuHQAQ	0.838	-4.93	2.12	0.0
0D-CuHQPY	0.971	-7.64	2.26	0.0
2D-CuHQBPA	0.526	-37.70	2.20	5.5
1D-CuHQ	1.014	-312.00	2.25	0.2

[a] $\chi_m T$ value at room temperature. [b] Calculated value of the constant of magnetic coupling. [c] Paramagnetic impurity percentage.

For Cu(II) dinuclear complexes, the constant of magnetic coupling can be defined with this equation ($J = 2j + 4\beta S = J_F + J_{AF}$)^[96] where j , β and S are the bielectronic exchange, mono-electronic resonance and overall integrals between the two magnetic orbitals centred at the two metal atoms. The first term is positive and represents the ferromagnetic contribution (J_F), favouring parallel alignment of the spins, while the second one is negative and represents the antiferromagnetic contribution (J_{AF}), favouring antiparallel alignment of the spins.

In compounds 0D-CuHQMEOH and 0D-CuHQAQ the magnetic coupling is dominated by the features of the double μ -HQ- κ O: κ O bridge in which each O-bridge atom shows an axial-equatorial arrangement with regard the magnetic orbital (Figure 2.30). Note that according to the distorted square-pyramid coordination geometry of the Cu(II) atoms, the unpaired electron resides primarily on a $d_{x^2-y^2}$ orbital, and therefore, the axial bonds established by the bridging O-atom are almost perpendicular to the magnetic plane. This type of disposition leads to small overlap between the localized magnetic orbitals and thus weak antiferromagnetic or ferromagnetic interactions are observed with J values usually ranging from -5 to $+1$ cm⁻¹.^[97] The nature and magnitude of the magnetic coupling constant of complexes with asymmetric

⁹⁵ (a) Hall, J. W. PhD Dissertation, University of North Carolina, 1977. (b) Bonner, J. Fisher, M. *Phys. Rev.*, **1964**, *135*, A640.

⁹⁶ Kahn, O. *Molecular Magnetism*; VCH: New York, 1993.

⁹⁷ (a) Chiari, B.; Helms, J. H.; Piovesana, O.; Tarantelli, T.; Zanazzi, P. *Inorg. Chem.*, **1986**, *25*, 2408. (b) Greenaway, A. M.; O'Connor, J. C.; Overman, J. W.; Sinn, E. *Inorg. Chem.*, **1981**, *20*, 1508. (c) Pasini, A.; Demartin, F.; Piovesana, O.; Chiari, B.; Cinti, A.; Crispu, O. *J. Chem. Soc., Dalton. Trans.*, **2000**, 3467. (d) Escribá, E.; Server-Carrió, J.; Lezama, L.; Folgado, J. V.; Pizarro, J. L.; Ballesteros, R.; Abarca, B. *J. Chem. Soc., Dalton. Trans.*, **1997**, 2033.

double μ -oxo bridges, depend largely on the angle ϕ ($\text{Cu}-\text{O}\cdots\text{Cu}$) and the out of plane bond length R_o ($\text{Cu}\cdots\text{O}$), since these factors determine the degree of overlap between $d_{x^2-y^2}$ magnetic orbitals.^[98] For ϕ values greater than 97.5° antiferromagnetic term prevails, which is in agreement with the J values observed for 0D-CuHQMEOH and 0D-CuHQAQ (ϕ : 104° and 100° , respectively).

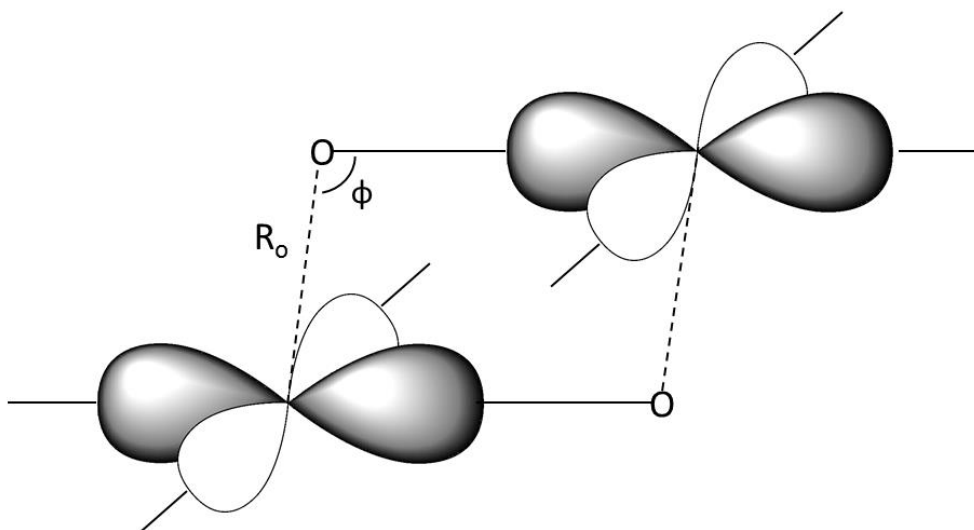


Figure 2.30. Schematic representation of a Cu(II) dimer in which the double bridge μ -oxo establishes a parallel disposition between the magnetic planes.

With regard to 0D-CuHQPY compound, despite the double μ -HQ- $\kappa\text{O}:\kappa\text{O}'$ bridge establishes larger $\text{Cu}\cdots\text{Cu}$ distance (7.25 \AA) than the those found in the previous two complexes (3.44 and 3.39 \AA for 0D-CuHQMEOH and 0D-CuHQAQ, respectively), the antiferromagnetic coupling is slightly greater. This probably can be attributed to the delocalization of the magnetic orbital into the π -system of the HQ ligand and the related spin polarization taking place along the bridge.^[99]

For compounds 1D-CuHQ and 2D-CuHQBPA, where the metal atoms are bridged through the carboxylate group of the HQ ligand (μ -HQ- $\kappa\text{O}_{\text{carboxylate}}:\kappa\text{O}'_{\text{carboxylate}}$), the nature and magnitude of the coupling constant is intimately associated to the coordination geometry of the carboxylate (Figure 2.31). While *anti-syn* and *anti-anti* coordination modes^[100] exhibit very

⁹⁸ (a) Hatfield, W. E. *Inorg. Chem.*, **1983**, *22*, 833. (b) Hatfield, W. E. *Comments Inorg. Chem.*, **1981**, *1*, 105. (c) Bencini, A. Gatteschi, D. *Inorg. Chim. Acta*, **1978**, *31*, 11. (d) A. van Albada, G.; Mutikainen, I.; J.J. Smeets, W.; L. Spek, A.; Turpeinen, U.; Reedijk, J. *Inorg. Chim. Acta*, **2002**, *327*, 134–139.

⁹⁹ (a) Beobide, G.; Castillo, O.; Luque, A.; García-Couceiro, U.; García-Teran, J.P.; Román, P. *Dalton Trans.*, **2007**, 2669-2680. (b) Ruiz, E.; Rodríguez-Fortea, A.; Alvarez, S. *Inorg. Chem.*, **2003**, *42*, 4881. (c) Thompson, A. M. W. Gatteschi, D.; McCleverty, J.A.; Navas, J.A.; Rentschler, E.; Ward, M.D. *Inorg. Chem.*, **1996**, *35*, 2701. (d) McConell, S. H. *J. Chem. Phys.*, **1963**, *39*, 1910

¹⁰⁰ (a) Delgado, F. S.; Hernandez-Molina, M.; Sanchez, J.; Ruiz-Perez, C.; Rodriguez-Martin, Y.; Lopez, T.; Lloret, F.; Julve, M. *Cryst. Eng. Comm.*, **2004**, *6*, 106. (b) Montney, M. R.; LaDuca, R. L. *Inorg. Chem. Comm.*, **2007**, *10*, 1518–1522. (c) Colacio, E.; Ghazi, M.; Kivekäs, R.; Moreno, J. M. *Inorg. Chem.* **2000**, *39*, 2882-2890. (e) Colacio, E.; Domínguez-Vera, J.M.; Ghazi, M.; Kivekäs, R.; Klinga,

weak ferro- or antiferromagnetic couplings (from +1.7 to -82.0 cm^{-1}) and weak antiferromagnetic couplings (from -1.1 to -41.0 cm^{-1}), respectively, the *syn-syn* coordination mode leads to stronger antiferromagnetic couplings (from -156 to -378 cm^{-1}).^[101] In compound 2D-CuHQBPAA, each pair of copper atoms are bridged by both *syn-syn* and *syn-anti* carboxylate with equatorial···equatorial and equatorial···axial arrangement, respectively. Therefore, the magnetic coupling of the Cu(II) atoms is mainly driven through the *syn-syn* carboxylate bridge. In fact, the resulting *J* value fits reasonably well respect to the expect one. In compound 1D-CuHQ, the Cu(II) atoms are bridged simultaneously by four *syn-syn* carboxylate bridges within the dinuclear cores, $[\text{Cu}_2(\mu\text{-HQ-}\kappa\text{O}_{\text{carboxylate}}:\kappa\text{O}'_{\text{carboxylate}})_4]$, and reasonably, the magnetic coupling is notably greater than that of the previous case, but comparable to other reported Cu(II) paddle-wheel structures based on carboxylate bridges.

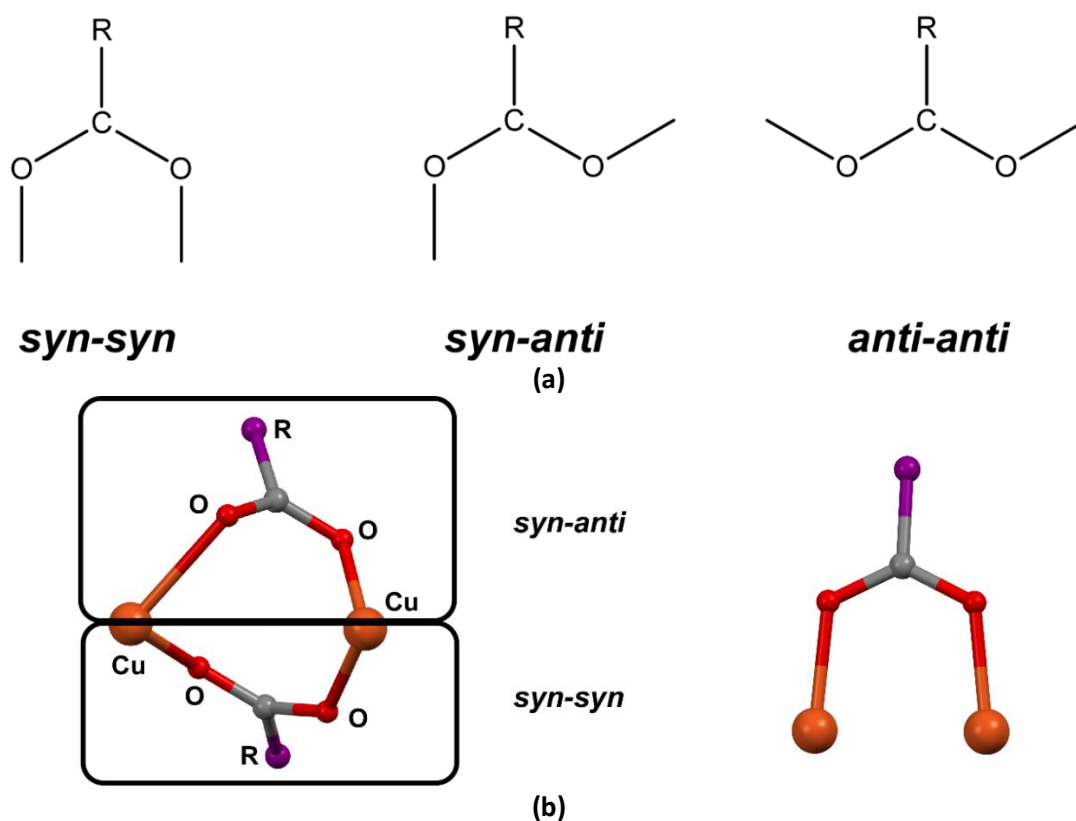


Figure 2.31. Coordination geometries of a bidentate carboxylate bridge (A) and the coordination modes found in compound 2D-CuHQBPAA and 1D-CuHQ respectively (B).

M.; Moreno, J. M. *Eur. J. Inorg. Chem.* **1999**, 441–445. (f) Delgado, F. S.; Sanchiz, J.; Ruiz-Perez, C.; Lloret, F.; Julve, M. *CrystEngComm*, **2004**, 6(73), 443–450. (g) Delgado, F. S.; Sanchiz, J.; Ruiz-Perez, C.; Lloret, F.; Julve, M. *Inorg. Chem.*, **2003**, 42, 5938–5948. (h) Suarez-Varela, J.; Mota, A. J.; Aouryaghal, H.; Cano, J.; Rodriguez-Dieguez, A.; Luneau, D.; Colacio, E. *Inorg. Chem.* **2008**, 47, 8143–8158.

¹⁰¹ (a) Dali, S.; Mukherjee, P. S.; Zangrando, E.; Lloret, F.; Chaudhuri, N. R. *J. Chem. Soc., Dalton Trans.*, **2000**, 822. (b) de Campos, N. R.; Ribeiro, M. A.; Oliveira, W. X. C.; Reis, D. O.; Stumpf, H. O.; Doriguetto, A. C.; Machado, F. C.; Pinheiro, C. B.; Lloret, F.; Julve, M.; Canof, J.; Marinho, M. V. *Dalton Trans.*, **2016**, 45, 172–189. (c) Bravo-García, L.; Barandika, G.; Fidalgo-Marijuan, A.; Bazan, B.; Urtiaga, M. K.; Lezama, L.; Arriortua, M. I., *Eur. J. Inorg. Chem.* **2016**, 4783–4791.

The magnetization vs applied field (M-H) curves at 2K of all compounds are gathered at Figure 2.32. On one hand, the magnetization curves of 1D-CuHQ ($J = -312.0 \text{ cm}^{-1}$) and 0D-CuHQBPA ($J = -37.7 \text{ cm}^{-1}$) are in good agreement with the expected ones for antiferromagnetic sample with smaller slope. Thus, the antiferromagnetic interaction increases and the magnetization values at 70 kOe are far below from the theoretical saturation magnetic moment ($2 \mu_B$ per Cu dinuclear unit). On the other hand, it is noteworthy that the curves of 0D-CuHQMeOH, 0D-CuHQQAQ and 0D-CuHQPY resemble sigmoidal shapes, which suggests the occurrence of a metamagnetic phase transition, from an antiferromagnetic state to an intramolecular ferromagnetic state. Moreover, take into account that the first slope change observed in compound CUHQQAQ (also in compound CUHQBPA) is due to the presence of the paramagnetic impurities detailed in the magnetic susceptibility measurement.

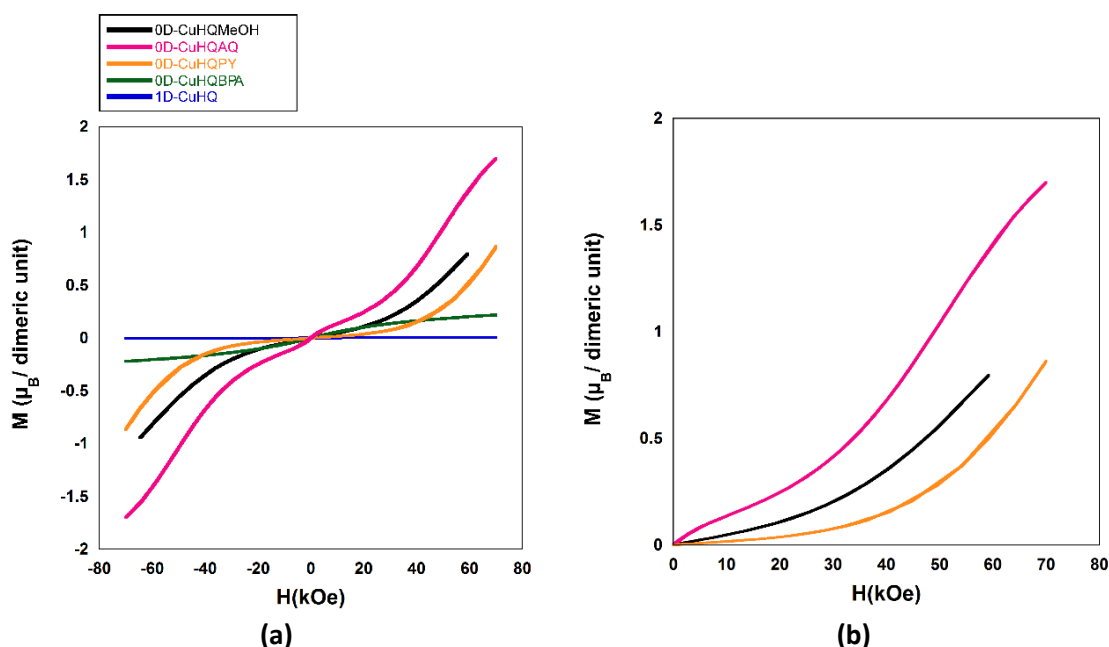


Figure 2.32. Magnetization (M) vs applied field (H) curves at 2 K for compounds of Chapter 2: (a) 0D-CuHQMeOH (black), 0D-CuHQQAQ (pink), 0D-CuHQPY (orange), 0D-CuHQBPA (green) and 1D-CuHQ (blue). (b) Clear observation of the metamagnetic effect in compounds 0D-CuHQMeOH (black), 0D-CuHQQAQ (pink) and 0D-CuHQPY (orange).

This kind of magnetic phenomena is favoured in compounds with very weak antiferromagnetic interactions in which the latter is overcome by an external applied field.^[102] This transition can be explained by the split of the spin states caused by the applied magnetic field (i.e. Zeeman effect) (Figure 2.33). At null magnetic field, antiferromagnetically coupled Cu(II) atoms yield an $S = 0$ ground state and an $S = 1$ excited state separated by an energy gap

¹⁰² (a) Son, K; Kim, J. Y; Schütz, G; Kang, S. G; Moon, H. R; Oh, H; *Inorg. Chem.* **2019**, *58*, 8895–8899. (b) Zheng, L. M; Gao, S; Song, H.-H; Decurtins, S; Jacobson, A. J; *Xin Chem. Mater.*, **2002**, *14*, 7, 3143-3147. (c) Pasán, J; Sanchiz, J; Ruiz-Pérez, C; Campo, J; Lloret, F; Julved, M. *Chem. Commun.*, **2006**, *27*, 2857–2859.

(J). Under an applied external magnetic field, the degeneracy of the triplet state is broken, so that there is a critical field (H_c) at which the energy gap between the ground state and the lower branch of the excited state is suppressed. At this point, the ground state is no longer than the singlet state but it is higher than the $|1, -1\rangle$ level derived from the triplet state. The general expression for the energy of the spin-state (equation 1) and the magnetic coupling J parameter definition (equation 1) can be assembled to provide an estimation of the critical field (equation 3) at which this transition takes place.

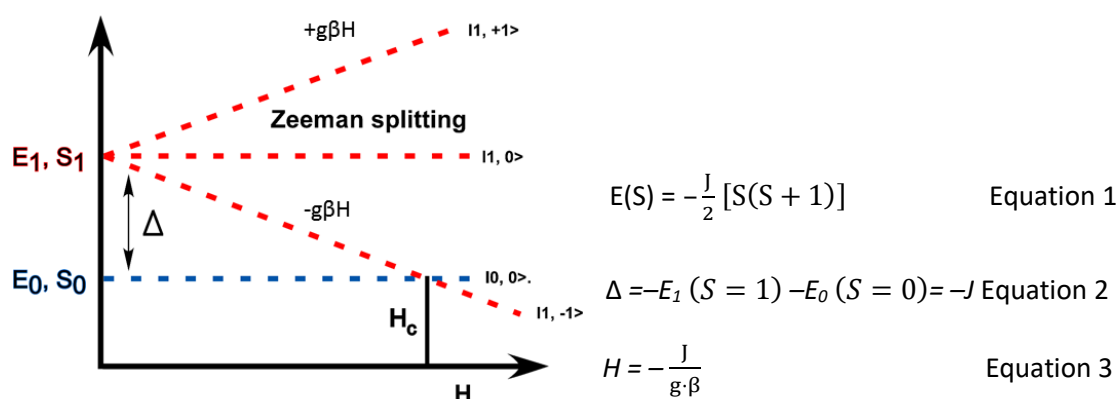


Figure 2.33. Energy diagram for a antiferromagnetically coupled Cu(II) dimer, showing the splitting produced under an applied magnetic field.

Accordingly to it, the stronger the antiferromagnetic coupling, the greater the critical magnetic field. This qualitative assertion is in good agreement with the trend observed for the H_c experimental values (Table 2.18). The H_c calculated values using equation 3 slightly overestimate the experimental ones, but they follow the same trend. Finally, the compounds with almost the same J value also show very similar H_c values.

Table 2.18. Comparison of the experimental and calculated critical magnetic fields with the magnetic coupling constants of compounds OD-CuHQMEOH, OD-CuHQAQ and OD-CuHQPYP.¹

	$H_{c(\text{exp.})}$ (kOe)	$H_{c(\text{calc.})}$ (kOe)	J (cm^{-1}) ^[b]
OD-CuHQMEOH	31.6	48.7	-4.86
OD-CuHQAQ	31.1	49.8	-4.93
OD-CuHQPYP	44.0	72.4	-7.64

¹ $H_{c(\text{exp.})}$: experimental critical magnetic field estimated from the magnetization data. $H_{c(\text{calc.})}$: calculated critical magnetic field using equation 3.

Chapter 3: Homometallic adenine nucleobase based SMOFs

3.1. Introduction

3.2. Synthesis and chemical characterization

3.3. Results and discussion

3.1. INTRODUCTION

Considering the results obtained in the previous chapter, it was decided to go a step further in the formation of SMOFs, using instead the HQ ligand, the well-known puric base adenine. Adenine (6-aminopurine) is the most widely used nucleobase for the formation of coordination compounds since it has five nitrogen atoms that give it great versatility as a ligand. Adenine, as many nitrogen bases, is characterized by its acid-base balance, which allows it to be found both in neutral (adenine: HAD), cationic (adeninium: H₂AD) and anionic (adeninate: AD) forms depending on the pH of the medium, with the consequent modification of its coordinative properties (Figure 3.1). Being a stronger base, it allows obtaining not only monomeric^[103] and polynuclear compounds,^[104,105] but also 3D networks.^[30]

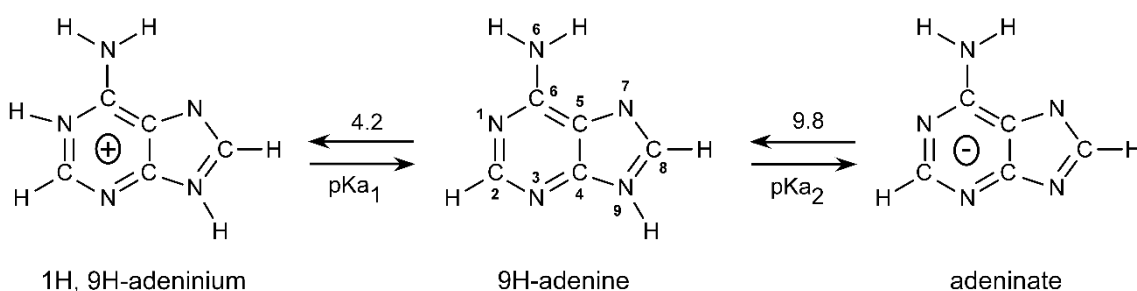


Figure 3.1. Acid-base equilibria of adenine.

In order to synthesize SMOFs, this ligand provides, at one hand, the advantage of the increased rigidity of the supramolecular building block due to the coordination through multiple positions, and, at the other hand, it presents many edges capable of establishing complementary hydrogen bonding interactions that provide rigid and predictable synthons capable of promoting the self-assembly of the building blocks (Figure 3.2 and Figure 3.3).^[106]

¹⁰³ Beck, W. M.; Calabrese, J.C.; Kottmair, N. *Inorg. Chem.* **1979**, *18*, 176.

¹⁰⁴ Hubert, J.; Beauchamp, A. L. *Acta Crystallogr.* **1980**, *B36*, 2613.

¹⁰⁵ (a) Prizant, L.; Olivier, M.J.; Rivest, R.; Beauchamp, A.L. *Acta Crystallogr.* **1982**, *B38*, 88. (b) Beauchamp, A. L. *J. Cryst. Mol. Struct.* **1980**, *10*, 149.

¹⁰⁶ Shinoda, K.; Shinoda, W.; Liew, C.C.; Tsuzuki, S.; Morikawa, Y.; Mikami, M. *Surface Science*, **2004**, *556*, 109–120.

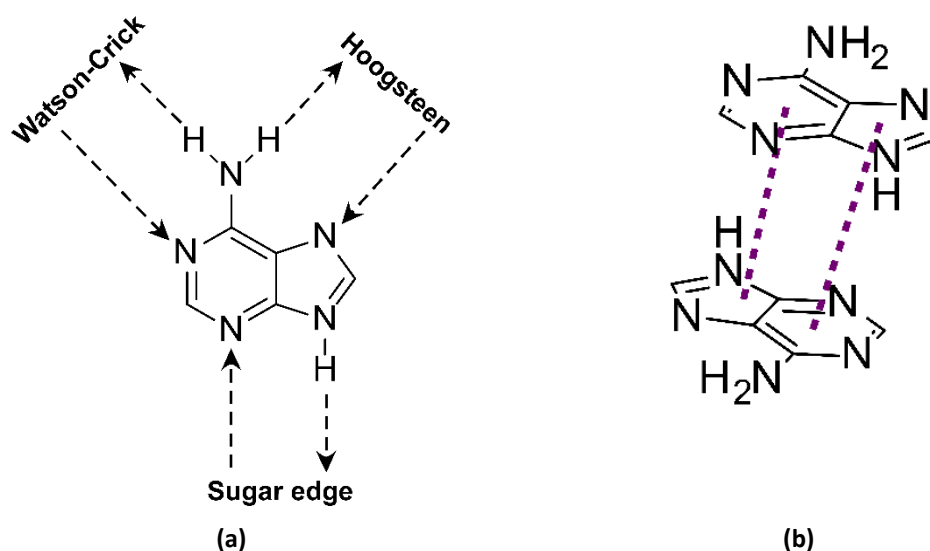


Figure 3.2. Capability of adenine to establish supramolecular interactions through hydrogen bonding (a) and π - π stacking (b).

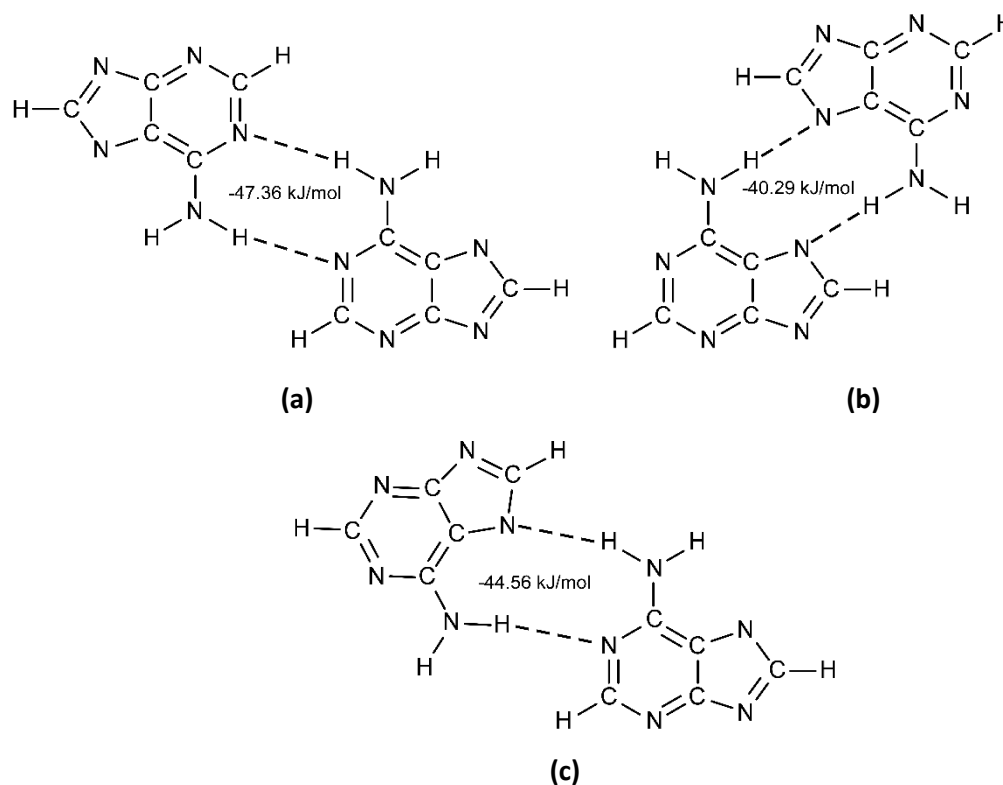


Figure 3.3. Hydrogen-bonding patterns of the adenine dimers and their bond energy.

Due to the large amount of copper(II) puric-base compounds described, whose most recurrent coordination mode in the bibliography is the entity with the shape paddle-wheel (consisting of a metal-organic dimer in which the metal centres are joined through four organic ligands that act as a bridge), it was decided to go a step further in the formation of these compounds, trying to synthesize polynuclear complexes different to recurrent paddle wheel, in

order to assess novel SMOF assemblies. Note that presumably, greater building blocks would allow the formation of larger cavities.

Accordingly, it was decided to explore the syntheses of Cu/adeninato complexes at basic pH values, where the hydroxide can act as co-ligand and give rises to new and more extended building blocks. In a first approach, of a solution containing a Cu(II) source (CuSO_4) and adenine was acidified with H_2SO_4 and thereafter, basified by the addition of triethylamine (NEt_3) up to $\text{pH} \approx 9$. This process led to obtain an octanuclear complex of formula $[\text{Cu}_8(\mu_3\text{-OH})_4(\mu_4\text{-OH})_4(\text{ade})_4(\mu\text{-ade})_4(\mu\text{-Hade})_2]$ (Cu_8AD), builds up by the stacking of Cu(II) dimeric entities. Seeing that the synthetic route allowed the formation of an entity that fulfilled the aimed goal, it was decided to exploit the synthetic route more exhaustively. Thereby we obtained, firstly, a compound built from neutral dinuclear Cu(II) entities and secondly, a family of porous compounds based on cationic heptameric copper(II) entities (Figure 3.4).

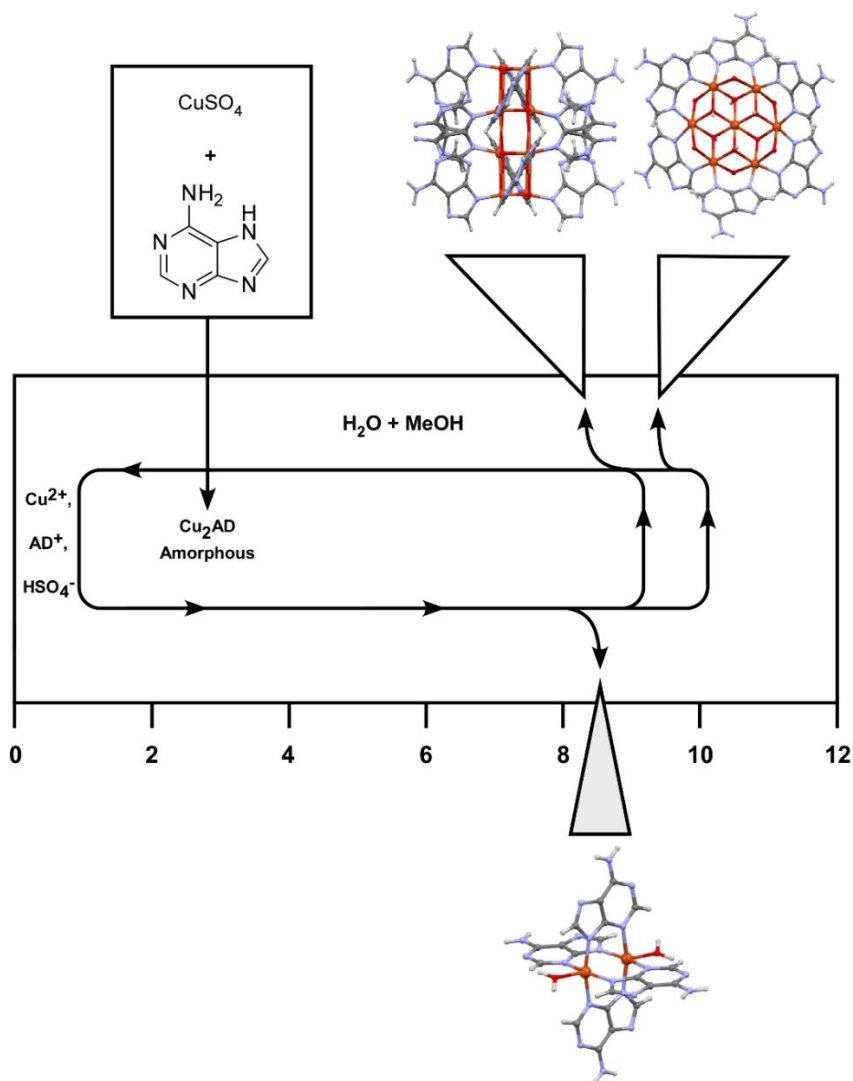


Figure 3.4. Scheme of pH variation in the synthetic route of Cu-AD complexes.

At a pH value below that providing the octanuclear complex, a dinuclear entity of formula $[\text{Cu}_2(\mu\text{-ade-}\kappa\text{N3:}\kappa\text{N9})_4(\text{H}_2\text{O})_2]$ was obtained ($\text{Cu}_2\text{ADSO}_4\text{NHEt}_3$). The assembly of the neutral dimeric entities gives rise to an open 3D supramolecular architecture in which the pores are occupied by solvent, sulfate and triethylammonium molecules. Nonetheless, it deserves to note that this complex lacks of hydroxide co-ligands, being in fact the recurrent paddle-wheel structure.

Consequently, it was decided to explore the influence of higher pH values in the synthesis process. In this way, the compounds labelled as $\text{Cu}_7\text{ADSO}_4\text{NHEt}_3\text{-1}$ and $\text{Cu}_7\text{ADSO}_4\text{NHEt}_3\text{-2}$ were obtained, featured by a heptanuclear complex of formula $[\text{Cu}_7(\mu\text{-H}_2\text{O})_6(\mu_3\text{-OH})_6(\mu\text{-ade-}\kappa\text{N3:}\kappa\text{N9})_6]^{2+}$. The complex entity contains a central $[\text{Cu}(\text{OH})_6]^{4-}$ core linked to six additional copper(II) metal centres which are further connected by bridging adeninato ligands. This building block also fulfils the requirements to yield a SMOF in which the porous network hosts solvent, sulfate and triethylammonium molecules. Taking these results in mind, the base, triethylammonium, was replaced by sodium hydroxide, resulting in the formation of the compound Cu_7ADSO_4 , which is comprised by the heptanuclear entities, sulfate counterions and solvent molecules.

As the overall supramolecular network of these compounds involves a strong interaction not only with the sulfate anions but also with the solvent molecules present in the channels, their crystal structures are very sensitive to the solvent. Thus, their release caused, as for example, by slight temperature changes, collapses the crystal structure when attempting to empty the channels. Therefore, 6-hydroxynicotinate (*HN*) was used as alternative counterion, due to its ability to form complementary hydrogen bonds and π - π stacking interactions that could allow yielding more stable supramolecular networks. This synthetic approach yielded two new compounds based on the heptanuclear entity, labelled as $\text{Cu}_7\text{ADHN-1}$ and $\text{Cu}_7\text{ADHN-2}$.

3.2. SYNTHESIS AND CHEMICAL CHARACTERIZATION

3.2.1 Synthesis

This chapter describes the synthesis and characterization of eight different compounds, listed in Table 3.1. Suitable single-crystals have been obtained from all of them to carry out the structural characterization by X-ray diffraction. Figure 3.5 shows a scheme that summarizes the synthetic procedures described in this chapter.

It is worth to mention that each pair of compounds, $\text{Cu}_7\text{ADSO}_4\text{NHEt}_3\text{-1/-2}$ and $\text{Cu}_7\text{ADHN-1/-2}$, without taking into consideration the solvent molecules hosted in the pores

can be considered as polymorphs. In the case of $\text{Cu}_7\text{ADSO}_4\text{NHEt}_3$ -1 and -2, employing different crystallization times, we can obtain the compound $\text{Cu}_7\text{ADSO}_4\text{NHEt}_3$ -1, which is the kinetically favoured or compound $\text{Cu}_7\text{ADSO}_4\text{NHEt}_3$ -2 which is the thermodynamically favoured one.

Table 3.1. Synthetized compounds.

Compound	Code
$[\text{Cu}_2(\mu\text{-ade-}\kappa\text{N3:}\kappa\text{N9})_4(\text{H}_2\text{O})_2] \cdot 2\{(\text{NHEt}_3)_2(\text{SO}_4)\} \cdot 10\text{H}_2\text{O} \cdot 2\text{CH}_3\text{OH}$	$\text{Cu}_2\text{ADSO}_4\text{NHEt}_3$
$[\text{Cu}_8(\mu_3\text{-OH})_4(\mu_4\text{-OH})_4(\text{ade-}\kappa\text{N9})_4(\mu\text{-ade-}\kappa\text{N3:}\kappa\text{N9})_4(\mu\text{-Hade-}\kappa\text{N3:}\kappa\text{N9})_2]$	Cu_8AD
$[\text{Cu}_7(\mu\text{-H}_2\text{O})_6(\mu_3\text{-OH})_6(\mu\text{-ade-}\kappa\text{N3:}\kappa\text{N9})_6](\text{NHEt}_3)_2(\text{SO}_4)_2 \cdot 42\text{H}_2\text{O}$	$\text{Cu}_7\text{ADSO}_4\text{NHEt}_3$ -1
$[\text{Cu}_7(\mu\text{-H}_2\text{O})_6(\mu_3\text{-OH})_6(\mu\text{-ade-}\kappa\text{N3:}\kappa\text{N9})_6](\text{NHEt}_3)_2(\text{SO}_4)_2 \cdot 23\text{H}_2\text{O}$	$\text{Cu}_7\text{ADSO}_4\text{NHEt}_3$ -2
$[\text{Cu}_7(\mu\text{-H}_2\text{O})_6(\mu_3\text{-OH})_6(\mu\text{-ade-}\kappa\text{N3:}\kappa\text{N9})_6](\text{SO}_4) \cdot 18\text{H}_2\text{O}$	Cu_7ADSO_4
$[\text{Cu}_7(\mu\text{-H}_2\text{O})_6(\mu_3\text{-OH})_6(\mu\text{-ade-}\kappa\text{N3:}\kappa\text{N9})_6](\text{C}_6\text{H}_4\text{NO}_3)_2 \cdot 20\text{H}_2\text{O}$	$\text{Cu}_7\text{ADHN-1}$
$[\text{Cu}_7(\mu\text{-H}_2\text{O})_6(\mu_3\text{-OH})_6(\mu\text{-ade-}\kappa\text{N3:}\kappa\text{N9})_6](\text{C}_6\text{H}_4\text{NO}_3) \cdot 29\text{H}_2\text{O}$	$\text{Cu}_7\text{ADHN-2}$

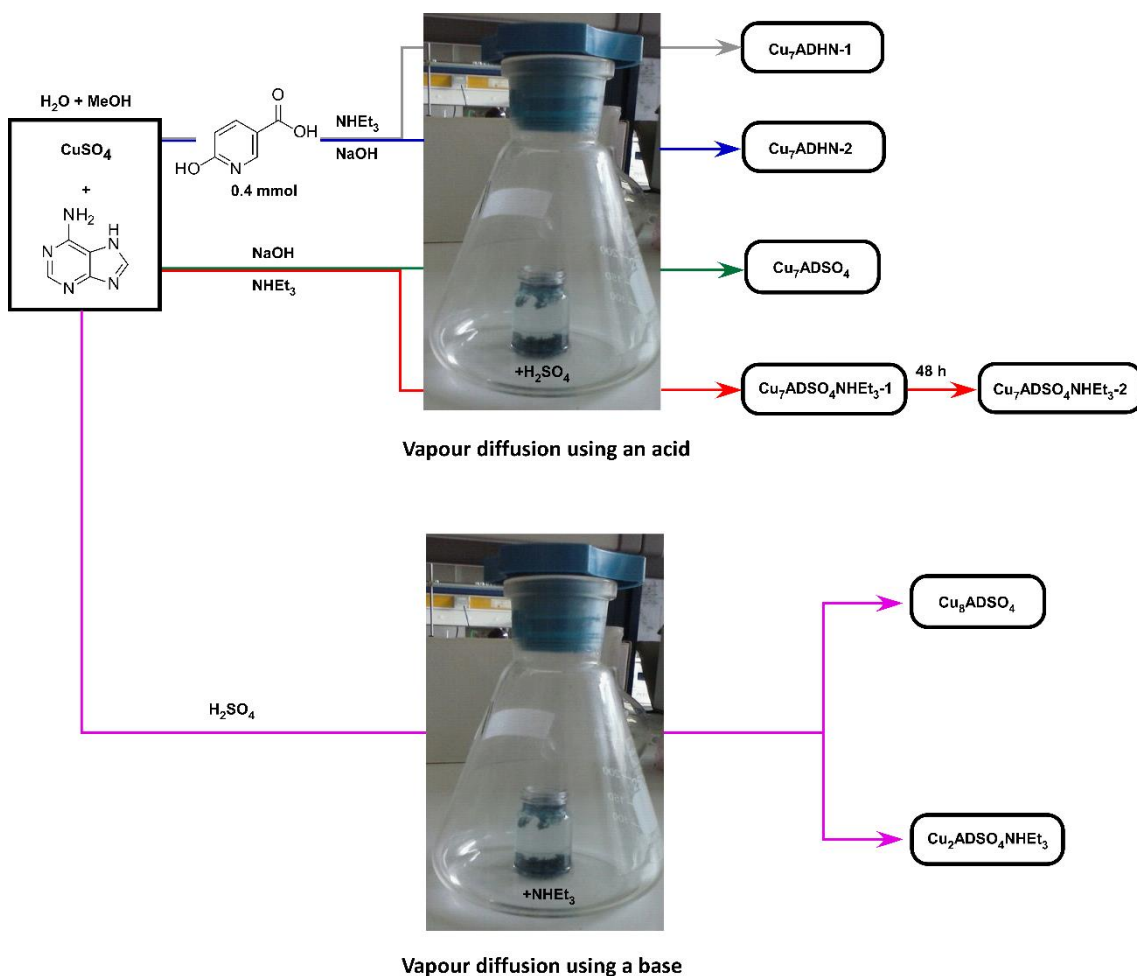


Figure 3.5. Synthesis scheme for all the compounds of this chapter (except Cu_8AD).

3.2.1.1. Synthesis of $\text{Cu}_2\text{ADSO}_4\text{NHET}_3$

0.200 g of $\text{CuSO}_4 \cdot 5\text{H}_2\text{O}$ (0.8 mmol) dissolved in 20 mL of water were added dropwise to an aqueous/methanolic (10 mL/10 mL) solution of 0.108 g of adenine (0.8 mmol). The resulting deep blue mixture was acidified to pH 1.5 by adding H_2SO_4 . The resulting pale blue solution was placed in a small crystal beaker that was introduced into an Erlenmeyer flask containing a triethylamine aqueous solution (1/20 volume ratio). The vapour diffusion taking place inside the closed Erlenmeyer flask slowly basified the copper–adenine solution prompting the growing of purple crystals of $\text{Cu}_2\text{ADSO}_4\text{NHET}_3$ four days later (solution pH = 8.6). Yield: ca. 40% (based on metal).

3.2.1.2. Synthesis of compound Cu_8ADSO_4

20 mL of an aqueous methanolic solution (1:1) containing adenine (0.8 mmol, 0.108 g) were added to 20 mL of an aqueous solution of $\text{CuSO}_4 \cdot 5\text{H}_2\text{O}$ (0.4 mmol, 0.100 g) leading to a solution of pH = 3. Immediately a dark blue precipitate appeared. Then, sulfuric acid was added until complete dissolution of the precipitate (pH = 1.5). A glass vial with the resulting solution was placed in an Erlenmeyer flask containing triethylamine favouring the diffusion of the base into the solution. A few days later, at pH = 8.5, a small amount of purple crystals of Cu_8ADSO_4 appeared.

3.2.1.3. Synthesis of compound $\text{Cu}_7\text{ADSO}_4\text{NHET}_3\text{-1}$ and $\text{Cu}_7\text{ADSO}_4\text{NHET}_3\text{-2}$

A solution of 0.200 g (0.8 mmol) of copper(II) sulfate pentahydrate dissolved in 20 mL of water was added dropwise to a 20 mL aqueous-methanolic (1/1) solution containing 0.108 g (0.8 mmol) of adenine. Immediately a dark blue precipitate appeared which was dissolved adding few drops of H_2SO_4 concentrated to set the pH value at 1.5. Later the pH was fixed at 10 by adding triethylamine and the resulting mixture was placed in a small beaker that was introduced into an Erlenmeyer flask containing a 1/5 (v/v) sulfuric acid solution. The vapor diffusion taking place inside the closed Erlenmeyer flask slowly acidified the solution allowing the growth of blue prismatic crystals of compound $\text{Cu}_7\text{ADSO}_4\text{NHET}_3\text{-1}$ four days later (pH = 8). If the beaker containing the reaction mixture is removed from the Erlenmeyer flask and left open in contact with atmosphere air, crystals of compound $\text{Cu}_7\text{ADSO}_4\text{NHET}_3\text{-1}$ appears, which evolves towards new blue cubic crystals belonging to compound $\text{Cu}_7\text{ADSO}_4\text{NHET}_3\text{-2}$ (pH = 7.0). Yield: 42% for compound $\text{Cu}_7\text{ADSO}_4\text{NHET}_3\text{-1}$ and 33% for compound $\text{Cu}_7\text{ADSO}_4\text{NHET}_3\text{-2}$, respectively.

3.2.1.4. Synthesis of compound Cu₇ADSO₄

Adenine (0.8 mmol, 0.108 g) was dissolved in a mixture of 20 mL water / methanol in a 1:1 ratio under continuous stirring and heating. Thereafter, it was added to an aqueous solution of 20 mL of copper(II) sulfate pentahydrate (0.8 mmol, 0.200 g). The appearance of a bluish suspension was observed at pH = 2.9. The suspension was redissolved by adding sulfuric acid dropwise to pH = 1.8. Then, 1 M sodium hydroxide was added dropwise obtaining a new dark blue suspension (pH = 10.1) that was placed in a small beaker and introduced into an Erlenmeyer flask containing a 1/5 (v/v) sulfuric acid solution. The vapor diffusion taking place inside the closed Erlenmeyer flask acidified the solution slowly. After four days, blue cubic crystals of Cu₇ADSO₄ were obtained (pH = 9.1). Yield: 60%.

3.2.1.5. Synthesis of compound Cu₇ADHN-1 and Cu₇ADHN-2

A solution of 0.200 g (0.8 mmol) of copper(II) sulfate pentahydrate was dissolved in 20 mL of water. After the complete dissolution, the mixture was added dropwise to a 20 mL aqueous-methanolic (1/1) solution containing 0.108 g (0.8 mmol) of adenine and 0.110 g (0.8 mmol) of HN. Then, a few drops of H₂SO₄ were added to reduce the pH value to 1.0. As soon as the pH was stable, trimethylamine (in compound Cu₇ADHN-1) or NaOH 1M (in compound Cu₇ADHN-2) was added to increase the pH up to 9.1 and 10.5. Thereafter, the solution was introduced into an Erlenmeyer flask containing of 1/5 (v/v) sulfuric acid solution. The vapor diffusion taking place inside the closed Erlenmeyer flask promoted the growth of blue prismatic crystals of Cu₇ADHN-1 and Cu₇ADHN-2, respectively, five days later (pH = 8.6 and 9.3). Yield: 25 % for both compounds.

3.2.2. Infrared spectroscopy

Infrared spectroscopy with attenuated total reflection (ATR-FTIR) has been used to determine qualitatively the presence of sulfate counterions, adeninato and 6-hydroxynicotinato ligands. Figures 3.6 and 3.7 show the IR spectrum of all the compounds and Tables 3.2 and 3.3 gather the assignment of the most relevant bands, with their relative intensity and wave numbers.

At ca. 3430 cm⁻¹ all the compounds exhibit an intense and broad band attributable to the O–H stretching of hydroxide and water molecules. At lower wave number, ca. 3200 cm⁻¹, the N–H stretching of the amine group of the adeninato emerges as an overlapped peak or shoulder. The signals corresponding to the C_{ar}–H stretching of AD and C–H stretching of NHET₃, expected around 3000–3100 and 3000–2850 cm⁻¹ respectively, are masked or appear as very weak peaks. The intense band around 1600 cm⁻¹, is attributed to the C=C stretching vibration

or to deformation vibration of NH_2 group of the adenine. In those compounds containing the sulfate anion, the $\text{S}=\text{O}$ stretching vibration is observed at 1108 cm^{-1} . In the case of the compounds containing the HN counterion, the representative asymmetric stretching vibration of the carboxylate group (expected for the free anion at around 1680 cm^{-1}) is overlapped with that adenine $\text{C}=\text{C}$ and $\text{C}=\text{N}$ stretching.^[86,107]

Table 3.2. Infrared spectroscopy bands (cm^{-1}) of the AD ligand and the compounds described in this chapter.^[a]

Adenine	$\text{Cu}_2\text{ADSO}_4\text{NHET}_3$	$\text{Cu}_7\text{ADSO}_4\text{NHET}_3\text{-1}$	$\text{Cu}_7\text{ADSO}_4\text{NHET}_3\text{-2}$	Cu_7ADSO_4	Assignment ^[b]
--	3430vs	3438vs	3439vs	3433vs	ν (O–H)
3303s	3386sh	3422sh	3416sh	3422sh	ν (N–H)
3123s	3120vw	3200sh	3194sh	3200sh	ν (C8–H + C2–H)
-	2980s	2982s	--	--	ν ($\text{C}_{\text{Et}}\text{-H} + \text{C}_{\text{Et}}\text{-H}$)
	1644vs	1652vs	1652vs	1641vs	
1605vs	1600vs	1605vs	1605vs	1605vs	ν (C=N) + ν (C=C) + δ (NH_2)
1560s	1564m	1586s	1585s	1547s	ν (C4–C5 + N3–C4–C5)
1471m	1462s	1461m	1461m	1463m	δ (C2–H + C8–N9) + ν (C8–H)
1419s	1400s	1408m	1408m	1400m	δ (N1–C6–H6)
1309s	1306s	1305m	1306m	1305m	
	1271vs	1277m	1277m	1275m	ν (N9–C8 + N3–C2) + δ (C–H)
1263s	1190s	1198m	1198m	1198m	
	1150m	1152m	1148m	1148m	δ (C8–H) + ν (N7–C8)
--	1110s	1102s	1102s	1108s	ν (S=O)
1023w	1030m	1033w	1030w	1028w	τ (NH_2)
940s	940w	935w	933w	933w	ν (N1–C6) + τ (NH_2)

^[a] vs = very strong, s = strong, m = medium, w = weak, sh = shoulder. ^[b] over = overlapped, ν = tension vibrations, δ = deformation vibrations, τ = torsion.

¹⁰⁷ Santos, C. R.; M. B. B. M. Figueira, R.; M. Piedade, M. F.; P. Diogo, H.; Minas da Piedade, M. E. *J. Phys. Chem.* **2009**, *113*, 14291–14309.

Table 3.3. Infrared spectroscopy bands (cm^{-1}) of the AD ligand and the compounds described in this chapter (cont.).^[a]

6-Hydroxynicotinic acid	Adenine	Cu ₇ ADHN-1	Cu ₇ ADHN-2	Assignment ^[b]
	--	3388vs	3355vs	ν (O–H)
	3303s	3342sh	3333sh	ν (NH ₂)
	3123s	3188sh	3169sh	ν (C8–H + C2–H)
	--	3197vs	3198vs	ν (O–H)
1639vs		1640vs	1641vs	ν_{as} (COO) + ν (C=N) +
	1605vs	1601vs	1602vs	ν (C=C) + δ (NH ₂)
1560s		1566s	1566s	ν_{s} (COO)
		1550s	1548s	ν (C4–C5 + N3–C4–C5)
	1471m	1462m	1464m	δ (C2–H + C8–N9) + ν (C8–H)
	1419s	1400m	1399m	δ (N1–C6–H6)
	1309s	1306m	1306m	
		1276m	1275m	ν (N9–C8 + N3–C2) + δ (C–H)
	1263s	1198m	1195m	
		1155m	1150m	δ (C8–H) + ν (N7–C8)
	1108s	1108s	1108s	ν (S=O)
	1023w	1032w	1029w	τ (NH ₂)
	940s	935w	933w	ν (N1–C6) + τ (NH ₂)

^[a] vs = very strong, s = strong, m = medium, w = weak, sh = shoulder. ^[b] over = overlapped, ν = tension vibrations, δ = deformation vibrations, τ = torsion.

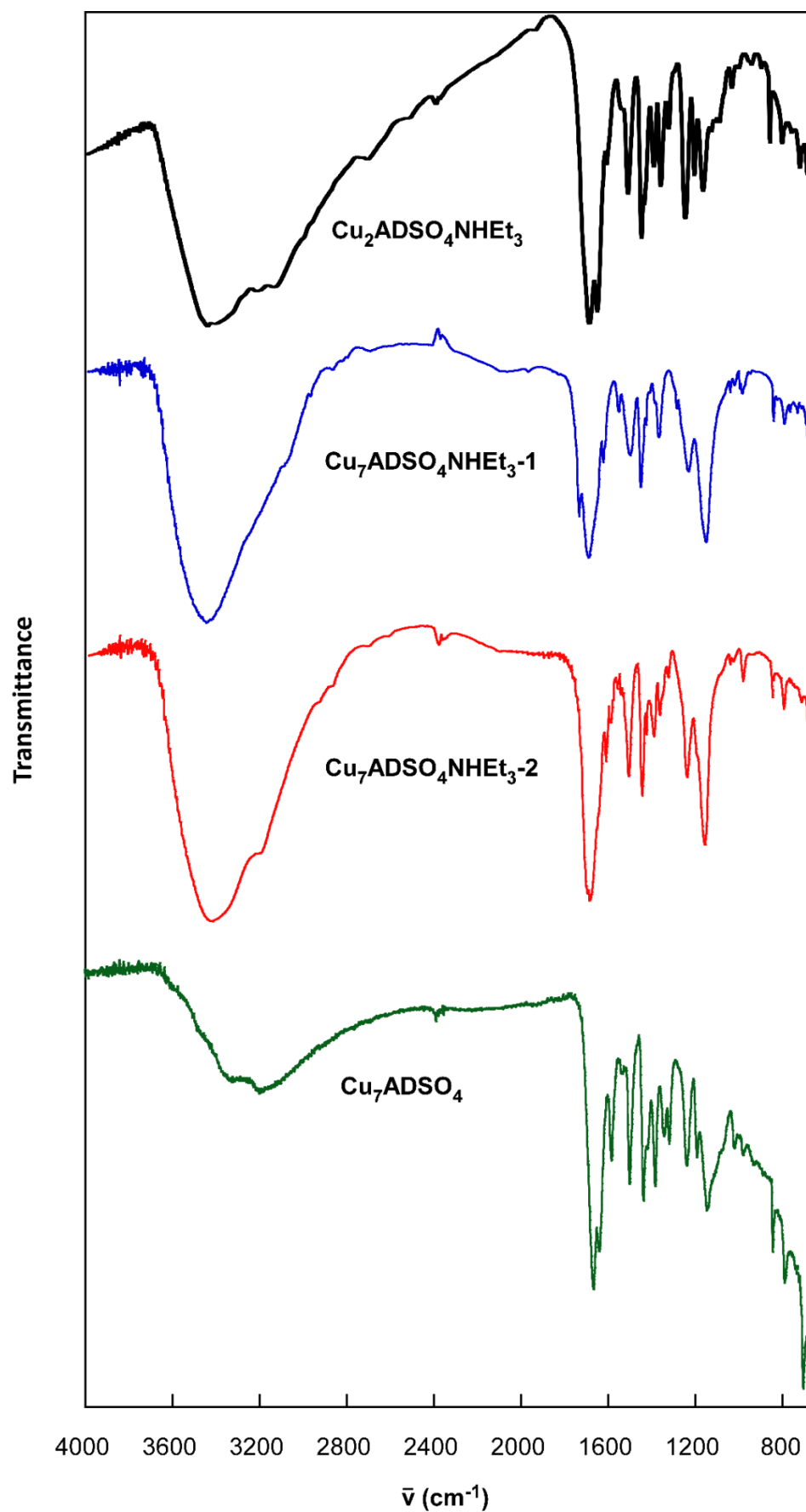


Figure 3.6. Infrared spectrum of compounds $\text{Cu}_2\text{ADSO}_4\text{NHEt}_3$, $\text{Cu}_7\text{ADSO}_4\text{NHEt}_3\text{-1}$ (blue), $\text{Cu}_7\text{ADSO}_4\text{NHEt}_3\text{-2}$ (red) and Cu_7ADSO_4 (green).

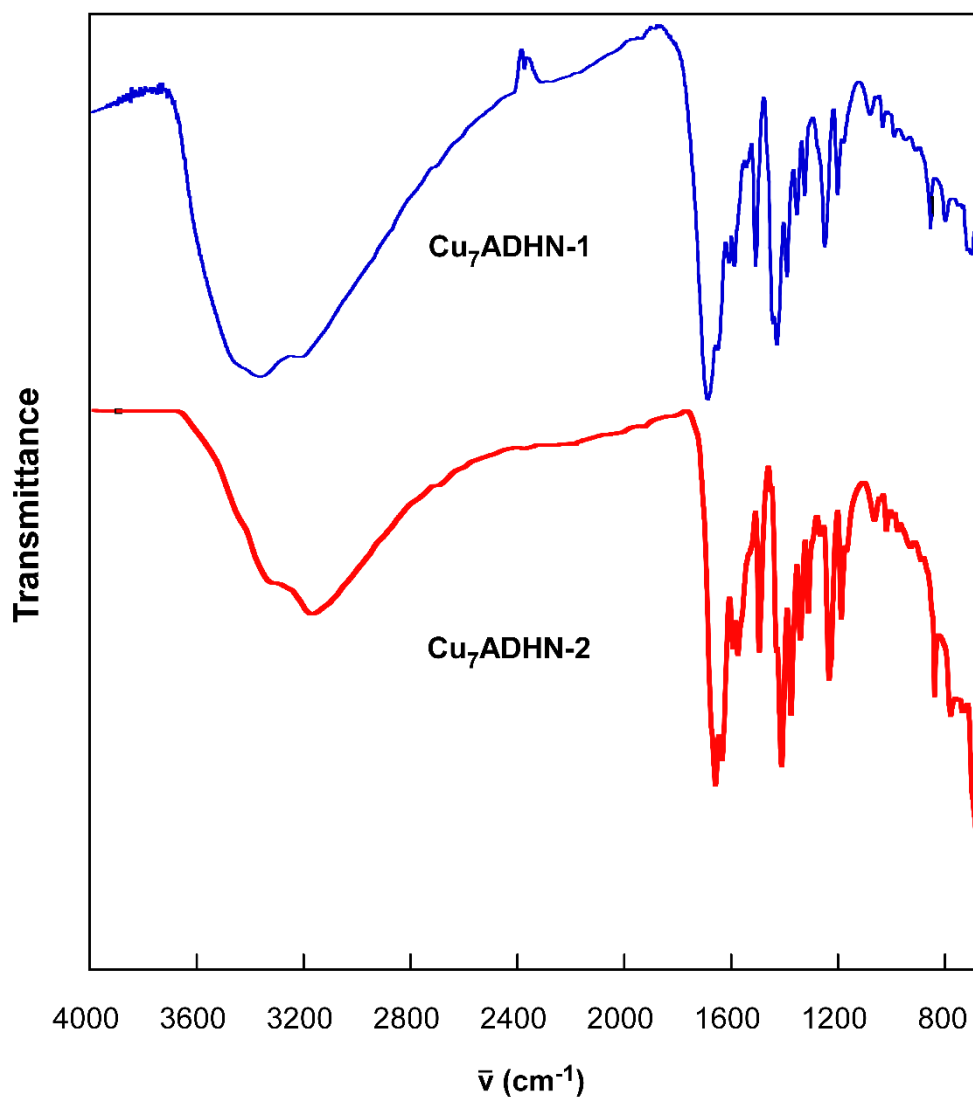


Figure 3.7. Infrared spectrum of compounds Cu₇ADHN-1 (blue) and Cu₇ADHN-2 (red).

3.2.3. Thermal analysis

The thermal behaviour of the synthesized compounds (TG/ATD curves) are plotted in Figure 3.8. The degradation processes taking place in each compound are analysed in Table 3.4. All measurements were performed using synthetic air (79 % N₂, 21 % O₂) as atmosphere.

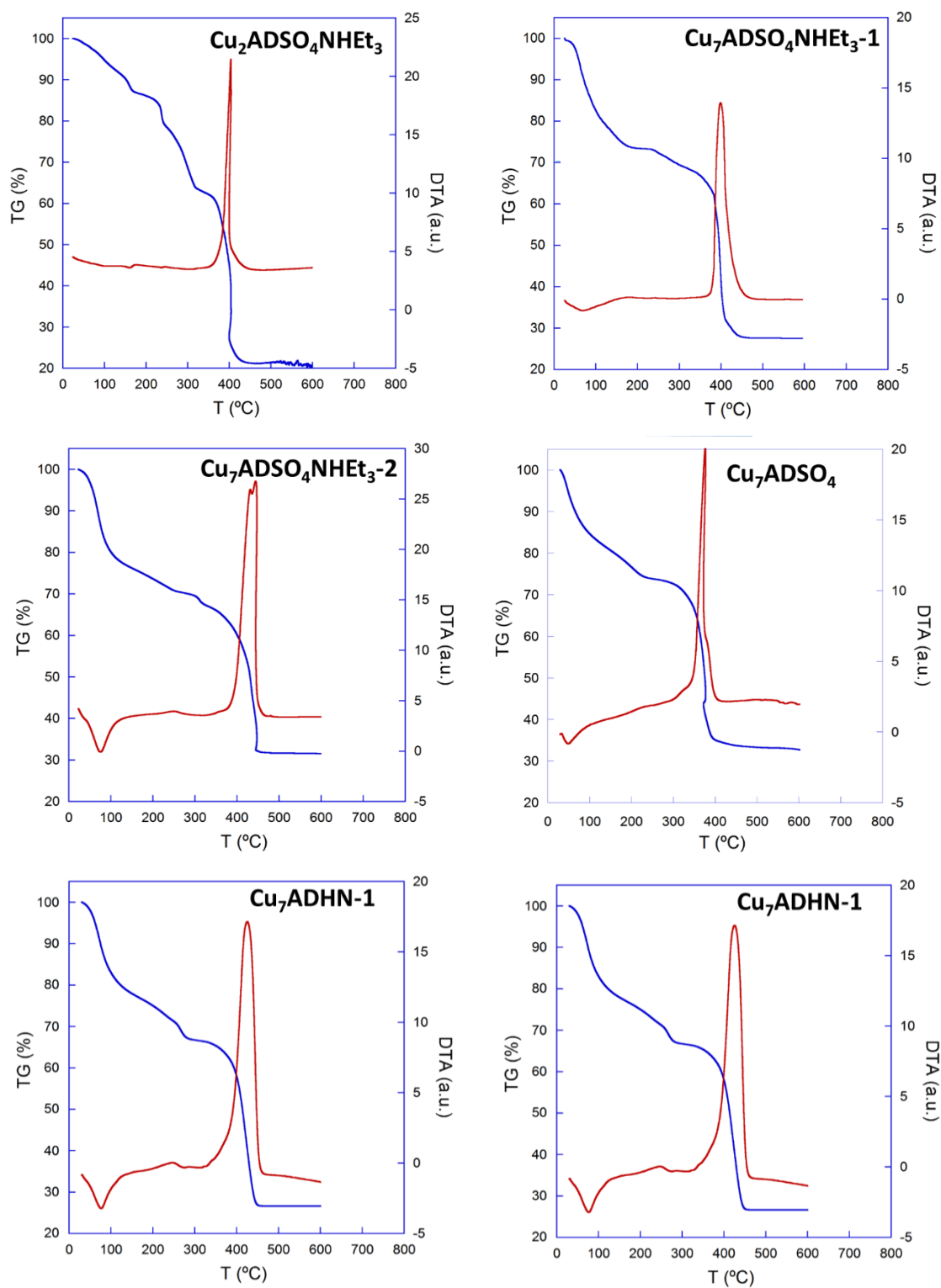


Figure 3.8. Thermogravimetric measurements performed upon representative samples.

Table 3.4. Thermoanalytic data of the compounds described in the chapter.

Step	T _i	T _f	T _{peak}	ΔH	Δm(%)	ΣΔm(%)	ΣΔm(%) _{theo}
Cu₂ADSO₄NHET₃							
1	25	140	--	Endo	8.8	8.8	8.3 (–(10H ₂ O + 2CH ₃ OH)) 11.9 (–6H ₂ O)
2	150	180	--	Endo	4.1	12.9	18.8 (–2NEt ₃)
3	215	250	--	Endo	8.2	21.1	34.8 (–2NEt ₃ + C ₅ H ₅ N ₅)
4	260	330		Endo	15.3	36.4	78.3 (4CuO + 2CuSO ₄)
5	350	440	400	Exo	42.5	78.9	
Cu₇ADSO₄NHET₃-1							
1	30	200	70	Endo	26.7	26.7	26.4 (–24H ₂ O –9H ₂ O – (N(Et) ₃))
2	230	475	400	Exo	45.8	72.5	72.5 (7CuO)
Cu₇ADSO₄NHET₃-2							
1	30	250	70	Endo	30.3	30.3	30.0 (–23H ₂ O –9H ₂ O – (N(Et) ₃))
2	280	320	300	Endo	4.6	34.9	34.4 (–N(Et) ₃)
3	320	465	400	Exo	32.3	67.2	68.4 (5CuO + 2 CuSO ₄)
Cu₇ADSO₄							
1	30	100	50	Endo	17.0	17.0	17.2 (–18H ₂ O)
2	100	235	-	--	8.9	25.9	25.8 (–9H ₂ O)
3	235	450	375	Exo	40.3	66.2	66.2 (6CuO +CuSO ₄)
Cu₇ADHN-1							
1	30	100	75	Endo	17.2	17.2	17.2 (–20H ₂ O)
2	100	220	--	--	7.8	25.0	25.0 (–9H ₂ O)
3	265	300			9.0	34.0	34.0 (–2C ₅ H ₄ NO)
4	330	465	425	Exo	40.4	73.4	73.4 (7CuO)
Cu₇ADHN-2							
1	30	115	85	Endo	17.9	23.2	24.6 (–29H ₂ O)
2	115	215	--	--	7.7	30.5	32.2 (–9H ₂ O)
3	260	285	--	--	6.5	32.1	36.6 (–C ₅ H ₃ NO)
4	350	495	480	Exo	41.6	73.7	73.8 (7CuO)

[a] T_i = initial temperature; T_f = final temperature; T_{peak} = peak temperature ATD; Δm(%) = loss mass percentage in each step; ΔH = type of process according to ATD; ΣΔm(%) = total loss mass after each step; ΣΔm(%)_{theo} = total loss mass theoretically calculated. [b] Eliminate water molecules and final residue per compound formula.

All the compounds described in this chapter display similar decomposition processes. First, from room temperature to values below 100 °C, the loss of the crystallization water molecules is observed through an endothermic process. Secondly, above 100 °C, the loss of coordination water molecules takes place. In the case of the heptanuclear complexes, is followed by the release of water molecules yielded by the dehydroxilation of the cluster, summing up nine water molecules per heptamer, six bridging waters and three more water molecules obtained in the condensation process of the six hydroxide bridges. In those compounds containing NHEt_3^+ cation, the loss of amine form (NEt_3) takes place at different temperatures, which is probably due to differences on the eventual porosity of the sample and the stability of ionic pairs formed. In the compounds $\text{Cu}_7\text{ADHN-1}$ and -2 , after the dehydration process at ca. 260 °C, the HNA ligands are decomposed pyrolytically to yield $\text{Cu}_7\text{O}_3(\text{C}_5\text{H}_4\text{N}_4)_6(\text{C}_2\text{O}_4)$. The formation of oxalate derivate is similar to that described for HQ ligand in Chapter 2. Finally, in the last stage, the decomposition of the adeninato ligands occurs through a strong exothermic process, generating the corresponding copper oxide or a mixture with copper sulfate.

3.3. RESULTS AND DISCUSSION

3.3.1. Crystallographic analysis

The crystallographic data and details of the refinement parameters of each compound are gathered in Table 3.5 and Table 3.6. Single crystal diffraction data were collected at 100(2) K on Agilent Technologies Supernova diffractometers ($\lambda_{\text{Cu-K}\alpha} = 1.54184 \text{ \AA}$ for compounds $\text{Cu}_7\text{ADSO}_4\text{NHHet}_3\text{-1}$, $\text{Cu}_7\text{ADSO}_4\text{HN-1}$ and $\text{Cu}_7\text{ADSO}_4\text{HN-2}$ and $\lambda_{\text{Mo-K}\alpha} = 0.71073 \text{ \AA}$ for compounds $\text{Cu}_2\text{ADSO}_4\text{NHet}_3$, Cu_8AD , $\text{Cu}_7\text{ADSO}_4\text{NHHet}_3\text{-2}$ and Cu_7ADSO_4). The data reduction was done with the CrysAlisPro program.^[108] Crystal structures were solved by direct methods using the SIR92 program^[109] and refined by full-matrix least-squares on F^2 including all reflections (WinGX).^[110] In the compounds $\text{Cu}_2\text{ADSO}_4\text{NHet}_3$, $\text{Cu}_7\text{ADSO}_4\text{NHet}_3\text{-1}$, $\text{Cu}_7\text{ADSO}_4\text{NHet}_3\text{-2}$ and Cu_7ADSO_4 almost one adeninato ligands is disordered in two coplanar arrangements with inverted orientation regarding the coordination mode ($\mu\text{-}\kappa\text{N}3\text{:}\kappa\text{N}9 / \mu\text{-}\kappa\text{N}9\text{:}\kappa\text{N}3$).^[111] In compounds $\text{Cu}_7\text{ADSO}_4\text{NHHet}_3\text{-1}$, $\text{Cu}_7\text{ADSO}_4\text{NHet}_3\text{-2}$ and Cu_7ADSO_4 there are two symmetry related to sulfate anions per heptamer. Therefore, the occupation factors of the sulfate molecule have been fixed to the stoichiometrically required, i.e., 0.75 from compound $\text{Cu}_7\text{ADSO}_4\text{NHHet}_3\text{-1}$ and 0.5 from

¹⁰⁸ CrysAlisPro, version 1.171.35.19; Agilent Technologies:Yarnton, UK, 2011.

¹⁰⁹ Altomare, A.; Casciaro, M.; Giacovazzo, C.; Guagliardi, A. *J. Appl. Cryst.* **1993**, *26*, 343-350.

¹¹⁰ (a) Farrugia, L. J. *J. Appl. Cryst.* **1999**, *32*, 837-838. (b) Sheldrick, G. M. *Acta Crystallogr.* **2008**, *A64*, 112-122.

¹¹¹ (a) Cepeda, J.; Castillo, O.; García-Terán, J. P.; Luque, A.; Pérez-Yáñez, S.; Román, P. *Eur. J. Inorg. Chem.* **2009**, 2344-2353. b) Pérez-Yáñez, S.; Beobide, G.; Castillo, O.; Cepeda, J.; Luque, A.; Román, P. *Cryst. Growth Des.* **2013**, *13*, 3057-3067.

$\text{Cu}_7\text{ADSO}_4\text{NHET}_3\text{-2}$ and Cu_7ADSO_4 . On the other hand, compound $\text{Cu}_7\text{ADHN-1}$ presents two heptameric clusters and HN ligands crystallographically independents. One of the six adeninato ligands of each cluster and one of the HN ligand are disordered in two positions. It is noteworthy that the crystal structure of all compounds display the presence of great channels in which the solvent molecules and co-crystallized ions are placed. The high disorder of some of these entities (solvent molecules in most of the cases or triethylammonium-sulfate ionic ensembles in $\text{Cu}_7\text{ADSO}_4\text{NHHET}_3\text{-1}$ and -2) precluded their modeling and, as a consequence, the electron density at the voids of the crystal structure was subtracted from the reflection data by the SQUEEZE method^[112] as implemented in PLATON.^[89] The electron density provided by the SQUEEZE routine matches the expected from the number of the species hosted in the channels. Although in most compounds there is not a big difference with respect to the water molecules observed between single crystal and thermogravimetric analysis, in the case of $\text{Cu}_7\text{ADSO}_4\text{NHHET}_3\text{-1}$ there is a significant difference probably due to a partial dehydration process. In all cases, the molecular weight used in the magnetic analysis was the obtained by single crystal data.

¹¹² Van der Sluis, P.; Spek, A. L. *Acta Crystallogr.* **1990**, *A46*, 194-201.

Table 3.5. Crystallographic data and refinement details of compounds of Cu₂ADSO₄NHET₃, Cu₈AD, Cu₇ADSO₄NHET₃-1 and Cu₇ADSO₄NHET₃-2.

	Cu ₂ ADSO ₄ NHET ₃	Cu ₈ AD	Cu ₇ ADSO ₄ NHET ₃ -1	Cu ₇ ADSO ₄ NHET ₃ -2
Formula	C ₈₆ H ₁₅₂ Cu ₆ N ₆₄ O ₂₆ S ₂	C ₅₀ H ₅₀ Cu ₈ N ₅₀ O ₈	C ₄₂ H ₁₅₈ Cu ₇ N ₃₂ O ₆₂ S ₂	C ₄₂ H ₁₂₀ Cu ₇ N ₃₂ O ₄₃ S ₂
M (g mol ⁻¹)	2944	1987	2612	2270
Cryst. Syst.	Monoclinic	Orthorhombic	Monoclinic	Trigonal
Space group	<i>P2₁/n</i>	<i>Ccca</i>	<i>C2/c</i>	<i>R$\bar{3}c$</i>
<i>a</i> (Å)	13.0248(3)	20.1899(5)	15.5705(6)	18.9582(5)
<i>b</i> (Å)	20.9011(4)	28.964(2)	22.3823(10)	18.9582(5)
<i>c</i> (Å)	23.1090(7)	16.5403(5)	27.2969(9)	43.2908(14)
α (°)	90	90	90	90
β (°)	102.207(2)	90	101.102(4)	90
γ (°)	90	90	90	120
<i>V</i> (Å ³)	6148.8(3)	9672.6(8)	9335.0(6)	13474.7(7)
<i>Z</i>	2	4	4	6
ρ_{calcd} (g·cm ⁻³)	1.590	1.365	1.778	1.258
Colour	Purple	Purple	Blue	Blue
F(000)	3060	3984	3260	5070
μ (cm ⁻¹)	1.149	1.790	2.666	1.739
θ range (°)	1.660–27.000	1.740–27.000	3.630–66.464	1.560–27.000
<i>hkl</i> range	–16 ≤ <i>h</i> ≤ 15; –26 ≤ <i>k</i> ≤ 26; –29 ≤ <i>l</i> ≤ 29	–8 ≤ <i>h</i> ≤ 22; –26 ≤ <i>k</i> ≤ 26; –36 ≤ <i>l</i> ≤ 37	–18 ≤ <i>h</i> ≤ 18; –26 ≤ <i>k</i> ≤ 26; –23 ≤ <i>l</i> ≤ 32	–19 ≤ <i>h</i> ≤ 24; –23 ≤ <i>k</i> ≤ 21; –55 ≤ <i>l</i> ≤ 52
Meas./indep. refl.	50515/13317	33482/5277	16386/8210	34104/3280
<i>R</i> eqv.	0.0456	0.0630	0.0849	0.0516
Obs. Refl. [<i>I</i> > 2 σ (<i>I</i>)]	10772	3803	5128	2014
<i>R</i> , <i>R</i> _w [<i>a</i> , <i>b</i>]	0.0714/0.1541	0.0721/0.2115	0.1205/0.3766	0.0969/0.3083
<i>R</i> , <i>R</i> _w (all)	0.0893/0.1625	0.0872/0.2221	0.1479/0.4025	0.1142/0.3237
Gof(S)[<i>c</i>]	1.133	1.092	1.519	1.157
Parameters	823	272	423	122
Weighting sch.[<i>d</i>]	Shelxl	Shelxl	Shelxl	Shelxl
Max./min. $\Delta\rho$ (e Å ⁻³)	1.796/–0.637	3.959/–1.064	1.528/–1.018	1.914/–0.591
Diffractometer	SuperNova	SuperNova	SuperNova	SuperNova
λ (Å)	0.71073	0.71073	1.54184	0.71073
Temperature (K)	100(2)	100(2)	100(2)	100(2)

[a] $S = [\sum w(F_o^2 - F_c^2)^2 / (N_{\text{obs}} - N_{\text{param}})]^{1/2}$ [b] $R_1 = \sum ||F_o| - |F_c|| / \sum |F_o|$ [c] $wR_2 = [\sum w(F_o^2 - F_c^2)^2 / \sum wF_o^2]^{1/2}$; $w = 1/[\sigma^2(F_o^2) + (aP)^2 + bP]$ where $P = (\max(F_o^2, 0) + 2F_c^2)/3$. a) Cu₂ADSO₄NHET₃ (0.0365), Cu₈AD (0.1845), Cu₇ADSO₄NHET₃-1 (0.2000) and Cu₇ADSO₄NHET₃-2 (0.2000). b) Cu₂ADSO₄NHET₃ (31.9990) and Cu₈AD (162.7088).

Table 3.6. Crystallographic data and refinement details of compounds of Cu₇ADSO₄, Cu₇ADHN-1 and Cu₇ADHN-2.

	Cu₇ADSO₄	Cu₇ADHN-1	Cu₇ADHN-2
Formula	C ₃₀ H ₇₄ Cu ₇ N ₃₀ O ₃₂ S	C ₄₂ H ₉₀ Cu ₇ N ₃₂ O ₄₈	C ₃₆ H ₁₀₃ Cu ₇ N ₃₁ O ₄₄
M (g mol ⁻¹)	1880	2096	2119
Cryst. Syst.	Orthorhombic	Monoclinic	Triclinic
Space group	<i>Cccm</i>	<i>P2₁/c</i>	<i>P</i> $\bar{1}$
<i>a</i> (Å)	10.5044(3)	19.3489(4)	10.4648(7)
<i>b</i> (Å)	24.8711(10)	20.0870(4)	15.9781(15)
<i>c</i> (Å)	27.0088(11)	21.7594(5)	24.6138(11)
α (°)	90	90	88.970(5)
β (°)	90	94.845(2)	83.389(5)
γ (°)	90	90	73.308(7)
<i>V</i> (Å ³)	7056.2(5)	8426.8(3)	3915.5(5)
<i>Z</i>	4	4	2
ρ_{calcd} (g·cm ⁻³)	1.770	1.652	1.353
Colour	Light blue	Blue	Blue
F(000)	3796	4252	1598
μ (cm ⁻¹)	2.202	2.796	2.629
θ range (°)	3.091–27.421	2.999–76.300	3.383–74.341
hkl range	–13≤h≤13; –32≤k≤31; –34≤l≤34	–23≤h≤24; –24≤k≤23; –21≤l≤27	–13≤h≤9; –19≤k≤19; –30≤l≤27
Meas./indep. refl.	29071/3879	40513/17237	29877/15469
R eqv.	0.0791	0.0372	0.0485
Obs. Refl. [<i>I</i> > 2σ(<i>I</i>)]	3000	12494	7746
R, Rw[a,b]	0.1123/0.2717	0.0737/0.2033	0.1453/0.4271
R, Rw(all)	0.1324/0.2813	0.0963/0.2237	0.1929/0.4729
Gof(S)[c]	1.135	1.028	1.489
Parameters	221	876	759
Weighting sch.[d]	Shelxl	Shelxl	Shelxl
Max./min. Δρ (e Å ⁻³)	2.835/–1.585	2.190/–0.829	1.870/–0.647
Diffractometer	SuperNova	SuperNova	SuperNova
λ (Å)	0.71073	1.54184	1.54184
Temperature (K)	100(2)	100(2)	100(2)

[a] $S = [\sum w(F_o^2 - F_c^2)^2 / (N_{\text{obs}} - N_{\text{param}})]^{1/2}$ [b] $R_1 = \sum ||F_o| - |F_c|| / \sum |F_o|$ [c] $wR_2 = [\sum w(F_o^2 - F_c^2)^2 / \sum wF_o^2]^{1/2}$; $w = 1/[\sigma^2(F_o^2) + (aP)^2 + bP]$ where $P = (\max(F_o^2, 0) + 2F_c^2)/3$. a) Cu₇ADSO₄ (0.0576), Cu₇ADHN-1 (0.1006) and Cu₇ADHN-2 (0.2000). b) Cu₇ADSO₄ (501.8563) and Cu₇ADHN-1 (29.1698).

3.3.2. Structural description

3.3.2.1. Structural description of dimeric compound.

The dimeric entity consists of two crystallographically independent neutral paddlewheel shaped [Cu₂(μ-ade-κN3:κN9)₄(H₂O)₂] discrete entities (A and B dimers) crystallized with triethylammonium sulfate and solvent molecules (water and methanol). In the dimeric entities, four bridging adeninato ligands connect the copper(II) atoms through their N3 and N9 nitrogen atoms to provide the core of the paddle-wheel shaped dinuclear entity.

Moreover, two water molecules are located in the apical positions of the elongated square pyramidal coordination environment of the metal centres (Figure 3.9, Table 3.7).

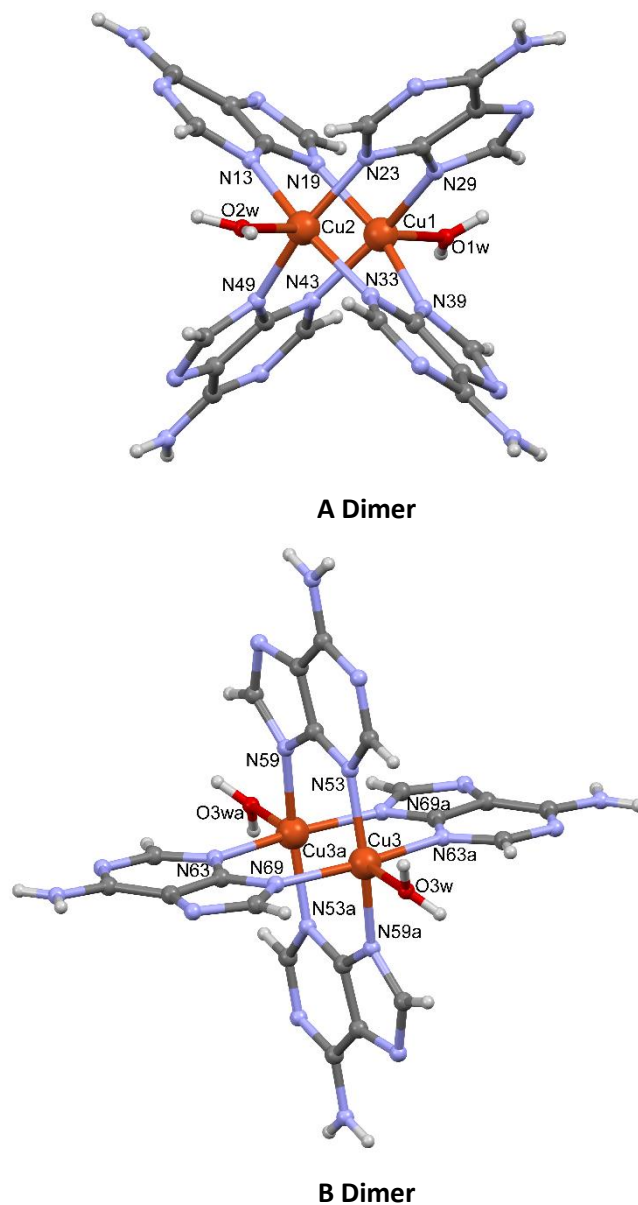


Figure 3.9. Crystallographically independent $[\text{Cu}_2(\mu\text{-ade-}\kappa\text{N3}:\kappa\text{N9})_4(\text{H}_2\text{O})_2]$ entities in compound $\text{Cu}_2\text{ADSO}_4\text{NHET}_3$.

Table 3.7. Coordination bond distances (Å) of compound Cu₂ADSO₄NHET₃.

Cu₂ADSO₄NHET₃			
Cu1–N19	2.020(4)	Cu2–N49	1.994(4)
Cu1–N29	2.004(4)	Cu2–O2w	2.185(4)
Cu1–N39	1.979(4)	Cu1…Cu2	2.956(9)
Cu1–N43	2.024(4)	Cu3–N53	2.024(4)
Cu1–O1w	2.246(4)	Cu3–N59a	1.992(4)
Cu2–N13	2.028(5)	Cu3–N63a	2.031(4)
Cu2–N23	1.994(4)	Cu3–N69	2.011(4)
Cu2–N33	2.038(4)	Cu3…Cu3a	2.965(12)

^aSymmetry codes: (a) $-x + 2, -y, -z + 1$.

The coordination mode of the adenine ensures the rigid built unit of the discrete dimeric entities, (as it was required by our first requirement to achieve porous materials; see Chapter 1). “A” dimers are crosslinked through hydrogen bonding interactions involving the Watson–Crick and Hoogsteen faces of adjacent nucleobases to give a $R_2^2(9)$ ring (by four adjacent symmetry related to other ones). The dihedral angles between the base pairing adenines (171/137 °) allow a 2D propagation interactions in the supramolecular 2D square grid (Figure 3.10, Table 3.8) give rise to a significant ondulation on the dimeric entities arrangement along this b-direction (dihedral angle: 137 °).

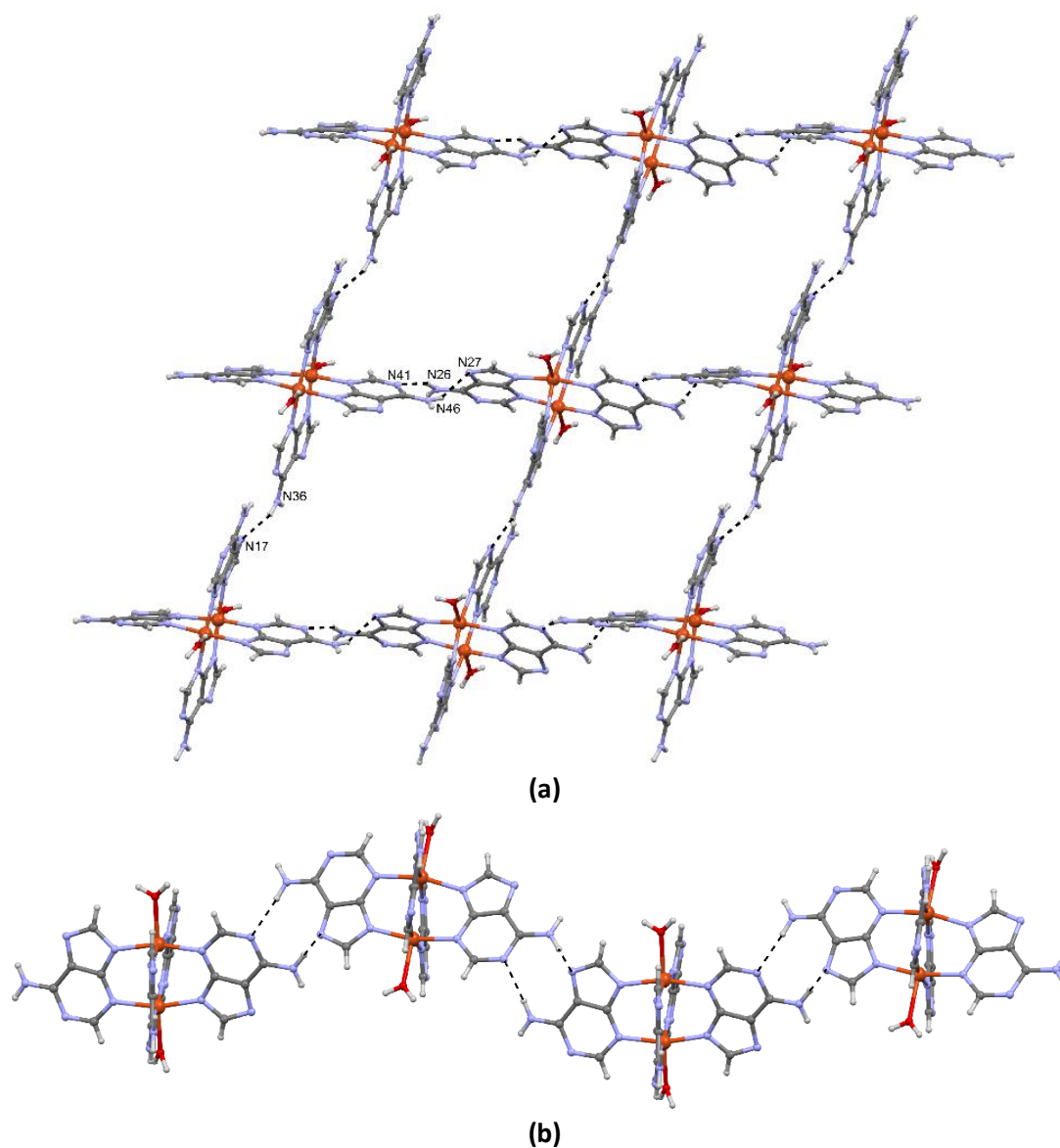


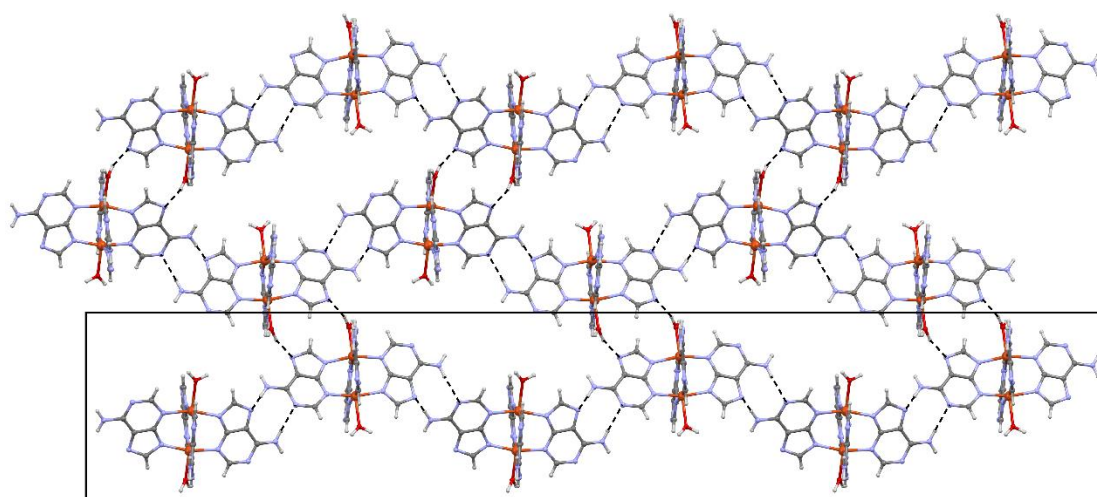
Figure 3.10. Base pairing assembled 2D supramolecular sheets of $[\text{Cu}_2(\mu\text{-ade-}\kappa\text{N3:}\kappa\text{N9})_4(\text{H}_2\text{O})_2]$ "A" entities: frontal (a) and lateral (b) views. The disorder of one of the adeninato ligands has been omitted for clarity.

Table 3.8. Hydrogen-bonding parameters (Å, °) in compound Cu₂ADSO₄NHET₃.^a

D–H···A ^b	H···A	D···A	D–H···A
N16A–H16A···N31a	2.56	3.405(11)	166.3
N16A–H···O3a	2.03	2.807(10)	150.7
N16B–H···N31a	2.05	2.894(11)	166.5
N16B–H···O3a	2.46	3.227(12)	149.0
N26–H···N61b	2.40	3.209(6)	157.9
N26–H···N41c	2.18	2.990(6)	157.0
N36–H···O3wd	2.39	3.216(7)	160.8
N36–H···N17e	2.13	2.966(6)	163.0
N46–H···N27f	2.10	2.885(7)	150.8
N46–H···O6wg	2.34	2.982(7)	132.1
N56–H···O8wd	2.18	2.862(8)	136.4
N66–H···N61h	2.12	2.943(6)	160.8
N66–H···O1wi	2.36	3.196(6)	163.8
O1w–H···N67j	1.97	2.752(5)	152.5
O2w–H···N47g	1.90	2.798(6)	163.5
O3w–H···N37k	1.82	2.666(6)	172.6
O5w–H···N11j	2.08	2.858(6)	150.9
O7w–H···N21	1.99	2.838(6)	175.0
O1M–H···N57	1.97	2.780(6)	155.1

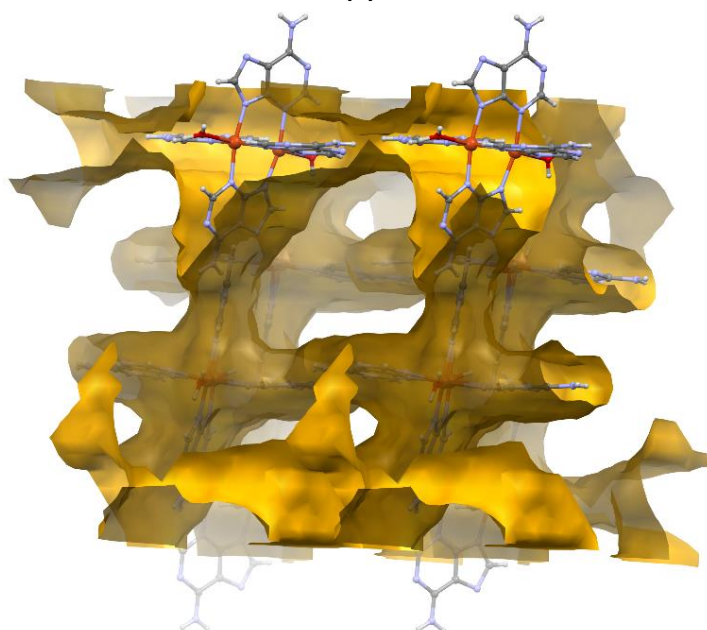
^aSymmetry codes: (a) $x - 1, y, z$; (b) $-x + 2, -y, -z + 1$; (c) $x + 1/2, -y + 1/2, z + 1/2$; (d) $-x + 5/2, y + 1/2, -z + 1/2$; (e) $x + 1, y, z$; (f) $x - 1/2, -y + 1/2, z - 1/2$; (g) $-x + 2, -y, -z$; (h) $-x + 1, -y, -z + 1$; (i) $-x + 3/2, y - 1/2, -z + 1/2$; (j) $-x + 3/2, y + 1/2, -z + 1/2$; (k) $-x + 5/2, y - 1/2, -z + 1/2$. ^bD: donor; A: acceptor.

Additionally, the base pairing assembled [Cu₂(μ-ade-κN3:κN9)₄(H₂O)₂] layers are held together through an additional hydrogen bonding interaction involving the coordinated water molecule as donor and the N7 position of the adeninato ligand as acceptor. As a consequence, a 3D architecture (Figure 3.11) with hexagonal BN (**bnn**) topology^[90], point symbol (4⁶.6⁴), and network of channels with a diameter of 4.6–8.2 Å is observed. The estimated surface area, 2200 m²/g based on theoretical calculations, displays of 45% of the total void space.



Base pairing assembled 2D sheet

(a)



(b)

Figure 3.11. (a) Assembly of the base pairing 2D sheets into a 3D supramolecular network. (b) Potential 3D interconnected channel system generated by the assembly of $[\text{Cu}_2(\mu\text{-ade-}\kappa\text{N3:}\kappa\text{N9})_4(\text{H}_2\text{O})_2]$ “A” entities.

The space present in the channels is not enough to allow the interpenetration of a second supramolecular network of the same type. However, there is space enough to permit the interpenetration of a second but different supramolecular network of base pairing $[\text{Cu}_2(\mu\text{-ade-}\kappa\text{N3:}\kappa\text{N9})_4(\text{H}_2\text{O})_2]$ entities (dimer B). These dimeric entities only employ two of their four adeninato ligands, in *trans* arrangement, to self-assemble through base pairing interactions. Interestingly, in this case, the base pairing interactions involve only the Watson–Crick faces and the interacting adeninato ligands are parallel. As a result, it generates 1D supramolecular linear chains that propagate along the space generated in between the 2D supramolecular sheets during their assembly into the 3D supramolecular architecture previously described

(Figure 3.12). The two subnetworks interact through the hydrogen bonding interaction established between the O1w coordinated water molecule of dimer "A" and the N7 position of the adeninato ligand of an adjacent dimer "B".

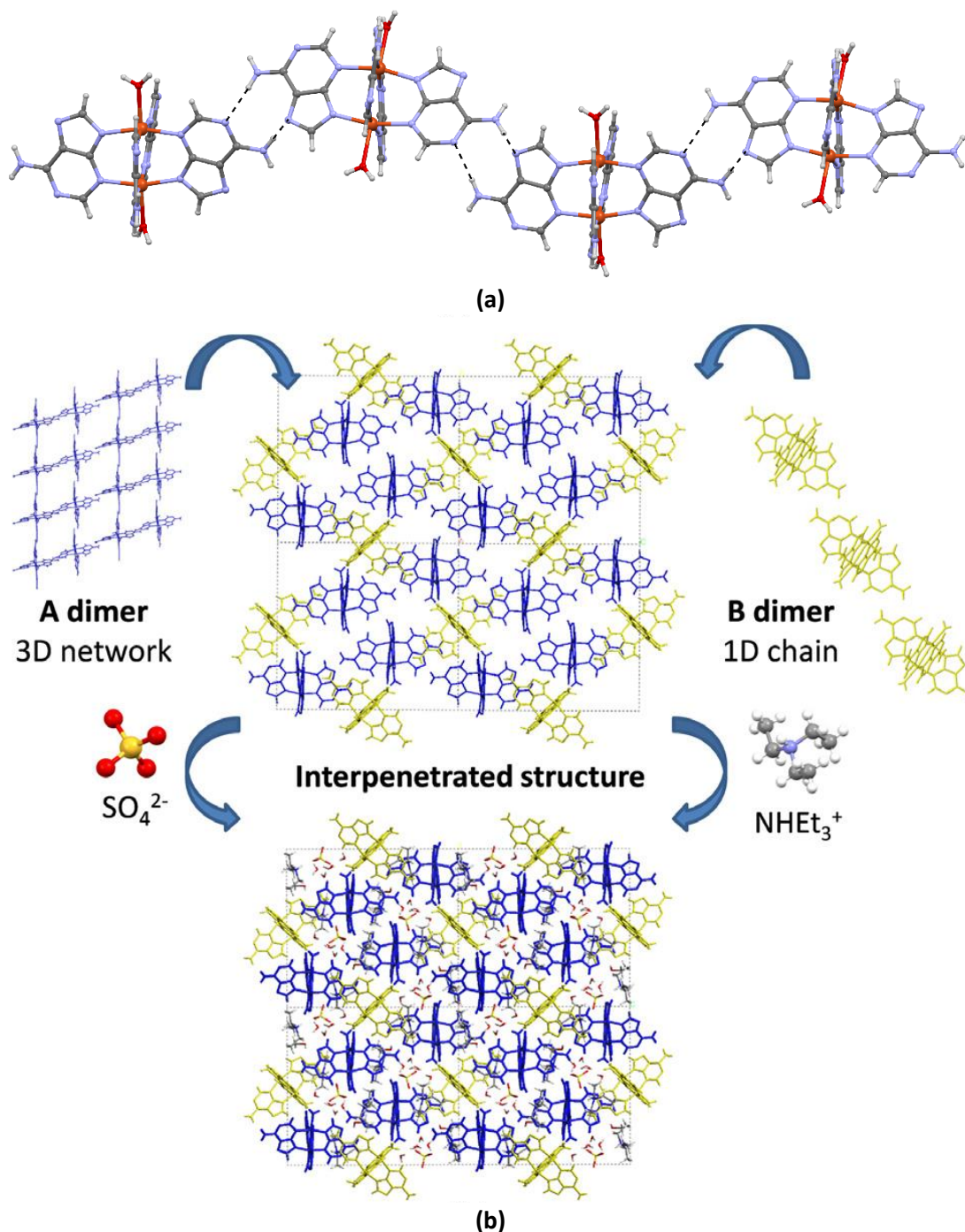


Figure 3.12. (a) Base pairing assembled supramolecular chain of $[\text{Cu}_2(\mu\text{-ade-}\kappa\text{N3:}\kappa\text{N9})_4(\text{H}_2\text{O})_2]$ "B" entities. (b) Overall description of the interpenetration of both $[\text{Cu}_2(\mu\text{-ade-}\kappa\text{N3:}\kappa\text{N9})_4(\text{H}_2\text{O})_2]$ subnetworks and the cocrystallization of $(\text{NH}_2\text{Et}_2)_2\text{SO}_4$ in the voids of the crystal structure.

The remaining available space within the channels is occupied by triethylammonium cations, sulfate anions, crystallization water and methanol molecules that establish a complex

hydrogen bond network involving also the donor/acceptor positions of the adeninato ligands not involved in the base pairing interactions.

3.3.2.2. Structural description of octameric compound.

This compound consists of $[\text{Cu}_8(\mu_4\text{-OH})_4(\mu_3\text{-OH})_4(\text{ade-}\kappa\text{N9})_4(\mu\text{-ade-}\kappa\text{N3}:\kappa\text{N9})_4(\mu\text{-adenine-}\kappa\text{N3}:\kappa\text{N9})_2]$ octameric clusters formed by the stacking of four $\text{Cu}_2(\mu\text{-OH})_2$ dimers that are 90° rotated and linked by a semicoordination to the neighbouring Cu(II) atoms through the hydroxide bridges (Figure 3.13, Table 3.9). The resulting aggregate can be described as the stacking of three cubanes (cubes with the vertices alternatively occupied by the metal and the bridging ligand). The surface of each octamer is occupied by eight adeninato and two neutral adenine ligands. Four adeninato and the neutral adenine entities act as bidentate N3, N9-bridging ligands. These bridging ligands are disordered into two coplanar arrangements with inverted orientation regarding the coordination mode ($\mu\text{-}\kappa\text{N3}:\kappa\text{N9}/\mu\text{-}\kappa\text{N9}:\kappa\text{N3}$). The remaining adeninato ligands are anchored to the corners of the cluster as terminal ligands through N9, and their stiffness is reinforced by intramolecular hydrogen bonds involving the hydroxide bridges and the N3 positions of the nucleobases. All the adenines, adeninatos, and hydroxides are rigidly anchored to the octameric entity because of their multiple coordination bond (OH/adenine/adeninato) or the combination of a coordination bond and an intramolecular hydrogen bond (adeninato).

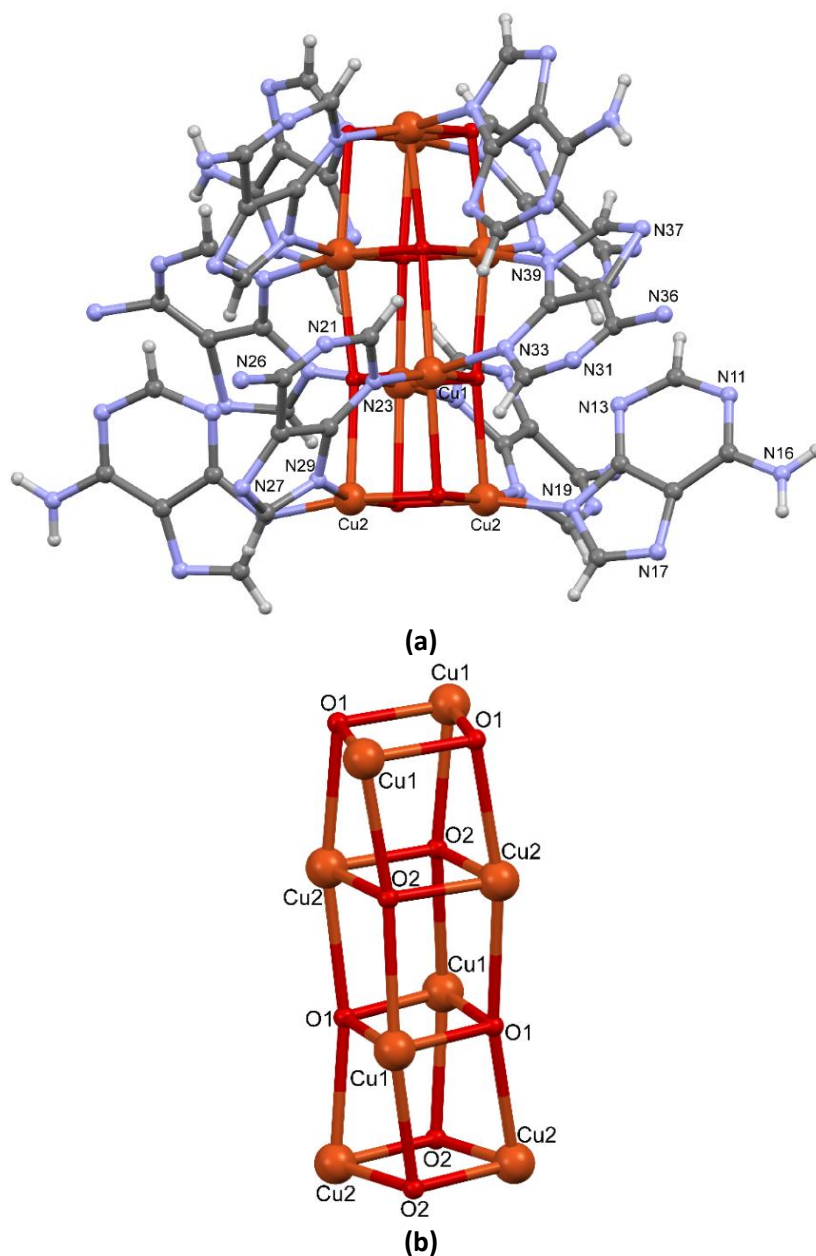


Figure 3.13. Whole octameric entity (a) and $[\text{Cu}_8(\mu_4\text{-OH})_4(\mu_3\text{-OH})_4]$ unit (b).

Table 3.9. Coordination bond distances (\AA) of compound Cu_8AD .^a

Cu_8AD			
Cu1–N33	1.960(1)	Cu2–O2	1.920(8)
Cu1–O1	1.967(6)	Cu2–O2a	1.994(8)
Cu1–O1a	1.998(5)	Cu2–N19	1.962(7)
Cu1–N23	1.974(9)	Cu2–N29	1.962(9)
Cu1–N39b	2.031(1)	Cu1...Cu1a	3.018(2)
		Cu2...Cu2a	2.988(2)

^aSymmetry codes: (a) $-x + 3/2, y, -z + 1/2$; (b) $x, -y, -z + 1/2$.

The interaction of each octamer with the adjacent ones is by means of a hydrogen bonding scheme involving the hydroxide anions and the N7 imidazolic atom of terminal adeninato ligands giving rises to a bidimensional network (Figure 3.14, Table 3.10). Moreover, the bridging adeninato ligands direct their Watson–Crick and Hoogsteen faces outward in those supramolecular layers in such a way that they establish complementary hydrogen bonding interactions with neighbouring tectons. As in previous compounds the Watson–Crick faces establish a $R_2^2(8)$ hydrogen bonding ring. The combination of the above described interactions leads to a 3D 8-connected uninodal supramolecular net with a **sqc3** topology, point symbol being $(4^4 \cdot 6^2)$,^[90] where the geometrical requirements imposed by the rigidity of the octameric unit and the hydrogen bonding interactions avoid the full occupancy of the space. This is reflected by the presence of large monodimensional channels of ca. 4.9 Å (Figure 3.14B) spreading along the [1 0 0] direction, which corresponds to a calculated surface area of 366 m²/g and a 30% of void space.

Table 3.10. Hydrogen-bonding parameters (Å, °) in compound Cu₈AD.^a

D–H···A ^a	H···A	D···A	D–H···A
N16–H16A···N11Ab	2.51	3.340(3)	161
N36–H36B···N13a	2.56	3.317(7)	148
O1–H1···N37c	2.09	2.947(5)	177
O2–H2···N33d	2.18	3.015(6)	167

^aSymmetry codes: (a) $x, -y + 1/2, -z + 1/2$; (b) $-x + 3/2, y, z - 1/2$; (c) $-x + 3/2, -y + 1, z$; (d) $-x + 3/2, y, z + 1/2$. ^bD: donor; A: acceptor.

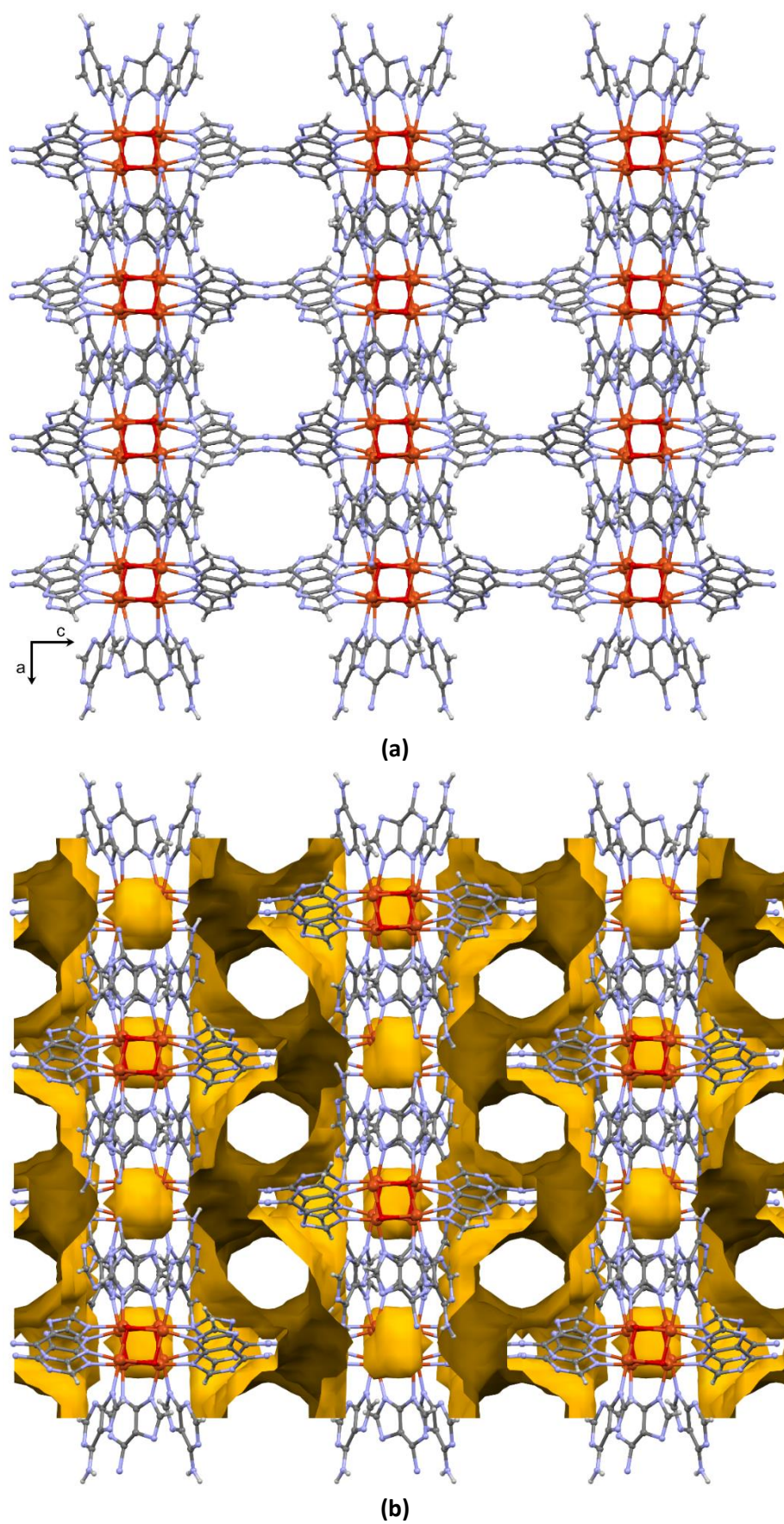


Figure 3.14. Crystal packing of compound Cu_8AD (a) showing the voids in yellow (b).

3.3.2.3. Structural description of heptameric compounds.

The crystal structure of all of the heptameric compounds contains cationic $[\text{Cu}_7(\mu\text{-H}_2\text{O})_6(\mu_3\text{-OH})_6(\mu\text{-ade-}\kappa\text{N3}:\kappa\text{N9})_6]^{2+}$ heptanuclear entities which consists of a central $[\text{Cu}(\text{OH})_6]^{4+}$ core, connected to six additional copper(II) metal centers in a radial and planar arrangement through the hydroxides with μ_3 -bridging mode (Figure 3.15). It generates a wheel shaped entity in which water molecules and $\mu\text{-}\kappa\text{N3}:\kappa\text{N9}$ adeninato ligands bridge the peripheral copper atoms. All the metal centers present an octahedral geometry with the usual Jahn-Teller tetragonal elongation but it is far more pronounced for the peripheral copper(II) centers ($\Delta d \approx 0.5\text{-}0.6 \text{ \AA}$) than for the central one ($\Delta d = 0.2 \text{ \AA}$), probably because of the rigidity of the wheel shaped heptanuclear entity. The elongation at the peripheral copper atoms takes place along the metal-water coordination bonds, in such a way that the coordinated water molecules are less strongly held to the complex entity than the adeninato ligands that establish shorter coordination bonds. In any case, the heptameric entity can be considered as a rigid building unit as all the components establish at least two coordination bonds.

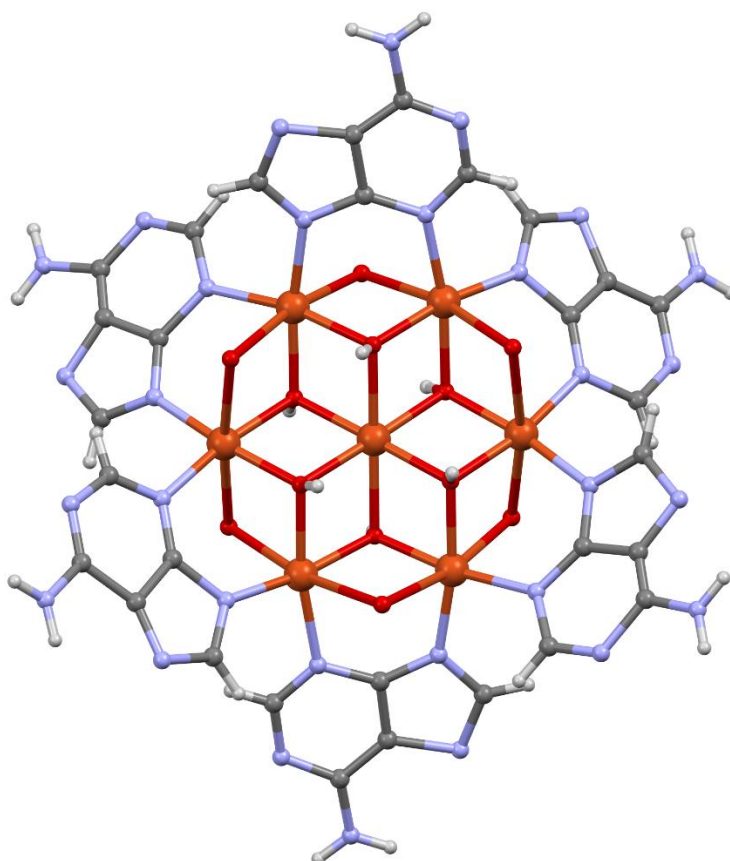


Figure 3.15. Heptameric cationic entity of compounds $\text{Cu}_7\text{ADSO}_4\text{NHEt}_3\text{-1}$, $\text{Cu}_7\text{ADSO}_4\text{NHEt}_3\text{-2}$, Cu_7ADSO_4 , $\text{Cu}_7\text{ADHN-1}$ and $\text{Cu}_7\text{ADHN-2}$.

The scheme of supramolecular interactions between adjacent heptameric units of each compound has significance differences for several reasons. On one hand, the type of counterion or co-crystallization species conditions the way in which the heptanuclear complexes are self-assembled. On the other hand, minor changes in the synthesis conditions also influence the assembly of the structural units, and as consequence, it yields to compounds that can be considered polymorphous, if the solvent molecules hosted in the pore are neglected ($\text{Cu}_7\text{ADSO}_4\text{NHET}_3\text{-1/-2}$ and $\text{Cu}_7\text{ADHN-1/-2}$). As mentioned in the synthesis section of the current chapter, as $\text{Cu}_7\text{ADSO}_4\text{NHET}_3\text{-1}$ and -2 differ on the crystallization times, $\text{Cu}_7\text{ADSO}_4\text{NHET}_3\text{-1}$ can be regarded as the kinetically favoured polymorph, while compound $\text{Cu}_7\text{ADSO}_4\text{NHET}_3\text{-2}$ would be the thermodynamically favoured one.

3.3.2.3.1. Structural description of compounds $\text{Cu}_7\text{ADSO}_4\text{NHET}_3\text{-1}$, $\text{Cu}_7\text{ADSO}_4\text{NHET}_3\text{-2}$ and Cu_7ADSO_4 .

Compounds $\text{Cu}_7\text{ADSO}_4\text{NHET}_3\text{-1}$ and -2 contain doubly capped sulfate/heptamer/sulfate rigid assemblies, where the hydrogen bond donor positions of the $[\text{Cu}(\text{OH})_6]^{4-}$ core are employed to tightly anchor the two sulfate anions, above and below the complex. In fact, the doubly capped sulfate/heptamer/sulfate rigid assembly is not only the key structural unit that fulfils the SMOF building criteria expounded in the introductory section, but it is also the point of disparity between the supramolecular schemes of these two polymorphous compounds (see below). Note, that the presence of two sulfate anions per heptanuclear complex is in agreement with the chemical formulas gathered in Table 3.1. Contrarily, in compound Cu_7ADSO_4 there is one sulfate anion per heptamer which links successively upper and lower $[\text{Cu}(\text{OH})_6]^{3-}$ cores of neighbouring complexes giving rise to a one-dimensional heptamer/sulfate rigid aggregate.

In compound $\text{Cu}_7\text{ADSO}_4\text{NHET}_3\text{-1}$ (Figure 3.16, Table 3.11), the hydrogen-bond donor positions of the $[\text{Cu}(\text{OH})_6]^{4-}$ core are employed to tightly anchor two sulfate anions, above and below the complex, through three $\text{O-H}\cdots\text{O}$ hydrogen bonds to each anion (Figure 3.16b). This doubly capped heptamer-sulfate rigid assembly is the key structural unit that fulfils the SMOF building criteria expounded in the introductory section, since it allows interacting with four adjacent ones through two different rigid synthons (Figure 3.17 and Table 3.12). The first one comes from double adeninato \cdots adeninato π - π stacking interactions taking place between the heptamer and two of the four adjacent heptamers. The second one involves a single adeninato \cdots adeninato π - π stacking and a $\text{N6}_{\text{adeninato}}\cdots\text{O}_{\text{sulfate}}\cdots\text{OH}_{\text{coordinated}}$ hydrogen bond chain. The rigidity of both the heptameric discrete entity and the synthons, built from the

combination of two relatively loose supramolecular interactions, generates a CdSO_4 -like **cds** topology with a $(6^5.8)$ point symbol (nodes being the heptameric units and connectors being the π - π stacking interactions between the adenines).^[90] This supramolecular network presents one-dimensional (1D) channels (mode: 5.5 Å) that imply a 49.0% of unit cell volume in which disordered solvent molecules and triethylammonium cations are placed.

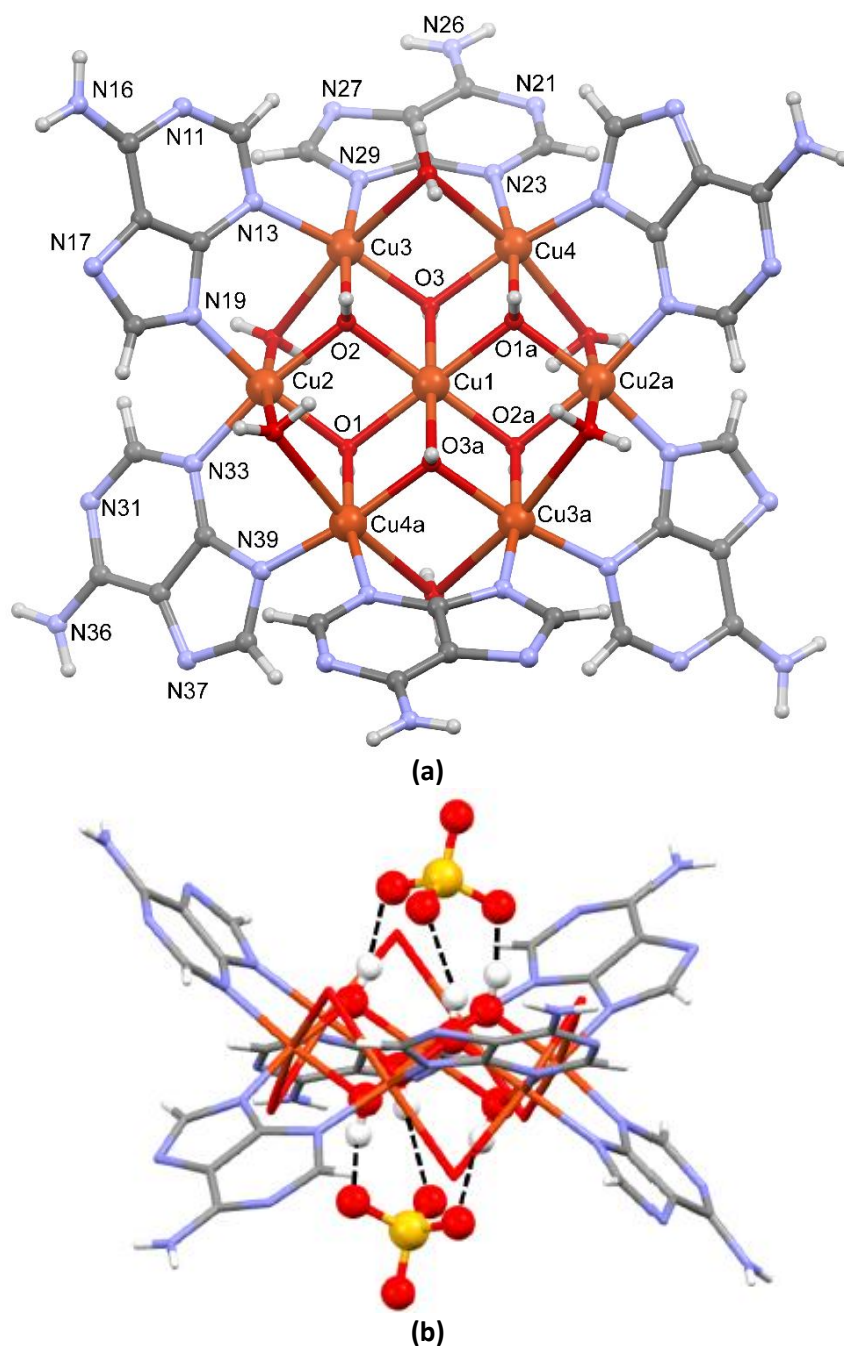


Figure 3.16. $[\text{Cu}_7(\mu\text{-H}_2\text{O})_6(\mu_3\text{-OH})_6(\mu\text{-ade-}\kappa\text{N3:}\kappa\text{N9})_6]^{2+}$ heptanuclear entity (a) and hydrogen bond anchorage of the sulfate anions (b) in compound $\text{Cu}_7\text{ADSO}_4\text{NHET}_3\cdot 1$. Dashed lines indicates hydrogen bond.

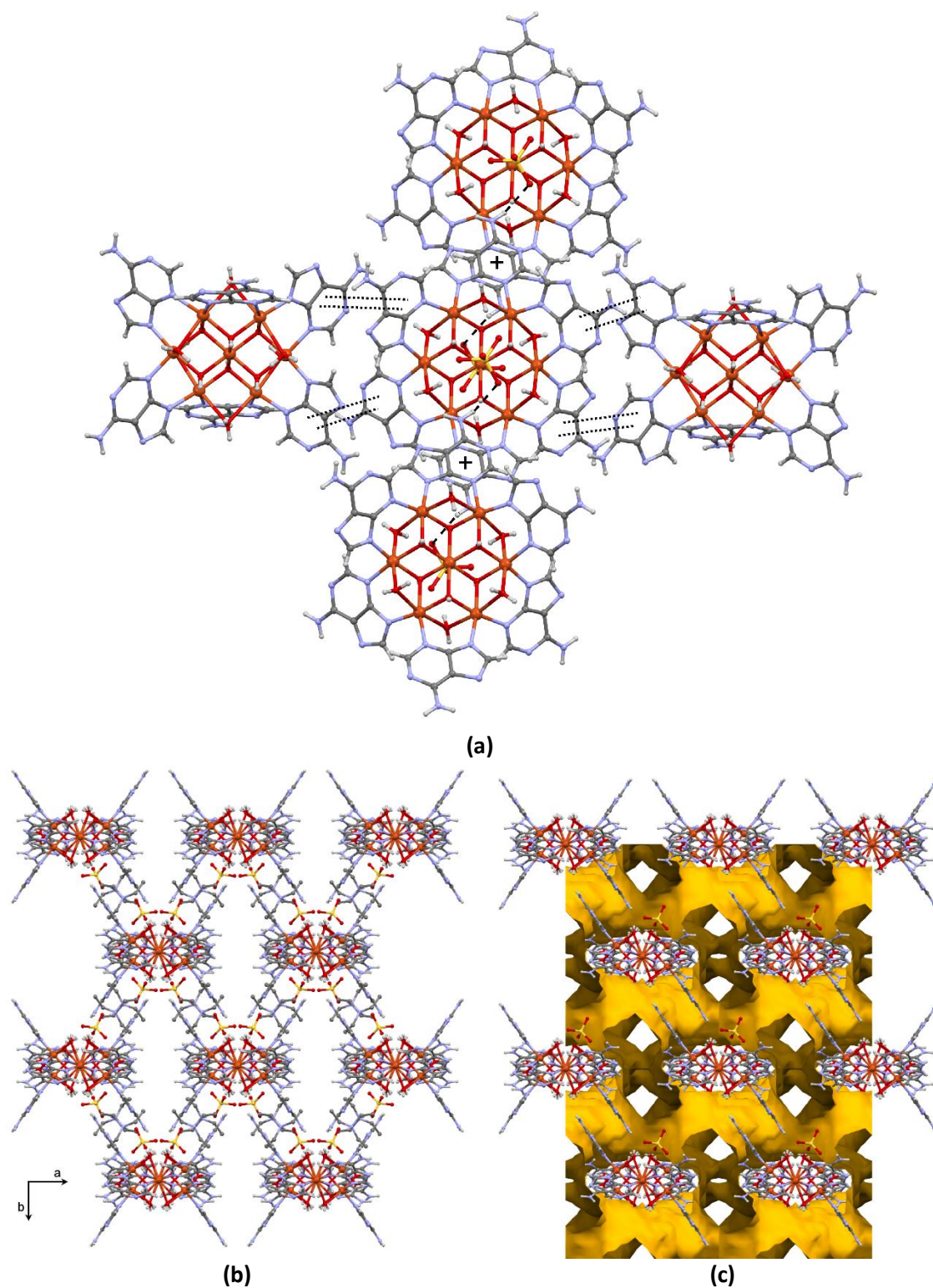


Figure 3.17. Supramolecular interactions connecting each $[\text{Cu}_7(\mu\text{-H}_2\text{O})_6(\mu_3\text{-OH})_6(\mu\text{-ade-}\kappa\text{N3}:\kappa\text{N9})_6]^{2+}$ heptanuclear entity to four adjacent ones (a) and projection of the crystal packing along the crystallographic c axis (b) for compound 1 showing the voids in yellow (c). Double dotted lines and “+” indicate π - π stacking interactions.

In compound $\text{Cu}_7\text{ADSO}_4\text{NH}_4\text{Et}_3\text{-2}$ (Figure 3.18, Table 3.11), the sulfate anions, although still occupying the top and bottom of the heptameric entity, are only anchored through two

hydrogen bonds to the hydroxide bridges (Figure 3.18b). It decreases the steric hindrance around the complex entity allowing the adeninato ligands to supramolecularly connect each complex entity to six adjacent ones (Figure 3.19 and Table 3.13). The same rigid synthon, involving adenine...adenine π - π interactions and a $N7_{\text{adeninato}} \cdots O_{\text{crystallization}} \cdots O_{\text{coordinated}}$ hydrogen bond chain, accounts for all the interactions between the heptamers. The sulfate counterions, although disordered, are held to the Hoogsteen edge of the adeninato ligands through hydrogen bonds. Again, an open structure is achieved, with α -**Po** primitive cubic pcu topology and a $(4^{12}.6^3)$ point symbol, in which 1D channels (mode: 5.8 Å) that encompass the 41.5 % of the unit cell volume are present.

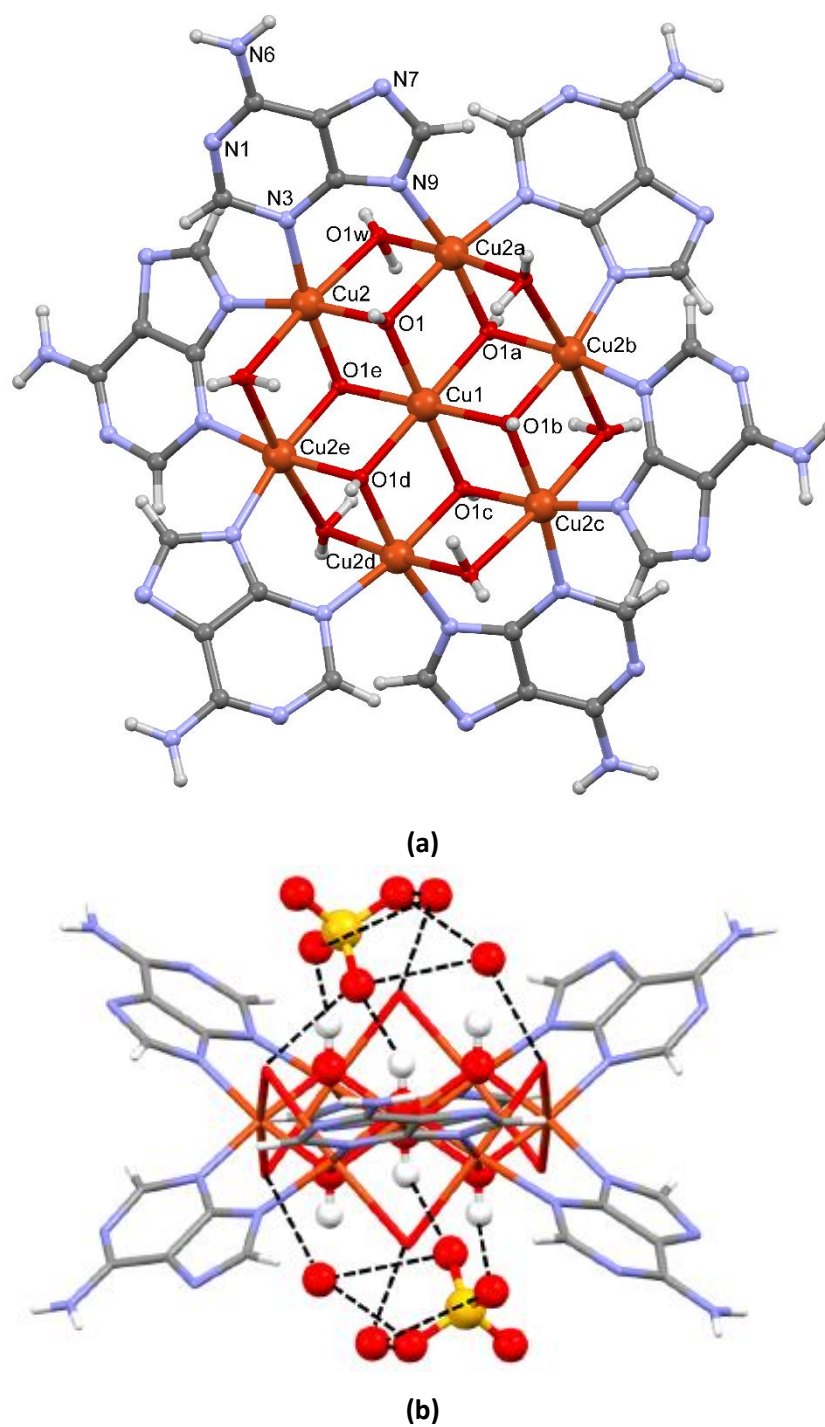


Figure 3.18. $[\text{Cu}_7(\mu\text{-H}_2\text{O})_6(\mu_3\text{-OH})_6(\mu\text{-ade-}\kappa\text{N3}:\kappa\text{N9})_6]^{2+}$ heptanuclear entity (a) and hydrogen bond anchorage of the sulfate anions (b) in compound $\text{Cu}_7\text{ADSO}_4\text{NHET}_3\cdot 2$. Dashed lines indicate hydrogen bond.

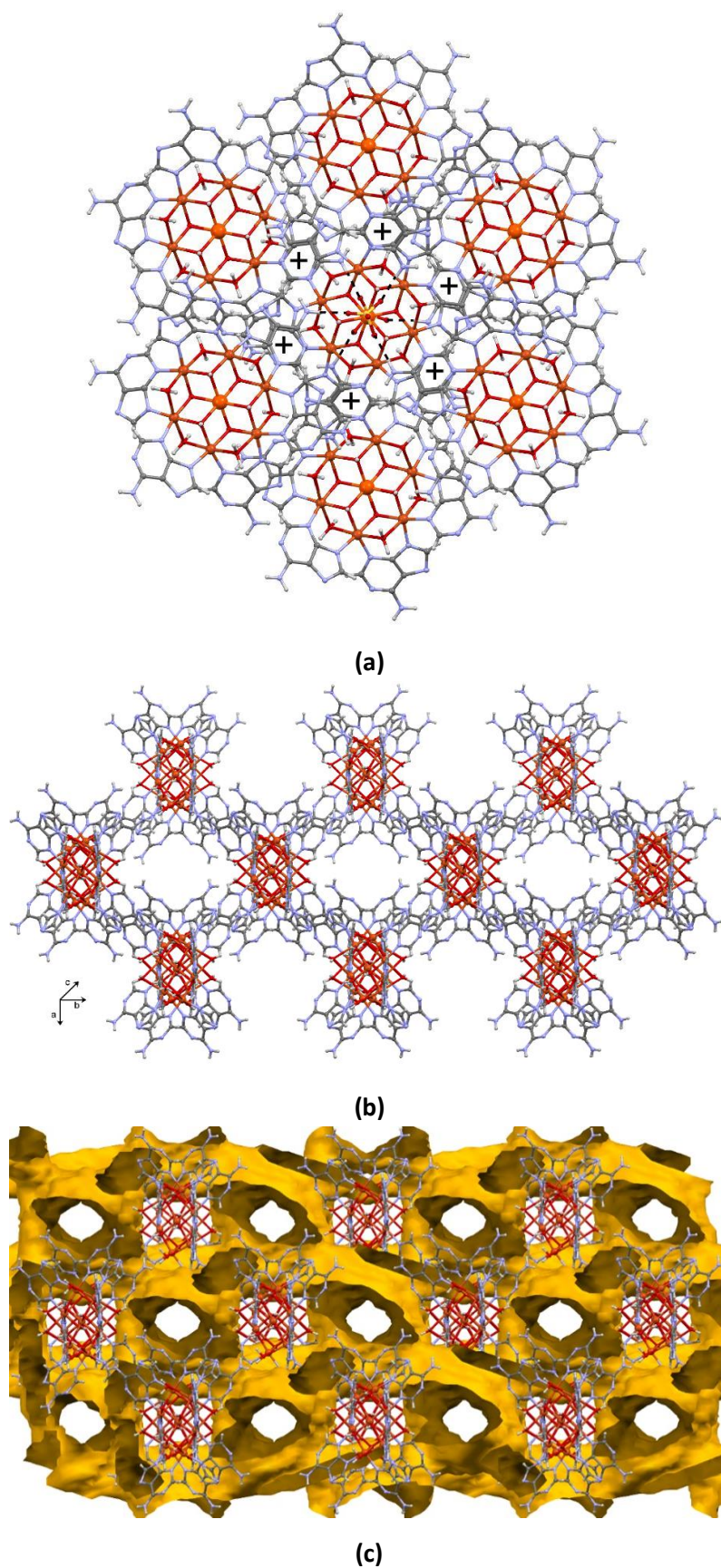


Figure 3.19. Supramolecular interactions connecting each $[\text{Cu}_7(\mu\text{-H}_2\text{O})_6(\mu_3\text{-OH})_6(\mu\text{-ade-}\kappa\text{N3}:\kappa\text{N9})_6]^{2+}$ heptanuclear entity to six adjacent ones (a) and crystal packing of the structure showing the presence of 1D channels (b and c).

In compound Cu_7ADSO_4 (Figure 3.20, Table 3.11), each sulfate anion connects successively upper and lower $[\text{Cu}(\text{OH})_6]^{4-}$ cores of neighbouring heptamers by means of four hydrogen bonding interactions, yielding a one-dimensional heptamer/sulfate supramolecular assembly (Figure 3.21, Table 3.14). Its heptanuclear complex is connected to four surrounding ones again by rigid double synthon that imply adenine...adenine π - π interactions and a $\text{N1}/7_{\text{adeninato}} \cdots \text{Ow}_{\text{coordinated}}$ hydrogen bond. Two of them seem to be excessively long to be considered as π - π interactions. However, the quasi-perfect overlap of adeninatos and references suggest otherwise.^[90] This rigid synthon provides again a porous supramolecular 4-connected unidodal structure with **sql** Shubnikov tetragonal plane net topology and a $(4^4.6^2)$ point symbol, containing 1D channels that account for 26.7% of the unit cell volume.

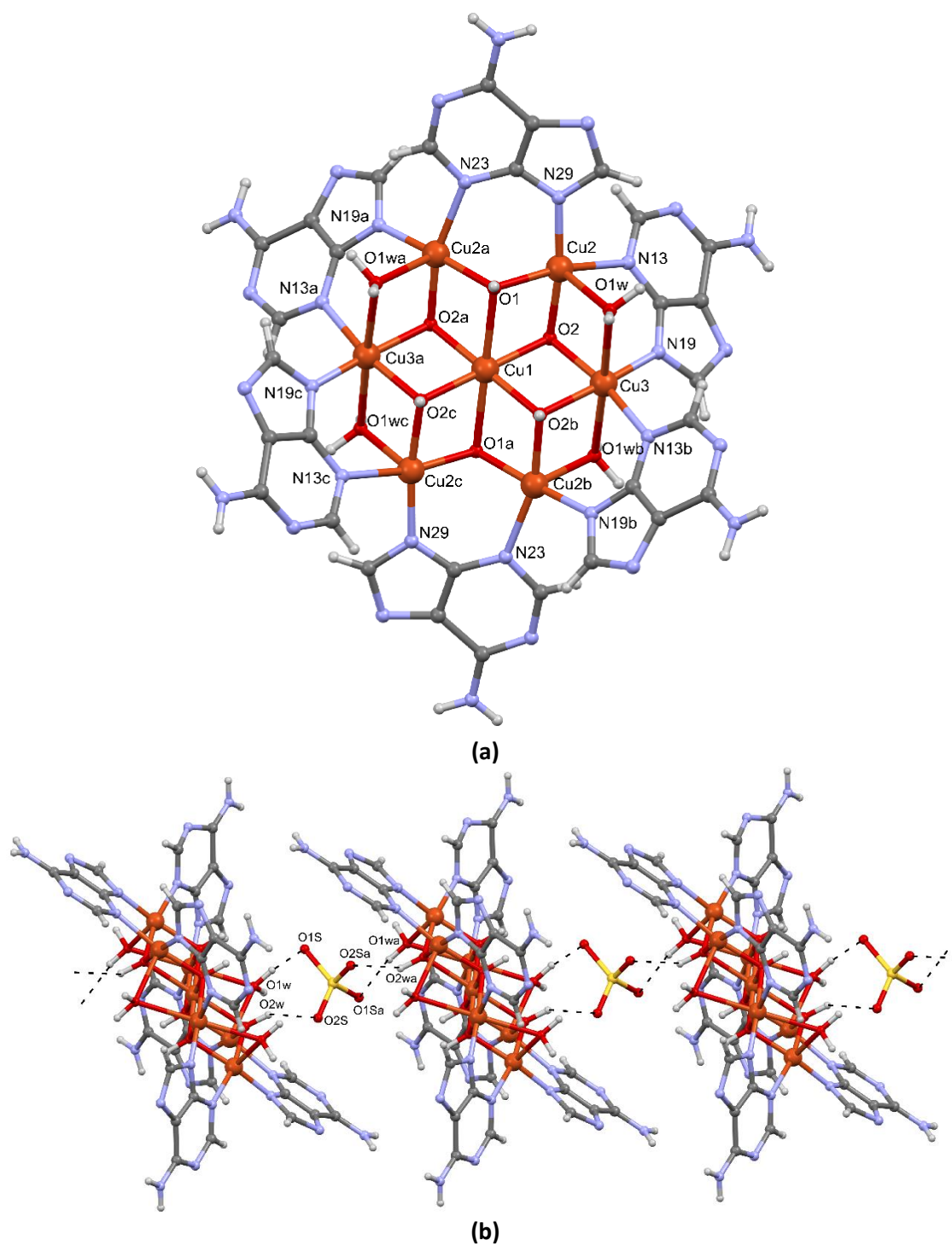


Figure 3.20. (a) $[\text{Cu}_7(\mu\text{-H}_2\text{O})_6(\mu_3\text{-OH})_6(\mu\text{-ade-}\kappa\text{N3}:\kappa\text{N9})_6]^{2+}$ entity and (b) hydrogen bond anchorage of sulfate anions in compound Cu_7ADSO_4 .

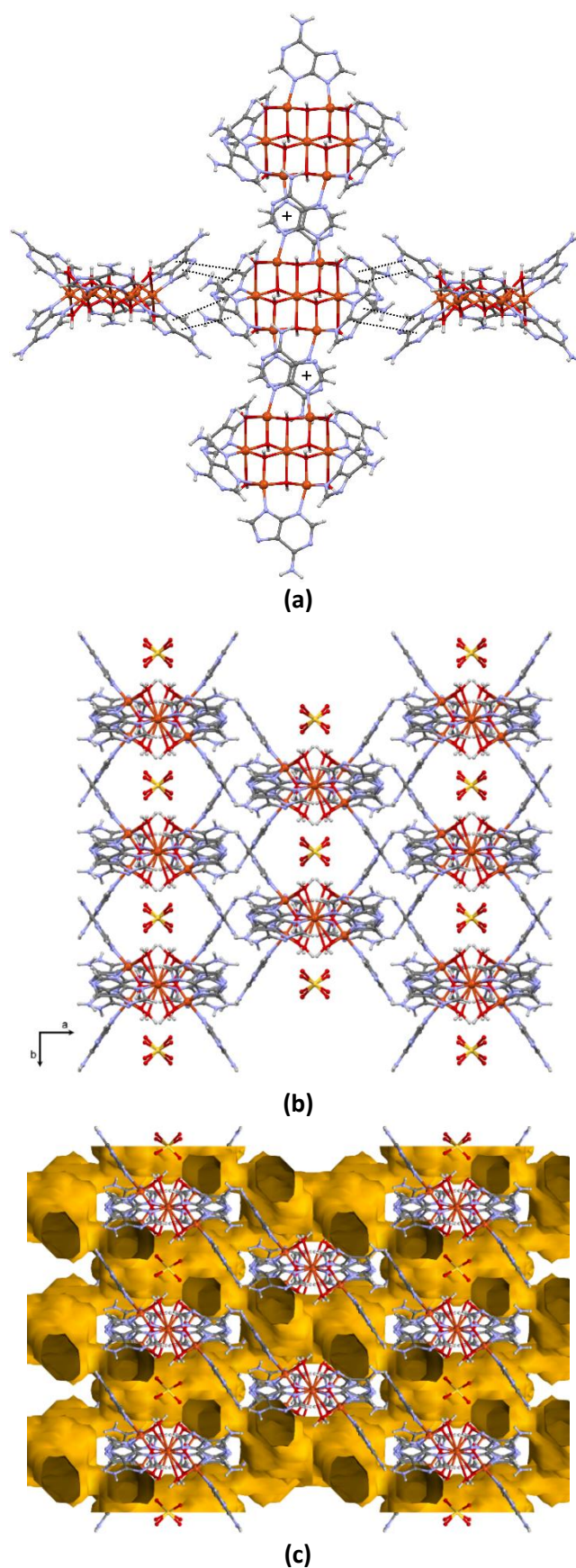


Figure 3.21. Supramolecular interactions connecting each $[\text{Cu}_7(\mu\text{-H}_2\text{O})_6(\mu_3\text{-OH})_6(\mu\text{-ade-}\kappa\text{N3}:\kappa\text{N9})_6]^{2+}$ heptanuclear entity to four adjacent ones (a) and crystal packing of the structure showing the presence of 1D channels (b and c).

Table 3.11. Coordination bond distances (Å) of compounds Cu₇ADSO₄NHET₃-1¹ Cu₇ADSO₄NHET₃-2 and Cu₇ADSO₄.^a

Cu₇ADSO₄NHET₃-1					
Cu1...O1	1.975(5)	Cu3-O2	1.995(6)	Cu4-N23	2.031(9)
Cu1...O2	1.973(6)	Cu3-O3	1.973(6)	Cu4-N39 ⁱ	1.945(8)
Cu1...O3	2.117(5)	Cu3-N13	2.017(11)	Cu4-O3w	2.516(9)
Cu2-O1	1.937(6)	Cu3-N29	1.973(9)	Cu1... Cu2	3.047(2)
Cu2-O2	1.965(5)	Cu3-O1w	2.459(9)	Cu2... Cu4a	3.126(2)
Cu2-O1w	2.409(9)	Cu3-O2w	2.465(9)	Cu1... Cu3	3.138(2)
Cu2-O3w	2.509(9)	Cu4-O1a	2.026(6)	Cu2... Cu3	3.129(2)
Cu2-N33	1.996(8)	Cu4-O3	1.957(5)	Cu1...Cu4	3.153(2)
Cu2-N19	1.945(9)	Cu4-O2w	2.510(9)	Cu3... Cu4	3.086(2)
Cu₇ADSO₄NHET₃-2					
Cu1-O1	2.047(4)	Cu2-O1 ^a	1.977(4)	Cu2-O1w	2.444(5)
Cu2-O1w ^b	2.463(5)	Cu2-N3 ^b	1.988(5)	Cu1... Cu2	3.1037(7)
Cu2-O1	1.961(4)	Cu2-N9	2.012(4)	Cu2... Cu2 ^b	3.1042(7)
Cu₇ADSO₄					
Cu1-O1	2.313(1)	Cu2-O1w	2.307(1)	Cu3-N19B	1.820(2)
Cu1-O1a	2.313(1)	Cu2-N13	2.113(2)	Cu3-N19Bc	1.820(2)
Cu1-O2	1.975(1)	Cu2-N19A	1.942(7)	Cu1...Cu2	3.161(1)
Cu1-O2a	1.975(1)	Cu2-N23	2.108(1)	Cu1...Cu2a	3.161(1)
Cu1-O2b	1.975(1)	Cu3-O2	1.962(1)	Cu1...Cu3	3.002(2)
Cu1-O2c	1.975(1)	Cu3-O2c	1.962(1)	Cu1...Cu3a	3.002(2)
Cu2-O1	1.942(7)	Cu3-N13A	2.101(1)		
Cu2-O2	1.999(8)	Cu3-N13Ac	2.101(1)		

^a Symmetry codes Cu₇ADSO₄NHET₃-1: (a) -x+2, -y, -z+1. Cu₇ADSO₄NHET₃-2: (a) x-y+1, x, -z+1; (b) y, -x+y+1, -z+1. Cu₇ADSO₄: (a) -x, -y, -z; (b) x, y, -z; (c) -x, -y, z.

Table 3.12. Hydrogen bonding parameters (Å, °) and π - π interactions of compound Cu₇ADSO₄NHET₃-1.^a

Hydrogen bonding interactions					
D-H...A ^[b]	H...A	D...A	D-H...A		
O1-H1...O13	1.939	2.739	158		
O2-H2...O11 ^a	2.093	2.740	139		
O3-H3...O14	2.340	2.976	139		
N26-H26B...O14 ^b	2.144	2.976	163		
N41-H41...O12	2.008	2.894	164		
N41-H41...O11	2.608	3.293	133		
O1w-H1w2...O14	1.960	2.807	175		
O2w-H2w2...O13 ^a	2.058	2.892	166		
O3w-H3w1...O11	1.989	2.811	161		
π-π interactions^[c]					
Ring...Ring ^[d]	α	DC	β	DZ	DXY
p1...h3 ^c	4.7	3.91	26.6	3.50	1.75
h2...h2 ^b	0.0	4.13	31.6	3.51	2.16

^a Symmetry codes: (a) $-x+2, -y, -z+1$; (b) $-x+3/2, -y+1/2, -z+1$; (c) $2-x, y, 1/2-z$. ^[b] D: donor; A: acceptor. ^[c] Angle: dihedral angle between the planes (°), DC: distance between the centroids of the rings (Å), α : angle (°) between mean plane of the rings. β : angle (°) between the normal to the first ring and the DC vector (°), DZ: interplanar distance (Å), DXY: lateral displacement (Å), ^[d] h: hexagonal ring of the adeninato and p: pentagonal ring of the adeninato. The numbers 1, 2 and 3 are related with each of the crystallographically independent adenines. ^[d] p₁: C14, C15A, N17, C18, N19; h₂: N21, C22, N23, C24, C25, C26; h₃: N31, C32, N33, C34, C35, C36.

Table 3.13. Hydrogen bonding parameters (Å, °) and π - π interactions in compound $\text{Cu}_7\text{ADSO}_4\text{NHET}_3\cdot 2$.^a

Hydrogen bonding interactions					
D-H...A ^[b]	H...A	D...A	D-H...A		
O1-H1...O2Sa	2.058	2.788	162		
O1-H1...O2Sb	2.211	2.839	141		
N16-H16A...O2S	1.979	2.834	173		
N16-H16A...O2Sc	2.189	2.960	149		
π-π interactions^[c]					
Ring...Ring ^[d]	α	DC	β	DZ	DXY
h...p ^d	0.0	3.89	27.1	3.47	1.77
h...h ^d	0.0	3.77	24.6	3.43	1.57
p...h ^d	0.0	3.89	28.3	3.43	1.84
p...p ^d	0.0	4.00	30.0	3.47	2.00

^aSymmetry codes: (a) $-x+y+2/3, y+1/3, z-1/6$; (b) $-y+5/3, -x+4/3, z-1/6$; (c) $-x+y, -x+1, z$; (d) $4/3-X, 2/3-X+Y, 7/6-Z$. ^[b] D: donor; A: acceptor. ^[c] Angle: dihedral angle between the planes (°), DC: distance between the centroids of the rings (Å), α : angle (°) between mean plane of the rings. β : angle (°) between the normal to the first ring and the DC vector (°), DZ: interplanar distance (Å), DXY: lateral displacement (Å), ^[d] h: hexagonal ring of the adeninato and p: pentagonal ring of the adeninato.

Table 3.14. Hydrogen bonding parameters (Å, °) and π - π interactions in compound Cu_7ADSO_4 .^a

D-H...A ^[b]	H...A	D...A	D-H...A		
N26-H26A... N26 ^a	2.61	2.98(2)	107		
O1-H1...O2S ^b	1.87	2.75(2)	148		
O1w-H1wA...O1S	1.91	2.74(2)	149		
π-π interactions^[c]					
Ring...Ring ^[d]	α	DC	DZ		
p1A... p1A ^c	12.0	5.72(4)	56.6	3.15(1)	4.77
p1A... p1B ^c	8.0	5.07(4)	45.9	3.52(9)	3.64
p2A...p2A ^b	0.1	4.62	4.58		

^aSymmetry codes: (a) $-x + 3/2, -y - 1/2, z$; (b) $-x + 1, -y, z$; (c) $-x, y, -z - 1/2$. ^[b] D: donor; A: acceptor. ^[c] Angle: dihedral angle between the planes (°), DC: distance between the centroids of the rings (Å), α : angle (°) between mean plane of the rings. β : angle (°) between the normal to the first ring and the DC vector (°), DZ: interplanar distance (Å), DXY: lateral displacement (Å), ^[d] h: hexagonal ring of the adeninato, p: pentagonal ring of the adeninato.

3.3.2.3.2. Structural description of compound $\text{Cu}_7\text{ADHN-1}$ and $\text{Cu}_7\text{ADHN-2}$.

The asymmetric unit of compound $\text{Cu}_7\text{ADHN-1}$ consists of two half heptamer and two HN counterions (Figure 3.22, Table 3.15). The capability of HN to behave as hydrogen bond donor/acceptor and as π -bonding platform, give rises to an interaction scheme among the

building completely different to those above described, controlling in great extent the resulting crystal packing, as described below. The parameters representing the principal supramolecular interactions are gathered in Table 3.16.

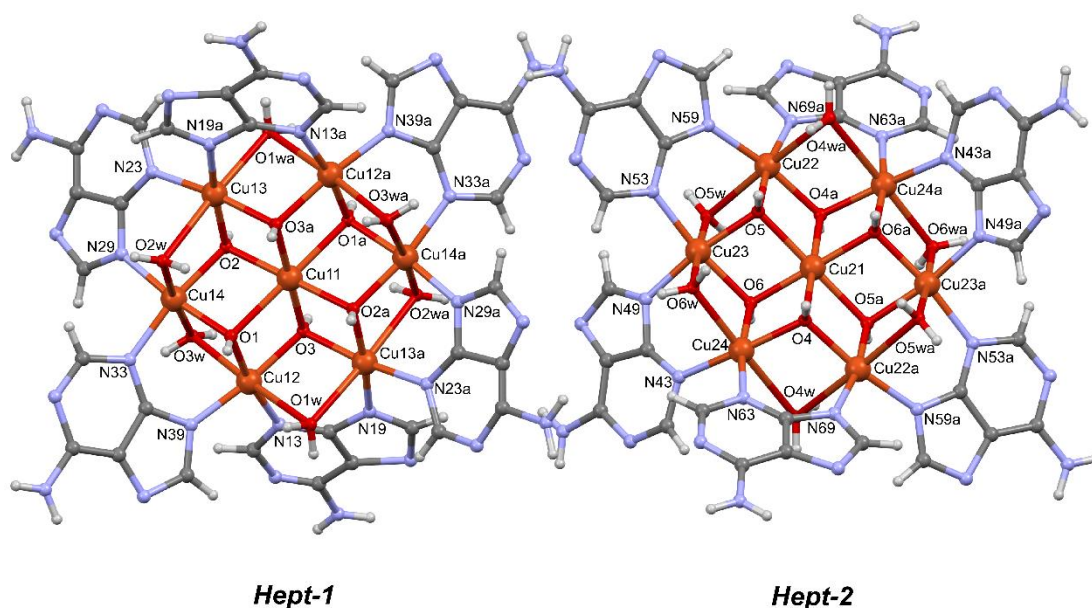


Figure 3.22. Both $[\text{Cu}_7(\mu\text{-H}_2\text{O})_6(\mu_3\text{-OH})_6(\mu\text{-ade-}\kappa\text{N3}:\kappa\text{N9})_6]^{2+}$ entities in compound $\text{Cu}_7\text{ADHN-1}$.

Figure 3.23a shows the supramolecular 2D framework (parallel to *cb* crystallographic plane) with *sql* topology consisting of 4-connected heptamer-2 units bridged by the rigid synthon established by one of the 6-hydroxynicotinate anions (HN-2) which is hydrogen bonded to hydroxide and water ligands ($\text{O78}\cdots\text{H-O6w}$, $\text{O77}\cdots\text{H-O4}$, $\text{O72}\cdots\text{H-O4w}$) and sandwiched by π - π interactions between two adeninos (AD-5 and AD-6) of the neighboring heptamers. Heptamer-2 units of neighboring layers are crosslinked by the interactions established by the HN-1/heptamer-1/HN-1 ensemble (Figure 3.23b) to yield a like 3D supramolecular network. Note that HN-1 bridges neighboring heptamer-1 and heptamer-2 by double rigid synthons: (1) it binds to heptamer-1 by means of a double hydrogen bonding established by the carboxylate O-atoms with hydroxide and water ligands ($\text{O87}\cdots\text{H-O3w}$, $\text{O88}\cdots\text{H-O2}$, $\text{O72}\cdots\text{H-O4w}$) and by π - π interactions with an adeninato (AD-2), and (2) it binds to heptamer-2 again through a double hydrogen bonding established by the carbonyl O-atom and the neighboring aromatic H-atom with Hoogsteen face of an adeninato (AD-4) ($\text{O82}\cdots\text{H-N46}$, $\text{C83-H}\cdots\text{N47}$). Some other weaker interactions (displaced π -interactions and $\text{H}\cdots\pi$ interactions) have been omitted from the discussion for clarity. The overall crystal structure contains an intricate system of 3D channels that imply a 26.2% of unit cell volume, which host the crystallization solvent molecules (Figure 3.24).

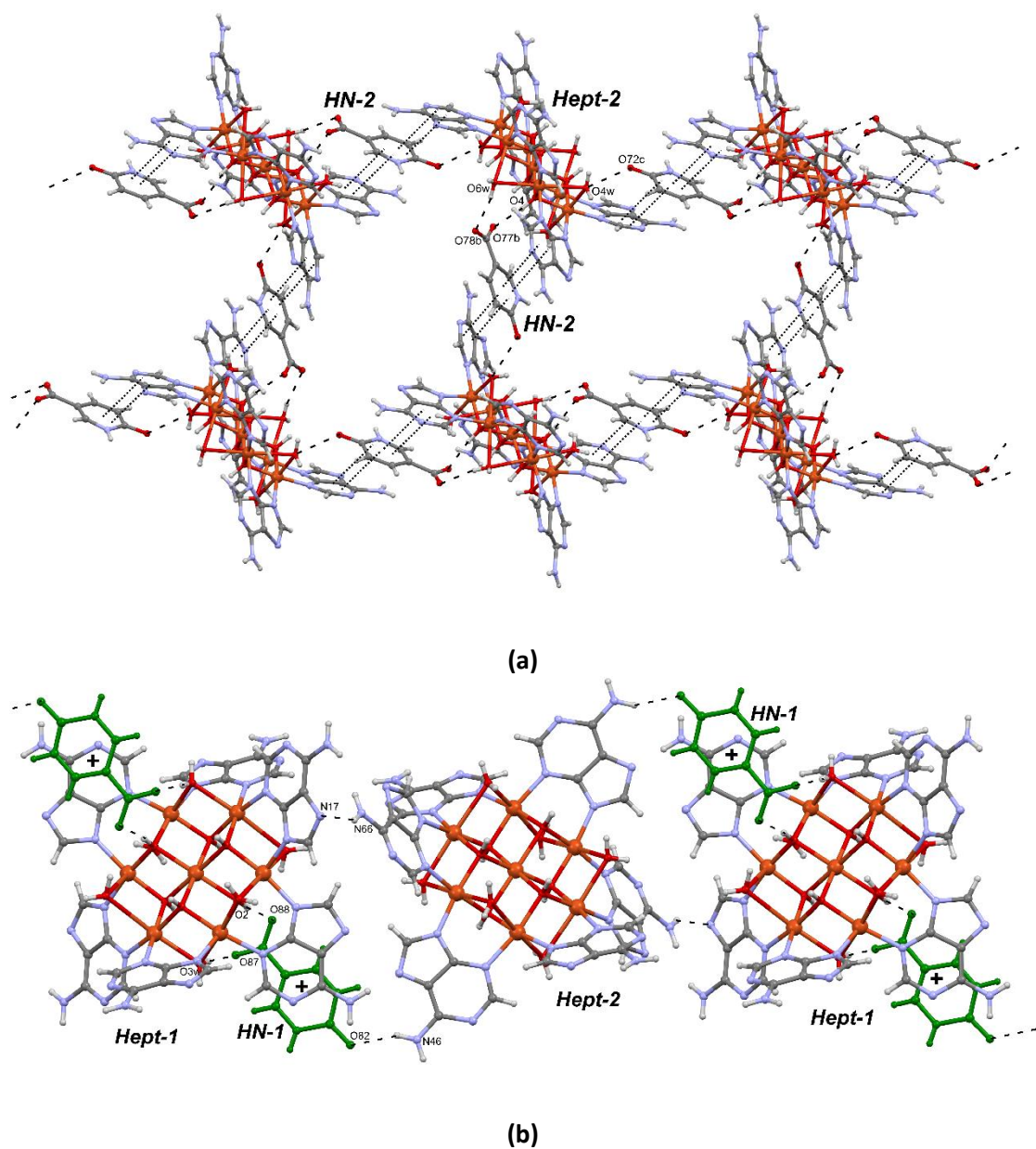


Figure 3.23. Supramolecular chain formed by the assembly of heptamer-2/HN-2 units (a). HN-1/heptamer-1/HN-1 supramolecular ensemble crosslinking of upper layers (b).

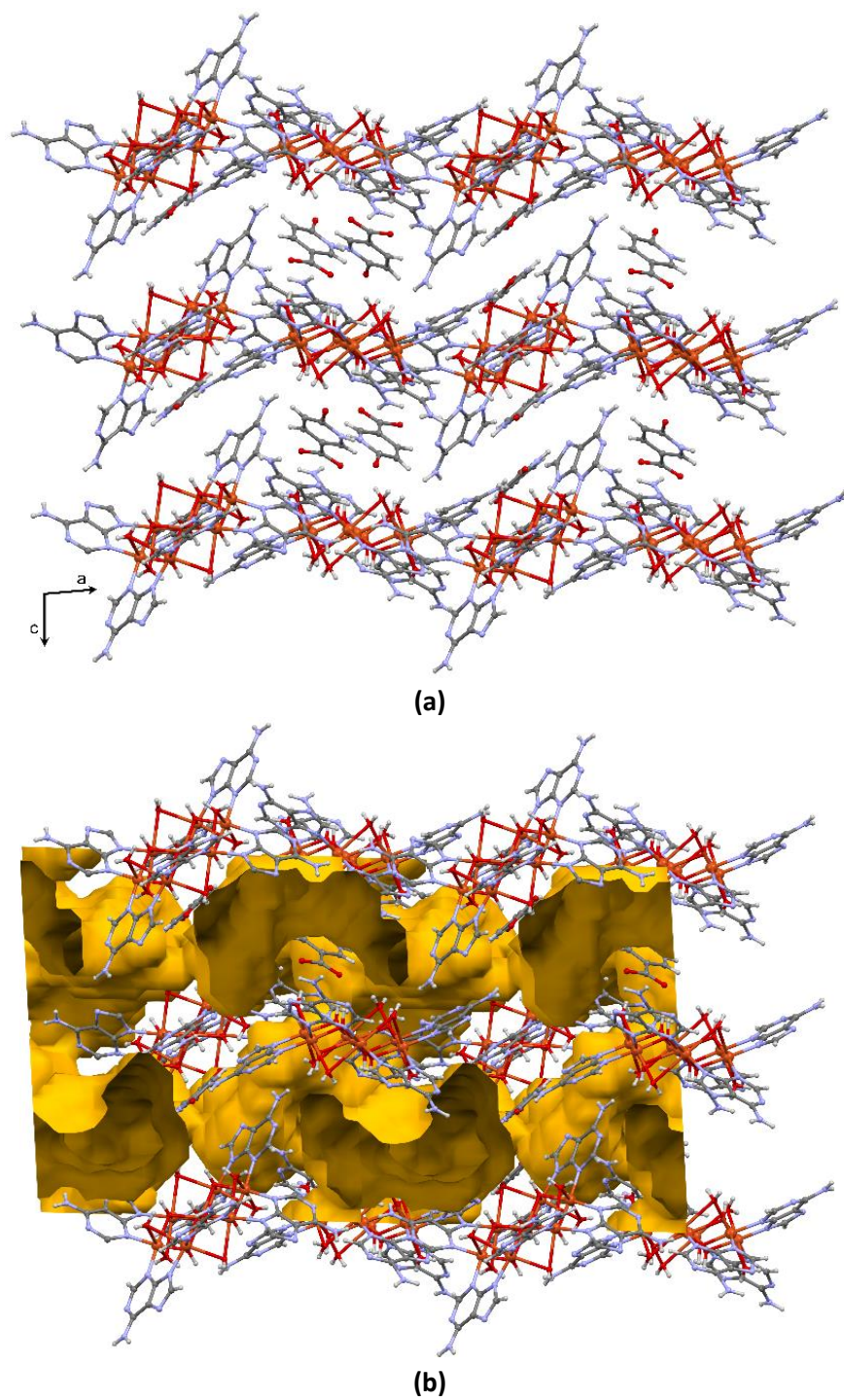


Figure 3.24. Crystal packing of compound $\text{Cu}_7\text{ADHN-1}$ (a) showing the voids in yellow (b).

Table 3.15. Coordination bond distances (Å) of compound Cu₇ADHN-1.^a

Cu₇ADHN-1			
Cu11–O1	1.954(4)	Cu22–N53	2.003(6)
Cu11–O1a	1.954(4)	Cu22–N69b	1.981(6)
Cu11–O2	2.104(4)	Cu22–O4	1.988(4)
Cu11–O2a	2.104(4)	Cu22–O5	1.956(4)
Cu11–O3	2.180(4)	Cu23–N43	2.025(6)
Cu11–O3a	2.180(4)	Cu23–N59a	1.967(7)
Cu12–N13	1.995(6)	Cu23–O5	1.992(4)
Cu12–N39	1.998(6)	Cu23–O6	1.943(4)
Cu12–O1a	1.997(4)	Cu23–O5w	2.437(5)
Cu12–O3	1.949(4)	Cu24–N49	1.964(6)
Cu12–O3wa	2.333(4)	Cu24–N63	1.983(6)
Cu13–N19	1.985(5)	Cu24–O4b	1.980(4)
Cu13–N29	1.996(5)	Cu24–O6	1.956(6)
Cu13–O2	1.988(4)	Cu11…Cu12	3.095(5)
Cu13–O3	1.971(4)	Cu11…Cu12a	3.095(5)
Cu14–N23	2.013(6)	Cu11…Cu13	3.189(6)
Cu14–N23a	1.979(6)	Cu11…Cu13a	3.189(6)
Cu14–O1	1.990(4)	Cu11…Cu14	3.071(5)
Cu14–O2	1.965(4)	Cu11…Cu14a	3.071(5)
Cu14–O3w	2.425(4)	Cu21…Cu22	3.050(9)
Cu21–O4	2.014(4)	Cu21…Cu22b	3.050(9)
Cu21–O4b	2.014(4)	Cu21…Cu23	3.140(9)
Cu21–O5	2.016(4)	Cu21…Cu23b	3.140(9)
Cu21–O5b	2.016(4)	Cu21…Cu24	3.153(8)
Cu21–O6	2.224(4)	Cu21…Cu24b	3.153(8)
Cu21–O6b	2.224(4)		

^a Symmetry codes: (a) $-x + 1, -y + 1, -z + 1$; (b) $-x + 2, -y, -z + 1$.

Table 3.16. Hydrogen bonding parameters (Å, °) and π - π interactions in compound Cu₇ADHN-1.^a

D-H...A ^[b]	H...A	D...A	D-H...A
N26-H26A... N26b	2.60	3.15(1)	123
N46b-H46Ab...O82	2.09	2.87(9)	151
N66A-H66A...N17a	2.22	2.99(2)	149
C28-H28...N61b	2.67	3.47(1)	145
C83-H83...N47b	1.90	2.83(8)	175
O2-H2...O88	1.85	2.82(7)	171
O4-H4...O77Ac	1.88	2.84(6)	170
O4-H4...O77Bc	1.77	2.70(6)	158
O1w-H1wA...O88	2.35	3.21(9)	176
O3w-H3wA...O87	1.92	2.77(6)	170
O4w-H4wA...N16a	2.40	3.15(8)	147
O4w-H4wA...O72b	2.59	2.88(3)	100
O5w-H5wB...O77Bc	1.97	2.79(7)	160
O6w-H6wB...O78Ab	2.05	2.89(9)	163
O6w-H6wB...O78Bb	2.11	2.97(8)	173

π - π interactions ^[c]					
Ring...Ring ^[d]	α	DC	β	DZ	DXY
hh1B...p5 ^a	9.8	5.37(1)	53.7	3.18(1)	3.74
hh1B ...h5 ^b	8.0	4.27(2)	37.0	3.38(3)	2.57
hh1B ...p6 ^b	5.6	3.76(1)	19.8	3.40(9)	1.27
hh2...p1 ^a	32.0	3.96(4)	13.8	2.89(2)	--
hh2...p2 ^a	13.4	4.55(4)	46.9	3.47(4)	3.32
hh1A...p5 ^a	14.3	5.71(8)	43.1	3.08(9)	3.90
hh1A ...h6 ^b	5.0	4.04(1)	29.1	3.37(3)	1.96
hh1A ...p6 ^b	4.9	3.79(1)	25.0	3.41(5)	1.60

^aSymmetry codes: (a) $x - 1, -y + 1/2, z - 1/2$; (b) $-x + 1, -y, -z + 1$; (c) $x + 1, y, z$. ^[b]D: donor; A: acceptor. ^[c]Angle: dihedral angle between the planes (°), DC: distance between the centroids of the rings (Å), α : angle (°) between mean plane of the rings. β : angle (°) between the normal to the first ring and the DC vector (°), DZ: interplanar distance (Å), DXY: lateral displacement (Å), ^[d]h: hexagonal ring of the adeninato, p: pentagonal ring of the adeninato and hh: ring of the hydroxynicotinato. The numbers from 1 to 6 are related with each of the crystallographically independent adenines and hydroxynicotinato. p1: C14, C15, N17, C18, N19. p2: C24, C25, N27, C28, N29. h5: N51, C52, N53, C54, C55. p5: C54, C55, N57, C58, N59. h6: N61, C62, N63, C64, C65. p6: C64, C65, N67, C68, N69. hh1A: N71A, C72A, C73A, C74A, C75A, C76A. hh1B: N71B, C72B, C73B, C74B, C75B, C76B. Hh2: N81, C82, C83, C84, C85, C86.

The asymmetric unit of compound $\text{Cu}_7\text{ADHN-2}$ consist of two half heptamers (heptamer-1 and heptamer-2) and a whole dianionic HN counterion (Figure 3.25, Table 3.17). Thus, the heptamer/HN ratio is reduced to 1/1, which induces significant differences in the crystal packing with regard to the previous case which contains two counterions per heptamer. It must be noted that the pH values in the synthesis of $\text{Cu}_7\text{ADHN-2}$ (10.5) is higher than that of $\text{Cu}_7\text{ADHN-1}$, and is also close to the pK_a_2 (ca. 11) corresponding to the amidic proton of 2-pyridone form, which might explain the inclusion of HN as dianion in this latter structure.

Table 3.18 gathers the parameters describing the main non-covalent interactions of $\text{Cu}_7\text{ADHN-2}$. Heptamer-1 and heptamer-2 entities assemble successively by means of a double set of $\pi-\pi$ stacking interactions (AD-1 \cdots AD-4 and AD-3 \cdots AD-5) to yield a supramolecular strip heptamers extending along the [101] direction. Each HN counterion is hydrogen bonded to hydroxide and water ligands (O71 \cdots H-O6w, O72 \cdots H-O4, O6N \cdots H-O1) and sandwiched by $\pi-\pi$ interactions between two adeninatos (AD-1 and AD-4) of heptamer-1 and heptamer-2 entities of neighbouring chains (Figure 3.26A). This rigid synthon is the same as that described for HN-2 in $\text{Cu}_7\text{ADHN-1}$. As a result, the connection between heptamer-1 and heptamer-2 entities yields 2D supramolecular ensemble parallel to *ac*-plane. These layers are connected by means of the displaced $\pi-\pi$ interactions taking place between adjacent heptamer-2 entities (Figure 3.26). The resulting crystal structure contains a 3D channel system that hosts the solvent molecules and accounts for 26.1 % of the total volume (Figure 3.27).

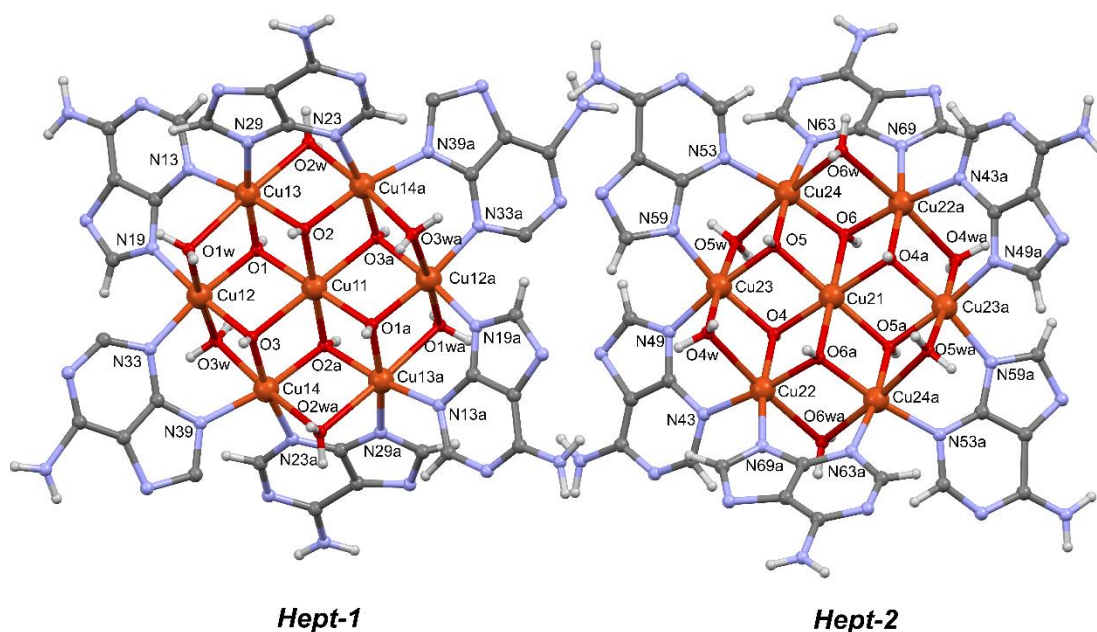


Figure 3.25. The two $[\text{Cu}_7(\mu\text{-H}_2\text{O})_6(\mu_3\text{-OH})_6(\mu\text{-ade-}\kappa\text{N3:}\kappa\text{N9})_6]^{2+}$ entities in compound $\text{Cu}_7\text{ADHN-2}$.

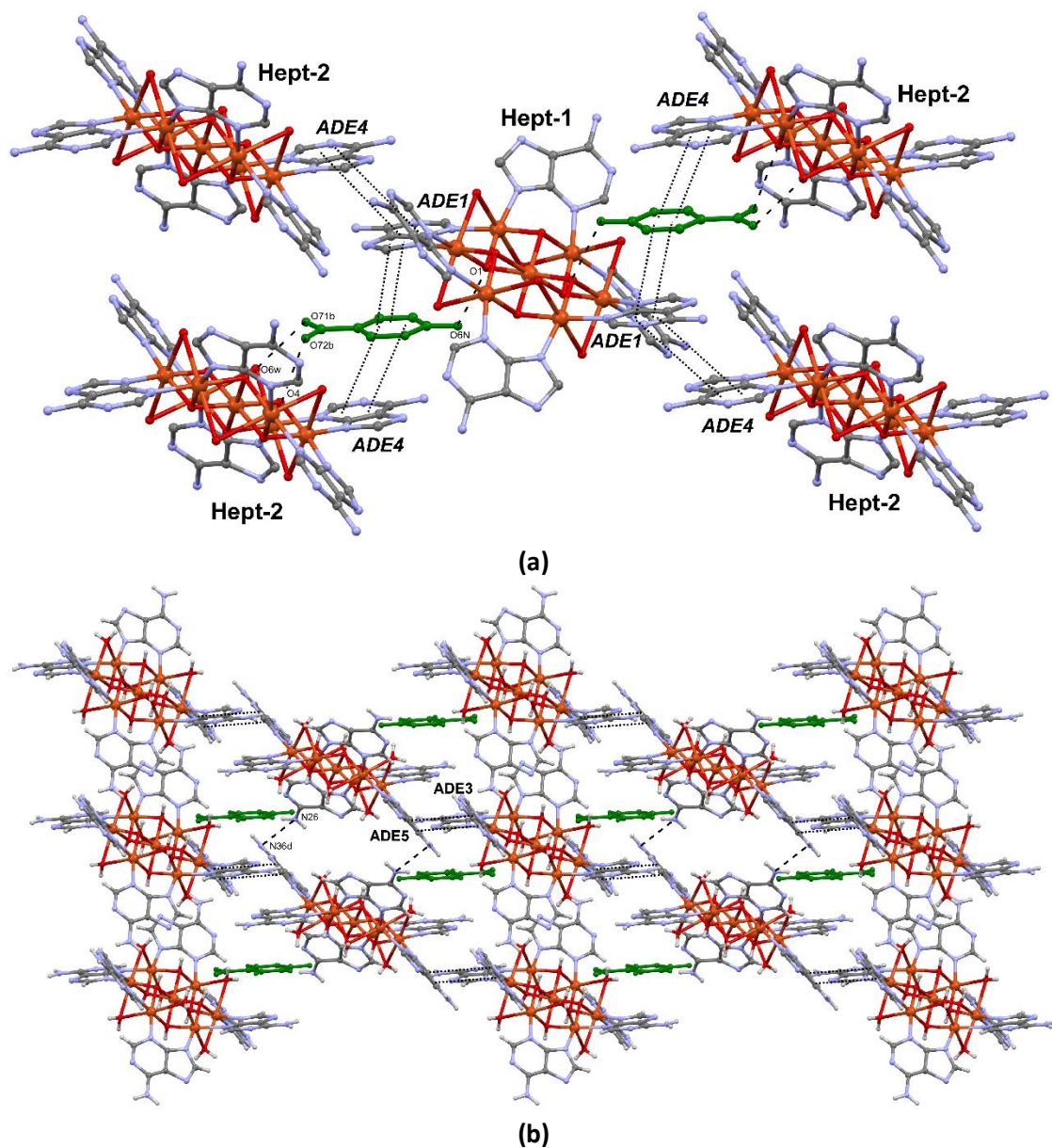


Figure 3.26. Set of interactions connecting hept-1 and hept-2 entities (A) and resulting supramolecular 2D ensemble in compound $\text{Cu}_7\text{ADHN-2}$ (B). In (A) H-atoms were omitted and HN anions were coloured in green for clarity.

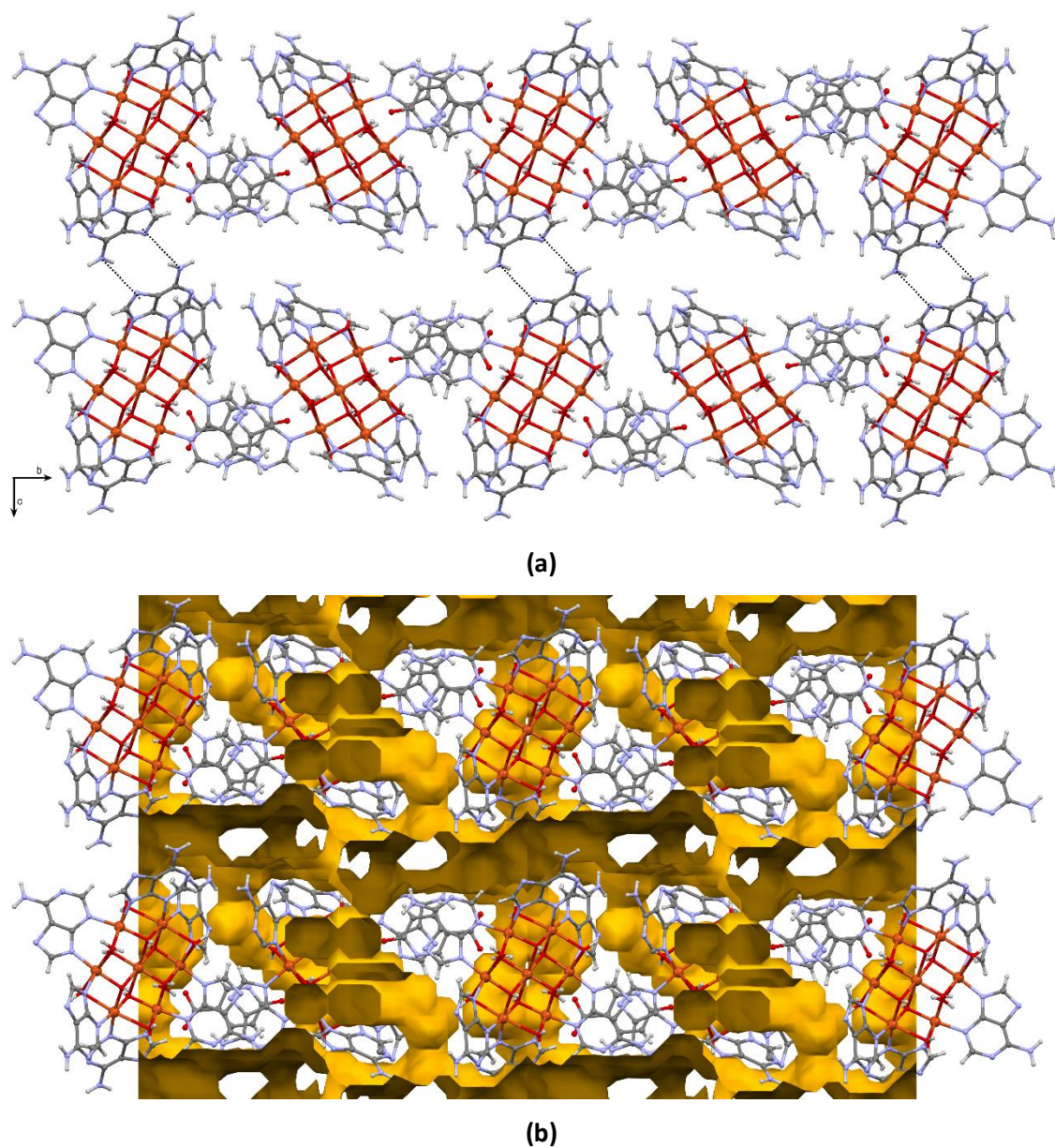


Figure 3.27. Crystal packing of Cu₇ADHN-2 viewed along [1 0 0] crystallographic direction (a) and representation of the voids (b).

Table 3.17. Coordination bond distances (Å) of compound Cu₇ADHN-2.^a

Cu₇ADHN-2			
Cu11–O1	2.014(8)	Cu22–N49	1.955(11)
Cu11–O1a	2.014(8)	Cu22–N69	1.973(13)
Cu11–O2	2.064(10)	Cu22–O4	1.966(8)
Cu11–O2a	2.064(10)	Cu22–O5	1.981(8)
Cu11–O3	2.167(9)	Cu22–O4w	2.422(12)
Cu11–O3a	2.167(9)	Cu22–O6w	2.506(12)
Cu12–N19	1.966(11)	Cu23–O5	1.972(8)
Cu12–N33	1.970(14)	Cu23–O6	1.962(8)
Cu12–O1	1.982(8)	Cu23–N49	1.955(11)
Cu12–O3a	1.962(9)	Cu23–N53	1.978(9)
Cu12–O1w	2.494(4)	Cu23–N59	1.978(9)
Cu12–O2w	2.454(4)	Cu23–O4w	2.482(4)
Cu13–O1	1.962(9)	Cu23–O5w	2.512(4)
Cu13–O2	1.996(8)	Cu24–O4	1.958(10)
Cu13–N13	1.997(11)	Cu24–O6b	1.967(9)
Cu13–N23	2.024(9)	Cu24–N53b	2.009(9)
Cu13–N29	2.024(9)	Cu24–N59b	2.009(9)
Cu13–O2w	2.454(4)	Cu24–N63	1.999(14)
Cu13–O3w	2.447(4)	Cu24–O5w	2.462(4)
Cu14–O2	1.976(9)	Cu24–O6w	2.562(4)
Cu14–O3	1.944(10)	Cu11…Cu12	3.098(10)
Cu14–N23	1.994(9)	Cu11…Cu12a	3.098(10)
Cu14–N29	1.994(9)	Cu11…Cu13	3.080(11)
Cu14–N39a	2.003(13)	Cu11…Cu13a	3.080(11)
Cu14–O1w	2.512(4)	Cu11…Cu14	3.150(12)
Cu14–O3w	2.532(4)	Cu11…Cu14a	3.150(12)
Cu21–O4	2.253(9)	Cu21…Cu22	3.142(11)
Cu21–O4b	2.253(9)	Cu21…Cu22b	3.142(11)
Cu21–O5	1.982(7)	Cu21…Cu23	3.040(14)
Cu21–O5b	1.982(7)	Cu21…Cu23b	3.040(14)
Cu21–O6	2.058(9)	Cu21…Cu24	3.161(10)
Cu21–O6b	2.058(9)	Cu21…Cu24b	3.161(10)

^a Symmetry codes: (a) $-x + 1, -y, -z + 1$; (b) $-x, -y, -z$.

Table 3.18. Hydrogen bonding parameters (Å, °) and π - π interactions in compound Cu₇ADHN-2.^a

D–H...A ^[b]	H...A	D...A	D–H...A
O1–H1...O6Na	2.14	2.90(2)	170
O4–H4...O72b	1.92	2.74(2)	160
O6w–H1W6...O71b	2.12	2.77(3)	133
O3w–H1w3...N1c	2.47	3.14(2)	136
N26A–H26A...N36d	2.52	2.93(5)	110

π - π interactions ^[c]					
Ring...Ring ^[d]	α	DC	β	DZ	DXY
p1...p4 ^b	2.0	3.98(9)	30.3	3.43(6)	2.00
p1...h4 ^b	2.0	4.83(1)	44.5	3.44(7)	3.39
hh...p1 ^a	4.3	3.54(9)	10.4	3.48(6)	0.64
p3...p5A ^b	3.0	5.50(1)	54.0	3.23(6)	4.45
h1...p4 ^b	2.3	4.77(9)	44.9	3.38(6)	3.36
h1...h4 ^b	2.9	4.90(1)	46.3	3.39(1)	3.54
hh...h1 ^a	4.2	4.09(1)	30.9	3.51(6)	2.10
hh...p4 ^c	6.0	3.85(9)	24.7	3.49(6)	1.60

^a Symmetry codes: (a) $-x + 1, -y + 1, -z + 1$; (b) $-x + 1, -y, -z + 1$; (c) $x - 1, y - 1, z$; (d) $2 - x, -y, 1 - z$. ^[b] D: donor; A: acceptor. ^[c] Angle: dihedral angle between the planes (°), DC: distance between the centroids of the rings (Å), α : angle (°) between mean plane of the rings. β : angle (°) between the normal to the first ring and the DC vector (°), DZ: interplanar distance (Å), DXY: lateral displacement (Å), ^[d] h: hexagonal ring of the adeninato, p: pentagonal ring of the adeninato and hh: ring of the hydroxynicotinato. The numbers from 1 to 6 are related with each of the crystallographically independent adenines and hydroxynicotinato. p1: C14, C15, N17, C18, N19. p3: C34, C35, N37, C38, N39. p4: C44, C45, N47, C48, N49. p5A: C54a, C55a, N57a, C58a, N59a. h1: N11, C12, N13, C14, C15, C16. h4: N41, C42, N43, C44, C45, C46. hh1A: N1, C2, C3B, C4, C5, C6.

3.3.2.4. Temperature variable PXRD experiments.

In these compounds, whose channels have a considerable size, the number of solvent molecules, especially water, is usually very variable. The structural stability depends on the network of supramolecular interactions taking place among the [Cu₇(μ -H₂O)₆(μ_3 -OH)₆(μ -ade- κ N3: κ N9)₆]²⁺ cations and the counterions (SO₄²⁻ or HN), but it is also influenced by the presence of the solvent molecules contained in the channels. Temperature variable PXRD measurements were made for compounds Cu₇ADSO₄NHET₃-1, Cu₇ADSO₄ and Cu₇ADHN-1 in order to analyse how the crystal structure evolves upon the desolvation caused by the increases of the temperature. Accordingly, PXRD were collected from room temperature to 200 °C (Figure 3.28a).

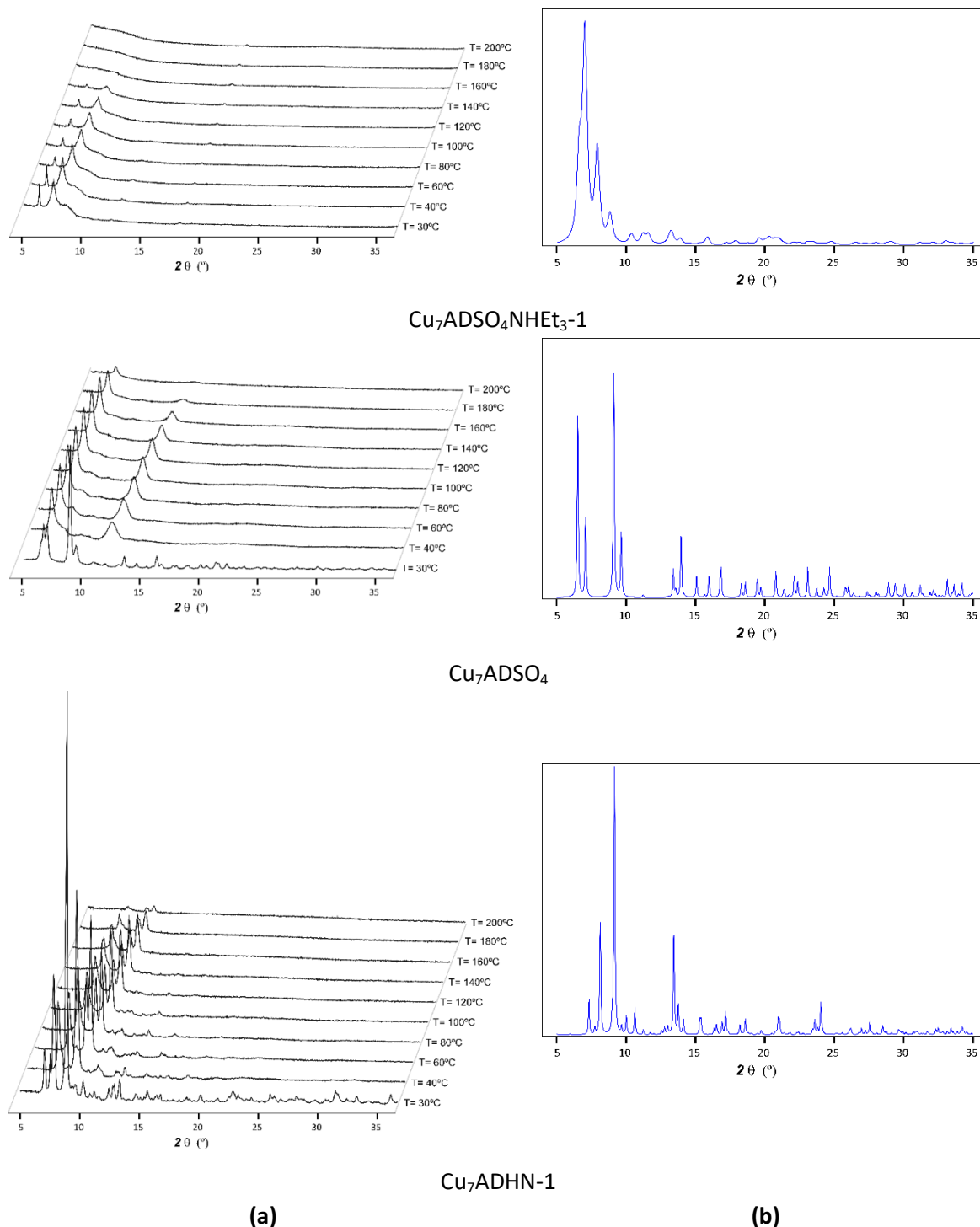


Figure 3.28. (a) Temperature variable PXRD plots for compounds $\text{Cu}_7\text{ADSO}_4\text{NHET}_3\text{-1}$, Cu_7ADSO_4 and $\text{Cu}_7\text{ADHN-1}$. Initially, the temperature increases from 30 to 40 °C and after that, increases 20 °C per measurement up to 200 °C. Compound $\text{Cu}_7\text{ADSO}_4\text{NHET}_3\text{-2}$ has not been included in this study because it shared the same thermal stability than its analogue, compound $\text{Cu}_7\text{ADSO}_4\text{NHET}_3\text{-1}$. (b) Theoretical PXRD patterns computed from the pristine crystal structures. In the case of $\text{Cu}_7\text{ADHN-1}$, the diffraction pattern was simulated using [0 3 1] as preferred orientation.

As it can be observed, the temperature evolution of the PXRD patterns of compounds Cu_7ADSO_4 and $\text{Cu}_7\text{ADHN-1}$ shows significant changes immediately after room temperature (40 °C), which can be ascribed to a structural change caused by a partial solvent evaporation.

Compound $\text{Cu}_7\text{ADSO}_4\text{NHEt}_3\text{-1}$ does not show this change in its reflections because it had previously occurred, when it had been in contact with the atmosphere while the sample was manipulated for the experiment preparation. Therefore, it becomes clear that the initial diffraction pattern might change depending on factors such as the exposition at room temperature, relative humidity and storage time during the sample manipulation. As an example, Figure 3.29 shows a time dependence PXRD of compound Cu_7ADSO_4 collected at 30 °C.

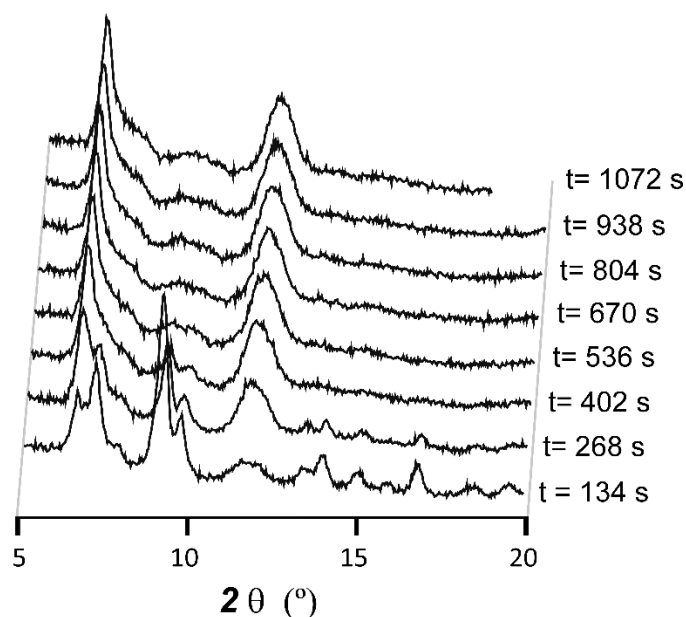


Figure 3.29. Time dependence PXRD at 30 °C with 134 second steps between each measurement for compound Cu_7ADSO_4 .

Something quite significant is the temperature at which the crystal structure of the compounds collapses and renders an amorphous product. In compound $\text{Cu}_7\text{ADSO}_4\text{NHEt}_3\text{-1}$ this amorphization takes place at ca. 160 °C, which probably can be ascribed to the evacuation of crystallization solvent molecules in such a way that the supramolecular interactions among the tectons are not robust enough to retain the crystallinity. Contrarily, Cu_7ADSO_4 and $\text{Cu}_7\text{ADHN-1}$, remain crystalline after the solvent release, and do not collapse until ca. 200 °C, probably due to the dihydroxylation of the cluster. It is interesting to analyse further the case of compounds $\text{Cu}_7\text{ADSO}_4\text{NHEt}_3\text{-1}$ and Cu_7ADSO_4 . Despite in both compounds the connection among the $[\text{Cu}_7(\mu\text{-H}_2\text{O})_6(\mu_3\text{-OH})_6(\mu\text{-ade-}\kappa\text{N}3:\kappa\text{N}9)_6]^{2+}$ entities is similar (4-connected nodes by $\pi\text{-}\pi$ stacking of adenines and coordination water molecules mediated hydrogen bonding with N1/N7 atoms of adenines), in Cu_7ADSO_4 the sulfate counter ions connect further the heptanuclear entities giving rise to a supramolecular ensemble that extends into one-dimension (...sulfate/heptamer/ sulfate/heptamer...). This feature seems to explain the superior stability of Cu_7ADSO_4 respect to $\text{Cu}_7\text{ADSO}_4\text{NHEt}_3\text{-1}$. In the case of compound $\text{Cu}_7\text{ADHN-1}$, the stability of

the crystal structure after pore evacuation, is not only explained by the direct interactions between the heptamers, but also by the π - π interactions and hydrogen bonding interaction implying the $-\text{COOH}$ and the $-\text{C}=\text{O}$ of the 6-hydroxynicotinate counterion, that connect further the adjacent heptameric clusters.

To analyse the reversibility of the desolvation process, fresh samples of compounds $\text{Cu}_7\text{ADHN-1}$ and Cu_7ADSO_4 were heated in an oven at $40\text{ }^\circ\text{C}$ under vacuum during 30 minutes to promote the release of the solvent molecules hosted in the pores. The blue colour characteristic of the crystal turned to green during this process. The samples (hereafter called $\text{Cu}_7\text{ADHN-1green}$ and $\text{Cu}_7\text{ADSO}_4\text{green}$) were weighed to check the mass loss. $\text{Cu}_7\text{ADSO}_4\text{green}$ and $\text{Cu}_7\text{ADHN-1green}$ samples were exposed to ambient humidity, while a follow-up of the mass evolution along the time was made (Figure 3.30). $\text{Cu}_7\text{ADSO}_4\text{green}$, behaves as a highly hygroscopic solid, re-adsorbing water very quickly in an almost completely reversible process. In fact, its colour turned from green to blue immediately after it was exposed to ambient humidity. However, $\text{Cu}_7\text{ADHN-1}$ practically do not change its mass, which is probably ascribed to the robust set of interactions provided by the HN counterion.

Thus, Cu_7ADSO_4 behaves as flexible structure that can realise and reabsorb water. In this sense, further experiments would be desirable taking into account the increasing interest on the application of porous solid for fresh water supply.

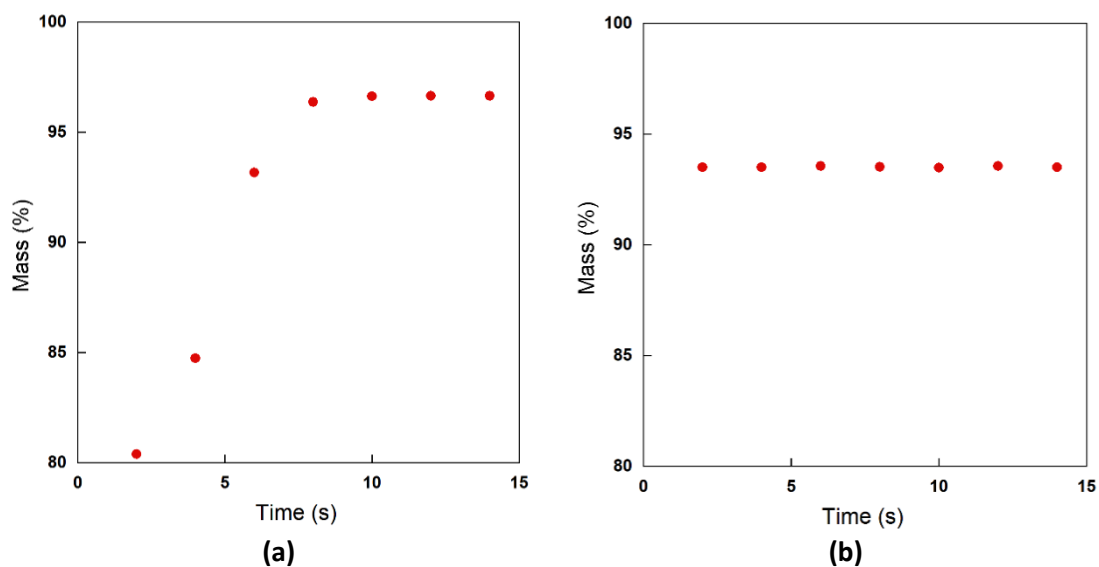


Figure 3.30. Mass (%) gained comparison between compounds $\text{Cu}_7\text{ADSO}_4\text{green}$ (A) and $\text{Cu}_7\text{ADHN-1green}$ (B) in contact with atmospheric humidity. 100% correspond fresh Cu_7ADSO_4 and $\text{Cu}_7\text{ADHN-1}$ samples.

3.3.3. Magnetic properties.

Figure 3.31 shows the temperature dependence of the molar magnetic susceptibility (χ_m) and $\chi_m T$ curves of compounds $\text{Cu}_2\text{ADSO}_4\text{NHEt}_3$, $\text{Cu}_7\text{ADSO}_4\text{NHEt}_3\text{-1}$, $\text{Cu}_7\text{ADSO}_4\text{NHEt}_3\text{-2}$, and Cu_7ADSO_4 respectively, measured at 1 kOe after cooling without an applied magnetic field (ZFC). As it can be seen, in the case of compound $\text{Cu}_2\text{ADSO}_4\text{NHEt}_3$, the $\chi_m T$ curve suffers an initial rise upon cooling from room temperature to gain the maximum value at 200 K. Afterwards, it decreases and reaches a minimum value in the vicinity of 60 K and increases again at lower temperatures as a result of the presence of paramagnetic impurities. Room-temperature $\chi_m T$ values are lower than that expected for two uncoupled paramagnetic $S = 1/2$ centre ($0.75 \text{ cm}^3 \text{ mol}^{-1} \text{ K}$, $g = 2.0$) which is indicative of strong intradimeric interactions. The experimental magnetic data were fitted by using the Bleaney–Bowers equation ($H = -JS_1S_2$) for a dinuclear copper(II) complex modified to take into account the presence of the paramagnetic impurities.

In contrast with the aforementioned compound, the molar magnetic susceptibility in the heptameric compounds increases with decreasing temperature up to 2 K for all compounds. The $\chi_m T$ reaches a value of 2.92 ($\text{Cu}_7\text{ADSO}_4\text{NHEt}_3\text{-1}$), 3.08 ($\text{Cu}_7\text{ADSO}_4\text{NHEt}_3\text{-2}$), and 3.19 (Cu_7ADSO_4) emu K/mol Oe at 300 K per heptameric complex, which is moderately larger than the spin-only value (2.63 emu K/mol Oe) expected for seven magnetically non-interacting Cu^{2+} ions with $S = 1/2$ and $g = 2.0$.^[113] These values slightly diminish as temperature decreases to achieve a minimum at 140 K (2.83 emu K/mol Oe), 155 K (3.03 emu K/mol Oe), and 228 K (3.13 emu K/mol Oe), respectively. Upon further cooling it increases rapidly to reach a maximum at 6 K (4.24 emu K/mol Oe), 3 K (4.93 emu K/mol Oe), and 6 K (4.88 emu K/mol Oe), respectively.

¹¹³ Handbook of Magnetochemical Formulae; Boca, R. A Elsevier: 1013 Amsterdam, The Netherlands, 2012, 1010.

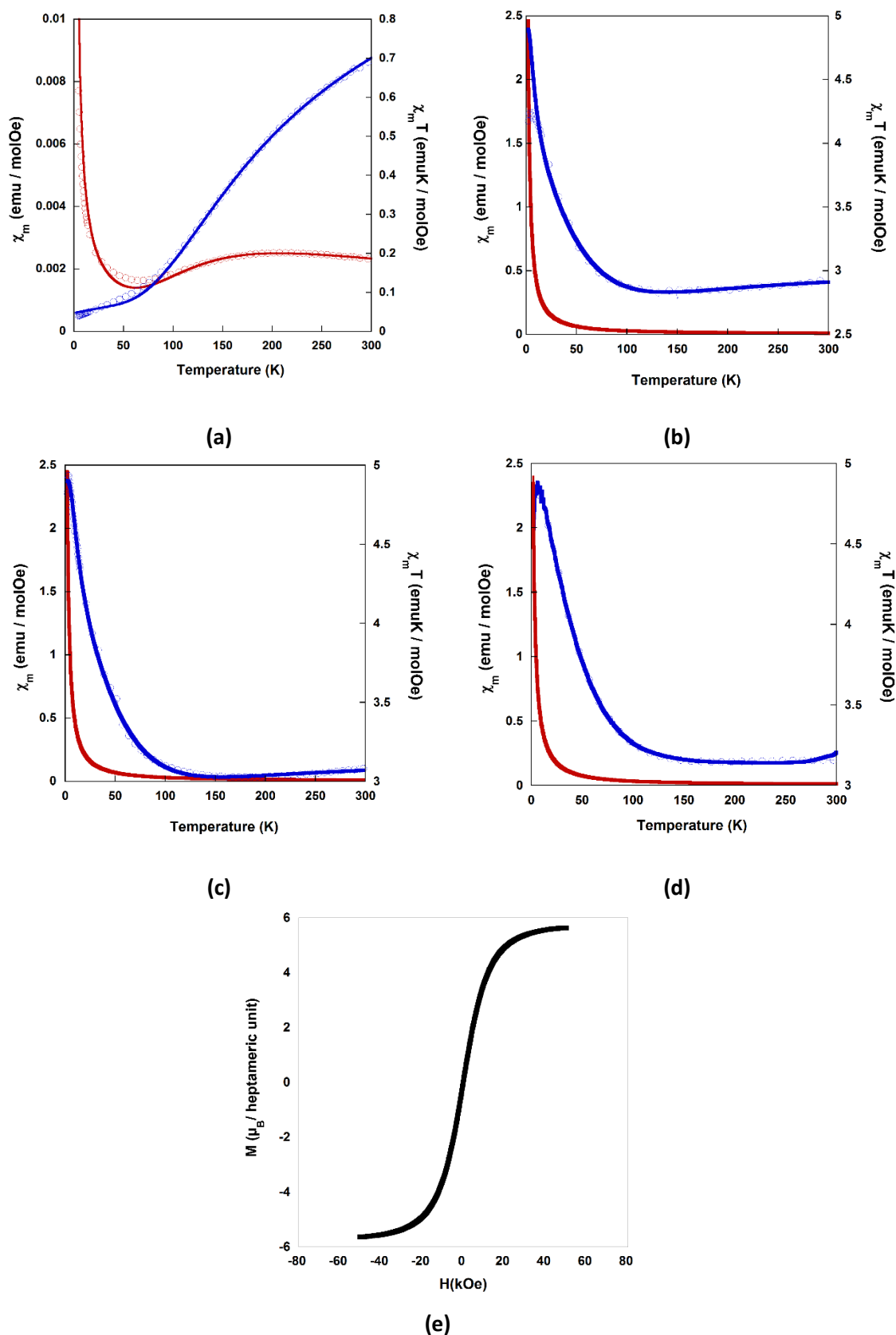


Figure 3.31. Thermal evolution of the molar magnetic susceptibility (χ_m) (red) and the $\chi_m T$ product (blue) in compounds $\text{Cu}_2\text{ADSO}_4\text{NHET}_3$ (a), $\text{Cu}_7\text{ADSO}_4\text{NHET}_3\text{-1}$ (b), $\text{Cu}_7\text{ADSO}_4\text{NHET}_3\text{-2}$ (c) and Cu_7ADSO_4 (d). Due to the similarity in the magnetization curves of all compounds in Chapter 3, as representative case, the magnetization at 2 K of compound $\text{Cu}_7\text{ADSO}_4\text{NHET}_3\text{-1}$ is only presented (e), while the remaining ones can be found in Figure A.5.1 of Appendix 5.

The field dependence of the magnetization at 2 K of the three compounds (Figure 3.31E and Figure A.5.1 of Appendix A.5) displays a linear dependence, from 0 to 15 kOe, which slowly tends to saturate at 50 kOe (5.65, 5.15 and 5.15 $\mu_B/\text{Cu}^{\text{II}}$ ion for compounds $\text{Cu}_7\text{ADSO}_4\text{NHEt}_3\text{-1}$, $\text{Cu}_7\text{ADSO}_4\text{NHEt}_3\text{-2}$ and Cu_7ADSO_4). The values obtained at this magnetic field are lower than the theoretical saturation moment for seven Cu^{II} ions ferromagnetically coupled with a magnetic spin $S = 1/2$ and $g \approx 2$ (7.00 μ_B) but agrees fairly well with a $S=5/2$ ground state. This behaviour seems to indicate the presence of ferrimagnetic heptameric entities in which the central copper(II) atom is antiferromagnetically coupled to the external ferromagnetic hexanuclear ring. Moreover, the magnetization at 2 K shows no hysteresis (have neither coercivity nor remanence).

The magnetic susceptibility measurements of compounds $\text{Cu}_7\text{ADHN-1}$ and $\text{Cu}_7\text{ADHN-2}$ show that, although the change of counterion modifies the supramolecular set of synthons, the overall magnetic properties of the heptameric cluster are not significantly affected. Figure 3.32 shows the temperature dependence of the molar magnetic susceptibility (χ_m) and $\chi_m T$ curves of these compounds. The room temperature $\chi_m T$ values are 3.12 ($\text{Cu}_7\text{ADHN-1}$) and 3.38 ($\text{Cu}_7\text{ADHN-2}$) emu K/mol Oe per heptameric complex. Upon further cooling it increases quite fast to reach a maximum at 3 K (4.92 emu K/mol Oe) and 6 K (4.85 emu K/mol Oe), respectively. The field dependence of the magnetization at 2 K (Figure A.5.1 of Appendix A.5), like in the previous compounds, displays a linear dependence, from 0 to 15 kOe, which slowly tends to saturate at 50 kOe (4.77 and 4.95 $\mu_B/\text{Cu}^{\text{II}}$ ion for $\text{Cu}_7\text{ADHN-1}$ and $\text{Cu}_7\text{ADHN-2}$, respectively, which are slightly lower than in the previous compounds, probably due to the contribution at low temperature of the intermolecular interactions provided by the HN counterion).

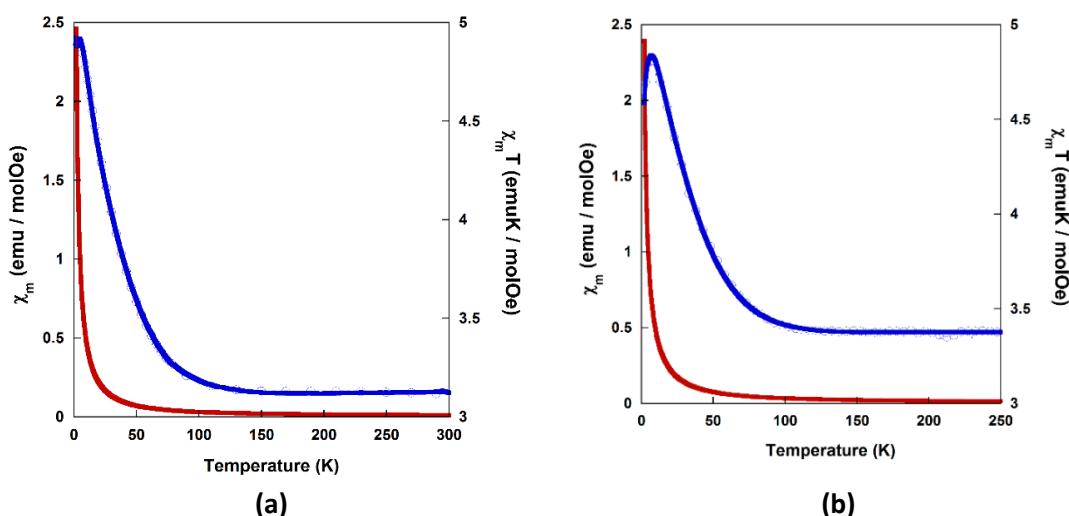


Figure 3.32. Thermal evolution of the molar magnetic susceptibility (χ_m) and the $\chi_m T$ product of $\text{Cu}_7\text{ADHN-1}$ (a) and $\text{Cu}_7\text{ADHN-2}$ (b).

Additionally, the magnetic susceptibility of the compound resulting from the dehydration $\text{Cu}_7\text{ADHN-1}$, i.e. $\text{Cu}_7\text{ADHN-1green}$ (see section 3.3.2.3) was also measured (Figure 3.33). This compound exhibits similar magnetic behaviour as its counterpart, except for the $\chi_m T$ values below 10 K. Here, a significant decrement is observed, with a value of 64 emu K/mol Oe at the maximum sited, 4 K. This issue could be ascribed to the influence of stronger intermolecular antiferromagnetic interactions caused by the compaction of the crystal structure upon dehydration process.

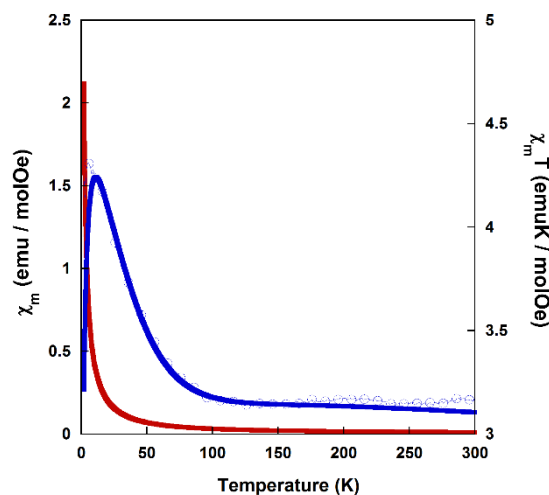


Figure 3.33. Thermal evolution of the molar magnetic susceptibility (χ_m), the $\chi_m T$ product of $\text{Cu}_7\text{ADHN-1green}$.

Taking into account the molecular structure of the $[\text{Cu}_7(\mu\text{-H}_2\text{O})_6(\mu_3\text{-OH})_6(\mu\text{-ade-}\kappa\text{N3}:\kappa\text{N9})_6]^{2+}$ heptanuclear entities and the Jahn-Teller elongated octahedron of the central copper(II) atom, the simplest Hamiltonian (Equation 1) describing the magnetic behaviour of these compounds involves three different superexchange magnetic exchanges between the copper ions and its first neighboring ones (J_1 , J_2 and J_3 ; see Figure 3.34).

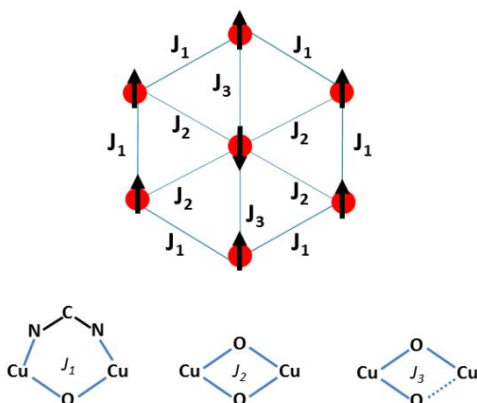


Figure 3.34. The magnetic topology and the magnetic exchange coupling scheme for all compounds of Chapter 3.

$$H = -J_1 (\vec{S}_2 \cdot \vec{S}_3 + \vec{S}_3 \cdot \vec{S}_4 + \vec{S}_4 \cdot \vec{S}_5 + \vec{S}_5 \cdot \vec{S}_6 + \vec{S}_6 \cdot \vec{S}_7 + \vec{S}_7 \cdot \vec{S}_2) - J_2 (\vec{S}_1 \cdot \vec{S}_2 + \vec{S}_1 \cdot \vec{S}_3 + \vec{S}_1 \cdot \vec{S}_5 + \vec{S}_1 \cdot \vec{S}_6) - J_3 (\vec{S}_1 \cdot \vec{S}_4 + \vec{S}_1 \cdot \vec{S}_7) - g\mu_B \vec{B} \cdot \vec{S}$$

Equation 1.

J_1 represents the superexchange interaction between the external Cu^{II} ions bridged by μ -adeninato and μ -OH₂ bridges. J_2 and J_3 are assigned to the superexchange interactions between the central and the exterior copper ions taking place through double μ -OH bridges. J_3 involves a mixture of equatorial-equatorial and equatorial-axial coordinated μ -OH bridges, whereas J_2 presents only an equatorial-equatorial arrangement of the bridging hydroxides. The fitting of the $\chi_m T$ experimental data above 10 K to this model was performed using the MagProp software tool distributed with DAVE.^[114] The best fitting parameters from compounds Cu₇ADSO₄NHET₃-1, Cu₇ADSO₄NHET₃-2, Cu₇ADSO₄, Cu₇ADHN-1, Cu₇ADHN-2 and Cu₇ADHN-1green (see the red continuous line in Figure 3.27) are gathered in Table 3.19.

Table 3.19. Magnetic properties of compounds Cu₇ADSO₄NHET₃-1, Cu₇ADSO₄NHET₃-2 and Cu₇ADSO₄.

Compound	J_1	J_2	J_3
Cu ₂ ADSO ₄ NHET ₃	-248.00		
Cu ₇ ADSO ₄ NHET ₃ -1	75.01	-228.02	14.88
Cu ₇ ADSO ₄ NHET ₃ -2	97.52	-221.13	6.98
Cu ₇ ADSO ₄	96.88	-212.35	49.45
Cu ₇ ADHN-1	90.94	-205.31	63.93
Cu ₇ ADHN-2	96.00	-184.28	53.48
Cu ₇ ADHN-1green	95.83	-192.77	64.59

The results of the fitting show similar ferromagnetic values for the three compounds in the coupling constant involving the external copper(II) ions bridged by adenine and hydroxide ligands (J_1). Usually, both the presence of non-linear NCN bridges or wide angle μ -oxido bridges (*ca.* 104°) cause strong antiferromagnetic couplings.^[115] However, the coexistence of these two types of bridges counterbalances their effects.^[116] In fact, the splitting of the molecular magnetic orbitals is reversed for each type of bridging ligand, thus leading to an almost negligible energy difference between them and, as a consequence, to the observed

¹¹⁴ Azuah, R. T.; Kneller, L. R.; Qiu, Y.; Tregenna-Piggott, P. L. W.; Brown, C. M.; Copley, J. R. D.; Dimeo, R. M. *J. Res. Natl. Inst. Stan. Technol.* **2009**, *114*, 341-358.

¹¹⁵ (a) Sonnenfroh, D.; Kreilick, R. W. *Inorg. Chem.* **1980**, *19*, 1259-1262. (b) Cañadillas-Delgado, L.; Fabelo, O.; Pasán, J.; Delgado, F. S.; Lloret, F.; Julve, M.; Ruiz-Pérez, C. *Inorg. Chem.* **2007**, *46*, 7458-7465.

¹¹⁶ (a) Pérez-Yáñez, S.; Castillo, O.; Cepeda, J.; García-Terán, J. P.; Luque, A.; Román, P. *Eur. J. Inorg. Chem.* **2009**, 3889-3899. (b) Nishida, Y.; Kida, S. *J. Chem. Soc., Dalton Trans.* **1986**, 2633-2640. (c) McKee, V.; Zvagulis, M.; Reed, C. A. *Inorg. Chem.* **1985**, *24*, 2914-2919.

ferromagnetic interaction. On the other hand, there are some significant differences on the coupling constants involving the central and external copper atoms (J_2 and J_3). In these compounds, J_2 (involving two short μ -hydroxide bridges and Cu-O-Cu angles around 99-103 °) is antiferromagnetic and stronger than the ferromagnetic J_3 which implies a short and a long hydroxide bridge. The antiferromagnetic nature of J_2 agrees with the stated by Hatfield et al. for symmetrically double bridged hydroxido dinuclear complexes, in which angles larger than 98.5° promote an antiferromagnetic coupling, while a ferromagnetic coupling is established for smaller angles.^[117] On the other hand, the weak ferromagnetic J_3 interaction is related to the orthogonality between the magnetic orbitals imposed by the combination of symmetric and asymmetric μ -OH bridges. Searching in the literature, copper(II) centres usually bridged by this arrangement of the hydroxide bridges showing a ferromagnetic behaviour with J values ranging from +10 to +90 cm^{-1} .^[118] We are aware of the fact that the over-parameterization of the model could lead to similar fitting agreements using different parameter values, but the similarity of the achieved superexchange constants and the reports found in the literature for similar bridging modes of the hydroxides make us to be confident on the experimental data fitting results. These results also agree with the reported ones for analogous wheel shaped heptanuclear copper(II) entities in which the external copper(II) centres are ferromagnetically coupled among them and antiferromagnetically to the central one.^[119,120] A single crystal with a larger size (*ca.* of 1 cm^3) would allow to compare in detail these data with an experimental determination from polarized-neutron-diffraction experiments.^[121]

3.3.4. Specific heat.

The temperature dependences of the molar heat capacity, C_p , for zero magnetic field are represented between 0.4 and 300 K in Figure 3.35a and Figure 3.35b for compounds $\text{Cu}_7\text{ADSO}_4\text{NHET}_3\text{-1}$ and $\text{Cu}_7\text{ADSO}_4\text{NHET}_3\text{-2}$, respectively. In both cases C_p have a tiny maximum of magnetic origin at low temperatures (*ca.* 11 K) and then it increases continuously due to the phonon contribution. The experimental data do not show any tendency to saturation not even at room temperature, where the values of C_p are 2100 and 1700 $\text{J K}^{-1} \text{mol}^{-1}$ for compounds $\text{Cu}_7\text{ADSO}_4\text{NHET}_3\text{-1}$ and $\text{Cu}_7\text{ADSO}_4\text{NHET}_3\text{-2}$, respectively, still far from the expected values according to the Dulong and Petit law, 75574 and 6136 $\text{J K}^{-1} \text{mol}^{-1}$ for compounds $\text{Cu}_7\text{ADSO}_4\text{NHET}_3\text{-1}$ and $\text{Cu}_7\text{ADSO}_4\text{NHET}_3\text{-2}$, respectively. This behaviour is attributable to the

¹¹⁷ Crawford, V. H.; Richardson, H. W.; Wasson, J. R.; Hodgson, D. J.; Hatfield, W. E. *Inorg. Chem.* **1976**, *15*, 2107-2110.

¹¹⁸ Tercero, J.; Ruiz, E.; Alvarez, S.; Rodríguez-Fortea, A.; Alemany, P. J. *Mater. Chem.* **2006**, *16*, 2729-2735.

¹¹⁹ Liu, Z. Y.; Zhang, H. Y.; Yang, E. C.; Liu, Z. Y.; Zhao, X. J. *Dalton Trans.* **2015**, *44*, 5280-5283.

¹²⁰ Ferreira, B. J. M. L.; Brandão, P.; Dos Santos, A. M.; Gai, Z.; Cruz, C.; Reis, M. S.; Santos, T. M.; Félix, V. J. *Coord. Chem.* **2015**, *68*, 2770-2787.

¹²¹ Campo, J.; Luzón, J.; Palacio, F.; McIntyre, G. J.; Millán, A.; Wildes, A. R. *Phys. Rev. B* **2008**, *78*, 054415.

presence of a high number of hydrogen atoms within the compounds, which display very high excitation energies. At very low temperatures, where the phonon contribution is negligible, C_p displays a second broad maximum ($\Delta C_p = 4.2$ J/mol K in both compounds) centred at 0.6 and 0.5 K for $\text{Cu}_7\text{ADSO}_4\text{NHEt}_3\text{-1}$ and $\text{Cu}_7\text{ADSO}_4\text{NHEt}_3\text{-2}$, respectively (see upper insets in Figure 3.35). Although these anomalies do not present the characteristic λ shape appearance of a second order transition, it can be attributed to the establishment of a three-dimensional magnetic order. This behaviour is confirmed by the effects of the magnetic field on C_p , since the field increase promotes the peak growing and shifting to higher temperatures, and apparently, disappearing for fields higher than 30 kOe in both compounds. This behaviour is later clarified analysing the magnetic contribution to the heat capacity (C_{mag}).

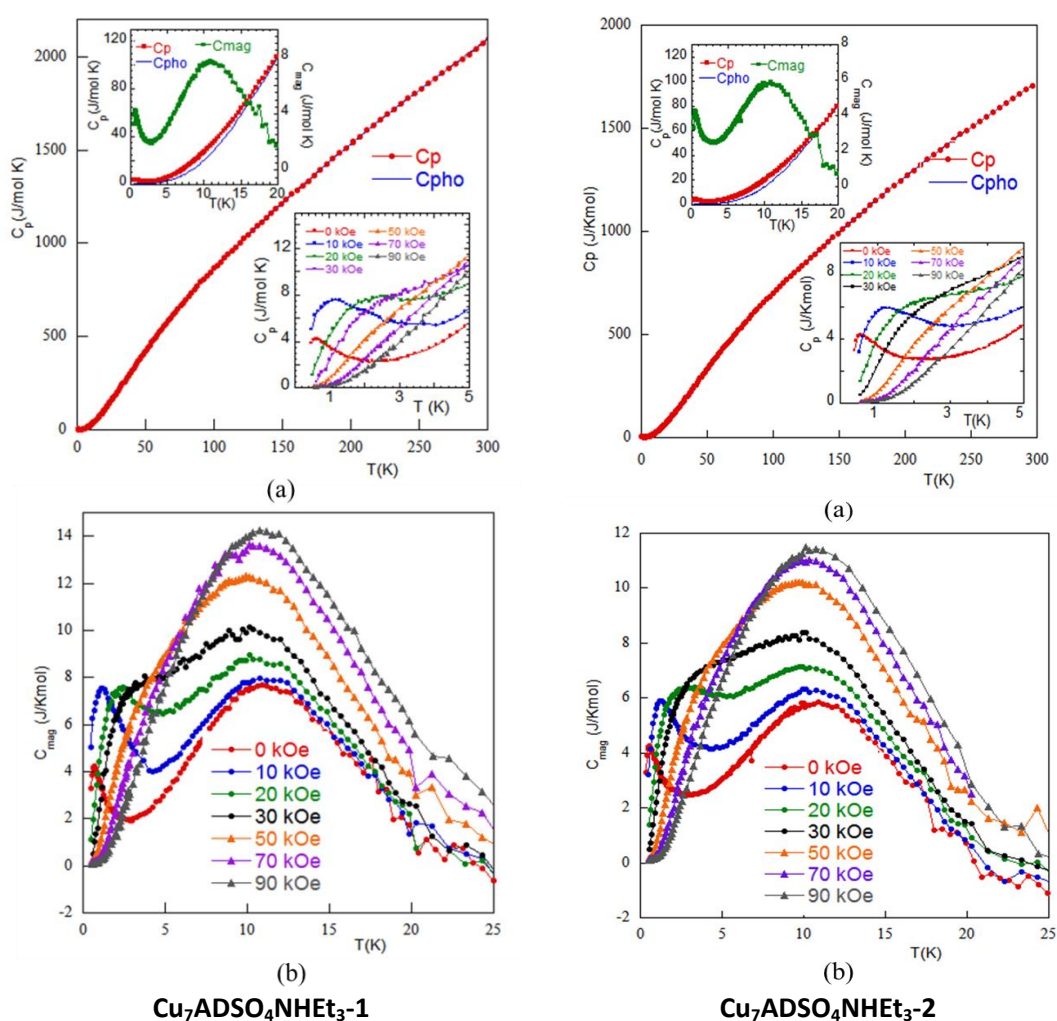


Figure 3.35. Specific heat of compounds $\text{Cu}_7\text{ADSO}_4\text{NHEt}_3\text{-1}$ and $\text{Cu}_7\text{ADSO}_4\text{NHEt}_3\text{-2}$ between 2 and 300 K (a). Upper inset shows the experimental data (red full dots), estimated phonon contribution (blue dashed line) and magnetic contribution (brown full dots). The lower inset is the specific heat at different applied magnetic field ($H \leq 90$ kOe). Magnetic specific heat as a function of temperature in the presence of external magnetic fields (b).

In order to extract C_{mag} from the heat capacity measurements, we determined the phonon contribution (C_{pho}) and then subtracted it from the experimental data. In the absence of a nonmagnetic isomorphous compound, we used a theoretical model to determine C_{pho} , with the Debye model being the most common. However, due to the large differences in the atomic weights of the elements, more than one phonon spectra are expected. This approach has been used successfully in previous studies in other complex insulators materials.^[122] In the present case, due to the large amount of ions and solvent molecules, the minimum number of Debye temperatures that is required to fit the heat capacity has been five. The good quality of the fits (see the blue continuous line in Figure 3.35) allows us to consider that this phenomenological model determines reasonably well the phonon contribution.

The temperature dependence of the magnetic contribution, determined as $C_{\text{mag}} = C_p - C_{\text{pho}}$, is depicted in Figure 3.35 for both compounds, respectively. In these figures are also included the temperature dependences of C_{mag} under applied magnetic fields up to 90 kOe. In both compounds, at zero field, the most significant features are **i)** the jump in C_{mag} at the order temperature has a small value, suggesting the existence of a complex magnetic order^[123] and **ii)** in addition to the low temperature peak, appears a broad maximum centred around 11 K, which usually is attributed to the existence of two-dimensional magnetic order, crystalline electrical field or the presence of short-range magnetic interactions.^[124]

Therefore, in the present case, these results suggest that at 11 K appears a local magnetic order inside the wheels and, by decreasing the temperature around 0.5 K, the wheels are coupled magnetically resulting in a three-dimensional (3D) magnetic ordering. The general effect of the magnetic field on C_{mag} is to increase the size of both peaks and to shift the low temperature peak to higher temperatures. This shift is characteristic of a ferromagnetic coupling. In addition, we should point out that the low temperature peak has a strong increase for 10 kOe and then tends to saturate for fields above 30 kOe, in concordance with the saturation of the magnetization curves. Taking into account the structural features of the compounds, the long-range ordering detected at low temperatures probably comes from the adeninato...adeninato π - π stacking interactions taking place between the heptamers units. From the 3D magnetic ordering temperature values ($T_c = 0.5$ and 0.6 K) and the Curie-Weiss

¹²² (a) de Pedro, I.; Rojo, J. M.; Fernández, J. R.; Fernandez-Díaz, M. T.; Rojo, T. *Phys. Rev. B* **2010**, *81*, 134431. (b) de Pedro, I.; Rojo, J. M.; Rius, J.; Vallcorba, O.; De Larramendi, I. R.; Rodríguez Fernández, J.; Lezama, L.; Rojo, T. *Inorg. Chem.* **2012**, *51*, 5246-5256.

¹²³ Orive, J.; Fernández de Luis, R.; Rodríguez Fernández, J.; Legarra, E.; Plazaola, F.; Arriortua, M. I. *CrystEngComm* **2014**, *16*, 6066-6079.

¹²⁴ (a) Sengupta, P.; Sandvik, A. W.; Singh, R. R. P. *Phys. Rev. B* **2003**, *68*, 094423. (b) Durand, A. M.; Klavins, P.; Currucini, L. R. *J. Phys. Condens. Matter.* **2008**, *20*, 235208. (c) Yaouanc, A.; Dalmas de Reotier, P.; Glazkov, V.; Marin, C.; Bonville, P.; Hodges, J. A.; Gubbens, P. C. M.; Sakarya, S.; Baines, C. *Phys. Rev. Lett.* **2005**, *95*, 047203.

temperature ($\theta_p = 20.7$ and 11.0 K for $\text{Cu}_7\text{ADSO}_4\text{NHET}_3\text{-1}$ and $\text{Cu}_7\text{ADSO}_4\text{NHET}_3\text{-2}$, respectively) we can obtain information of the magnetic spin frustration, f , given by $|\theta/T_c|$ of these open supramolecular structures^[125] where f parameter reaches values of 41.4 and 18.3 for $\text{Cu}_7\text{ADSO}_4\text{NHET}_3\text{-1}$ and $\text{Cu}_7\text{ADSO}_4\text{NHET}_3\text{-2}$ respectively. A value above 10 indicates the presence of strong frustration.^[126] Therefore, it indicates that both SMOFs display complex 3D magnetic structures with the presence of stronger spin frustration in the $\text{Cu}_7\text{ADSO}_4\text{NHET}_3\text{-1}$ compound.

¹²⁵ Ramirez, A. P. *Annu. Rev. Mater. Sci.* **1994**, *24*, 453-480.

¹²⁶ Shores, M. P.; Nytko, E. A.; Bartlett, B. M.; Nocera, D. G. *J. Am. Chem. Soc.* **2005**, *127*, 13462-13463.

Chapter 4: Heterometallic adenine nucleobase based SMOFs

4.1. Introduction

4.2. Synthesis and chemical characterization

4.3. Results and discussion

4.1. INTRODUCTION

In the previous chapter it was observed how the supramolecular network built up from the heptameric $[\text{Cu}_7(\mu\text{-H}_2\text{O})_6(\mu_3\text{-OH})_6(\mu\text{-ade-}\kappa\text{N3}:\kappa\text{N9})_6]^{2+}$ entity underwent significant changes depending on the added counterion. Despite the supramolecular rearrangements induced by such counterions, the impact on the intramolecular magnetic behaviour is slight and only appreciable at very low temperatures, where the magnetic ordering through non-covalent interaction pathways is more relevant.^[127–128]

In this chapter, the goal relies on the fine tuning of the intramolecular magnetic properties by conveniently selecting the paramagnetic metal ions that comprise the central position of the heptameric wheel. Precisely, the central Cu(II) has been replaced by Cr(III), Mn(III), Co(II), Ni(II) and Zn(II), while retaining the radial Cu(II) whose coordination plasticity and affinity towards N-donor ligands make it particularly suitable to fit such position (Figure 4.1). As a result, we show how the magnetic superexchange scheme and the total spin of the heptanuclear complex can predetermined in rationalized manner.

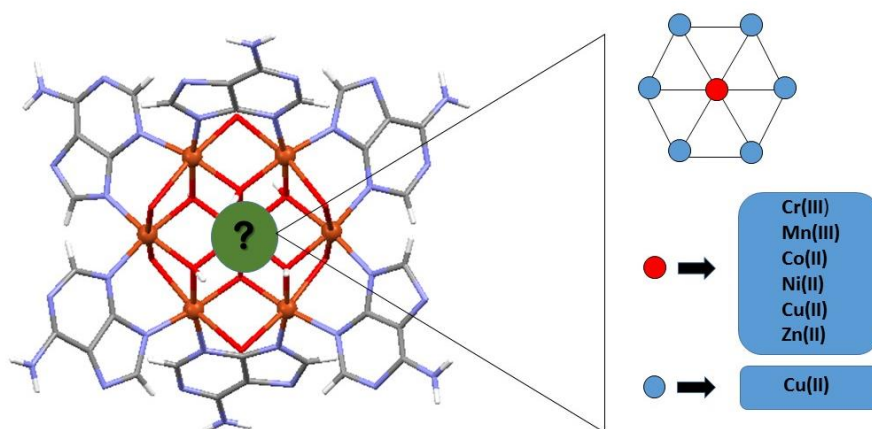


Figure 4.1. Heptameric cluster depicting the targeted replacement of the central metal atom.

Heterometallic MOFs have led to remarkable advances in molecular magnetism, electrochemistry, catalysis, and gas absorption partly due to the charge transfer phenomena and synergistic effects between different metal centres.^[129–130] Regarding the magnetic properties, it deserves to note that the combination of different paramagnetic centres has

¹²⁷ Zheng, Y. Z.; Tong, M. L.; Xue, W.; Zhang, W. X.; Chen, X. M.; Grandjean, F.; Long, G. J. *Angew. Chem.* **2007**, *119*, 6188–6192.

¹²⁸ (a) Sharples, J. W.; Collison, D.; McInnes, E. J.; Schnack, J.; Palacios, E.; Evangelisti, M. *Nature Commun.* **2014**, *5*, 1–6. (b) Mondal, K. C.; Mereacre, V.; Kostakis, G. E.; Lan, Y.; Anson, C. E.; Prisecaru, I.; Powell, A. K. *Chem. Eur. J.* **2015**, *21*, 10835–10842.

¹²⁹ (a) Qi, Y.-J.; Zhao, D.; Li, X.-X.; Ma, X.; Zheng, W.-X.; Zheng, S.-T. *Cryst. Growth Des.*, **2017**, *17*, 1159–1165. (b) Li, X. X.; Gong, Y. Q.; Zhao, H. X.; Wang, R. H. *Cryst. Eng. Comm.* **2014**, *16*, 8818–8824.

¹³⁰ (a) Buchwalter, P.; Rose, J.; Braunstein, P. *Chem. Rev.* **2015**, *115*, 28–126. (b) Matsunaga, S.; Shibasaki, M. *Chem. Comm.* **2014**, *50*, 1044–1057.

demonstrated to be well suited tool to modulate the magnetic anisotropy and total spin of the system.^[131–132]

Within these heterometallic MOFs, both transition metal ions and lanthanide ions have been widely used as excellent magnetic building blocks. Particularly, lanthanide ions are very suitable to build up single-molecule magnets (SMMs) due to the large magnetic moment and significant single-ion anisotropy derived from spin–orbit coupling which are not easily satisfied in transition-metal.^[133] However, the octahedral coordination geometry and coordination bond lengths required to fit central position of the heptameric cluster, led us to disregard lanthanides and limit our selection to certain transition metal centres, as it is discussed below.

As depicted in the analysis performed in the CSD database (Figure 4.2), the coordination index (C.I. = 6) of the central position of the heptameric wheel is not located between the preferred bonding of lanthanide ions (Ln(III), C.I. = 8 and 9). Contrarily, selected transition metals (Cr, Mn, Co, Ni, Cu and Zn) are prone to exhibit a coordination index equal to 6. At this point, it can be proposed that the coordination sphere of a central Ln(III) atom might be completed by solvent molecules. However, there is a second fact that points again as a suitable option the selected transition metal centres and discourages a replacement of the central position using lanthanides: i.e. adjustability of the ionic radii (Figure 4.3). Selected transition ions do not differ greatly in size with regard to Cu(II), so the replacement of the central position should not cause a significant strain of the outer Cu₆-ring. Adversely, the greater ionic radii of Ln(III) series would imply an increase of the radial distance and therefore, a lengthening of the arc or Cu···Cu distances, which would weaken (destabilize) the Cu₆-ring.

¹³¹ (a) Griffiths, K.; Tsipis, A. C.; Kumar, P.; Townrow, O. P. E.; Abdul-Sada, A.; Akién, G. R.; Baldansuren, A.; Spivey, A. C.; Kostakis, G. E. *Inorg. Chem.* **2017**, *56*, 9563–9573. (b) Chandrasekhar, V.; Bag, P.; Kroener, W.; Gieb, K.; Müller, P. *Inorg. Chem.* **2013**, *52*, 13078–13086.

¹³² (a) Mondal, K. C.; Sundt, A.; Lan, Y.; Kostakis, G. E.; Waldmann, O.; Ungur, L.; Chibotaru, L. F.; Anson, C. E.; Powell, A. K. *Angew. Chem., Int. Ed.* **2012**, *51*, 7550–7554. (b) Perez-Temprano, M. H.; Casares, J. A.; Espinet, P. *Chem. Eur. J.* **2012**, *18*, 1864–1884.

¹³³ Ruiz, E.; Cirera, J.; Cano, J.; Alvarez, S.; Loose, C.; Kortus, J. *Chem. Comm.* **2008**, *44*, 52–54.

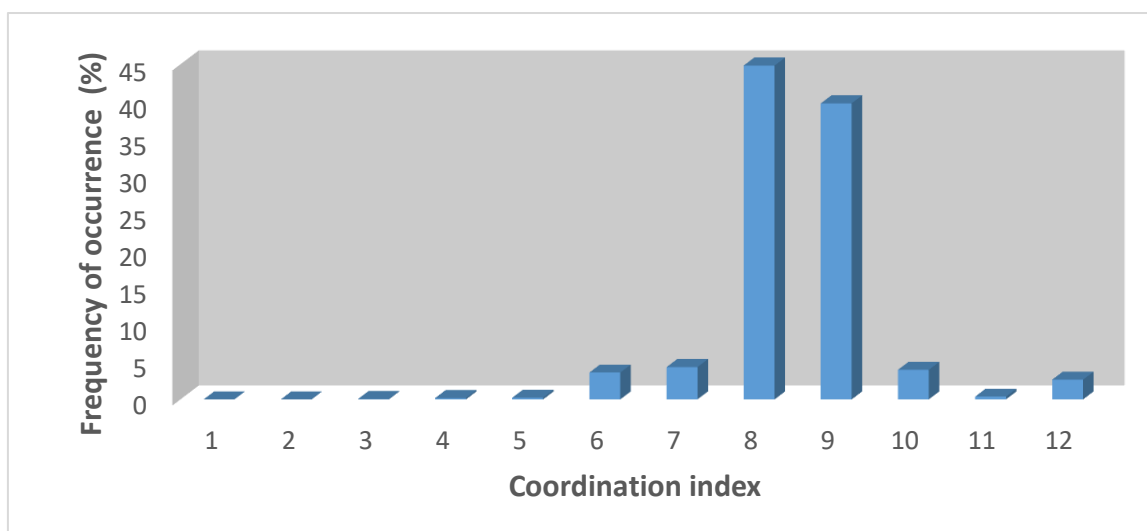


Figure 4.2. Coordination-index and frequency of occurrence for lanthanide ions.

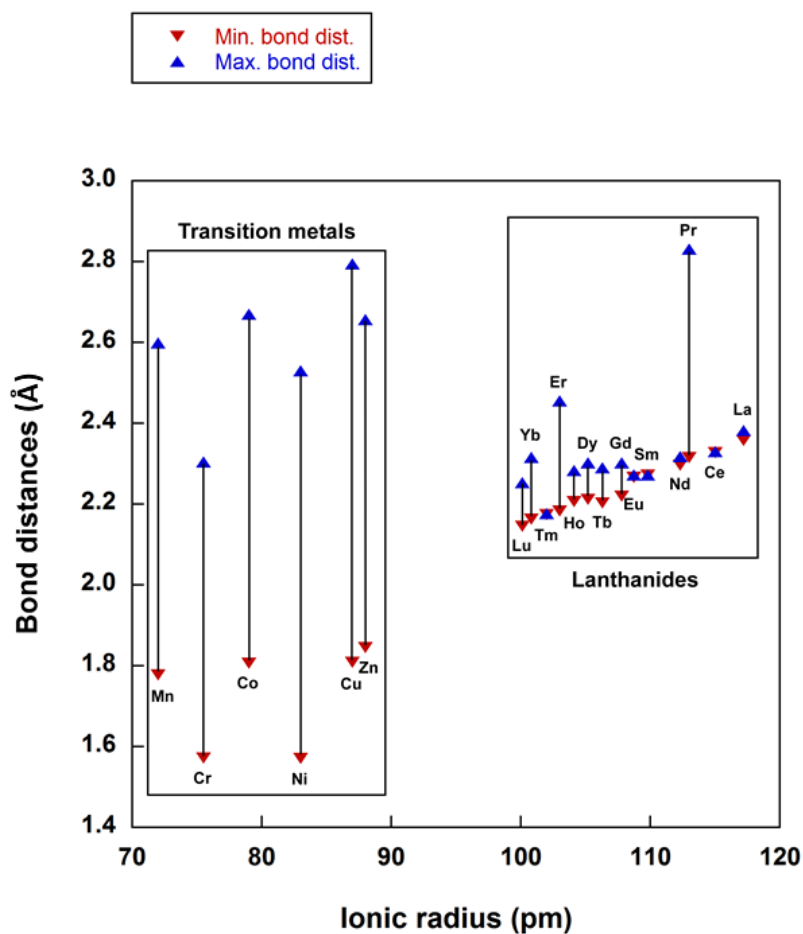


Figure 4.3. Minimum and maximum bond distances vs ionic radius in octahedral coordination complexes of lanthanides(III) and selected transition metals (M(III): Mn, Cr; M(II): Co, Ni, Cu, Zn). Bond distances were obtained from a parametrized search in the CSD database^[81] while ionic radius data was obtained from Database of Ionic Radii.^[134]

¹³⁴ Shannon, R.D.; *Acta Cryst.*, **1976**, *32*, 751-767.

4.2. SYNTHESIS AND CHEMICAL CHARACTERISATION

4.2.1. Synthesis

The formula and name of the compounds synthesized and characterized in this chapter are provided in Table 4.1. Figure 4.4 shows a scheme depicting the synthesis procedure of each compound, while detailed descriptions are provided below. It must be emphasized that the amount of the reagent used for the central metal source, exceeded slightly the stoichiometrically demanded (1.5:6 vs 1:6 for $M_{\text{central}}:\text{Cu}_{\text{ring}}$), in order to favour the formation of the heterometallic wheel.

Despite the described synthesis procedures exhibit relatively high yields, the quality of the obtained crystals was not good enough for the elucidation of the crystal structure from single-crystal diffraction data. Accordingly, applying the base-vapour diffusion driven crystallization described in Chapter 3, suitable single-crystals were obtained in all cases except for compound Cu_6NiAD whose structural analysis is based on PXRD data. The vapour diffusion process provided few crystals and therefore, it was disregarded for bulk sample characterisation purposes.

Table 4.1. Formula and code of the compounds synthesized with the heterometallic heptameric cluster.

Compound	Code
$[\text{Cu}_6\text{Cr}(\mu\text{-H}_2\text{O})_6(\mu_3\text{-OH})_6(\mu\text{-ade-}\kappa\text{N3}:\kappa\text{N9})_6](\text{SO}_4)_{1.5}\cdot 17\text{H}_2\text{O}$	Cu_6CrAD
$[\text{Cu}_6\text{Mn}(\mu\text{-H}_2\text{O})_6(\mu_3\text{-OH})_6(\mu\text{-ade-}\kappa\text{N3}:\kappa\text{N9})_6](\text{SO}_4)(\text{OH})\cdot 12\text{H}_2\text{O}$	Cu_6MnAD
$[\text{Cu}_6\text{Co}(\mu\text{-H}_2\text{O})_6(\mu_3\text{-OH})_6(\mu\text{-ade-}\kappa\text{N3}:\kappa\text{N9})_6](\text{SO}_4)\cdot 14\text{H}_2\text{O}$	Cu_6CoAD
$[\text{Cu}_6\text{Ni}(\mu\text{-H}_2\text{O})_6(\mu_3\text{-OH})_6(\mu\text{-ade-}\kappa\text{N3}:\kappa\text{N9})_6](\text{SO}_4)\cdot 12\text{H}_2\text{O}$	Cu_6NiAD
$[\text{Cu}_6\text{Zn}(\mu\text{-H}_2\text{O})_6(\mu_3\text{-OH})_6(\mu\text{-ade-}\kappa\text{N3}:\kappa\text{N9})_6](\text{SO}_4)\cdot 16\text{H}_2\text{O}$	Cu_6ZnAD

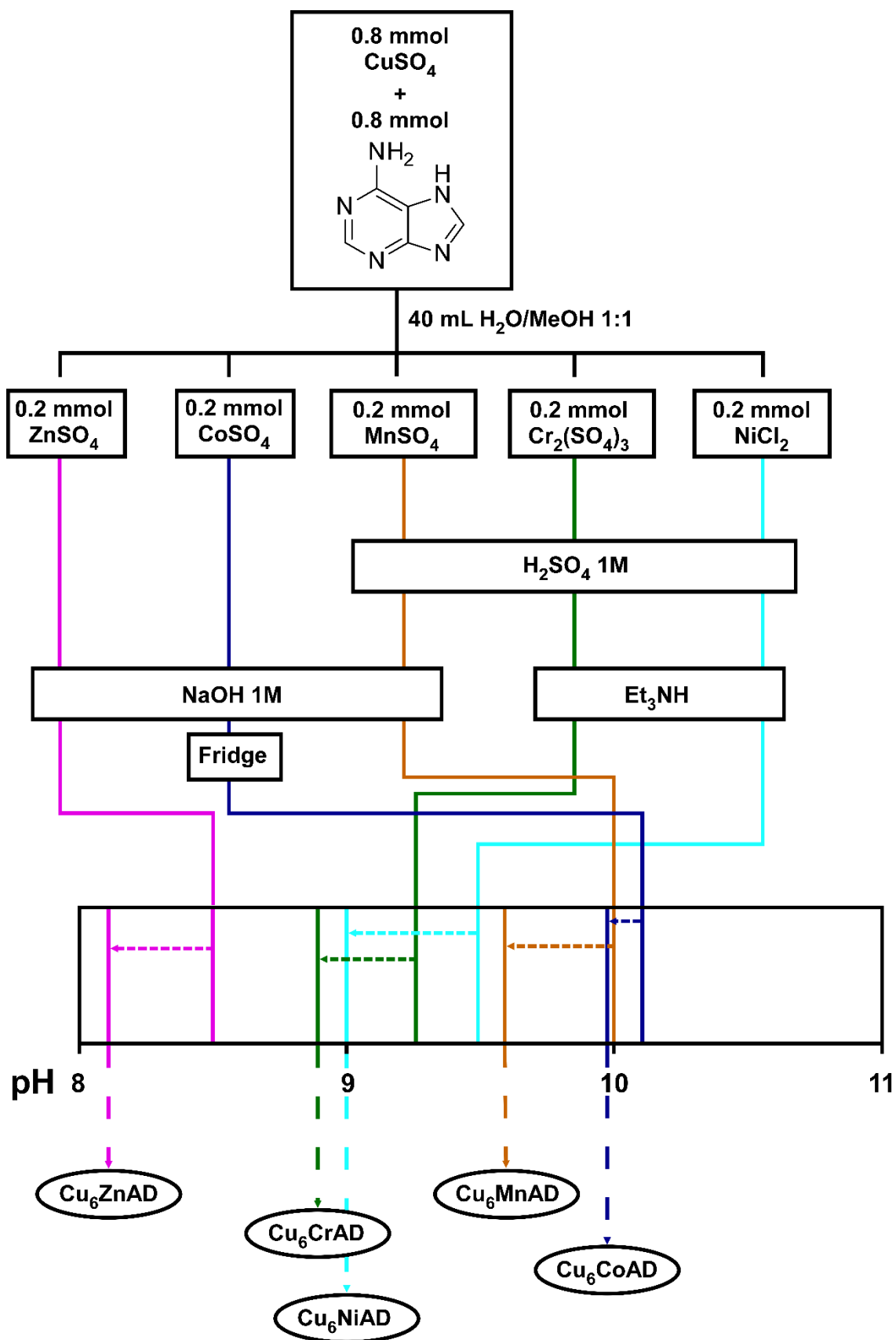


Figure 4.4. Synthetic route of the heterometallic compounds of Chapter 4.

4.2.1.1. Synthesis of compound Cu₆CrAD

Adenine (0.8 mmol, 0.108 g) was dissolved in 20 mL of water/methanol mixture (1:1 volume ratio), heating under continuous stirring for 20 minutes. Then, a 20 mL aqueous solution of copper(II) sulfate pentahydrate (0.8 mmol, 0.200 g) and chromium(III) sulfate monohydrate (0.2 mmol, 0.078 g) was added. Immediately after mixing the solutions a green suspension was formed with pH = 3.02. This suspension was dissolved by acidifying with sulfuric acid until a light green solution is obtained at pH = 1.46. Subsequently, the solution pH was shifted to 9.2 by adding triethylamine, obtaining a green suspension which was left in a crystallizer sealed with sealing film (Parafilm™) slightly holed to allow the slow solvent evaporation. After three days, the suspension recrystallized as green needle-shaped crystals. Yield: 75–85 %.

4.2.1.2. Synthesis of compound Cu₆MnAD

20 mL of an aquo-methanolic (1:1 volume ratio) solution of adenine (0.8 mmol, 0.108 g) was mixed with 20 mL of an aqueous solution containing copper(II) sulfate pentahydrate (0.8 mmol, 0.200 g) and manganese(II) sulfate monohydrate (0.2 mmol, 0.079 g). As a result, a bluish suspension formed (pH = 3.67) which was dissolved by adding sulfuric acid until pH = 2.7. After that, sodium hydroxide 1 M was added until a green-brown suspension appears at pH = 10 and the resulting suspension was transferred to a crystallizer that was closed with a sealing film. After five days, dark green plate-like crystals of Cu₆MnAD were formed. It deserves to note that Mn(II) was oxidized to Mn(III) upon the synthesis conditions. Yield: 60–65 %.

4.2.1.3. Synthesis of compound Cu₆CoAD

An aqueous solution containing copper(II) sulfate pentahydrate (0.8 mmol, 0.200 g) and cobalt(II) sulfate heptahydrate (0.2 mmol, 0.056 g) was added to a solution of adenine (0.8 mmol, 0.108 g) in 20 mL of methanol/water (1:1 volume ratio), heating under continuous stirring. After 10 minutes, the reaction mixture was left to temper, obtaining a blue suspension with pH = 3.78 which was left stirring for one hour (the colour turns to violet). Then, sodium hydroxide (1 M) was added dropwise until a pH value of 10.1 is reached. Finally, the resulting suspension was placed into a crystallizer covered with sealing film and left in a fridge at 6 °C. After five days, blue needle-shaped crystals were obtained. Yield: 60–70 %.

4.2.1.4. Synthesis of compound Cu₆NiAD

Adenine (0.8 mmol, 0.108 g) and nickel(II) chloride (0.2 mmol, 0.048 g) were added into a solution of 20 mL of methanol/water (1:1 volume ratio), heating it up under continuous stirring until a green solution was obtained. To that, 20 mL of an aqueous solution of copper(II) sulfate pentahydrate (0.8 mmol, 0.200 g) was added, obtaining a bluish suspension with pH = 3.27 which was acidified with sulfuric acid until it was completely dissolved (pH = 2.1) into a light green solution. Thereafter, triethylamine was added until the formation of a blue-green suspension at pH = 9.48 which was transferred to a crystallizer covered with a sealing film. After two days, rectangular blue crystals were obtained. Yield: 52–58 %.

4.2.1.5. Synthesis of compound Cu₆ZnAD

20 mL of an aqueous solution of copper(II) sulfate pentahydrate (0.8 mmol, 0.200 g) and zinc(II) sulfate pentahydrate (0.2 mmol, 0.055 g) were poured onto 20 mL of a hot water/methanol solution containing adenine (0.8 mmol, 0.108 g). The pH of the resulting light blue suspension (pH = 3.1) was shifted to 8.5 by adding dropwise 1 M solution of sodium hydroxide. After six days, needle-like light blue crystals were formed. Yield: 52–57 %.

4.2.2. Infrared spectroscopy

As in the previous chapter, infrared spectroscopy has been able to determine efficiently the presence of the bands corresponding to the adenine ligand and sulfate counterion. The infrared spectra of the compounds are presented in Figure 4.5 and Figure 4.6. Table 4.2 shows the wavenumber, the relative intensity and the assignment of the observed bands.

In all cases, the infrared spectra show a wide band around 3400 cm⁻¹ characteristic of the O–H stretching of the bridging hydroxides, coordination water molecules and crystallization water molecules. The extent of the latter band, allows fairly identifying the N–H stretching of the amine group of the adenine as a fine shoulder at ca. 3200 cm⁻¹, but it masks the signals corresponding to the C_{ar}–H stretching expected around 3100 cm⁻¹. Over 1600 cm⁻¹, appears one of the most intense bands of the spectra which is mainly attributable to C=C stretching vibration and deformation vibration of NH₂ group of the adenine. Another representative band of this series of heterometallic compounds appears near of 1108 cm⁻¹ which corresponds to S=O vibration of the sulfate counterion.^[87]

Table 4.2. Infrared spectra bands (cm^{-1}) of the neutral adenine ligand and compounds of Chapter 4.^[a]

Adenine	Cu ₆ CrAD	Cu ₆ MnAD	Cu ₆ CoAD	Cu ₆ NiAD	Cu ₆ ZnAD	Assignment ^[b]
	3388vs	3355vs	3333vs	3333vs	3400vs	v (O–H)
3303s	3200sh	3200sh	3200sh	3200sh	3200sh	v (NH ₂) ⁺
3123s	over	over	over	over	over	v (C8–H + C2–H)
	1642vs	1642vs	1638vs	1638vs	1642vs	
1605vs	1603vs	1603vs	1600vs	1600vs	1608vs	v (C=N) + v (C=C) + δ (NH ₂)
1560s	1548s	1545s	1545s	1546s	1551s	v (C4–C5 + N3–C4–C5)
1471m	1463m	1463m	1466m	1463m	1466m	δ (C2–H + C8–N9) + v (C8–H)
1419s	1402m	1397m	1397m	1396m	1400m	δ (N1–C6–H6)
	1304m	1306m	1305m	1306m	1306m	
1309s	1277m	1277m	1275m	1275m	1271m	v (N9–C8 + N3–C2) + δ (C–H)
	1195m	1195m	1198m	1198m	1195m	
1263s	1152m	1148m	1148m	1150m	1148m	δ (C8–H) + v (N7–C8)
1108m	1108m	1105m	1109m	1108m	1108m	v (S–O)
1023w	1033w	1028w	1030w	1030w	1031w	τ (NH ₂)
940w	935w	933w	933w	935w	937w	v (N1–C6) + τ (NH ₂)

^[a] vs = very strong, s = strong, m = medium, w = weak, sh = shoulder. ^[b] over = overlapped, v = tension vibrations, δ = deformation vibrations, τ = torsion.

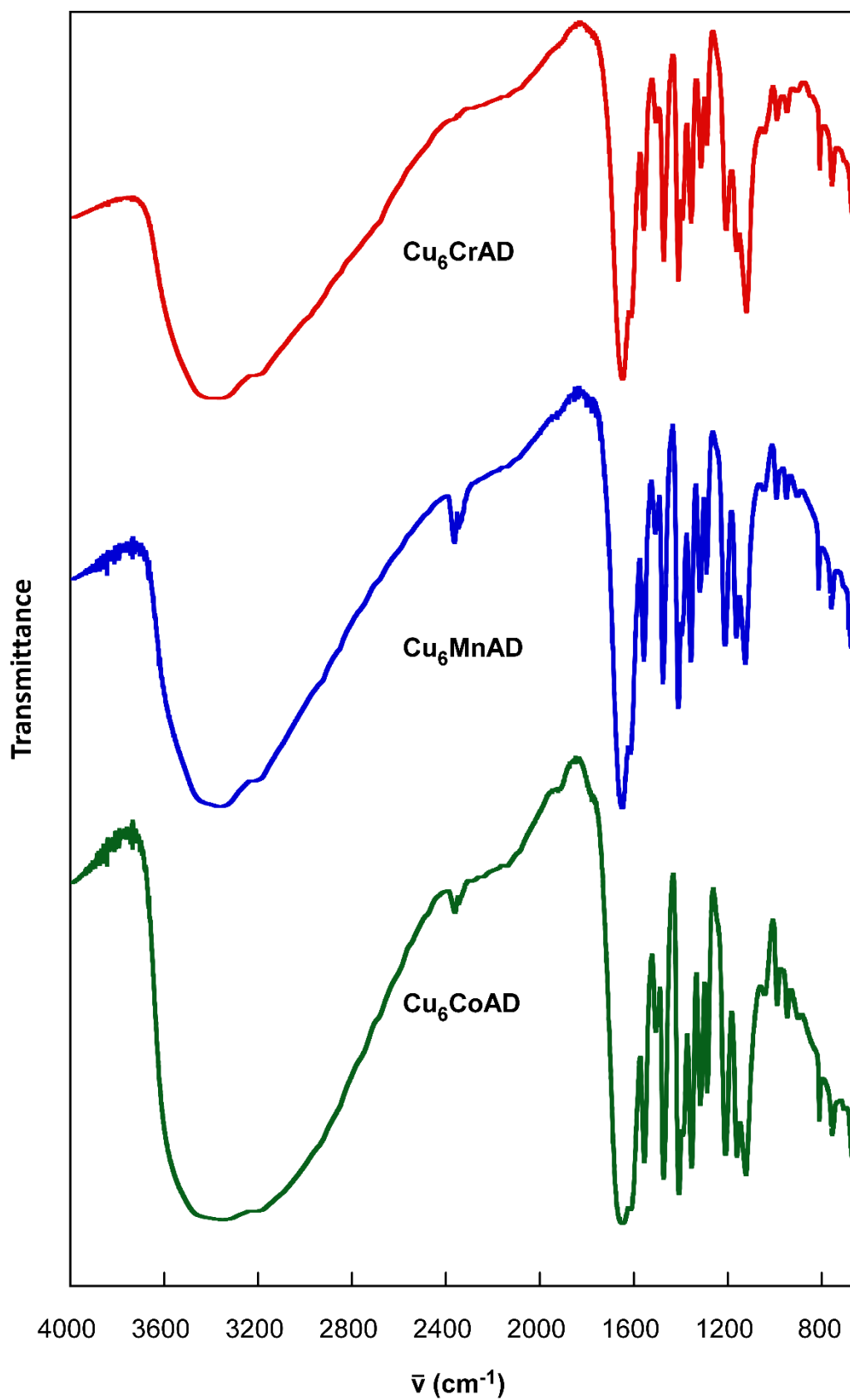


Figure 4.5. Infrared spectra of compounds Cu_6CrAD (red), Cu_6MnAD (blue) and Cu_6CoAD (green).

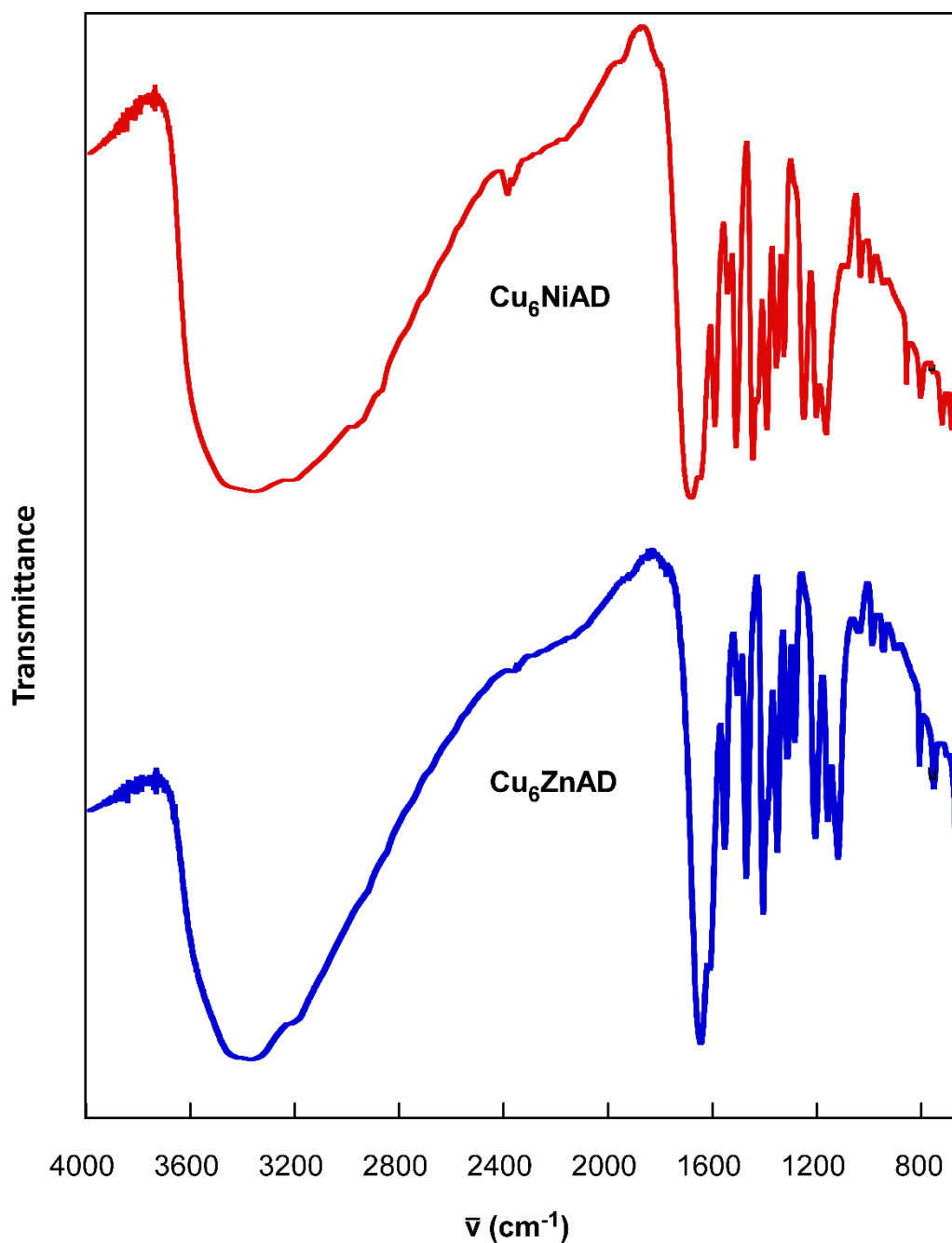


Figure 4.6. Infrared spectra of compounds Cu_6NiAD (red) and Cu_6ZnAD (blue).

4.2.3. Thermal analysis

Thermogravimetric and thermal differential analysis of these compounds are plotted in Figure 4.7, while the decomposition processes in each degradation stage are gathered in Table 4.3. All measurements were performed under a synthetic air atmosphere (79 % N_2 , 21 % O_2).

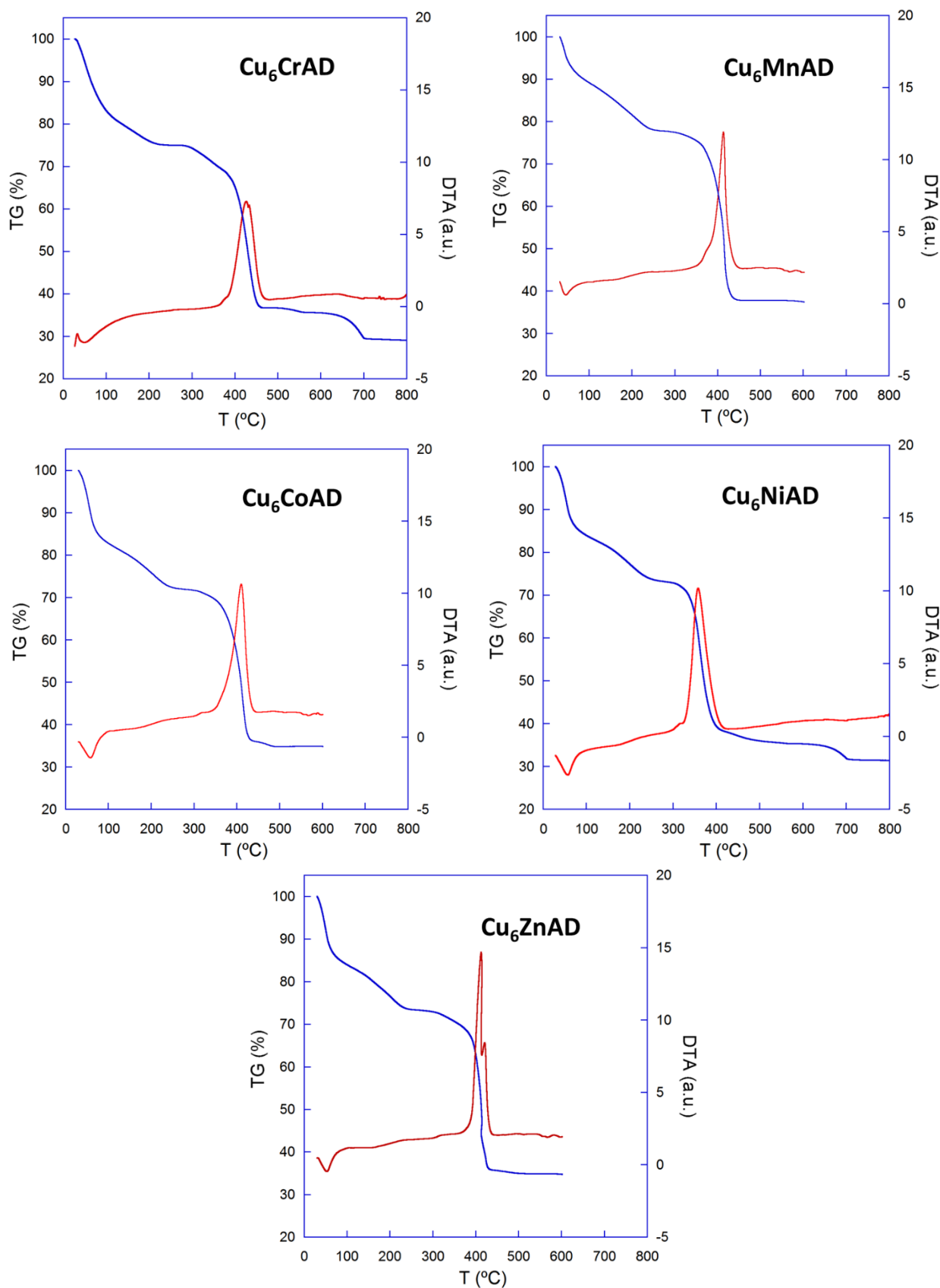


Figure 4.7. Thermogravimetric measurements performed upon representative samples.

Table 4.3. Thermoanalytic data of the compounds of Chapter 4.^[a]

Step	T _i	T _f	T _{peak}	ΔH	Δm(%)	ΣΔm(%)	ΣΔm(%) _{theo.} ^[b]
Cu ₆ CrAD							
1	30	95	50	Endo	16.3	16.3	16.3 (-17H ₂ O)
2	95	230		--	10.3	26.6	26.6 (-9H ₂ O)
3	300	475	425	Exo	37.9	64.5	64.5 (Cu ₆ CrO ₆ (SO ₄) _{1.5})
4	475	800			6.3	70.8	70.8 (6CuO + 0.5Cr ₂ O ₃)
Cu ₆ MnAD							
1	30	90	45	Endo	12.8	12.8	12.8 (-10.4H ₂ O)
2	90	255		--	11.4	21.6	21.6 (- (2.6 + 9) H ₂ O)
3	300	465	415	Exo	41.4	63.0	63.0 (Cu ₆ MnO ₆ (SO ₄) ₁)
Cu ₆ CoAD							
1	30	65	60	Endo	14.0	14.0	14.0 (-14H ₂ O)
2	65	265		--	9.0	23.0	23.0 (-9H ₂ O)
3	290	470	410	Exo	41.8	64.8	64.8 (Cu ₆ CoO ₆ (SO ₄) ₁)
Cu ₆ NiAD							
1	30	85	60	Endo	12.5	12.5	12.2 (-12H ₂ O)
2	85	260		--	8.9	21.4	21.4 (-9 H ₂ O)
3	290	515	355	Exo	42.7	64.1	64.2 (Cu ₆ NiO ₆ (SO ₄) ₁)
4	515	800			4.5	68.6	68.6 (6CuO+NiO)
Cu ₆ ZnAD							
1	30	85	55	Endo	15.0	15.0	15.6 (-16 H ₂ O)
2	85	250		--	9.3	24.3	23.7 (- 9H ₂ O)
3	290	465	415	Exo	39.0	65.3	65.3 (Cu ₆ ZnO ₆ (SO ₄) ₁)

^[a] T_i = initial temperature; T_f = final temperature; T_{peak} = peak temperature ATD; Δm(%) = loss mass percentage in each step; ΔH = type of process according to ATD; ΣΔm(%) = total loss mass after each step; ΣΔm(%)_{theo.} = total loss mass theoretically calculated. ^[b] Eliminate water molecules and final residue per compound formula.

All the compounds gathered in this chapter display a similar decomposition process. First, the loss of the crystallization water molecules occurs, in an endothermic process, from room temperature to a value below 100 °C. Subsequently, partially overlapped with the previous mass loss process, it takes place the loss of nine water molecules, corresponding to the six bridging waters and to the three water molecules formed upon the condensation process of the six hydroxide bridges. Despite water desorption and hydroxide condensation

reaction are endothermic and exothermic processes, respectively, no clear peak in the DTA curve is observed.

Thereafter, the decomposition of the organic part occurs through a strong exothermic process, generating a residue consisting on copper(II) oxide and the central metal sulfate according to PXRD analysis. In compounds Cu₆MnAD, Cu₆CoAD and Cu₆ZnAD, where the final analysis temperature was set at 600 °C, no further mass changes are observed. On the other hand, in compounds Cu₆CrAD and Cu₆NiAD, the analysis was performed until 800 °C, in such a way that the decomposition process of the metal sulfate to the corresponding oxide is observed. This process allows corroborating the sulphur content set from the crystallographic analysis, as the mass loss is ascribed to the release of SO₃.

4.3. RESULTS AND DISCUSSION

4.3.1. Crystallographic analysis.

The crystallographic data and details of the refinement parameters of each compound are gathered in Table 4.4. All non-hydrogen atoms were refined anisotropically, except those corresponding to disordered entities. The hydrogen atoms belonging to adeninato ligands have been geometrically fixed and refined according to a riding model with an isotropic thermal parameter linked to the atom to which they are attached (120 %). The hydrogen atoms of the coordination crystallisation water molecules and hydroxide groups have been located in the difference Fourier map or using the routine CALC-OH^[87] implemented in WinGX interface. The refinement of the latter hydrogen atoms has been performed with an isotropic thermal parameter of 150 % respect to their parent atom. Regarding the crystallization water molecules, not all of them could be located due their high disorder and therefore, their contribution was removed using the SQUEEZE^[112] procedure as implemented in the PLATON^[135] software. Accordingly, the hydrogen atoms of the located crystallization water molecules were not included due to high disorder present within the voids. Compound Cu₆MnAD show the peculiarity of only being possible to locate one SO₄²⁻ entity per heptameric unit, which is not enough to ensure the charge balance in this compound ([Cu₆Mn(μ-H₂O)₆(μ₃-OH)₆(μ-ade)₆]³⁺). Therefore, it has been assumed the remaining negative charge comes from an additional non coordinated hydroxide anion as it has been reported for some other MOFs synthesized under highly basic conditions.^[136]

¹³⁵ Spek, A. L. *Acta Crystallogr., Sect. D*, **2009**, *65*, 148–155.

¹³⁶ Sadakiyo, M.; Kasai, H.; Kato, K.; Takata, M.; Yamaudi, M. *J. Am. Chem. Soc.*, **2014**, *136*, 1702–1705.

Compounds Cu₆MnAD and Cu₆ZnAD were refined as a two component twin with a batch scale factor (BASF) parameter of 0.286 and 0.420 respectively. During the structural resolution of the heptameric entities of Cu₆CrAD, Cu₆MnAD and Cu₆CoAD, the initial resolution showed anomalous elongated ellipsoids for a series of atoms attributed to the adeninato ligands. These large values of the thermal movements were related to a disorder implying two coplanar puric bases with inverted dispositions regarding the bridging mode (μ - $\kappa N3:\kappa N9$ / μ - $\kappa N9:\kappa N3$). This disorder has been modelled by refining the occupation of each part (A and B) and ensure they sum up a total occupation factor of one. Furthermore, in compounds Cu₆MnAD and Cu₆CoAD the use of several restraints (DFIX and FLAT) were required in order to retain the expected geometry of the adeninato ligands during the data refinement process.

In compounds Cu₆CrAD and Cu₆CoAD, there are two symmetry related sulfate anions per heptamer. Thus, the occupation factors of the atoms comprising the sulfate have been fixed to the stoichiometrically required, i.e., 0.75 and 0.5 respectively. In compound Cu₆ZnAD, there are also two sulfate anions per heptamer, but each sulfate appears grouped together with two crystallization water molecules (O2w, O4w) in such a way that this ensemble is disordered in three position related by a ternary axis crossing along the sulfate O3S atom. Accordingly, the occupation factor of the atoms comprising the ensemble has been set to 1/6.

Although the lack of suitable single crystals has prevented the structural resolution of Cu₆NiAD compound, a profile fitting of its PXRD pattern has yielded similar cell parameters (Table 4.5 and Figure 4.8) to those of compound Cu₇ADSO₄, described in Chapter 3. Therefore, they can be considered isostructural compounds.

Table 4.4. Crystallographic data and refinement details of the compounds of Chapter 4.

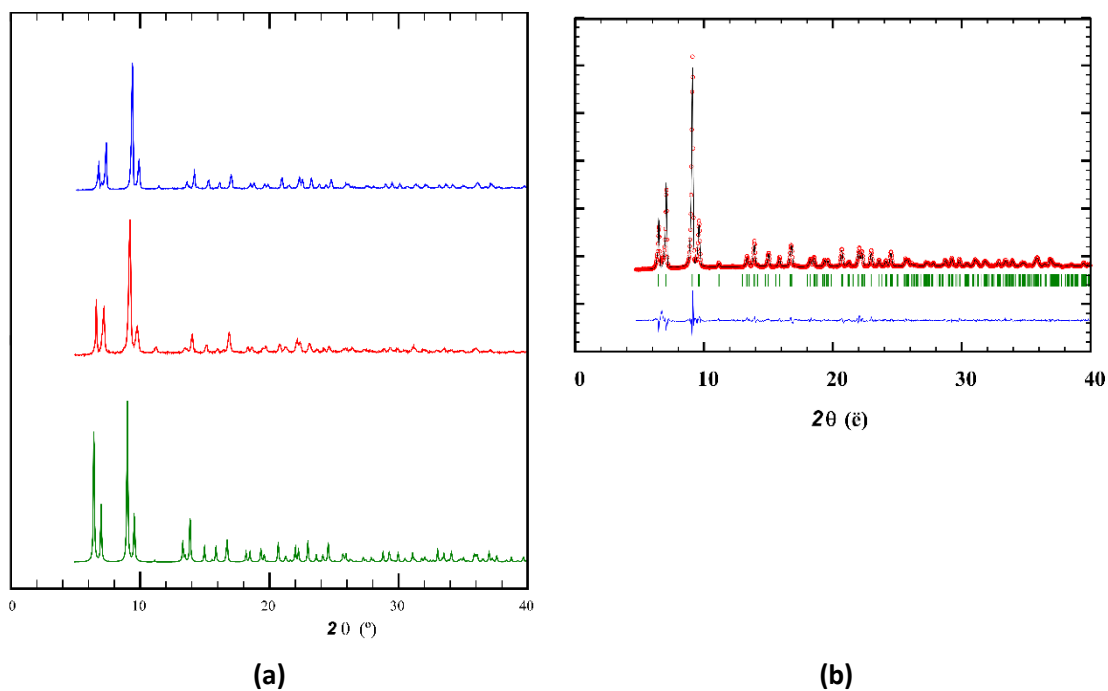
	Cu₆CrAD	Cu₆MnAD	Cu₆CoAD	Cu₆ZnAD
Formula	C ₃₀ H ₇₆ Cu ₆ CrN ₃₀ O ₃₅ S _{1.5}	C ₃₀ H ₆₇ Cu ₆ MnN ₃₀ O ₂₁ S	C ₃₀ H ₇₀ Cu ₆ ZnN ₃₀ O ₂₈ S	C ₃₀ H ₇₄ Cu ₆ ZnN ₃₀ O ₃₂ S
M (g mol ⁻¹)	1898.48	1780.32	1803.33	1845.82
Cryst. Syst.	Monoclinic	Monoclinic	Trigonal	Trigonal
Space group	<i>C2/c</i>	<i>P2₁/c</i>	<i>R$\bar{3}c$</i>	<i>R$\bar{3}c$</i>
<i>a</i> (Å)	15.583(3)	9.383(1)	19.058(3)	19.108(1)
<i>b</i> (Å)	22.219(4)	27.106(5)	19.058(3)	19.108(1)
<i>c</i> (Å)	27.400(3)	27.732(2)	43.157(9)	43.046(3)
α (°)	90	90	90	90
β (°)	101.386(14)	90.677(8)	90	90
γ (°)	90	90	120	120
<i>V</i> (Å ³)	9300.0(3)	7052.9(16)	13575.0(5)	13610.9(17)
<i>Z</i>	4	4	6	6
ρ_{calcd} (g·cm ⁻³)	1.124	1.676	1.378	1.654
Colour	Green	Dark green	Blue	Light blue
F(000)	3120	3660	5515	7020
μ (cm ⁻¹)	3.224	4.506	4.124	1.775
θ range	3.291–59.871	3.581–59.991	3.371–64.999	3.106–23.499
HKL range	-17≤h≤10; -21≤k≤24; -30≤l≤30	-7≤h≤10; -30≤k≤30; -31≤l≤31	-22≤h≤22; -22≤k≤21; -50≤l≤50	-20≤h≤21; -20≤k≤21; -48≤l≤48
Meas./indep. refl.	14606/6738	23766/5609	27448/2581	29410/5438
R _{eqv.}	0.0982	0.3726	0.4476	0.3814
Obs. refl. [<i>I</i> > 2σ(<i>I</i>)]	2202	1591	571	1367
R, R _w ^[a,b]	0.1149/0.3034	0.1593/0.4070	0.1190/0.3128	0.1252/0.3443
R, R _w (all)	0.2119/0.3789	0.3359/0.4852	0.2646/0.3810	0.2676/0.3747
Gof (S) ^[c]	0.958	1.020	0.785	0.967
Parameters	413	440	118	151
Weighting sch. ^[d]	Shelxl	Shelxl	Shelxl	Shelxl
Máx./min. Δρ (e Å ⁻³)	0.675/-0.406	1.089/-1.162	1.018/-0.467	1.143/-0.658
Diffractionmeter	SuperNova	SuperNova	SuperNova	SuperNova
λ (Å)	1.54184	1.54184	1.54184	0.71073
Temperature (K)	100(2)	100(2)	100(2)	100(2)

[a] $S = [\sum w(F_o^2 - F_c^2)^2 / (N_{\text{obs}} - N_{\text{param}})]^{1/2}$ [b] $R_1 = \sum ||F_o| - |F_c|| / \sum |F_o|$ [c] $wR_2 = [\sum w(F_o^2 - F_c^2)^2 / \sum wF_o^2]^{1/2}$; $w = 1/[\sigma^2(F_o^2) + (aP)^2]$ where $P = (\max(F_o^2, 0) + 2F_c^2)/3$. a: Cu₆CrAD (0.1803), Cu₆MnAD (0.2000), Cu₆CoAD (0.1864) and Cu₆ZnAD (0.1458).

Table 4.5. Crystal data and refinement details obtained from PXRD data for compound Cu₆NiAD.

Cu₆NiAD			
Formula	C ₃₀ H ₆₆ Cu ₆ NiN ₃₀ O ₂₈ S	Z	4
M (g mol ⁻¹)	1767.07	Colour	Blue
Cryst. Syst.	Orthorhombic	ρ _{calcd} (g·cm ⁻³)	1.345
Space group	<i>Cccm</i>	2θ range (°)	5.01–69.98
<i>a</i> (Å)	10.559(1)	Δ2θ step (°)	0.026
<i>b</i> (Å)	25.048(2)	Time per step (s)	2
<i>c</i> (Å)	27.301(4)	χ ²	3.66
α(°)	90	R _f ^a	1.73
β(°)	90	R _b ^b	1.44
γ(°)	90	R _p ^c	20.4
V (Å ³)	7220.6(1)	R _{wp} ^d	20.2

$${}^a R_f = \frac{\sum (|I_{\text{obs}}|^{1/2} - |I_{\text{calc}}|^{1/2})}{\sum |I_{\text{obs}}|^{1/2}} \quad {}^b R_b = \frac{\sum |I_{\text{obs}} - I_{\text{calc}}|}{\sum I_{\text{obs}}} \quad {}^c R_p = \frac{\sum |I_{\text{obs}} - I_{\text{calc}}|}{\sum I_{\text{obs}}} \quad {}^d R_{\text{wp}} = \left[\frac{\sum \omega_i |I_{\text{obs}} - I_{\text{calc}}|^2}{\sum \omega_i (I_{\text{obs}})^2} \right]^{1/2}$$

**Figure 4.8.** (a) Comparison of the experimental PXRD of Cu₆NiAD (blue) with the simulated (green) and experimental (red) ones of Cu₇ADSO₄. (b) Profile fitting of the PXRD pattern of Cu₆NiAD.

4.3.2. Structural description

All the crystal structures herein described consist of $[\text{Cu}_6\text{M}^{\text{III}}(\mu\text{-H}_2\text{O})_6(\mu_3\text{-OH})_6(\mu\text{-ade-}\kappa\text{N3}:\kappa\text{N9})_6]^{3+}$ or $[\text{Cu}_6\text{M}^{\text{II}}(\mu\text{-H}_2\text{O})_6(\mu_3\text{-OH})_6(\mu\text{-ade-}\kappa\text{N3}:\kappa\text{N9})_6]^{2+}$ heterometallic heptanuclear entities (M^{III} : Cr, Mn; M^{II} : Co, Ni, Zn), sulfate counterions and crystallization water molecules. The connectivity within the heptanuclear entities is essentially identical, in such a way that a central $[\text{M}^{\text{III}}(\text{OH})_6]^{3-}$ or $[\text{M}^{\text{II}}(\text{OH})_6]^{4-}$ core is connected to the six copper(II) metal centers comprising the external ring. The peripheral copper atoms are further connected among them through the double $\mu\text{-H}_2\text{O}$ and $\mu\text{-ade-}\kappa\text{N3}:\kappa\text{N9}$ bridge.

In addition, XPS (X-ray photoelectronic spectroscopy) measurements suggest that the external copper(II) ring has remained unaltered during the replacement process of the central metal atom (Figure 4.9). In the same way, the expected binding energies for Cu(II) are compared with experimental values of Cu_6MAD compounds. The bonding energies of the Cu(II) and the substituted central metals are reflected in Table 4.6.

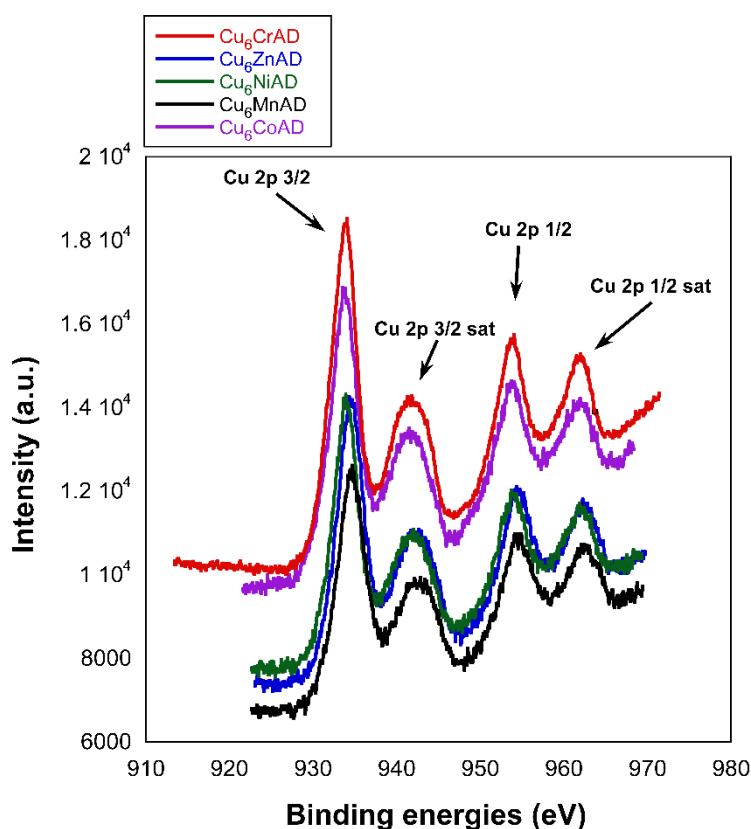


Figure 4.9. Bonding energies of the Cu(II) ions of all compounds of Chapter 4.

Table 4.6. Expected and experimental binding energies values for Cu(II).^[137]

	B.E (eV) _{Theo.}	Cr B.E (eV) _{exp.}	Mn B.E (eV) _{exp.}	Co B.E (eV) _{exp.}	Ni B.E (eV) _{exp.}	Zn B.E (eV) _{exp.}
Cu 2p 3/2	934.4	933.9	934.5	933.6	933.8	934.4
Cu 2p 3/2 sat	941.9	941.4	942.3	941.4	941.6	942.1
Cu 2p 1/2	953.7	953.7	954.5	953.7	954.3	954.3
Cu 2p 1/2 sat	961.9	961.9	962.5	961.9	962.3	962.3

The comparison of the theoretical data with the experimental one of the substituted metal centres demonstrates qualitatively the presence of the metal centres in the oxidation states; M^{III}: Cr^[138], Mn^[139] and M^{II}: Co^[140], Ni^[141], Zn^[142]. See the appendix A.2.6 for more details of the spectra and binding energies. Manganese compound was also measured using a Mg X-ray source, due to the overlap of the peak with the Auger Cu LMM line. The binding energies observed for this compound do not allow a firm assertion of the oxidation state present in the structure due to the proximity of the binding energies of the +2 and +3 states. However, more references have been found for Mn(III) compounds that fit the peaks of Cu₆MnAD comparing to the reported for Mn(II) compounds.^[144] The slight discrepancies between the binding energies of these compounds and those reported in bibliography could be attributable to the differences with in the coordination environment or the experimental conditions of the measurements.

It is noteworthy that, Cu₆CoAD and Cu₆ZnAD are isostructural to Cu₇ADSO₄NHET₃-2, Cu₆CrAD to Cu₇ADSO₄NHET₃-1 and Cu₆NiADE to Cu₇ADSO₄. In spite of that, in certain cases, slight differences have been observed in the balance of the supramolecular interactions caused by the different content of guest molecules hosted in the pores. No equivalent crystal structure was found for Cu₆MnAD among the compounds reported in the current PhD thesis. Next, the description of each crystal structure is gathered, providing in each case a view of the

¹³⁷ NIST X-ray Photoelectron Spectroscopy Database, Version 4.1 (National Institute of Standards and Technology, Gaithersburg, **2012**); <http://srdata.nist.gov/xps/>.

¹³⁸ (a) El-Mehalmey, W. A.; Ibrahim, A. H.; Abugable, A. A.; Hassan, M. H.; Haikal, R. R.; Karakalos, S. G.; Zaki, O.; Alkordi, M. H. *J. Mater. Chem. A*, **2018**, *6*, 2742. (b) Flores-Cano, J. V.; Leyva-Ramos, R.; Carrasco-Marin, F.; Aragon-Piña, A.; Salazar-Rabago, J. J.; Leyva-Ramos S. *Adsorption*, **2016**, *22*, 297–308.

¹³⁹ (a) Van De Vondel, D.F.; Wuyts, L.F.; Van Der Kelen, G.P.; Bevernage, L. *J. Electron Spectrosc. Relat. Phenom.*, **1977**, *10*, 389. (b) Vannerberg, N.G. *Chem. Scr.*, **1976**, *9*, 122. (c) Ivanov-Emin, B.N.; Nevskaya, N.A.; Zaitsev, B.E.; Ivanova, T.M., *Zh. Neorg. Khimii*, **1982**, *27*, 3101. (d) Carver, J.C.; Schweitzer, G.K.; Carlson, T.A. *J. Chem. Phys.*, **1972**, *57*, 973.

¹⁴⁰ A. M., Su; L. S., Wang; Q. F., Zhang; J., Xie; Q., Luo; D. L., Peng, *J. of Mat. Sci.: Mat. in Elec.*, **2018**, *29*, 9814–9820.

¹⁴¹ Alamar, T.; Shekhah, O.; Wohlgemuth, J.; Mudring, A.-V. *J. Mater. Chem.*, **2012**, *22*, 18252.

¹⁴² (a) Wayu, M. B.; King, J. E.; Johnson, J. A.; Chusuei, C. C. *Electroanalysis*, **2015**, *27*, 2552–2558. (b) Cano, A.; Rodríguez-Hernández, J.; Reguera, L.; Rodríguez-Castellón, E.; Reguera E., *Eur. J. Inorg. Chem.* **2019**, 1724–1732.

heptanuclear entity with its numbering scheme, coordination bond-lengths and main details on the crystal packing.

4.3.2.1. Structural description of compound Cu₆CrAD.

The heptanuclear complex of compound Cu₆CrAD together with its numbering scheme is shown in Figure 4.10, while the corresponding coordination bond lengths are gathered in Table 4.7. As expected, all the coordination bonds around the central Cr(III) atom are similar, since it is not affected by the Jahn-Teller effect. Note that in the analogous Cu₇ADSO₄NHET₃-1 compound, the coordination polyhedron around central Cu(II) resembles an elongated octahedron with 4 short coordination distances (1.97–2.00 Å) and two longer ones (2.11–2.16 Å). The [Cr(OH)₆]³⁻ core is tightly anchored to two sulfate anions, below and above the heptameric entity, through three O–H···O hydrogen bonds to each anion. As a result, the supramolecular packing is driven by the self-assembling of these robust sulfate/heptamer/sulfate supramolecular ensembles (Figure 4.11; Table 4.8). In this regard, each heptamer acts as a four-connected node showing the same connectivity features as those described for Cu₇ADSO₄NHET₃-1: firstly, each heptamer binds to two neighbouring ones through double adeninato π–π interactions (ADE-2···ADE-3; minimum distances: 3.42–3.61 Å; tilt angle between mean planes: 2.91°) and secondly to another two heptamers again through additional adeninato π–π interactions (ADE-1···ADE-1; minimum distances: 3.45–3.67 Å; tilt angle between mean planes: 0.50°) and sulfate mediated hydrogen bonding (N16_{adeninato}-H···O_{sulfate}···OH_{coordinated}). It deserves to note that these π–π interactions imply both the endocyclic atoms and the exocyclic amino group, whose lone electron pair is delocalized in the π–system of the adenine. As in Cu₇ADSO₄NHET₃-1, the rigidity of both the heptameric discrete entity and the double synthons connecting the entities, generate a supramolecular porous architecture with **cds** (CdSO₄ like) topology with a (6⁵.8) point symbol. The pore system is comprised by 1D channels that imply a 44.3 % of unit cell volume as it can be observed in Figure 4.12. This porosity is somewhat smaller than that probed for Cu₇ADSO₄NHET₃-1 (49 %) which can be related to the different content of guest molecules and to certain structural flexibility.

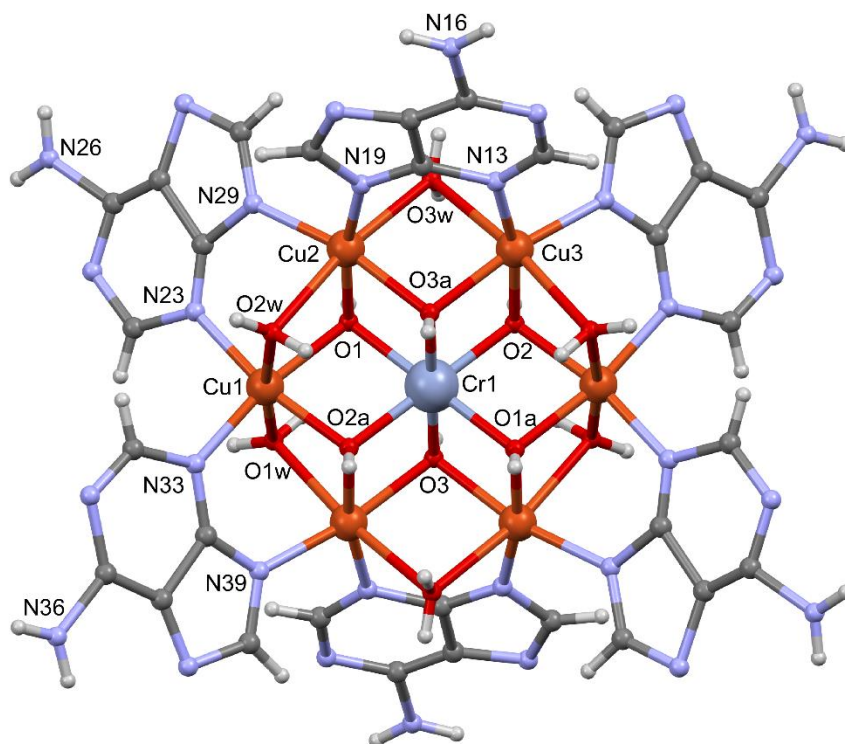


Figure 4.10. Heptameric entity of compound Cu_6CrAD .

Table 4.7. Coordination bond distances (\AA) of compound Cu_6CrAD .¹

Cu_6CrAD					
Cr1–O1	1.999(9)	Cu1–O2w	2.384(1)	Cu3–O2a	2.016(1)
Cr1–O1a	1.999(9)	Cu1–N29	1.982(2)	Cu3–O3	2.019(8)
Cr1–O2	1.961(8)	Cu1–N33	1.982(1)	Cu3–O1wa	2.380(1)
Cr1–O2a	1.961(8)	Cu2–O1	1.967(1)	Cu3–O3w	2.442(8)
Cr1–O3	1.992(1)	Cu2–O3	2.030(9)	Cu3–N13	1.935(1)
Cr1–O3a	1.992(1)	Cu2–O2w	2.412(1)	Cu3–N39a	1.999(1)
Cu1–O1	2.013(9)	Cu2–O3w	2.414(1)	Cr1...Cu1	3.058(1)
Cu1–O2	1.964(9)	Cu2–N19	1.862(2)	Cr1...Cu2	3.097(2)
Cu1–O1w	2.429(1)	Cu2–N23	2.032(4)	Cr1...Cu3	3.100(2)

¹ Symmetry-codes: (a): $-x, -y+1, -z+1$.

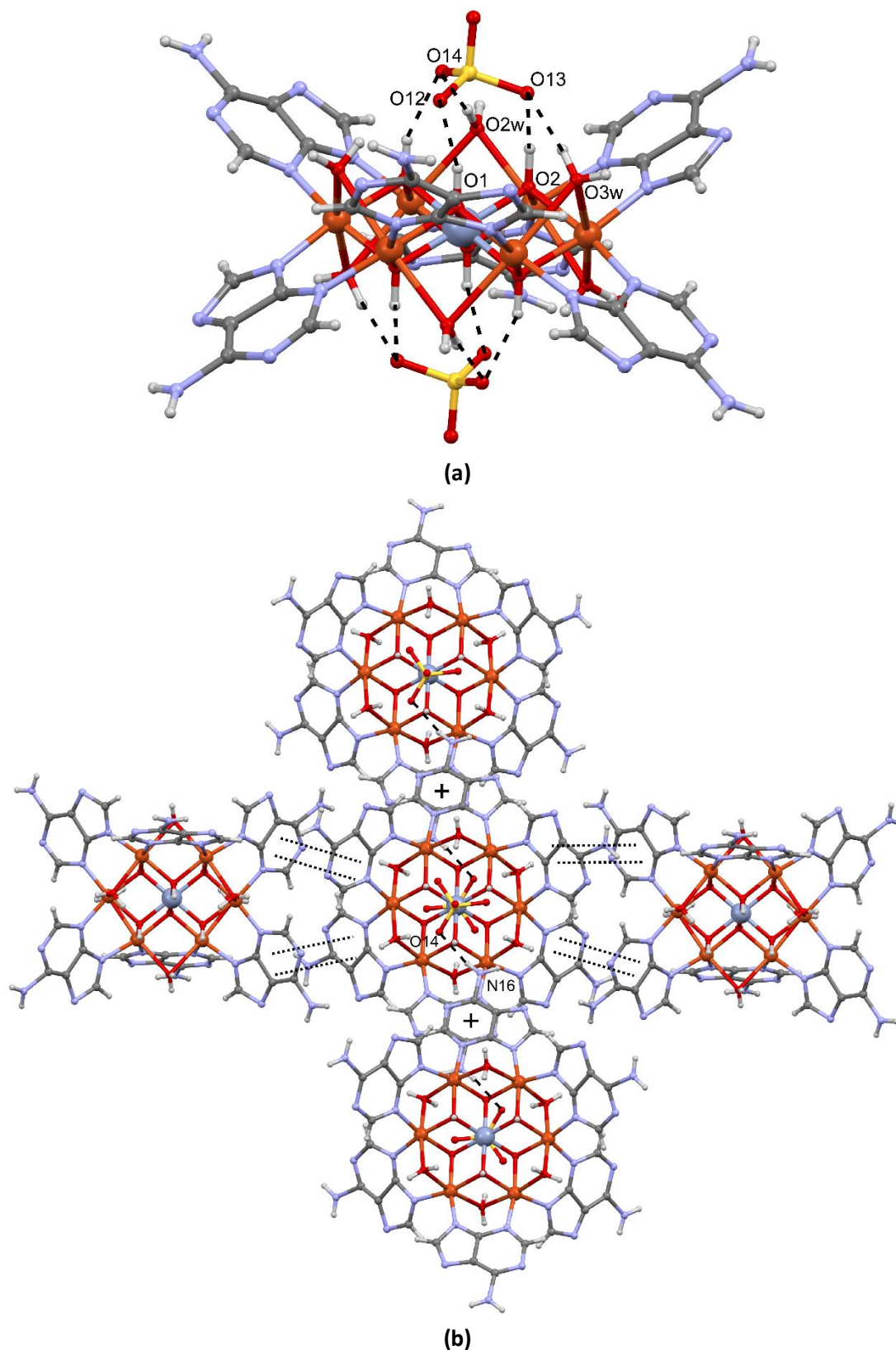


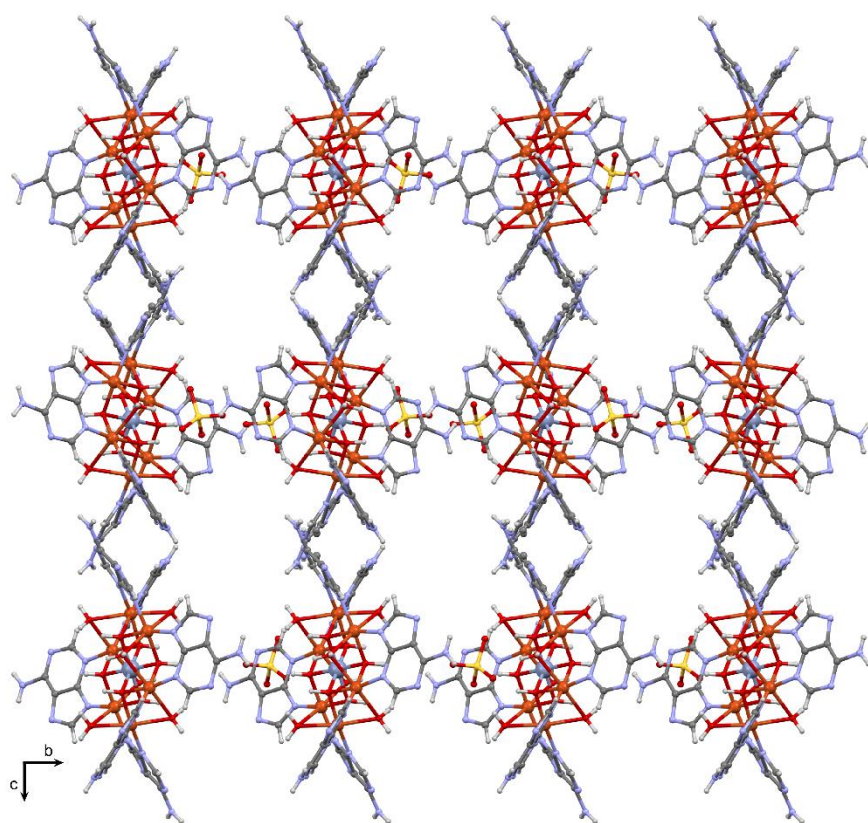
Figure 4.11. (a) Detail of the sulfate/heptamer/sulfate supramolecular ensemble and (b) non-covalent interactions among neighbouring heptamers in compound Cu_6CrAD .

Table 4.8. Hydrogen-bonding parameters (Å, °) and π - π interactions in compound Cu₆CrAD.^a

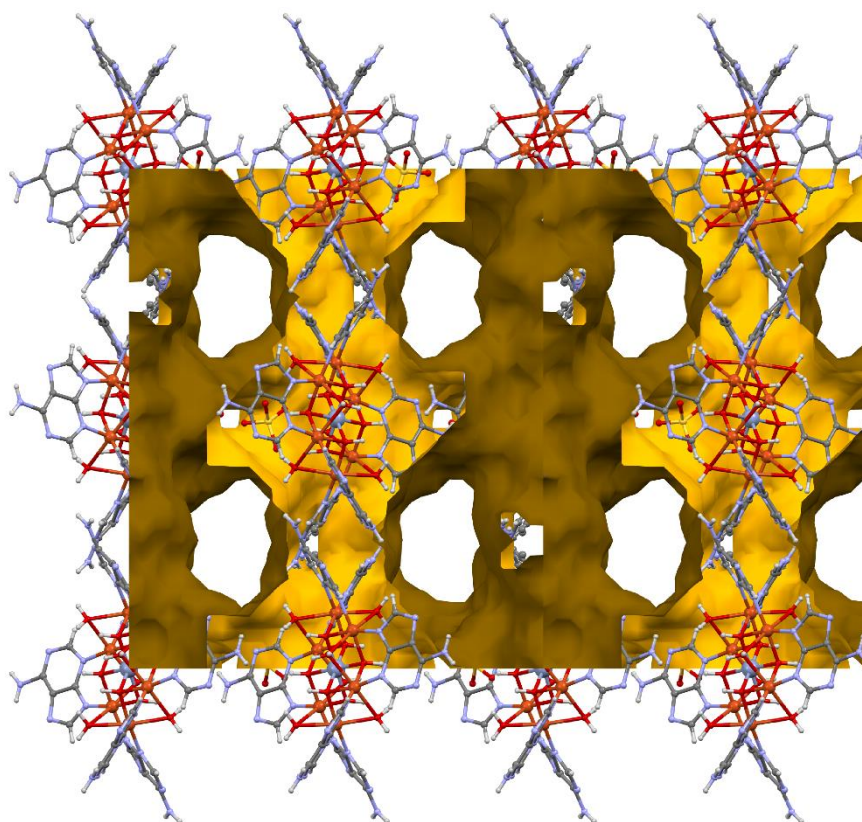
D-H...A ^[b]	H...A	D...A	D-H...A
N16-H16B...O14a	2.08	2.92(3)	167
O4w... N31	--	2.71(2)	--
N36-H16B...O4w	2.56	3.18(2)	130
O1w-H12w...O12c	2.29	3.05(2)	149
O2w-H21w...O4wb	1.89	2.68(18)	154
O2w-H22w...O14	1.98	2.85(19)	176
O3w-H32w...O13c	2.15	2.96(2)	157
O1-H1...O12c	1.73	2.66(2)	157
O2-H2...O13c	1.67	2.61(2)	159
O3-H3...O14	1.90	2.81(3)	153

π-π interactions^[c]					
Ring...Ring ^[d]	α	DC	β	DZ	DXY
p3...h2 ^b	1.0	5.62(1)	52.8	3.40(9)	4.47
p2...p3 ^b	5.0	5.12(1)	48.6	3.38(9)	3.84
h1...h1 ^b	0.5	3.55(3)	32.1	3.45(2)	4.29

^a Symmetry-codes: (a) $-x, -y+3/2, -z+1$; (b) $-x, y, -z+3/2$; (c) $-x, -y+1, -z+1$. ^[b] D: donor; A: acceptor. ^[c] Angle: dihedral angle between the planes (°), DC: distance between the centroids of the rings (Å), α : angle (°) between mean plane of the rings. β : angle (°) between the normal to the first ring and the DC vector (°), DZ: interplanar distance (Å), DXY: lateral displacement (Å), ^[d] h: hexagonal ring of the adeninato and p: pentagonal ring of the adeninato. The numbers 1, 2 and 3 are related with each of the crystallographically independent adenines. h1: N11, C12, N13, C14, C15, C16. h2: N21, C22, N23, C24, C25, C26. p2: C24, C25, N27, C28, N29. p3: C34, C35, N37, C38, N39.



(a)



(b)

Figure 4.12. Crystal packing of compound Cu_6CrAD (a) showing the voids in yellow (b).

4.3.2.2. Structural description of compound Cu_6MnAD .

Figure 4.13 and Table 4.9 show the heptameric entity and coordination bond distances of compound Cu_6MnAD . The central manganese atom shows four short coordination bond distances (2.06–2.09 Å) and two longer ones (*ca.* 2.2 Å). This observation led us to disregard +2 oxidation-state, as $\text{Mn}^{\text{II}}\text{-O}$ bond distances are expected to be more isotropic and range between 2.15 and 2.25 Å.^[8] A central Mn(II) is neither compatible with the observed magnetic behaviour. Therefore, Mn(III) can be assigned as central atom, which is also influenced by the Jahn-Teller effect ($t_{2g}^3 e_g^1$). We have analysed the distribution of coordination bond lengths in $\text{Mn}^{\text{III}}\text{O}_6$ -type coordination polyhedra using the ConQuest [version 2.05] search engine implemented in the CSD (Figure 4.14 and Table 4.10). The equatorial bond lengths range roughly between 1.9 and 2.0 Å (mean: *ca.* 1.94 Å), while the axial mean bond lengths are 2.2(1) Å and 1.87(2) Å for elongated and compressed polyhedra, respectively. This seems to indicate that a central Mn^{III} with a Jahn-Teller elongation is the most likely option despite, certain disorder might be affecting it, as the equatorial bond distances are somewhat larger than expected. It must be indicated that the aerobic oxidation of Mn(II) to Mn(III) is favoured in aqueous alkaline media, such as that employed in the synthesis of these compounds. In any case the presence of Mn(III), matches with the thermogravimetric analysis and XPS observations, and it is further supported by the magnetic data (see section 4.3.3.).

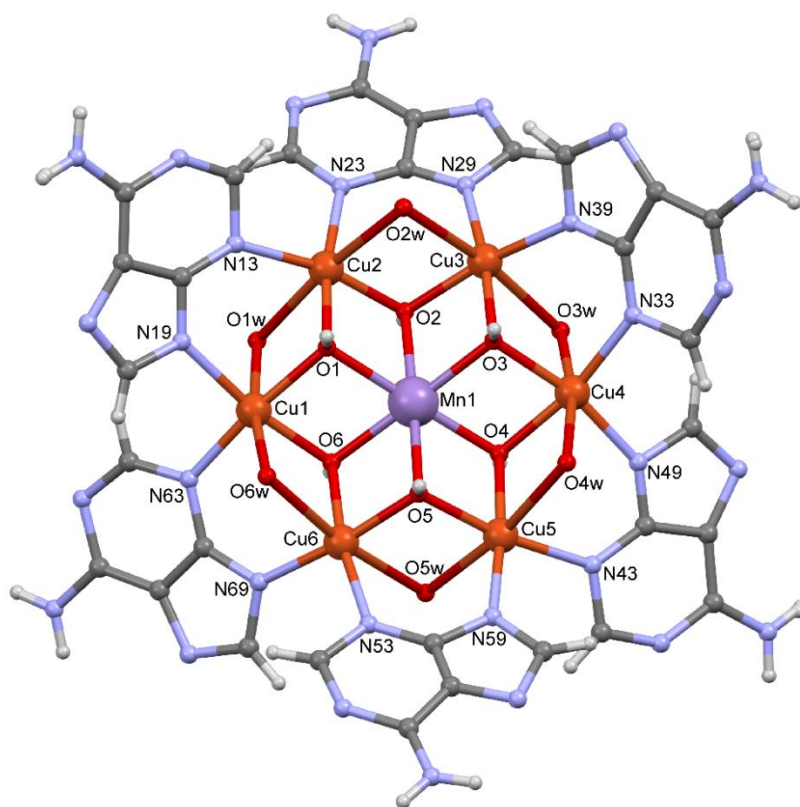


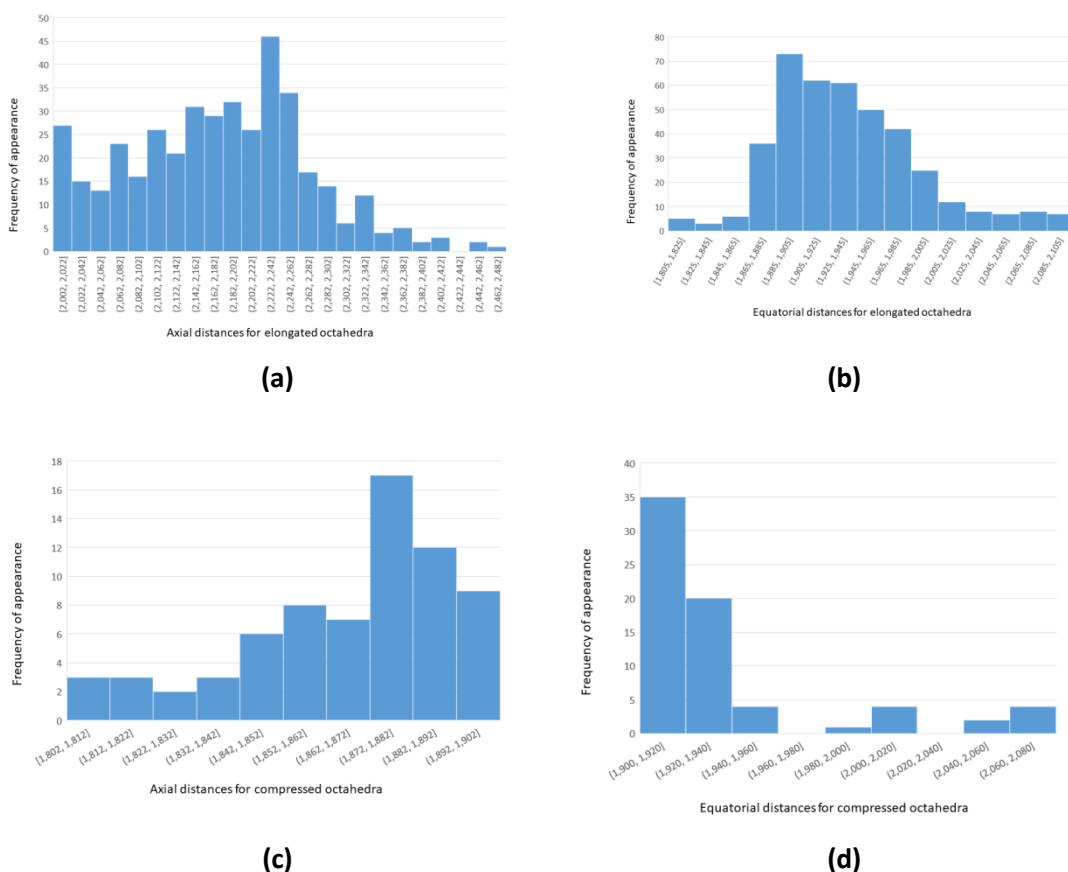
Figure 4.13. Heptameric entity of compound Cu_6MnAD .

Table 4.9. Coordination bond distances (Å) compounds Cu₆MnAD.¹

Cu₆MnAD			
Mn1–O1	2.090(2)	Cu4–N33	2.043(5)
Mn1–O2	2.200(2)	Cu4–N49	1.977(6)
Mn1–O3	2.066(1)	Cu4–O3	1.960(2)
Mn1–O4	2.068(2)	Cu4–O4	1.974(1)
Mn1–O5	2.158(2)	Cu4–O3w	2.482(2)
Mn1–O6	2.088(1)	Cu4–O4w	2.594(1)
Cu1–N19	2.072(5)	Cu5–N43	2.066(5)
Cu1–N63	1.987(4)	Cu5–N59	1.987(6)
Cu1–O1	1.975(1)	Cu5–O4	1.954(2)
Cu1–O6	1.957(2)	Cu5–O5	1.950(2)
Cu1–O1w	2.749(1)	Cu5–O4w	2.577(1)
Cu1–O6w	2.419(2)	Cu5–O5w	2.488(1)
Cu2–N13	2.033(5)	Cu6–N53	2.105(5)
Cu2–N23	2.046(4)	Cu6–N69	1.977(5)
Cu2–O1	1.936(2)	Cu6–O5	1.918(2)
Cu2–O2	1.910(2)	Cu6–O6	1.955(2)
Cu2–O1w	2.667(2)	Cu6–O5w	2.589(1)
Cu2–O2w	2.481(2)	Cu6–O6w	2.505(1)
Cu3–N29	1.927(5)	Mn1…Cu1	3.115(6)
Cu3–N39	2.050(4)	Mn1…Cu2	3.159(4)
Cu3–O2	1.972(2)	Mn1…Cu3	3.144(5)
Cu3–O3	1.990(2)	Mn1…Cu4	3.106(7)
Cu3–O2w	2.519(1)	Mn1…Cu5	3.146(7)
Cu3–O3w	2.556(2)	Mn1…Cu6	3.121(5)

Table 4.10. Equatorial and axial mean bond lengths in elongated and compressed $Mn^{III}O_6$ type polyhedra.¹

	Elongated		Compressed	
	Mean (Å)	σ (Å)	Mean (Å)	σ (Å)
Axial	2.185	0.101	1.868	0.023
Equatorial	1.942	0.052	1.935	0.043

¹: σ : standard deviation.**Figure 4.14.** Distribution of equatorial and axial bond lengths (Å) in elongated and compressed $Mn^{III}O_6$ type polyhedral showing the amount of compounds with each length distribution.

Despite the complex wheel has the same ionic charge as that of compound Cu_6CrAD compound, the set of supramolecular interactions involving the heptameric entity show significant differences (Figure 4.15, Table 4.11). Each sulfate anion links successively upper and lower $[Mn(OH)_6]^{3-}$ cores of neighbouring heptamers by means of four hydrogen bonding interactions (Figure 4.15a) to give rise to a one-dimensional heptamer/sulfate aggregate. On the other hand, each heptamer is connected to seven surrounding heptamers through an intricate network of interactions: (1) it binds to three neighbouring heptamers by means of the $\pi-\pi$ interactions (see green entities in Figure 4.15b) established through five of its adenines (ADE-1, -2, -3, -5 and -6), (2) it is hydrogen bonded to one neighbouring complex by means

of the pairing interaction (N46–H···N41) taking place between Watson-Crick faces of adeninato ligands (ADE–4, blue entity), and (3) it establishes less robust single-hydrogen bonding interactions (N26–H26B···N31, N26–H26B···N31, N56–H56A···N47, N66–H66X···N21) with three surrounding heptamers (depicted as yellow entities). Thus, if we consider each heptameric entity as a node of the network and both π - π interactions and hydrogen bonds between adeninato ligands as linkers, the structure can be described as a 7-connected uninodal net with $(3^3.4^3.5^{12}.6^3)$ point symbol that affords an unprecedented topology. The resulting supramolecular network presents 1D channels that imply a 22.2 % of unit cell volume as it can be observed in Figure 4.16.

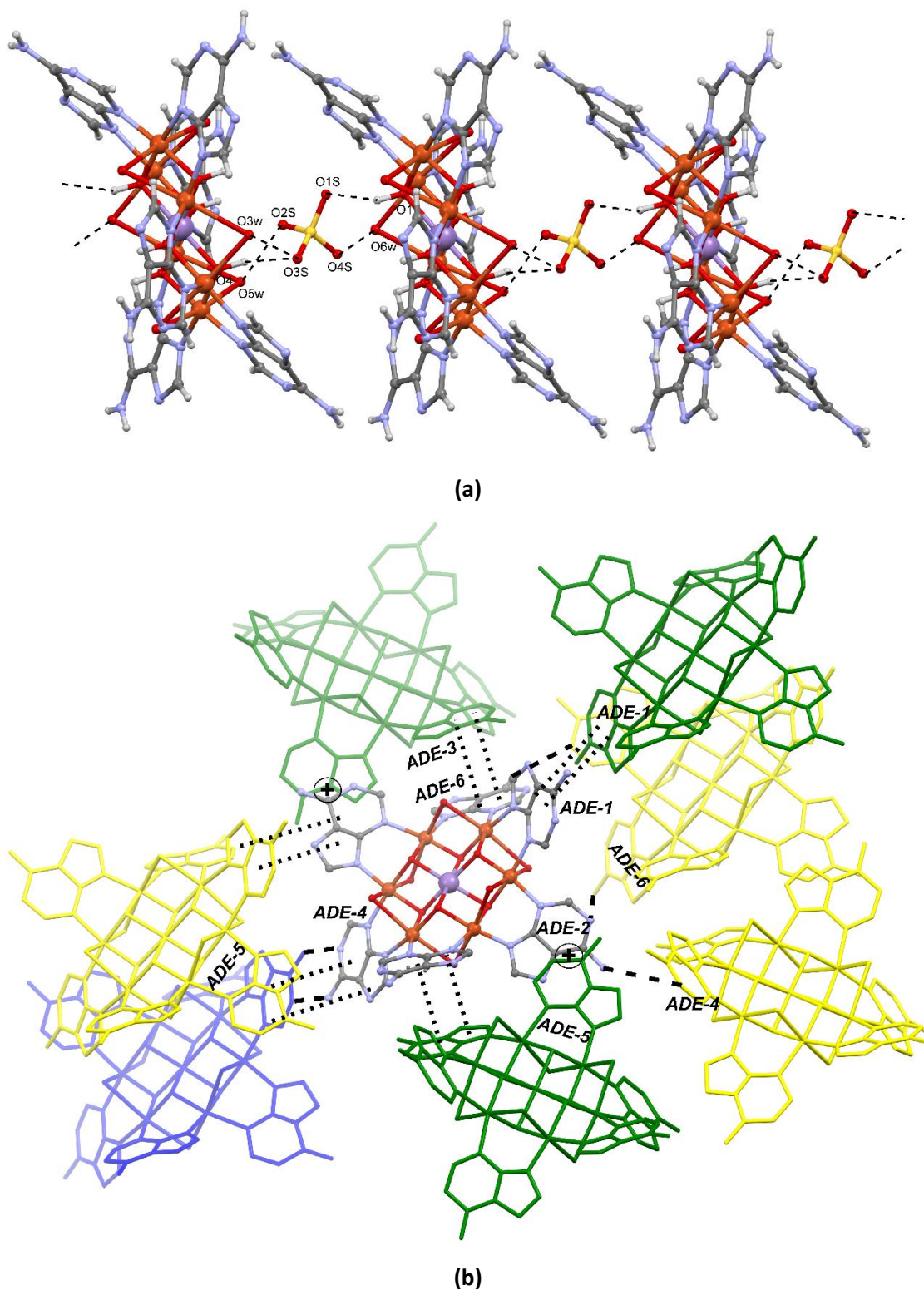


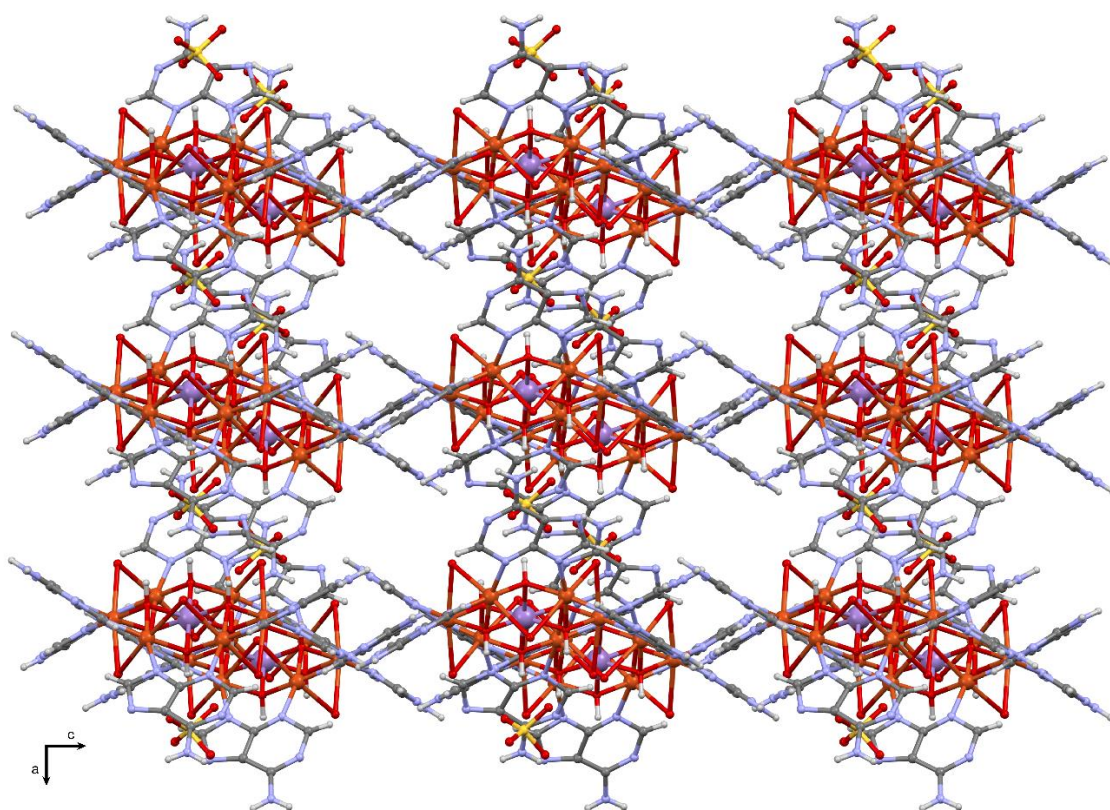
Figure 4.15. Sulfate/heptamer 1D supramolecular ensemble (a) and interaction of a heptameric entity with seven surrounding ones in compound Cu_6MnAD (b). Hydrogen atoms were omitted for clarity; green, blue and yellow entities are assembled by means of π - π , pairing interaction through Watson-Crick face and single-hydrogen bonding interactions, respectively.

Table 4.11. Hydrogen-bonding parameters (Å, °) and π - π interactions in compound Cu₆MnAD.^a

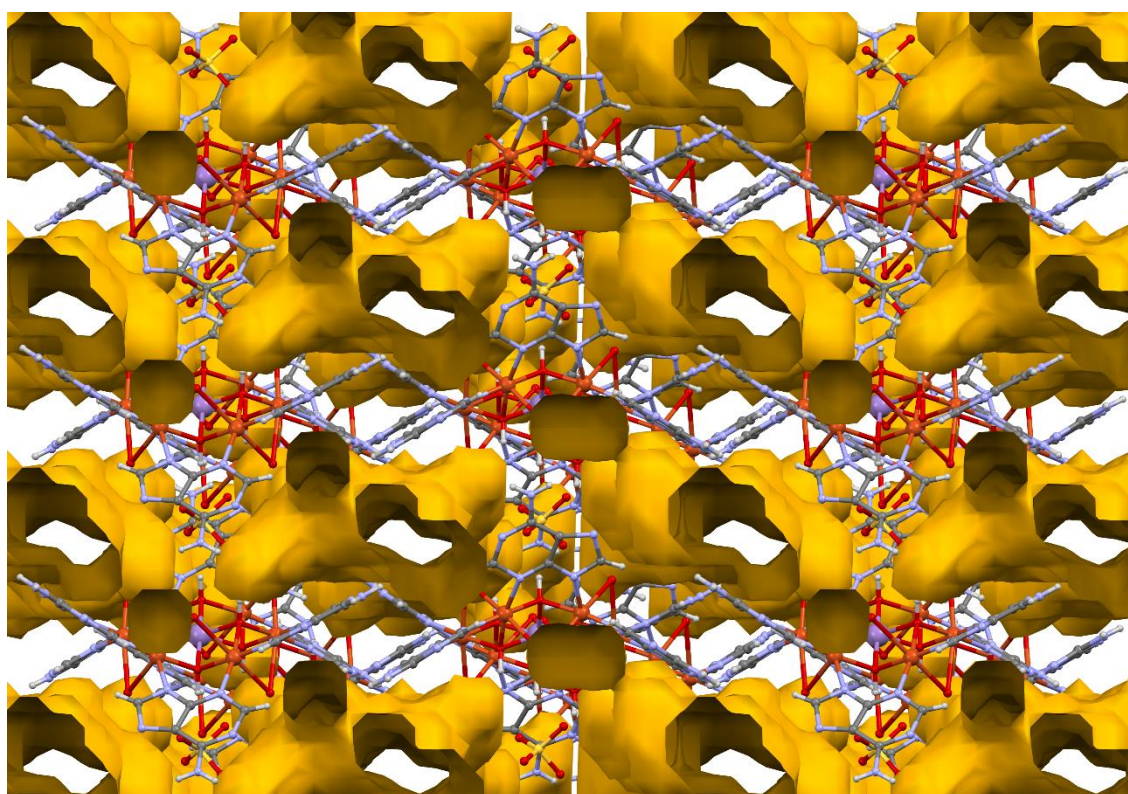
D-H...A ^[b]	H...A	D...A	D-H...A
N26-H26B...N31a	2.41	3.25(3)	166
N46-H46B...N41b	1.89	2.71(3)	159
N56-H56A...N47c	2.57	3.36(5)	153
N66-H66B...N21d	2.30	3.142(6)	168
O3w-H3...O3Se		2.87(2)	
O5w-H5...O2Se		2.88(3)	
O1-H1...O1S	1.93	2.86(4)	158
O3-H3...O4S	2.44	3.22(4)	136
O4-H4...O2Se	2.43	3.24(3)	140
O4-H4...O3Se	1.99	2.90(5)	153

π-π interactions^[c]					
Ring...Ring ^[d]	α	DC	β	DZ	DXY
h1...p1 ^f	0.0	5.43(2)	50.3	3.47(1)	4.18
p2...p5 ^g	3.0	5.53(2)	50.1	3.35(1)	4.24
h3...p6 ^g	3.3	4.89(3)	45.0	3.26(8)	3.46
p3...p6 ^g	3.3	3.84(2)	25.9	3.38(1)	1.68
h4...p5 ^c	54.1	4.47(7)	26.0	1.96(1)	--
p4...p5 ^c	54.1	4.49(4)	26.7	0.78(8)	--

^a Symmetry-codes: (a) 2-x, -1/2+y, 3/2-z. (b) -x+3, -y+1, -z+2. (c) -x+2, -y+1, -z+2. (d) -x+2, -y, -z+2. (e) x+1, y, z. (f) -x+1, -y, -z+2. (g) x, -y+1/2, z-1/2. ^[b] D: donor; A: acceptor. ^[c] Angle: dihedral angle between the planes (°), DC: distance between the centroids of the rings (Å), α : angle (°) between mean plane of the rings. β : angle (°) between the normal to the first ring and the DC vector (°), DZ: interplanar distance (Å), DXY: lateral displacement (Å), ^[d] h: hexagonal ring of the adeninato and p: pentagonal ring of the adeninato. The numbers from 1 to 6 are related with each of the crystallographically independent adenines. h1: N11, C12, N13, C14, C15, C16. p1: C14, C15, N17, C18, N19. p2: C24, C25, N27, C28, N29. h3: N31, C32, N33, C34, C35, C36. p3: C34, C35, N37, C38, N39. h4: N41, C42, N43, C44, C45. p4: C44, C45, N47, C48, N49. p5: C54, C55, N57, C58, N59. p6: C64, C65, N67, C68, N69.



(a)



(b)

Figure 4.16. Crystal packing of compound Cu_6MnAD (a) showing the voids in yellow (b).

4.3.2.3. Structural description of compounds Cu₆CoAD and Cu₆ZnAD.

As mentioned in the introductory section of the structural description of this chapter, the compounds Cu₆CoAD and Cu₆ZnAD are isostructural to Cu₇ADSO₄NHET₃-2, described in Chapter 3. Although in general terms the crystal packings are analogous, some slight differences are observed in the coordination bond distances (Figure 4.17 and Table 4.12) and in some supramolecular interactions implying the sulfate anions. The central metal atom (Co or Zn) is sited on a special position containing an inversion centre and a ternary axis. Interestingly, despite the symmetry site of the central metal atom forces all the M–OH coordination bond distances to be equal, the hydroxide O-atoms could be refined anisotropically, as both exchanged central metal atoms have a weak or lack of Jahn-Teller effect (Co^{II} and Zn^{II}, respectively), i.e. there should not be great differences between coordination bond lengths. Contrarily, in compound Cu₇ADSO₄NHET₃-2, the O-atoms of the [Cu(OH)₆]⁴⁻ core could only be refined using isotropic displacement parameters because if anisotropic ones are employed too elongated ellipsoid are generated indicative of an unresolved disorder.

Table 4.13 and Table 4.14 show the structural parameters of the hydrogen bonding of compounds Cu₆CoAD and Cu₆ZnAD, respectively. In these compounds, the heptameric entities appear sandwiched between sulfates, but they display some dissimilarities with regard to Cu₇ADSO₄NHET₃-2 in terms of disposition and/or site occupancy of the sulfate entities (Figure 4.18). In the Co(II) compound, each sulfate anion is hydrogen bonded like a tripod to three OH groups of the heptamer, similarly to Cu₆CrAD and Cu₇ADSO₄NHET₃-1, but the total site occupancy for each sulfate is set to 1/2 to counterbalance the charge of the complex entity. Note that the ternary axis crosses through apical S–O1s bond of the sulfate. In the Zn(II) analogous compound, the disposition of the sulfate anion is similar to that of Cu₇ADSO₄NHET₃-2: a ternary axis crosses through a peripheral sulfate O-atom (O3s) in such a way that the anion and two related crystallization water molecules (O2w and O4w) appear disordered in three symmetry related positions and therefore, the heptamers are sandwiched by two sets of three sulfates (each with a total occupancy of 1/6). Furthermore, in Cu₆ZnAD, as it occurs in the isostructural parent compound (Cu₇ADSO₄NHET₃-2), each sulfate is only anchored through two hydrogen bonds to the hydroxide bridges.

Regarding the self-assembly of the heptamers, each entity is six-connected by means of π–π interactions (comprising its six adeninatos) to three upper and to three lower ones, resembling a close packing model of spheres (Figure 4.19). However, again, some mild differences are observed due to the unlike disposition of sulfate counterions. In compound

Cu_6CoAD , the sulfate, anchored as tripod to the three hydroxide of a heptamer, bridges surrounding heptamers by means of the hydrogen bonding interaction established with the amino group of the adenine. In compound Cu_6ZnAD , similarly to $\text{Cu}_7\text{ADSO}_4\text{NHET}_3\text{-2}$, the heptamers are further connected by means of the hydrogen bonding that establishes the capping sulfate/water ensemble with the Hoogsteen face of the adeninato ligands of neighbouring heptamers. In both cases, the rigid synthons generated from the combined set of π - π and hydrogen bonding interactions lead to, an open structure, with α -Po primitive cubic **pcu** topology and a $(4^{12}.6^3)$ point symbol. The resulting 3D channels comprise the 46.1% and 49.0% of the unit cell of compounds Cu_6CoAD and Cu_6ZnAD , respectively (Figure 4.20).

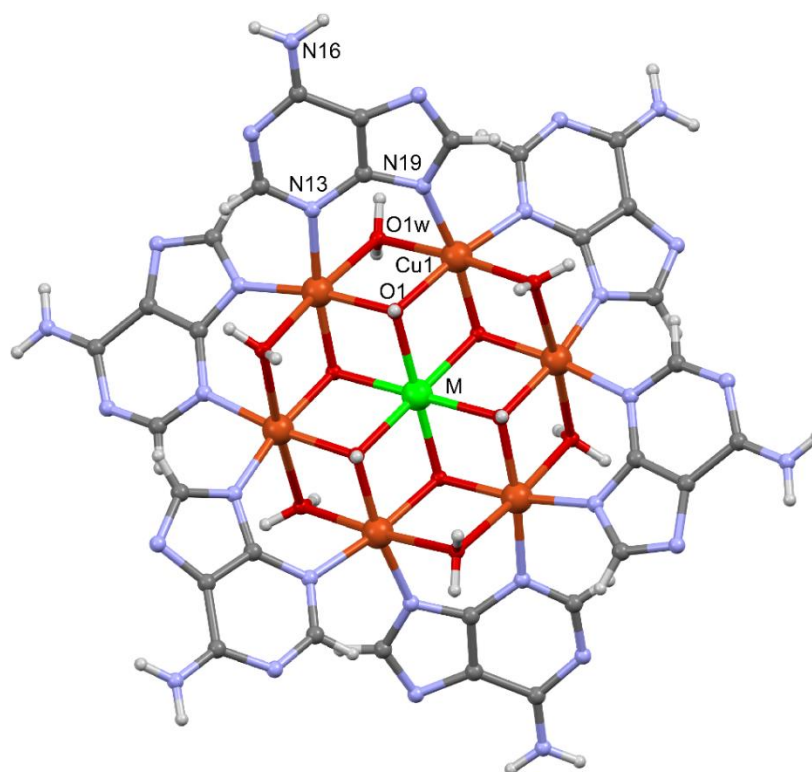


Figure 4.17. Heptameric entity of compound Cu_6CoAD and Cu_6ZnAD , M being Co(II) or Zn(II).

Table 4.12. Coordination bond distances (Å) compounds Cu₆CoAD and Cu₆ZnAD.^a

Cu₆CoAD			
Co1–O1	2.066(1)	Cu1–N13Be	1.892(1)
Co1–O1a	2.066(1)	Cu1–N19Ae	1.890(1)
Co1–O1b	2.066(1)	Cu1–N19B	1.894(1)
Co1–O1c	2.066(1)	Cu1–O1e	1.992(1)
Co1–O1d	2.066(1)	Cu1–O1	1.993(1)
Co1–O1e	2.066(1)	Co1···Cu2	3.104(4)
Cu1–N13A	1.892(1)		
Cu₆ZnAD			
Zn1–O1	2.078(1)	Zn1–O1c	2.078(1)
Zn1–O1a	2.078(1)	Zn1–O1d	2.078(1)
Zn1–O1b	2.078(1)	Zn1–O1e	2.078(1)
Cu2–N3a	2.013(2)	Cu2–O1c	1.985(1)
Cu2–N9	1.947(2)	Cu2–O1wa	2.411(1)
Cu2–O1	1.970(1)	Zn1···Cu2	3.117(2)

^a Symmetry-codes. Cu₆CoAD: (a) $-x, -y, -z+1$; (b) $x-y, x, -z+1$; (c) $-x+y, -x, z+1$; (d) $-y, x-y, z+1$; (e) $y, -x+y, -z+1$. Cu₆ZnAD: (a) $y, -x+y+1, -z+1$; (b) $-y+2, x-y+1, z$; (c) $x-y, x, -z+1$; (d) $-x+2, -y+2, -z+1$; (e) $-x+y+1, -x+2, z$.

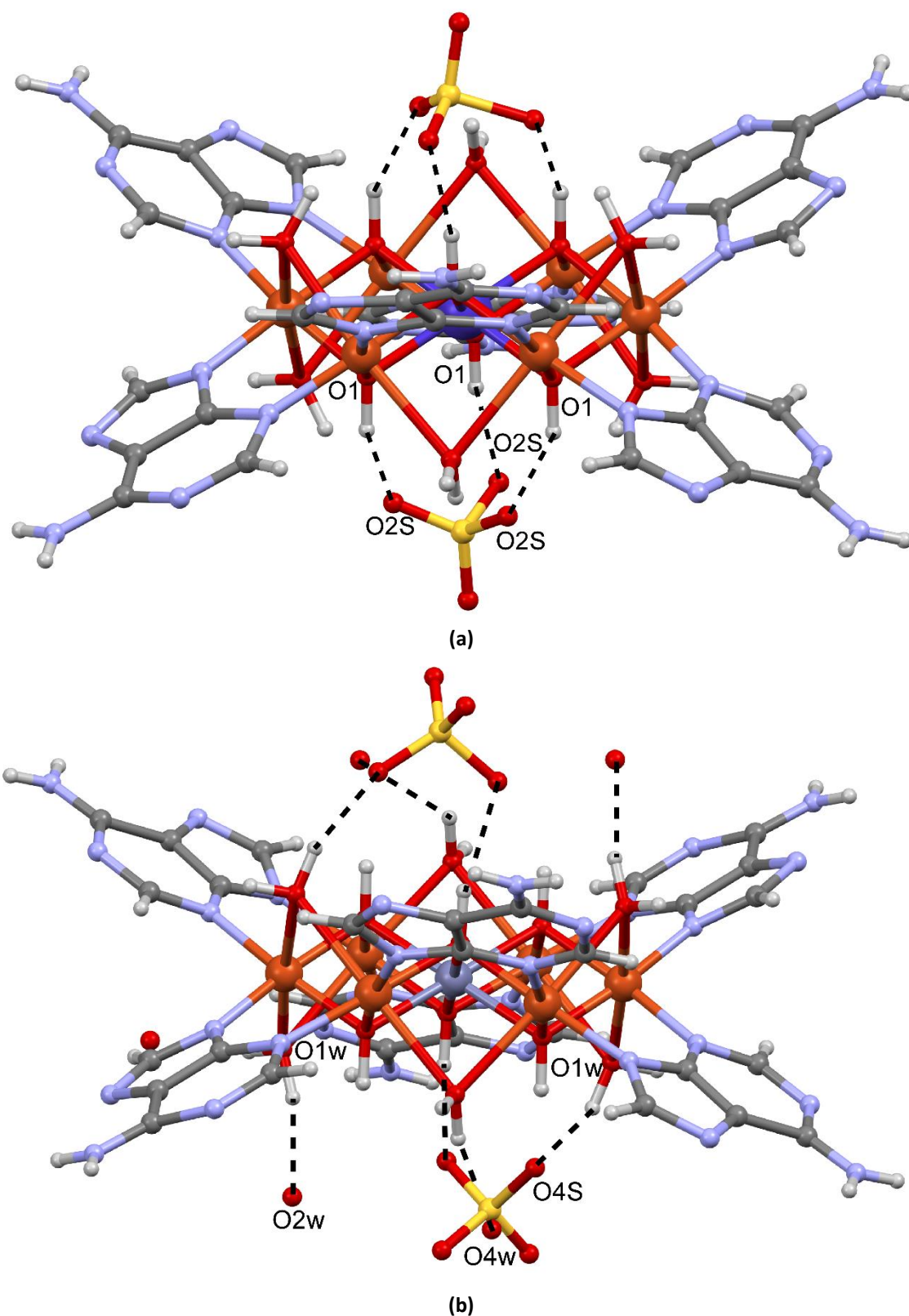
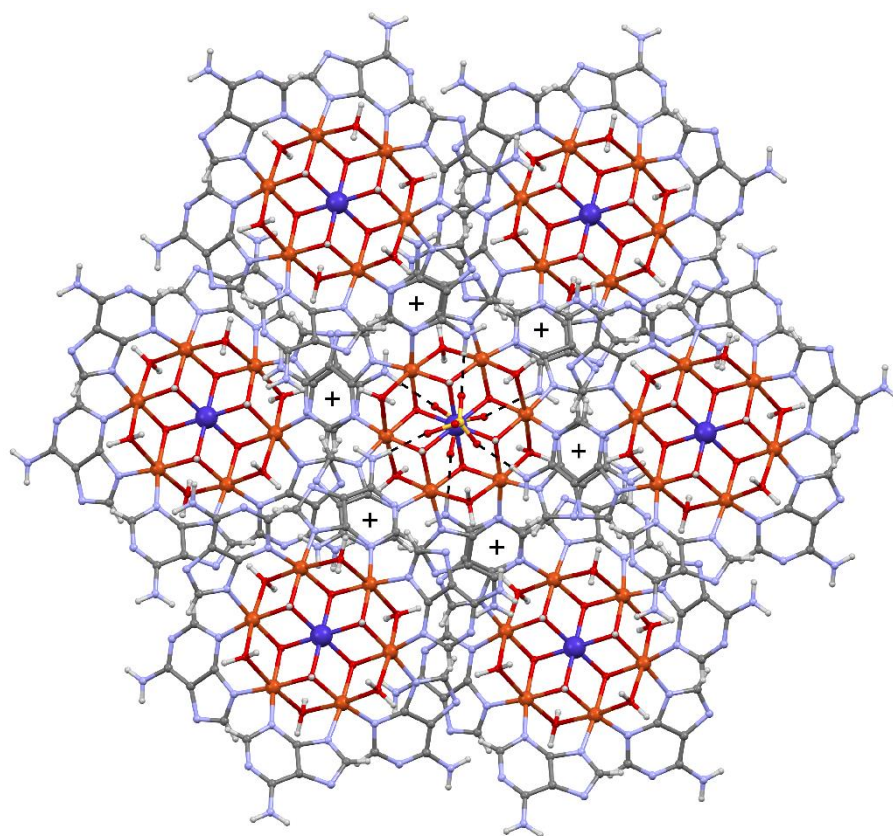
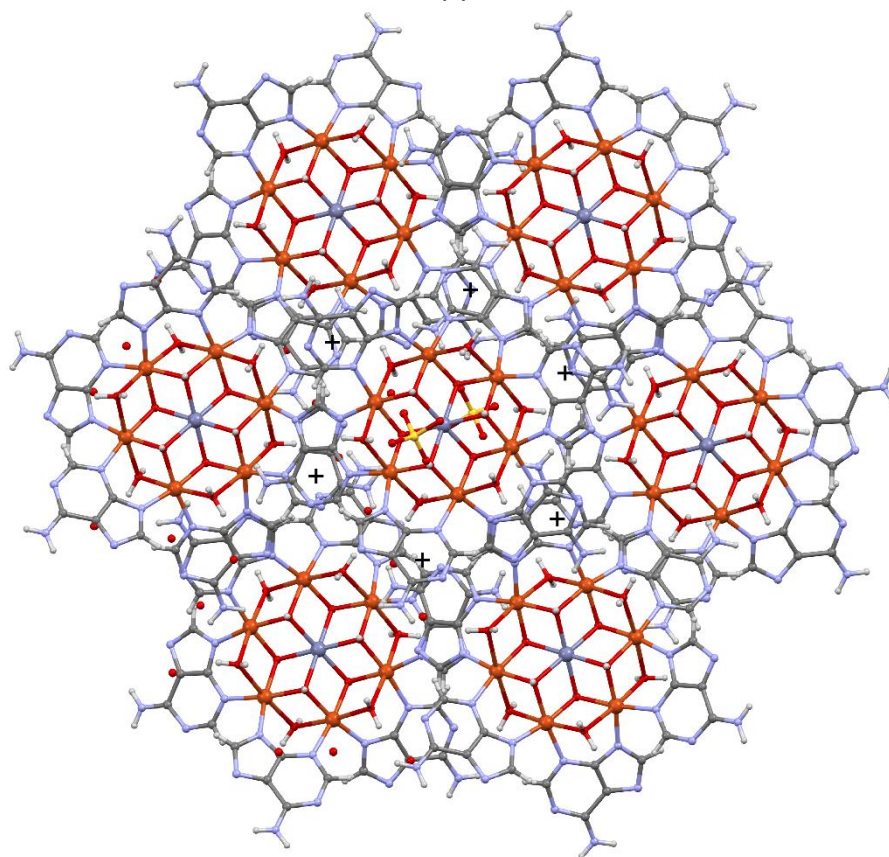


Figure 4.18. Interaction of the sulfate anion with a heptameric in entity of Cu₆CoAD (a) and Cu₆ZnAD (b) compounds. For clarity, in compound Cu₆ZnAD two of the disordered sulfate/water ensembles (related by the ternary axis) were omitted.



(a)



(b)

Figure 4.19. Supramolecular interactions between neighbouring heptameric entities in compounds Cu₆CoAD (a) and Cu₆ZnAD (b).

Table 4.13. Hydrogen-bonding parameters (Å, °) and π - π in compound Cu₆CoAD.^a

Cu₆CoAD					
D–H\cdotsA^[b]	H\cdotsA	D\cdotsA	D–H\cdotsA		
N16A–H16A \cdots O2S	1.84	2.70(4)	173		
O1–H1 \cdots O2S	1.89	2.83(4)	160		
π-π interactions^[c]					
Ring \cdots Ring ^[d]	α	DC	β	DZ	DXY
p1A \cdots p1A ^a	0.0	4.79(5)	50.9	3.02(1)	3.72
p1A \cdots p1B ^a	0.0	5.20(2)	43.7	3.76(1)	3.59
p1A \cdots p1B ^b	33.0	3.99(9)	57.8	2.13(1)	--
p1B \cdots p1A ^c	71.0	4.00(2)	55.6	2.26(1)	--
p1A \cdots h1A ^a	0.0	4.74(7)	39.5	3.66(2)	3.02
p1A \cdots h1B ^a	0.0	4.50(2)	43.0	3.29(8)	3.07
p1B \cdots p1B ^a	0.0	3.99(9)	32.0	3.39(2)	2.11
p1B \cdots h1A ^a	0.0	4.14(3)	34.9	3.39(6)	2.37
p1B \cdots h1B ^a	0.0	4.63(1)	47.7	3.11(8)	3.42
h1A \cdots h1B ^a	0.0	4.28(3)	39.7	3.29(3)	2.73
h1A \cdots h1A ^a	0.0	4.06(6)	25.9	3.65(8)	1.77
h1B \cdots h1B ^a	0.0	4.16(5)	41.6	3.11(2)	2.76

^a Symmetry-codes : (a) 1/3+x-y, -2/3-y, 5/6-z. (b) x-y, x, 1-z. (c) y, -x+y, 1-z. ^[b] D: donor; A: acceptor. ^[c] Angle: dihedral angle between the planes (°), DC: distance between the centroids of the rings (Å), α : angle (°) between mean plane of the rings. β : angle (°) between the normal to the first ring and the DC vector (°), DZ: interplanar distance (Å), DX Y: lateral displacement (Å), ^[d] h: hexagonal ring of the adeninato and p: pentagonal ring of the adeninato ligand. h1A: N11A, C12A, N13A, C14A, C15A, C16A. h1B: N11B, C12B, N13B, C14B, C15B, C16B. p1A: C14A, C15A, N17A, C18A, N19A. p1B: C14B, C15B, N17B, C18B, N19B.

Table 4.14. Hydrogen-bonding parameters (Å, °) and π - π in compound Cu₆ZnAD.^a

Cu₆ZnAD					
D–H···A^[b]	H···A	D···A	D–H···A		
N16–H16A···O1S	2.09	2.95(4)	178		
N16–H16B···O2w	2.38	3.21(7)	163		
N16–H16B···O4S	2.07	2.85(5)	149		
O1w–H11w···O2w	2.32	3.04(7)	136		
O1w–H11w···O4w	1.92	2.81(6)	164		
O1w–H11w···O5w	2.05	2.89(4)	160		
O1w–H11w···O4S	2.09	2.77(3)	131		
π-π interactions^[c]					
Ring···Ring^[d]	α	DC	β	DZ	DXY
p1···p1 ^a	0.0	4.02(5)	31.8	3.42(1)	2.12

^a Symmetry-codes : (a) 1+x–y, x, 1–z. ^[b] D: donor; A: acceptor. ^[c] Angle: dihedral angle between the planes (°), DC: distance between the centroids of the rings (Å), α : angle (°) between mean plane of the rings. β : angle (°) between the normal to the first ring and the DC vector (°), DZ: interplanar distance (Å), DXY: lateral displacement (Å), ^[d] h: hexagonal ring of the adeninato and p: pentagonal ring of the adeninato. p1: C14, C15, N17, C18, N19.

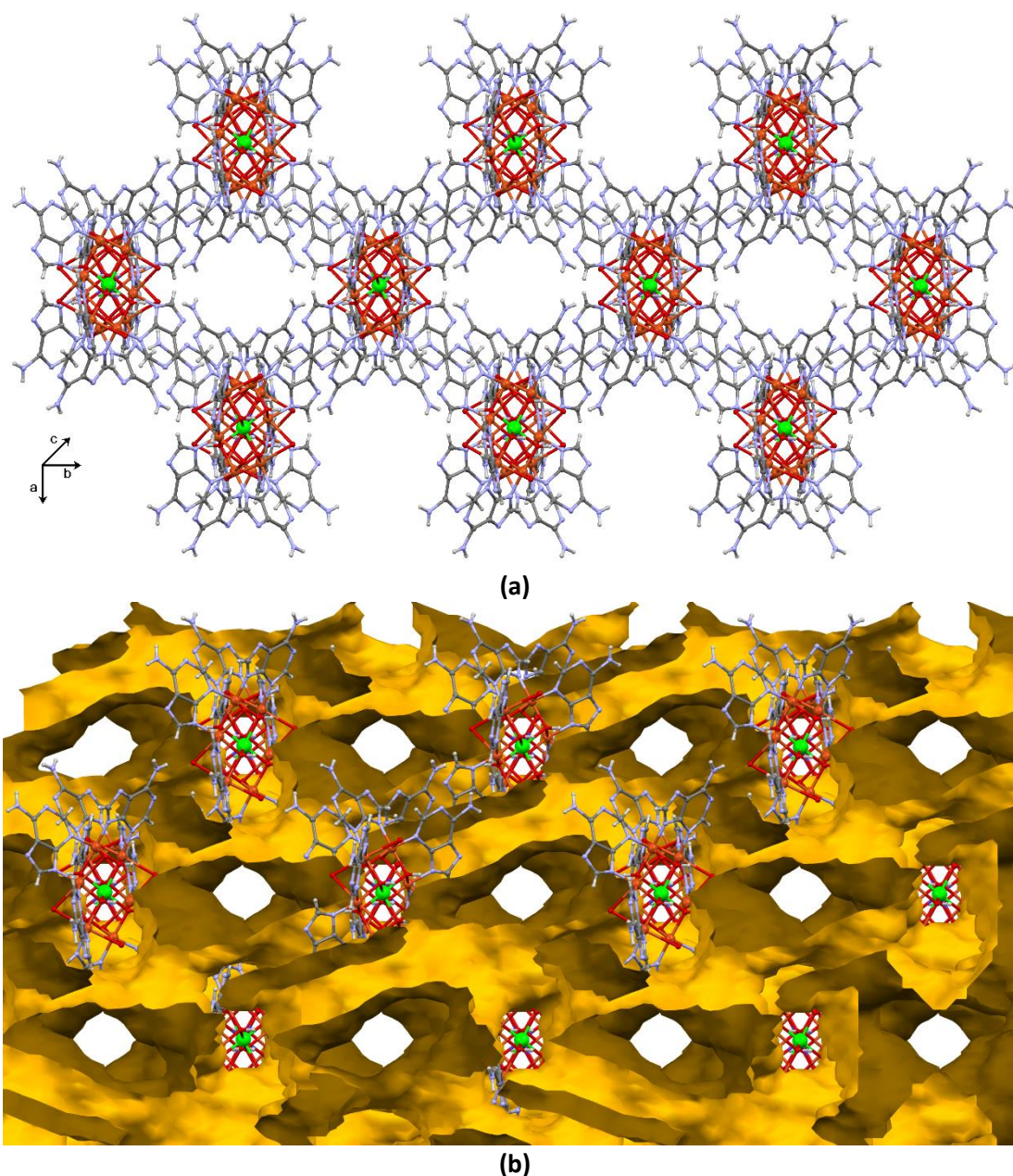


Figure 4.20. Crystal packing of compounds Cu_6CoAD and Cu_6ZnAD (a) showing the voids in yellow (b).

As it can be seen in Figure 4.21, although both compounds are isostructural, the simulated PXRD shows slight differences. This is explainable by the different number of water molecules present in the channels of the compounds, which is affected by the ambient humidity or temperature and probably preferential orientation effects.

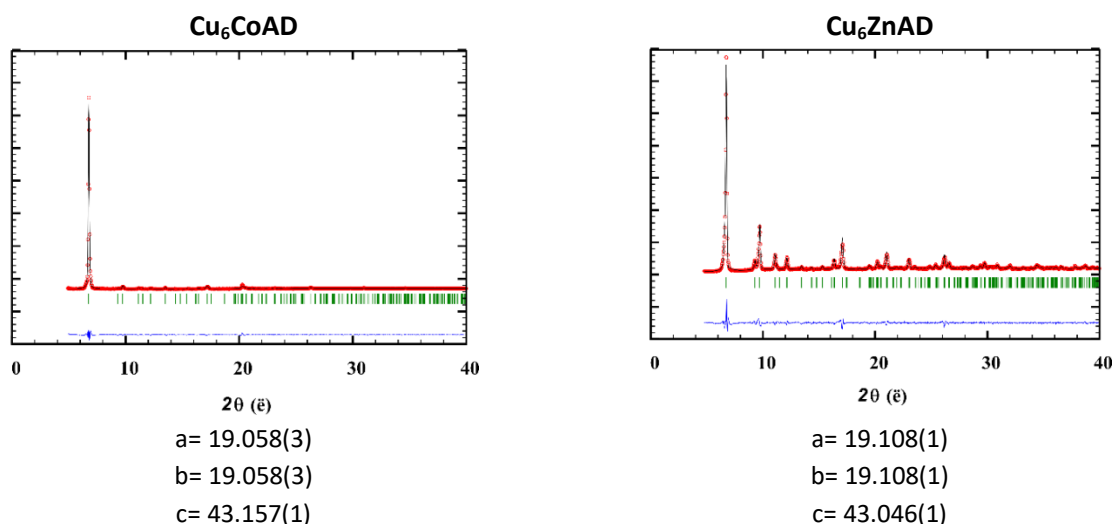


Figure 4.21. Comparison between the PXRD taken at 293 K of compounds Cu₆CoAD and Cu₆ZnAD. Cell parameters obtained from the pattern matching analysis are also included.

4.3.3. Magnetic properties.

Figure 4.22 shows the molar magnetic susceptibility (χ_m) and the $\chi_m T$ product for compounds Cu₆M^{III}AD and Cu₆M^{II}AD (M(III): Cr, Mn; M(II): Co, Ni, Zn), measured at 1 kOe after cooling without an applied magnetic field (ZFC). Table 4.15 compares the experimental $\chi_m T$ values at room temperature with those values calculated ($\chi_m T_{\text{calc}}$) from the van Vleck equation (equation 2 of appendix A.3) for magnetically non interacting six Cu(II) and one central M^{III} or M^{II} atom. In most cases, the experimental $\chi_m T$ value at RT are close to the calculated values. However, in the case of Cr(III) the experimental value is significantly larger than the calculated one, which could be attributed to the influence of the intramolecular magnetic interactions, that require higher temperatures than RT to decay.

In the case of Cu₆CrAD and Cu₆ZnAD analogues, $\chi_m T$ value increases as temperature decreases from room temperature, which is associated to intramolecular ferromagnetic interactions. Indeed in the Cr(III) compound, the maximum in $\chi_m T$ is found at 25 K (3.88 emu K/mol Oe), after which it decreases sharply probably due to intermolecular antiferromagnetic interactions, similar to those observed in the homometallic Cu-heptamers (see chapter 1). In the case of Cu₆MnAD and Cu₆NiAD, the $\chi_m T$ values slightly diminish upon cooling until a minimum close to 108 K (5.76 emu K/mol Oe) and 85 K (3.91 emu K/mol Oe), respectively. Further cooling of the compounds leads to a sharp increase of $\chi_m T$ values to get a maximum at 6 K (8.05 emu K/mol Oe) and 8 K (4.85 emu K/mol Oe) for manganese and nickel analogues, respectively. Finally, the $\chi_m T$ product of Cu₆CoAD remains almost constant in the high temperature range (4.78 emu K/mol Oe) to start smoothly decreasing upon cooling below 150 K down to 18 K and then more sharply. This magnetic behaviour can be attributed to both a

zero-field splitting ground state of cobalt(II) ion ($S = 3/2$)^[143] and to intermolecular antiferromagnetic interactions.

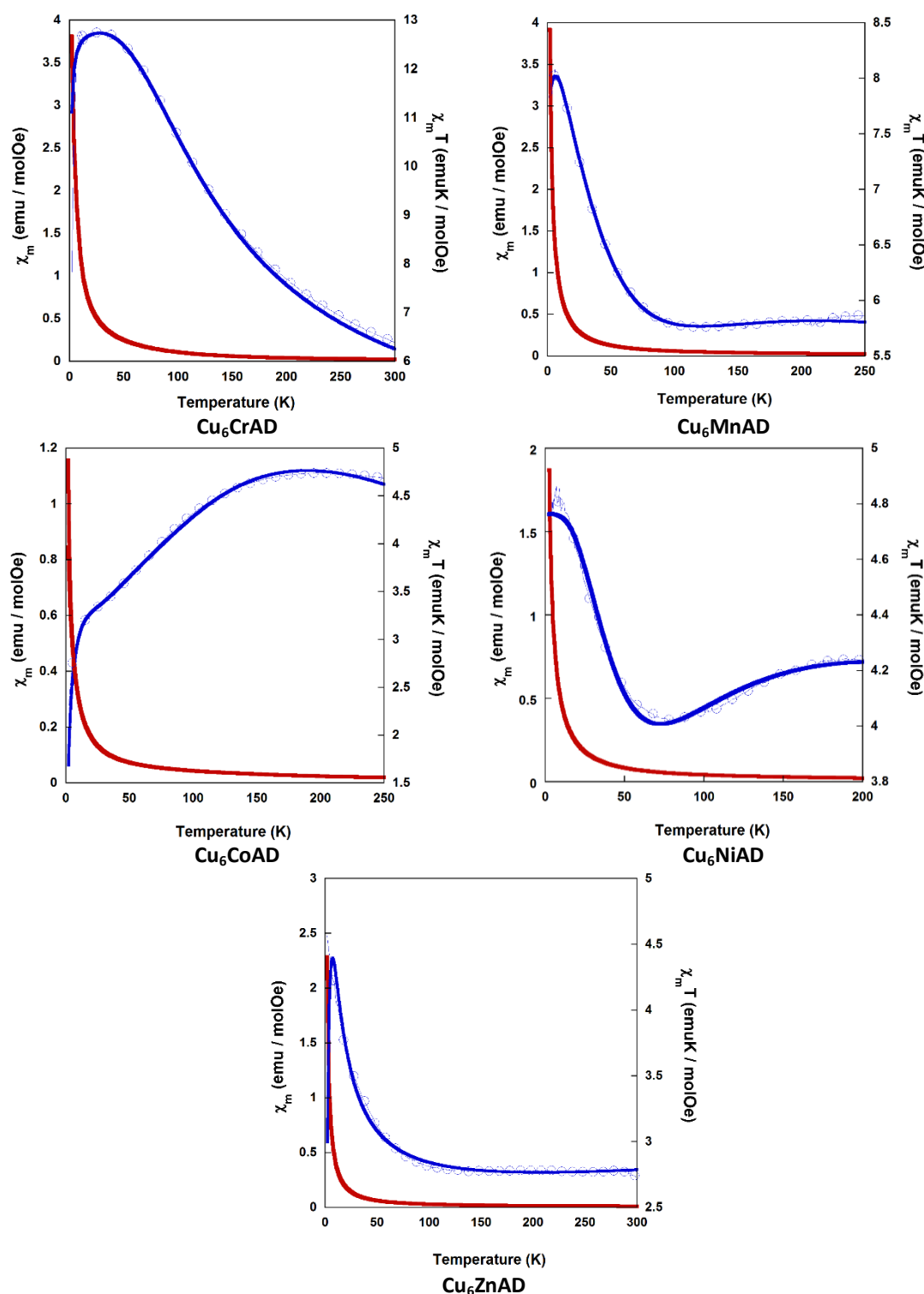


Figure 4.22. Thermal evolution of χ_m (red) and $\chi_m T$ product (blue) for the heterometallic compounds of Chapter 4. Experimental $\chi_m T$ values are represented by blue circles, while the fitting to the magnetic data is depicted by a continuous line.

¹⁴³ (a) Krzystek, J.; Zvyagin, S. A.; Ozarowski, A.; Fiedler, A. T.; Brunold, C. T.; Telser, J., *J. Am. Chem. Soc.*, **2004**, *126*, 2148–2155. (b) Kobak, J.; Bogucki, A.; Smoleński, T.; Papaj, M.; Koperski, M.; Potemski, M.; Kossacki, P.; Golnik, A.; Pacuski, W. *Phys. Rev.*, **2018**, *97*, 4–15. (c) Idešicová, M.; Titiš, J.; Krzystek, J.; Boča, R. *Inorg. Chem.* **2013**, *52*, 9409–9417.

Figure 4.23 represents the field dependence of the magnetization at 2 K of all compounds. In general, between 0 and 10 kOe, all the curves show a linear dependence with regard to the magnetic field applied and then, they tend to saturate without the presence of a hysteresis loop (have neither coercivity nor remanence). In Table 4.13 the saturation magnetization values (M_s) at 2K are compared with the theoretical saturation moment (S_T) of each heterometallic heptamer considering various scenarios. First, in the case Cu_6CrAD , the M_s value ($9.36 \mu_B$ per heptamer molecule) agrees with a total spin of $9/2$ resulting from a ferromagnetic Cu_6 -ring ($6.00 \mu_B$, assuming $S_{\text{Cu}_6\text{-ring}} = 6/2$ and $g \approx 2$) coupled ferromagnetically with the central chromium ion ($3.00 \mu_B$, $S_{\text{Cr}} = 3/2$). Note that a ferromagnetic coupling among the central atom and the peripheral Cu(II) atoms is expected considering the orbital orthogonality taking place between copper(II) (e_g)¹ and chromium(III) (t_{2g})³ magnetic orbitals. Second, for Cu_6CoAD and Cu_6NiAD , the values obtained are near from the theoretical saturation moment corresponding to an antiferromagnetic coupling between Cu_6 -ring and metal centre ($S_{\text{Co}} = 3/2$, $S_{\text{Ni}} = 1$) i.e. a total $S = 3/2$ and 2 per heptameric entity, respectively. Third, in Cu_6ZnAD with a central diamagnetic ion (Zn(II) ; d^{10}) the saturation magnetisation ($5.79 \mu_B$) is close to that for six isolated Cu(II) ions ferromagnetically coupled (Cu_6 -ring).

Table 4.15. Relevant data on magnetic susceptibility and magnetization measurements.^a

Compound	$\chi_M T_{\text{RT}}$	$\chi_M T_{\text{calc.}}$	M_s	S_T	Compound	$\chi_M T_{\text{RT}}$	$\chi_M T_{\text{calc.}}$	M_s	S_T
Cu_6CrAD	6.36	4.40	9.36	9/2	Cu_6NiAD	4.23	3.58	4.83	2
Cu_6MnAD	5.73	5.52	6.78	3	Cu_6ZnAD	2.62	2.52	5.79	3
Cu_6CoAD	4.68	4.40	3.57	3/2					

^a: $\chi_M T$ (RT): experimental $\chi_M T$ values ($\text{emu}\cdot\text{K}\cdot\text{mol}^{-1}\cdot\text{Oe}^{-1}$) at room temperature. $\chi_M T_{\text{calc.}}$: calculated $\chi_M T$ values for non-interacting paramagnetic centres. M_s : saturation magnetization (μ_B per heptamer molecule). S_T : total spin resulting from the magnetic coupling scheme.

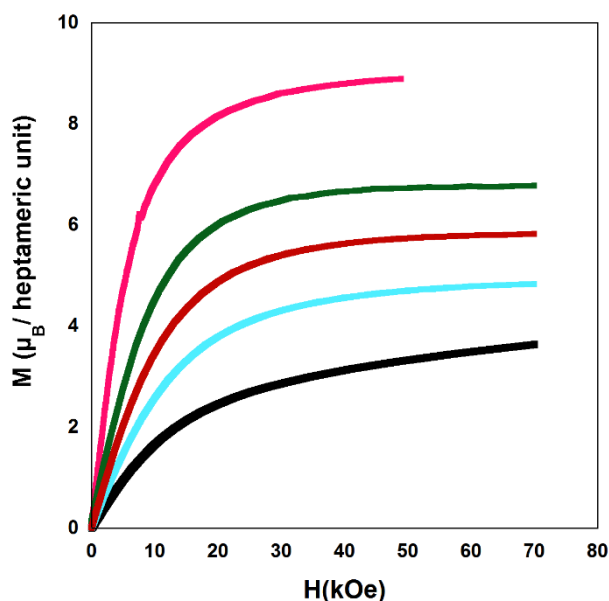


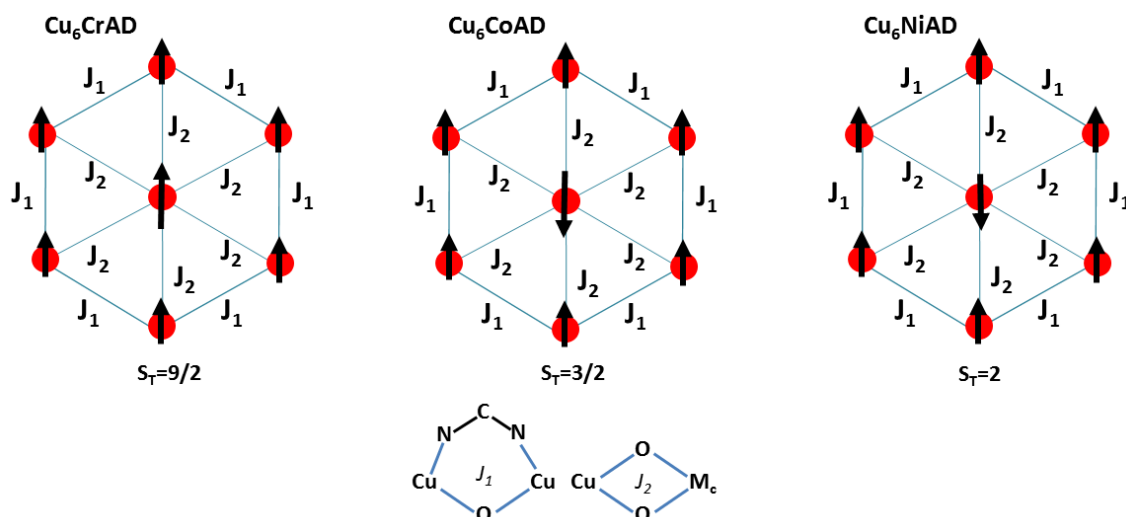
Figure 4.23. Compendium of the magnetization curves at 2 K for compounds of Chapter 4. Cu_6CrAD (pink), Cu_6MnAD (green), Cu_6ZnAD (red), Cu_6NiAD (blue) and Cu_6CoAD (black), respectively.

Finally, Cu_6MnAD presents a saturation magnetization of $6.78 \mu_B$ per heptamer. If the central manganese(III) atom displays a high spin configuration, $t_{2g}^3 e_g^1$, $S_{\text{Mn(H.S.)}} = 2$, coupled ferromagnetically to four of the peripheral copper(II) atoms and antiferromagnetically to the other ones, the total spin of 3 per heptamer will be $6.00 \mu_B$. In the case of Mn(III) in low spin configuration, t_{2g}^4 , $S_{\text{Mn(L.S.)}} = 1$, a ferromagnetic coupling with the outer Cu_6 -ring, reaches a saturation magnetization value of $8 \mu_B$ with $S_{\text{T(L.S.)}} = 4$ or even assuming an antiferromagnetic coupling, which would be highly unusual due to symmetry orthogonality between the copper(II) e_g and Mn(III)_{LS} t_{2g} magnetic orbital, a saturation magnetization value of $4 \mu_B$ with $S_{\text{T(L.S.)}} = 2$.

Mn(II) ($S = 5/2$) in high spin configuration, $(t_{2g})^5$ coupled ferromagnetically with the Cu_6 -ring would render a total spin of $11/2$ and antiferromagnetically coupled a total spin of 2. In low spin configuration ($S = 1/2$) a ferromagnetic coupling with the outer Cu_6 -ring, reaches a saturation magnetization value of $7/2$, close to the observed one. However, as a first row transition metal ion in a low oxidation state and weak field ligands (hydroxide) would imply a small crystal-field splitting parameter (Δ_o). Moreover, Mn(II) is disregarded from the discussion, as the observation of two elongated coordination bonds which suggest that the electronic configuration of the central metal atom must be compatible with a Jahn-Teller effect. All in all, coupling scheme envisaged for a high spin Mn(III) centre is compatible with the calculated coupling constants (see discussion below).

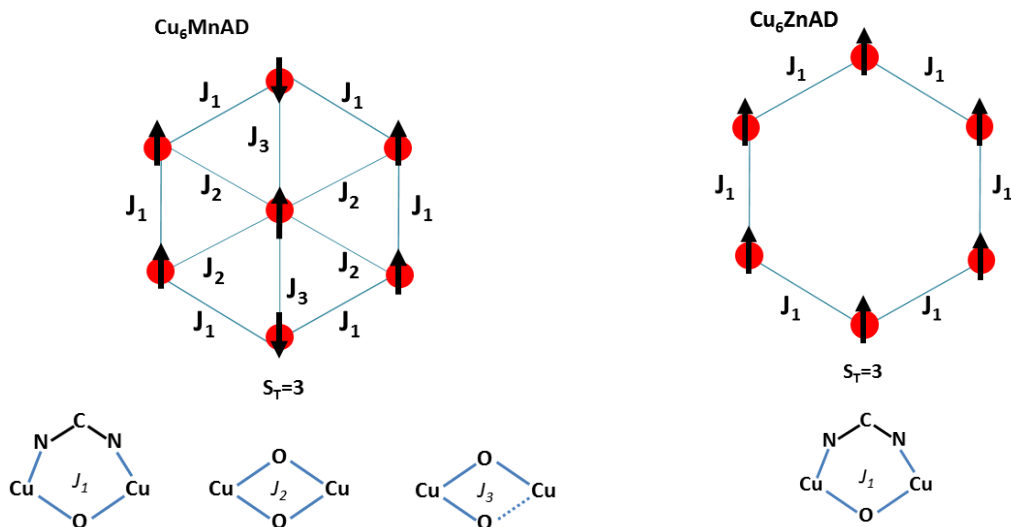
To determine the Hamiltonian for the calculation of superexchange magnetic coupling constants of the compounds detailed in this chapter, the influence of the Jahn-Teller effect on the central metal atom in each heptanuclear entity $[\text{Cu}_6\text{M}(\mu\text{-H}_2\text{O})_6(\mu_3\text{-OH})_6(\mu\text{-ade-}\kappa\text{N3}:\kappa\text{N9})_6]^{n+}$ ($n = 2$ or 3) has to be considered. In the case of Cu_6CrAD , Cu_6CoAD and Cu_6NiAD , with lack of Jahn-Teller distortion (with Cr(III), Ni(II) and Co(II) oxidation states) the $\text{M}_{\text{central}}\text{-(OH)}_2\text{-Cu}_{\text{ring}}$ bridges can be considered equivalent. Therefore, for this series of compounds a Hamiltonian consisting of two different magnetic superexchanges (Figure 4.24a) that account for the couplings within the Cu_6 -ring (J_1) and between the central paramagnetic centre and the peripheral copper(II) atoms (J_2).^[144] On the contrary, in Cu_6MnAD , the $[\text{Mn}(\text{OH})_6]^{3-}$ core exhibits two elongated coordination bond distances and four shorter ones (see Table 4.9 of the structural description) as consequence of a sizeable Jahn-Teller effect. Accordingly, a third coupling constant (J_3) has been included (Figure 4.24b) to account for the magnetic superexchange taking place along the elongated bridge. Finally, in compound Cu_6ZnAD , the proposed Hamiltonian (Figure 4.24c) only considers the coupling among the neighbouring peripheral Cu(II), as the central Zn(II) is diamagnetic.

¹⁴⁴ Estes, E. D.; Hatfield, W. E.; Hodgson, D. J. *Inorg. Chem.*, **1974**, *13*, 1654–1657.



$$H = -J_1 (\vec{S}_2 \cdot \vec{S}_3 + \vec{S}_3 \cdot \vec{S}_4 + \vec{S}_4 \cdot \vec{S}_5 + \vec{S}_5 \cdot \vec{S}_6 + \vec{S}_6 \cdot \vec{S}_7 + \vec{S}_7 \cdot \vec{S}_2) - J_2 (\vec{S}_1 \cdot \vec{S}_2 + \vec{S}_1 \cdot \vec{S}_3 + \vec{S}_1 \cdot \vec{S}_4 + \vec{S}_1 \cdot \vec{S}_5 + \vec{S}_1 \cdot \vec{S}_6 + \vec{S}_1 \cdot \vec{S}_7) - g\mu_B \vec{B} \cdot \vec{S}$$

(a)



$$H = -J_1 (\vec{S}_2 \cdot \vec{S}_3 + \vec{S}_3 \cdot \vec{S}_4 + \vec{S}_4 \cdot \vec{S}_5 + \vec{S}_5 \cdot \vec{S}_6 + \vec{S}_6 \cdot \vec{S}_7 + \vec{S}_7 \cdot \vec{S}_2) - J_2 (\vec{S}_1 \cdot \vec{S}_2 + \vec{S}_1 \cdot \vec{S}_3 + \vec{S}_1 \cdot \vec{S}_5 + \vec{S}_1 \cdot \vec{S}_6) - J_3 (\vec{S}_1 \cdot \vec{S}_4 + \vec{S}_1 \cdot \vec{S}_7) - g\mu_B \vec{B} \cdot \vec{S}$$

(b)

(c)

Figure 4.24. The magnetic topologies and their corresponding J coupling hamiltonian for the Cu_6M_c clusters.

The fitting of the $\chi_{\text{M}}T$ data above 10 K was performed on the basis of the above described equations using the MagProp software tool distributed with DAVE.^[115] The resulting magnetic coupling constants (Table 4.16) are in concordance with the expectations on the

magnetic topology inferred from the saturation magnetization of Cu_6M clusters. In general terms, the peripheral Cu(II) atoms are coupled ferromagnetically ($J_1 > 0$) due to the counterbalance between the magnetic orbitals induced by the double bridge adenine/hydroxide (see further details in Chapter 3, section 3.3.3).^[145] The differences on the magnitude of the J_1 coupling constants are attributable to the accuracy of the data fitting but also to the slight differences in the coordination bond lengths and angles of each compound and disposition of the hydrogen atom of the hydroxide group. Note, that the displacements on the hydrogen atoms of bridging hydroxide groups caused by the counterions present in the structures, have demonstrated to strongly influence the sign and magnitude of the magnetic interaction.^[146]

With regard to the coupling taking place between the central metal atom and the Cu_6 -ring, the fitting of the magnetic data reveals a ferromagnetic J_2 value for Cu_6CrAD , which is in good agreement with the envisaged magnetic topology and with the orthogonality between the magnetic orbitals of Cu(II) and Cr(III) (see above). In compound Cu_6CoAD and Cu_6NiAD , the symmetry of the magnetic orbitals of the central metal atom (Co(II) or Ni(II)) and the peripheral Cu(II), ensures an efficient overlap through the hydroxide bridges, thus it would favour an antiferromagnetic coupling (J_2).^[147] In a simplified approach the magnetic coupling between two paramagnetic centres can be expressed as the sum of a ferromagnetic term (J_F) and an anti-ferromagnetic term (J_{AF}), i.e. $J = J_F + J_{AF}$.^[148] J_{AF} is proportional to the energy difference between the singly occupied molecular orbitals (Δ between SOMOs), $J_{AF} \propto \sum \Delta^2$, which strictly depends on the overlap between magnetic atomic orbitals. While J_F depends on the exchange bielectronic integrals (j), $J_F \propto \sum j$. Thus, an efficient overlap between the magnetic orbitals, increases the energy difference between the SOMOs, it favours a low spin state or an antiferromagnetic coupling.

¹⁴⁵ Pérez-Aguirre, R.; Beobide, G.; Castillo, O.; de Pedro, I.; Luque, A.; Pérez-Yañez, S.; Rodríguez Fernandez, J.; Román, P. *Inorg. Chem.* **2016**, *55*, 7755–7763.

¹⁴⁶ Ruiz, E.; Alemany, P.; Alvarez, S.; Cano, J., *J. Am. Chem. Soc.* **1997**, *119*, 1297–1303.

¹⁴⁷ (a) Hatfield, W. E. *ACS*, **1974**, *5*, 108–141. (b) Lewis, D. L.; McGregor, K. T.; Hatfield, W. E.; Hodgson, D. J. *Inorg. Chem.*, **1974**, *13*, 1013–1019. (b) McGregor, K. T.; Watkins, N. T.; Lewis, D. L.; Drake, R. F.; Hodgson, D. J.; Hatfield, W. E. *Inorg. Nucl. Chem. Lett.*, **1973**, *9*, 423–428.

¹⁴⁸ Hay, P. J.; Thibault, J. C.; Hoffmann, R. *J. Am. Chem. Soc.* **1975**, *97*, 4884.

Table 4.16. Magnetic data obtained from the fitting of the magnetic susceptibility curves.^a

Compound	J_1	J_2	J_3	D	S_T (2K)
Cu ₆ CrAD	80.06	50.50	--		9/2
Cu ₆ MnAD	70.09	-66.81	18.59		3
Cu ₆ CoAD	63.15	-19.11	--	55.71	3/2
Cu ₆ NiAD	47.26	-30.58	--		2
Cu ₆ ZnAD	18.20	--	--		3

^a: J_{1-3} and D: magnetic coupling constants (cm^{-1}) and zero field splitting parameter (cm^{-1}).

The case of the manganese(III) heterometallic cluster is more interesting as only one of the two e_g orbitals is occupied by an unpaired electron ($t_{2g}^3 e_g^1$). It leads to the crystallographically observed Jahn-Teller elongation but also to the differentiated magnetic coupling interactions that it establishes with the external Cu(II) metal centers. At this point, it deserves to note that there are two type of radial magnetic interactions, those involving $e_g(\text{Mn}) \cdots e_g(\text{Cu})$ of antiferromagnetic nature, as previously observed for the homometallic Cu₇ clusters, and the $t_{2g}(\text{Mn}) \cdots e_g(\text{Cu})$ interaction of ferromagnetic nature due to symmetry dictated strict orthogonality between the involved orbitals. Therefore, as the main lobules of the single occupied dz^2 orbital only extends along the z direction while not in the x and y directions it is expected the magnetic interactions to be ordered in the same way: 2 antiferromagnetic interactions involving the dz^2 orbital and 4 ferromagnetic interactions coming from the orbital orthogonality. This situation comes very similar to the situation observed for Cu₇ heptamers in which we also observe a similar radial distribution of 2 antiferromagnetic interactions and four ferromagnetic ones in addition to the peripheral ferromagnetic interactions among the external copper(II) metal centers. However, the relative magnitude value of these interactions differ:

Cu₇: $|J_{AF}(\text{radial})|, |J_F(\text{peripheral})| > |J_F(\text{radial})|$ which leads to the ferrimagnetic spin arrangement described in the previous chapter to provide a $S_T = 5/2$ at low temperature.

Cu₆Mn: $|n_1 \cdot n_2 \cdot J_{AF}(\text{radial})|, |n_1 \cdot n_2 \cdot J_F(\text{radial})| > |J_F(\text{peripheral})|$ (n_1 and n_2 being the unpaired electrons at copper and manganese metal centers, respectively) which adopts a different arrangement of the spins with the interactions established by the central manganese(III) atom imposing their preferences over the, this time weaker, J_F peripheral interactions to generate a $S_T = 3$ at low temperature (n_1 and n_2 , stand for the unpaired electrons of Cu(II) and Mn(III), so that $n_1 \cdot n_2$ term (4·1) must be considered in order to scale the magnetic interaction).

In both compounds, a spin frustration situation arises as there is no an optimal spin ordering within the heptameric entity that could fulfill all the magnetic interaction preferences (notice that the $J_F(\text{radial})$ and $J_F(\text{peripheral})$ coupling preferences are unfulfilled in compounds Cu_7AD and Cu_6CrAD , respectively). However, the strength ordering of the magnetic interactions change due to the contribution of the t_{2g} magnetic orbitals, not present in the copper(II) magnetic centers, which strengthen the radial ferromagnetic term above the peripheral one. The latter one coming from the previously explained orbital countercomplementarity of the $\mu\text{-N3:N9}$ -adenine and $\mu\text{-OH}$ bridging ligand.

4.3.4. Magnetic sustentation experiments.

As previously stated, these compounds establish complex magnetic interactions at low temperatures but at room temperature they are well placed in the paramagnetic regime as it can be deduced from their $\chi_M T$ product at room temperature. Therefore, the attraction force exerted by a relatively strong external magnetic field (i.e. that of magnets or electromagnets) on the particle of the samples is very weak not being able to overcome the earth gravity attraction under normal conditions and as a consequence, no displacement takes place on these particles. However, under reduced gravity conditions such as when the particles are immersed in a liquid, the magnetic field attraction is strong enough to avoid them from depositing at the bottom (Figure 4.25) and even to move them if the magnetic field is strong enough (Figure 4.26). In this sense, a double pole electromagnet was employed in order to get fine control on the applied magnetic field. The equation mediating the attraction between the paramagnetic particles and the magnetic field implies: $F = \nabla(m \cdot H)$, where the gradient ∇ is the change of the quantity $m \cdot H$ per unit distance (m : magnetic dipole of the particle and H : external magnetic field), and the direction is that of maximum increase of $m \cdot H$. If m is in the same direction as H , as it happens for paramagnetic particles, then the gradient pulls the particles into regions of maximum H -field. This equation is strictly only valid for zero size magnets, but is often a good approximation for tiny particles as it is the case.

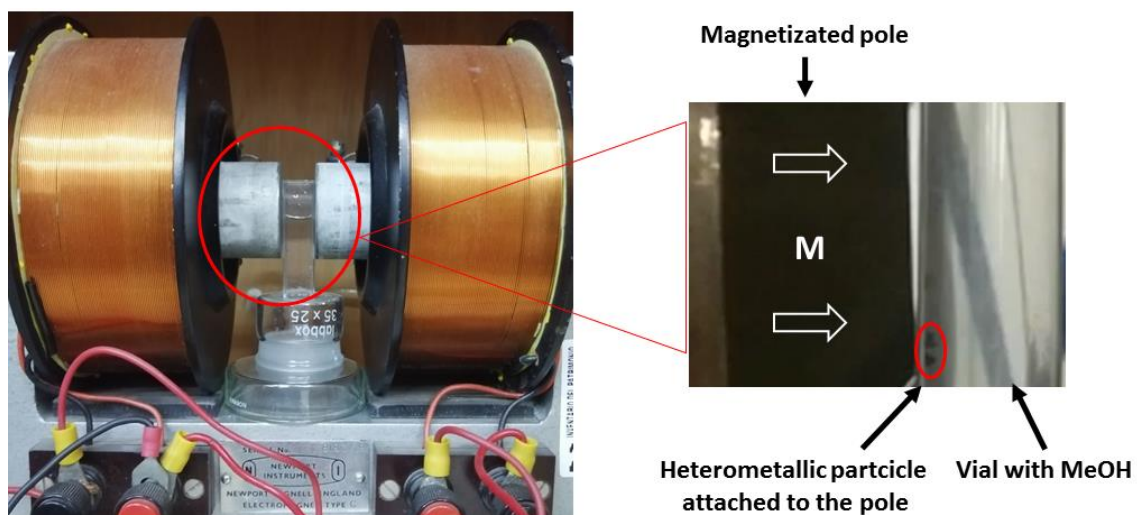


Figure 4.25. Image of compound Cu_6CrAD particles sustained by the pole of an electromagnet while immersed in methanol.

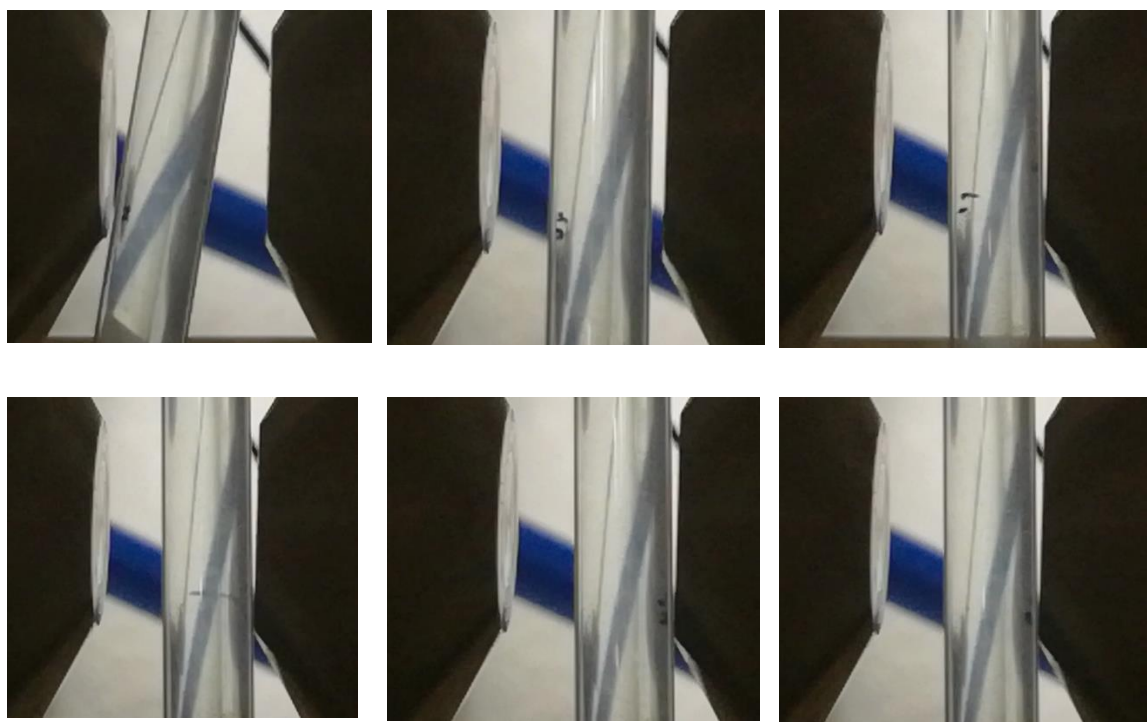


Figure 4.26. Image of particles jumping to the closest electromagnet pole while the vial is displaced from one to another.

Taking into account the paramagnetic nature of the particles, the magnetic dipole of the particles can be expressed based on the external magnetic field and taken away from gradient as the particles being so small the magnetic dipole moment can be considered constant all along the particle (equation 1):

$$F_p = \mu_0 \frac{\chi_M}{MW} \cdot \rho_p \cdot V_p \cdot H \cdot \nabla(H_p) \quad (1)$$

Being F_p the magnetic attraction force on particle, μ_0 the permeability of vacuum, χ_M molar susceptibility, MW the molecular weight of the compound framework (excluding the solvent molecules located in the pores), ρ_p the density of the compound framework, V_p particle volume, H and $\nabla(H_p)$ magnetic field and field gradient in the centre of the particle.

It implies that the magnetic force on the particles is not going to be uniform on the whole surface of the pole but achieves a maximum value on the edge of the pole pointing toward the central axis of the pole. It means that only at the bottom of the pole perimeter where the magnetic attraction force is opposite to the gravitation force, the particles of these compounds can accumulate (Figure 4.25). This phenomenon was corroborated using three different solvents: CCl_4 , H_2O and MeOH (see Table 4.17). The denser the solvent a lower magnetic field is required to maintain the particles attached to the pole of the electro-magnet. However, due to wettability related problem found for water the experiment was far easier to perform with MeOH and CCl_4 and due to environmental and health concerns, the following experiments were performed using MeOH .

Table 4.17. Physical properties of the solvents under normal room conditions.

Properties	CCl_4	H_2O	MeOH
Density (g/cm^{-3})	1.59	1.00	0.79
Surface tension (mN/m)	26.95	71.97	22.60

The use of an electromagnet provides a unique opportunity to exactly determine the minimum magnetic field required by each compound for their particles to fall from the pole bottom edge. Accordingly to equation (1), it must be dependent on the molecular susceptibility which can be estimated using spin-only expression depicted by equation (2):

$$\chi_M = \frac{[4S_M(S_M+1)] + 6 \cdot [4S_{Cu}(S_{Cu}+1)]}{8T} \quad (2)$$

It allows to calculate the exact magnetic field value at which the particles will fall from the pole by matching the opposite gravitation and magnetic attraction forces. However, having in mind the flotation force exerted by the solvent on the particles, it only applies to the compound framework and not to the volume occupied by the pores of the material as the molecules placed there, freely exchange with the solvent. It leads to equation (3):

$$\mu_0 \frac{[4S_M(S_M+1)]+6 \cdot [4S_{Cu}(S_{Cu}+1)]}{8T \cdot MW} \cdot \rho_P \cdot V_P \cdot H \cdot \nabla(H_P) = (\rho_P - \rho_S) \cdot V_P \cdot g \quad (3)$$

where ρ_S is the solvent density and g is gravity of earth.

At this point, it is necessary to perform two approximations in order to simplify the previous equation. The first one relies on the molecular mass similarity of most of the compounds reported in this chapter (see Table 4.18) that allows to assume the MW parameter remains essentially constant. The same applies for the density of the compound framework (ρ_P).

Table 4.18. Formula and molecular mass of all the heterometallic compounds.

Name code	Formula	MW	ρ_P (cm ³ /g)	$4S_M(S_M + 1)$
Cu ₆ ZnAD	[Cu ₆ Zn(H ₂ O) ₆ (OH) ₆ (C ₅ H ₄ N ₅) ₆](SO ₄)	1557	2.09	0
Cu ₇ AD	[Cu ₇ (H ₂ O) ₆ (OH) ₆ (C ₅ H ₄ N ₅) ₆](SO ₄)	1555	2.13	3
Cu ₆ NiAD	[Cu ₆ Ni(H ₂ O) ₆ (OH) ₆ (C ₅ H ₄ N ₅) ₆](SO ₄)	1550	--	4
Cu ₆ CoAD	[Cu ₆ Co(H ₂ O) ₆ (OH) ₆ (C ₅ H ₄ N ₅) ₆](SO ₄)	1551	2.11	15
Cu ₆ CrAD	[Cu ₆ Cr(H ₂ O) ₆ (OH) ₆ (C ₅ H ₄ N ₅) ₆](SO ₄) _{1.5}	1592	2.18	15
Cu ₆ MnAD	[Cu ₆ Mn(H ₂ O) ₆ (OH) ₆ (C ₅ H ₄ N ₅) ₆](SO ₄)(OH)	1564	2.11	24

Accepting those two approximations implies that now there are only two variables: $4S_M(S_M + 1)$ and $H \cdot \nabla(H_P)$. The remaining parameters in the formula can be simplified into A and B constants (equations 4 and 5) to lead equation (6):

$$[4S_M(S_M + 1)] + 6 \cdot [4S_{Cu}(S_{Cu} + 1)] = \frac{(\rho_P - \rho_S) \cdot V_P \cdot g \cdot 8T \cdot MW}{\mu_0 \cdot \rho_P \cdot V_P \cdot H \cdot \nabla(H_P)} = \frac{(\rho_P - \rho_S) \cdot g \cdot 8T \cdot MW}{\mu_0 \cdot \rho_P \cdot H \cdot \nabla(H_P)} \quad (4)$$

$$[4S_M(S_M + 1)] + A = \frac{B}{H \cdot \nabla(H_P)} \quad (5)$$

$$[4S_M(S_M + 1)] = \frac{B}{H \cdot \nabla(H_P)} - A \quad (6)$$

Therefore, the experimental points at which the particles detach from the pole must fit to a $4S_M(S_M + 1)$ vs $\frac{1}{H \cdot \nabla(H_P)}$ a straight line.

In order to check the validity of these equations the magnetic field and its gradient was measured on the pole surface of the electromagnet at different current I values. Figure 4.27 depicts the magnetic field measured along the plane corresponding to the surface of the magnetic pole in the vertical z-axis. The magnetic data were fitted to a fourth order polynomial expression and ∇H and $H \cdot \nabla H$ were computed. The particles are keep sustained at the

position where the upwards force is maximum, according to equation (1) it corresponds to the position of most negative $H \cdot \nabla H$ product: close to the lower end of the pole. Figure 4.28 shows the dependence of the most negative $H \cdot \nabla H$ product for each current value with the magnetic field measured in the center of the pole.

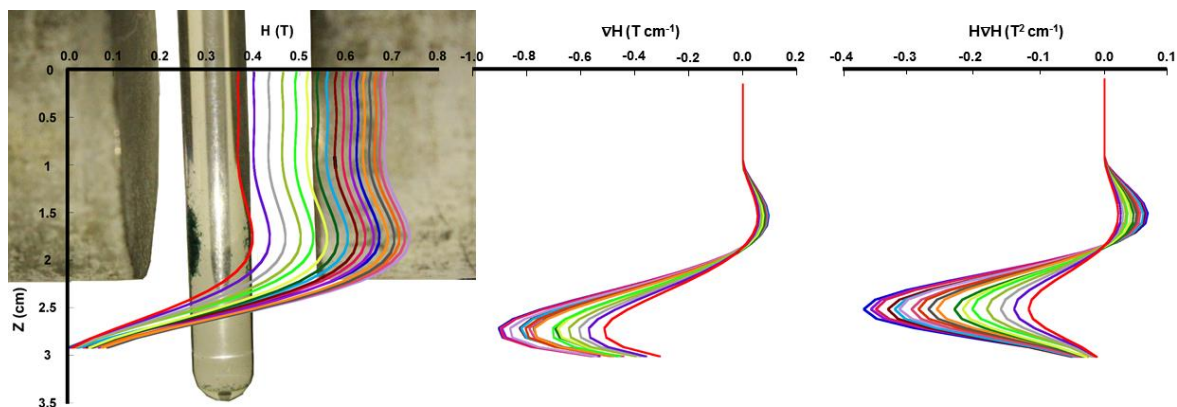


Figure 4.27. Magnetic field measured along the plane corresponding to the surface of the magnetic pole in the vertical z-axis for intensity currents increasing from 0.0 to 2.5 mA (step: 0.1 mA) and the computed ∇H and $H \cdot \nabla H$ values. The $z = 0$ value corresponds to the pole centre.

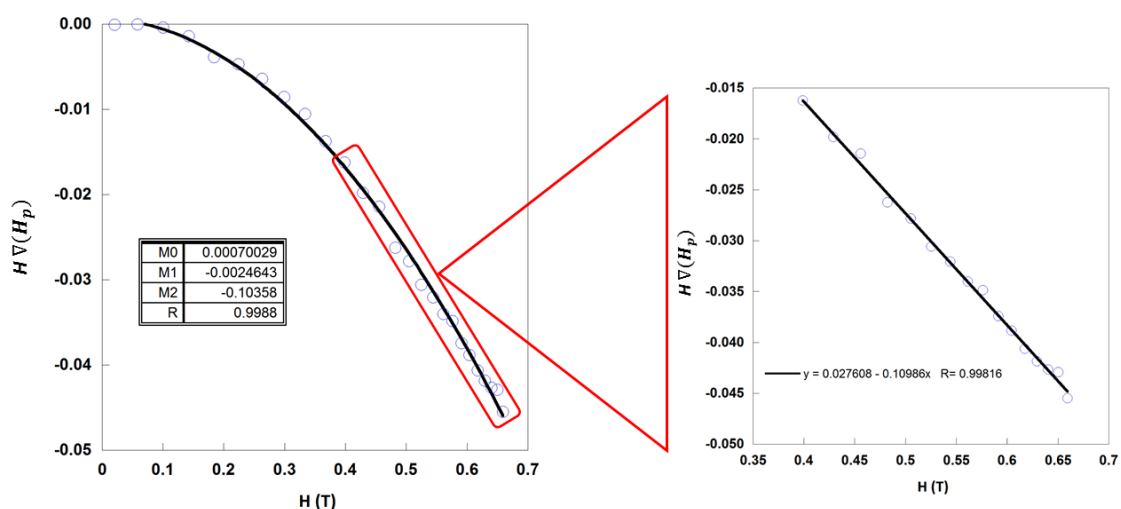


Figure 4.28. Polynomic equation of the gradient field vs the magnetic field at the centre of the pole. Left second order polynomial fitting of the entire magnetic field range and right linear fit within the range at which the experimental data appear for these compounds.

Now depicting the experimental data in the $4S_M(S_M + 1)$ vs $\frac{1}{H \cdot \nabla(H_P)}$ graph (Figure 4.29), the values lie in a straight with positive slope as predicted with the exception Cu_6CoAD probably due to the well-known orbital contribution of Co(II) that significantly deviates the spin-only susceptibility towards greater values. The second exception correspond to Cu_6CrAD which is the compound with a greater deviation of the PM with respect to the other members of this family because of the presence of 1.5 sulfate anions per formula instead a single sulfate. It is worthy to note that at magnetic fields above 0.4 T there is a linear relationship between

ΔH and H (Figure 4.30 left), as a consequence the experimental data, all of them lying within this H region, show also a linear correlation between $4S_M(S_M + 1)$ and $\frac{1}{H}$.

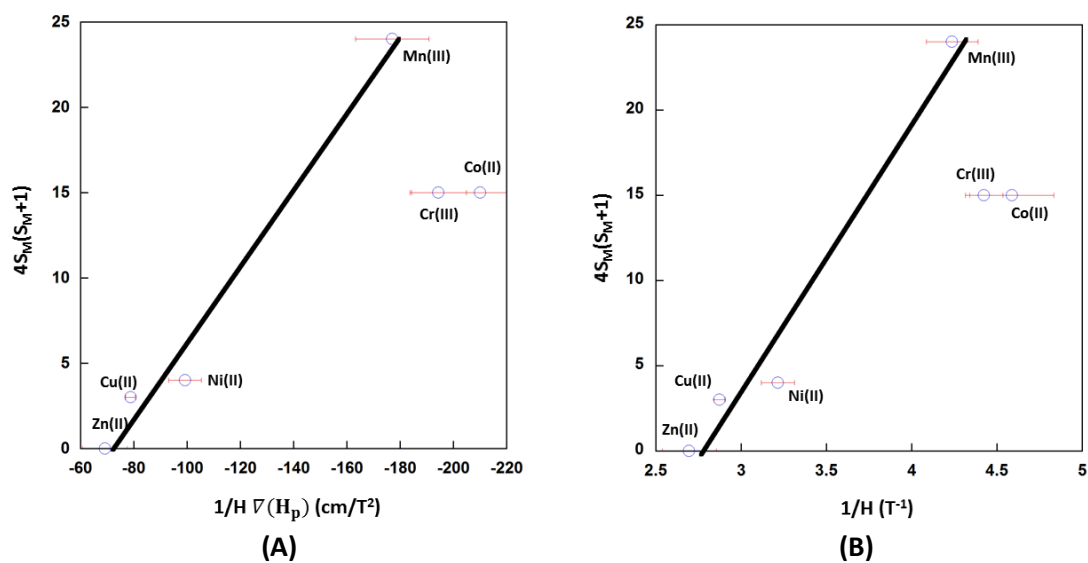


Figure 4.29. Spin-term dependence with respect to the $\frac{1}{H \cdot \nabla(H_p)}$ (A) and $\frac{1}{H}$ (B) values at which the particles are detached from the electromagnet pole.

Chapter 5: Application on the drug capture and magnetic sensing

5.1. Introduction

5.2. Drug active-capture experiments

5.3. Electromagnet sustentation experiment on drug loaded Cu_6CrAD samples

5.1. INTRODUCTION

Emerging pollutants are nowadays one of the ever-increasing environmental concerns due to the adverse ecological and human health effects.^[149] These pollutants (pesticides, drugs, food additives, etc.) are ubiquitously found in the world and have been detected in lot of environmental matrices, including aquatic media (groundwater, wastewater, drinking water, ...).^[150] That is why there is a global emergency to employ quick and effective methodologies for the removal of those emerging pollutants. Among all the methodologies explored so far, the one based on adsorbents is considered one of the most appropriate options given that it shows an excellent removal capacity.^[151] More specifically, up to now, the most commonly used adsorbents have been activated carbon, zeolites, mesoporous silica, cyclodextrins and chitosan beads.^[152] In this challenging quest for the ideal adsorbent MOFs have emerged as a suitable platform.^[153] These ordered crystalline porous materials are renowned due to their high surface areas, tunable pores and intriguing functionalities which make them fulfil several applications.^[56] Thus far, Férey's group first described promising adsorption and release properties of ibuprofen on non-toxic porous iron(III)-based MOFs.^[58] In fact, only a few MOFs allow high amounts of drugs to be loaded, with a complete delivery time range from 6 to 23 days.^[154] A related burgeoning field is that of SMOFs (supramolecular metal-organic frameworks) in which the coordination bonds are released from guiding the crystal structure and supramolecular interactions (π - π stacking interactions and/or hydrogen bonds) play this role.^[40]

5.2. DRUG ACTIVE-CAPTURE EXPERIMENTS

In the previous chapter it has been shown several SMOFs that have bring together intrinsic porosity (pore volume greater than 40%) and interesting magnetic features that range from ferrimagnetic to ferromagnetic behaviour at low temperatures.^[145] In the first compound of this family, the heptanuclear $[\text{Cu}_7(\mu\text{-H}_2\text{O})_6(\mu_3\text{-OH})_6(\mu\text{-ade-}\kappa\text{N3}:\kappa\text{N9})_6]^{2+}$ wheels are joined

¹⁴⁹ (a) Zhang, Y., *Emerging Chemicals and Human Health*, Ed.; Springer: Singapore, **2019**. (b) Barceló D.; Alastuey, A., *Emerging Organic Contaminants and Human Health; The Handbook of Environmental Chemistry*, V. 20; Springer: Heidelberg, **2012**.

¹⁵⁰ Geissen, V.; Mol, H.; Klumpp, E.; Umlauf, G.; Nadal, M.; van der Ploeg, M.; van de Zee, S.E.A.T.M.; Ritsema, C.J. Emerging pollutants in the environment: a challenge for water resource management. *International Soil and Water Conservation Research*. **2015**, *3*, 57–65.

¹⁵¹ Gupta, V. K.; Ali, I.; Saleh, T. A.; Nayak, A.; Agarwal, S., *RSC Advances*, **2012**, *2*, 6380–6388.

¹⁵² Sophia, C.A.; Lima, E.C. *Ecotoxicology and environmental safety*, **2018**, *150*, 1–17.

¹⁵³ Dhaka, S.; Kumar, R.; Deep, A.; Kurade, M. B.; Ji, S.-W.; Jeon, B.-Y., *Coord. Chem. Rev.* **2019**, *380*, 330–352.

¹⁵⁴ Agostoni, W.; Chalati, T.; Horcajada, P.; Willaime, H.; Anand, R.; Semiramoth, N.; Baati, T.; Hall, S.; Mauri, G.; Chacun, H.; Bouchemal, K.; Martineau, C.; Taulelle, F.; Couverur, P.; Rogez-Kreuz, C.; Clayette, P.; Monti, S.; Serre, C.; Gref, R. *Adv. Healthcare Mater.*, **2013**, *2*, 1630–1637.

together by means of π - π stacking interactions and the central copper(II) centre is antiferromagnetically coupled to external ones which are ferromagnetically coupled among them leading to a $S = 5/2$ ground state, while for the heterometallic heptanuclear $[\text{Cu}_6\text{Cr}(\mu\text{-H}_2\text{O})_6(\mu_3\text{-OH})_6(\mu\text{-ade-}\kappa\text{N3}:\kappa\text{N9})_6]^{3+}$ entity all magnetic interactions are ferromagnetic giving rise to a $S = 9/2$ ground state. In addition to that, the above-mentioned heptanuclear entity has been recurrently described in other SMOFs^[155] and it has been recently reported as a building unit of a MOF.^[156] Worthy to mention the case of the SMOFs given that the nature and size of the voids have proved to accommodate different types of anionic molecules not only inorganic but also organic ones through the molecular recognition capabilities provided by the adeninato ligands decorating the outer surface of the wheel shaped heptamers.

Among the heterometallic members of this family of heptameric entities, compound $[\text{Cu}_6\text{Cr}(\mu\text{-H}_2\text{O})_6(\mu_3\text{-OH})_6(\mu\text{-ade-}\kappa\text{N3}:\kappa\text{N9})_6](\text{SO}_4)_{1.5} \cdot n_{\text{solvent}}$ (now called $\text{Cu}_6\text{CrAD}(1)$) outstands as a very interesting candidate to capture potentially hazardous molecules from water but, as it will be described below, not only through a passive diffusion dominated procedure as it is usually employed for classical porous materials and MOFs. In these compounds, the rich acid-base chemistry of the adenine nucleobase allows its solution in acid aqueous solutions while retaining the molecular structure of the heptameric entities. The $\mu\text{-}\kappa\text{N3}:\kappa\text{N9}$ coordination bridging mode for the adeninato leaves the N1 and the N7 positions as suitable acceptor positions for protonation without, in principle, altering the key features of the wheel shaped heptamer. In our first trials, it was attempted to carry out this experiment with the homometallic Cu_7 analogue, but the lability of copper(II) makes the acid media not only attacking the base positions in the adeninato ligand but also the hydroxide anions bridging the central metal atom to the peripheral ones, leading to its dissociation as clearly deduced from the adeninium sulfate $((\text{C}_5\text{H}_6\text{N}_5)_2\text{SO}_4)$ precipitation. However, the presence of the chromium(III) atom at the central position plays a crucial role as its kinetical inertness provides stability to the $[\text{Cr}(\text{OH})_6]^{3-}$ central core, in such a way that the protonation takes place only at the nucleobases that are able to deal with it without collapsing the molecular structure of the heptameric entities. This fact allows its complete solution at pH below 2.0. The obtained solution is stable for a few hours before starting the thermodynamically favoured breakdown of the heptameric unit with the appearance of the previously mentioned adeninium sulfate precipitate. It confirms the kinetical stability of the Cu_6Cr entity in an acid media. Furthermore,

¹⁵⁵ (a) Pascual-Colino, J.; Beobide, G.; Castillo, O.; da Silva, I.; Luque, A.; Pérez-Yáñez, S., *Cryst. Growth Des.* **2018**, *18*, 3465–3476.
(b) Pascual-Colino, J.; Beobide, G.; Castillo, O.; Lodewyckx, P.; Luque, A.; Pérez-Yáñez, S.; Román, P.; Velasco, L. F., *J. Inorg. Biochem.* **2020**, *202*, 110865.

¹⁵⁶ Li, J.; Jiang, L.; Chen, S.; Kirchon, A.; Li, B.; Li, Y.; Zhou, H.-C., *J. Am. Chem. Soc.* **2019**, *141*, 3807–3811.

if the solution is not allowed to stand for long at these very acid pH values, for example by basifying with NaOH up to pH 6.5, it provides again the starting compound (Figure 5.1) with the peculiar magnetic features provided by the presence of the Cu_6Cr entity. Note that the stoichiometric mixture of the reagents at acid pH, followed by a comparable pH increase provides an amorphous product which chemical and magnetic characterization could not be related with the presence of heptanuclear entities. This indirect evidence further supports the toughness of the Cu_6Cr entity at acid solution.

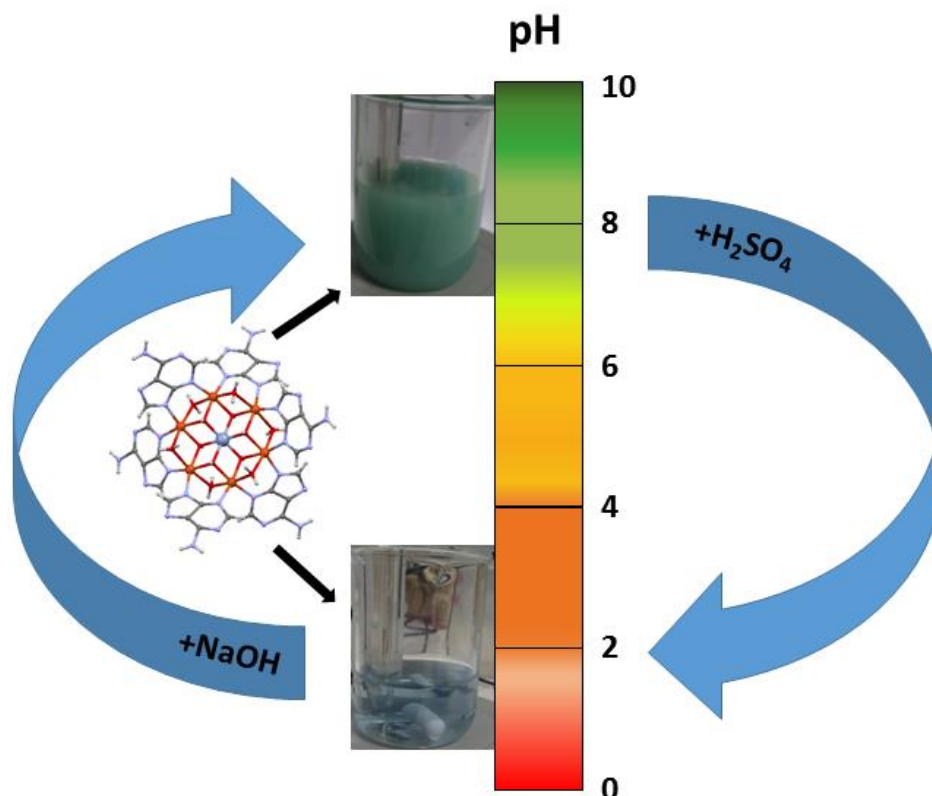


Figure 5.1. pH induced reversible solubilisation/precipitation of the Cu_6CrAD compound.

Figure 5.2 shows how the magnetization value of the recycled $\text{Cu}_6\text{CrAD}(2)$ compound remains at the expected values ($M_s = 9.21$). Similarly, Figure 5.3 and Table 5.1 shows a comparison between the thermogravimetric measurements of both Cu_6Cr heptanuclear entities, being the greater difference only due to a different amount of water molecules present in each compound. The IR spectra also reflect this similarity (Figure 5.4). The integrity of the heptameric unit has also been ensured by XPS (X-ray photoelectronic spectroscopy) measurements as we will describe later.

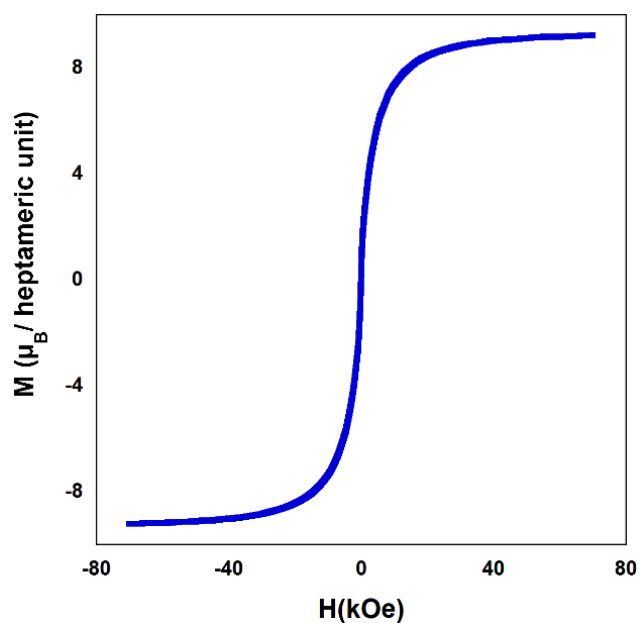


Figure 5.2. Magnetization curve at 2 K for compound Cu_6CrAD after the solution/recrystallization process.

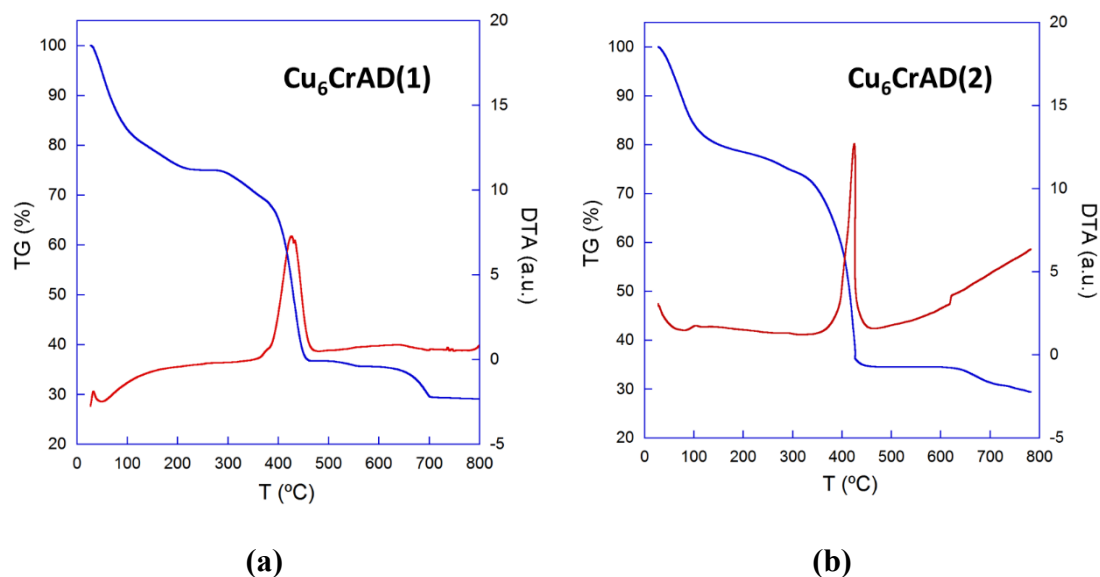
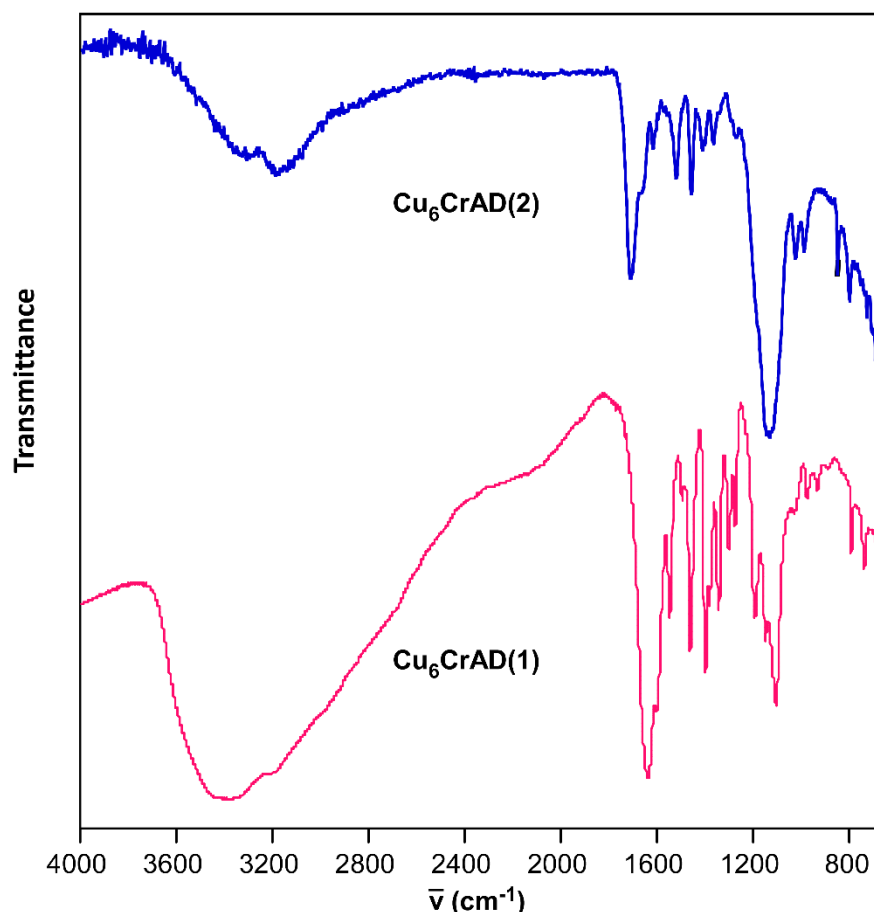


Figure 5.3. Thermogravimetric measurements of the heptameric Cu_6Cr entity before (a) and after (b) the dissolution/recrystallization process.

Table 5.1. Thermoanalytic data of the compounds of Chapter 5.^[a]

Step	T _i	T _f	T _{peak}	ΔH	Δm(%)	ΣΔm(%)	ΣΔm(%) _{theor.} ^[b]
Cu ₆ CrAD(1)							
1	30	95	50	Endo	16.3	16.3	16.3 (−17H ₂ O)
2	95	230		--	10.3	26.6	26.6 (−9H ₂ O)
3	280	475	425	Exo	37.9	64.5	64.5 (Cu ₆ CrO ₆ (SO ₄) _{1.5})
4	625	715			6.3	70.8	70.8 (6CuO + 0.5Cr ₂ O ₃)
Cu ₆ CrAD(2)							
1	30	255	55	Endo	23.0	23.0	23.9 (−(16 + 9H ₂ O))
2	255	460	425	Exo	42.6	65.6	65.6 (Cu ₆ CrO ₆ (SO ₄) _{1.5})
3	600	800	--	--	5.1	70.7	70.7 (6CuO + 0.5Cr ₂ O ₃)

^[a] T_i = initial temperature; T_f = final temperature; T_{peak} = peak temperature ATD; Δm(%) = loss mass percentage in each step; ΔH = type of process according to ATD; ΣΔm(%) = total loss mass after each step; ΣΔm(%)_{theo} = total loss mass theoretically calculated.^[b] Eliminated water molecules and final residue per compound formula.

**Figure 5.4.** IR spectra of the original (1) and reconstituted (2) Cu₆CrAD samples.

However, it deserves to note here that the PXRD pattern indicates that the crystal structure of the reconstituted compound has been altered, but it is not so unusual as several

cases of polymorphism has been also reported for the homometallic Cu₇ analogues (Figure 5.5).^[10–11]

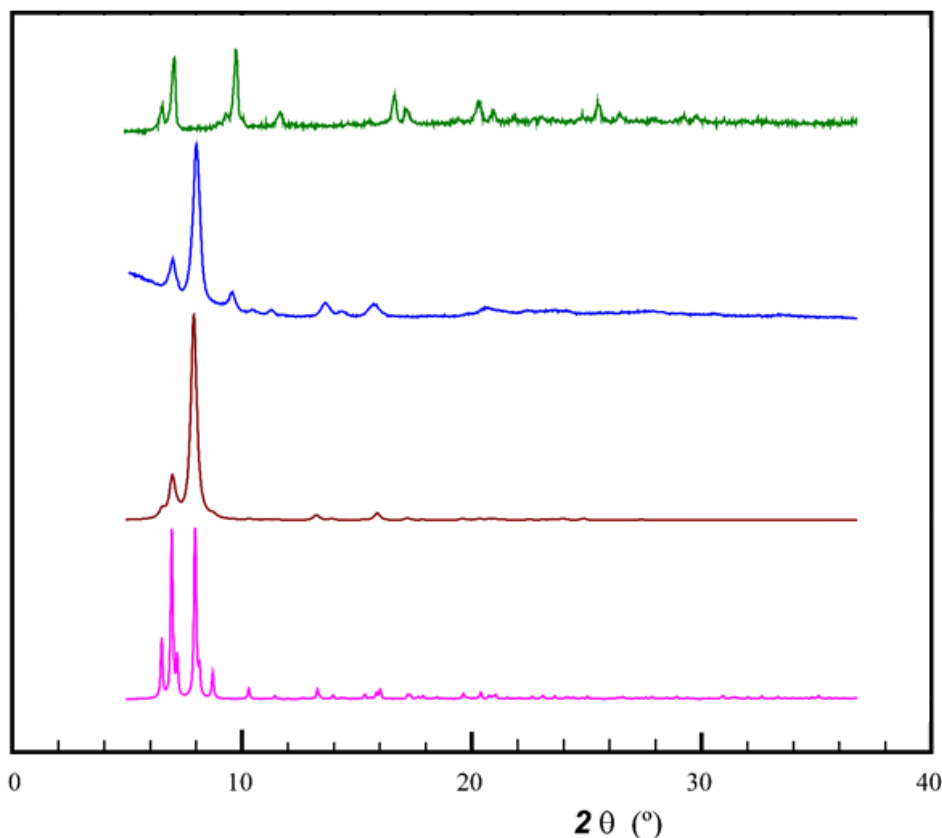


Figure 5.5. Comparison between PXRD of compound Cu₆CrAD, simulated without preferred orientation (pink), with preferred orientation (brown), experimental (blue) and after the dissolution/recrystallization process. The preferred orientation was set using $hkl = 0\ 1\ 0$, with a peak shape FWHM 0.3 and a March–Dollase parameter being 0.6, which is typical of platy shape crystals.

At this point, we decided to combine all these features to provide a material that could actively entrap medically extensively employed molecules such as the nonsteroidal anionic anti-inflammatory drugs (NSAIDs) naproxen and ibuprofen molecules which are nowadays a source of water contamination concern.^[157] These drugs have been selected because of their the capability to form supramolecular interactions with the heptameric entity, either hydrogen bonding or π – π stacking. Second, the anionic nature of these drugs allows them to replace the SO₄²⁻ anions to balance the positive charge of the heptameric cluster.

¹⁵⁷ (a) Sun, W.; Li, H.; Li, H.; Li, S.; Cao, X. *Chem. Eng. J.*, **2019**, *360*, 645-653. (b) Paunovic, O.; Pap, S.; Maletic, S.; Taggart, M.A.; Boskovic, N.; Sekulic, M.T. *J. Colloid. Interf. Sci.*, **2019**, *547*, 350-360. (c) Górny, D.M.; Guzik, U.; Hupert-Kocurek, K.; Wojcieszynska, D. *Ecotox. Environ. Safe.*, **2019**, *167*, 505-512. (d) Li, Z.; Liu, G.; Su, Q.; Jin, X.; Wen, X.; Zhang, G.; Huang, R. *Arab. J. Chem.*, **2018**, *11*, 910-917. (e) Domínguez, J.R.; González, T.; Palo, P.; Cuerda-Correa, E.M. *Desalination.*, **2011**, *269*, 231-238.

NSAIDs are members of a drug class that reduces pain, decreases fever, prevents blood clots, and in higher doses, decreases inflammation.^[158-159] These drugs act as nonselective inhibitors of the cyclooxygenase (COX) enzymes, inhibiting both the cyclooxygenase-1 (COX-1) and cyclooxygenase-2 (COX-2) isoenzymes (Figure 5.6).^[160] The COX enzymes produces prostaglandins, a family of chemicals that promote inflammation that is necessary for healing, but also results in pain, and fever; support the blood clotting function of platelets; and protect the lining of the stomach from the damaging effects of acid.^[161] This inhibition is competitively reversible (albeit at varying degrees of reversibility), as opposed to the mechanism of aspirin, which is irreversible inhibition.^[162]

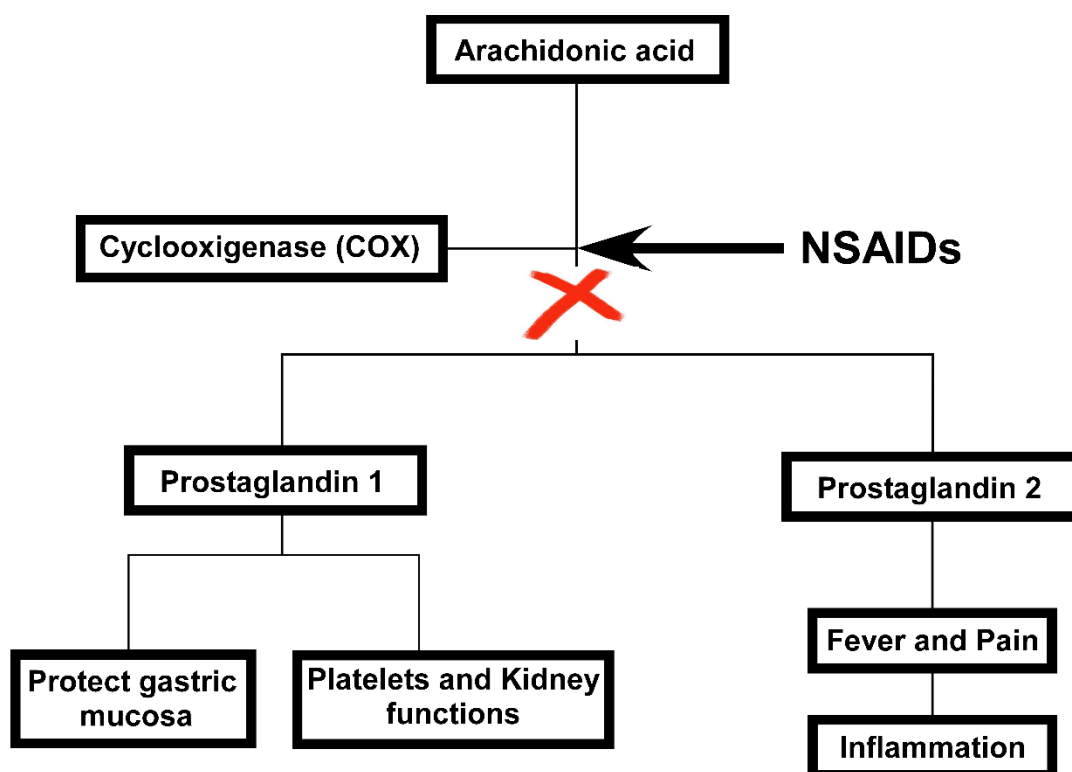


Figure 5.6. Schematic action mechanism of the drugs employed in this chapter.

These two drugs (ibuprofen and naproxen) have been derived from propionic acid (Figure 5.7). Ibuprofen is a widely available and moderately potent NSAID that has a low systemic toxicity, and, unlike some other NSAIDs, such as aspirin, indomethacin, and piroxicam, it has a relatively low risk of side-effects caused by gastric damage.^[17] Ibuprofen has not only been considered for acute pain relief, but it has also been used to treat chronic

¹⁵⁸ Bally, M; Dendukuri, N; Rich, B; Nadeau, L; Helin-Salmivaara, A; Garbe, E; Brophy, BMJ., *Clinical Research Ed.*, **2017**, *357*, j1909.

¹⁵⁹ Lanas, A; Chan, FK. *Lancet.*, **2017**, *390*, 613–624.

¹⁶⁰ Harris, Randall E. *COX-2 Blockade in Cancer Prevention and Therapy*, SPRINGER SCIENCE + BUSINESS MEDIA, LLC, 2003.

¹⁶¹ Vane, J. R.; Botting, R. M. *Am. J. Med.* **1998**, *104*, 2S–8S.

¹⁶² Knights, Kathleen. *Expert Review of Clinical Pharmacology.*, **2010**, *3*, 769–776.

inflammatory and degenerative diseases^[163] and is also under consideration for treating a variety of cancers.^[164-165] The drug naproxen shares the same characteristics as ibuprofen, being from the same family.

NONSTEROIDAL ANTI-INFLAMMATORY DRUGS (NSAIDs)

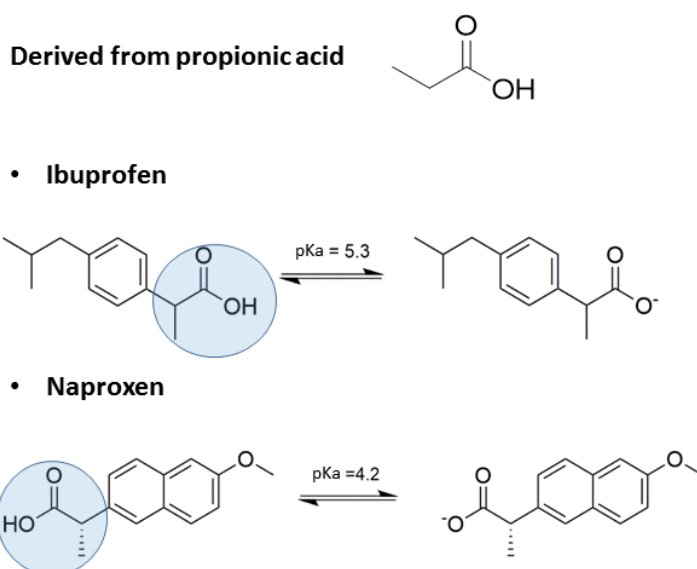


Figure 5.7. Acid-base equilibrium of ibuprofen and naproxen drugs.

One of the biggest problems caused by this type of medication is its high consumption, being easy to obtain anti-inflammatory drugs (no prescription is necessary). The concentration of each capsule is substantially higher than that needed by the body, because the drug travels throughout the body instead of being selective to the affected area. This causes that large concentrations of the same are excreted by the organism, ending up into the residual waters. Thus drugs have been continually detected in groundwater, seawater, polluted water and drinking water because they were not treated completely by the wastewater treatment plant.^[157] It has been reported that naproxen may not only affect the water quality and organisms resulting in the reduction of the biodiversity,^[157] but also induces heart disease and causes endocrine disruption.^[157-166] Hence, it is crucial to develop effective methods for the removal of these drugs from wastewater.

To accomplish the active capture experiments of these drugs, 0.0413 mmol of $\text{Cu}_6\text{CrADSO}_4$ (0.0785 g) were added to 5 mL of water and H_2SO_4 was added dropwise until its

¹⁶³ Wyss-Coray, T.; Mucke, L. *Nat. Med.* **2000**, *6*, 973–974.

¹⁶⁴ Khwaja, F.; Allen, J.; Lynch, J.; Andrews, P.; Djakiew, D. *Cancer Res.*, **2004**, *64*, 6207–6213.

¹⁶⁵ Harris, R. E.; Alshafie, G. A.; Abou-Issa, H.; Seibert, K. *Oncol. Rep.*, **2000**, *60*, 2101–2103.

¹⁶⁶ Domínguez, J.R.; González, T.; Palo, P.; Cuerda-Correa, E.M. *Desalination.*, **2011**, *269*, 231–238.

complete dissolution around pH 1.7–2.0. Throughout the synthesis process, pH control takes special relevance. In this case, the pH value at which it dissolves must not be lower than 1.6, if so, the heptameric cluster would break, making its reconstruction impossible. Simultaneously, three 1 L diluted solutions for each of the two drugs were prepared with concentrations of 248, 413 and 826 μM (corresponding to 51, 85 and 170 mg/L for ibuprofen and 57, 95 and 190 mg/L for naproxen). These two will be mixed leading to a Cu_6CrAD heptamer:drug ratios of 1:6, 1:10 and 1:20, respectively. During the addition of the highly acidic solution of the heptamer, the pH of the solution was kept between pH 7–8 by the simultaneous addition of 1M NaOH in order to prevent the precipitation of the highly insoluble neutral forms of the drugs. As the heptamer was added to the drug, a green suspension appeared, but interestingly the amount of precipitate clearly increases as the concentration of the drug solution increases. The characterization of the resulting precipitates indicated that the amount of the anionic form of the drug captured by the heptameric entities differ from 1:3 (for naproxen), 1:6 (for ibuprofen and naproxen) and 1:9 (for ibuprofen and naproxen). The 1:3 ratio ibuprofen sample was achieved as the result with the less concentrated ibuprofen sodium salt solution provided what seemed to be a mixture of 1:3 and 1:6 precipitates.

The infrared spectroscopy has been able to determine efficiently in these precipitates the presence of the bands corresponding to the adenine ligand and the drugs ibuprofen and naproxen, respectively. The infrared spectra of the compounds are presented in Figures 5.8 and 5.9. Tables 5.2 and 5.3 show the wave number, relative intensity and the assignment of the observed signals.

The absence of a signal around $1700\text{--}1730\text{ cm}^{-1}$ takes out the presence of protonated carboxylic groups in these precipitates, excluding the possibility of a coprecipitation or incorporation of ibuprofen and naproxen in their neutral forms which are highly insoluble. On the contrary, the sodium salt form of these drugs are highly soluble in water ($\geq 100\text{ mg/mL}$), therefore their precipitation can be also excluded. In addition to that, the bands corresponding to ibuprofenato and naproxenato anions can be clearly observed. First of all, the assignment of the CH_3 asymmetric stretching, as well as the CH_2 asymmetric stretching vibration ($2860\text{--}2975\text{ cm}^{-1}$) are clearly noticeable in contrast with the Cu_6CrAD compound. Secondly, the COO^- asymmetric stretching band of the drugs ($1630\text{--}1640\text{ cm}^{-1}$) was also detected among others. In both spectra, the presence of the C–O stretching (1183 cm^{-1}),^[167] CH_2 scissoring vibration (1462 cm^{-1}) and CH–CO deformation (1420 cm^{-1}) are also detected. The specific stretching vibration of the metoxil group at 1366 cm^{-1} is only observed in the naproxenato anion containing

¹⁶⁷ Pretsch, E.; Bühlmann, P.; Badertscher, M., *Structure Determination of Organic Compounds*, Ed. 4th, Springer, 2009.

samples, which is a referential feature in the naproxen related compounds.^[168] In all the cases, the characteristic band of the C=C stretching vibration and deformation vibration of NH₂ group of the adenine among others appears in the original Cu₆CrAD and drug containing samples. Finally, the IR of the drug containing samples clearly showed the disappearance of sulfate characteristic ν (S–O) band around 1108 cm⁻¹.^[87]

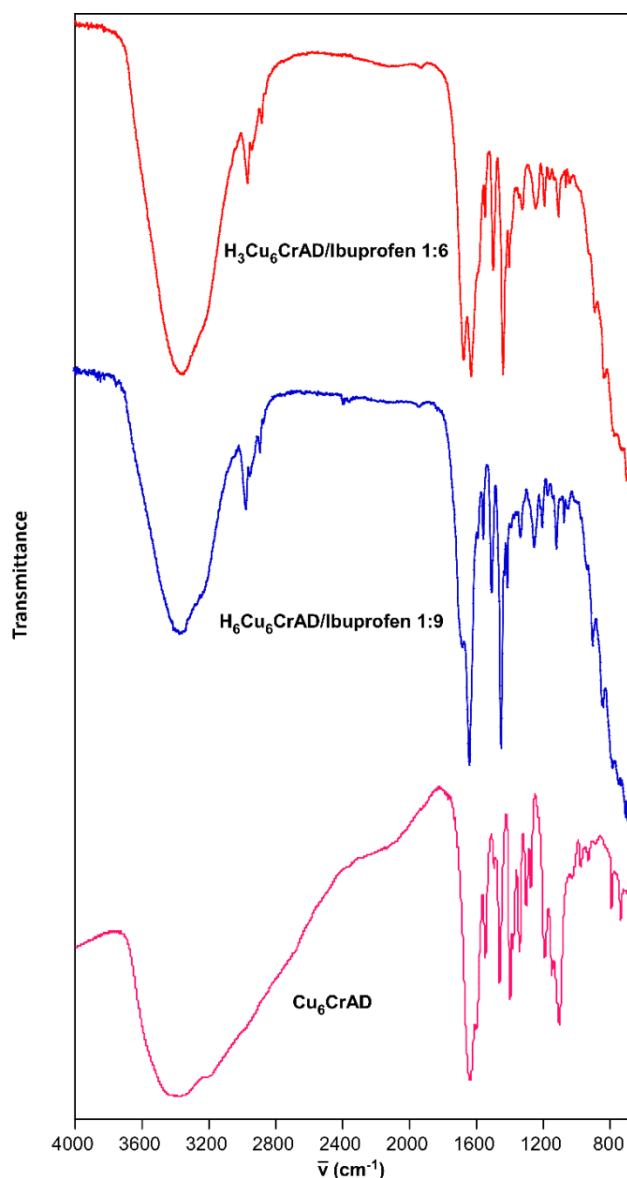


Figure 5.8. Infrared spectra of compounds Cu₆CrAD/ibuprofen 1:6 (red), Cu₆CrAD/ibuprofen 1:6 (blue) and Cu₆CrAD (pink).

¹⁶⁸ (a) Acharya, M.; Mishra, Satyaki, Sahoo, R.; Mallick, S., *Acta Chim. Slov.*, **2017**, *64*, 45–54. (b) Saji, R.; Prasana, J.; Muthu, S.; George, J.; Kuruvilla, T.; Raajaraman, B.R., *Spectrochimica Acta Part A*, **2020**, *226*, 117614.

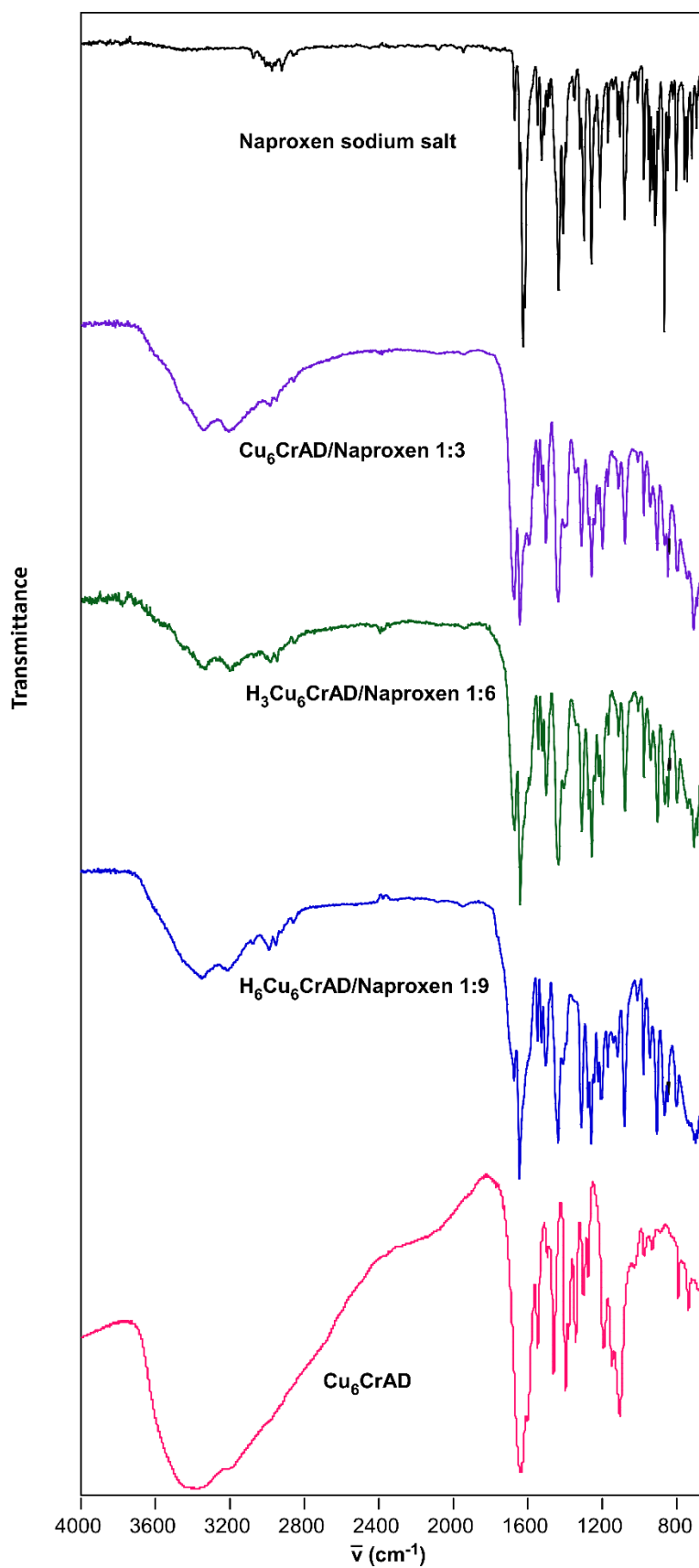


Figure 5.9. Infrared spectra of Naproxen sodium, Cu₆CrAD/Naproxen 1:3 (purple), Cu₆CrAD/Naproxen 1:6 (green), Cu₆CrAD/Naproxen 1:9 (blue) and Cu₆CrAD (pink).

Table 5.2. Infrared spectra bands (cm^{-1}) of the ibuprofen molecule, Cu_6CrAD and the samples obtained during the ibuprofen capture experiments.^[a]

Ibuprofen	Cu_6CrAD	Ibu 1:6	Ibu 1:9	Assignment ^[b]
	3388vs	3346vs	3355vs	ν (O–H)
	3200sh	3217vs	3217vs	ν (NH_2) ⁺
	over	--	--	ν (C8–H + C2–H)
2958vs		2955vs	2955vs	ν_{as} (CH_3)
2868vs		2866vs	2866vs	ν_{s} (CH_2)
1650s	1642vs	1644s	1647s	ν_{as} (COO^-)
	1603vs	1597s	1597s	ν (C=N) + ν (C=C) + δ (NH_2)
	1548s	1545s	1533s	ν (C4–C5 + N3–C4–C5)
	1463m	1463m	1463m	δ (C2–H + C8–N9) + ν (C8–H)
1462s		1461s	1461s	δ_{as} (CH_3) + τ (CH_2)
1420s	1402m	1405s	1405s	δ (N1–C6–H6) + δ (CH–CO)
	1304m			
	1277m	1285m	1288m	ν (N9–C8 + N3–C2) + δ (C–H)
	1195m	1203m	1202m	δ (C8–H) + ν (N7–C8)
	1152m	1150m	1152m	
1183s		1200s	1200s	ν_{as} (CO)
	1108m	--	--	ν (S–O)
	1033w	1020w	1022w	τ (NH_2)
	935w	921vw	922vw	ν (N1–C6) + τ (NH_2)

^[a] vs = very strong, s = strong, m = medium, w = weak, sh = shoulder. ^[b] over = overlapped, ν = tension vibrations, δ = deformation vibrations, τ = torsion.

Table 5.3. Infrared spectra bands (cm^{-1}) of the naproxen molecule, Cu_6CrAD and the samples obtained during the naproxen capture experiments.^[a]

Naproxen	Cu_6CrAD	Nap 1:3	Nap 1:6	Nap 1:9	Assignment ^[b]
	3388vs	3338vs	3340vs	3336vs	ν (O–H)
	3200sh	3190vs	3190vs	3193vs	ν (NH_2) ⁺
	over	--	--	--	ν (C8–H + C2–H)
2958vs		2973vs	2975vs	2970vs	ν_{as} (CH_3)
2900vs		2903vs	2906vs	2900vs	ν_{s} (CH_2)
1630s	1642vs	1633s	1635s	1633s	ν_{as} (COO^-)
	1603vs	1603s	1603s	1603s	ν (C=N) + ν (C=C) + δ (NH_2)
	1548s	1551s	1551s	1550s	ν (C4–C5 + N3–C4–C5)
1503s		1501s	1502s	1503s	ν (C=C) + δ (CH_2)
	1463m	1463m	1463m	1463m	δ (C2–H + C8–N9) + ν (C8–H)
1462s		1461s	1461s	1461s	δ_{as} (CH_3) + τ (CH_2)
	1402m	1393s	1397s	1393s	δ (N1–C6–H6)
1366s					ν_{s} (C–O) + δ (CH)
	1304m				
	1277m	1265m	1266m	1265m	ν (N9–C8 + N3–C2) + δ (C–H)
	1195m	1210m	1209m	1210m	δ (C8–H) + ν (N7–C8)
	1152m	1150m	1150m	1152m	
1190w		1210s	1209s	1210s	ν_{as} (CO)
	1108m	--	--	--	ν (S–O)
	1033w	1033w	1030w	1033w	τ (NH_2)
	935w	926w	926vw	926w	ν (N1–C6) + τ (NH_2)
855s		852s	852s	852s	ν_{s} (C–O)

^[a] vs = very strong, s = strong, m = medium, w = weak, sh = shoulder. ^[b] over = overlapped, ν = tension vibrations, δ = deformation vibrations, τ = torsion.

The incorporation of a maximum of 9 monoanionic drug molecules per heptameric entity enables to assume that in the acidic solution of Cu_6CrAD , the heptameric entities have been able to incorporate 6 H^+ probably located on the non-coordinated endocyclic nitrogen atoms of the adenines in such a way that the discrete entities acquire a 9^+ charge allowing so to capture up to 9 anions of these drugs per formula. Apparently, depending on the concentration/ratio of the drug solution, the addition of these highly protonated 9^+ entities into a nearly neutral solution leads to two competing processes: (a) the neutralization of these

acidic entities and (b) their precipitation in the form of a cationic heptamer – anionic drug insoluble compound (Figure 5.10). At high concentrations, the second process takes place before any neutralization process and it results in the isolation of H_6Cu_6CrAD/Ibu 1:9 (ibu: ibuprofen) and H_6Cu_6CrAD/Nap 1:9 (Nap: naproxen) compounds. At intermediate concentrations, partial neutralization takes place before the anionic drug is able to precipitate it, giving rise to samples H_3Cu_6CrAD/Ibu 1:6 and H_3Cu_6CrAD/Nap 1:6 compounds. At the lower end of employed concentrations, the neutralization can be completed for Cu_6CrAD/Nap 1:3 but for the ibuprofen analogue on a mixture of the apparently 1:3 and 1:6 compounds is achieved as previously mentioned.

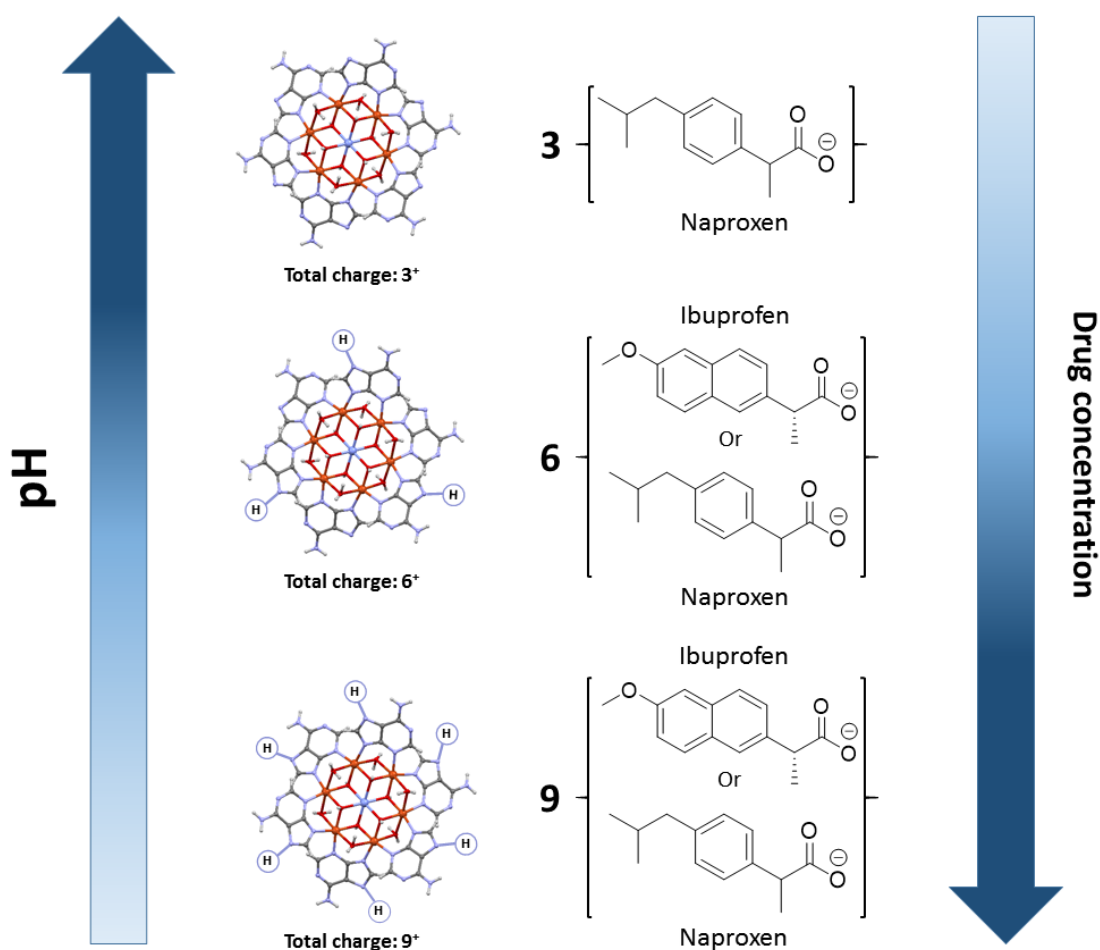


Figure 5.10. Protonation of the adeninato ligand with the increment of the drug concentration.

The drug contents have been corroborated by the elemental analysis of the precipitated compounds. Table 5.4 shows the experimental values obtained in the elemental analysis of the compounds, compared with the calculated values, and the proposed formulas.

Table 5.4. Calculated and experimental elemental analysis values for the compounds with the proposed formulas.

Compound	N(%)		C(%)		H(%)		S(%)	
	Exp.	Cal.	Exp.	Cal.	Exp.	Cal.	Exp.	Cal.
Cu ₆ CrAD [Cu ₆ Cr(H ₂ O) ₆ (OH) ₆ (C ₅ H ₄ N ₅) ₆](SO ₄) _{1.5} ·17H ₂ O·3CH ₃ OH	19.75	21.07	18.87	19.87	3.46	4.44	2.19	2.41
H ₃ Cu ₆ CrAD/Ibu 1:6 [Cu ₆ Cr(H ₂ O) ₆ (OH) ₆ (C ₅ H ₅ N ₅) ₃ (C ₅ H ₄ N ₅) ₃](C ₁₃ H ₁₇ O ₂) ₆ ·7CH ₃ OH 2H ₂ O	14.20	14.27	45.98	46.93	6.22	6.13	0.00	0.00
H ₆ Cu ₆ CrAD/Ibu 1:9 [Cu ₆ Cr(H ₂ O) ₆ (OH) ₆ (C ₅ H ₅ N ₅) ₆](C ₁₃ H ₁₇ O ₂) ₉ ·9CH ₃ OH	11.76	11.89	52.04	52.29	6.64	6.16	0.01	0.01
Cu ₆ CrAD/Nap 1:3 [Cu ₆ Cr(H ₂ O) ₆ (OH) ₆ (C ₅ H ₄ N ₅) ₆](C ₁₄ H ₁₃ O ₃) ₃ ·CH ₃ OH·H ₂ O	16.55	16.82	39.88	39.91	6.02	5.40	0.00	0.00
H ₃ Cu ₆ CrAD/Nap 1:6 [Cu ₆ Cr(H ₂ O) ₆ (OH) ₆ (C ₅ H ₅ N ₅) ₃ (C ₅ H ₄ N ₅) ₃](C ₁₄ H ₁₃ O ₃) ₆ ·CH ₃ OH·2H ₂ O	14.45	14.48	47.89	47.61	4.84	4.76	0.00	0.00
H ₆ Cu ₆ CrAD/Nap 1:9 [Cu ₆ Cr(H ₂ O) ₆ (OH) ₆ (C ₅ H ₅ N ₅) ₉](C ₁₄ H ₁₃ O ₃) ₉ ·5CH ₃ OH·H ₂ O	11.43	11.37	52.30	52.32	5.27	5.10	0.00	0.00

The thermogravimetric analysis (TGA) also confirmed the above described amount of drug incorporated per heptamer (Figure 5.11 and Table 5.5). All measurements were performed using synthetic air (79 % N₂, 21 % O₂) as atmosphere under a 5 °C/min heating ramp.

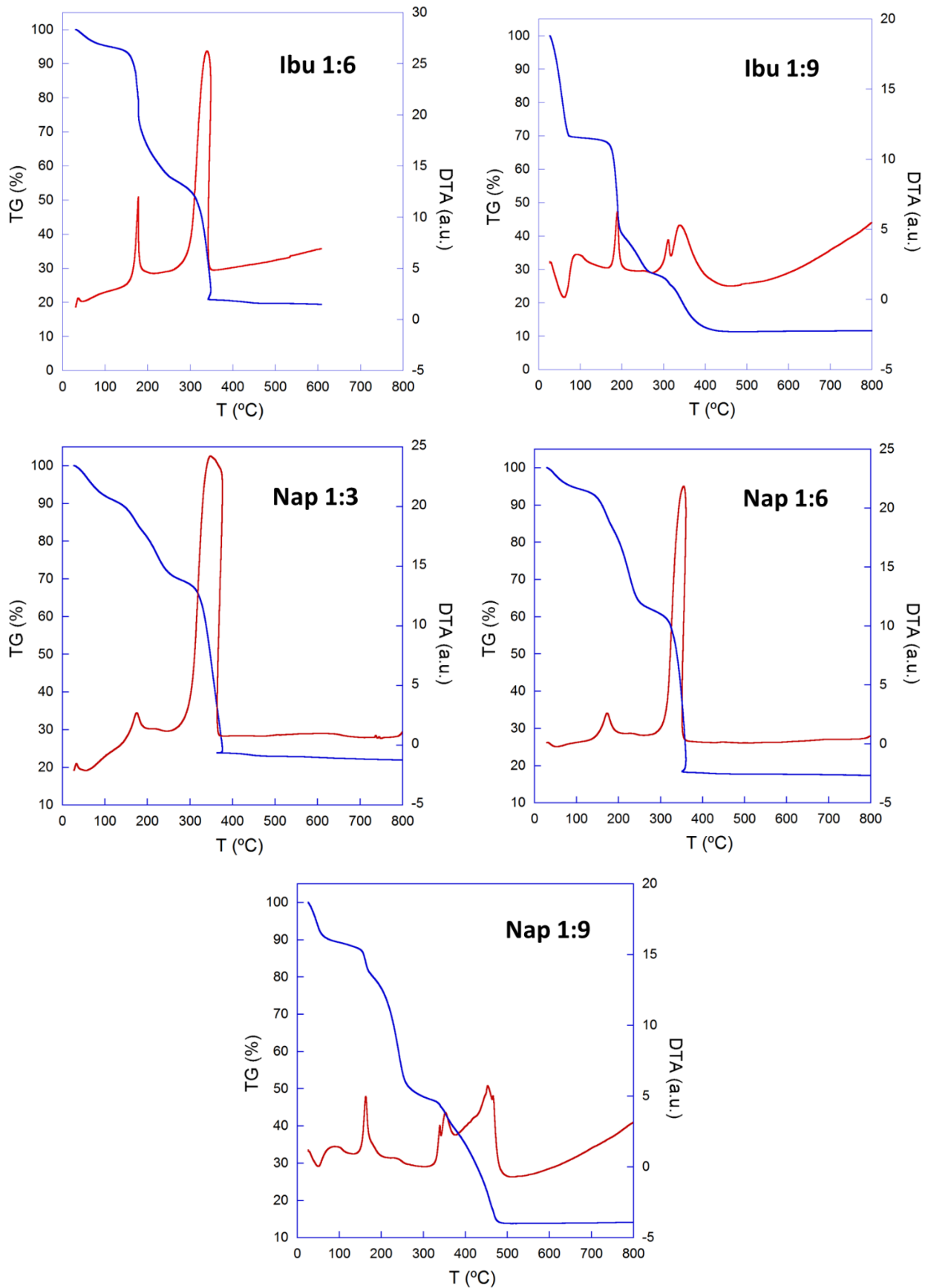


Figure 5.11. Thermogravimetric measurements performed upon representative samples.

Table 5.5. Thermoanalytic data of the compounds of Chapter 5.^[a]

Step	T _i	T _f	T _{peak}	ΔH	Δm(%)	ΣΔm(%)	ΣΔm(%) _{theo} ·[b]
Ibu 1:6							
1	30	120	--	--	4.0	5.3	4.5 (-7H ₂ O)
2	140	280	175	Exo	38.5	45.7	46.9 -(6H ₂ O + 6C ₁₀ H ₁₄) [Cu ₆ Cr(OH) ₆ (C ₅ H ₅ N ₅) ₃ (C ₅ H ₄ N ₅) ₃](C ₃ H ₃ O ₂) ₆
3	280	480	335	Exo	37.8	80.3	80.3 (6CuO + 0.5(Cr ₂ O ₃))
Ibu 1:9							
1	30	85	60	Endo	31.0	31.0	31.2 (-83H ₂ O)
2	150	195	190	--	27.6	58.6	59.1 -(6H ₂ O + 9C ₁₀ H ₁₄) [Cu ₆ Cr(OH) ₆ (C ₅ H ₅ N ₅) ₆](C ₃ H ₃ O ₂) ₉
3	190	450	210/340	Exo	29.9	88.5	88.5 (6CuO + 0.5(Cr ₂ O ₃))
Nap 1:3							
1	30	130	60	Endo	8.2	8.2	11.2 (-15H ₂ O)
2	130	260	170	Exo	23.8	32.0	35.4 -(6H ₂ O + 3C ₁₁ H ₁₀ O) [Cu ₆ Cr(OH) ₆ (C ₅ H ₄ N ₅) ₆](C ₃ H ₃ O ₂) ₆
3	285	450	350	Exo	45.0	77.0	77.0 (6CuO + 0.5(Cr ₂ O ₃))
Nap 1:6							
1	30	105	--	--	5.5	5.5	7.1 (-12H ₂ O)
2	135	270	170	Exo	34.5	38.0	41.3 -(6H ₂ O + 6C ₁₁ H ₁₀ O) [Cu ₆ Cr(OH) ₆ (C ₅ H ₅ N ₅) ₃ (C ₅ H ₄ N ₅) ₃](C ₃ H ₃ O ₂) ₆
3	300	385	400	Exo	41.8	81.8	81.8 (6CuO + 0.5(Cr ₂ O ₃))
Nap 1:9							
1	30	80	55	Endo	10.5	10.5	11.8 (-26H ₂ O)
2	140	290	165	Exo	41.1	50.0	49.6 -(6H ₂ O + 9C ₁₁ H ₁₀ O) [Cu ₆ Cr(OH) ₆ (C ₅ H ₅ N ₅) ₆](C ₃ H ₃ O ₂) ₉
3	290	500	multi	Exo	31.6	86.1	83.2 (6CuO + 0.5(Cr ₂ O ₃))

^[a] T_i = initial temperature; T_f = final temperature; T_{peak} = peak temperature ATD; Δm(%) = loss mass percentage in each step; ΔH = type of process according to ATD; ΣΔm(%) = total loss mass after each step; ΣΔm(%)_{theo} = total loss mass theoretically calculated. ^[b] Eliminate water molecules and final residue per compound formula.

All the compounds gathered in this chapter undergo a similar decomposition process. First, the loss of the crystallization water molecules is observed which is featured by an endothermic DTA peak and usually spans from room temperature to values between 70–150 °C depending on the amount of water in the pores. Shortly after the previous process, the

release of the six water molecules coordinated to the discrete heptameric entities takes place altogether with the fragmentation and release of the drug molecules as depicted in Figure 5.12. This fragmentation of the drug molecules has been previously reported^[169] and leaves behind a propenoate anion that ensures the charge balance of the resulting product. The mass loss observed in this step increases with the amount of captured anionic drug molecules. Thereafter, the combustion of the organic part occurs through a strong exothermic process, generating the corresponding metal oxides. A very informative decomposition step is that corresponding to the decomposition of the sulfate anion into SO_3 and O^{2-} (which takes place around 650-700 °C and it is clearly observed in the sulfate containing Cu_6CrAD compound) which it is not observed in these samples. The absence of this latter process corroborates also the substitution of the sulfate anion by these anionic drugs.

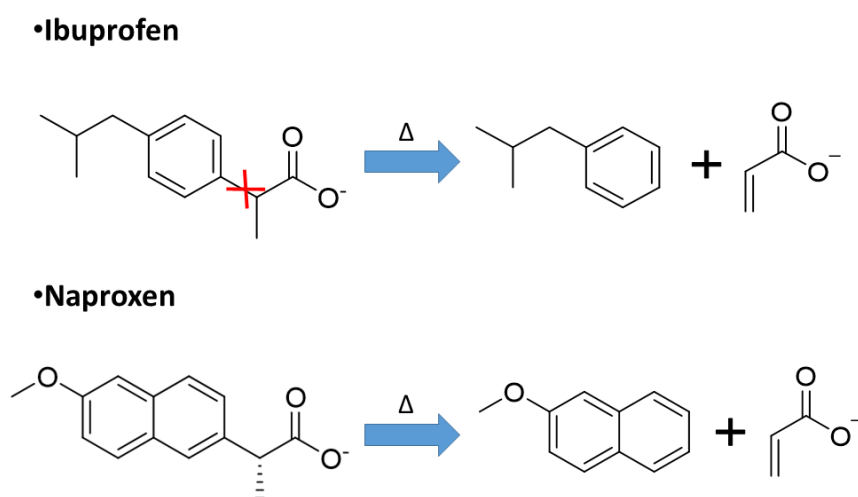


Figure 5.12. Pyrolytic fragmentation process of the anionic drugs.

Finally, the integrity of the heptameric discrete units has been further ensured by XPS (X-ray photoelectronic spectroscopy) measurements. The bond energies of both the external ring copper(II) and the central chromium(III) metal centres do not change, indicating that their chemical environment has remained unaltered (Figure 5.13).^[138]

¹⁶⁹ (a) Zayed, M.; Hawash, M.; Fahmey, M.; El-Gizouli, A., *J. Therm. Anal. Calorim.*, **2012**, *108*, 315–322. (b) Zayed, M.; Hawash, M.; El-Desawy, M.; El-Gizouli, A., *Arabian Journal of Chem.*, **2017**, *10*, 351–359.

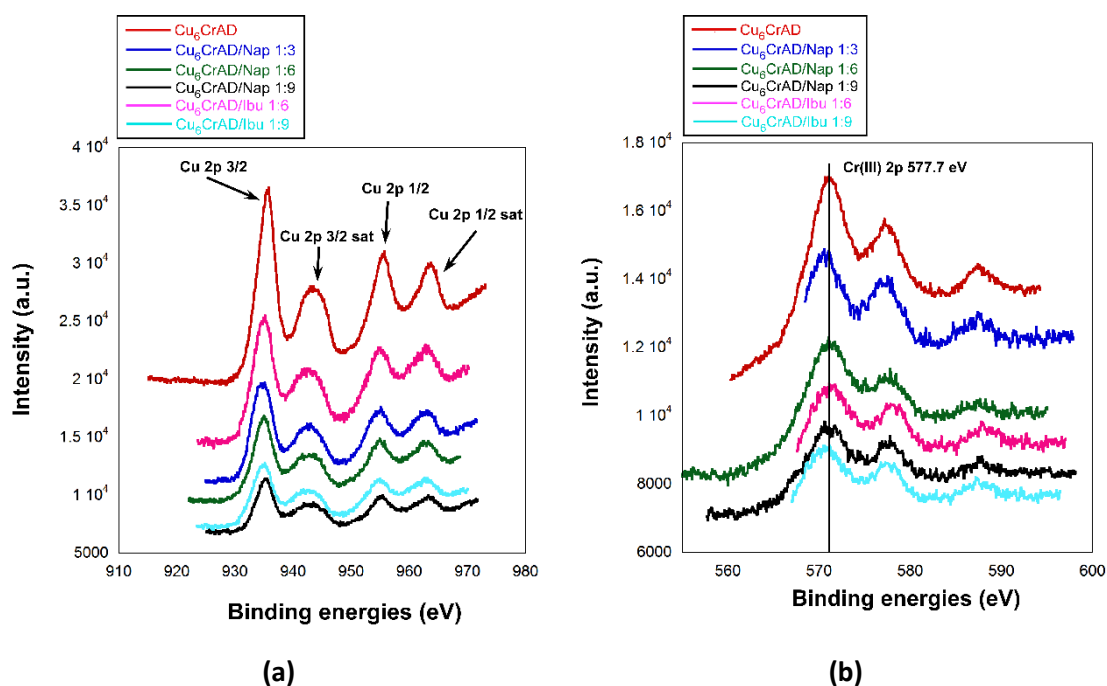


Figure 5.13. X-ray photoemission spectra of the Cu(II) (a) and Cr(III) (b) ions of all compounds of Chapter 5.

5.3. ELECTROMAGNET SUSTENTATION EXPERIMENT ON DRUG LOADED Cu₆CrAD SAMPLES

As previously stated in section 4.3.3 of Chapter 4, under the strong magnetic field generated by the electromagnet, the paramagnetic response of these compounds is enough to provide mobility to the particles immersed in a solvent and to attach them to the lower end of the magnetic pole. In this case, all the samples contain the same paramagnetic heptameric Cu₆CrAD entity but differ on the nature and amount of the counterions. In this case, the variation of the magnetic field at which the sustentation of the particles ends will not depend on the number of unpaired electrons as the metal atoms in the heptameric entity did not differ. However, they do on the counterion total mass that makes the gravitation attraction to increase and necessarily displaces the critical magnetic field towards higher values (Figure 5.14). To find the dependence between the counterion total mass and the magnetic field required to keep the particles attached to the electromagnet pole. For that purpose, the framework volume of the particle must now be divided into the volumes occupied by the heptameric entity (V_H) and by the counterions (V_C): $V_F = V_H + V_C$. The attraction by the magnetic field can be expressed only on V_H as it is the only source of the paramagnetism responsible of this attraction, but the gravitation-flotation part requires both terms V_H and V_C , equation (1):

$$\mu_0 \frac{[4S_{Cr}(S_{Cr}+1)]+6 \cdot [4S_{Cu}(S_{Cu}+1)]}{8T \cdot MW_H} \cdot \rho_H \cdot V_H \cdot H \cdot \nabla(H_p) = (\rho_H - \rho_S) \cdot V_H \cdot g + (\rho_C - \rho_S) \cdot V_C \cdot g \quad (1)$$

It is possible to relate V_H and V_C , equations (2) and (3), through the molecular density and molecular weights of both components, equations (4) and (5):

$$V_H \propto \frac{MW_H}{\rho_H} \quad (2)$$

$$V_C \propto \frac{n \cdot MW_C}{\rho_C} \quad (3)$$

$$\frac{V_C}{V_H} = \frac{n \cdot MW_C \cdot \rho_H}{MW_H \cdot \rho_C} \quad (4)$$

$$V_C = \frac{n \cdot MW_C \cdot \rho_H}{\rho_C \cdot MW_H} \cdot V_H \quad (5)$$

Replacing this value in equation (1) an expression is obtained from which the volume term can be removed, equations (6) and (7):

$$\mu_0 \frac{[4S_{Cr}(S_{Cr}+1)]+6 \cdot [4S_{Cu}(S_{Cu}+1)]}{8T \cdot MW_H} \rho_H \cdot V_H \cdot H \cdot \nabla(H_P) = (\rho_H - \rho_S)V_H \cdot g + (\rho_C - \rho_S) \frac{n \cdot MW_C \cdot \rho_H}{\rho_C \cdot MW_H} \cdot V_H \cdot g \quad (6)$$

$$\mu_0 \frac{[4S_{Cr}(S_{Cr}+1)]+6 \cdot [4S_{Cu}(S_{Cu}+1)]}{8T \cdot MW_H} \rho_H \cdot H \cdot \nabla(H_P) = (\rho_H - \rho_S)g + (\rho_C - \rho_S) \frac{n \cdot MW_C \cdot \rho_H}{\rho_C \cdot MW_H} g \quad (7)$$

Now isolating nMW_C :

$$nMW_C = \frac{\mu_0 \frac{[4S_{Cr}(S_{Cr}+1)]+6 \cdot [4S_{Cu}(S_{Cu}+1)]}{8T \cdot MW_H} \rho_H \cdot H \cdot \nabla(H_P) - (\rho_H - \rho_S)g}{\frac{(\rho_C - \rho_S)\rho_H}{\rho_C \cdot MW_H}} \quad (8)$$

$$nMW_C = \mu_0 \cdot \rho_C \frac{[4S_{Cr}(S_{Cr}+1)]+6 \cdot [4S_{Cu}(S_{Cu}+1)]}{8T \cdot (\rho_C - \rho_S)} H \cdot \nabla(H_P) - \frac{(\rho_H - \rho_S)g \cdot \rho_C \cdot MW_H}{(\rho_C - \rho_S)\rho_H} \quad (9)$$

Assuming the counterions molecular density is similar and that the remaining parameters apart from nMW_C and $H \cdot \nabla(H_P)$ are constant, equation (9) can be simplified into a linear equation with two constants (A and B), equation (10).

$$nMW_C = A \cdot H \cdot \nabla(H_P) + B \quad (10)$$

Accordingly, the experimental data depicted on a nMW_C vs $H \cdot \nabla(H_P)$ fits satisfactory to a straight line (Figure 5.15). The same can be observed if the experimental data are plotted on a nMW_C vs H graph due to linear relationship between $H \cdot \nabla(H_P)$ and H for magnetic fields above 0.4 T (see Figure 4.28 of Chapter 4).

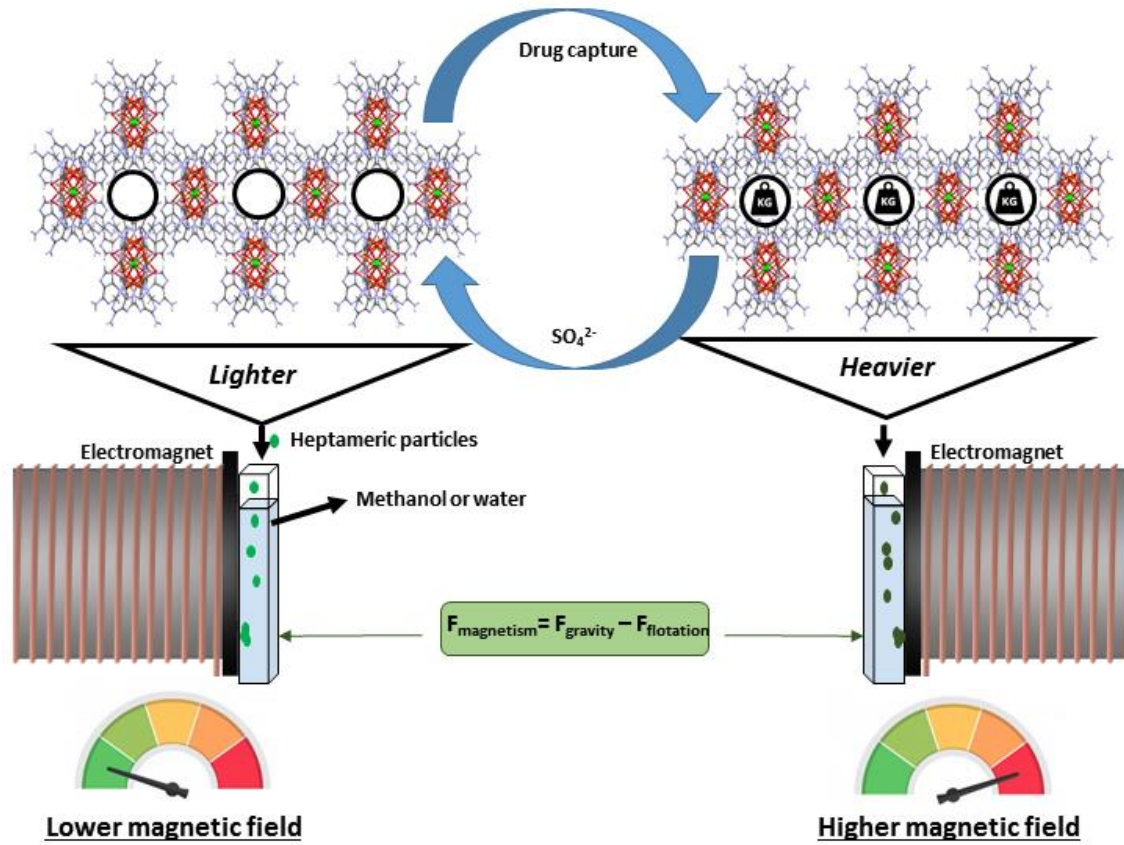


Figure 5.14. Scheme simulating the replacement of the anionic part, changing the minimum magnetic force needed to attach a particle in the magnetic pole.

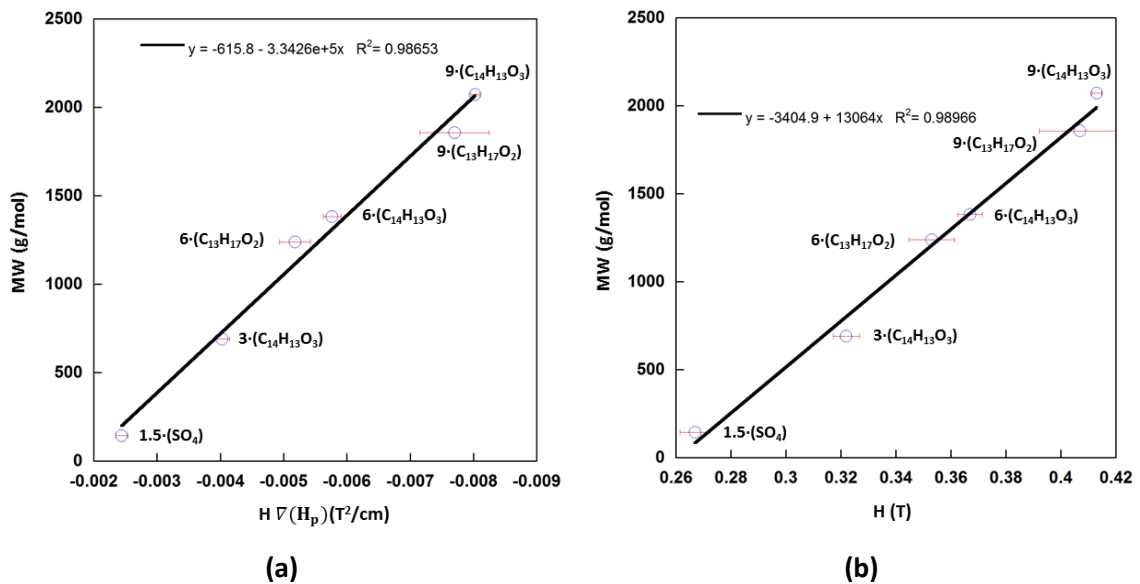


Figure 5.15. Dependence of the molecular weight of the captured drug with respect to $H \nabla(H_p)$ (a) and H (b) values at which the particles are detached from the electromagnet pole.

Conclusions

6.1. CONCLUSIONS

Seventeen new metal-organic compounds have been synthesized and characterized using either 2-hydroxyquinoline-4-carboxylate or adeninate as bridging ligands and Cu(II) as major metal centre. Furthermore, in certain cases, co-ligands (pyridine or 4,4'-bipyridinethane) or additional transition metal centres (Cr(III), Mn(III), Co(II), Ni(II), or Zn(II)) were employed to enrich the structural and chemical diversity of the compounds. The major conclusions arising from this work are listed below:

- The coordinative versatility of the HQ ligand has allowed to obtain three dimeric structures (0D-CuHQMEOH, 0D-CuHQAQ and 0D-CuHQPY) and two polymeric ones (1D-CuHQ and 2D-HQBPA).

- Initially obtained 0D-CuHQMEOH and 0D-CuHQAQ, met the first and second criteria to build up an SMOF, but not the third one. For this reason, several co-ligands (BPA and PY) have been added with the aim of favouring the formation of non-coplanar synthons that could provide alternative growth vectors necessary to achieve a robust three-dimensional structure sustained by a combination of complementary synthons. However, both approaches were unsuccessful. The steric hindrance of the PY ligand led to a change into the bridging mode of the HQ ligand, rearranging the structure in such a way that the parallel synthons were maintained. Similarly, the addition of the BPA ligand has led to an increase of the dimensionality of the network.

- Through the use of higher synthesis temperature, a polymeric structure (1D-CuHQ) and a paddle-wheel shaped structure (0D-CuCBDQ) (433 K) were obtained. Whereas the polymeric structure was built up from the semi-coordination through the carbonyl-O atoms of $[\text{Cu}_2(\text{HQ})_4]$ paddle-wheel shaped complexes with UUDD configuration, the HQ of the 0D-CuCBDQ experiments a cycloaddition, to generate cyclobutadiquinoline (CBDQ), obtaining as a result, a paddle-wheel-shaped $[\text{Cu}_2(\text{CBDQ})_4]$ dinuclear entity with UDUD configuration.

- Each dinuclear complex fulfils the three criteria required to yield a SMOF, and accordingly, they self-assemble by complementary hydrogen bonding ($\text{N-H}\cdots\text{O}=\text{C}_{\text{carbonyl}}$) to yield **lvt**-type and **dia**-type supramolecular porous network, respectively. However, the large pore size generated causes a double and a triple interpenetration of the network that has almost completely eliminated the porosity of the compound 1D-CuHQ and left compound 0D-CuCBDQ with a remaining pore volume of ca. 19%.

- The nature and magnitude of the magnetic coupling constant is closely related to the coordination mode displayed by the HQ ligand. Those based on $\mu\text{-HQ-}\kappa\text{O}_{\text{carboxylate}}:\kappa\text{O}_{\text{carboxylate}}$ or $\mu\text{-HQ-}\kappa\text{O}_{\text{carboxylate}}:\kappa\text{O}_{\text{carbonyl}}$ yield weak intramolecular antiferromagnetic interactions that are the

source of the metamagnetic behaviour observed in the magnetization curves. Contrarily, compounds exhibiting $\mu\text{-HQ-}\kappa\text{O}_{\text{carboxylate}}:\kappa\text{O}'_{\text{carboxylate}}$ coordination modes, present intermediate or strong antiferromagnetic coupling constant values depending on the syn–syn or syn–anti disposition of the carboxylate bridge.

- Regarding to the Cu(II)/adeninato system, the nuclearity of the resulting complex is highly affected by the pH of the synthesis, obtaining from dinuclear entities to octanuclear and heptanuclear ones upon the increase of the basicity of the reaction media.

- The obtained neutral $[\text{Cu}_2(\mu\text{-ade})_4(\text{H}_2\text{O})_2]$ paddle-wheel dimer self-assemble through pairing interactions into a 3D supramolecular network with **bnn** topology and a 45% of void volume ($\text{Cu}_2\text{ADSO}_4\text{NHET}_3$). Voids are big enough to host not only solvent molecules but also $\text{NHET}_3^+/\text{SO}_4^{2-}$ ion pairs and a 1D-supramolecular chain of $[\text{Cu}_2(\mu\text{-ade})_4(\text{H}_2\text{O})_2]$ complexes.

- The octameric clusters, $[\text{Cu}_8(\mu_3\text{-OH})_4(\mu_4\text{-OH})_4(\text{ade})_4(\mu\text{-ade})_4(\mu\text{-Hade})_2]$ (Cu_8AD), fulfil also the criteria to yield an SMOF, and accordingly they self-assemble by hydrogen bonding to yield a porous 3D network with **sqc3** topology and a 30% of void space (Cu_8AD).

- The cationic nature of the heptanuclear $[\text{Cu}_7(\mu\text{-H}_2\text{O})_6(\mu_3\text{-OH})_6(\mu\text{-ade})_6]^{2+}$ complexes makes the packing very sensitive to the ionic species present in the media and as consequence five different porous crystal packings were obtained using this complex entity ($\text{Cu}_7\text{ADSO}_4\text{NHET}_3\text{-1}$, $\text{Cu}_7\text{ADSO}_4\text{NHET}_3\text{-2}$, Cu_7ADSO_4 , $\text{Cu}_7\text{ADHN-1}$ and $\text{Cu}_7\text{ADHN-2}$). The porosity, the scheme of the supramolecular interactions, and the stability of the structure is closely related to the counterions hosted in each crystal structure with a void space ranging from 26% to 49%.

- The magnetic characterization indicates the central Cu(II) atom is anti-ferromagnetically coupled to the external ferromagnetic Cu_6 -ring, leading to a $S = 5/2$ ground state.

- The robustness of the heptameric entity allowed us to replace the central Cu(II) atom by Cr(III), Mn(III), Co(II), Ni(II) and Zn(II), giving rise to a novel family of heterometallic complexes of general formula $[\text{Cu}_6\text{M}^{\text{III}}(\mu\text{-H}_2\text{O})_6(\mu_3\text{-OH})_6(\mu\text{-ade-}\kappa\text{N3}:\kappa\text{N9})_6]^{3+}$ or $[\text{Cu}_6\text{M}^{\text{II}}(\mu\text{-H}_2\text{O})_6(\mu_3\text{-OH})_6(\mu\text{-ade-}\kappa\text{N3}:\kappa\text{N9})_6]^{2+}$ ($\text{Cu}_6\text{MADSO}_4$; M: Cr, Mn, Co, Ni, Zn)

- The replacement of the central atom allowed us to tune the magnetic behaviour of the complex obtaining total spins that vary from $3/2$ to $9/2$. The paramagnetic behaviour of these porous heptanuclear compounds at room temperature is enough to attach them to the magnetic pole of an electromagnet when the particles are immersed in a liquid. Interestingly, it was showed how the field at which the material particles are detached, keeps a linear dependence with the paramagnetic contribution of the central metal atom ($4S_M(S_M + 1)$).

- Finally, we observed that the Cr(III) heptanuclear (Cu_6CrAD) complex is able to disassemble and reassemble at room temperature conditions upon controlled pH changes. This exclusive behaviour together with its cationic nature and anchored nucleobases provide the ability to capture anionic drugs. Furthermore, it was demonstrated how the critical magnetic field at which the material is detached from the magnetic pole, shows a linear relationship with the molecular weight of the trapped drug, which could be a valuable tool for drug identification purposes.

References

7.1. Introduction

7.2. References

7.1. INTRODUCTION

In this work, the references are mentioned as footnotes in the different chapters. In this section, the full references can be found, displayed in alphabetical order of the first author and, then, the rest of the authors are considered. When this criterion is not enough, the publication name and the first page will be taken into account. The reference style followed is the recommended by the American Chemical Society.

7.2. REFERENCES

- A. M., SU; L. S., WANG; Q. F., ZHANG; J., XIE; Q., LUO; D. L., PENG, *J. of Mat. Sci.: Mat. in Elec.*, **2018**, *29*, 9814–9820.
- A. VAN ALBADA, G.; MUTIKAINEN, I.; J.J. SMEETS, W.; L. SPEK, A.; TURPEINEN, U.; REEDIJK, J. *Inorg. Chim. Acta*, **2002**, *327*, 134–139.
- ACHARYA, M.; MISHRA, SATYAKI, SAHOO, R.; MALLICK, S. *Acta Chim. Slov.*, **2017**, *64*, 45–54.
- AGOSTONI, W.; CHALATI, T.; HORCAJADA, P.; WILLAIME, H.; ANAND, R.; SEMIRAMOTH, N.; BAATI, T.; HALL, S.; MAURI, G.; CHACUN, H.; BOUCHEMAL, K.; MARTINEAU, C.; TAULELLE, F.; COUVERUR, P.; ROGEZ-KREUZ, C.; CLAYETTE, P.; MONTI, S.; SERRE, C.; GREF, R. *Adv. Healthcare Mater.*, **2013**, *2*, 1630–1637.
- AIDA, T.; MEIJER, E. W.; STUPP, S. I. *Science*, **2012**, *335*, 813–817.
- ALAMMAR, T.; SHEKHAH, O.; WOHLGEMUTH, J.; MUDRING, A.-V. *J. Mater. Chem.*, **2012**, *22*, 18252.
- ALTOMARE, A.; CASCARANO, M.; GIACOVAZZO, C.; GUAGLIARDI, A. *J. Appl. Cryst.* **1993**, *26*, 343-350.
- AMO-OCHOA, P.; GIVAJA, G.; SANZ MIGUEL, P. J.; CASTILLO, O.; ZAMORA, F. *Inorg. Chem. Comm.*, **2007**, *10*, 921–924.
- AMO-OCHOA, P.; ZAMORA, F., *Chem. Soc. Rev.*, **2005**, *34*, 9–21.
- AN, J.; FARHA, O.K.; HUPP, J.T.; POHL, E.; YEH, J.I.; ROSI, N.L., *Nat. Comm.*, **2012**, *3*, 604.
- AN, J.; FIORELLA, R.P.; GEIB, S.J.; ROSI, N.L., *JACS*. **2009**, *131*, 8401–8403.
- AN, J.; GEIB, S.J.; ROSI, N.L. *J. Am. Chem. Soc.*, **2010**, *132*, 38–39.
- AN, J.; GEIB, S.J.; ROSI, N.L. *J. Am. Chem. Soc.* **2009**, *131*, 8376–8377.
- ARUNAN, E.; DESIRAJU, G. R.; KLEIN, R. A.; SADLEJ, J.; SCHEINER, S.; ALKORTA, I.; CLARY, D. C.; CRABTREE, R. H.; DANNENBERG, J. J.; HOBZA, P.; KJAERGAARD, H. G.; LEGON, A. C.; MENNUCCI, B.; NESBITT, D. J. DEFINITION OF THE HYDROGEN BOND (IUPAC RECOMMENDATIONS 2011). *Pure Appl. Chem.* **2011**, *83*, 1637–1641.
- AZUAH, R. T.; KNELLER, L. R.; QIU, Y.; TREGENNA-PIGGOTT, P. L. W.; BROWN, C. M.; COPLEY, J. R. D.; DIMEO, R. M. *J. Res. Natl. Inst. Stan. Technol.* **2009**, *114*, 341-358.

- BALLY, M.; DENDUKURI, N.; RICH, B.; NADEAU, L.; HELIN-SALMIVAARA, A.; GARBE, E.; BROPHY, BMJ. *Clinical Research Ed.*, **2017**, 357, j1909.
- BAO, Z.; ALNEMRAT, S.; YU, L.; VASILIEV, I.; REN, Q.; LU, X.; DENG, S. *J. Col. Int. Sci.*, **2011**, 357, 504–509.
- BARCELÓ D.; ALASTUEY, A., *Emerging Organic Contaminants and Human Health; The Handbook of Environmental Chemistry*, V. 20; Springer: Heidelberg, **2012**.
- BATTEN, S.R.; CHAMPNESS, N.R.; CHEN, X.M.; GARCIA-MARTINEZ, J.; KITAGAWA, S.; OHRSTROM, L.; O'KEEFFE, M.; SUH, M.P.; REEDIJK, J. *Pure Appl. Chem.*, **2013**, 85, 1715–1724.
- BATTEN, S.R.; CHAMPNESS, N.R.; CHEN, X.M.; GARCIA-MARTINEZ, J.; KITAGAWA, S.; OHRSTROM, L.; O'KEEFFE, M.; SUH, M.P.; REEDIJK, J. *CrystEngComm*, **2012**, 14, 3001–3004.
- BATTEN, S.R.; HOSKINS, B.F.; ROBSON, R. *J. Am. Chem. Soc.*, **1995**, 117, 5385–5386.
- BEAUCHAMP, A. L. *J. Cryst. Mol. Struct.* **1980**, 10, 149.
- BECK, W. M.; CALABRESE, J.C.; KOTTMAIR, N. *Inorg. Chem.* **1979**, 18, 176.
- BENCINI, A. GATTESCHI, D. *Inorg. Chim. Acta*, **1978**, 31, 11.
- BEOBIDE, G.; CASTILLO, O.; LUQUE, A.; GARCÍA-COUCEIRO, U.; GARCÍA-TERAN, J.P.; ROMÁN, P. *Dalton Trans.*, **2007**, 2669-2680.
- BEOBIDE, G.; CASTILLO, O.; CEPEDA, J.; LUQUE, A.; PÉREZ-YAÑEZ, S.; ROMAN, P.; THOMAS-GIPSON, J. *Coord. Chem. Rev.*, **2013**, 257, 2716–2736.
- BEOBIDE, G.; CASTILLO, O.; LUQUE, A.; PÉREZ-YAÑEZ, S. *Cryst. Eng. Comm.* **2015**, 17, 3051-3059.
- BERLIN, A.A.; MATVEEVA, N.G. *Russ. Chem. Rev.* **1960**, 29, 119–128.
- BU, LINTAO; E. HIMMEL, M; R. NIMLOS, M. *ACS Symposium Series*, **2010**, 1052, 99–117.
- BUCHWALTER, P.; ROSE, J.; BRAUNSTEIN, P. *Chem. Rev.* **2015**, 115, 28–126.
- C. HANSELL, *Nat. Chem.*, **2014**, 6, 459.
- CAMBRIDGE STRUCTURAL DATABASE (CSD). Version 5.41 (**2019**).
- CAMPO, J.; LUZÓN, J.; PALACIO, F.; MCINTYRE, G. J.; MILLÁN, A.; WILDES, A. R. *Phys. Rev. B* **2008**, 78, 054415.
- CAÑADILLAS-DELGADO, L.; FABELO, O.; PASÁN, J.; DELGADO, F. S.; LLORET, F.; JULVE, M.; RUIZ-PÉREZ, C. *Inorg. Chem.* **2007**, 46, 7458-7465.
- CANO, A.; RODRÍGUEZ-HERNÁNDEZ, J.; REGUERA, L.; RODRÍGUEZ-CASTELLÓN, E.; REGUERA E. *Eur. J. Inorg. Chem.* **2019**, 1724–1732.
- CARVER, J.C.; SCHWEITZER, G.K.; CARLSON, T.A. *J. Chem. Phys.*, **1972**, 57, 973.

- CEJUDO, R.; ALZUET, G.; BORRÁS, J.; LIU-GONZÁLEZ, M.; SANZ-RUIZ, F. *Polyhedron* **2002**, *21*, 1057.
- CEPEDA, J.; CASTILLO, O.; GARCÍA-TERÁN, J. P.; LUQUE, A.; PÉREZ-YÁÑEZ, S.; ROMÁN, P. *Eur. J. Inorg. Chem.* **2009**, 2344-2353.
- CHANDRASEKHAR, V.; BAG, P.; KROENER, W.; GIEB, K.; MÜLLER, P. *Inorg. Chem.* **2013**, *52*, 13078–13086.
- CHIARI, B.; HELMS, J. H.; PIOVESANA, O.; TARANTELLI, T.; ZANAZZI, P. *Inorg. Chem.*, **1986**, *25*, 2408.
- CHOWDHURY, P.; MEKALA, S.; DREISBACH, F.; GUMMA, S. *Micr. and Mes. Mat.* **2012**, *152*, 246–252.
- COLACIO, E.; DOMÍNGUEZ-VERA, J.M.; GHAZI, M.; KIVEKÄS, R.; KLINGA, M.; MORENO, J. M. *Eur. J. Inorg. Chem.* **1999**, 441–445.
- COLACIO, E.; GHAZI, M.; KIVEKÄS, R.; MORENO, J. M. *Inorg. Chem.* **2000**, *39*, 2882-2890.
- COOPER, A. I. *Angew. Chem., Int. Ed.*, **2012**, *51*, 7892.
- CRAWFORD, V. H.; RICHARDSON, H. W.; WASSON, J. R.; HODGSON, D. J.; HATFIELD, W. E. *Inorg. Chem.* **1976**, *15*, 2107-2110.
- CrysAlisPro, version 1.171.35.19*; Agilent Technologies:Yarnton, UK, **2011**.
- CZAJA, A. U.; TRUKHAN, N.; MÜLLER, U., *Chem. Soc. Rev.* **2009**, *38*, 1284.
- DALI, S.; MUKHERJEE, P. S.; ZANGRANDO, E.; LLORET, F.; CHAUDHURI, N. R. *J. Chem. Soc., Dalton Trans.*, **2000**, 822.
- DE CAMPOS, N. R.; RIBEIRO, M. A.; OLIVEIRA, W. X. C.; REIS, D. O.; STUMPF, H. O.; DORIGUETTO, A. C.; MACHADO, F. C.; PINHEIRO, C. B.; LLORET, F.; JULVE, M.; CANOF, J.; MARINHO, M. V. *Dalton Trans.*, **2016**, *45*, 172–189.
- DE MEESTER, P.; SKAPSKI, A. C. *J. Chem. Soc., Dalton Trans.* **1973**, 424.
- DE PEDRO, I.; ROJO, J. M.; FERNÁNDEZ, J. R.; FERNANDEZ-DIAZ, M. T.; ROJO, T. *Phys. Rev. B* **2010**, *81*, 134431.
- DE PEDRO, I.; ROJO, J. M.; RIUS, J.; VALLCORBA, O.; DE LARRAMENDI, I. R.; RODRIGUEZ FERNANDEZ, J.; LEZAMA, L.; ROJO, T. *Inorg. Chem.* **2012**, *51*, 5246-5256.
- DELGADO, F. S.; HERNÁNDEZ-MOLINA, M.; SANCHIZ, J.; RUIZ-PÉREZ, C.; RODRÍGUEZ-MARTÍN, Y.; LÓPEZ, T.; LLORET, F.; JULVE, M. *CrystEngComm* **2004**, *6*, 106-111.
- DELGADO, F. S.; SANCHIZ, J.; RUIZ-PÉREZ, C.; LLORET, F.; JULVE, M. *CrystEngComm*, **2004**, *6*(73), 443–450.
- DELGADO, F. S.; SANCHIZ, J.; RUIZ-PÉREZ, C.; LLORET, F.; JULVE, M. *Inorg. Chem.*, **2003**, *42*, 5938–5948.
- DESIRAJU, G. D. *Crystal Engineering: The Design of Organic Solids*; Elsevier: New York, **1989**.
- DESIRAJU, G. R. *Acc. Chem. Res.* **2002**, *35*, 565–573.

- DESIRAJU, G. R. *Angew. Chem., Int. Ed. Engl.* **1995**, *34*, 2311–2327.
- DESIRAJU, G. R. *Prog. Solid State Chem.* **1987**, *17*, 295–353.
- DHAKA, S.; KUMAR, R.; DEEP, A.; KURADE, M. B.; JI, S.-W.; JEON, B.-Y. *Coord. Chem. Rev.* **2019**, *380*, 330–352.
- DOMÍNGUEZ, J.R.; GONZÁLEZ, T.; PALO, P.; CUERDA-CORREA, E.M. *Desalination.*, **2011**, *269*, 231-238.
- DURAND, A. M.; KLAVINS, P.; CURRUCCINI, L. R. *J. Phys. Condens. Matter.* **2008**, *20*, 235208.
- DYBTSEV, DN; CHUN, H; YOON, SH; KIM, D; KIM, K., *J. Am. Chem. Soc.* **2004**, *126*, 32–33.
- EDDAOUDI, M.; MOLER, D.; LI, H.; CHEN, B.; REINEKE, T.; O'KEEFFE, M.; YAGHI, O. M. *Acc. Chem. Res.*, **2001**, *34*, 319–330.
- EDDAOUDI, M; KIM, J; ROSI, N; VODAK, D; WACHTER, J; O'KEEFFE, M; YAGHI, O. M. *Science*, **2002**, *295*, 469–472.
- EL-MEHALMEY, W. A.; IBRAHIM, A. H.; ABUGABLE, A. A.; HASSAN, M. H.; HAIKAL, R. R.; KARAKALOS, S. G.; ZAKI, O.; ALKORDI, M. H. *J. Mater. Chem. A*, **2018**, *6*, 2742.
- ESCRIBÁ, E.; SERVER-CARRIÓ, J.; LEZAMA, L.; FOLGADO, J. V.; PIZARRO, J. L.; BALLESTEROS, R.; ABARCA, B. *J. Chem. Soc., Dalton. Trans.*, **1997**, 2033.
- ESTES, E. D.; HATFIELD, W. E.; HODGSON, D. J. *Inorg. Chem.*, **1974**, *13*, 1654–1657.
- ETTER, M. C. *Acc. Chem. Res.* **1990**, *23*, 120–126.
- ETTER, M. C. *J. Phys. Chem.* **1991**, *95*, 4601–4610.
- ETTER, M. C.; URBANCZYK-LIPKOWSKA, Z.; ZIA-EBRAHIMI, M.; PANUNTO, T. W. *J. Am. Chem. Soc.* **1990**, *112*, 8415–8426.
- FARRUGIA, L. J. *J. Appl. Cryst.* **1999**, *32*, 837-838.
- FÉREY, G.; SERRE, C. *Chem. Soc. Rev.* **2009**, *38*, 1380.
- FERREIRA, B. J. M. L.; BRANDÃO, P.; DOS SANTOS, A. M.; GAI, Z.; CRUZ, C.; REIS, M. S.; SANTOS, T. M.; FÉLIX, V. *J. Coord. Chem.* **2015**, *68*, 2770-2787.
- FLORES-CANO, J. V.; LEYVA-RAMOS, R.; CARRASCO-MARIN, F.; ARAGON-PIÑA, A.; SALAZAR-RABAGO, J. J.; LEYVA-RAMOS S. *Adsorption*, **2016**, *22*, 297–308.
- FONTANET, M.; POPESCU, A-R.; FONTRDONA, X.; RODRÍGUEZ, M.; ROMERO, I.; TEIXIDOR, F.; VIÑAS, C.; ALIAGA-ALCALDE, N.; RUIZ, E. *Chem. Eur. J.* **2011**, *17*, 13217.
- FORGAN, RS.; SMALDONE, RA.; GASSENSMITH, JJ.; FURUKAWA, H.; CORDES, DB.; LI, Q.; WILMER, CE.; BOTROS, YY.; SNURR, RQ.; SLAWIN, AMZ.; STODDART, JF. *J. Am. Chem. Soc.* **2012**, *134*, 406–417.
- FORSTER, PM; CHEETHAM, AK. *Angew. Chem.*, **2002**, *41*, 457–459.
- FURUKAWA, H.; KO, N.; GO, Y.B.; ARATANI, N.; CHOI, S.B.; CHOI, F.; YAZAYDIN, A.; SNURR, R.Q.; O'KEEFFE, M.; KIM, J.; YAGHI, O.M. *Science*, **2010**, *329*, 424-428.
- G. M. SHELDRIK. *SHELXL97*, University of Göttingen, Göttingen, Germany, **1997**.

- GARCÍA-TERAN, J. P.; CASTILLO, O.; LUQUE, A.; GARCÍA-COUCEIRO, U.; ROMAN, P.; LEZAMA, L. *Inorg. Chem.* **2004**, *43*, 4549.
- GARCÍA-TERÁN, J.P.; CASTILLO, O.; LUQUE, A.; GARCÍA-COUCEIRO, U.; BEOBIDE, G.; ROMÁN, P. *Dalton Transactions*, **2006**, 902–911.
- GARDNER, G.B.; VENKATARAMANI, D.; MOORE, J.S.; LEE, S. *Nature*, **1994**, *374*, 792–795.
- GASSENSMITH, J.J.; FURUKAWA, H.; SMALDONE, R.A.; FORGAN, S.S.; BOTROS, Y.Y.; YAGHI, O.M.; STODDART, J.F. *J. Am. Chem. Soc.* **2011**, *133*, 15312–15315.
- GAVEZZOTTI, A., *New J. Chem*, **2016**, *40*, 6848–6853.
- GEISSEN, V.; MOL, H.; KLUMPP, E.; UMLAUF, G.; NADAL, M.; VAN DER PLOEG, M.; VAN DE ZEE, S.E.A.T.M.; RITSEMA, C.J. Emerging pollutants in the environment: a challenge for water resource management. *International Soil and Water Conservation Research*. **2015**, *3*, 57–65.
- GHOSE, R. *Inorg. Chim. Acta* **1989**, *156*, 303.
- GHOSE, R. *Synth. React. Inorg. Met. Org. Chem.* **1992**, *22*, 379.
- GILLI, G.; GILLI, P. Oxford University Press: Oxford, **2009**.
- GIMÉNEZ-MARQUÉS, M.; HIDALGO, T.; SERRE, C.; HORCAJADA, P., *Coord. Chem. Rev.*, **2016**, *307*, 342–360.
- GONZALEZ-PEREZ, J.M.; ALARCON-PAYER, C.; CASTINEIRAS, A.; PIVETTA, T.; LEZAMA, L.; CHOQUESILLO-LAZARTE, D.; CRISPONI, G.; NICLOS-GUTIERREZ, J. *Inorg. Chem.*, **2006**, *45*, 877.
- GÓRNY, D.M.; GUZIK, U.; HUPERT-KOCUREK, K.; WOJCIESZYŃSKA, D. *Ecotox. Environ. Safe.*, **2019**, *167*, 505-512.
- GREENAWAY, A. M.; O'CONNOR, J. C.; OVERMAN, J. W.; SINN, E. *Inorg. Chem.*, **1981**, *20*, 1508.
- GRIFFITHS, K.; TSIPIIS, A. C.; KUMAR, P.; TOWNROW, O. P. E.; ABDUL-SADA, A.; AKIEN, G. R.; BALDANSUREN, A.; SPIVEY, A. C.; KOSTAKIS, G. E. *Inorg. Chem.* **2017**, *56*, 9563–9573.
- GROOM, C. R.; BRUNO, I. J.; LIGHTFOOT, M. P.; WARD, S. C. *Acta Cryst.* **2016**, *72*, 171-179.
- GUPTA, V. K.; ALI, I.; SALEH, T. A.; NAYAK, A.; AGARWAL, S. *RSC Advances*, **2012**, *2*, 6380–6388.
- GUTIÉRREZ, L.; ALZUET, G.; BORRAS, J.; CASTIÑEIRAS, A.; RODRIGUEZ-FORTEA, A.; RUIZ, E. *Inorg. Chem.* **2001**, *40*, 3089–3096.
- HADJILIADIS, N; SLETTEN, E. *Metal Complex-DNA Interactions*; John Wiley & Sons: Chichester, **2009**.
- HALL, J. W. PhD Dissertation, University of North Carolina, **1977**.
- HANDBOOK OF MAGNETOCHEMICAL FORMULAE; Boca, R. A Elsevier: 1013 Amsterdam, The Netherlands, **2012**, 1010.
- HARRIS, R. E.; ALSHAFIE, G. A.; ABOU-ISSA, H.; SEIBERT, K. *Oncol. Rep.*, **2000**, *60*, 2101–2103.
- HARRIS, RANDALL E. COX-2 Blockade in Cancer Prevention and Therapy, SPRINGER SCIENCE + BUSINESS MEDIA, LLC, **2003**.
- HATFIELD, W. E. *ACS*, **1974**, *5*, 108–141.

- HATFIELD, W. E. COMMENTS *Inorg. Chem.*, **1981**, *1*, 105.
- HATFIELD, W. E. *Inorg. Chem.*, **1983**, *22*, 833.
- HAY, P. J.; THIBEAULT, J. C.; HOFFMANN, R. *J. Am. Chem. Soc.* **1975**, *97*, 4884.
- HEINE, T.; MAVRANDONAKIS, A.; SUPRONOWICZ, B.; *J. Phys. Chem. C* **2015**, *119*, 3024–3032.
- HERMANN, W.A. Synthetic Methods of Organometallic and Inorganic Chemistry, Georg Thieme Verlag Stuttgart, New York **1977**.
- HOBZA, P.; JUREČKA, P.; ŠPONER, J.; *J. Am. Chem. Soc.* **2004**, *126*, 10142–10151.
- HORCAJADA, P.; SERRE, C.; VALLET-REG, M.; SEBBAN, M.; TAULELLE, F.; FREY, G. *Angew. Chem. Int. Ed.* **2006**, *45*, 5974–5978.
- HOSKINS, B.F.; ROBSON, R. *J. Am. Chem. Soc.*, **1990**, *112*, 1546–1554.
- HUBERT, J.; BEAUCHAMP, A. L. *Acta Crystallogr.* **1980**, *B36*, 2613.
- IDEŠICOVÁ, M.; TITIŠ, J.; KRZYTEK, J.; BOČA, R. *Inorg. Chem.* **2013**, *52*, 9409–9417.
- IMAZ, I.; RUBIO-MARTÍNEZ, M.; AN, J.; SOLÉ-FONT, I.; ROSI, N. L.; MASPOCH, D. *Chem. Commun.* **2011**, *47*, 7287–7302.
- INGLESON, M.J.; BARRIO, J.P.; BACSA, J.; DICKINSON, C.; PARK, H.; ROSSEINSKY, M.J. *Chem. Commun.* **2008**, *11*, 1287–1289.
- IVANOV-EMIN, B.N.; NEVSKAYA, N.A.; ZAITSEV, B.E.; IVANOVA, T.M. *Zh. Neorg. Khimii*, **1982**, *27*, 3101.
- JEFFREY, G. A. An Introduction to Hydrogen Bonding; Oxford University Press: Oxford, **1997**.
- JIAO, L.; JOANNE, S.; SKINNER, W.; WANG, Z.; JIANG, H.-L. *Materials Today*. **2019**, *27*, 43–68.
- KAHN, O. Molecular Magnetism, VCH Publishers Inc., **1993**.
- KANEKO, K.; RODRÍGUEZ-REINOSO, F. *Nanoporous Materials for Gas Storage*, Singapore : Springer, **2019**.
- KHWAJA, F.; ALLEN, J.; LYNCH, J.; ANDREWS, P.; DJAKIEW, D. *Cancer Res.*, **2004**, *64*, 6207–6213.
- KIKHTYANIN, O.; KUBIČKA, D.; ČEJKA, J. *Catalysis Today*, **2015**, *243*, 158–162.
- KINOSHITA, Y.; MATSUBARA, I.; HIGUCHI, T.; SAITO, Y. *Bull. Chem. Soc. Jpn.* **1959**, *32*, 1221–1226.
- KITAGAWA, S.; KAWATA, S.; NOZAKA, Y.; MUNAKATA, M. *J. Chem. Soc. Dalton Trans.*, **1993**, *9*, 1399–1404.
- KNIGHTS, KATHLEEN. *Expert Review of Clinical Pharmacology.*, **2010**, *3*, 769–776.
- KNOBLOCH, F.W.; RAUSCHER, W.H. *J. Polym. Sci.* **1959**, *38*, 261–262.
- KOBAK, J.; BOGUCKI, A.; SMOLEŃSKI, T.; PAPAJ, M.; KOPERSKI, M. POTEMSKI, M.; KOSSACKI, P.; GOLNIK, A.; PACUSKI, W. *Phys. Rev.*, **2018**, *97*, 4–15.

- KRZYSTEK, J.; ZVYAGIN, S. A.; OZAROWSKI, A.; FIEDLER, A. T.; BRUNOLD, C. T.; TELSER, J. *J. Am. Chem. Soc.*, **2004**, *126*, 2148–2155.
- KUBO, M.; KISHITA, M.; KURODA, Y. *J. Polym. Sci.* **1960**, *48*, 467–471.
- LANAS, A; CHAN, FK. *Lancet.*, **2017**, *390*, 613–624.
- LANCHAS, M. (2015). “Métodos no convencionales para la preparación de polimeros de coordinación porosos. Una aproximación económica, medioambientalmente amigable y escalable”, D. Tesis, UPV-EHU, Leioa (España).
- LARREA, E. S.; FERNÁNDEZ DE LUIS, R.; ORIVE, J.; IGLESIAS, M.; ARRIORTUA, M. I. *Eur. J. Inorg. Chem.* **2015**, *10*, 4699–4707.
- LEHN, J. M. *Angew. Chem., Int. Ed.*, **1990**, *29*, 1304–1319.
- LEHN, J. M. *Chem. Scr.*, **1988**, *28*, 237–262.
- LEHN, J. M. *Supramolecular Chemistry: Concepts and Perspectives*, Wiley VCH, **1995**.
- LEWIS, D. L.; MCGREGOR, K. T.; HATFIELD, W. E.; HODGSON, D. J. *Inorg. Chem.*, **1974**, *13*, 1013–1019.
- LI, H; EDDAOUDI, M; O'KEEFFE, M.; YAGHI, O. M. *Nature*, **1999**, *402*, 276–279.
- LI, J.; JIANG, L.; CHEN, S.; KIRCHON, A.; LI, B.; LI, Y.; ZHOU, H.-C. *J. Am. Chem. Soc.* **2019**, *141*, 3807–3811.
- LI, J.-R.; KUPPLER, R. J.; ZHOU, H.-C. *Chem. Soc. Rev.*, **2009**, *38*, 1477–1504.
- LI, T.; CHEN, D.-L.; SULLIVAN, J.E.; KOZLOWAKI, M.T.; JOHNSON, J.K.; ROSI, N.L. *Chemical Science*, **2013**, *4*, 1746–1755.
- LI, X. X.; GONG, Y. Q.; ZHAO, H. X.; WANG, R. H. *Cryst. Eng. Comm.* **2014**, *16*, 8818–8824.
- LI, Z.; LIU, G.; SU, Q.; JIN, X.; WEN, X.; ZHANG, G.; HUANG, R. *Arab. J. Chem.*, **2018**, *11*, 910-917.
- LIPPERT, B. *Coord. Chem. Rev.* **2000**, *200–202*, 487.
- LIU, Y.; HU, C.; COMOTTI, A.; WARD, M. D. *Science*, **2011**, *333*, 436.
- LIU, Z. Y.; ZHANG, H. Y.; YANG, E. C.; LIU, Z. Y.; ZHAO, X. *J. Dalton Trans.* **2015**, *44*, 5280-5283.
- MACRAE, C. F.; SOVAGO, I. S.; COTTRELL, J.; GALEK, P. T. A.; MCCABE, P.; PIDCOCK, E.; PLATINGS, M.; SHIELDS, G. P.; STEVENS, J. S.; TOWLER, M.; WOOD, P. A.; *J. Appl. Cryst.*, **2020**, *53*, 226–235.
- MASTALERZ, M.; OPPEL, I. M. *Angew. Chem., Int. Ed.*, **2012**, *51*, 5252.
- MATSUNAGA, S.; SHIBASAKI, M. *Chem. Comm.* **2014**, *50*, 1044–1057.
- MCCONELL, S. H. *J. Chem. Phys.*, **1963**, *39*, 1910
- MCGREGOR, K. T.; WATKINS, N. T.; LEWIS, D. L.; DRAKE, R. F.; HODGSON, D. J.; HATFIELD, W. E. *Inorg. Nucl. Chem. Lett.*, **1973**, *9*, 423–428.
- MCKEE, V.; ZVAGULIS, M.; REED, C. A. *Inorg. Chem.* **1985**, *24*, 2914-2919.

- MEEK, S. T.; GREATHOUSE, J. A.; ALLENDORF, M. D. *Adv. Mat.*, **2011**, *23*, 249.
- MENGER, F. M. *Proc. Natl. Acad. Sci. U. S. A.*, **2002**, *99*, 4818–4822.
- MILLER, SR.; HERTAUX, D.; BAATI, T.; HORCAJADA, P.; GRENECHE, JM.; SERRE, C. *Chem. Commun.* **2010**, *46*, 4526–4528.
- MOELLMERA, J.; MOELLERA, A.; DREISBACH, F.; GLAESER, R.; STAUDT, R. *Micr. and Mes. Mat.* **2011**, *138*, 140–148.
- MONDAL, K. C.; MEREACRE, V.; KOSTAKIS, G. E.; LAN, Y.; ANSON, C. E.; PRISECARU, I.; POWELL, A. K. *Chem. Eur. J.* **2015**, *21*, 10835–10842.
- MONDAL, K. C.; SUNDT, A.; LAN, Y.; KOSTAKIS, G. E.; WALDMANN, O.; UNGUR, L.; CHIBOTARU, L. F.; ANSON, C. E.; POWELL, A. K. *Angew. Chem., Int. Ed.* **2012**, *51*, 7550–7554.
- MONTNEY, M. R.; LADUCA, R. L. *Inorg. Chem. Comm.*, **2007**, *10*, 1518–1522.
- NAKAMOTO, K. Infrared and Raman spectra of inorganic and coordination compounds; *John Wiley & Sons: New York*, **1997**.
- NARDELLI M., *J. Appl. Crystallogr.* **1999**, *32*, 563–571.
- NIEBING, S.; JANIAK, C. *Molecular Catalysis*, **2019**, *467*, 70–77.
- NISHIDA, Y.; KIDA, S. *J. Chem. Soc., Dalton Trans.* **1986**, 2633–2640.
- NIST X-ray Photoelectron Spectroscopy Database, Version 4.1 (National Institute of Standards and Technology, Gaithersburg, **2012**); <http://srdata.nist.gov/xps/>.
- O'KEEFFE, M.; YAGHI, O. M. *Chem. Rev.* **2012**, *112*, 675.
- OHRSTROM, L.; LARSSON, K. *Molecular Based Materials: The Structural Network Approach*; Elsevier: Amsterdam, **2005**.
- ORIVE, J.; FERNÁNDEZ DE LUIS, R.; RODRÍGUEZ FERNÁNDEZ, J.; LEGARRA, E.; PLAZAOLA, F.; ARRIORTUA, M. I. *CrystEngComm* **2014**, *16*, 6066–6079.
- PANELLA, B.; HIRSCHER, M.; PÜTTER, H.; MÜLLER, U. *Adv. Funct. Mater.* **2006**, *16*, 520–524.
- PANUNTO, T. W.; URBANCZYK-LIPKOWSKA, Z.; JOHNSON, R.; ETTER, M. C. *J. Am. Chem. Soc.* **1987**, *109*, 7786–7797.
- PASÁN, J.; SANCHIZ, J; RUIZ-PÉREZ, C; CAMPO, J; LLORETD, F; JULVED, M. *Chem. Commun.*, **2006**, *27*, 2857–2859.
- PASCUAL-COLINO, J.; BEOBIDE, G.; CASTILLO, O.; DA SILVA, I.; LUQUE, A.; PÉREZ-YÁÑEZ, S. *Cryst. Growth Des.* **2018**, *18*, 3465–3476.
- PASCUAL-COLINO, J.; BEOBIDE, G.; CASTILLO, O.; LODEWYCKX, P.; LUQUE, A.; PÉREZ-YÁÑEZ, S., ROMÁN, P.; VELASCO, L. F. *J. Inorg. Biochem.* **2020**, *202*, 110865.
- PASINI, A.; DEMARTIN, F.; PIOVESANA, O.; CHIARI, B.; CINTI, A.; CRISPU, O. *J. Chem. Soc., Dalton. Trans.*, **2000**, 3467.
- PAUL, A.K.; SANYAL, U.; NATARAJAN, S., *Crystal Growth & Desing*, **2010**, *10*, 4161–4175.

- PAUNOVIC, O.; PAP, S.; MALETIC, S.; TAGGART, M.A.; BOSKOVIC, N.; SEKULIC, M.T. *J. Colloid. Interf. Sci.*, **2019**, *547*, 350-360.
- PÉREZ-AGUIRRE, R.; BEOBIDE, G.; CASTILLO, O.; DE PEDRO, I.; LUQUE, A.; PÉREZ-YÁÑEZ, S.; RODRÍGUEZ FERNÁNDEZ, J.; ROMÁN, P. *Inorg. Chem.* **2016**, *55*, 7755–7763.
- PEREZ-TEMPRANO, M. H.; CASARES, J. A.; ESPINET, P. *Chem. Eur. J.* **2012**, *18*, 1864–1884.
- PÉREZ-YAÑEZ, S.; BEOBIDE, G.; CASTILLO, O.; CEPEDA, J.; GARCÍA-TERÁN, J.P.; LUQUE, A.; AGUAYO, A.T.; A.; ROMÁN, P. *Inorg. Chem.*, **2011**, *50*, 5330–5332.
- PÉREZ-YAÑEZ, S.; BEOBIDE, G.; CASTILLO, O.; CEPEDA, J.; LUQUE, A.; ROMÁN, P. *Crystal Growth & Desing.*, **2012**, *12*, 3324–3334.
- PÉREZ-YÁÑEZ, S.; BEOBIDE, G.; CASTILLO, O.; CEPEDA, J.; LUQUE, A.; ROMÁN, P. *Cryst. Growth Des.* **2013**, *13*, 3057-3067.
- PÉREZ-YÁÑEZ, S.; CASTILLO, O.; CEPEDA, J.; GARCÍA-TERÁN, J. P.; LUQUE, A.; ROMÁN, P. *Eur. J. Inorg. Chem.* **2009**, 3889-3899.
- PÉREZ-YAÑEZ, S.; CASTILLO, O.; CEPEDA, J.; GARCÍA-TERÁN, J.P.; LUQUE, A.; ROMÁN, P. *Inorg. Chem. Acta*, **2011**, *365*, 211–219.
- PHAN, A.; CZAJA, A. U.; GÁNDARA, F.; KNOBLER, C. B.; YAGHI, O. M. *Inorganic Chemistry*, **2011**, *50*, 7388-7390
- PRETSCH, E.; BÜHLMANN, P.; BADERTSCHER, M. *Structure Determination of Organic Compounds*, Ed. 4th, Springer, **2009**.
- PRINS, L. J.; HUSKENS, J.; DE JONG, F.; TIMMERMAN, P.; REINHOUDT, D. N. *Nature*, **1999**, *398*, 498–502.
- PRIZANT, L.; OLIVIER, M.J.; RIVEST, R.; BEAUCHAMP, A.L. *Acta Crystallogr.* **1982**, *B38*, 88.
- QI, Y.-J.; ZHAO, D.; LI, X.-X.; MA, X.; ZHENG, W.-X.; ZHENG, S.-T. *Cryst. Growth Des.*, **2017**, *17*, 1159–1165.
- RABONE, J.; YUE, Y. F.; CHONG, S. Y.; STYLIANOU, K. C.; BACSA, J.; BRADSHAW, D.; DARLING, G. R.; BERRY, N. G.; KHIMYAK, Y. Z.; GANIN, A. Y.; WIPER, P.; CLARIDGE, J. B.; ROSSEINSKY, M. J. *Science*, **2010**, *329*, 1053–1057.
- RAMIREZ, A. P. *Annu. Rev. Mater. Sci.* **1994**, *24*, 453-480.
- RAP, V. M.; MANOHAR, H. *Inorg. Chim. Acta* **1979**, *34*, L213.
- REN, Y.-W.; LIANG, J.-X.; LU, J.-X.; CAI, B.-W.; SHI, D.-B.; QI, C.-R. JIANG, H.-F.; CHEN, J.; ZHENG, D. *Eur. J. Inorg. Chem.* **2011**, *28*, 4369–4376.
- RIOU, D.; FERREY, G. *J. Mater. Chem.*, **1998**, *8*, 2733–2735.
- RODRIGUEZ, HS.; HINESTROZA, JP.; OCHOA-PUENTES, C.; SIERRA, CA.; SOTO, CY. *J. Appl. Polym. Sci.* **2014**, *131*, 40815.
- RODRÍGUEZ-FORTEA, A. ALEMANY, P.; ALVAREZ, S.; RUIZ, E. *Chem. Eur. J.* **2001**, *7*, 627.
- ROJAS, S.; DEVIC, T.; HORCAJADA, P. *J. Mater. Chem. B*, **2017**, *5*, 2560–2573.

- ROWSELL, J. L.C.; YAGHI, O. M. *Micropor. Mesopor. Mat.* **2004**, *73*, 3.
- ROWSELL, J.L.C.; YAGHI, O.M. *J. Am. Chem. Soc.* **2006**, *128*, 1304–1315.
- RUI, F.; FEI-LONG, J.; MING-YAN, W.; LIAN, C.; CHUN-FENG, Y.; MAO-CHUN, H.; *Cryst. Growth Des.* **2010**, *10*, 2306–2313.
- RUIZ, E.; ALEMANY, P.; ALVAREZ, S.; CANO, J. *J. Am. Chem. Soc.* **1997**, *119*, 1297–1303.
- RUIZ, E.; CIRERA, J.; CANO, J.; ALVAREZ, S.; LOOSE, C.; KORTUS, J. *Chem. Comm.* **2008**, *44*, 52–54.
- RUIZ, E.; RODRIGUEZ-FORTEA, A.; ALVAREZ, S. *Inorg. Chem.*, **2003**, *42*, 4881.
- S. KITAGAWA, S. MATSUYAMA, M. MUNAKATA, T. EMORI, *J. Chem. Soc. Dalton Trans.* **1991**, *11*, 2869–2874.
- SAHA, D.; SEN, R.; MAITY, T.; KONER, S. *Langmuir*, **2013**, *29*, 3140–3151.
- SAHA, D.; WEI, Z.; DENG, S.; *Int. J. Hydr. En.* **2008**, *33*, 7479–7488.
- SAJI, R.; PRASANA, J.; MUTHU, S.; GEORGE, J.; KURUVILLA, T.; RAAJARAMAN, B.R. *Spectrochimica Acta Part A*, **2020**, *226*, 117614.
- SANTOS, C. R.; M. B. B. M. FIGUEIRA, R.; M. PIEDADE, M. F.; P. DIOGO, H.; MINAS DA PIEDADE, M. E., *J. Phys. Chem. B* **2009**, *113*, 14291–14309.
- SCHERMAN, O. A. *Nat. Chem.*, **2009**, *1*, 524–525.
- SCHLESINGER, M.; SCHULZE, S.; HIETSCHOLD, M.; MEHRING, M. *Micropor. Mesopor. Mater.*, **2010**, *132*, 121.
- SEKI, K.; TAKAMIZAWA, S.; MORI, W. *Chem. Lett.* **2001**, *30*, 122–123.
- SENGUPTA, P.; SANDVIK, A. W.; SINGH, R. R. P. *Phys. Rev. B* **2003**, *68*, 094423.
- SHANNON, R.D.; *Acta Cryst.*, **1976**, *32*, 751-767.
- SHARPLES, J. W.; COLLISON, D.; MCINNES, E. J.; SCHNACK, J.; PALACIOS, E.; EVANGELISTI, M. *Nature Commun.* **2014**, *5*, 1-6.
- SHELDRIK, G. M. *Acta Crystallogr.* **2008**, *A64*, 112-122.
- SHINODA, K.; SHINODA, W.; LIEW, C.C.; TSUZUKI, S.; MORIKAWA, Y.; MIKAMI, M. *Surface Science*, **2004**, *556*, 109–120.
- SHORES, M. P.; NYTKO, E. A.; BARTLETT, B. M.; NOCERA, D. G. *J. Am. Chem. Soc.* **2005**, *127*, 13462-13463.
- SON, K.; KIM, J. Y.; SCHÜTZ, G.; KANG, S. G.; MOON, H. R.; OH, H.; *Inorg. Chem.* **2019**, *58*, 8895–8899.
- SONNENFROH, D.; KREILICK, R. W. *Inorg. Chem.* **1980**, *19*, 1259-1262.
- SOPHIA, C.A.; LIMA, E.C. *Ecotoxicology and environmental safety*, **2018**, *150*, 1–17.
- SPEK, A. L. *Acta Crystallogr.* **2009**, *D56*, 148.

- SPEK, A. L. *Acta Crystallogr., Sect. D*, **2009**, *65*, 148–155.
- SPOKOYNY, A. M.; KIM, D.; SUMREIN, A.; MIRKIN, C. A. *Chem. Soc. Rev.* **2009**, *38*, 1218–1227.
- STANG, P.J.; OLENYUK, B. *Acc. Chem. Res.*, **1997**, *30*, 502–518.
- STEIN, A.; KELLER, S. W.; MALLOUK, T. E. *Science*, **1993**, *259*, 1558–1563.
- STYLIANOU, K.C.; WARREN, J.E.; CHONG, S.Y.; RABONE, J.; BASCA, J.; BRADSHAW, D.; ROSSEINSKY, M.J. *Chem. Comm.*, **2011**, *47*, 3389–3391.
- SUAREZ-VARELA, J.; MOTA, A. J.; AOURYAGHAL, H.; CANO, J.; RODRIGUEZ-DIEGUEZ, A.; LUNEAU, D.; COLACIO, E. *Inorg. Chem.* **2008**, *47*, 8143–8158.
- SUN, W.; LI, H.; LI, H.; LI, S.; CAO, X. *Chem. Eng. J.*, **2019**, *360*, 645–653.
- SWEYGERS, N.; ALEWATERS, N.; DEWIL, R.; APPELS, L., *Scientific Reports*, **2018**, *8*, 7719.
- TERCERO, J.; RUIZ, E.; ALVAREZ, S.; RODRÍGUEZ-FORTEA, A.; ALEMANY, P. *J. Mater. Chem.* **2006**, *16*, 2729–2735.
- THI DANG, Y.; TRUNG HOANG, H.; CAO DONG, H.; THI BUI, K.-B.; HO THUY NGUYEN, L.; BACH PHAN, T.; KAWAZOE, Y.; LE HOANG DOAN, T. *Micr. Meso. Mat.*, **2020**, *298*, 110064.
- THOMAS-GIPSON, J.; BEOBIDE, G.; CASTILLO, O.; FRÖBA, M.; HOFFMANN, F.; LUQUE, A.; PÉREZ-YÁÑEZ, S.; ROMÁN, P., *Cryst. Growth Des.* **2014**, *14*, 4019–4029.
- THOMAS-GIPSON, J.; BEOBIDE, G.; CASTILLO, O.; LUQUE, A.; PASCUAL-COLINO, J.; PÉREZ-YÁÑEZ, S.; ROMÁN, P., *Cryst. Eng. Comm.* **2018**, *20*, 2528–2539.
- THOMAS-GIPSON, J.; PEREZ-AGUIRRE, R.; BEOBIDE, G.; CASTILLO, O.; LUQUE, A.; PEREZ-YÁÑEZ, S.; ROMAN, P. *Cryst. Growth Des.* **2015**, *15*, 975–983.
- THOMPSON, A. M. W. GATTESCHI, D.; MCCLEVERTY, J.A.; NAVAS, J.A.; RENTSCHLER, E.; WARD, M.D. *Inorg Chem.*, **1996**, *35*, 2701.
- TIAN, Y.-Q.; ZHAO, Y.-M.; CHEN, Z.-X.; ZHANG, G.-N.; WENG, L.-H.; ZHAO, D.-Y. *Chem. Eur. J.*, **2007**, *13*, 4146.
- TOKAY, N.; ÖGRETIR, C. *J. Mol. Struct. (Theochem)*. **2002**, *594*, 185–197.
- TOMIC, E.A. *J. Appl. Polym. Sci.*, **1965**, *9*, 3745–3752.
- TOPOS Main Page. <http://www.topos.ssu.samara.ru> (accessed Jan. **2015**).
- UHL, W.; STEFANIAK, C.; VO, M.; LAYH, M.; ROGEL, F.; KOSTERS, J. *Z. Anorg. Allg. Chem.* **2015**, *641*, 253.
- VALTCHEV, V.; MINTOVA, S.; TSAPATSI, M. *Ordered Porous Solids, Recent Advances and Prospects*, Elsevier Science, **2009**.
- VALVEKENS, P.; VANDICHEL, M.; WAROQUIER, M.; VAN SPEYBROECK, V.; DE VOSA, D. *Journal of Catalysis*, **2014**, *317*, 1–10.
- VALVEKENS, P.; VERMOORTELE, F.; VOS, D. D. *Catal. Sci. Technol.* **2013**, *3*, 1435–1445.
- VAN DE VONDEL, D.F.; WUYTS, L.F.; VAN DER KELEN, G.P.; BEVERNAGE, L. *J. Electron Spectrosc. Relat. Phenom.*, **1977**, *10*, 389.

- VAN DER SLUIS, P.; SPEK, A. L. *Acta Crystallogr., Sect. A*, **1990**, *46*, 194–201.
- VAN NIEKERK, J. N.; SCHOENING, F. R. L. *Acta Crystallogr.* **1953**, *6*, 227.
- VAN VLECK, J.H, Physics, Nobel Lecture World Scientific Publishing Co., Singapore, **1992**.
- VANE, J. R.; BOTTING, R. M. *Am. J. Med.* **1998**, *104*, 2S–8S.
- VANNERBERG, N.G. *Chem. Scr.*, **1976**, *9*, 122.
- VERMA, S.; MISHRA, A. K.; KUMAR, J. *Acc. Chem. Res.* **2010**, *43*, 79–91.
- VERMA, S.; MISHRA, A.K.; KUMAR, J., *Acc. Chem. Res.*, **2009**, *43*, 79–91.
- WANG, F.; TAN, Y.-X.; YANG, H.; ZHANG, H.-X.; KANG, Y.; ZHANG, J., *Chem. Comm.*, **2011**, *47*, 5828–5830.
- WANG, X.G.; DONG, Z.Y.; CHENG, H.; WAN, S.S.; CHEN, W.H.; ZOU, M.Z.; HUO, J.W.; DENG, H.X.; ZHANG, X.Z. *Nanoscale*, **2015**, *7*, 16061.
- WANG, Z.; COHEN, S. M. *Chem. Soc. Rev.* **2009**, *38*, 1315.
- WAYU, M. B.; KING, J. E.; JOHNSON, J. A.; CHUSUEI, C. C. *Electroanalysis*, **2015**, *27*, 2552–2558.
- WERNER, U.; CHRISTINA, S.; MATTHIAS, V.; MARCUS, L.; FRIEDHELM, R.; JUTTA, K. *Z. Anorg. Allg. Chem.* **2015**, *641*, 253–260.
- WU, X.; BAO, Z.; YUAN, B.; WANG, J.; SUN, Y.; LUO, H.; DENG, S. *Micr. Meso. Mat.*, **2013**, *180*, 114–122.
- WYSS-CORAY, T.; MUCKE, L. *Nat. Med.* **2000**, *6*, 973–974.
- XU, Z.; ZHAO, G.; ULLAH, L.; WANG, M.; WANG, A.; ZHANG, Y.; ZHANG, S. *RSC Adv.*, **2018**, *8*, 10009–10016.
- YAGHI, O. M.; LI, H.; DAVIS, C.; RICHARDSON, D.; GROU, T. L. *Acc. Chem. Res.*, **1998**, *31*, 474–484.
- YAGHI, O. M.; O'KEEFFE, M.; KANATZIDIS, M. G. *J. Solid State Chem.*, **2000**, *152*, 1–2.
- YAGHI, O. M.; O'KEEFFE, M.; OCKWIG, N. W.; CHAE, H. K.; EDDAOUDI, M.; KIM, J. *Nature*, **2003**, *423*, 705.
- YAGHI, O.M.; LI, H.L. *J. Am. Chem. Soc.*, **1995**, *117*, 10401–10402.
- YAMANAKA, M.; UEKUSA, H.; OHBA, S.; SAITO, Y.; IWATA, S.; KATO, M.; TOKII, T.; MUTO, Y.; STEWARD, O. W. *Acta Crystallogr.* **1991**, *B47*, 344.
- YANG, E.-C.; ZHAO, H.-K. FENG, Y.; ZHAO, X.J. *Inorg. Chem.*, **2009**, *48*, 3511–3513.
- YAOUANC, A.; DALMAS DE REOTIER, P.; GLAZKOV, V.; MARIN, C.; BONVILLE, P.; HODGES, J. A.; GUBBENS, P. C. M.; SAKARYA, S.; BAINES, C. *Phys. Rev. Lett.* **2005**, *95*, 047203.
- YOUNGME, S.; CHEANSIRISOMBOON, A.; DANVIRUTAI, C.; PAKAWATCHAI, C.; CHAICHIT, N.; ENKAGUL, C.; A. VAN ALBADA, G.; SANCHEZ-COSTA, J.; REEDIJK, J. *Polyhedron* **2008**, *27*, 1875.
- YUAN, G.; QIN, J.-S.; SU Z.-M.; SHAO, K.-Z.; FU, Y.-M. *Acta Cryst.* **2008**, *64*, m389-390.

- ZACHER, D.; SHEKHAH, O.; WÖLL, C.; FISCHER, R. A. *Chem. Soc. Rev.* **2009**, *38*, 1418.
- ZAYED, M.; HAWASH, M.; EL-DESAWY, M.; EL-GIZOULI, A. *Arabian Journal of Chem.*, **2017**, *10*, 351–359.
- ZAYED, M.; HAWASH, M.; FAHMEY, M.; EL-GIZOULI, A. *J. Therm. Anal. Calorim.*, **2012**, *108*, 315–322.
- ZHANG, Y., *Emerging Chemicals and Human Health*, Ed.; Springer: Singapore, **2019**.
- ZHAO, S.-N.; SONG, X.-Z.; SONG, S.-Y.; ZHANG, H.-J. *Coord. Chem. Rev.* **2017**, *337*, 80–96.
- ZHENG, L. M; GAO, S; SONG, H.-H; DECURTINS, S; JACOBSON, A. J; *Xin Chem. Mater.*, **2002**, *14*, 7, 3143-3147.
- ZHENG, Y. Z.; TONG, M. L.; XUE, W.; ZHANG, W. X.; CHEN, X. M.; GRANDJEAN, F.; LONG, G. J. *Angew. Chem.* **2007**, *119*, 6188-6192.
- ZHU, L.; LIU, X.-Q.; JIANG, H.-L.; SUN, L.-B. *Chem. Rev.* **2017**, *117*, 8129–8176
- ZUBIETA, J.: *Comprehensive Coordination Chemistry II*, Elsevier Ltd, **2004**, *1*, 697.

Appendices

A.1. Chemicals

A.2. Instrumental techniques

A.3. Thermal ellipsoid plot representations

A.4. XPS analysis

A.5. Magnetic fitting models

A.6. Magnetization curves of compounds of chapter 3

A.7. Publications arising from this work

A.1. CHEMICALS

All chemicals employed for the synthesis of the compounds were of reagent grade and used as commercially obtained. Tables A.1.1 and A.1.2 gather the reactants, formula, commercial supplier (CS), assay (AS), molecular weight (MW), Chemical Abstracts Service number (CAS), and risk (R) and safety (S) statements for their manipulation.

Table A.1.1. Employed reactants.

Name	Formula	CS	AS	M.W. (g/mol)	CAS	R	S
Chromium(III) sulfate monohydrate	$\text{Cr}_2(\text{SO}_4)_3 \cdot \text{xH}_2\text{O}$	Aldrich	≥98%	392.18	15244–38–9	36/37/38	24/25
Cobalt(II) sulfate heptahydrate	$\text{CoSO}_4 \cdot 7\text{H}_2\text{O}$	Aldrich	≥95%	281.10	10026–24–1	22/42–43/49/50–53/60/68	45/53/60–61
Copper(II) sulfate pentahydrate	$\text{CuSO}_4 \cdot 5\text{H}_2\text{O}$	Aldrich	≥98%	249.69	7758–99–8	22–36/38–50/53	22–60–61
Manganese(II) sulfate monohydrate	$\text{MnSO}_4 \cdot \text{xH}_2\text{O}$	Aldrich	≥99%	169.02	10034-96-5	48/20/22–51/53	22/61
Methanol	CH_3OH	Scharlau	≥99%	32.04	67-56-1	11–23/24/25	7–16–36/37–45
Nickel(II) chloride	NiCl_2	Aldrich	≥98%	129.60	7718-54-9	23–25/38/42–43/49/50–53/61/68	45/53/60/61
Zinc(II) sulfate pentahydrate	$\text{ZnSO}_4 \cdot 5\text{H}_2\text{O}$	Aldrich	≥99%	251.53	7446–20–0	22/41/50–53	60–61

Table A.1.2. Employed ligands.

Name	Formula	CS	AS	M.W. (g/mol)	CAS	R	S
2–hydroxyquinoline–4–carboxylate acid	$\text{C}_{10}\text{H}_7\text{NO}_3$	Aldrich	≥97%	189.17	84906–81–0	36/37/38–22	26–36
4,4′–bipyridinethane	$\text{C}_{10}\text{H}_8\text{N}_2$	Aldrich	≥98%	156.18	553–26–4	25	22–24/25–37–45
6–hydroxynicotinic acid	$\text{C}_6\text{H}_5\text{NO}_3$	Aldrich	≥98%	139.11	5006–66–6	315/319	264/280/302/305/332/337/362
Adenine	$\text{C}_5\text{H}_5\text{N}_5$	Aldrich	≥99%	135.13	73–24–5	22	26–36
Aspirin	$\text{C}_9\text{H}_8\text{O}_4$	Aldrich	≥99%	180.16	50–78–2	302	301/312/330
DMF	$\text{C}_3\text{H}_7\text{NO}$	Scharlau		73.09	68–12–2	20/21/36/61	45/53
Ibuprofen	$\text{C}_{13}\text{H}_{18}\text{O}_2$	Aldrich	≥98%	206.28	15687–27–1	22/61	45/53
Naproxen sodium	$\text{C}_{14}\text{H}_{13}\text{O}_3\text{Na}$	Aldrich	≥98%	252.24	26159–34–2	22/61	45/53
Pyridine	$\text{C}_5\text{H}_5\text{N}$	Aldrich	≥99%	79.10	110–86–1	11–20/21/22/36/38–52	26–28
Triethylamine	$\text{C}_6\text{H}_{15}\text{N}$	Aldrich	≥99%	101.19	121–44–8	11–20/21/22–35	3–16–26–29–36/37/39–45

A.2. INSTRUMENTAL TECHNIQUES

A.2.1. Infrared spectroscopy

The IR spectra were recorded on a FTIR 8400S Shimadzu spectrometer of the Inorganic Department of the Science and Technology Faculty of the UPV/EHU in the 4000–400 cm^{-1} spectral region (Figure A.2.1). The measurements were made using the attenuated total reflection (ATR) technique with approximately using 3 mg of each compound. A spectrum correction was made in 2000–1000 cm^{-1} bands in order to palliate the background noise and be able to appreciate more precisely the IR spectra in this region.

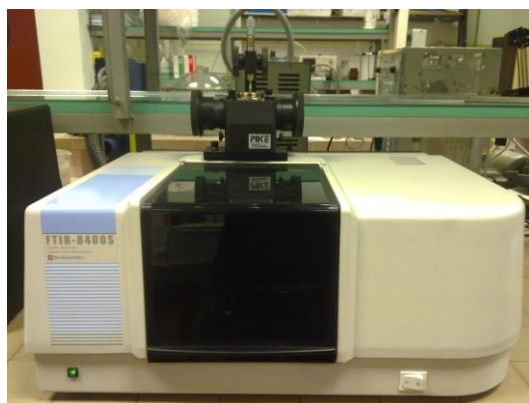


Figure A.2.1. FTIR 8400S Shimadzu spectrophotometer.

A.2.2. Thermal analysis

The thermogravimetric studies (TG, DTG, and DTA) were carried out in a METTLER TOLEDO TGA/SDTA851 thermal analyser of the Inorganic Department of the Science and Technology Faculty of the UPV/EHU (Figure A.2.2). The measures were performed in an atmosphere of synthetic air (79% N_2 / 21% O_2) with a flow rate of 150 $\text{cm}^3 \text{min}^{-1}$, between 25 and 600 or 800 $^\circ\text{C}$, with a heating rate of 5 $^\circ\text{C} / \text{min}$.



Figure A.2.2. METTLER TOLEDO TGA/SDTA851 thermal analyser.

A.2.3. Elemental analyses

Elemental analyses (C, H, N) were performed on an Organic elemental Thermo Scientific Modelo FLASH 2000 microanalyser (Figure A.2.3A) provided by Burgos University,

whereas the metal content was determined by inductively coupled plasma (ICP–AES) performed on a Horiba Yobin Yvon Activa spectrometer (Figure A.2.3B), provided by the SGiker of the University of the Basque Country (UPV/EHU).

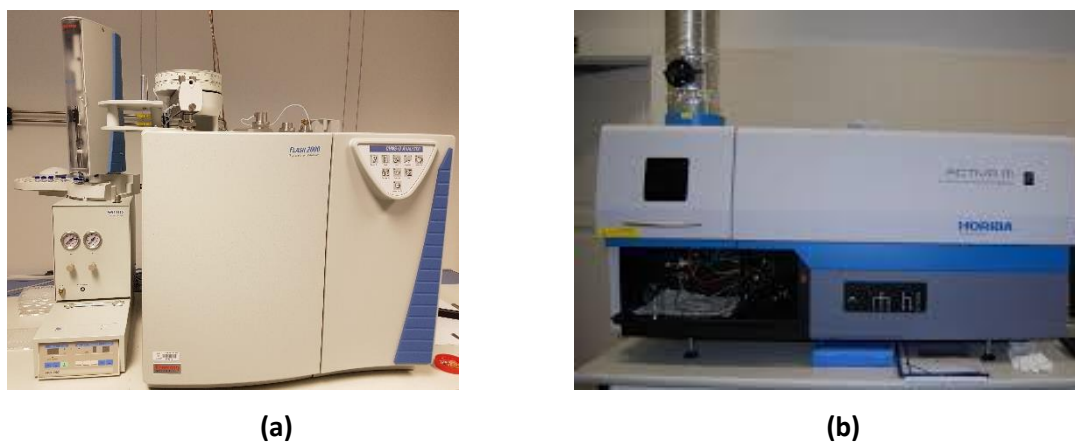


Figure A.2.3. Organic elemental Thermo Scientific Modelo FLASH 2000 microanalyser (A) and Horiba Yobin Yvon Activa spectrometer (B).

A.2.4. Single-crystal X-ray diffraction

The single crystal X-ray diffraction data collections were done at 293(2) K and at 100(2) K on an on an Agilent Technologies Supernova ($\lambda_{\text{Mo-K}\alpha} = 0.71073 \text{ \AA}$ and $\lambda_{\text{Cu-K}\alpha} = 1.5418 \text{ \AA}$) diffractometers of the SGiker of the UPV/EHU (Figure A.2.4).

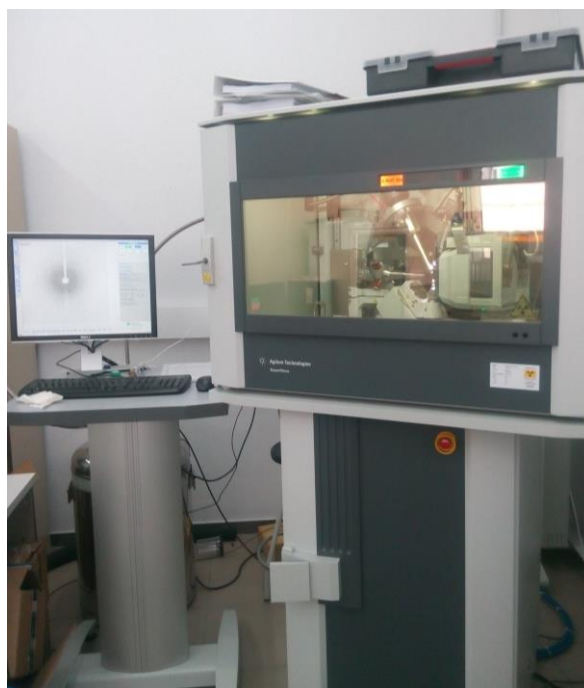


Figure A.2.4. Agilent Technologies Supernova diffractometer.

The data reduction was done with the CrysAlis PRO. Most of the structures were solved by direct methods using the SIR92 program^[111] and refined by full-matrix least-squares

on F2 including all reflections (SHELXL97),^[170] with all calculations performed using the WINGX crystallographic software package. The representation of the crystal structures has been made by MERCURY.^[171]

A.2.5. X-ray powder diffraction

The X-ray powder diffraction patterns were collected on a Phillips X'PERT powder diffractometer of the SGIKer of the UPV/EHU with Cu-K α radiation ($\lambda = 1.5418 \text{ \AA}$) over the range $5 < 2\theta < 50^\circ$ with a step size of 0.02° and an acquisition time of 2.5 s per step at $25 \text{ }^\circ\text{C}$ (Figure A.2.5). Indexation of the diffraction profiles were made by means of the FULLPROF program (pattern-matching analysis) on the basis of the space group and the cell parameters found for isostructural compounds by single crystal X-ray diffraction.



Figure A.2.5. Phillips X'PERT powder diffractometer.

A Bruker D8 Advance Vario powder diffractometer of the SGIKer of the UPV/EHU with Cu-K α 1 ($\lambda = 1.5406 \text{ \AA}$) was used to perform the variable-temperature X-ray powder diffraction measurements, heating the samples from room temperature with a heating rate of $5 \text{ }^\circ\text{C}\cdot\text{min}^{-1}$ and measuring a complete diffractogram every 20 or 30 $^\circ\text{C}$ as appropriate (Figure A.2.6).

¹⁷⁰ G. M. Sheldrick, *SHELXL97*, University of Göttingen, Göttingen, Germany, **1997**.

¹⁷¹ Macrae, C. F.; Sovago, I. S.; Cottrell, J.; Galek, P. T. A.; McCabe, P.; Pidcock, E.; Platings, M.; Shields, G. P.; Stevens, J. S.; Towler, M.; Wood, P. A.; *J. Appl. Cryst.*, **2020**, *53*,226–235.



Figure A.2.6. Bruker D8 Advance Vario powder diffractometer.

A.2.6. X-Ray Photoelectron Spectroscopy

X-Ray Photoelectron Spectroscopy (XPS) measurements were performed on a SPECS system (Berlin, Germany) equipped with Phoibos 150 1D-DLD analyser and Al K α monochromatic radiation source (1486.7 eV) (Figure A.2.7).



Figure A.2.7. SPECS system equipped with Phoibos 150 1D-DLD analyser.

A.3. THERMAL ELLIPSOID PLOT REPRESENTATIONS

All the compounds described below have been drawn using the MERCURY program.^[3] The ellipsoids are represented with a probability factor of 50%. Hydrogen atoms have been omitted for clarity.

A.3.1. Chapter 2

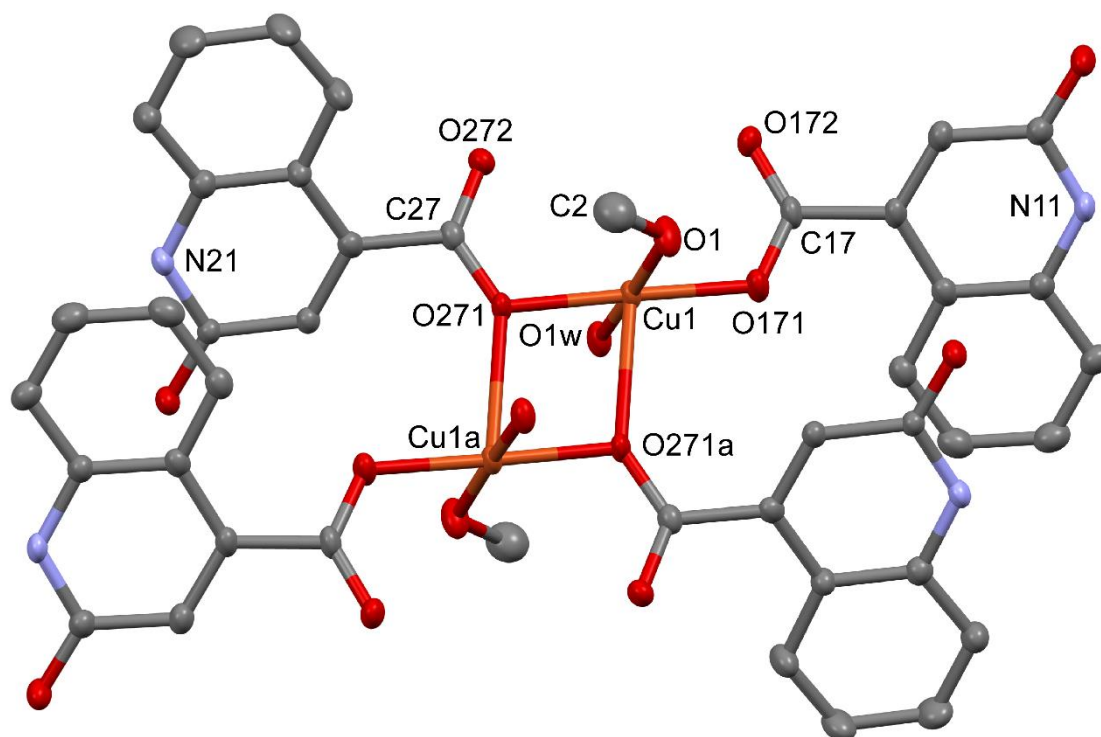


Figure A.3.1. Compound 0D-CuHQMEOH.

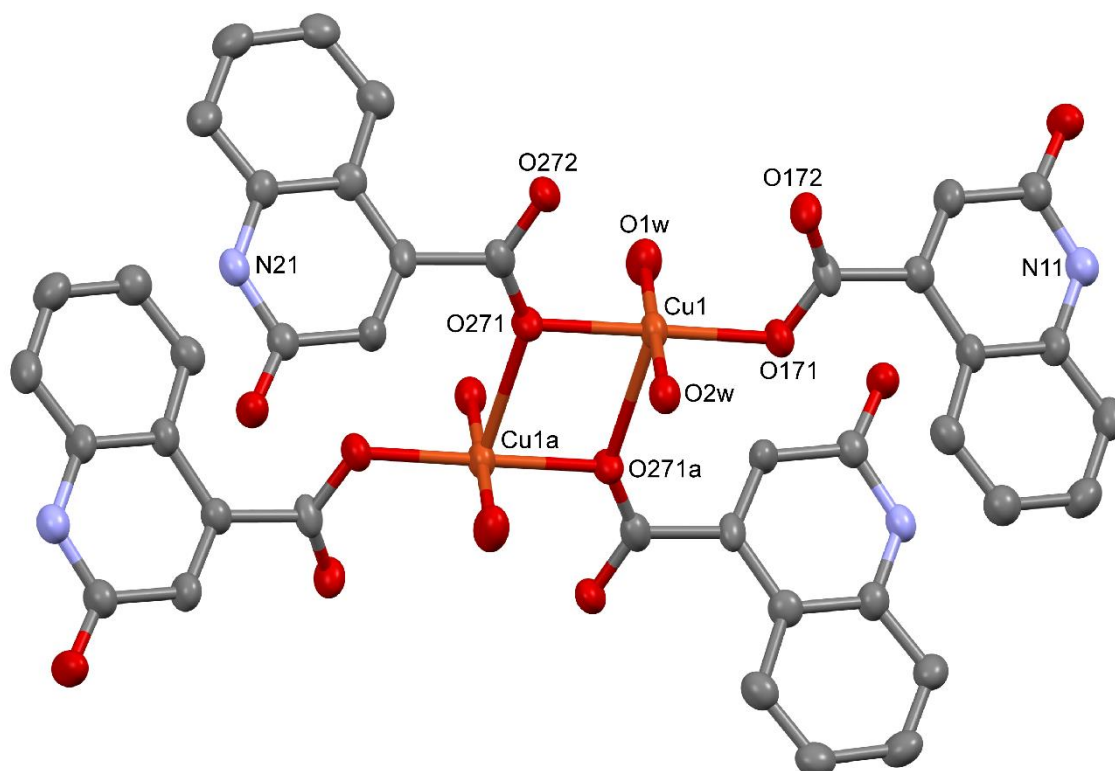


Figure A.3.2. Compound 0D-CuHQAQ.

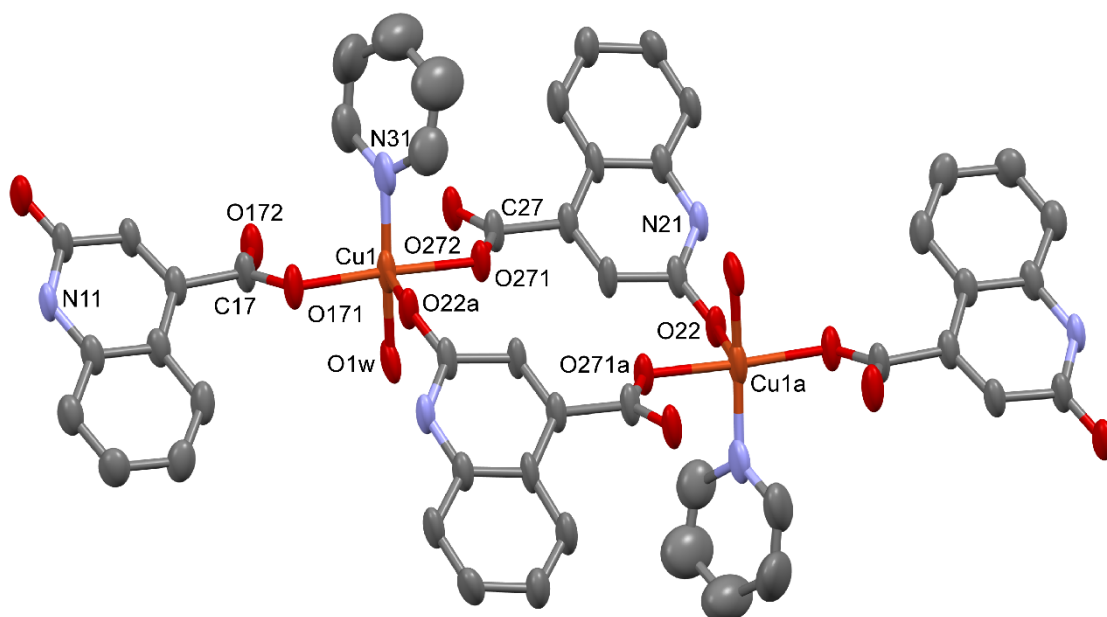


Figure A.3.3. Compound 0D-CuHQPY.

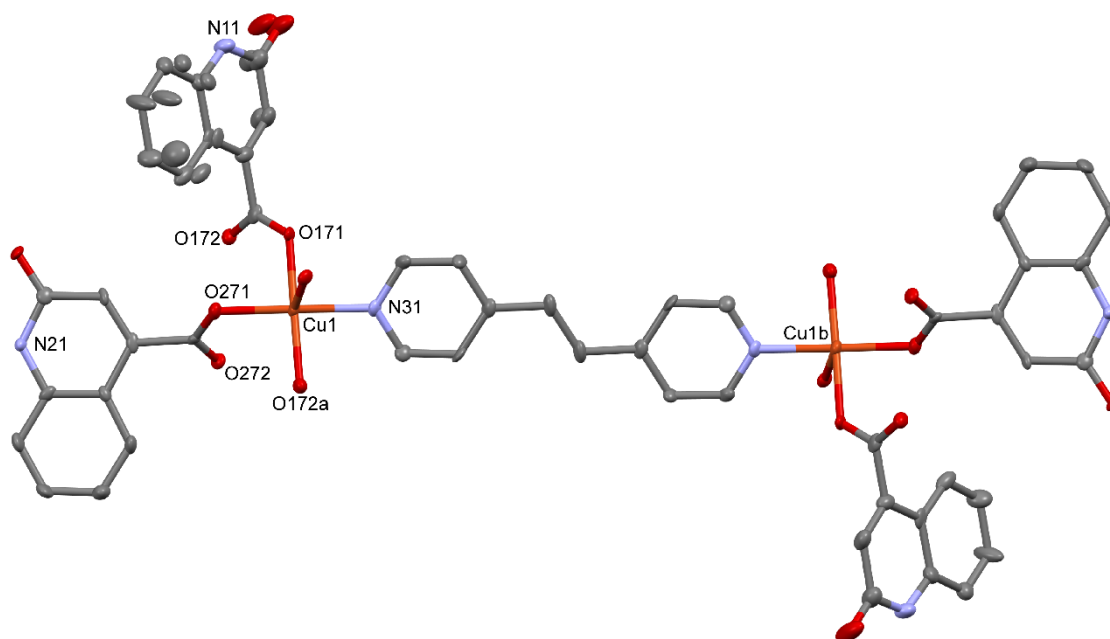


Figure A.3.4. Compound 2D-CuQBPA.

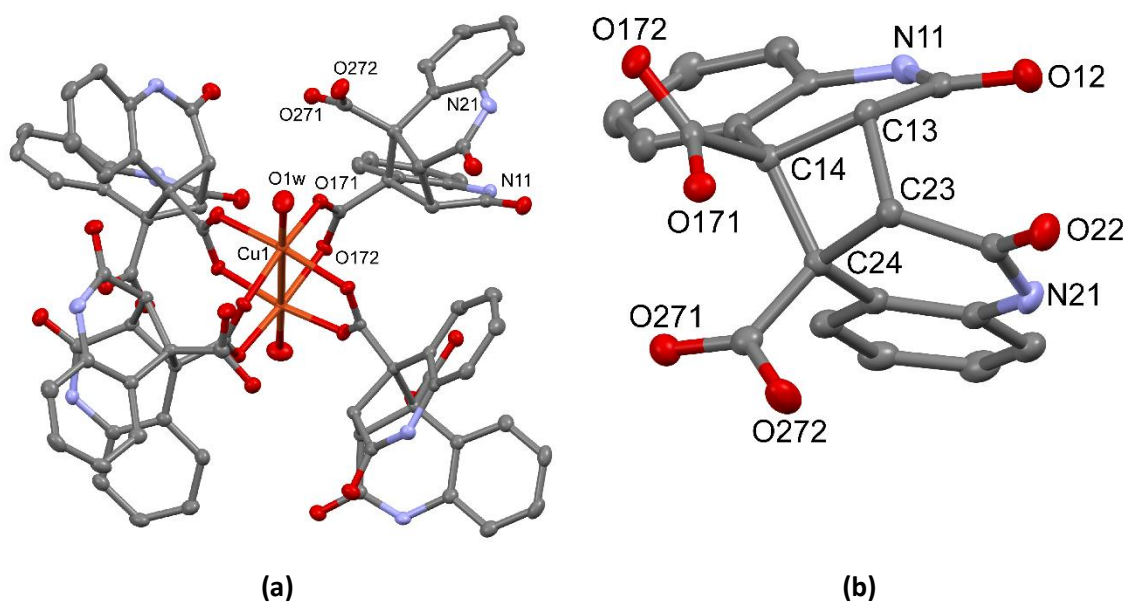


Figure A.3.5. Compound 0D-CuCBDQ (A) and the CBDQ ligand (B).

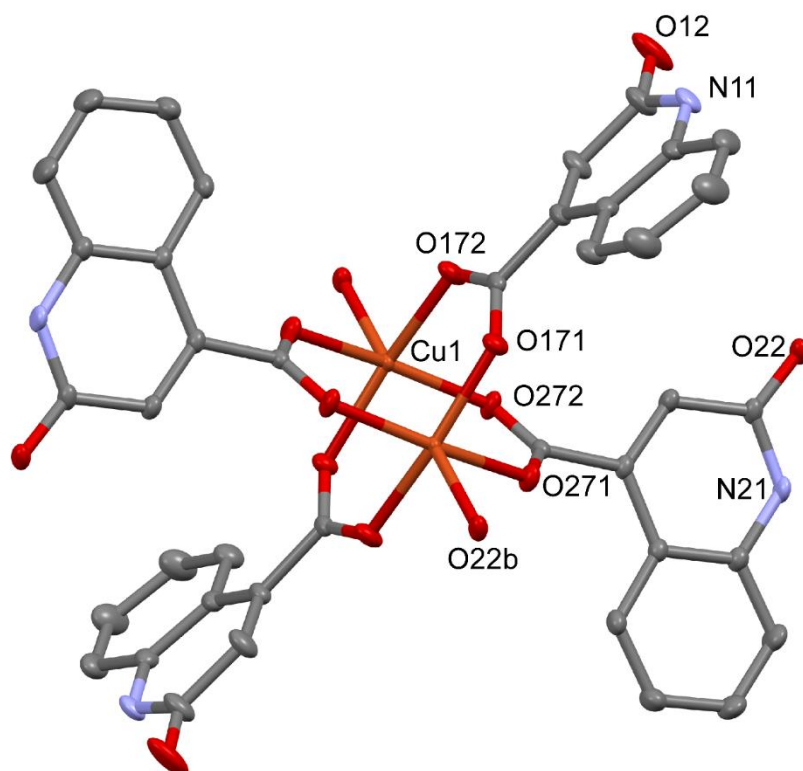
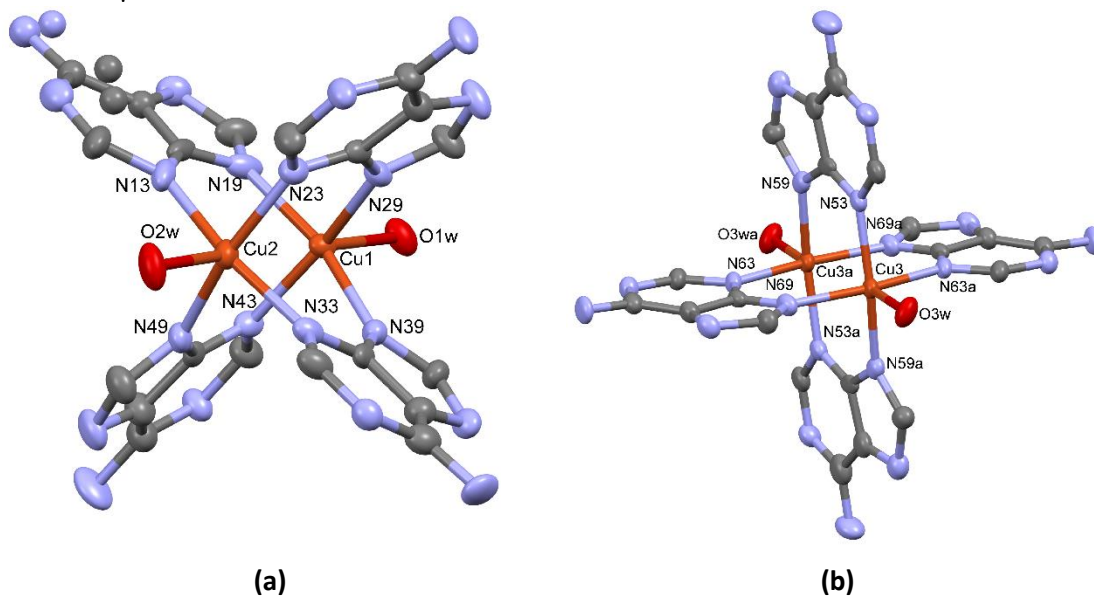
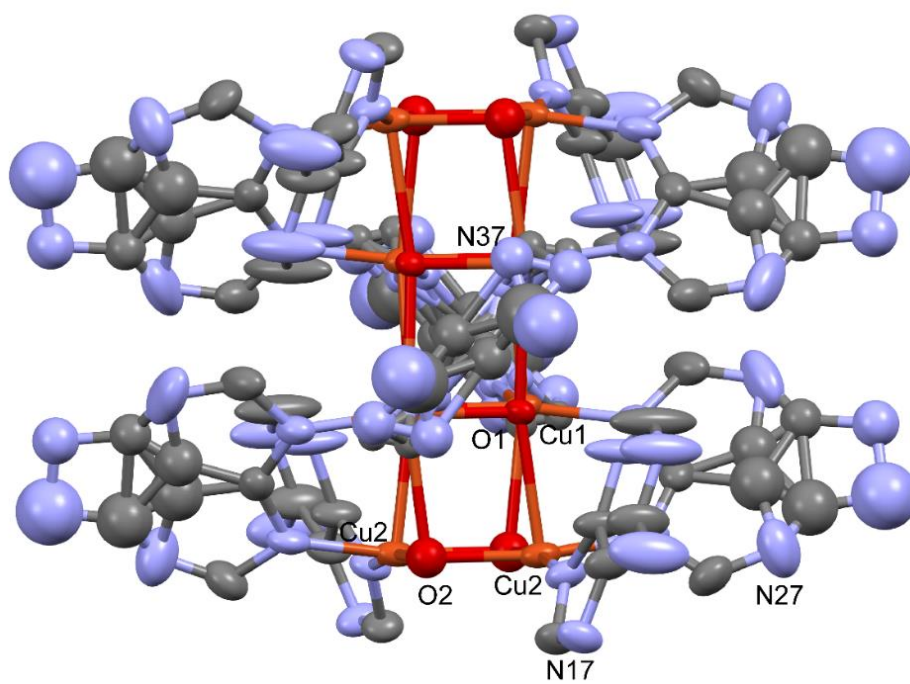


Figure A.3.6. Compound 1D-CuHQ.

A.3.2. Chapter 3

Figure A.3.7. Compound $\text{Cu}_2\text{ADSO}_4\text{NHET}_3$.Figure A.3.8. Compound Cu_8ADSO_4 .

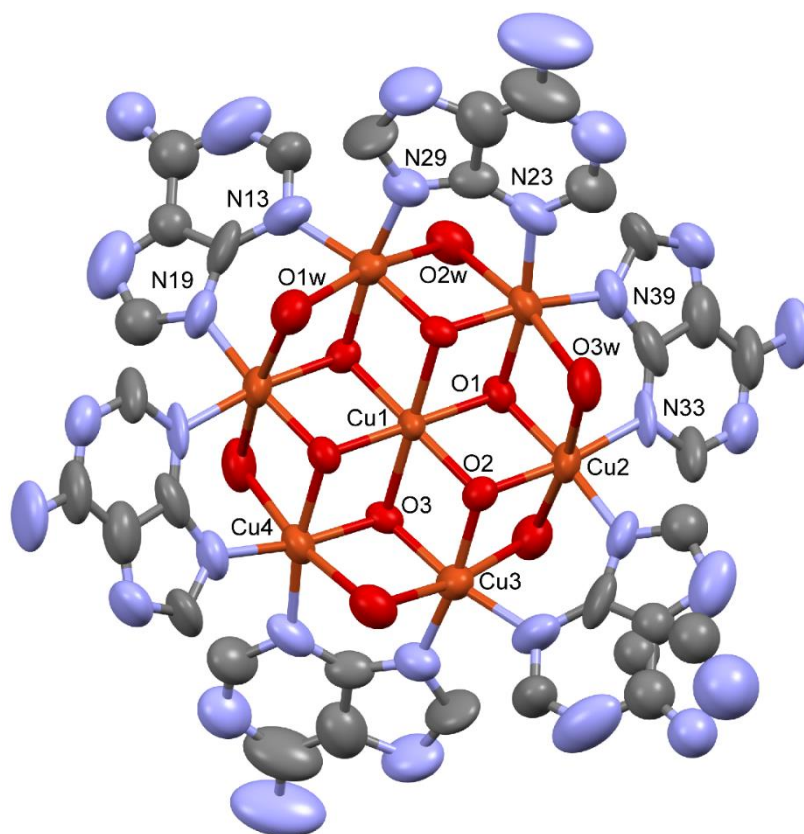


Figure A.3.9. Compound $\text{Cu}_7\text{ADSO}_4\text{NHt}_3\text{-1}$.

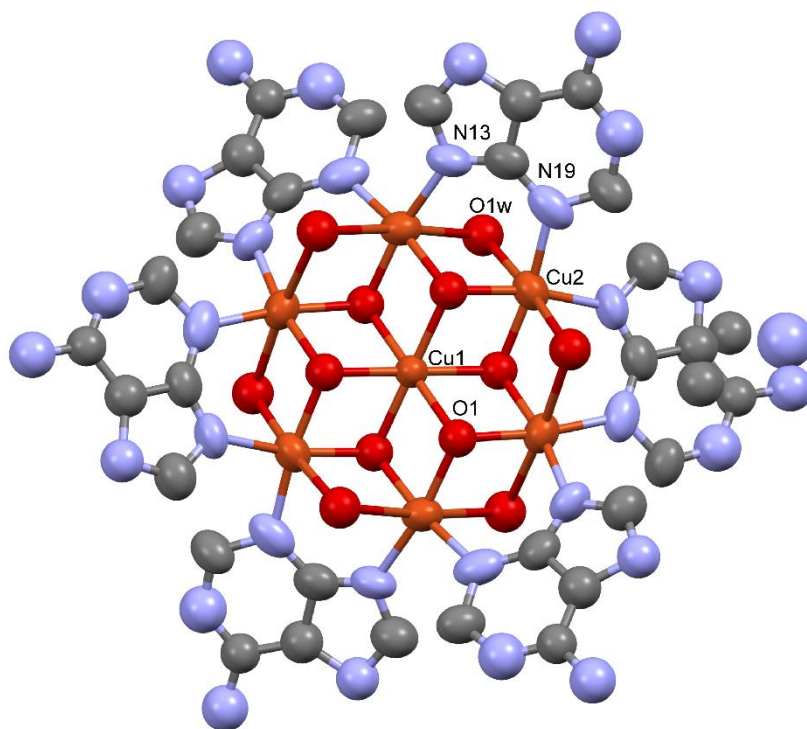


Figure A.3.10. Compound $\text{Cu}_7\text{ADSO}_4\text{NHt}_3\text{-2}$.

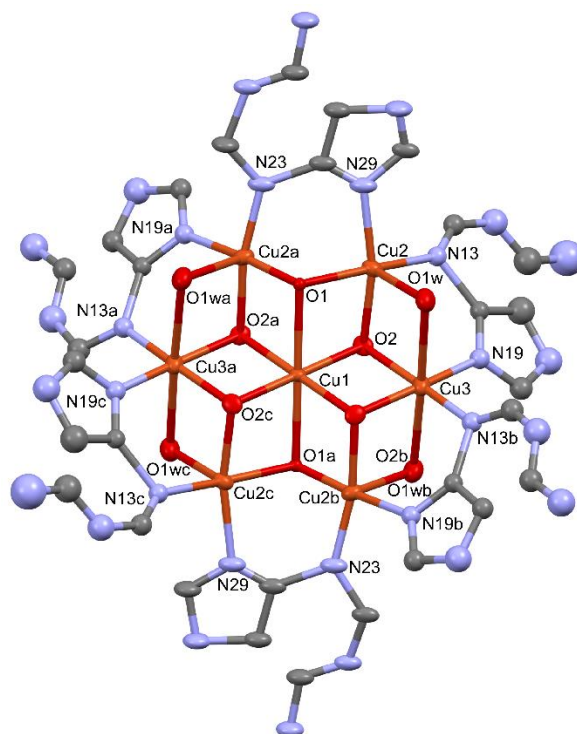


Figure A.3.11. Compound Cu_7ADSO_4 .

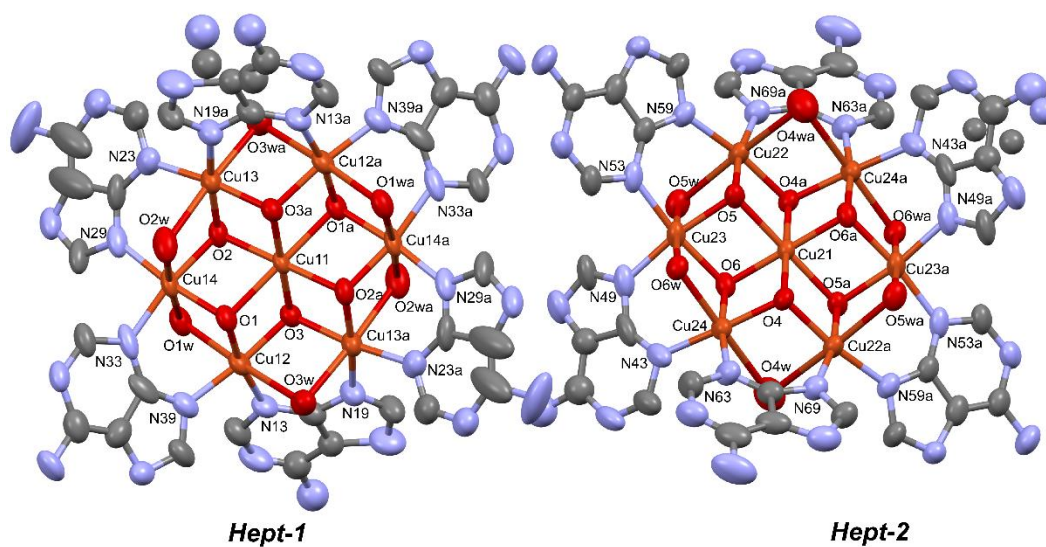


Figure A.3.12. Compound $\text{Cu}_7\text{ADSO}_4\text{HN-1}$.

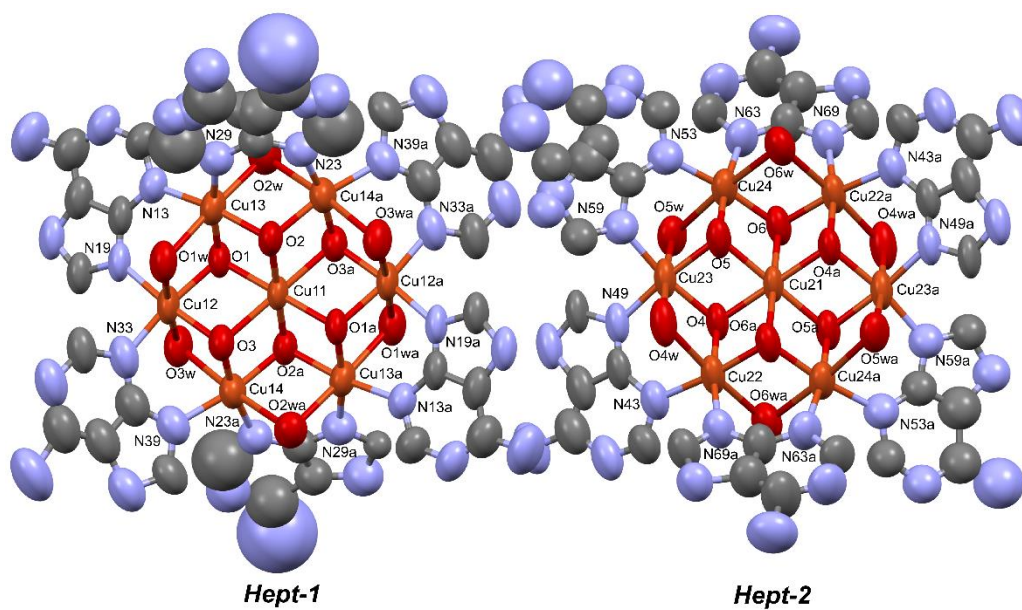


Figure A.3.13. Compound $\text{Cu}_7\text{ADSO}_4\text{HN-2}$.

A.3.3. Chapter 4

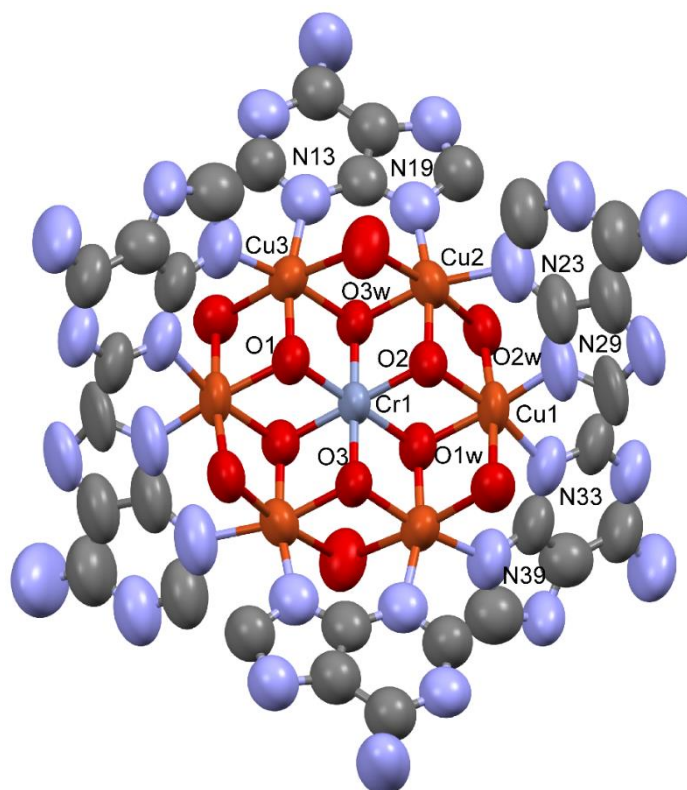


Figure A.3.14. Compound $\text{Cu}_6\text{CrADSO}_4$.

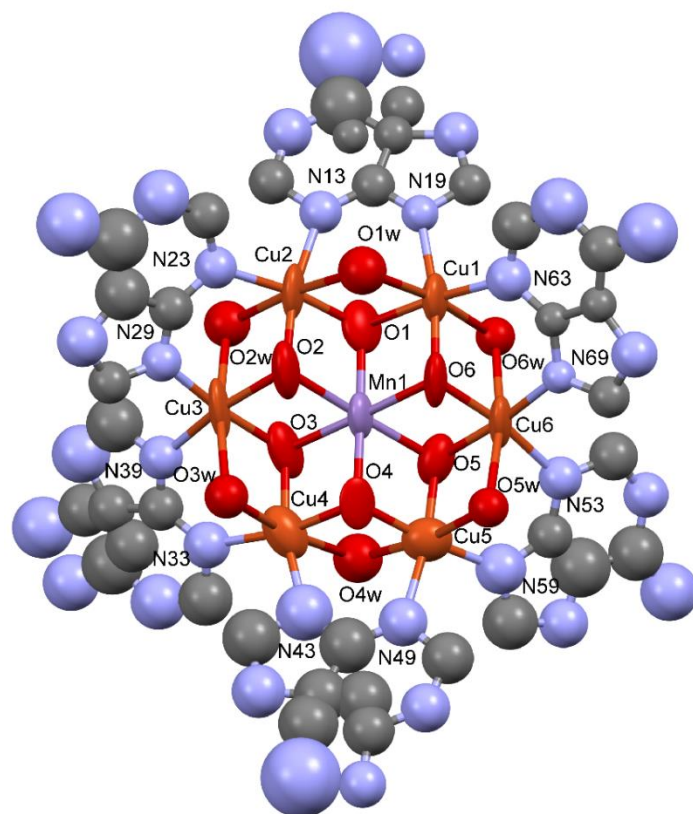


Figure A.3.15. Compound $\text{Cu}_6\text{MnADSO}_4$.

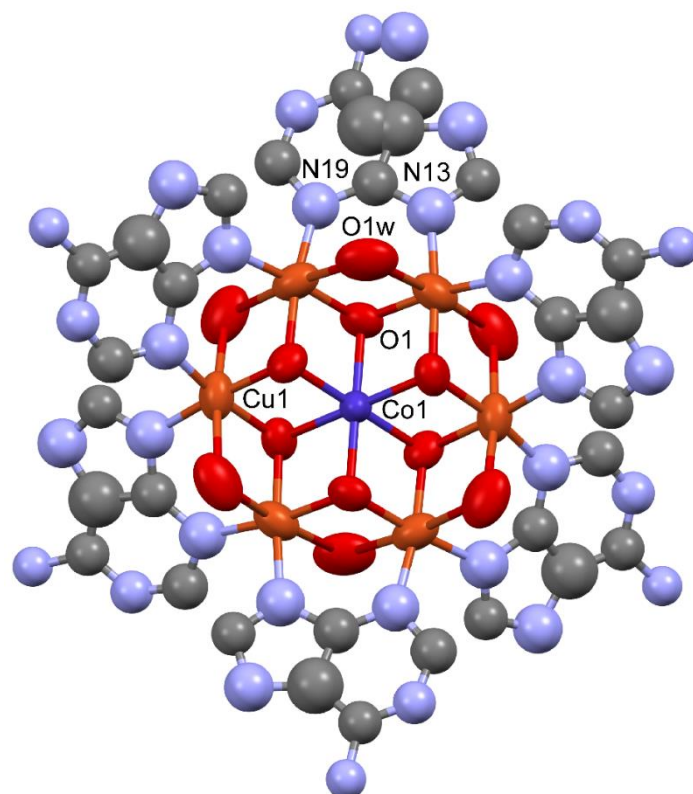


Figure A.3.16. Compound $\text{Cu}_6\text{CoADSO}_4$.

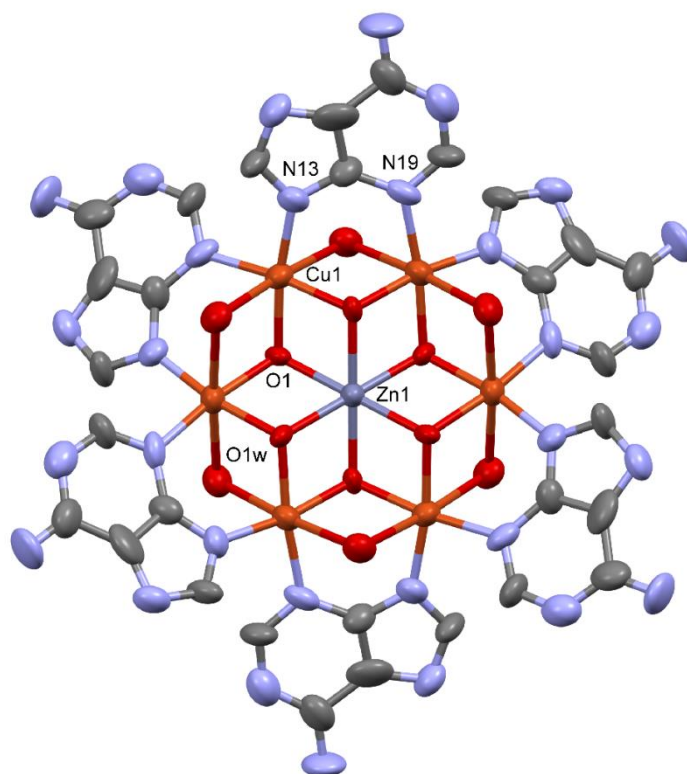


Figure A.3.17. Compound $\text{Cu}_6\text{ZnADSO}_4$.

A.4. XPS ANALYSIS

An initial analysis was carried out to determine the elements present (wide scan: step energy 1 eV, dwell time 0.1 s, pass energy 80 eV; X-ray source: Al anode) and detailed analyses of the detected elements were performed (detail scan: step energy 0.08 eV, dwell time 0.1 s, pass energy 30 eV) with an electron exit angle of 90 °. The spectra were adjusted using the CasaXPS 2.3.16 software, which models the Gauss-Lorentzian contributions, after a subtraction of the background (Shirley). Figure A.4.1 represent the shape and intensity of the XPS peaks used to validate the composition and determine the oxidation state of all the heterometallic centres.

Additional analysis of the Cu_6MnAD sample was carried out using Mg anode as X-ray source, in order to analyse better the Mn 2p line, due to the observed overlap of the Mn 2p and Cu LMM lines (Figure A.4.2).

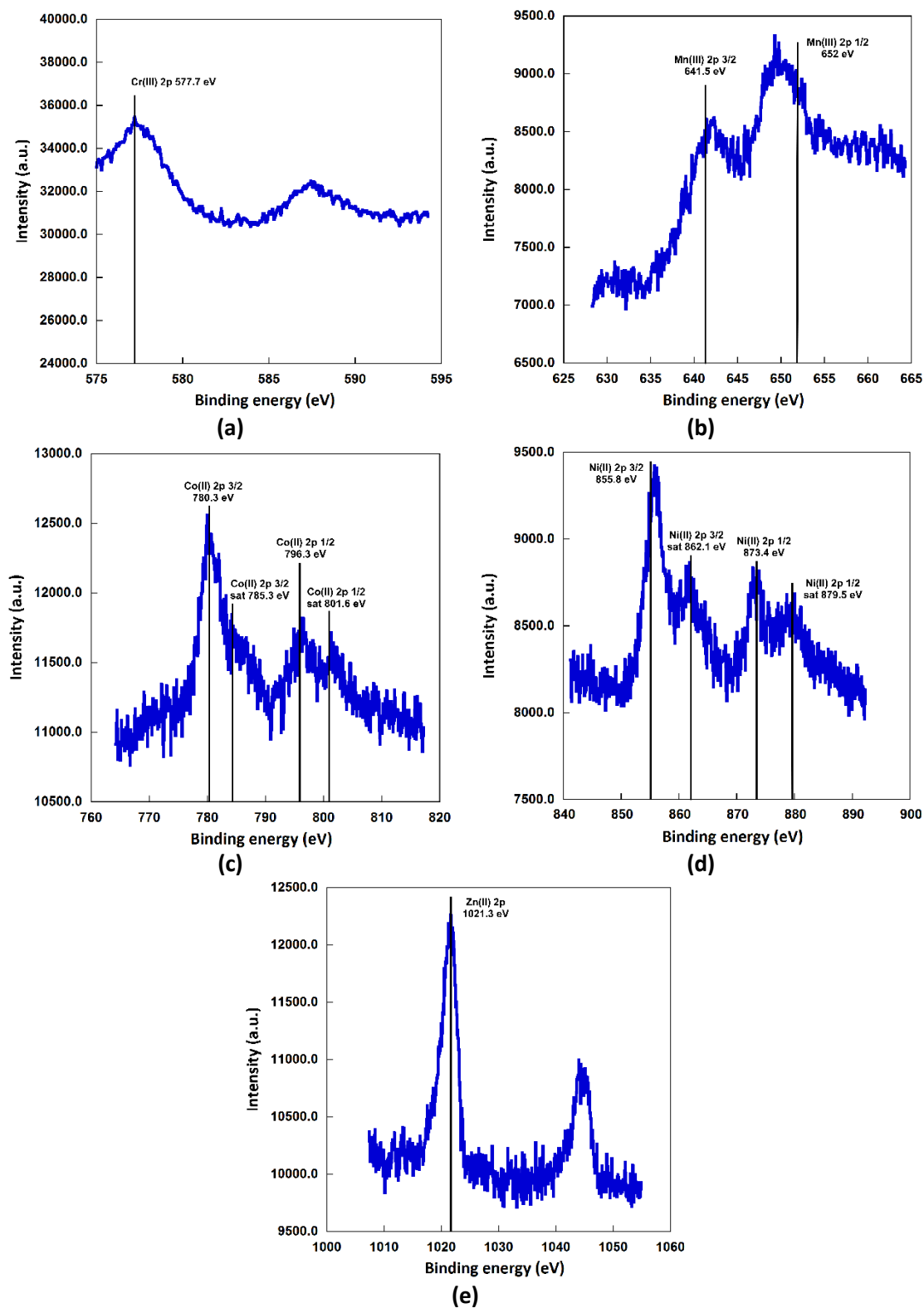


Figure A.4.1. XPS representation of all heterometallic centres being (a) Cr, (b) Mn, (c) Co, (d) Ni and (e) Zn using Al anode as X-ray source.

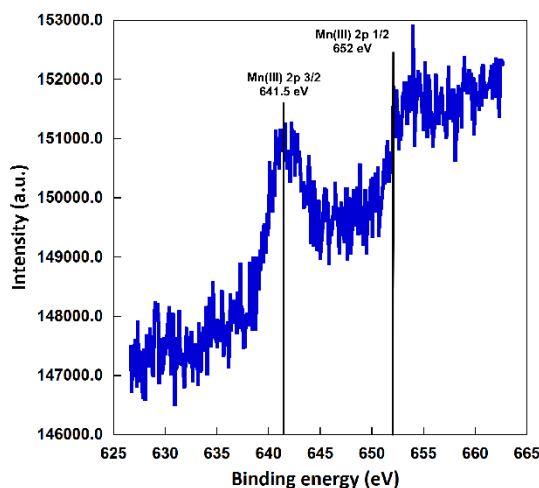


Figure A.4.2. XPS of compound Cu_6MnAD using Mg anode as X-ray source.

A.5. MAGNETIC FITTING MODELS

Then, the different models and equations used in the analysis of the molar magnetic susceptibility (χ_m) data are exposed. For the dimeric compounds calculations described in Chapter 2 and Chapter 3, the mathematical model used corresponds to the Bleaney-Bowers dimeric model of $S = 1/2$ interacting paramagnetic centres (Equation 1):

$$\chi_m = \frac{Ng^2\beta^2}{kT} f(x) \quad \text{where } f(x) = \frac{2 \exp(x)}{1+3\exp(x)} \quad (x = J/KT) \quad (1)$$

In Chapter 4, where the scheme of the magnetic interactions is far more complex, the fitting of the $\chi_m T$ experimental data above 10 K to obtain the superexchange parameters was performed using the MagProp software tool distributed with DAVE.^[114]

The DAVE software package is an experimental neutron scattering data reduction, visualization, and analysis system. In order to analyse the magnetic behaviour, the MagProp program module for the workup, visualisation and analysis of magnetic data is used (Figure A.5.1). This program incorporates a Hamiltonian matrix generator that allows generating a matrix representation of a given Hamiltonian from a symbolic expression (Figure A.5.2a). Then the desired magnetic couplings constants are added with the g value expressed as g_x , g_y and g_z , using the common Zeeman terms (Figure A.5.2b). Once the desired Hamiltonian is generated, the energy values of the magnetic excited states can be computed and placed in the Van Vleck equation (2) to calculate the compound χ_m and $\chi_m T$ values at different temperatures. The program incorporates a fitting algorithm that allows modifying the magnetic parameters (J, g, diamagnetisms, molecular field approximation...) (Figure A.5.3).

$$\chi = \frac{N_A \sum_n E_n^{(1)2} \exp(-E_n^{(0)}/kT)}{kT \sum_n \exp(-E_n^{(0)}/kT)} \quad (2)$$

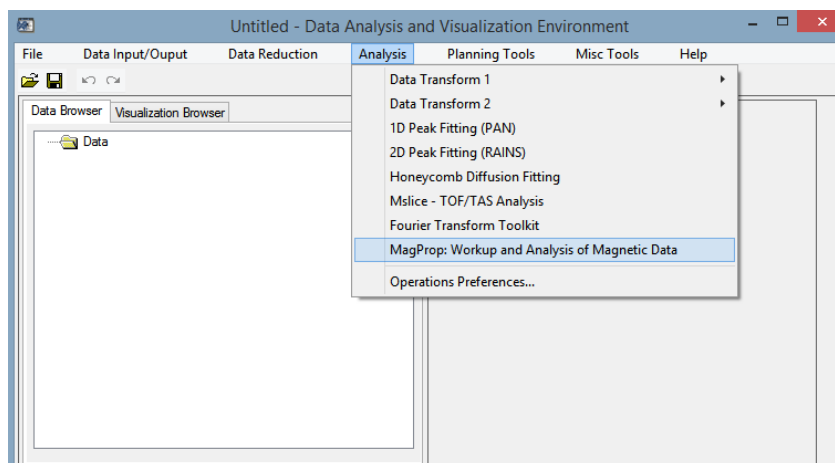
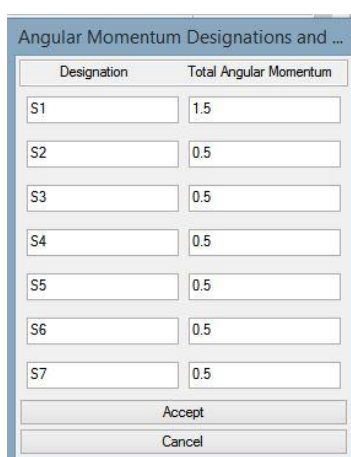
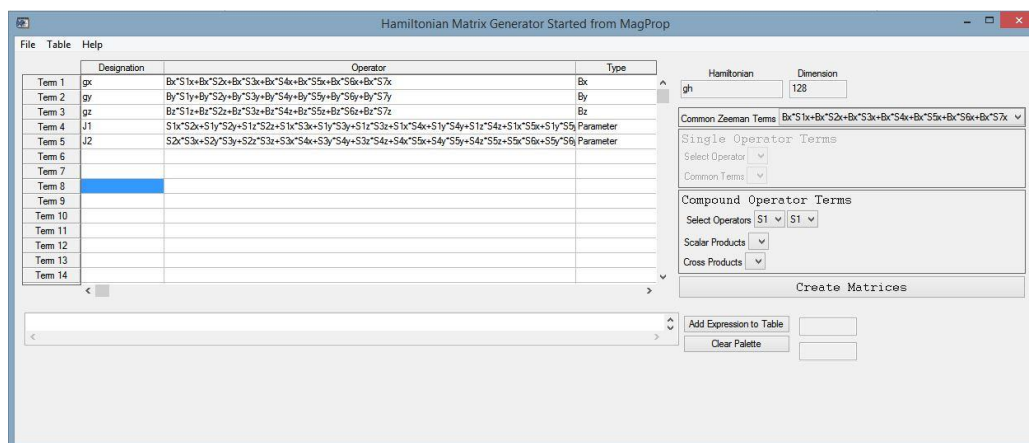


Figure A.5.1. The main application window of DAVE.



(a)



(b)

Figure A.5.2. (a) Hamiltonian generation window corresponding to the Cu₆CrAD compound with a central Cr(III) and a ring of six Cu(II) metal centres and (b) the generated Hamiltonian including the superexchanges J constants and the Zeeman terms.

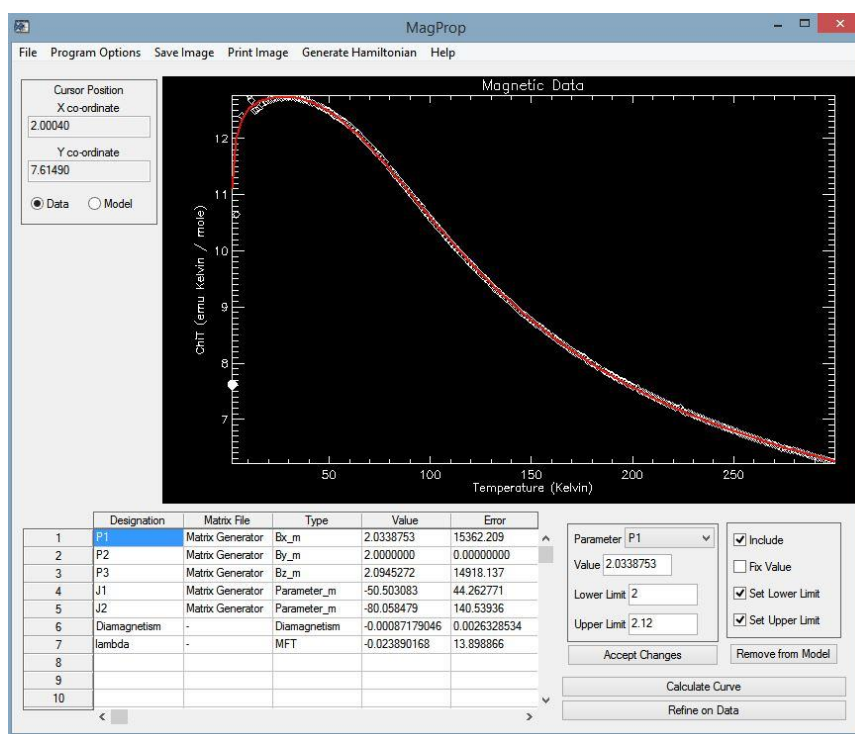


Figure A.5.3. Graphical display of a magnetic fitting, using the diamagnetism and molecular field approximation in addition to J and g parameters. The experimental $\chi_m T$ is indicated as the white line while the calculated is indicated as a red line.

A.6. MAGNETIZATION CURVES OF COMPOUNDS OF CHAPTER 3

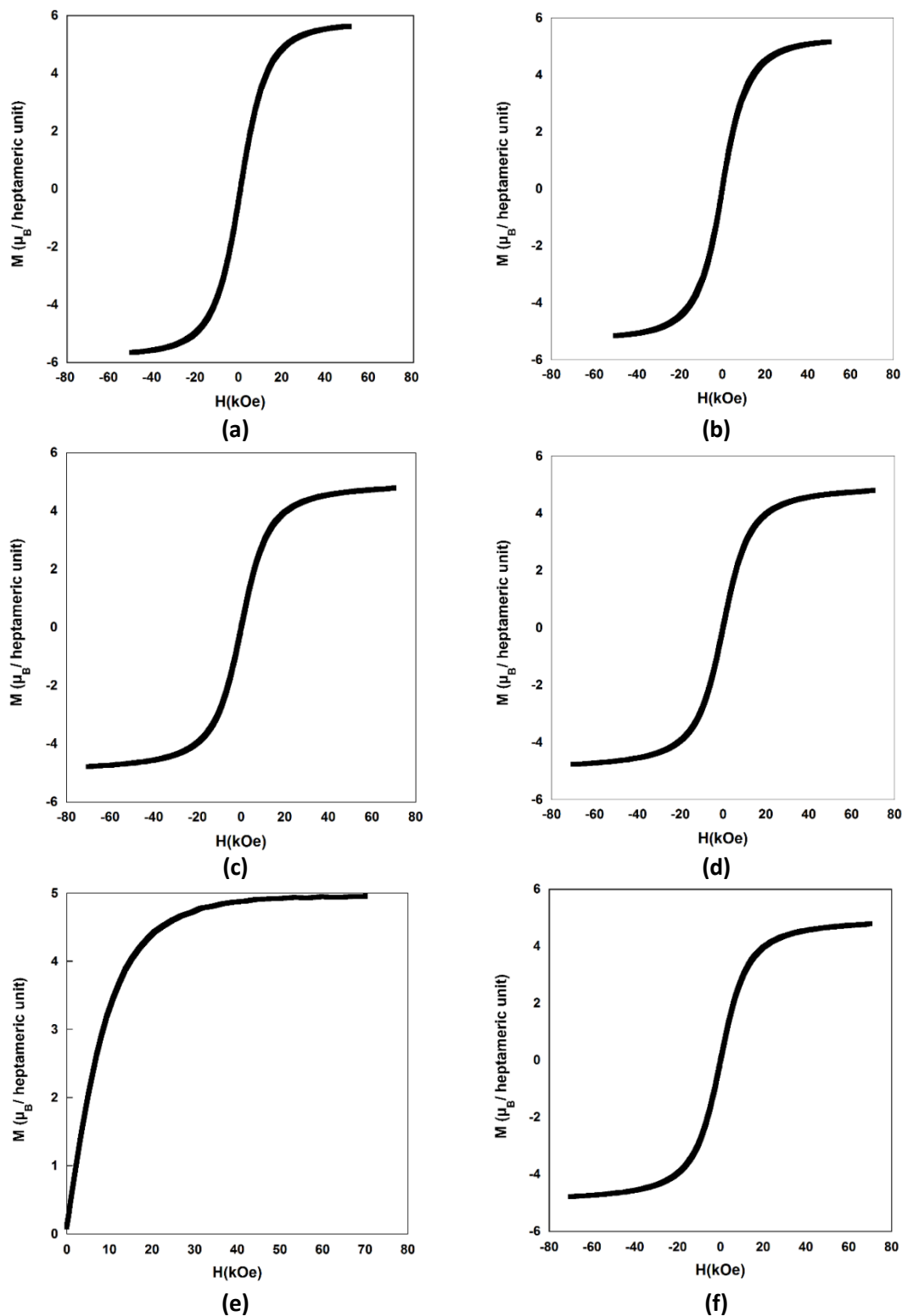


Figure A.6.1. Field dependence of the magnetization at 2 K of (A) $\text{Cu}_7\text{ADSO}_4\text{NHET}_3\text{-1}$, (B) $\text{Cu}_7\text{ADSO}_4\text{NHET}_3\text{-2}$, (C) Cu_7ADSO_4 , (D) $\text{Cu}_7\text{ADHN-1}$, (E) $\text{Cu}_7\text{ADHN-2}$ and (F) $\text{Cu}_7\text{ADHN-1green}$.

A.7. PUBLICATIONS ARISING FROM THIS WORK

This work has led to the publication of some articles in international scientific journals that are attached below:

1. Thomas–Gipson, J.; Pérez–Aguirre, R.; Beobide, G.; Castillo, O.; Luque, A.; Pérez–Yañez, S.; Román, P.: Unravelling the Growth of Supramolecular Metal–Organic Frameworks Based on Metal–Nucleobase Entities. *Cryst. Growth Des.* **2015**, *15*, 975–983.
2. Pérez–Aguirre, R.; Beobide, G.; Castillo, O.; de Pedro, I.; Pérez–Yañez, S.: Supramolecular extended systems based on discrete paddle-wheel shaped metal–adeninate entities. *Inorganica Chimica Acta*, **2016**, *452*, 222–228.
3. Pérez–Aguirre, R.; Beobide, G.; Castillo, O.; de Pedro, I.; Luque, A.; Pérez–Yañez, S.; Rodríguez–Fernandez, J.; Román, P.: 3D Magnetically Ordered Open Supramolecular Architectures Based on Ferrimagnetic Cu/Adenine/Hydroxide Heptameric Wheels. *Inorg. Chem.* **2016**, *55*, 7755–7763.

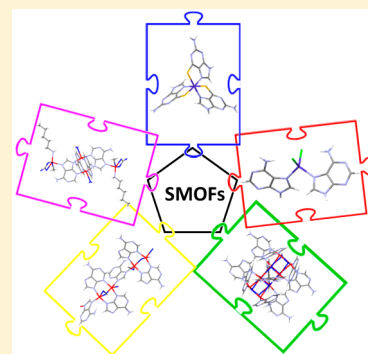
Unravelling the Growth of Supramolecular Metal–Organic Frameworks Based on Metal–Nucleobase Entities

Jintha Thomas-Gipson,[‡] Rubén Pérez-Aguirre,[‡] Garikoitz Beobide, Oscar Castillo,* Antonio Luque, Sonia Pérez-Yáñez,* and Pascual Román

Departamento de Química Inorgánica, Facultad de Ciencia y Tecnología, Universidad del País Vasco (UPV/EHU), Apartado 644, E-48080 Bilbao, Spain

Supporting Information

ABSTRACT: The present work provides the basis to obtain three-dimensional (3D) extended porous supramolecular assemblies named supramolecular metal–organic frameworks (SMOFs). This goal can be achieved by considering three key factors: (i) the use of rigid building units, (ii) the establishment of predictable and rigid synthons between the building units, and (iii) the non-coplanarity of functional groups involved in the predictable synthons. Throughout this report we demonstrate the suitability of this synthetic strategy supported by six new SMOFs based on metal–nucleobase entities which fulfill the stated requirements: [Co(ThioG)₃] (SMOF-4; ThioG = thioguaninato), [Co(Hade)₂X₂] (SMOF-5, SMOF-6; Hade = adenine and X = Cl[−], Br[−]), [Cu₈(μ₃-OH)₄(μ₄-OH)₄(ade)₄(μ-ade)₄(μ-Hade)₂] (SMOF-7; ade = adeninato), [Cu₄(μ₃-ade)₄(μ-ade)₂(pentylNH₂)₂(CH₃OH)₂(CO₃)₂(H₂O)₂] (SMOF-8; pentylNH₂ = 1-pentylamine), and [Cu₂(μ-ade)₂(ade)(μ-OH)(H₂O)(CH₃OH)]_n (SMOF-9). SMOF-4 is built up from monomeric entities in which bidentate thioguaninato ligands establish complementary hydrogen bonding interactions in non-coplanar directions leading to supramolecular layers that are further connected resulting in a porous structure with one-dimensional (1D) channels. The hydrogen bonding interactions among Watson–Crick and sugar edges of monomeric entities in SMOF-5 give rise to a triply interpenetrated supramolecular framework. Octameric clusters in SMOF-7 are self-assembled by hydrogen bonding to yield a porous 3D network. SMOF-8 is built up from tetranuclear units that are linked via base pairing interactions involving Watson–Crick faces to afford layers whose assembly generates a two-dimensional pore system. SMOF-9 is in between pure MOFs and SMOFs since it consists of 1D infinite coordination polymers held together by complementary hydrogen bonding interactions into a 3D supramolecular porous structure.



INTRODUCTION

Metal–organic frameworks (MOFs) encompass an area of chemistry that has experienced impressive growth during the last decades because of their various potential applications in catalysis, gas storage, chemical separations, sensing, ion exchange, drug delivery, and optics.¹ Regarding the adsorption field, it is worth mentioning that their large surface areas, adjustable pore sizes, and controllable functionalities are key factors that make MOFs promising candidates for adsorptive separations and purification purposes.^{2,3} Taking into account the great potential of MOFs, we decided to explore a related type of material, in which the coordination bonds are replaced with hydrogen bonds as connectors, which are also directional and predictable interactions, to sustain the three-dimensional (3D) crystal building containing potentially accessible voids (Figure 1).^{4,5} Although such kinds of alternative materials can arise a similar fascination to that of MOFs, the crystal engineering principles and the synthetic approach are not yet settled, and examples of this kind of material are rather scarce. In this sense a first clue to reach this goal can be inferred using the naive analogy of soft and rigid balls. Soft balls can adjust their shape to provide an efficient packing leaving almost no space in between. However, rigid balls do not have the option

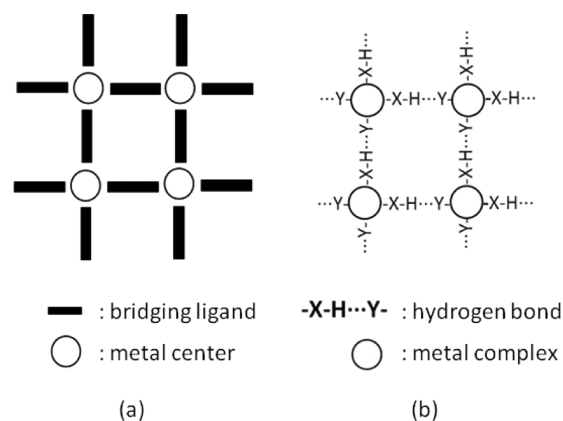


Figure 1. Similarity between (a) coordination bonds and (b) hydrogen bonding interactions as structure directing agents.

Received: December 10, 2014

Revised: January 7, 2015

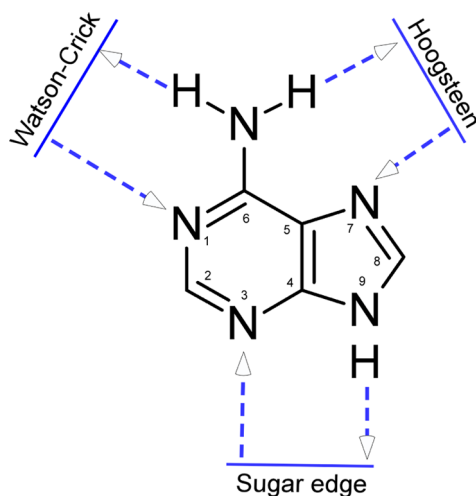
Published: January 12, 2015

of changing their shape, and, as a consequence, their packing is less effective giving rise to the presence of voids. In other words, flexible objects pack effectively, while rigid objects do not unless they present very specific and appropriate shape, such as cubes, triangular, rectangular and hexagonal prisms, etc.⁶ This simple idea has helped us develop a synthetic strategy to obtain supramolecular metal–organic frameworks (SMOFs)^{7,8} with potentially accessible voids as an alternative to more conventional metal–organic frameworks (MOFs).

The synthetic strategy is based on the following key factors: (i) the use of rigid building units, (ii) the establishment of predictable and rigid synthons between the building units, and (iii) the noncoplanarity of functional groups involved in the predictable synthons. The rigidity of the building units (discrete complexes) can be achieved using rigid ligands bonded through multiple positions. It means, in most common cases, a double anchoring of the ligand by means of two simultaneous coordination bonds or the combination of a coordination bond and an intramolecular hydrogen bond. The predictability and rigidity of the synthons require the presence of adjacent functional groups, incorporated into the rigid ligands, able to establish complementary hydrogen bonding interactions. Finally, the requisite of noncoplanar arrangement of the synthons comes from our objective of obtaining 3D extended systems that is achieved by the presence of at least three noncoplanar synthons. The use of nonplanar coordination geometries for the complexes makes this last condition easy to accomplish.

From previous studies we realized that a suitable system that would fulfill all of the above-described requirements for obtaining SMOFs are the discrete metal–nucleobase systems, especially those based on purine nucleobases.^{9–11} These ligands provide, on the one hand, the advantage of increased rigidity of the supramolecular building block due to the coordination through multiple positions, and, on the other hand, they present many edges capable of establishing complementary hydrogen bonding interactions that provide rigid and predictable synthons (Scheme 1). Therefore, the adequate selection of the metal–nucleobase discrete entity that would afford a non-coplanar arrangement of the nucleobases could provide the desired supramolecular porous materials.

Scheme 1. Adenine Edges Capable of Establishing Rigid Complementary Double Hydrogen Bonding Synthons



The preliminary results were achieved employing $[\text{Cu}_2(\mu\text{-adenine})_4(\text{X})_2]^{2+}$ (SMOF-1 and SMOF-2; $\text{X} = \text{Cl}^-$, Br^-) as supramolecular building blocks in which two or more nucleobases are tightly anchored to the metal centers by two donor positions (N3 and N9 sites), imposing a rigid building unit.^{7,12} Moreover, this coordination motif imposes a rigid geometrical restraint among the nucleobases providing a set of noncoplanar synthons that otherwise would be very difficult to achieve. As many hydrogen donor/acceptor positions of the nucleobase remain free, these discrete entities are able to self-assemble among them by means of double hydrogen bonds to provide extended supramolecular solids in which great channels are present. These compounds present a surface instability that creates a diffusion barrier permeated only by strong interacting adsorbate molecules such as CO_2 but not N_2 , H_2 , and CH_4 , which makes them attractive for selective gas adsorption and separation technologies. Zaworotko et al. reported an analogous compound, based on the $[\text{Cu}_2(\mu\text{-adenine})_4(\text{X})_2]^{2+}$ dinuclear entity, replacing the halides by bulkier TiF_6^{2-} anions improving the chemical stability of the supramolecular network toward humidity, thus avoiding the surface instability, and therefore, being able to adsorb CO_2 , CH_4 , and N_2 .¹³ These studies also pointed out the relevance of the solvent selection because strong hydrogen bond donor and acceptor solvents such as water molecules could disrupt the direct hydrogen bonding interactions between the nucleobases that are the key factors to achieve this type of compound.

In this report we demonstrate the suitability of this synthetic strategy to afford the self-assembly of rigid mono- or polynuclear entities by means of a set of non-coplanar synthons into supramolecular porous materials.

■ EXPERIMENTAL SECTION

Synthesis of SMOF-4, $[\text{Co}(\text{ThioG})_3]$. 0.59 mL (0.4 mmol) of pentylamine was added dropwise to 0.0685 g (0.4 mmol) of 6-thioguanine dissolved in 20 mL of water, and the mixture was stirred in an ice bath for 1 h. To this mixture was added a 10 mL solution of 0.0291 g (0.1 mmol) of $\text{Co}(\text{NO}_3)_2 \cdot 6\text{H}_2\text{O}$ dissolved in water. The brown-colored solution was then stirred for 2 h in an ice bath and then left for evaporation. Brown-colored single-crystals were separated after 2 weeks. The compound was also obtained on replacing $\text{Co}(\text{NO}_3)_2 \cdot 6\text{H}_2\text{O}$ with $\text{CoSO}_4 \cdot 7\text{H}_2\text{O}$. Yield: 60%. Anal. Calcd (found) for $\text{C}_{15}\text{H}_{12}\text{CoN}_5\text{S}_3 \cdot 6.7\text{H}_2\text{O}$: C, 26.56 (26.68); H, 3.78 (3.70); N, 30.98 (31.29); S, 14.18 (14.21); Co, 8.69 (8.75). Main IR features (cm^{-1} ; KBr pellets): 3422s, 1611m, 1498w, 1459w, 1385m, 1306sh, 1243vs, 1190m, 1146s, 983s, 933w, 893w, 836w, 803w, 743w, 716w, 680w, 630w, 523w.

Synthesis of SMOF-5, $[\text{Co}(\text{Hade})_2\text{Cl}_2]$. This compound was obtained as deep blue polycrystalline form by the dropwise addition of a propanolic solution of adenine (0.0270 g, 0.2 mmol) into a stirring solution of 0.0238 g of $\text{CoCl}_2 \cdot 6\text{H}_2\text{O}$ (0.1 mmol). When the synthesis was performed in methanol bad quality crystals were obtained. Then, single crystals of good quality were obtained by using diffusion techniques. Yield: precipitate 70%, crystals 50%. Anal. Calcd (found) for $\text{C}_{10}\text{H}_{10}\text{Cl}_2\text{CoN}_{10}$: C, 30.02 (30.09); H, 2.52 (2.47); N, 35.01 (34.93); Co, 14.73 (14.82)%. Main IR features (cm^{-1} ; KBr pellets): 3391vs, 3258vs, 3133vs, 3058vs, 2346w, 2280w, 2186w, 2016w, 1943w, 1790w, 1696vs, 1611s, 1498m, 1459w, 1397s, 1327m, 1237m, 1171m, 1105w, 1066w, 1016w, 942m, 895m, 856w, 778m, 712m, 631w, 610m, 530m.

Synthesis of SMOF-6, $[\text{Co}(\text{Hade})_2\text{Br}_2]$. The synthesis is the same as for SMOF-5 but replacing $\text{CoCl}_2 \cdot 6\text{H}_2\text{O}$ by CoBr_2 . Yield: precipitate 60%. All the attempts to grow single-crystals were unsuccessful. Anal. Calcd (found) for $\text{C}_{10}\text{H}_{10}\text{Br}_2\text{CoN}_{10}$: C, 24.56 (24.49); H, 2.06 (2.15); N, 28.64 (28.57); Co, 12.05 (12.01)%. Main IR features (cm^{-1} ; KBr pellets): 3450s, 3341vs, 3066s, 2817w, 2671w, 2284w, 1951w, 1663vs,

Table 1. Crystallographic Data and Structure Refinement Details^a

	SMOF-4	SMOF-5	SMOF-7	SMOF-8	SMOF-9
formula	C ₁₅ H ₁₂ CoN ₁₅ S ₃	C ₁₀ H ₁₀ Cl ₂ CoN ₁₀	C ₅₀ H ₅₀ Cu ₈ N ₅₀ O ₈	C _{30.85} H _{46.80} Cu _{3.55} N _{21.55} O _{8.20}	C ₁₆ H ₁₉ Cu ₂ N ₁₅ O ₃
MW (g mol ⁻¹)	557.51	400.11	1987.72	1076.37	596.54
crystal system	trigonal	monoclinic	monoclinic	triclinic	monoclinic
space group	P $\bar{3}$	C2/c	Ccca	P $\bar{1}$	C2/c
a (Å)	16.7297(14)	11.2442(18)	20.1899(5)	12.646(5)	23.472(7)
b (Å)	16.7297(14)	6.9401(7)	28.964(2)	13.136(5)	16.398(3)
c (Å)	6.5245(4)	18.760(2)	16.5403(5)	13.158(5)	18.803(5)
α (deg)	90	90	90	73.784(5)	90
β (deg)	90	95.000(13)	90	81.840(5)	112.30(3)
γ (deg)	120	90	90	62.368(5)	90
V (Å ³)	1581.4(2)	1458.4(3)	9672.6(8)	1859.2(12)	6696(3)
Z	2	4	4	1	8
ρ_{calcd} (g cm ⁻³)	1.171	1.822	1.365	0.961	1.184
μ (mm ⁻¹)	0.769	12.758	1.790	1.047	1.899
reflections collected	4690	5201	33482	6909	5529
unique data/parameters	2300/103	1462/109	5277/272	6909/269	5529/325
R _{int}	0.1278	0.0656	0.0630	0.1840	0.0972
goodness of fit (S) ^b	1.033	1.045	1.092	0.773	0.741
R ₁ ^c /wR ₂ ^d [all data]	0.0924/0.1673	0.0664/0.1606	0.0872/0.2221	0.2330/0.2882	0.1519/0.2091
R ₁ ^c /wR ₂ ^d [I > 2 σ (I)]	0.0646/0.1585	0.0606/0.1560	0.0721/0.2115	0.1044/0.2691	0.0800/0.1840

^aReported data do not include the variable amount of solvent molecules present in the channels. ^bS = $[\sum w(F_0^2 - F_c^2)^2 / (N_{\text{obs}} - N_{\text{param}})]^{1/2}$. ^cR₁ = $\sum \|F_0 - |F_c|\| / \sum |F_0|$. ^dwR₂ = $[\sum w(F_0^2 - F_c^2)^2 / \sum wF_0^2]^{1/2}$; w = 1/[$\sigma^2(F_0^2) + (aP)^2 + bP$] where P = (max(F₀², 0) + 2F_c²)/3 with a = 0.0691 (1), 0.0897 (2), 0.1440 (3), 0.1283 (4), 0.0584 (5) and b = 4.8645 (2), 1.6779 (3).

1596vs, 1513w, 1480s, 1416s, 1360w, 1343s, 1306s, 1246s, 1170w, 1120w, 1020w, 1063w, 1030w, 973m, 910m, 870w, 791m, 763m, 722s, 680w, 638m, 627m, 557s, 545m, 532s.

Synthesis of **SMOF-7**, [Cu₈(μ_3 -OH)₄(μ_4 -OH)₄(ade)₄(μ -ade)₄(μ -Hade)₂]. Twenty milliliters of an aqueous methanolic solution (1:1) containing adenine (0.8 mmol, 0.108 g) were added to 20 mL of an aqueous solution of CuSO₄·5H₂O (0.4 mmol, 0.0998 g) leading to a solution of pH = 3. Immediately a dark blue precipitate appeared. Then, sulfuric acid was added until complete dissolution of the precipitate (pH = 1.5). A glass vial with the resulting solution was placed in an Erlenmeyer flask containing triethylamine favoring the diffusion of the base into the solution. A few days later a small amount of purple crystals appeared mixed with a major unknown phase.

Synthesis of **SMOF-8**, [Cu₄(μ_3 -ade)₄(μ -ade)₂(pentylNH₂)₂-(CH₃OH)₂(CO₃)₂(H₂O)₂]. Single crystals of this compound were obtained by adding a 10 mL methanolic solution of 0.0198 g of Cu(OOCCH₃)₂·H₂O (0.1 mmol) to a methanolic solution (20 mL) of 0.0206 g of adenine (0.15 mmol) mixed with 0.59 mL of pentylamine. The green-colored solution was stirred for 1 h and left evaporating at room temperature. On evaporating the color of the solution started changing to blue-violet. After 2 weeks, violet-colored prismatic shaped crystals appeared. The crystals are unstable out from the mother liquid.

Synthesis of **SMOF-9**, [Cu₂(μ -ade)₂(ade)(μ -OH)(H₂O)-(CH₃OH)]_n. Single crystals of this compound were obtained by the slow addition of a 10 mL methanolic solution of 0.0199 g of Cu(OOCCH₃)₂·H₂O (0.1 mmol) into a methanolic solution (50 mL) of 0.0546 g of adenine (0.4 mmol) mixed with 0.59 mL of pentylamine. The green-colored solution was stirred for 1 h and left evaporating at room temperature. Few blue needle like crystals that correspond to **SMOF-9** appeared in a time period of 1 week, mixed with violet crystals of **SMOF-8**. Yield: 5%. Anal. Calcd (found) for C₁₆H₁₉Cu₂N₁₅O₃·8.5(CH₃OH): C, 33.87 (33.77); H, 6.15 (6.08); N, 24.18 (24.09); Cu, 14.63 (14.74) %. Main IR features (cm⁻¹; KBr pellets): 3446s, 3356vs, 3123s, 1671s, 1418m, 1398m, 1385m, 1333m, 1308s, 1268m, 1251w, 1191m, 1149m, 1123w, 1022w, 979w, 939m, 910w, 875w, 845w, 797m, 738w, 723s, 641m, 620w, 570w, 541m.

Physical Measurements. Elemental analyses (C, H, N, S) were performed on an Euro EA elemental analyzer, whereas the metal content was determined by inductively coupled plasma atomic emission spectrometer (ICP-AES) from Horiba Yobin Yvon Activa.

The IR spectra (KBr pellets) were recorded on a FTIR 8400S Shimadzu spectrometer in the 4000–400 cm⁻¹ spectral region. Dinitrogen (77 K) and carbon dioxide (273 K) physisorption data were recorded on activated samples (vacuum at 100 °C for 4 h) with a Quantachrome QUADRASORB-SI-MP and a Quantachrome Autosorb-iQ-MP, respectively. The specific surface area was calculated from the adsorption branch in the relative pressure interval from 0.01 to 0.10 using the Brunauer–Emmett–Teller (BET) method.

X-ray Diffraction Data Collection and Structure Determination. Single-crystal X-ray diffraction data were collected on an Oxford Diffraction Xcalibur diffractometer with graphite monochromated Mo K α radiation (λ = 0.71073 Å) at 100(2) K for **SMOF-4** and **SMOF-7**, and at 293 K for **SMOF-8**, and on an Agilent Technologies SuperNova diffractometer with Cu K α radiation (1.54185 Å) for **SMOF-5** and **SMOF-9**. Data reduction was done with the CrysAlisPro program.¹⁴ All the structures were solved by direct methods using the SIR92 program¹⁵ and refined by full-matrix least-squares on F² including all reflections (SHELXL97).¹⁶ All calculations for these structures were performed using the WINGX crystallographic software package.¹⁷ After the initial structure solution was completed, the difference Fourier map for **SMOF-4**, **-7**, **-8**, and **-9** showed the presence of substantial electron density at the voids of the crystal structure that was impossible to model. Therefore, its contribution was subtracted from the reflection data by the SQUEEZE method¹⁸ as implemented in PLATON.¹⁹ During the data reduction process it became clear that the crystal specimen of **SMOF-8** was a non-merohedric twin with a twin law: (1.026 -0.077 0.038/0.070 0.963 0.012/-0.023 -0.000 1.003). The final result showed a percentage of twinned component of 24.3%. Additionally, one of the metal centers (Cu2) and its coordinated ligands present a partial occupation of 0.78. Relevant data acquisition and refinement parameters are gathered in Table 1. CCDC 1038651–1038655 contain the supplementary crystallographic data for this paper.

RESULTS AND DISCUSSION

Structural Description of [Co(ThioG)₃] (SMOF-4). The basic media of the reaction favored the oxidation to Co(III), as ensured by its diamagnetic nature, giving rise to neutral monomeric [Co(ThioG)₃] entities. Three thioguaninato

ligands, in its 9*H*-tautomeric form, are coordinated in a bidentate chelating mode to the Co(III) atoms by their N7 and S6 atoms affording an octahedral coordination environment. Coordination bonds lengths and angles are gathered in the Supporting Information. The coordination mode of the nucleobase analogue renders a rigid metal-complex and, at the same time, exposes its Watson–Crick (N1, N2) and sugar edges (N3, N9) providing a set of non-coplanar synthons with dihedral angles of 87° (Figure 2a). Therefore, this discrete

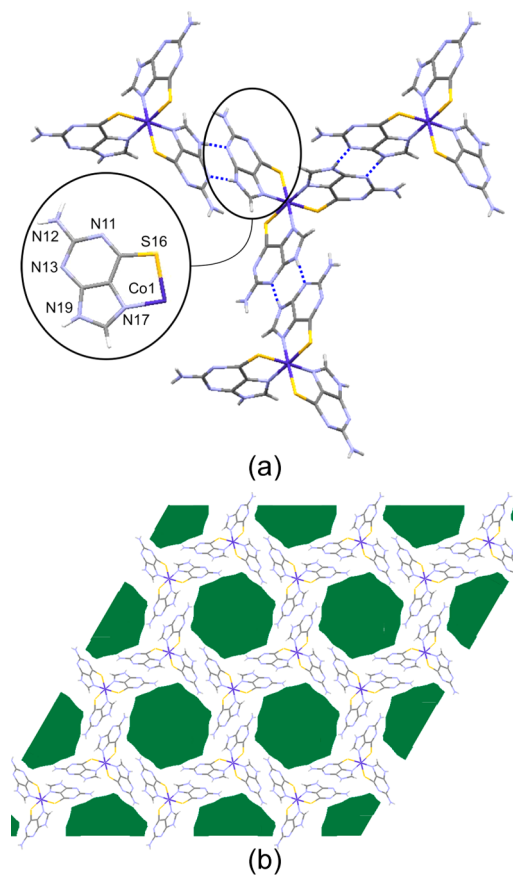


Figure 2. (a) Interactions among the monomeric entities and numbering scheme. (b) Projection of the crystal packing of SMOF-4 along the crystallographic *c* axis. Green-colored regions represent the solvent accessible void.

complex entity fulfils the previously stated requirements for the success in obtaining a supramolecular porous material. In fact, there is a previous work based on similar discrete entities but using 6-thioguanosine that provides a complementary hydrogen bonding interaction involving only the Watson–Crick face (N1, N2) as the sugar edge is blocked by the sugar residue. It affords a supramolecular assembly containing great voids that are occupied by the sugar residue of the thioguanosine.²⁰ In SMOF-4 both sides of the 6-thioguaninato are available to contribute to the supramolecular assembly. The sugar edge (N3, N9) of the nucleobases establishes a double hydrogen bonding interaction with the nucleobases of three neighboring entities to give a $R_2^2(8)$ ring (Table 2). This rigid synthon, based on direct thioguaninato⋯thioguaninato pairing interactions, leads to layers in the *ab* plane in which Δ and Λ isomers of the trischelate complex are sequentially arranged similarly to what happens in layered $[M(\text{ox})_3]^{n-}$ based compounds.^{21,22} The resulting arrangement corresponds to

Table 2. Structural Parameters (\AA , $^\circ$) of Noncovalent Interactions in SMOF-4^a

Hydrogen Bonding Interactions					
D–H⋯A ^b	H⋯A	D⋯A	D–H⋯A		
N19–H19⋯N13 ⁱ	2.03	2.875(5)	167		
N12–H12⋯S16 ⁱⁱ	2.69	3.467(4)	151		
C18–H18⋯S16 ⁱⁱⁱ	2.67	3.415(4)	138		
π – π Interactions ^c					
ring⋯ring ^d	angle	DC	α	DZ	DXY
h⋯h ^{iv}	0.0	3.46	18.5	3.28	1.10

^aSymmetry codes: (i) $-x, -y + 1, -z + 2$; (ii) $x - y, x, -z + 1$; (iii) $-x + y, -x + 1, z + 1$; (iv) $-x, -y + 1, -z + 1$. ^bD: donor; A: acceptor. ^cAngle: dihedral angle between the planes (deg), DC: distance between the centroids of the rings (\AA), α : angle between the normal to the first ring and the DC vector (deg), DZ: interplanar distance (\AA), DXY: lateral displacement (\AA). ^dh: hexagonal ring of the thioguanine.

the Shubnikov hexagonal **hcb** topology with a (6^3) point symbol.^{23–25} The interactions among the three-connected uninodal two-dimensional (2D) nets are linked via weaker hydrogen bonds (N2–H⋯S6 and C8–H⋯S6) and reinforced with π – π interactions, (Table 2) leading to an **acs** topology and $(4^9.6^6)$ point symbol that corresponds to a porous crystal structure with an estimated surface area of 887 m^2/g and 43% of void space based on theoretical calculations.^{26,19} The resulting porous structure consists of one-dimensional (1D) channels that run along the crystallographic *c* axis with a diameter of 8.2–9.4 \AA (Figure 2b). It is worth mentioning the template effect exerted by the pentylamine. This molecule provides the basic media that this reaction requires, and, at the same time, the tendency of the aliphatic tails to form aggregates in water promotes the growth of the supramolecular structure around them. In fact, the same synthesis but using different amines with shorter aliphatic tails does not provide this compound.

According to N_2 (77 K) and CO_2 (273 K) adsorption studies, this compound is highly selective toward CO_2 adsorption (Figure 3). The N_2 adsorption curve exhibits features of a nonporous material, and, accordingly, the fitting of the adsorption area to BET equation leads to a negligible value. However, it shows a significant CO_2 uptake with a non-saturating curve reaching a value of 1.4 mmol/g at 1 bar. This behavior has been described in the introduction section for

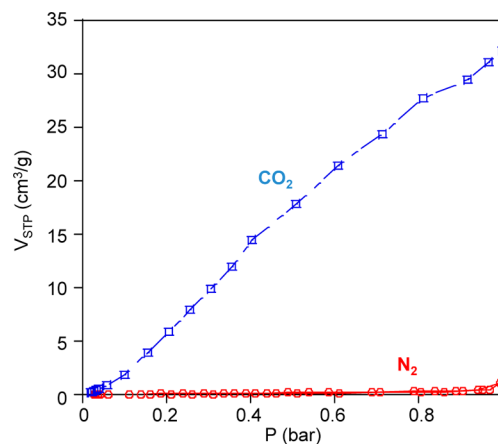


Figure 3. Adsorption isotherms for N_2 (77 K) and CO_2 (273 K), of a fresh sample of SMOF-4.

SMOF-1 and SMOF-2, and its explanation for SMOF-4 probably would also be related to a crystal surface instability.

Structural Description of [Co(Hade)₂Cl₂] (SMOF-5). SMOF-5 contains neutral monomeric [Co(Hade)₂Cl₂] units. 9H-Adenine acts as a monodentate ligand, and it is coordinated to the Co(II) metal center through the N7 position that it is very usual for unsubstituted adenine moieties, but it requires a second anchoring position of the nucleobase to be stiff enough to meet our requirements. Such stiffness is achieved by the presence of intramolecular hydrogen bonding interactions between the amino hydrogen atom and the chloride one. The adenine also exposes its Watson–Crick and sugar-edges to establish intermolecular complementary hydrogen bonding interactions with adjacent adenine molecules (Figure 4a).

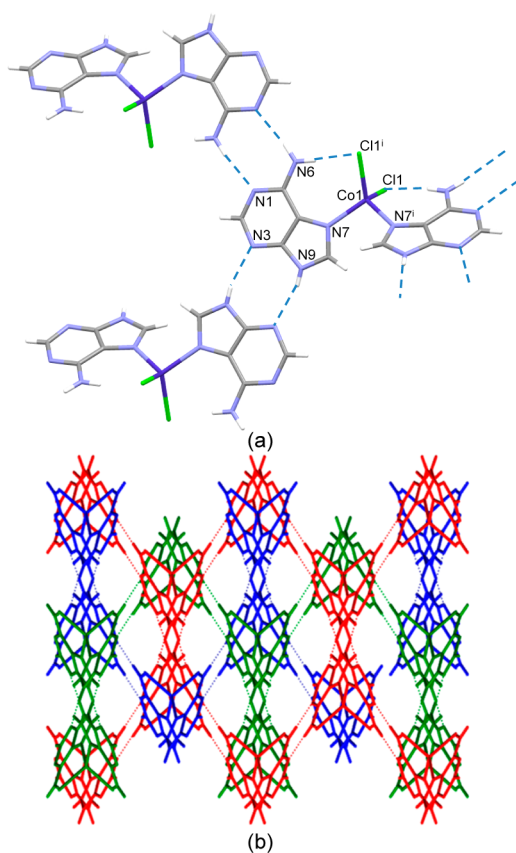


Figure 4. (a) Rigid synthon formed by direct supramolecular interactions in SMOF-5. (b) Triple interpenetrated crystal structure of SMOF-5. Each subnet is represented using a different color.

The rigid synthons involving WC...WC and sugar...sugar edges interactions give rise in both cases to $R_2^2(8)$ hydrogen bonding rings, that are well-known structural synthons between self-assembling adenine fragments.^{27–33} These interactions build up a four-connected uninodal 3D supramolecular net with dia topology and (6^6) point symbol that would represent a new porous material with an estimated internal surface area of 3600 m²/g and 67% of void space.

Nevertheless, it would contain such huge channels that the real crystal structure involves three interpenetrated networks that occupy all the available space providing a nonporous material. This entanglement problem is also common in MOFs.³⁴ Porous materials try to minimize the system energy through optimal filling of void space, but structural inter-

penetration may occur only if the pore space of an individual net is sufficiently large to accommodate an additional net. In addition to this, various weak supramolecular forces such as H-bonding, π - π aromatic stacking interactions, and van der Waals forces are believed to play vital roles in the formation of interpenetrated structures. SMOF-5 follows the same pattern, provided that it contains such a huge percentage of void. Thus, the resulting structure can be described as a 3-fold interpenetrated network as shown in Figure 4b. The attempt to avoid this interpenetration using the more voluminous bromide anion instead of chloride did not succeed, providing the same triple interpenetrated supramolecular structure (SMOF-6, see Supporting Information).

Table 3. Hydrogen Bonding Interactions (Å, °) in SMOF-5^a

D–H...A ^b	H...A	D...A	D–H...A
N6–H6A...N1 ⁱⁱ	2.06	2.912(6)	173
N6–H6B...Cl1 ⁱ	2.39	3.237(4)	167
N9–H9...N3 ⁱⁱⁱ	2.11	2.833(6)	165

^aSymmetry codes: (i) $-x, y, -z + 1/2$; (ii) $-x + 1/2, -y + 1/2, -z + 1$; (iii) $-x, -y - 1, -z + 1$. ^bD: donor; A: acceptor.

Structural Description of [Cu₈(μ_4 -OH)₄(μ_3 -OH)₄(ade)₄(μ -ade)₄(μ -Hade)₂] (SMOF-7). This compound consists of [Cu₈(μ_4 -OH)₄(μ_3 -OH)₄(adeninato- κ N9)₄(μ -adeninato- κ N3: κ N9)₄(μ -adenine- κ N3: κ N9)₂] octameric clusters formed by the stacking of four Cu₂(μ -OH)₂ dimers that are 90° rotated and linked by a semicoordination to the neighboring Cu(II) atoms through the hydroxide bridges (Figure 5a). The resulting aggregate can be described as the stacking of three cubanes (cubes with the vertices alternatively occupied by the metal and the bridging ligand). The surface of each octamer is occupied by eight adeninate and two neutral adenine ligands. Four adeninato and the neutral adenine entities act as bidentate N3,N9-bridging ligands. These bridging ligands are disordered into two coplanar arrangements with inverted orientation regarding the coordination mode (μ - κ N3: κ N9/ μ - κ N9: κ N3).^{35,36} The remaining adeninato ligands are anchored to the corners of the cluster as terminal ligands through N9, and their stiffness is reinforced by intramolecular hydrogen bonds involving the hydroxide bridges and the N3 positions of the nucleobases. All the adenines, adeninates, and hydroxides are rigidly anchored to the octameric entity because of their multiple coordination bond (OH/adenine/adeninato) or the combination of a coordination bond and an intramolecular hydrogen bond (adeninato).

The interaction of each octamer with the adjacent ones is by means of a hydrogen bonding scheme involving the hydroxide anions and the N7 imidazolic atom of terminal adeninato ligands giving rise to a bidimensional network. Moreover, the bridging adeninato ligands direct their Watson–Crick and Hoogsteen faces outward in those supramolecular layers in such a way that they establish complementary hydrogen bonding interactions with neighboring tectons. As in previous compounds the Watson–Crick faces establish a $R_2^2(8)$ hydrogen bonding ring. The combination of the above-described interactions leads to a 3D 8c uninodal supramolecular net with a sqc3 topology, point symbol being $(4^4.6^2)$, where the geometrical requirements imposed by the rigidity of the octameric unit and the hydrogen bonding interactions avoid the full occupancy of the space. This is reflected by the presence of large monodimensional channels of ca. 4.9 Å

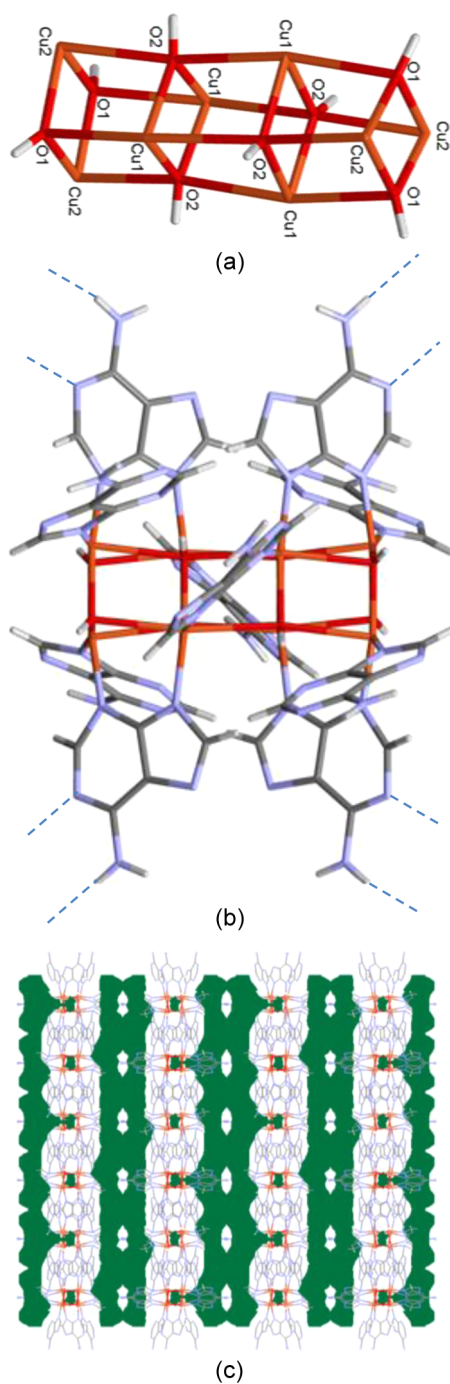


Figure 5. (a) $[\text{Cu}_8(\mu_4\text{-OH})_4(\mu_3\text{-OH})_4]$ unit, (b) whole octameric entity, and (c) three-dimensional packing of SMOF-7.

spreading along the $[100]$ direction, which corresponds to a calculated surface area of $366 \text{ m}^2/\text{g}$ and a 30% of void space.

Structural Description of $[\text{Cu}_4(\mu_3\text{-ade})_4(\mu\text{-ade})_2(\text{pentylNH}_2)_2(\text{CH}_3\text{OH})_2(\text{CO}_3)_2(\text{H}_2\text{O})_2]_n(\text{solvent})$ (SMOF-8). SMOF-8 is built up by tetranuclear $[\text{Cu}_4(\mu_3\text{-ade})_2(\mu\text{-ade})_2(\text{pentylNH}_2)_2(\text{CH}_3\text{OH})_2(\text{CO}_3)_2(\text{H}_2\text{O})_2]$ units in which two types of neutral building units coexist: a dimeric $[\text{Cu}_2(\mu\text{-ade})_4(\text{H}_2\text{O})_2]$ entity and two monomeric $[\text{Cu}(\text{pentylNH}_2)(\text{CH}_3\text{OH})(\text{CO}_3)]$ moieties (Figure 6).

The dimeric fragment is centrosymmetric and is made of two Cu(II) atoms bridged by four $\mu\text{-N}3, \text{N}9$ -adeninate anions in a paddle-wheel shaped arrangement. The apical position of the

Table 4. Hydrogen Bonding Interactions (\AA , $^\circ$) in SMOF-7^a

D–H...A ^b	H...A	D...A	D–H...A
N16–H16A...N11A ⁱⁱⁱ	2.51	3.34(3)	161
N36–H36B...N13 ⁱ	2.56	3.317(7)	148
O1–H1...N37 ^{iv}	2.09	2.947(5)	177
O2–H2...N33 ^v	2.18	3.015(6)	167

^aSymmetry codes: (i) $x, -y + 1/2, -z + 1/2$; (iii) $-x + 3/2, y, z - 1/2$; (iv) $-x + 3/2, -y + 1, z$; (v) $-x + 3/2, y, z + 1/2$. ^bD: donor; A: acceptor.

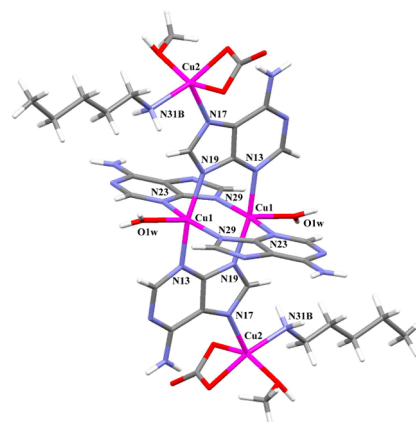


Figure 6. Structural unit of SMOF-8 with the atomic numbering scheme.

distorted square pyramidal coordination around Cu1 atom is completed with a water molecule. Each dimeric entity is linked to two neighboring monomeric units via the N7 imidazolic atoms of two adeninate ligands. Therefore, two adeninate anions behave as tridentate $\mu_3\text{-N}3, \text{N}7, \text{N}9$ bridging ligands, whereas the other two act as bidentate $\mu\text{-N}3, \text{N}9$. The basal plane of the square pyramidal chromophore around Cu2 atom is completed with two oxygen atoms from a carbonato ligand, an oxygen atom of a methanol molecule, and the nitrogen atom of a pentylamine molecule.

Each tetranuclear entity is linked to four adjacent ones via double N6–H...N1 hydrogen bonding interactions between the Watson–Crick faces of neighboring entities to give a $\text{R}_2^2(8)$ ring. This assembling of tetrameric entities gives rise to layers that can be described as a four-connected uninodal net with Shubnikov tetragonal *sql* topology and $(4^4.6^2)$ point symbol. It is worth noting that the dinuclear paddle-wheel entity of SMOF-1 and SMOF-2 presents analogous four-connected nodes (using Watson–Crick base pairing interactions), but the absence of the bulky capping monomeric entities allows the growth of a 3D supramolecular network (*nbo*, $6^4.8^2$). However, in SMOF-8 the 3D cohesion requires additional hydrogen bonding interactions involving the coordination water molecule, the carbonato ligand, and the pentylamine molecule (Figure 7, Table S4) leading to an $\alpha\text{-Po}$ *pcu* topology. The overall packing generates a 2D pore network with channels running along the *b* and *c* axes of 3–5 \AA of diameter, that represents 43% of void space and a calculated surface area of $402 \text{ m}^2/\text{g}$. However, the crystals decompose upon removal from the mother liquor and even when immersed in pure methanol. This fact is probably due to the loss of pentylamine that seems to play a key role stabilizing the crystal structure.

Structural Description of $[\text{Cu}_2(\mu\text{-ade})_2(\text{ade})(\mu\text{-OH})(\text{H}_2\text{O})(\text{CH}_3\text{OH})]_n(\text{solvent})$ (SMOF-9). The basic structural

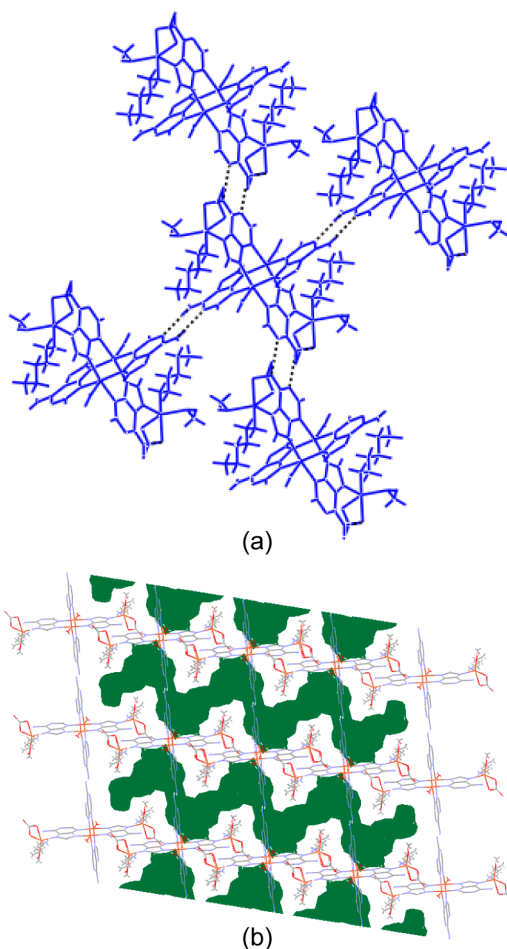


Figure 7. (a) Linkage of the tetranuclear entities by the Watson–Crick faces and (b) crystal packing along the *b* axis of SMOF-8, showing the generated voids.

Table 5. Hydrogen Bonding Interactions (Å, °) in SMOF-8^a

D–H...A ^b	H...A	D...A	D–H...A
N6–H6A...N11 ⁱⁱ	2.13	2.978(11)	167
N6–H6B...O1	2.11	2.965(13)	175
N6–H26B...N21 ⁱⁱⁱ	2.08	2.935(17)	172
O1w–H12w...O3 ^{iv}	1.94	2.790(13)	169
N31–H31A...O2 ^v	1.94	2.843(18)	176

^aSymmetry codes: (ii) $-x + 2, -y + 1, -z + 1$; (iii) $-x + 2, -y, -z$; (iv) $x - 1, y, z$; (v) $-x + 3, -y, -z + 1$. ^bD: donor; A: acceptor.

unit of this compound consists of 1D infinite coordination polymers held together by complementary hydrogen bonding interactions in a 3D supramolecular porous structure. The coordination polymer can be described as noncentrosymmetric dinuclear units (Figure 8) in which two Cu(II) atoms are bridged with two adeninate moieties by the N3 and N9 atoms and also by one hydroxyl group (Figure 9a). One of the metal centers is also coordinated to a water molecule while the other to the oxygen atom of a methanol molecule. These dinuclear units are connected by additional bridging adeninates that are coordinated to the Cu(II) centers by the N7 and N9 atoms to provide a 1D coordination chain. An interesting structural feature is that the bridging adeninates inside the dinuclear units are tilted by 22°, but they present wider tilt angle with respect to those connecting the dimeric units (56 and 78°, respectively)

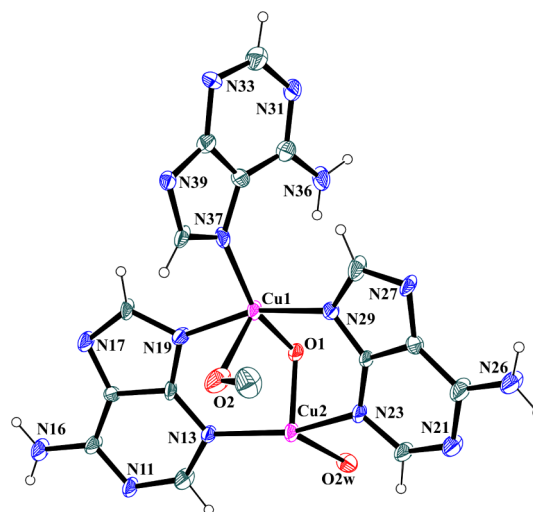


Figure 8. Ortep representation of the dimeric unit $[\text{Cu}_2(\mu\text{-ade})_2(\text{ade})(\text{H}_2\text{O})(\mu\text{-OH})(\text{CH}_3\text{OH})]$ together with the numbering scheme in SMOF-9.

in the polymeric chain. This fact together with the complementary double hydrogen bonding interactions of the nucleobases promotes a three-dimensional propagation of the supramolecular structure. The $\mu\text{-}\kappa\text{N3}:\kappa\text{N9}$ -adeninates are able to establish double WC...WC and H...H synthons leading to $R_2^2(8)$ and $R_2^2(10)$ hydrogen bonding rings, respectively. On the other hand, the $\mu\text{-}\kappa\text{N7}:\kappa\text{N9}$ -adeninates are hydrogen bonded to the bridging hydroxide and the coordinated water molecule of an adjacent polymeric chain through N1 and N6 positions of the Watson–Crick face. The resulting supramolecular crystal structure shows the presence of large channels along the *b* axis with a calculated surface area of 295 m²/g and 44% of void space.

This compound is an interesting case because it is in between pure MOFs and SMOFs as it polymerizes into 1D through coordination bonds and further extends to supramolecular array through complementary hydrogen bonding interactions resulting in a 3D porous network (Figure 9c).

CONCLUSIONS

In this report we have paid special attention to the design prerequisites of SMOFs: (i) rigid building unit/complex, (ii) rigid and predictable synthons, and (iii) at least three non-coplanar synthons. This approach is supported by six new SMOFs based on different metal centers, nucleobases, and synthetic conditions. It also highlights the suitability of metal-nucleobase systems, specially purine based ones, to obtain SMOFs since many of them accomplish the above stated requirements: (i) the rigidity of the building unit is achieved using nucleobases because they can be coordinated through multiple positions, normally by a double anchoring (double coordination bonds or the combination of a coordination bond and an intramolecular hydrogen bond), (ii) the well-known complementary hydrogen bonding interactions between the nucleobases ensures the necessary rigidity of the predictable synthons, and (iii) the metal coordination geometries impose, in many cases, a non-coplanar arrangement of the nucleobases affording a non-coplanar disposition of the synthons that allows three-dimensional propagation of the nucleobase...nucleobase complementary hydrogen bonding assembly.

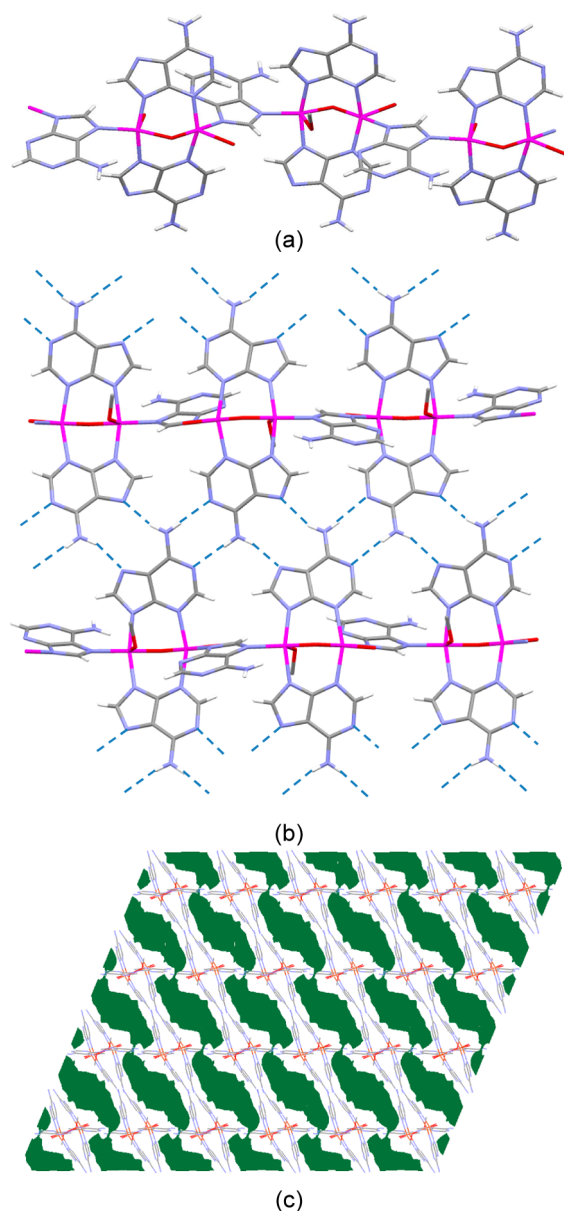


Figure 9. (a) Coordination polymeric chain. (b) Supramolecular complementary base pairing interactions among the adeninate entities. (c) Porous supramolecular architecture of SMOF-9 along the *b* axis.

Table 6. Hydrogen Bonding Interactions (Å, °) in SMOF-9^a

D–H...A ^b	H...A	D...A	D–H...A
N16–H16A...N11 ⁱⁱ	2.23	3.075(10)	170
N26–H26A...N21 ⁱⁱⁱ	2.06	2.920(11)	179
N26–H26B...N17 ^{iv}	2.08	2.904(11)	161
N36–H36B...O1 ^v	2.12	2.884(9)	148

^aSymmetry codes: (ii) $-x + 1, -y + 2, -z + 1$; (iii) $-x, -y + 2, -z$; (iv) $x - 1/2, -y + 3/2, z - 1/2$; (v) $-x + 1/2, -y + 3/2, -z$. ^bD: donor; A: acceptor.

■ ASSOCIATED CONTENT

Supporting Information

Tables of coordination bond lengths, figures of network topologies, XRPD patterns, and cif files. This material is available free of charge via the Internet at <http://pubs.acs.org>.

■ AUTHOR INFORMATION

Corresponding Authors

* (O.C.) E-mail: oscar.castillo@ehu.es. Fax: (internat): +34 946013500.

* (S.P.-Y.) E-mail: sonia.perez@ehu.es.

Author Contributions

[‡]These authors (J.T.-G and R.P.-A) contributed equally.

Notes

The authors declare no competing financial interest.

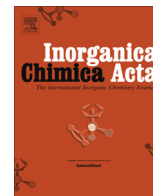
■ ACKNOWLEDGMENTS

This work has been funded by Ministerio de Economía y Competitividad (MAT2013-46502-C2-1-P), Eusko Jaurlaritza/Gobierno Vasco (Grant IT477-10, S-PE13UN016), and Universidad del País Vasco/Euskal Herriko Unibertsitatea (EHUA14/09, UFI 11/53, postdoctoral fellowship for S.P.Y.). Technical and human support provided by SGIKER (UPV/EHU, MINECO, GV/EJ, ERDF, and ESF) is gratefully acknowledged.

■ REFERENCES

- (1) Zhou, H.-C.; Long, J. R.; Yaghi, O. M. *Chem. Rev.* **2012**, *112*, 673.
- (2) Seo, J.; Jin, N.; Chun, H. *Inorg. Chem.* **2010**, *49*, 10833.
- (3) Bae, Y. S.; Farha, O. K.; Hupp, J. T.; Snurr, R. Q. *J. Mater. Chem.* **2009**, *19*, 2131.
- (4) Simard, M.; Su, D.; Wuest, J. D. *J. Am. Chem. Soc.* **1991**, *113*, 4696.
- (5) Kim, H.; Kim, Y.; Yoon, M.; Lim, S.; Park, S. M.; Seo, G.; Kim, K. *J. Am. Chem. Soc.* **2010**, *132*, 12200.
- (6) Holden, A. *Shapes, Space, and Symmetry*; Dover: New York, 1991; pp 154–163.
- (7) Thomas-Gipson, J.; Beobide, G.; Castillo, O.; Fröba, M.; Hoffmann, F.; Luque, A.; Pérez-Yáñez, S.; Román, P. *Cryst. Growth Des.* **2014**, *14*, 4019.
- (8) Reger, D. L.; Debreczeni, A.; Smith, M. D.; Jezierska, J.; Ozarowski, A. *Inorg. Chem.* **2012**, *51*, 1068.
- (9) Beobide, G.; Castillo, O.; Cepeda, J.; Luque, A.; Pérez-Yáñez, S.; Román, P.; Thomas-Gipson, J. *Coord. Chem. Rev.* **2013**, *257*, 2716.
- (10) Stylianou, K. C.; Warren, J. E.; Chong, S. Y.; Rabone, J.; Bacsá, J.; Bradshaw, D.; Rosseinsky, M. J. *Chem. Commun.* **2011**, *47*, 3389.
- (11) Kundu, S.; Mohapatra, B.; Mohapatra, C.; Verma, S.; Chandrasekhar, V. *Cryst. Growth Des.* **2015**, *15*, 247.
- (12) Thomas-Gipson, J.; Beobide, G.; Castillo, O.; Cepeda, J.; Luque, A.; Pérez-Yáñez, S.; Aguayo, A. T.; Román, P. *CrystEngComm* **2011**, *13*, 3301.
- (13) Nugent, P. S.; Rhodus, V. L.; Pham, T.; Forrest, K.; Wotjas, L.; Space, B.; Zaworotko, M. J. *J. Am. Chem. Soc.* **2013**, *135*, 10950.
- (14) *CrysAlis RED*, version 1.171.33.55; Oxford Diffraction: Wrocław, Poland, 2010.
- (15) Altomare, A.; Cascarano, M.; Giacovazzo, C.; Guagliardi, A. J. *Appl. Crystallogr.* **1993**, *26*, 343.
- (16) Sheldrick, G. M. *SHELXL-97, Program for X-ray Crystal Structure Refinement*; University of Göttingen: Göttingen, Germany, 1997.
- (17) Farrugia, L. J. *J. Appl. Crystallogr.* **1999**, *32*, 837.
- (18) Van der Sluis, P.; Spek, A. L. *Acta Crystallogr.* **1990**, *A46*, 194.
- (19) Spek, A. L. *J. Appl. Crystallogr.* **2003**, *36*, 7.
- (20) Amo-Ochoa, P.; Alexandre, S. S.; Hribesh, S.; Galindo, M. A.; Castillo, O.; Gómez-García, C. J.; Pike, A. R.; Soler, J. M.; Houlton, A.; Zamora, F. *Inorg. Chem.* **2013**, *52*, S290.
- (21) García-Couceiro, U.; Castillo, O.; Cepeda, J.; Lanchas, M.; Luque, A.; Pérez-Yáñez, S.; Román, P.; Vallejo-Sánchez, D. *Inorg. Chem.* **2010**, *49*, 11346.
- (22) Coronado, E.; Galán-Mascarós, J. R.; Gómez-García, C. J.; Laukhin, V. *Nature* **2000**, *408*, 447.
- (23) TOPOS Main Page. <http://www.topos.ssu.samara.ru> (accessed Apr. 2014).

- (24) Blatov, V. A. *IUCR CompComm Newsletter* **2006**, 7, 4.
- (25) O'Keeffe, M.; Yaghi, O. M. *Chem. Rev.* **2012**, 112, 675.
- (26) Sarkisov, L.; Harrison, A. *Molecular Simulation* **2011**, 37, 1248.
- (27) Pérez-Yáñez, S.; Beobide, G.; Castillo, O.; Cepeda, J.; Luque, A.; Román, P. *Cryst. Growth Des.* **2012**, 12, 3324.
- (28) Pandey, M. D.; Mishra, A. K.; Chandrasekhar, V.; Verma, S. *Inorg. Chem.* **2010**, 49, 2020.
- (29) Mishra, A. K.; Purohit, C. S.; Kumar, J.; Verma, S. *Inorg. Chim. Acta* **2009**, 362, 855.
- (30) Beck, W. M.; Calabrese, J. C.; Kottmair, N. D. *Inorg. Chem.* **1979**, 18, 176.
- (31) Sánchez-Moreno, M. J.; Choquesillo-Lazarte, D.; González-Pérez, J. M.; Carballo, R.; Castiñeiras, A.; Niclós-Gutiérrez, J. *Inorg. Chem. Commun.* **2002**, 5, 800.
- (32) Pérez-Yáñez, S.; Castillo, O.; Cepeda, J.; García-Terán, J. P.; Luque, A.; Román, P. *Inorg. Chim. Acta* **2011**, 365, 211.
- (33) An, J.; Fiorella, R. P.; Geib, S. J.; Rosi, N. L. *J. Am. Chem. Soc.* **2009**, 131, 8401.
- (34) Shekhah, O.; Wang, H.; Paradinas, M.; Ocal, M.; Schüpbach, B.; Terfort, A.; Zacher, D.; Fischer, R. A.; Wöll, C. *Nat. Mater.* **2009**, 8, 481.
- (35) Cepeda, J.; Castillo, O.; García-Terán, J. P.; Luque, A.; Pérez-Yáñez, S.; Román, P. *Eur. J. Inorg. Chem.* **2009**, 2344.
- (36) Pérez-Yáñez, S.; Beobide, G.; Castillo, O.; Cepeda, J.; Luque, A.; Román, P. *Cryst. Growth Des.* **2013**, 13, 3057.



Supramolecular extended systems based on discrete paddle-wheel shaped metal–adeninate entities



Rubén Pérez-Aguirre^{a,b}, Garikoitz Beobide^a, Oscar Castillo^{a,*}, Imanol de Pedro^b, Sonia Pérez-Yáñez^a

^a Departamento de Química Inorgánica, Facultad de Ciencia y Tecnología, Universidad del País Vasco, Apartado 644, E-48080 Bilbao, Spain

^b Facultad de Ciencias, Universidad de Cantabria, CITIMAC, E-39005 Santander, Spain

ARTICLE INFO

Article history:

Received 4 December 2015

Received in revised form 19 February 2016

Accepted 22 February 2016

Available online 3 March 2016

Keywords:

Supramolecular Metal–Organic Frameworks

Adenine

Paddle-wheel

Metal–nucleobase

ABSTRACT

The present work deals with the design and construction of supramolecular extended systems built up from paddle-wheel shaped metal–adeninate entities in which the deprotonation of the adenine affords a neutral $[\text{Cu}_2(\mu\text{-ade-}\kappa\text{N3}:\kappa\text{N9})_4(\text{H}_2\text{O})_2]$ (ade: adeninate anion) that would avoid the presence of counterions in the channels of the generated supramolecular architecture as happens for the cationic $[\text{Cu}_2(\mu\text{-Hade})_4(\text{X})_2]^{2+}$ (Hade: adenine) entity. This strategy allows us to obtain a new compound of formula $3[\text{Cu}_2(\mu\text{-ade-}\kappa\text{N3}:\kappa\text{N9})_4(\text{H}_2\text{O})_2] \cdot 2\{(\text{NHEt}_3)_2(\text{SO}_4)\} \cdot 10\text{H}_2\text{O} \cdot 2\text{CH}_3\text{OH}$ (**1**) in which the assembly of the neutral dimeric entities gives rise to an open 3D supramolecular architecture with a 45% of void volume. However, such a great available space allows its interpenetration by a second, although different, network of the same neutral $[\text{Cu}_2(\mu\text{-ade-}\kappa\text{N3}:\kappa\text{N9})_4(\text{H}_2\text{O})_2]$ entities assembled into 1D linear chains. The remaining available space within the channels is occupied by triethylammonium cations, sulphate anions, crystallization water and methanol molecules. The resulting crystal structure has been rationalized in terms of the rigidity of the building block, the predictability and rigidity of the synthons and the arrangement of these synthons around the metal–nucleobase discrete entity. The thermal and magnetic characterization of the compound has been also accomplished.

© 2016 Elsevier B.V. All rights reserved.

1. Introduction

Design and construction of metal–organic frameworks (MOFs) are of great interest because of their potential applications in areas such as gas storage, chemical separations, sensing, ion exchange, drug delivery and optics [1]. In order to create such materials, a careful choice of the metal ion and the organic ligand is a key issue [2]. In this sense, the unsubstituted adenine nucleobase is a good candidate because it contains at least five donor sites which endows it of great versatility as ligand [3]. In fact, there are several examples of metal–adenine based MBioFs that present permanent porosity [4]. However, at the present, we are focused on the adenine nucleobase as a molecule able to establish strong hydrogen bonding recognition processes in combination with its coordination capacity. Recently, we have developed a new family of porous materials in which the coordination bonds that sustain the 3D building of the MOFs are replaced with hydrogen bonds as connectors, which are also directional and predictable interactions (Fig. 1). These new materials containing accessible voids has been named Supramolecular Metal–Organic Frameworks (SMOFs) [5,6] and

constitute an alternative to more conventional Metal–Organic Frameworks (MOFs).

The crystal engineering principles and the synthetic approach to achieve this kind of materials are sustained in three requirements: (i) the use of rigid building units, (ii) the establishment of predictable and rigid synthons between the building units, and (iii) the non-coplanarity of functional groups involved in the predictable synthons. The rigidity requirement appearing in the first two conditions comes from the fact that condensed structures are preferred over the open ones. Flexible building units along with non rigid supramolecular interactions lead to systems with a potentially high structural diversity that mostly results in the crystallization of condensed structures. Therefore, a rational approach to get access to open structures would be working with systems in which the degrees of freedom inside the building units and the supramolecular interactions are reduced. In other words, rigid systems. The rigidity of the building units (discrete complexes) can be achieved using rigid ligands bonded through multiple positions. It means, in most common cases, a double anchoring of the ligand by means of two simultaneous coordination bonds or the combination of a coordination bond and an intramolecular hydrogen bond. The predictability and rigidity of the synthons requires the presence of adjacent functional groups, incorporated into the rigid

* Corresponding author. Tel.: +34 946 015 991; fax: +34 946 013 500.

E-mail address: oscar.castillo@ehu.es (O. Castillo).

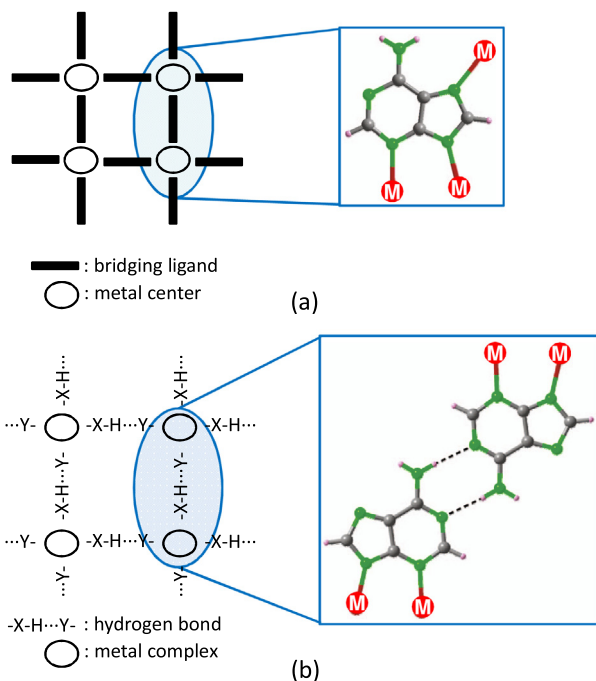


Fig. 1. Metal–nucleobase coordination-bond sustained MOFs (a) and base pairing assembled SMOFs (b).

ligands, able to establish complementary hydrogen bonding interactions. In this regard, the adenine nucleobase has been widely proven to provide both rigid discrete entities and rigid supramolecular synthons. It is usually anchored to the discrete complex entities through its N3 and N9 donor positions and exposes its Watson–Crick (N1/N6 positions) and Hoogsteen (N7/N6 positions) sides to provide rigid and predictable complementary hydrogen bonding interactions.

Finally, the requisite of non-coplanar arrangement of the synthons comes from our objective of obtaining three-dimensional extended systems that is achieved by the presence of at least three non-coplanar synthons. The use of non-planar coordination geometries for the complexes makes this last condition easy to accomplish.

Among our previously reported works on SMOFs, we can highlight two porous supramolecular compounds of formula $[\text{Cu}_2(\mu\text{-Hade})_4(\text{X})_2]^{2+}$ (**SMOF-1** and **SMOF-2**; $\text{X} = \text{Cl}^-$, Br^-) [3]. In these compounds the nucleobases are tightly anchored to the metal centers by two donor positions at the same time (N3 and N9 sites), imposing a rigid building unit. The metal coordination geometry imposes a rigid geometrical restraint among the nucleobases providing a set of non-coplanar synthons that otherwise would be difficult to achieve. As many hydrogen donor/acceptor positions of the nucleobase remain free, these discrete entities are able to self-assemble among them by means of complementary double hydrogen bonds (rigid synthons) prompting the growth of extended supramolecular solids in which great channels are present. However, the use of neutral adenines implies the presence of chloride counterions to balance the charge, reducing the accessible volume in the crystal structure.

In this work, we have focused our research on the use of deprotonated adenines (adeninates, ade) to obtain neutral paddle-wheel shaped $[\text{Cu}_2(\mu\text{-ade})_4]$ entities that could self assemble into an open structure without the need of additional ions in the channels to counterbalance the charge of the supramolecular network.

2. Experimental

2.1. Synthesis of $3[\text{Cu}_2(\mu\text{-ade-}\kappa\text{N3:}\kappa\text{N9})_4(\text{H}_2\text{O})_2] \cdot 2\{(\text{NHEt}_3)_2(\text{SO}_4)\} \cdot 10\text{H}_2\text{O} \cdot 2\text{CH}_3\text{OH}$ (**1**)

0.200 g of $\text{CuSO}_4 \cdot 5\text{H}_2\text{O}$ (0.8 mmol) dissolved in 20 mL of water were added dropwise to an aqueous/methanolic (10 mL/10 mL) solution of 0.108 g of adenine (0.8 mmol). The resulting deep blue mixture was acidified to pH 1.5 by adding H_2SO_4 . The resulting pale blue solution was placed in a small crystal beaker that was introduced into an Erlenmeyer flask containing a triethylamine aqueous solution (1/20 volume ratio). The vapour diffusion taking place inside the closed Erlenmeyer flask slowly basified the copper–adenine solution prompting the growing of purple crystals of **1** four days later. Yield of ca. 40% (based on metal). Main IR features of compound **1** (cm^{-1} , KBr pellet): 3430vs, 3197vs, 3120vs, 1644vs, 1600vs, 1564m, 1462s, 1400s, 1337m, 1306s, 1271vs, 1190s, 1150m, 1110s, 1071m, 1030m, 973w, 940w, 880w, 835w, 795m, 738m, 693m, 655m, 620m, 556m. *Anal. Calc.* for $\text{C}_{86}\text{H}_{152}\text{Cu}_6\text{N}_{64}\text{O}_{26}\text{S}_2$: C, 35.08; H, 5.20; Cu, 12.95; N, 30.45; S, 2.18. *Found*: C, 35.25; H, 5.07; Cu, 12.87; N, 30.42; S, 2.20%.

2.2. Physical measurements

Elemental analyses (C, H, N, S) were performed on a Euro EA elemental analyzer, whereas the metal content was determined by inductively coupled plasma atomic emission spectrometer (ICP-AES) from Horiba Yobin Yvon Activa. The IR spectra (KBr pellets) were recorded on a FTIR 8400S Shimadzu spectrometer in the $4000\text{--}400\text{ cm}^{-1}$ spectral region. Thermal analysis (TG/DTG/DTA) were performed on a TA Instruments SDT 2960 thermal analyzer in a synthetic air atmosphere (79% N_2 /21% O_2) with heating rate of 5 min^{-1} . The X-ray powder diffraction patterns (XRPD) were collected on a Phillips X'PERT powder diffractometer with Cu $K\alpha$ radiation. Magnetic measurements were performed on polycrystalline samples of the complexes taken from the same uniform batches used for the structural determinations with a Quantum Design SQUID susceptometer covering the temperature range $5.0\text{--}300\text{ K}$ at a magnetic field of 1000 G. The susceptibility data were corrected for the diamagnetism, as estimated from Pascal's tables [7], the temperature-independent paramagnetism and the magnetisation of the sample holder.

2.3. X-ray structure determination

A blocklike crystal ($0.35 \times 0.10 \times 0.10\text{ mm}$) was mounted on a Oxford Diffraction Xcalibur equipped with graphite-monochromated Mo $K\alpha$ radiation ($\lambda = 0.71073\text{ \AA}$) at 100(2) K. Data were processed and corrected for Lorentz and polarization effects. During the data reduction process it became clear that the crystal specimen was twinned containing a major domain and many minor ones. Therefore, the structure solution and refinement was performed using only the diffraction data belonging to the major domain. Additionally, one of the adeninato ligands is disordered in two coplanar arrangements with inverted orientation regarding the coordination mode ($\mu\text{-}\kappa\text{N3:}\kappa\text{N9}/\mu\text{-}\kappa\text{N9:}\kappa\text{N3}$), as it is relatively common for metal–adenine dimers [8]. Crystallographic details for structure **1** are summarized in Table 1.

The structure was solved by direct methods using the SIR97 program [9]. Full matrix least-squares refinements were performed on F^2 using SHELXL97 [10]. All non-hydrogen atoms were refined anisotropically. All calculations were performed using the WinGX crystallographic software package [11].

Table 1
Crystal data and structure refinement parameters for **1**.

Formula	C ₈₆ H ₁₅₂ Cu ₆ N ₆₄ O ₂₆ S ₂
Formula weight	2944.08
Crystal system	monoclinic
Space group	<i>P2₁/n</i>
<i>a</i> (Å)	13.0248(3)
<i>b</i> (Å)	20.9011(4)
<i>c</i> (Å)	23.1090(7)
<i>V</i> (Å ³)	6148.8(3)
<i>D</i> _{calc} (g cm ⁻³)	1.590
<i>μ</i> (mm ⁻¹)	1.149
<i>T</i> (K)	100(2)
<i>λ</i> (Å)	0.71073
<i>S</i> ^a	1.133
<i>R</i> ₁ , <i>wR</i> ₂ ^b [<i>I</i> > 2σ(<i>I</i>)]	0.0714, 0.1541
<i>R</i> ₁ , <i>wR</i> ₂ ^b [all]	0.0893, 0.1625

$$^a S = [\sum w(F_o^2 - F_c^2)^2 / (N_{obs} - N_{param})]^{1/2}$$

$$^b R_1 = \sum (|F_o| - |F_c|) / \sum |F_o|, wR_2 = [\sum w(|F_o| - |F_c|)^2 / \sum w|F_o|^2]^{1/2}$$

3. Results and discussion

Single-crystal X-ray diffraction analysis shows that compound **1** consist of two crystallographically independent neutral paddle-wheel shaped [Cu₂(μ-ade-κN3:κN9)₄(H₂O)₂] discrete entities (A and B dimers) cocrystallized with triethylammonium sulphate and crystallization solvent molecules (water and methanol). In the dimeric entities, four bridging adeninato ligands are linked to the copper(II) atoms through their N3 and N9 nitrogen atoms to provide the core of the paddle-wheel shaped dinuclear entity and two water molecules occupy the apical positions of the elongated square pyramidal coordination environment of the metal centers (Fig. 2). The structural parameters listed in Table 2 are similar to those reported for dimeric compounds containing μ-κN3:κN9 bridging purine ligands [12]. The coordination mode of the adenine ensures the rigidity of the building unit, the discrete dimeric entities, as required by our postulated first requirement to achieve porous materials.

It is well known that these entities can self-assemble through the base pairing of the Watson–Crick (N6–H, N1) and Hoogsteen faces (N6–H, N7) and by π–π stacking interactions. These base pairing interactions constitute the required predictable and rigid synthons (second requirement). Nonetheless, additional factors present in the reaction media, such as interactions with solvent molecules or counterions, can disrupt the direct hydrogen bonding interactions between the nucleobases.

The presence of non coplanar synthons propagating the supramolecular crystal structure in 3D can also be fulfilled in the case of the dimeric entities if both Watson–Crick and Hoogsteen faces are involved in the base pairing interactions.

Taking into account all the above mentioned requirements, the crystal structure shows a relatively unexpected result as each crystallographically independent [Cu₂(μ-adeninato-κN3:κN9)₄(H₂O)₂] entity establishes its own supramolecular network without significant interactions between the nucleobases belonging to each sub-network. “A” dimers are cross linked to four adjacent symmetry related ones through hydrogen bonding interactions involving the Watson–Crick and Hoogsteen faces of adjacent nucleobases to give a *R*₂²(9) ring. The propagation of this synthon gives rise to a supramolecular 2D square grid (Fig. 3). The topological analysis indicates a *sqI*/Shubnikov tetragonal plane net with point symbol (4⁴.6²) [13].

At this point, it is worth noting that the base pairing interaction between the [Cu₂(μ-Hade-κN3:κN9)₄Cl₂]²⁺ in reference [3a] leads to a 3D supramolecular network. The differences between both dimeric entities comes from the fact that in the cationic dimeric entity, only the Watson–Crick face (WC: N6–H and N1) is available

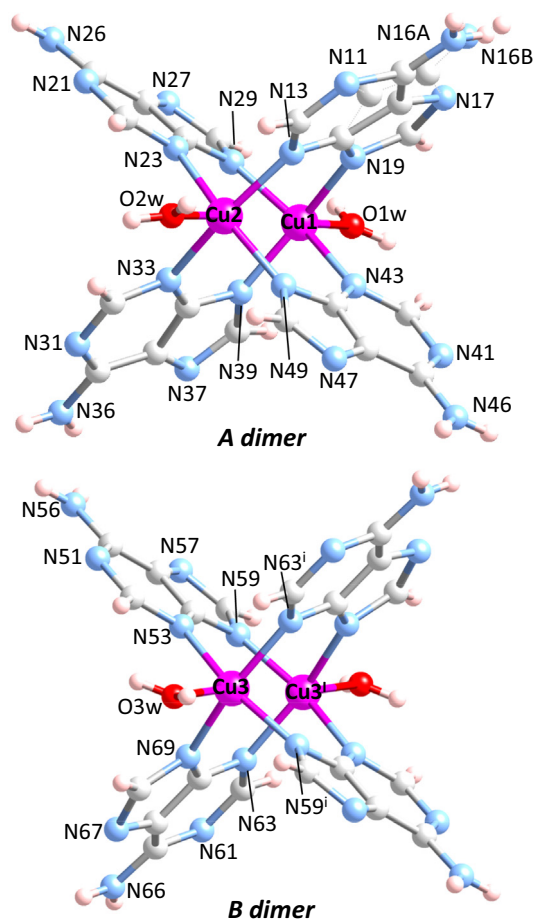


Fig. 2. Crystallographically independent [Cu₂(μ-ade-κN3:κN9)₄(H₂O)₂] entities found in compound **1**. The disorder present in one of the adeninato ligands is represented by dotted lines.

Table 2
Selected bond lengths [Å] for **1**.

Cu1–N19	2.020(4)	Cu2–N13	2.028(5)
Cu1–N29	2.004(4)	Cu2–N23	1.994(4)
Cu1–N39	1.979(4)	Cu2–N33	2.038(4)
Cu1–N43	2.024(4)	Cu2–N49	1.994(4)
Cu1–O1w	2.246(4)	Cu2–O2w	2.185(4)
Cu3–N53	2.024(4)	Cu3–N63 ⁱ	2.031(4)
Cu3–N59 ⁱ	1.992(4)	Cu3–N69	2.011(4)
Cu3–O3w	2.178(4)		
Cu1...Cu2	2.9562(9)	Cu3...Cu3 ⁱ	2.9653(12)

Symmetry codes: (i) $-x + 2, -y, -z + 1$.

for base pairing interaction whereas the Hoogsteen face (H: N6–H and N7–H) cannot establish complementary hydrogen bonds. As a consequence, direct adenine···adenine interactions involve WC···WC pairing. On the contrary, the neutral [Cu₂(μ-ade-κN3:κN9)₄(H₂O)₂] entity contains both the Watson–Crick (N6–H and N1) and Hoogsteen (N6–H and N7) faces available for base pairing and the interactions present in this crystal structure are almost all of them WC···H type. However, as each adeninato ligand only employ one of these faces on the base pairing interactions, this difference does not seem to be so relevant on determining the final supramolecular topology. There is a second main difference that in our opinion would account for it, the dihedral angle between the base pairing adenines: 117° for [Cu₂(μ-Hade-κN3:κN9)₄Cl₂]²⁺ entities and 171/137° for the neutral [Cu₂(μ-ade-κN3:κN9)₄(H₂O)₂] (Fig. 4). This difference implies that the relative orientation

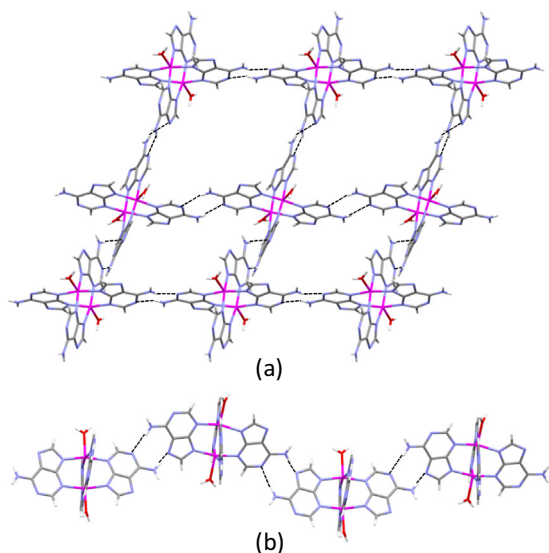


Fig. 3. Base pairing assembled 2D supramolecular sheets of $[\text{Cu}_2(\mu\text{-ade-}\kappa\text{N3:}\kappa\text{N9})_4(\text{H}_2\text{O})_2]$ "A" entities: frontal (a) and lateral (b) views. The disorder of one of the adeninato ligands has been omitted for clarity.

of the intradimeric $\text{Cu}\cdots\text{Cu}$ axes between adjacent dimeric entities also differs. It is nearly perpendicular in the case of the interacting $[\text{Cu}_2(\mu\text{-Hade-}\kappa\text{N3:}\kappa\text{N9})_4\text{Cl}_2]^{2+}$ entities, directing the supramolecular assembly into a 3D architecture. Probably because of the chloride counterion that interacts strongly with the Hoogsteen sides of the adenines and directs, in this sense, the final crystal structure. In

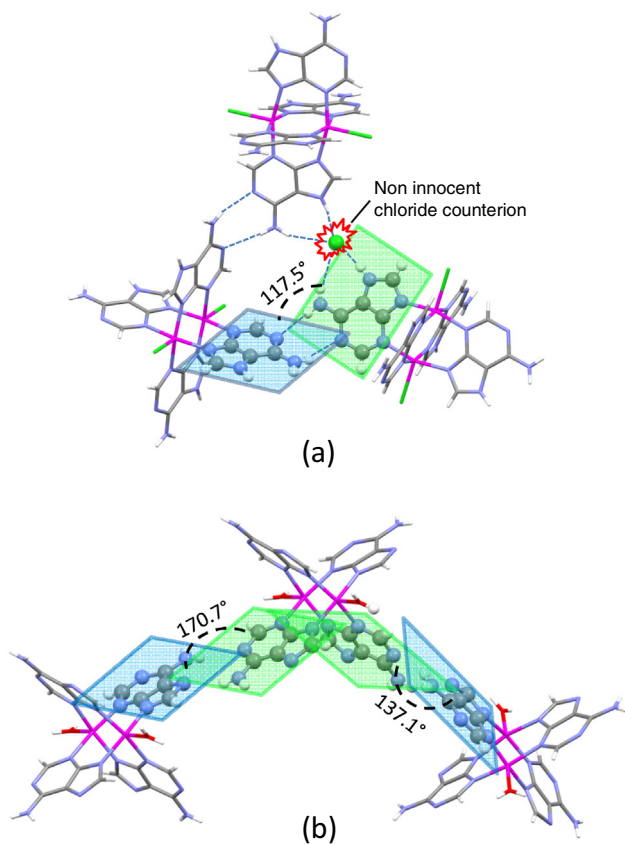


Fig. 4. Dihedral angles between the base pairing nucleobases between the cationic $[\text{Cu}_2(\mu\text{-adenine-}\kappa\text{N3:}\kappa\text{N9})_4\text{Cl}_2]^{2+}$ (a) and neutral $[\text{Cu}_2(\mu\text{-adeninato-}\kappa\text{N3:}\kappa\text{N9})_4(\text{H}_2\text{O})_2]$ (b) entities.

the case of neutral $[\text{Cu}_2(\mu\text{-ade-}\kappa\text{N3:}\kappa\text{N9})_4(\text{H}_2\text{O})_2]$ entities, the arrangement of the interacting nucleobases is more or less parallel, only allowing a 2D propagation of the base pairing interactions. This 2D pattern resembles a corrugated supramolecular sheet where the dimeric entities interacting through almost parallel adenines (dihedral angle: 171°) are collinear but those held together through less parallel interactions (dihedral angle: 137°) give rise to a significant undulation on the dimeric entities arrangement along this direction.

Coming back to the crystal structure of compound **1**, the base pairing assembled $[\text{Cu}_2(\mu\text{-ade-}\kappa\text{N3:}\kappa\text{N9})_4(\text{H}_2\text{O})_2]$ layers are held together through an additional hydrogen bond involving the coordinated water molecule as donor and the N7 position of the adeninato ligand as acceptor. It provides a 3D architecture (Fig. 5), with hexagonal BN (**bnn**) topology and point symbol $(4^6.6^4)$, which contains a 3D connected network of channels with a diameter of 4.6–8.2 Å, an estimated surface area of $2200\text{ m}^2/\text{g}$, and 45% of void space based on theoretical calculations [14,15].

The space present in the channels is not enough as to allow the interpenetration of a second supramolecular network of the same type as happens in the related supramolecular structure of compound $[\text{CoCl}_2(\text{Hade})_2]$ [6]. However, there is space enough to allow the interpenetration of a second but different supramolecular network of base pairing $[\text{Cu}_2(\mu\text{-ade-}\kappa\text{N3:}\kappa\text{N9})_4(\text{H}_2\text{O})_2]$ entities (dimer B). These dimeric entities only employ two of their four adeninato ligands, in *trans* arrangement, to self assemble through base pairing interactions. Interestingly, in this case the base pairing interactions involve only the Watson–Crick faces and the interacting adeninato ligands are parallel. As a result, it generates 1D supramolecular linear chains that propagate along the space generated in between the 2D supramolecular sheets during their assembly into the 3D supramolecular architecture previously described (Fig. 6). The two subnetworks interact through the hydrogen

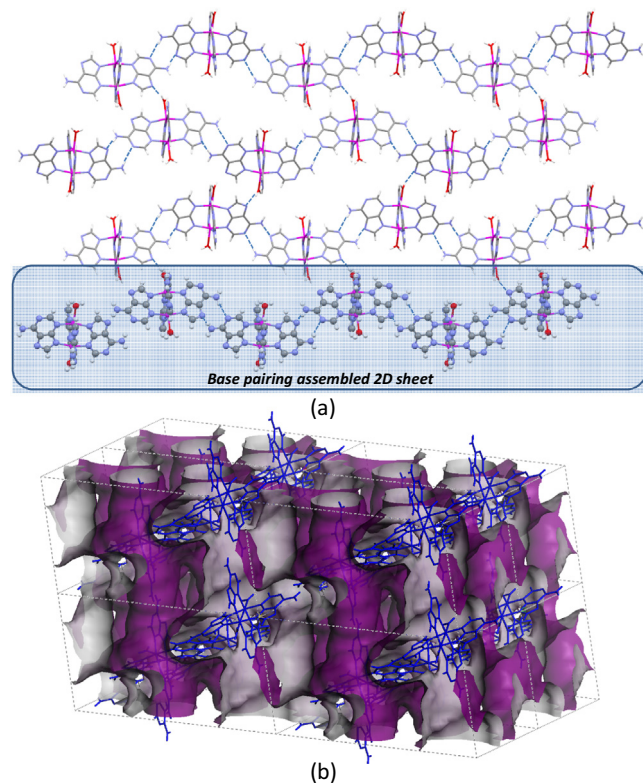


Fig. 5. (a) Assembly of the base pairing 2D sheets into a 3D supramolecular network. (b) Potential 3D interconnected channel system generated by the assembly of $[\text{Cu}_2(\mu\text{-ade-}\kappa\text{N3:}\kappa\text{N9})_4(\text{H}_2\text{O})_2]$ "A" entities.

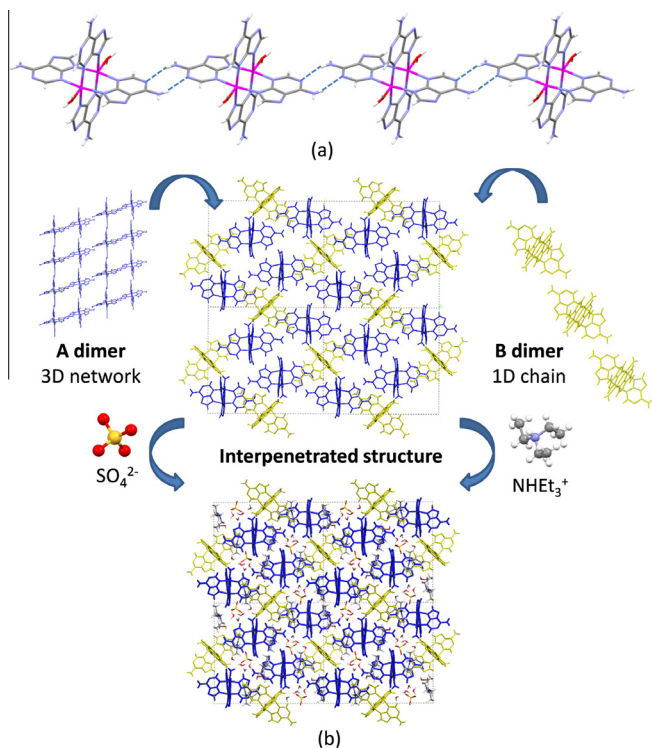


Fig. 6. (a) Base pairing assembled supramolecular chain of $[\text{Cu}_2(\mu\text{-ade-}\kappa\text{N3}:\kappa\text{N9})_4(\text{H}_2\text{O})_2]$ "B" entities. (b) Overall description of the interpenetration of both $[\text{Cu}_2(\mu\text{-ade-}\kappa\text{N3}:\kappa\text{N9})_4(\text{H}_2\text{O})_2]$ subnetworks and the cocrystallization of $(\text{NH}_2\text{Et}_2)_2\text{SO}_4$ in the voids of the crystal structure.

Table 3
Hydrogen bonding interactions (Å, °) involving the adeninato ligands.

	H...A	D...A	D-H...A
N16A-H...N31 ⁱ	2.56	3.405(11)	166.3
N16A-H...O3 ^j	2.03	2.807(10)	150.7
N16B-H...N31 ⁱ	2.05	2.894(11)	166.5
N16B-H...O3 ^j	2.46	3.227(12)	149.0
N26-H...N61 ⁱⁱ	2.40	3.209(6)	157.9
N26-H...N41 ⁱⁱⁱ	2.18	2.990(6)	157.0
N36-H...O3w ^{iv}	2.39	3.216(7)	160.8
N36-H...N17 ^v	2.13	2.966(6)	163.0
N46-H...N27 ^{vi}	2.10	2.885(7)	150.8
N46-H...O6w ^{vii}	2.34	2.982(7)	132.1
N56-H...O8w ^{iv}	2.18	2.862(8)	136.4
N66-H...N61 ^{viii}	2.12	2.943(6)	160.8
N66-H...O1w ^{ix}	2.36	3.196(6)	163.8
O1w-H...N67 ^x	1.97	2.752(5)	152.5
O2w-H...N47 ^{vii}	1.90	2.798(6)	163.5
O3w-H...N37 ^{xi}	1.82	2.666(6)	172.6
O5w-H...N11 ^x	2.08	2.858(6)	150.9
O7w-H...N21	1.99	2.838(6)	175.0
O1M-H...N57	1.97	2.780(6)	155.1

Symmetry codes: (i) $x - 1, y, z$; (ii) $-x + 2, -y, -z + 1$; (iii) $x + 1/2, -y + 1/2, z + 1/2$; (iv) $-x + 5/2, y + 1/2, -z + 1/2$; (v) $x + 1, y, z$; (vi) $x - 1/2, -y + 1/2, z - 1/2$; (vii) $-x + 2, -y, -z$; (viii) $-x + 1, -y, -z + 1$; (ix) $-x + 3/2, y - 1/2, -z + 1/2$; (x) $-x + 3/2, y + 1/2, -z + 1/2$; (xi) $-x + 5/2, y - 1/2, -z + 1/2$.

bonding interaction established between the O1w coordinated water molecule of dimer "A" and the N7 position of the adeninato ligand of an adjacent dimer "B". There is also a close contact between one of the N6-H position of dimer "B" pointing to the N9 position of dimer "A" (almost perpendicularly with respect to the adeninato mean plane), resembling a T type π interaction (N56...N19: 3.286(6) Å).

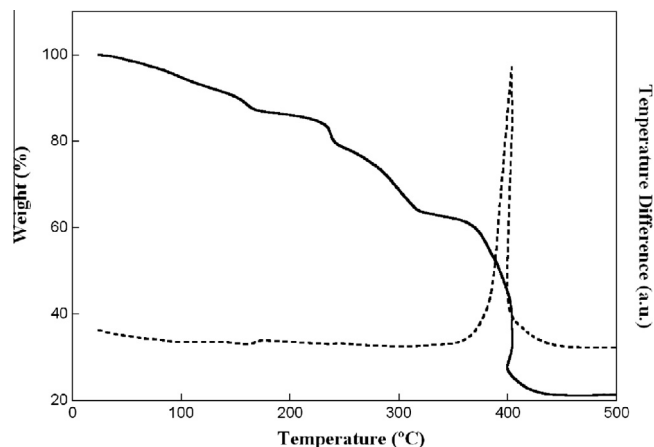


Fig. 7. Thermogravimetric curves (TG/DTA) in synthetic air atmosphere for compound **1**.

Table 4
Thermogravimetric data for compound **1**.

Step	$T_i - T_f$ (°C)	$\Delta m / \Sigma \Delta m$ (%)	$\Sigma \Delta m$ (%) _{teo}	ΔH
1	25–140	8.8/8.8	8.28 (–10H ₂ O + 2CH ₃ OH)	Endo
2	150–180	4.1/12.9	11.9 (–6H ₂ O)	Endo
3	215–250	8.2/21.1	18.8 (–2NEt ₃)	Endo
4	260–330	15.3/36.4	34.8 (–2NEt ₃ + 2C ₂ H ₅ N ₃)	Endo
5	350–440	42.5/78.9	80.4 (4CuO + 2CuSO ₄)	Exo

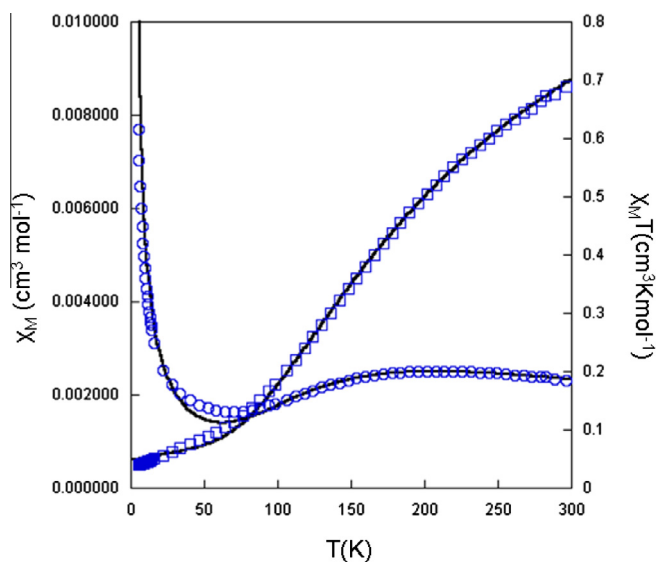


Fig. 8. χ_M and the $\chi_M T$ vs. T plots. Blue coloured circles correspond to experimental χ_M values while blue coloured squared correspond to experimental $\chi_M T$ ones. Black line corresponds to the best theoretical fit for both curves. (For interpretation of the references to colour in this figure legend, the reader is referred to the web version of this article.)

The remaining available space within the channels is occupied by triethylammonium cations, sulphate anions, crystallization water and methanol molecules that establish a complex hydrogen bond network involving also the donor/acceptor positions of the adeninato ligands not involved in the base pairing interactions. It is worth mentioning that although parallel π - π stacking of nucleobases is common in many systems, there is no evidence of this kind of interaction in compound **1**. Table 3 gathers the hydrogen bonding interactions present in this compound.

Table 5Structural parameters and *J* values of some representative compounds together with the observed for herein studied compound.^a

Compounds	Cu–N	Cu–X	Cu···Cu	<i>T</i> _{max}	<i>J</i> _{exp}	References
[Cu ₂ (ade) ₄ (NH ₃) ₂].6H ₂ O	—	—	—	222	—	[12c]
[Cu ₂ (ade) ₄ (H ₂ O) ₂].(bpa).8H ₂ O	2.01	2.21	2.95	180	–222	[8a]
[Cu ₂ (ade) ₄ (Pip) ₂].6H ₂ O	—	—	—	210	–246	[12c]
This work	1.99–2.04	2.19–2.25	2.96	200	–248	
[Cu ₂ (ade) ₄ (H ₂ O) ₂].5H ₂ O	2.02	2.20	2.95	—	–257	[12d]
[Cu ₂ (Hade) ₄ Br ₂].2H ₂ O	—	—	—	—	–284	[17]
[Cu ₂ (Hade) ₄ (H ₂ O) ₂](NO ₃) ₄ .2[Cu(Pic) ₂ (H ₂ O)].6H ₂ O	2.00	2.17	3.00	—	–288	[8a]
[Cu ₂ (Hade) ₄ Cl ₂].Cl ₂ .6H ₂ O	2.03	2.43	3.07	251	–285	[18]
[Cu ₂ (Hade) ₄ (H ₂ O) ₂](SO ₄).6H ₂ O	—	—	—	253	–305	[12c]
[Cu ₂ (Hade) ₄ (H ₂ O) ₂](ClO ₄).2H ₂ O	2.03	2.17	2.95	243	–312	[12c, 12e]
[Cu ₂ (Hypox) ₄ Cl ₂].Cl ₂ .6H ₂ O	2.00	2.43	3.02	212	–211	[12c, 19]
[Cu ₂ (Hypox) ₄ Br ₂].2H ₂ O	—	—	—	—	–284	[17]
[Cu ₂ (6ClPur) ₄ (H ₂ O) ₂].6H ₂ O	2.02	2.12	2.97	220	–250	[8a]

^a Cu–N: equatorial copper–nitrogen distance; Cu–X: axial copper–ligand distance; Cu···Cu: distance between intradimeric copper atoms.

The thermal degradation under synthetic air atmosphere (Fig. 7 and Table 4) shows that the compound starts losing the non coordinated solvent molecules from room temperature to 140 °C. Almost immediately, in a process that starts at 150 °C and ends at 180 °C, the coordinated water molecules are released. The resulting anhydrous product remains stable up to 215 °C after which it undergoes several decomposition processes to provide a mixture of CuO and CuSO₄ as the final residue at temperatures above 440 °C.

The thermal evolution of the molar magnetic susceptibility (χ_M) and the $\chi_M T$ product are indicative of strong intradimeric antiferromagnetic interactions. The χ_M curve suffers an initial rise upon cooling from room temperature to gain the maximum value at 200 K. Afterwards, it decreases and reaches a minimum value in the vicinity of 60 K and increases again at lower temperatures as a result of the presence of paramagnetic impurities. Room-temperature $\chi_M T$ values are lower than that expected for two uncoupled paramagnetic $S = 1/2$ centre (0.75 cm³ mol^{–1} K, $g = 2.0$) which is indicative of strong intradimeric interactions. Continuous drop is observed to reach a plateau below 50 K attributed to the presence of a small amount of paramagnetic impurities (Fig. 8). The experimental magnetic data were fitted by using the Bleaney–Bowers equation ($H = -JS_1S_2$) for a dinuclear copper(II) complex [16] modified to take into account the presence of the paramagnetic impurities. The obtained *J* value (–248 cm^{–1}) falls within the range of previously reported compounds with [Cu₂(μ-purine ligand)₄(X)₂]^{*n*+} (*n* = 0, 2, 4; X = H₂O, Cl, Br) entities (Table 5), in which the dispersion of the *J* values pointed out that structural/chemical parameters strongly influence the magnitude of the magnetic coupling. In particular, the *J* value can be related to the increase in the number of electron lone pairs in the bridging ligand (by means of the deprotonation or by substitution of the exocyclic amine group by a chlorine atom). This fact increases the extension of the molecular orbitals of the bridging ligands and the N3 and N9 atoms contribute to a lesser extent, so they overlap less efficiently with the metal-centered magnetic orbitals and a weaker antiferromagnetic interaction is observed, as it can be noticed for the herein studied compound.

4. Conclusions

The result shows that neutral [Cu₂(μ-ade-κN3:κN9)₄(H₂O)₂] neutral entities can effectively generate supramolecular open architectures, but some other subtle factors such as the solvent, the presence of other apparently innocent ions and the possibility of interpenetration play also a significant role in transforming these supramolecular open structures into real porous materials.

Acknowledgments

This work was supported by the Ministerio de Economía y Competitividad (MAT2013-46502-C2-1-P), Eusko Jaurlaritz/Gobierno Vasco (Grant IT477-10), and Universidad del País Vasco/Euskal Herriko Unibertsitatea (UFI 11/53, postdoctoral fellowship for S.P. Y.). Technical and human support provided by SGIKER (UPV/EHU, MINECO, GV/EJ, ERDF, and ESF) is gratefully acknowledged.

Appendix A. Supplementary material

CCDC 1440642 contains the supplementary crystallographic data for this paper. These data can be obtained free of charge from The Cambridge Crystallographic Data Centre via www.ccdc.cam.ac.uk/data_request/cif. Supplementary data associated with this article can be found, in the online version, at <http://dx.doi.org/10.1016/j.ica.2016.02.049>.

References

- [1] (a) H.-C. Zhou, S. Kitagawa, *Chem. Soc. Rev.* 43 (2014) 5415. and all articles of this special issue; (b) H.-C. Zhou, J.R. Long, O.M. Yaghi, *Chem. Rev.* 112 (2012) 673. and all articles of this special issue.
- [2] (a) M. Zhang, M. Bosch, T. Gentle, H.-C. Zhou, *CrystEngComm* 16 (2014) 4069; (b) H. Furukawa, K.E. Cordova, M. O’Keeffe, O.M. Yaghi, *Science* 341 (2013) 974; (c) M.G. Goesten, F. Kapteijn, J. Gascon, *CrystEngComm* 15 (2013) 9249.
- [3] (a) S. Verma, A.K. Mishra, J. Kumar, *Acc. Chem. Res.* 43 (2010) 79; (b) A. Domínguez-Martín, M.P. Brandi-Blanco, A. Matilla-Hernández, H. El Bakkali, V.M. Nurchi, J.M. González-Pérez, A. Castiñeiras, J. Niclós-Gutiérrez, *Coord. Chem. Rev.* 257 (2013) 2841.
- [4] (a) I. Imaz, M. Rubio-Martínez, J. An, I. Solé-Font, N.L. Rosi, D. Maspoch, *Chem. Commun.* 47 (2011) 7287; (b) G. Beobide, O. Castillo, J. Cepeda, A. Luque, S. Pérez-Yáñez, P. Román, J. Thomas-Gipson, *Coord. Chem. Rev.* 257 (2013) 2716; (c) G. Beobide, O. Castillo, A. Luque, S. Pérez-Yáñez, *CrystEngComm* 17 (2015) 3051.
- [5] (a) J. Thomas-Gipson, G. Beobide, O. Castillo, J. Cepeda, A. Luque, S. Pérez-Yáñez, A.T. Aguayo, P. Román, *CrystEngComm* 13 (2011) 3301; (b) J. Thomas-Gipson, G. Beobide, O. Castillo, M. Fröba, F. Hoffmann, A. Luque, S. Pérez-Yáñez, P. Román, *Cryst. Growth Des.* 14 (2014) 4019.
- [6] J. Thomas-Gipson, R. Pérez-Aguirre, G. Beobide, O. Castillo, A. Luque, S. Pérez-Yáñez, P. Román, *Cryst. Growth Des.* 15 (2015) 975.
- [7] A. Earnshaw, In: *Introduction to Magnetochemistry*, Academic Press, London, 1968.
- [8] (a) J. Cepeda, O. Castillo, J.P. García-Terán, A. Luque, S. Pérez-Yáñez, P. Román, *Eur. J. Inorg. Chem.* (2009) 2344; (b) S. Pérez-Yáñez, G. Beobide, O. Castillo, J. Cepeda, A. Luque, P. Román, *Cryst. Growth Des.* 13 (2013) 3057.
- [9] A. Altomare, M.C. Burla, M. Camalli, G.L. Casciarano, C. Giacovazzo, A. Guagliardi, A.G.G. Moliterni, R. Spagna, *J. Appl. Crystallogr.* 32 (1999) 115.
- [10] G.M. Sheldrick, *SHELXS97* and *SHELXL97*, University of Göttingen, Germany, 1997.
- [11] J. Farrugia, *WINGX*, A Windows Program for Crystal Structure Analysis, University of Glasgow, Glasgow, 1998.
- [12] (a) J.M. González-Pérez, C. Alarcón-Payer, A. Castiñeiras, T. Pivetta, L. Lezama, D. Chokesillo-Lazarte, G. Crisponi, J. Niclós-Gutiérrez, *Inorg. Chem.* 45 (2006) 877;

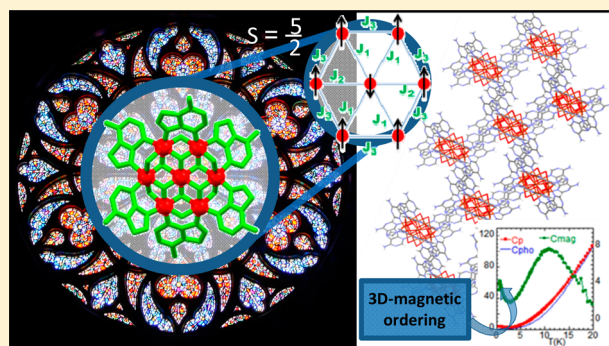
- (b) J.W. Suggs, M.J. Dube, M. Nichols, *J. Chem. Soc., Chem. Commun.* (1993) 307;
- (c) D. Sonnenfroh, R.W. Kreilick, *Inorg. Chem.* 19 (1980) 1259;
- (d) E. Sletten, *Acta Crystallogr., Sect. B: Struct. Crystallogr. Cryst. Chem.* 25 (1969) 1480;
- (e) A. Terzis, A.L. Beauchamp, R. Rivest, *Inorg. Chem.* 12 (1973) 1166.
- [13] (a) TOPOS Main Page. <http://www.topos.ssu.samara.ru> (accessed Nov. 2015).;
- (b) V.A. Blatov, *IUCR Comp. Comm Newslett.* 7 (2006) 4;
- (c) M. O'Keeffe, O.M. Yaghi, *Chem. Rev.* 112 (2012) 675;
- (d) V.A. Blatov, M. O'Keeffe, D.M. Proserpio, *CrystEngComm* 12 (2010) 44;
- (e) E.V. Alexandrov, V.A. Blatov, A.V. Kochetkov, D.M. Proserpio, *CrystEngComm* 13 (2011) 3947.
- [14] L. Sarkisov, A. Harrison, *Mol. Simulat.* 37 (2011) 1248.
- [15] A.L. Spek, *J. Appl. Crystallogr.* 36 (2003) 7.
- [16] B. Bleaney, K.D. Bowers, *Proc. Roy. Soc. Ser. A* 214 (1952) 451.
- [17] T. Asakawa, M. Innoue, K.-I. Hara, M. Kubo, *Bull. Chem. Soc. Jpn.* 45 (1972) 1054.
- [18] P. De Meester, A.C. Skapski, *J. Chem. Soc. A* 13 (1971) 2167.
- [19] E. Sletten, *Acta Crystallogr., Sect. B* 26 (1970) 1609.

3D Magnetically Ordered Open Supramolecular Architectures Based on Ferrimagnetic Cu/Adenine/Hydroxide Heptameric Wheels

Rubén Pérez-Aguirre,[‡] Garikoitz Beobide,[‡] Oscar Castillo,^{*,‡} Imanol de Pedro,^{*,§} Antonio Luque,[‡] Sonia Pérez-Yáñez,[‡] Jesús Rodríguez Fernández,[§] and Pascual Román[‡][‡]Departamento de Química Inorgánica, Facultad de Ciencia y Tecnología, Universidad del País Vasco, UPV/EHU, Apartado 644, E-48080 Bilbao, Spain[§]CITIMAC, Facultad de Ciencias, Universidad de Cantabria, E-39005 Santander, Spain

Supporting Information

ABSTRACT: The present work provides two new examples of supramolecular metal–organic frameworks consisting of three-dimensional extended noncovalent assemblies of wheel-shaped heptanuclear $[\text{Cu}_7(\mu\text{-H}_2\text{O})_6(\mu_3\text{-OH})_6(\mu\text{-adeninato-}\kappa\text{N3}:\kappa\text{N9})_6]^{2+}$ entities. The heptanuclear entity consists of a central $[\text{Cu}(\text{OH})_6]^{4+}$ core connected to six additional copper(II) metal centers in a radial and planar arrangement through the hydroxides. It generates a wheel-shaped entity in which water molecules and $\mu\text{-}\kappa\text{N3}:\kappa\text{N9}$ adeninato ligands bridge the peripheral copper atoms. The magnetic characterization indicates the central copper(II) center is anti-ferromagnetically coupled to external copper(II) centers, which are ferromagnetically coupled among them leading to an $S = 5/2$ ground state. The packing of these entities is sustained by $\pi\text{-}\pi$ stacking interactions between the adenine nucleobases and by hydrogen bonds established among the hydroxide ligands, sulfate anions, and adenine nucleobases. The sum of both types of supramolecular interactions creates a rigid synthon that in combination with the rigidity of the heptameric entity generates an open supramolecular structure (40–50% of available space) in which additional sulfate and triethylammonium ions are located altogether with solvent molecules. These compounds represent an interesting example of materials combining both porosity and magnetic relevant features.



INTRODUCTION

Metal–organic frameworks (MOFs) encompass an area of chemistry that has experienced impressive growth during the last decades because of their various potential applications in catalysis, gas storage, chemical separations, sensing, ion exchange, drug delivery, and optics.¹ Their large surface areas, adjustable pore sizes, and controllable functionalities are the key factors on their multiple applications.^{2,3} Recently, we explored a related type of material, supramolecular metal–organic frameworks (SMOFs), in which the three-dimensional (3D) crystal building containing potentially accessible voids is sustained by hydrogen bonds as connectors, which are also directional and predictable interactions. The design of this kind of material is based on the following key factors: (i) the use of rigid building units, (ii) the presence of rigid synthons connecting the building units, and (iii) the non-coplanarity of functional groups involved in the synthons.⁴ The stiffness of the building units (discrete complexes) can be achieved using nonflexible ligands anchored to the metal center through multiple positions. The predictability and rigidity of the synthons requires the presence of adjacent functional groups in the ligands able to establish complementary hydrogen-bonding interactions. Finally, the requisite of non-coplanar

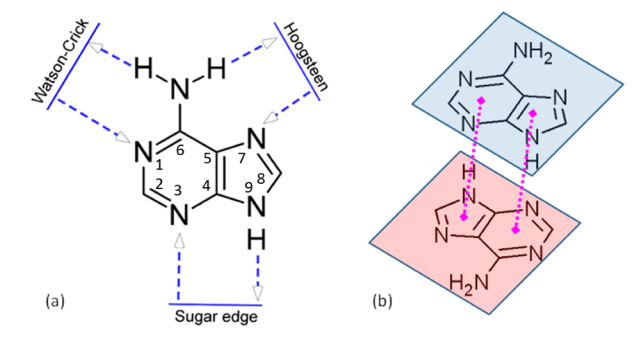
arrangement of the synthons comes from our objective of obtaining 3D extended systems that is achieved by the presence of at least three non-coplanar synthons. The use of nonplanar coordination geometries for the complexes makes this last condition easy to accomplish. From previous studies we realized that a suitable system that would fulfill all the above-described requirements for obtaining SMOFs are the discrete metal-nucleobase systems, especially those based on purine nucleobases.⁵ These ligands provide, on one hand, the advantage of the increased rigidity of the supramolecular building block due to the coordination through multiple positions, and, on the other hand, they present many edges capable of establishing complementary hydrogen-bonding interactions that provide rigid and predictable synthons (Scheme 1). However, some other factors such as pH, solvent molecules, or other species present in the reaction media can direct the resulting final crystal structure and are also factors that need to be kept in mind.

Moreover, the building of SMOFs from transition metal ions set up the possibility of designing functional nanoporous

Received: May 20, 2016

Published: July 13, 2016

Scheme 1. Capability of Adenine to Establish Supramolecular Interactions through Hydrogen Bonding (a) and π - π Stacking (b)



materials with additional physical properties. Among these, the development of magnetic open-framework structures based on nucleobases is an appealing challenge for sensing applications, as it would bring together porosity, magnetism, and the well-known molecular recognition ability of biomolecules.⁶

It must be pointed out that there exists a notable number of MOFs that successfully meet porosity and relevant magnetic properties. However, there are also enormous difficulties in increasing pore sizes without compromising the strength of magnetic couplings.⁷ Without a doubt, magnetic exchange interactions between metal ions take place through a superexchange coupling involving ligand orbitals, a mechanism that is strongly dependent on the distance and angle between interacting ions. Although some systematic rules have been defined for the design of bigger pore size and different topologies, such modifications are expected to decrease, or in the worst case disrupt, the superexchange magnetic coupling. To overcome these disadvantages, alternative methods are being explored. Among them, the use of metal clusters as nodes with a high-spin ground state or single-molecule magnet behavior outstand, which can be further connected by spacers (ligands) of any size without prejudicing the pristine magnetic properties of the nodes.⁸ A recent example published by Zhao et al. consists of a (3,6)-connected two-dimensional coordination polymer built from sulfoisophthalate/adeninato-derived Cu^{II} wheels and $S = 5/2$ ground state.⁹ It is worth mentioning the relationship of the spin topology of the wheels with the frustrated triangular anti-ferromagnetic (AF) lattice, which is one of the very few solvable models in spin-frustrated systems.¹⁰ It makes this system an attractive target for displaying magneto caloric effect (MCE) and using it for low-temperature refrigeration purposes. In fact, such effects have been recently observed in a molecular cluster based on Gd^{III} and Fe^{III} with this triangular AF lattice structure.¹¹

Herein we report two new SMOFs consisting of heptanuclear metal-nucleobase entities with a high-spin ground state ($S = 5/2$), which self-assemble by means of hydrogen bonding and π - π interactions into two supramolecular open architectures with long-range magnetic ordering.

EXPERIMENTAL PROCEDURES

Chemicals. All the chemicals were of reagent grade and were used as commercially obtained.

Synthesis of $[\text{Cu}_7(\mu\text{-H}_2\text{O})_6(\mu_3\text{-OH})_6(\mu\text{-Adeninato-}\kappa\text{N3}:\kappa\text{N9})_6](\text{NH}_4)_2(\text{SO}_4)_2 \cdot 42\text{H}_2\text{O}$ (1) and $[\text{Cu}_7(\mu\text{-H}_2\text{O})_6(\mu_3\text{-OH})_6(\mu\text{-Adeninato-}\kappa\text{N3}:\kappa\text{N9})_6](\text{NH}_4)_2(\text{SO}_4)_2 \cdot 23\text{H}_2\text{O}$ (2). A solution of 0.1996 g (0.8 mmol) of $\text{CuSO}_4 \cdot 5\text{H}_2\text{O}$ dissolved in 20 mL of water was added dropwise to a 20 mL aqueous methanolic (1/1) solution containing

0.1080 g (0.8 mmol) of adenine. Immediately a dark blue precipitate appeared, which was dissolved by adding a few drops of H_2SO_4 concentrated to set the pH value at 1.5. Later the pH was fixed at 10 by adding triethylamine, and the resulting mixture was placed in a small beaker that was introduced into an Erlenmeyer flask containing a 1/5 (v/v) sulfuric acid solution. The vapor diffusion taking place inside the closed Erlenmeyer flask slowly acidified the solution allowing the growth of blue prismatic crystals of **1** after 4 d (pH = 8; yield: 80–90%). If the beaker containing the reaction mixture is removed from the Erlenmeyer flask and left open in contact with atmosphere after the appearance of crystals of compound **1**, the solution evolves toward the disappearance of the prismatic crystals of **1** and the apparition of new blue cubic crystals belonging to compound **2** (pH = 7; yield: 60–70%).

Physical Measurements. The IR spectra (KBr pellets) were recorded on an FTIR 8400S Shimadzu spectrometer in the 4000–400 cm^{-1} spectral region. Variable-temperature magnetic susceptibility measurements were performed using a standard Quantum Design PPMS magnetometer while heating from 2 to 300 K at 1 kOe range after cooling in the absence (zero-field cooling, ZFC) of the applied field. Magnetization as a function of field (H) was measured using the same magnetometer in the $-50 \leq H/\text{kOe} \leq 50$ at 2 K after cooling the sample in zero field. The susceptibility data were corrected for the diamagnetism estimated from Pascal's Tables,¹² the temperature-independent paramagnetism and the magnetization of the sample holder. Heat capacity was measured with the same device between 0.40 and 300 K at several magnetic fields from 0 to 90 kOe using a standard relaxation method with a two-tau model. To guarantee a good thermal contact, a piezon N grease was used to glue the sample to the sample holder. The addenda (sample holder and grease) were measured under different magnetic fields before the sample measurements were taken and then subtracted from the total heat capacity to get the sample heat capacity. The sample used was a 4.54 and 4.38 mg plate for **1** and **2** obtained compressing the original thin powder. Thermal analyses (thermogravimetry (TG)/differential thermal analysis (DTA)) were performed on a TA Instruments SDT 2960 thermal analyzer in a synthetic air atmosphere (79% N_2 /21% O_2) with a heating rate of 5 $^\circ\text{C} \cdot \text{min}^{-1}$. The purity of the samples was assessed by powder X-ray diffraction, TG, and FTIR analyses (see Supporting Information).

X-ray Diffraction Data Collection and Structure Determination. Single-crystal diffraction data were collected at 100(2) K on Agilent Technologies Supernova diffractometers ($\lambda_{\text{Cu-K}\alpha} = 1.54184 \text{ \AA}$ for **1** and $\lambda_{\text{Mo-K}\alpha} = 0.71073 \text{ \AA}$ for **2**). The data reduction was done with the CrysAlisPro program.¹³ Crystal structures were solved by direct methods using the SIR92 program¹⁴ and refined by full-matrix least-squares on F^2 including all reflections (WINGX).^{15,16} One-third of the adeninato ligands in compound **1** and all of them in compound **2** are disordered into two coplanar arrangements with inverted orientation regarding the coordination mode ($\mu\text{-}\kappa\text{N3}:\kappa\text{N9}/\mu\text{-}\kappa\text{N9}:\kappa\text{N3}$).¹⁷ The crystal structure of both compounds revealed the presence of large channels in which the solvent molecules, triethylammonium, and sulfate anions are placed. The high disorder that these entities present precluded their modeling and, as a consequence, the electron density at the voids of the crystal structure was subtracted from the reflection data by the SQUEEZE method¹⁸ as implemented in PLATON.¹⁹ The electron density provided by the SQUEEZE routine matches the expected from the number of triethylammonium, sulfate, and solvation water molecules hosted in the channels. Details of the structure determination and refinement of all compounds are summarized in Table 1.

RESULTS AND DISCUSSION

The direct reaction between CuSO_4 and adenine immediately produces a very fine powder in a quantitative yield. All the attempts to grow X-ray diffraction suitable single crystals of this product were unsuccessful. Therefore, it was decided to acidify the reaction media until complete solubilization of this product is achieved. Later, the pH was increased by slow vapor diffusion

Table 1. Crystallographic Data and Structure Refinement Details of Compounds 1 and 2

	1	2
empirical formula	C ₄₂ H ₁₅₈ Cu ₇ N ₃₂ O ₆₂ S ₂	C ₄₂ H ₁₂₀ Cu ₇ N ₃₂ O ₄₃ S ₂
formula weight	2612.83	2270.54
crystal system	monoclinic	trigonal
space group	C2/c	R3c
a (Å)	15.5705(6)	18.9582(5)
b (Å)	22.3823(10)	
c (Å)	27.2969(9)	43.2908(14)
β (deg)	101.102(4)	
V (Å ³)	9335.0(6)	13 474.7(7)
Z	4	6
T (K)	100(2)	100(2)
λ (Å)	1.541 84	0.710 73
ρ _{calcd} (g·cm ⁻³)	1.320	1.258
μ (cm ⁻¹)	2.666	1.739
S ^a	1.519	1.158
R _{int}	0.0849	0.0516
final R indices		
[I > 2σ(I)] R ₁ ^b /wR ₂ ^c	0.1205/0.3766	0.0969/0.3083
all data R ₁ ^b /wR ₂ ^c	0.1479/0.4025	0.1142/0.3237

^aS = $[\sum w(F_o^2 - F_c^2)^2 / (N_{\text{obs}} - N_{\text{param}})]^{1/2}$. ^bR₁ = $\sum ||F_o| - |F_c|| / \sum |F_o|$. ^cwR₂ = $[\sum w(F_o^2 - F_c^2)^2 / \sum wF_o^4]^{1/2}$; w = $1/[\sigma^2(F_o^2) + (0.2000P)^2 + b]$ where P = $(\max(F_o^2, 0) + 2F_c^2)/3$.

of a weakly coordinating amine to precipitate again the copper–adenine product. This indirect route allowed us to get suitable single crystals of compounds **1** and **2** (depending on the crystallization time) that otherwise would be almost impossible to obtain by direct reaction of the reagents.

The crystal structure of compounds **1** and **2** contains cationic $[\text{Cu}_7(\mu\text{-H}_2\text{O})_6(\mu_3\text{-OH})_6(\mu\text{-adeninato-}\kappa\text{N3:}\kappa\text{N9})_6]^{2+}$ heptanuclear entities, sulfate, and triethylammonium ions. The complex entity consists of a central $[\text{Cu}(\text{OH})_6]^{4-}$ core that is connected to six additional copper(II) metal centers in a radial and planar arrangement through the hydroxides (Figures 1 and 2). The hydroxide anions adopt a μ_3 -bridging mode in such a way that they connect the central metal atom to two external ones. It generates a wheel-shaped entity in which water molecules and $\mu\text{-}\kappa\text{N3:}\kappa\text{N9}$ adeninato ligands bridge the peripheral copper atoms. All the metal centers present an octahedral geometry with the usual Jahn–Teller tetragonal elongation, but it is far more pronounced for the peripheral copper(II) centers ($\Delta d \approx 0.5\text{--}0.6$ Å) than for the central one ($\Delta d = 0.2$ Å), probably because of the rigidity of the wheel-shaped heptanuclear entity. The elongation at the peripheral copper atoms takes place along the metal–water coordination bonds in such a way that the coordinated water molecules are less strongly held to the complex entity than the adeninato ligands that establish shorter coordination bonds. In any case, the heptameric entity can be considered as a rigid building unit, as all the components establish at least two coordination bonds. Bond distances around the copper atoms are listed in Table S1 in the Supporting Information.

It is remarkable that the central copper(II) atom in the heptanuclear cluster of compound **2** shows an apparent regular octahedral geometry instead of the expected elongated one due to the Jahn–Teller effect. However, they are clearly pointing out that this is an artifact of the X-ray diffraction, which provides average arrangement of the atoms, as the M–O distance in this compound lies midway between the short (ca.

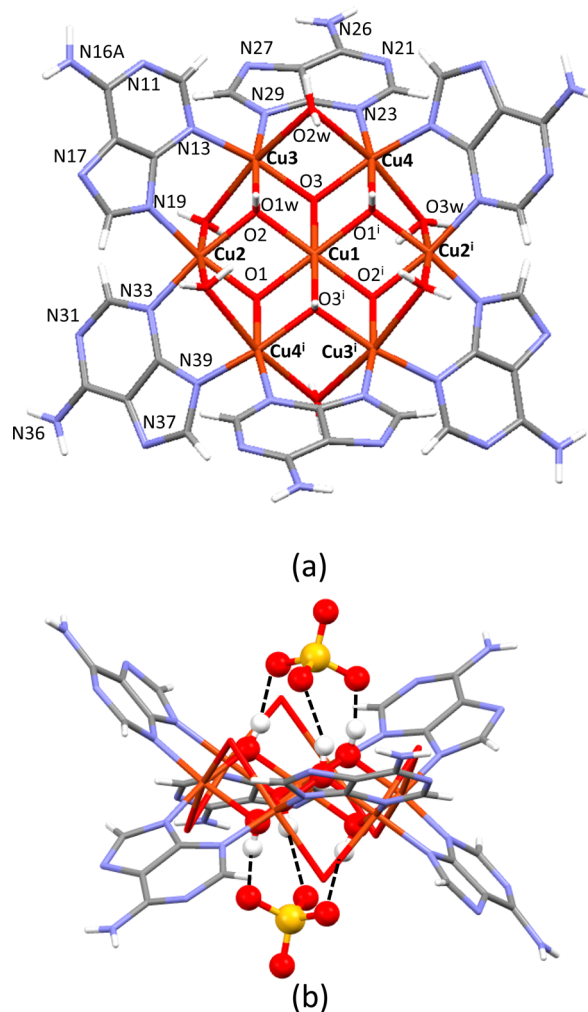


Figure 1. $[\text{Cu}_7(\mu\text{-H}_2\text{O})_6(\mu_3\text{-OH})_6(\mu\text{-adeninato-}\kappa\text{N3:}\kappa\text{N9})_6]^{2+}$ heptanuclear entity (a) and hydrogen bond anchorage of the sulfate anions (b) found in compound **1**. Dashed lines indicate hydrogen bonds.

1.97 Å) and long (ca. 2.12 Å) distances found in compound **1**. It could be due to a disorder of the elongation among the heptanuclear entities, which is evidenced by the fact the hydroxide oxygen atoms were refined isotropically, because when refining with anisotropic displacement parameters it provided very elongated ellipsoids that are a usual signal of disorder.

The difference between both crystal structures is due to the spatial arrangement of the heptameric entities. In compound **1**, the hydrogen-bond donor positions of the $[\text{Cu}(\text{OH})_6]^{4-}$ core are employed to tightly anchor two sulfate anions, above and below the complex, through three O–H...O hydrogen bonds to each anion (Figure 1b). This doubly capped heptamer-sulfate rigid assembly is the key structural unit that fulfills the SMOF building criteria expounded in the introductory section, since it allows interacting with four adjacent ones through two different rigid synthons (Figure 3 and Table 2). The first one comes from double adeninato...adeninato $\pi\text{-}\pi$ stacking interactions taking place between the heptamer and two of the four adjacent heptamers. The second one involves a single adeninato...adeninato $\pi\text{-}\pi$ stacking and a $\text{N6}_{\text{adeninato}}\cdots\text{O}_{\text{sulfate}}\cdots\text{OH}_{\text{coordinated}}$ hydrogen bond chain. The rigidity of both the heptameric discrete entity and the synthons, built from the combination of two relatively loose supramolecular interactions, generates a

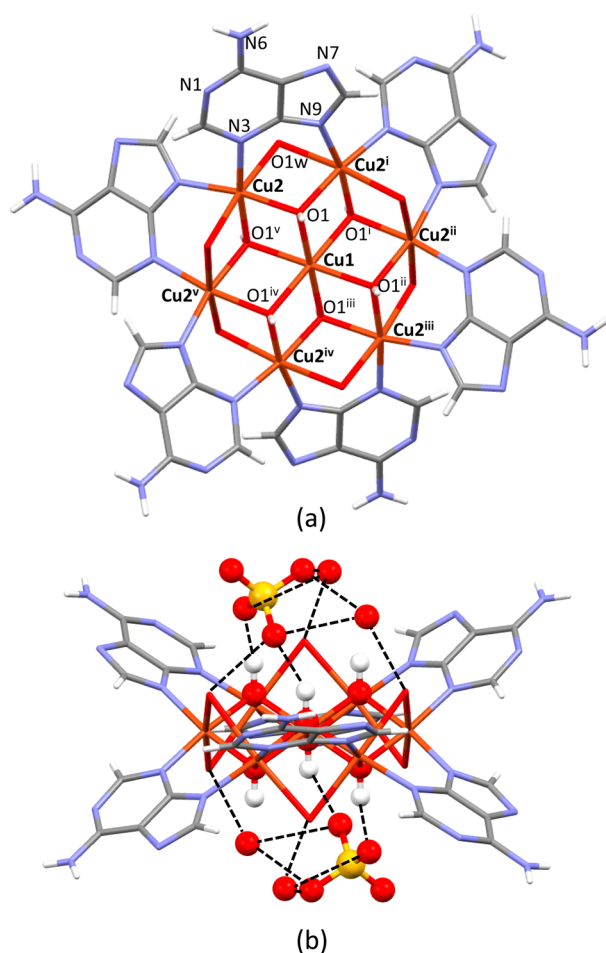


Figure 2. $[\text{Cu}_7(\mu\text{-H}_2\text{O})_6(\mu_3\text{-OH})_6(\mu\text{-adeninato-}\kappa\text{N3:}\kappa\text{N9})_6]^{2+}$ heptanuclear entity found in compound **2** (a), showing the hydrogen bond anchorage of the sulfate anions and crystallization water molecules to heptameric entity (b).

CdSO_4 -like *cds* topology with a $(6^5.8)$ point symbol (nodes being the heptameric units and connectors being the π - π stacking interactions between the adeninates).²⁰ This supramolecular network presents one-dimensional (1D) channels (mode: 5.5 Å) that imply a 49.0% of unit cell volume in which disordered solvent molecules and triethylammonium cations are placed.

In compound **2**, the sulfate anions, although still occupying the top and bottom of the heptameric entity, are only anchored through two hydrogen bonds to the hydroxide bridges (Figure 2b). It decreases the steric hindrance around the complex entity allowing the adeninato ligands to supramolecularly connect each complex entity to six adjacent ones (Figure 4 and Table 3). The same rigid synthon, involving adenine...adenine π - π interactions and a $\text{N7}_{\text{adeninato}} \cdots \text{Ow}_{\text{crystallization}} \cdots \text{Ow}_{\text{coordinated}}$ hydrogen bond chain, accounts for all the interactions between the heptamers. The sulfate counterions, although disordered, are held to the Hoogsteen edge of the adeninato ligands through hydrogen bonds. Again, an open structure is achieved, with α -Pc primitive cubic *pcu* topology and a $(4^{12}.6^3)$ point symbol, in which 1D channels (mode: 5.8 Å) that encompass the 41.5% of the unit cell volume are present.

If we do not pay attention to the different amount of crystallization water molecules, the two compounds can be considered as polymorphs, compound **1** being the kinetically

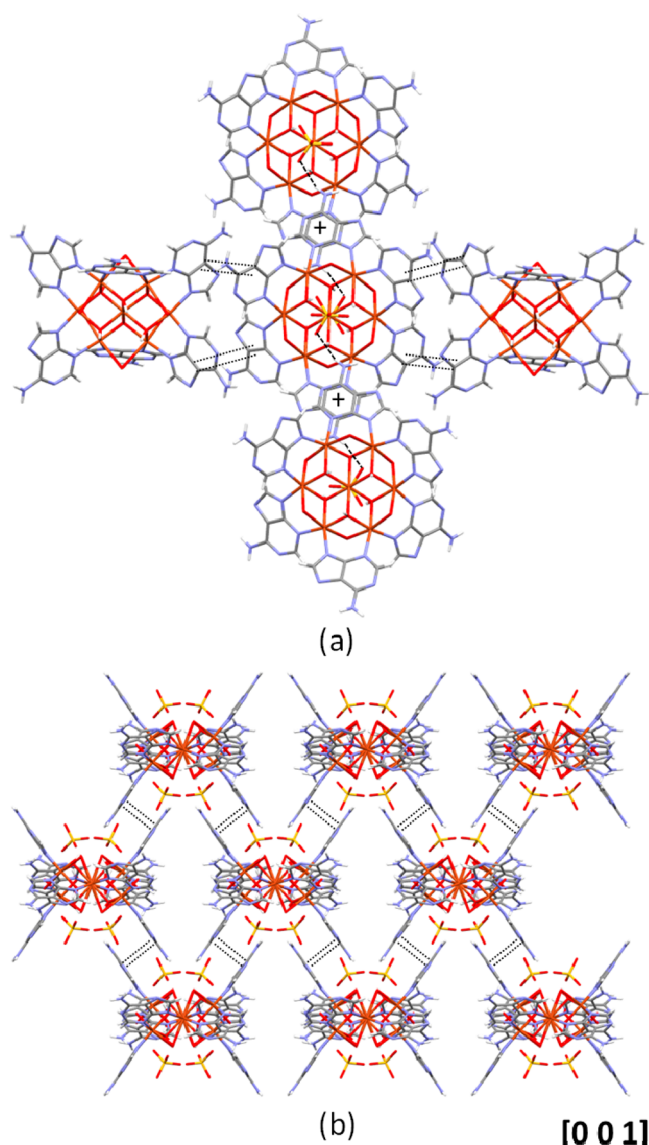


Figure 3. Supramolecular interactions connecting each $[\text{Cu}_7(\mu\text{-H}_2\text{O})_6(\mu_3\text{-OH})_6(\mu\text{-adeninato-}\kappa\text{N3:}\kappa\text{N9})_6]^{2+}$ heptanuclear entity to four adjacent ones (a) and projection of the crystal packing along the crystallographic *c* axis (b) for compound **1**. Double dotted lines and "+" indicate π - π stacking interactions.

preferred one, as it is formed at the beginning, and compound **2** the thermodynamically favored one.

Magnetic Properties. Figure 5 shows the temperature dependence of the molar magnetic susceptibility (χ_m) and $\chi_m T$ curves of **1** and **2**, measured at 1 kOe after cooling without an applied magnetic field (ZFC). As it can be seen, the molar magnetic susceptibility increases with decreasing temperature up to 2 K for both compounds. The $\chi_m T$ reaches a value of 2.92 (1) and 3.08 (2) emuK/molOe at 300 K per heptameric complex, which is moderately larger than the spin-only value (2.63 emuK/molOe) expected for seven magnetically non-interacting Cu^{2+} ions with $S = 1/2$ and $g = 2.0$.²¹ These values slightly diminish as temperature decreases to achieve a minimum at 140 K (2.83 emuK/molOe) and 155 K (3.03 emuK/molOe), respectively. When further cooled, it increases quite fast to reach a maximum at 6 K (4.24 emuK/molOe) and 3 K (4.93 emuK/molOe) for **1** and **2**, respectively. The temperature dependence of the inverse susceptibility ($1/\chi_m$)

Table 2. Structural Parameters (Å, deg) of More Relevant Noncovalent Interactions in Compound **1**^a

hydrogen-bonding interactions						
D–H...A ^b		H...A	D...A	D–H...A		
O1–H1...O13		1.939	2.739	158		
O2–H2...O11 ⁱ		2.093	2.740	139		
O3–H3...O14		2.340	2.976	139		
N26–H26B...O14 ⁱⁱ		2.144	2.976	163		
N41–H41...O12		2.008	2.894	164		
N41–H41...O11		2.608	3.293	133		
O1w–H1w2...O14		1.960	2.807	175		
O2w–H2w2...O13 ⁱ		2.058	2.892	166		
O3w–H3w1...O11		1.989	2.811	161		
π – π interactions ^c						
ring...ring ^d		angle	DC	α	DZ	DXY
p ₁ ...h ₃ ⁱⁱⁱ		4.7	3.91	26.6	3.50	1.75
h ₂ ...h ₂ ⁱⁱ		0.0	4.13	31.62	3.51	2.16

^aSymmetry codes: (i) $-x + 2, -y, -z + 1$; (ii) $-x + 3/2, -y + 1/2, -z + 1$; (iii) $2 - x, y, 1/2 - z$. ^bD: donor; A: acceptor. ^cAngle: dihedral angle between the planes (deg), DC: distance between the centroids of the rings (Å), α : angle between the normal to the first ring and the DC vector (deg), DZ: interplanar distance (Å), DXY: lateral displacement (Å). ^dp₁: C14, C15A, N17, C18, N19; h₂: N21, C22, N23, C24, C25, C26; h₃: N31, C32, N33, C34, C35, C36.

curves (not shown) were fitted in the paramagnetic range ($T > 10$ K) using the Curie–Weiss law for $S = 1/2$ in the molecular field approximation. The effective paramagnetic moment (μ_{eff}) and Curie–Weiss temperature (θ_{p}), obtained from the fitting, have a value of 1.73 and 1.82 μ_{B}/Cu ion and 20.7 and 11.0 K, for **1** and **2**, respectively. This is in good agreement with the expected value of 1.73 μ_{B} for Cu^{2+} ion with a magnetic spin $S = 1/2$ and other $\text{Cu}(\text{II})$ -containing complexes.²²

The field dependence of the magnetization at 2 K of both compounds (see inset of Figure 5) displays a linear dependence, from 0 to 15 kOe, which slowly tends to saturate at 50 kOe (5.65 and 5.15 $\mu_{\text{B}}/\text{Cu}^{\text{II}}$ ion for **1** and **2**, respectively). The values obtained at this magnetic field are lower than the theoretical saturation moment for seven isolated Cu^{II} ions ferromagnetically coupled with a magnetic spin $S = 1/2$ and $g \approx 2$ (7.00 μ_{B}) but agrees fairly well with a total $S = 5/2$ in the molecule. This behavior seems to indicate the presence of ferromagnetic heptameric entities in which the central copper(II) atom is anti-ferromagnetically coupled to the external ferromagnetic hexanuclear ring. Finally, the magnetization at 2 K shows no hysteresis (have neither coercivity nor remanence) at this temperature.

Taking into account the molecular structure of the $[\text{Cu}_7(\mu\text{-H}_2\text{O})_6(\mu_3\text{-OH})_6(\mu\text{-adeninato-}\kappa\text{N3:}\kappa\text{N9})_6]^{2+}$ heptanuclear entities and the Jahn–Teller elongated octahedron of the central copper(II) atom, the simplest Hamiltonian (eq 1) that would describe the behavior of this compound involves three different magnetic superexchange parameters accounting for the couplings between the copper ions and its first neighboring ones (J_1 , J_2 and J_3 ; see Figure 6).

$$\begin{aligned}
 H = & -J_1(\vec{S}_1 \cdot \vec{S}_2 + \vec{S}_1 \cdot \vec{S}_3 + \vec{S}_1 \cdot \vec{S}_5 + \vec{S}_1 \cdot \vec{S}_6) \\
 & -J_2(\vec{S}_1 \cdot \vec{S}_4 + \vec{S}_1 \cdot \vec{S}_7) - J_3(\vec{S}_2 \cdot \vec{S}_3 + \vec{S}_3 \cdot \vec{S}_4 + \vec{S}_4 \cdot \vec{S}_5 \\
 & + \vec{S}_5 \cdot \vec{S}_6 + \vec{S}_6 \cdot \vec{S}_7 + \vec{S}_2 \cdot \vec{S}_7) - g\mu_{\text{B}}\vec{B} \cdot \vec{S}
 \end{aligned}
 \quad (1)$$

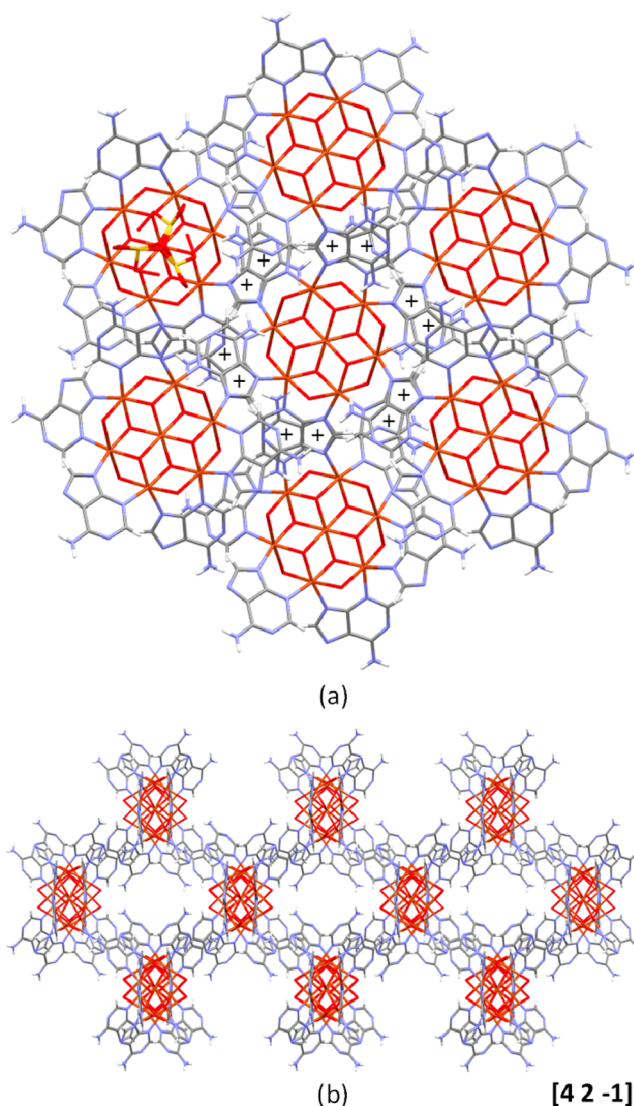


Figure 4. Supramolecular interactions connecting each $[\text{Cu}_7(\mu\text{-H}_2\text{O})_6(\mu_3\text{-OH})_6(\mu\text{-adeninato-}\kappa\text{N3:}\kappa\text{N9})_6]^{2+}$ heptanuclear entity to six adjacent ones (a) and crystal packing of the structure showing the presence of 1D channels (b).

J_1 and J_2 are assigned to the superexchange interactions between the central and the exterior copper ions taking place through double $\mu\text{-OH}$ bridges. J_1 involves a mixture of equatorial–equatorial and equatorial–axial coordinated $\mu\text{-OH}$ bridges, whereas J_2 presents only an equatorial–equatorial arrangement of the bridging hydroxides. J_3 represents the superexchange interaction between the external Cu^{II} ions bridged by $\mu\text{-adeninato}$ and $\mu\text{-OH}_2$ bridges. The fitting of the $\chi_{\text{m}}T$ experimental data above 10 K to this model was performed using the MagProp software tool distributed with DAVE.²³ The best fitting parameters (see the red continuous line in Figure 5) are gathered in Table 4.

The results of the fitting shows similar ferromagnetic values for **1** and **2** in the coupling constant involving the external copper(II) ions bridged by adenine and hydroxide ligands (J_3). Usually, both the presence of nonlinear NCN bridges or wide-angle $\mu\text{-oxido}$ bridges (ca. 104°) cause strong AF couplings.²⁴ However, the coexistence of these two types of bridges counterbalances their effects.²⁵ In fact, the splitting of the molecular magnetic orbitals is reversed for each type of bridging

Table 3. Structural Parameters (Å, deg) of More Relevant Noncovalent Interactions in Compound 2^a

hydrogen-bonding interactions					
D–H...A ^b		H...A	D...A	D–H...A	
O1–H1...O1A ⁱ		2.058	2.788	162	
O1–H1...O4A ⁱⁱ		2.211	2.839	141	
N6A–H6A2...O1A		1.979	2.834	173	
N6A–H6A2...O4A ⁱⁱⁱ		2.189	2.960	149	
N6B–H6B1...O2w ⁱⁱⁱ		2.620	3.201	126	
π – π interactions ^c					
ring...ring ^d	angle	DC	α	DZ	DXY
h...p ^{iv}	0.0	3.89	27.1	3.47	1.77
h...h ^{iv}	0.0	3.77	24.6	3.43	1.57
p...h ^{iv}	0.0	3.89	28.3	3.43	1.84
p...p ^{iv}	0.0	4.00	30.0	3.47	2.00

^aSymmetrycodes: (i) $-x + y + 2/3, y + 1/3, z - 1/6$; (ii) $-y + 5/3, -x + 4/3, z - 1/6$; (iii) $-x + y, -x + 1, z$; (iv) $4/3 - x, 2/3 - x + y, 7/6 - z$. ^bD: donor; A: acceptor. ^cAngle: dihedral angle between the planes (deg), DC: distance between the centroids of the rings (Å), α : angle between the normal to the first ring and the DC vector (deg), DZ: interplanar distance (Å), DXY: lateral displacement (Å). ^dh: hexagonal ring of the adeninate and p: pentagonal ring of the adeninate.

ligand, thus leading, on one hand, to an almost negligible energy difference between them and, as a consequence, to the observed ferromagnetic interaction. On the other hand, there are some significant differences on the coupling constants involving the central and external copper atoms (J_1 and J_2). In both compounds, J_2 (involving two short μ -hydroxide bridges and Cu–O–Cu angles around 99–103°) is AF and stronger than the ferromagnetic J_1 which implies a short and a long hydroxide bridge. The AF nature of J_2 agrees with the stated by Hatfield et al. for symmetrically double bridged hydroxo dinuclear complexes, in which angles larger than 98.5° promote an AF coupling, while a ferromagnetic coupling is established for smaller angles.²⁶ On the other hand the weak ferromagnetic J_1 interaction is related to the orthogonality between the magnetic orbitals imposed by the combination of symmetric and asymmetric μ -OH bridges. In the literature most cases of copper(II) centers bridged by this arrangement of the hydroxide bridges show a ferromagnetic behavior with J values ranging from +10 to +90 cm⁻¹.²⁷ We are aware of the fact that the overparameterization of the model could lead to similar fitting agreements using different parameter values, but the similarity of the achieved superexchange constants and the reports found in the literature for similar bridging modes of the hydroxides make us confident of the experimental data fitting results. These results also agree with the reported ones for analogous wheel-shaped heptanuclear copper(II) entities in which the external copper(II) centers are ferromagnetically coupled among them and antiferromagnetically to the central one.^{9,28} A single crystal with a larger size (ca. of 1 cm³) would allow to compare in detail these data with an experimental determination from polarized neutron-diffraction experiments.²⁹

The temperature dependences of the molar heat capacity C_p for zero magnetic field are represented between 0.4 and 300 K in Figures 7 and 8 for compounds 1 and 2, respectively. In both cases C_p has a tiny maximum of magnetic origin below 1 K, and then it increases continuously due to the phonon contribution. The experimental data do not show any tendency to saturation,

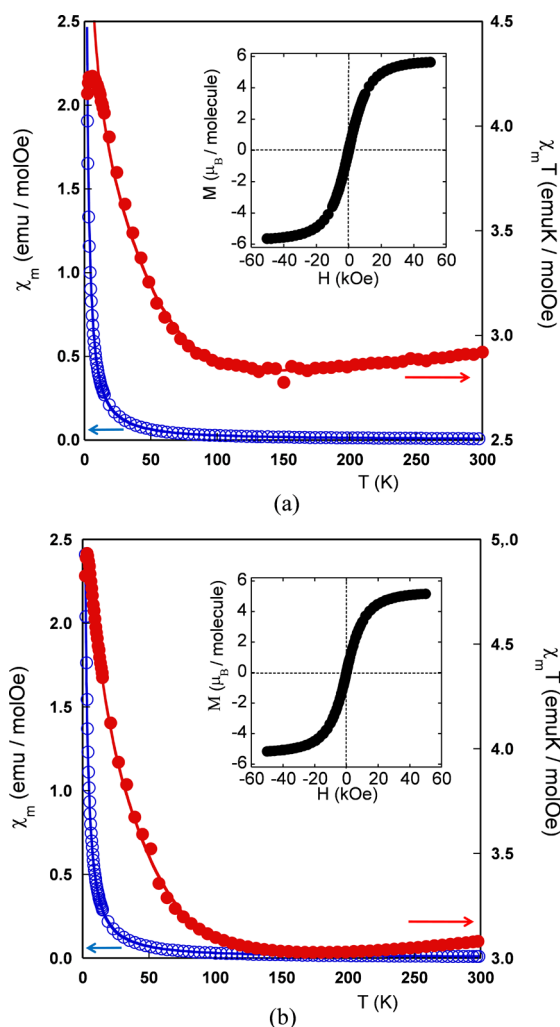


Figure 5. ZFC thermal evolution of the molar magnetic susceptibility (χ_m) and $\chi_m T$ product for 1 (a) and 2 (b). (insets) The magnetization curves at 2 K. The red line shows the fitting of the χT experimental data.

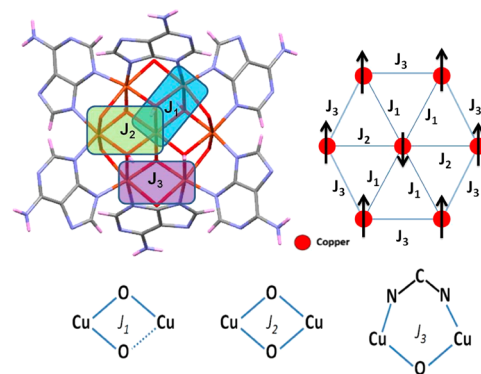


Figure 6. $[\text{Cu}_7(\mu\text{-H}_2\text{O})_6(\mu_3\text{-OH})_6(\mu\text{-adeninato-}\kappa\text{N3:}\kappa\text{N9})_6]^{2+}$ heptanuclear entity emphasizing the relationship of the magnetic topology and the 3- J coupling scheme for the local Cu^{II}_7 cluster.

even at room temperature, where the values of C_p are 2100 and 1700 J K⁻¹ mol⁻¹ for compounds 1 and 2, respectively, still far from the expected values according to the Dulong and Petit law, 7557 and 6136 J K⁻¹ mol⁻¹ for compounds 1 and 2, respectively. This behavior is attributable to the presence of a

Table 4. Main Magnetic Data for Compounds 1 and 2

	compound 1	compound 2
g	2.12	2.12
J_1 (cm ⁻¹)	+14	+6
J_2 (cm ⁻¹)	-228	-221
J_3 (cm ⁻¹)	+75	+97

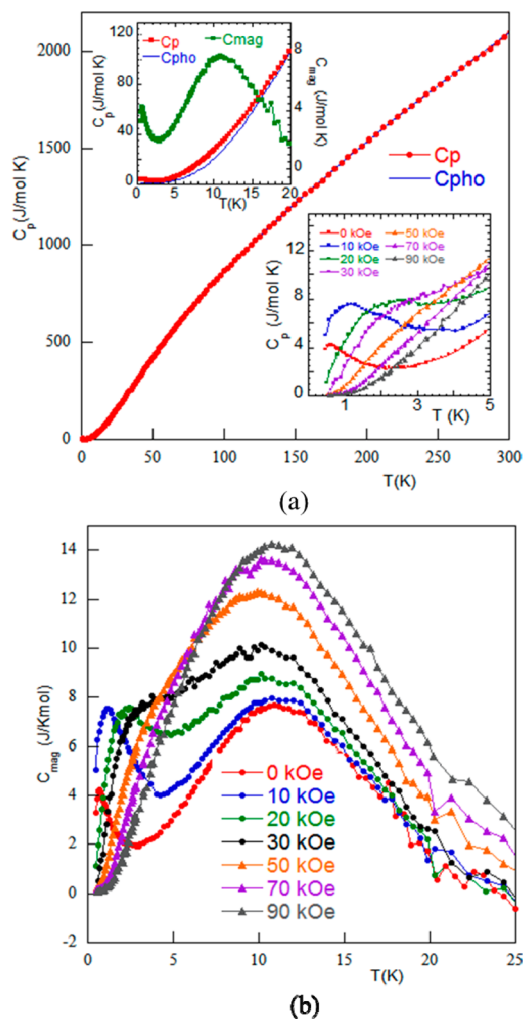


Figure 7. (a) Specific heat of 1 between 0.4 and 300 K. (upper inset) Experimental data (red ●), estimated phonon contribution (blue dashed line), and magnetic contribution (green ●). (lower inset) Specific heat at different applied magnetic field ($H \leq 90$ kOe). (b) Magnetic specific heat as a function of temperature in the presence of external magnetic fields.

high number of hydrogen atoms within the compounds, which display very high excitation energies. At very low temperatures, where the phonon contribution is negligible, as commented previously C_p displays a broad maximum ($\Delta C_p = 4.2$ J/mol K in both compounds) centered at 0.6 and 0.5 K for 1 and 2, respectively (see upper insets in Figures 7 and 8). Although these anomalies do not present the characteristic λ shape appearance of a second-order transition, it can be attributed to the establishment of a 3D magnetic order. This behavior is confirmed by the effects of the magnetic field on C_p , since the field increase promotes the peak growing and shifting to higher temperatures, and apparently disappearing for fields higher than

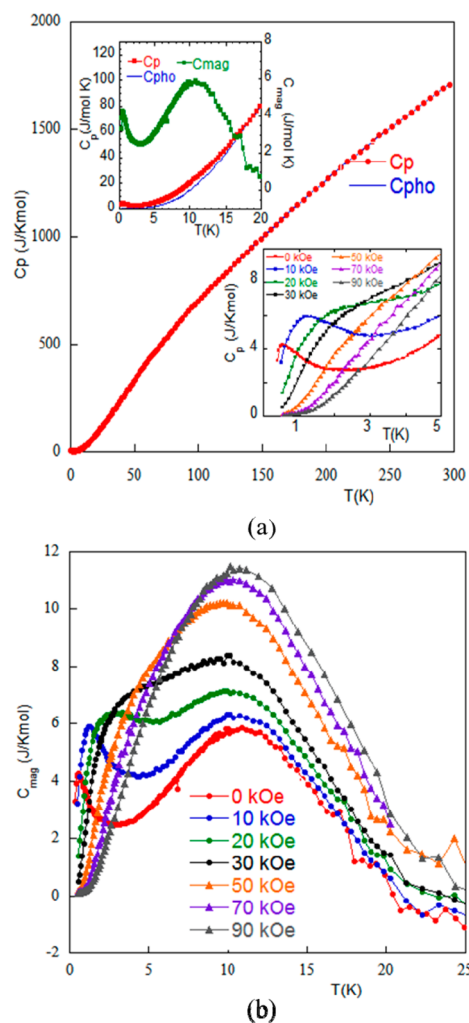


Figure 8. (a) Specific heat of 2 between 0.4 and 300 K. (upper inset) Experimental data (red ●), estimated phonon contribution (blue dashed line), and magnetic contribution (brown ●). (lower inset) Specific heat at different applied magnetic field ($H \leq 90$ kOe). (b) Magnetic specific heat as a function of temperature in the presence of external magnetic fields.

30 kOe in both compounds. This behavior is later clarified analyzing the magnetic contribution to the heat capacity (C_{mag}).

To extract C_{mag} we determine the phonon contribution (C_{pho}) and then subtract it from the experimental data. In the absence of a nonmagnetic isomorphous compound, we should use a theoretical model to determine C_{pho} , with the Debye model being the most common. However, because of the large differences in the atomic weights of the elements, more than one phonon spectrum is expected. This approach has been used successfully in previous studies in other complex insulators materials.³⁰ In the present case, because of the large amount of ions and solvent molecules, the minimum number of Debye temperatures that is required to fit the heat capacity was five. The good quality of the fits (see the blue continuous line in Figures 7 and 8) allows us to consider that this phenomenological model determines reasonably well the phonon contribution.

The temperature dependence of the magnetic contribution, determined as $C_{mag} = C_p - C_{pho}$, is depicted in Figures 7b and 8b for compounds 1 and 2, respectively. In these figures are also included the temperature dependences of C_{mag} under

applied magnetic fields up to 90 kOe. In both compounds, at zero field, the most significant features are (i) the jump in C_{mag} at the order temperature has a small value, suggesting the existence of a complex magnetic order,^{30,31} and (ii) in addition to the low-temperature peak, appears a broad maximum centered around 11 K, which usually is attributed to the existence of two-dimensional magnetic order, crystalline electrical field or the presence of short-range magnetic interactions.^{30,32}

Therefore, in the present case, these results suggest that at 11 K appears a local magnetic order inside the wheels, and by decreasing the temperature around 0.5 K, the wheels are coupled magnetically resulting in a 3D magnetic ordering. The general effect of the magnetic field on C_{mag} is to increase the size of both peaks and to shift the low-temperature peak to higher temperatures. This shift is characteristic of a ferromagnetic coupling. In addition, we should point out that the low-temperature peak has a strong increase for 10 kOe and then tends to saturate for fields above 30 kOe, in concordance with the saturation of the magnetization curves. Taking into account the structural features of the compounds, the long-range ordering detected at low temperatures probably comes from the adeninato...adeninato π - π stacking interactions taking place between the heptamer units. From the 3D magnetic ordering temperature values ($T_c = 0.5$ and 0.6 K) and the Curie-Weiss temperature ($\theta_p = 20.7$ and 11.0 K for **1** and **2**, respectively) we can obtain information on the magnetic spin frustration f , given by $|\theta/T_c|$ of these open supramolecular structures.³³ The f parameter reaches values of 41.4 and 18.3 for **1** and **2**, respectively, where a value above 10 indicates the presence of strong frustration.³⁴ Therefore, it indicates that both SMOFs display complex 3D magnetic structures with the presence of stronger spin frustration in the **1** compound.

CONCLUSIONS

The use of long spacer to connect the paramagnetic centers in MOFs and SMOFs (the spacer being a ligand or supramolecular synthon, respectively) is crucial in the porosity pursuit, but it tends to pauperize the magnetic interactions. A strategy to overcome such problem has been previously settled for MOFs in which a metal cluster with a high-spin ground state is employed as node that is further connected by extended ligand, giving rise to magnetically appealing porous materials. Herein, we have transferred this strategy to the burgeoning field of SMOFs. The fine-tuning of the synthesis conditions gave rise to a node consisting of heptanuclear $[\text{Cu}_7(\mu\text{-H}_2\text{O})_6(\mu_3\text{-OH})_6(\mu\text{-adeninato-}\kappa\text{N3:}\kappa\text{N9})_6]^{2+}$ wheel in which the spokes are built by short μ_3 -hydroxido bridges, while tire is formed by a μ -adenine and μ -aqua double bridge. The shape of the complex entity exposes the adeninato ligands available for supramolecular interactions. As previously stated, the nucleobases interact among them mainly by hydrogen bonding and π - π stacking interactions. There are several examples of porous supramolecular architectures based on complementary hydrogen-bonding interactions taking place among the nucleobases anchored to a metal center, but examples based on the nucleobase π - π stacking capacity as the driving force that sustains the 3D porous supramolecular structure are more scarce. In comparison to hydrogen bond, π - π stacking interactions do not define a highly preferential orientation between the interacting molecules. It is true that these molecules must arrange nearly parallel with an interplanar distance of ca. 3.5 Å, but the orientation within the plane is

looser. However, it is possible to achieve a rigid synthon by the combination of two of these interactions or by its combination with a second supramolecular interaction. Compounds **1** and **2** provide experimental evidence to the latter statement, as the Cu^{II}_7 wheels are simultaneously bridged by means of π - π stacking interactions among the adenine nucleobases and by hydrogen bonds established between the hydroxide ligands, the sulfate anions and adenine nucleobases. The sum of both types of interactions into a double supramolecular bridge creates a rigid synthon that in combination with the rigidity of the heptameric entity fulfills all the SMOF design criteria and generates an open supramolecular structure (40–50% of available space) in which additional sulfate and triethylammonium ions are located altogether with solvent molecules. Furthermore, the magnetic characterization indicates that the central copper(II) atom individual spins are coupled to yield an $S = 5/2$ ground state. The supramolecular assembly of Cu^{II}_7 wheels, mediated by π - π stacking interactions between the adenines, is able to provide a 3D ferromagnetic ordering below 1 K. Further work is in progress to analyze the influence of the guest molecules hosted in the channels of these compounds on the magnetic properties, as subtle changes such as the O–H bond displacement from the Cu_2O_2 core imply significant change on the mediated magnetic interactions.

ASSOCIATED CONTENT

Supporting Information

The Supporting Information is available free of charge on the ACS Publications website at DOI: 10.1021/acs.inorgchem.6b01231.

FTIR data, powder X-ray analysis, thermogravimetric measurements for compounds **1** and **2** (PDF)

X-ray crystallographic file in CIF format (CCDC 1481044) (CIF)

X-ray crystallographic file in CIF format (CCDC 1481045) (CIF)

AUTHOR INFORMATION

Corresponding Authors

*E-mail: oscar.castillo@ehu.eus, Fax: (international) +34-94601-3500. (O.C.)

*E-mail: manuel.depedro@unican.es. (M.D.)

Notes

The authors declare no competing financial interest.

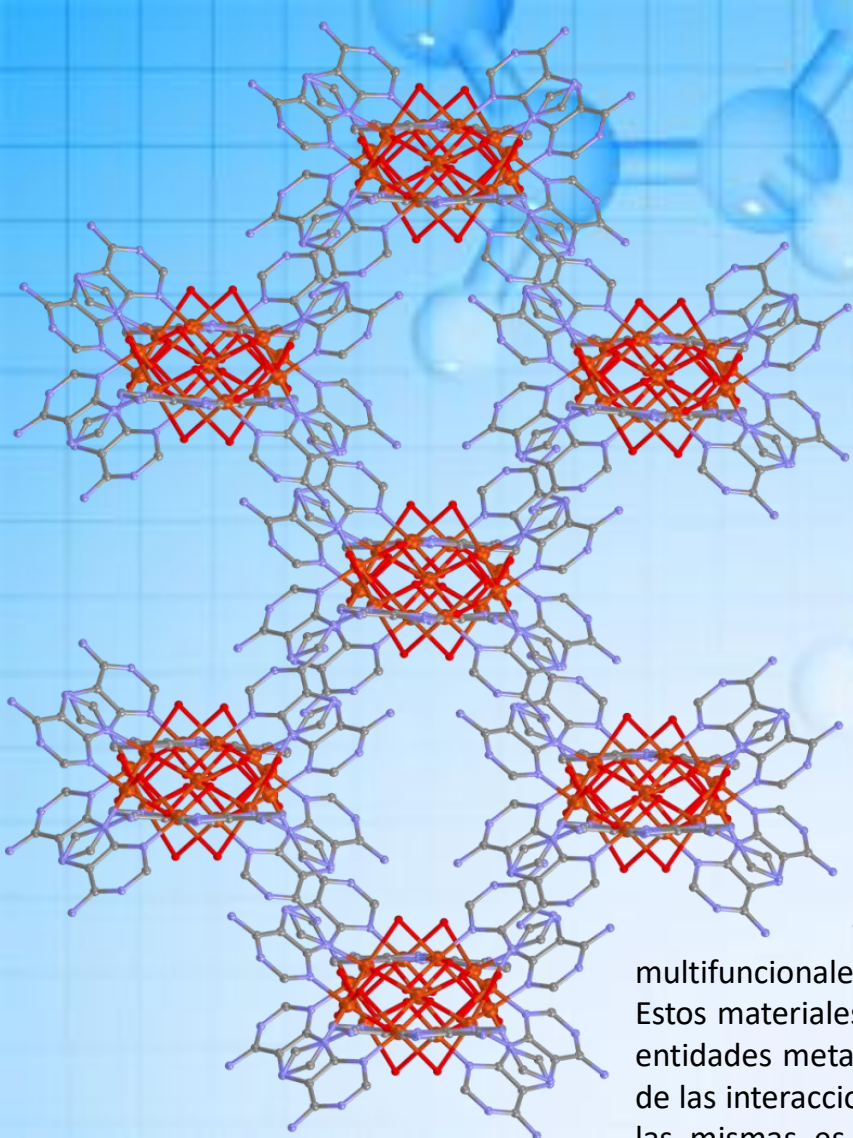
ACKNOWLEDGMENTS

This work has been funded by Eusko Jaurlaritza/Gobierno Vasco, Universidad del País Vasco/Euskal Herriko Unibertsitatea (predoctoral fellowship for R.P.A.), and Ministerio de Economía y Competitividad (MAT2013-46502-C2-1P and MAT2014-55049-C2-R). Technical and human support provided by SGIker (UPV/EHU, MICINN, GV/EJ, ESF) is also acknowledged.

REFERENCES

- (1) (a) Kitagawa, S.; Kondo, M. *Bull. Chem. Soc. Jpn.* **1998**, *71*, 1739–1753. (b) Batten, S. R.; Robson, R. *Angew. Chem., Int. Ed.* **1998**, *37*, 1460–1494. (c) Blake, A. J.; Champness, N. R.; Hubberstey, P.; Li, W. S.; Withersby, M. A.; Schröder, M. *Coord. Chem. Rev.* **1999**, *183*, 117–138. (d) Moulton, B.; Zaworotko, M. *Chem. Rev.* **2001**, *101*, 1629–1658. (e) Moulton, B.; Lu, J.; Mondal, A.; Zaworotko, M. J. *Chem. Commun.* **2001**, 863–864.

- (2) (a) Zhou, H.-C.; Kitagawa, S. *Chem. Soc. Rev.* **2014**, *43*, 5415–5418. (b) Tan, J.-C.; Civalieri, B. *CrystEngComm* **2015**, *17*, 197–198. (c) Cui, Y.; Yue, Y.; Qian, G.; Chen, B. *Chem. Rev.* **2012**, *112*, 1126–1162.
- (3) Kurmoo, M. *Chem. Soc. Rev.* **2009**, *38*, 1353–1379.
- (4) (a) Thomas-Gipson, J.; Beobide, G.; Castillo, O.; Fröba, M.; Hoffmann, F.; Luque, A.; Pérez-Yáñez, S.; Román, P. *Cryst. Growth Des.* **2014**, *14*, 4019–4029. (b) Thomas-Gipson, J.; Pérez-Aguirre, R.; Beobide, G.; Castillo, O.; Luque, A.; Pérez-Yáñez, S.; Román, P. *Cryst. Growth Des.* **2015**, *15*, 975–983.
- (5) Beobide, G.; Castillo, O.; Luque, A.; Pérez-Yáñez, S. *CrystEngComm* **2015**, *17*, 3051–3059.
- (6) Beobide, G.; Castillo, O.; Cepeda, J.; Luque, A.; Pérez-Yáñez, S.; Román, P.; Thomas-Gipson, J. *Coord. Chem. Rev.* **2013**, *257*, 2716–2736.
- (7) Moulton, B.; Lu, J.; Hajndl, R.; Hariharan, S.; Zaworotko, M. J. *Angew. Chem., Int. Ed.* **2002**, *41*, 2821–2824.
- (8) Dechambenoit, P.; Long, J. R. *Chem. Soc. Rev.* **2011**, *40*, 3249–3265.
- (9) Liu, Z. Y.; Zhang, H. Y.; Yang, E. C.; Liu, Z. Y.; Zhao, X. J. *Dalton Trans.* **2015**, *44*, S280–S283.
- (10) Zheng, Y. Z.; Tong, M. L.; Xue, W.; Zhang, W. X.; Chen, X. M.; Grandjean, F.; Long, G. J. *Angew. Chem.* **2007**, *119*, 6188–6192.
- (11) (a) Sharples, J. W.; Collison, D.; McInnes, E. J.; Schnack, J.; Palacios, E.; Evangelisti, M. *Nat. Commun.* **2014**, *5*, 1–6. (b) Mondal, K. C.; Mereacre, V.; Kostakis, G. E.; Lan, Y.; Anson, C. E.; Prisca, L.; Powell, A. K.; et al. *Chem. - Eur. J.* **2015**, *21*, 10835–10842.
- (12) Earnshaw, A. *Introduction to Magnetochemistry*; Academic Press: London, U.K, 1968.
- (13) *CrysAlisPro*, version 1.171.35.15; Agilent Technologies: Yarnton, U.K, 2011.
- (14) Altomare, A.; Cascarano, M.; Giacovazzo, C.; Guagliardi, A. J. *Appl. Crystallogr.* **1993**, *26*, 343–350.
- (15) Farrugia, L. J. *J. Appl. Crystallogr.* **1999**, *32*, 837–838.
- (16) Sheldrick, G. M. *Acta Crystallogr., Sect. A: Found. Crystallogr.* **2008**, *A64*, 112–122.
- (17) (a) Cepeda, J.; Castillo, O.; García-Terán, J. P.; Luque, A.; Pérez-Yáñez, S.; Román, P. *Eur. J. Inorg. Chem.* **2009**, 2344–2353. (b) Pérez-Yáñez, S.; Beobide, G.; Castillo, O.; Cepeda, J.; Luque, A.; Román, P. *Cryst. Growth Des.* **2013**, *13*, 3057–3067.
- (18) Van der Sluis, P.; Spek, A. L. *Acta Crystallogr., Sect. A: Found. Crystallogr.* **1990**, *A46*, 194–201.
- (19) Spek, A. L. *J. Appl. Crystallogr.* **2003**, *36*, 7–13.
- (20) (a) TOPOS Main Page. <http://www.topospro.com> (accessed Jan 2015). (b) Blatov, V. A. *IUCR CompComm Newsletter* **2006**, *7*, 4–38. (c) O’Keeffe, M.; Yaghi, O. M. *Chem. Rev.* **2012**, *112*, 675.
- (21) Boca, R. *Handbook of Magnetochemical Formulae*; Elsevier: Amsterdam, The Netherlands, 2012; p 1010.
- (22) (a) Mohamadou, A.; Moreau, J.; Dupont, L.; Wenger, E. *Inorg. Chim. Acta* **2012**, *383*, 267–276. (b) Pérez-Yáñez, S.; Beobide, G.; Castillo, O.; Cepeda, J.; Luque, A.; Aguayo, A. T.; Román, P. *Inorg. Chem.* **2011**, *50*, 5530–5532.
- (23) Azuah, R. T.; Kneller, L. R.; Qiu, Y.; Tregenna-Piggott, P. L. W.; Brown, C. M.; Copley, J. R. D.; Dimeo, R. M. *J. Res. Natl. Inst. Stand. Technol.* **2009**, *114*, 341–358.
- (24) (a) Sonnenfroh, D.; Kreilick, R. W. *Inorg. Chem.* **1980**, *19*, 1259–1262. (b) Delgado, F. S.; Hernández-Molina, M.; Sanchiz, J.; Ruiz-Pérez, C.; Rodríguez-Martín, Y.; López, T.; Lloret, F.; Julve, M. *CrystEngComm* **2004**, *6*, 106–111. (c) Cañadillas-Delgado, L.; Fabelo, O.; Pasán, J.; Delgado, F. S.; Lloret, F.; Julve, M.; Ruiz-Pérez, C. *Inorg. Chem.* **2007**, *46*, 7458–7465.
- (25) (a) Pérez-Yáñez, S.; Castillo, O.; Cepeda, J.; García-Terán, J. P.; Luque, A.; Román, P. *Eur. J. Inorg. Chem.* **2009**, 3889–3899. (b) Nishida, Y.; Kida, S. *J. Chem. Soc., Dalton Trans.* **1986**, 2633–2640. (c) McKee, V.; Zvagulis, M.; Reed, C. A. *Inorg. Chem.* **1985**, *24*, 2914–2919.
- (26) Crawford, V. H.; Richardson, H. W.; Wasson, J. R.; Hodgson, D. J.; Hatfield, W. E. *Inorg. Chem.* **1976**, *15*, 2107–2110.
- (27) Tercero, J.; Ruiz, E.; Alvarez, S.; Rodríguez-Fortea, A.; Alemany, P. *J. Mater. Chem.* **2006**, *16*, 2729–2735.
- (28) Leite Ferreira, B. J. M.; Brandão, P.; Dos Santos, A. M.; Gai, Z.; Cruz, C.; Reis, M. S.; Santos, T. M.; Félix, V. J. *Coord. Chem.* **2015**, *68*, 2770–2787.
- (29) Campo, J.; Luzón, J.; Palacio, F.; McIntyre, G. J.; Millán, A.; Wildes, A. R. *Phys. Rev. B: Condens. Matter Mater. Phys.* **2008**, *78*, 054415.
- (30) (a) de Pedro, I.; Rojo, J. M.; Rodríguez Fernández, J.; Fernández-Díaz, M. T.; Rojo, T. *Phys. Rev. B: Condens. Matter Mater. Phys.* **2010**, *81*, 134431. (b) de Pedro, I.; Rojo, J. M.; Rius, J.; Vallcorba, O.; Ruiz de Larramendi, I.; Rodríguez Fernández, J.; Lezama, L.; Rojo, T. *Inorg. Chem.* **2012**, *51*, 5246–5256.
- (31) Orive, J.; Fernández de Luis, R.; Rodríguez Fernández, J.; Legarra, E.; Plazaola, F.; Arriortua, M. I. *CrystEngComm* **2014**, *16*, 6066–6079.
- (32) (a) Sengupta, P.; Sandvik, A. W.; Singh, R. R. P. *Phys. Rev. B: Condens. Matter Mater. Phys.* **2003**, *68*, 094423. (b) Durand, A. M.; Klavins, P.; Corruccini, L. R. *J. Phys.: Condens. Matter* **2008**, *20*, 235208. (c) Yaouanc, A.; Dalmás de Reotier, P.; Glazkov, V.; Marin, C.; Bonville, P.; Hodges, J. A.; Gubbens, P. C. M.; Sakarya, S.; Baines, C. *Phys. Rev. Lett.* **2005**, *95*, 047203.
- (33) Ramirez, A. P. *Annu. Rev. Mater. Sci.* **1994**, *24*, 453–480.
- (34) (a) Shores, M. P.; Nytko, E. A.; Bartlett, B. M.; Nocera, D. G. *J. Am. Chem. Soc.* **2005**, *127*, 13462–13463. (b) Zheng, Y. Z.; Tong, M. L.; Xue, W.; Zhang, W. X.; Chen, X. M.; Grandjean, F.; Long, G. J. *Angew. Chem.* **2007**, *119*, 6188–6192.



Se ha sintetizado y caracterizado una extensa familia de nuevos materiales metal-orgánicos multifuncionales que combinan porosidad y magnetismo. Estos materiales se caracterizan por estar basados en entidades metal-orgánicas discretas, donde la especificidad de las interacciones supramoleculares que tienen lugar entre las mismas es el origen de la naturaleza porosa de estos materiales. Esta especificidad en las interacciones supramoleculares es obtenida mediante la apropiada selección de la parte orgánica de estas entidades, normalmente nucleobases o piridinas funcionalizadas con grupos dadores y aceptores de enlaces de hidrógeno adyacentes.

En lo que hace referencia a las propiedades magnéticas los centros paramagnéticos que constituyen los centros metálicos interactúan entre sí de forma eficaz a través de los diversos puentes μ -adeninato, μ -hidróxido y μ -carboxilato presentes en las entidades. En este sentido cabe destacar las entidades heptaméricas $[\text{Cu}_6\text{M}(\text{OH})_6(\text{adeninato})_6(\text{H}_2\text{O})_6]^{n+}$ (M^{3+} : Cr, Mn y M^{2+} : Co, Ni, Cu, Zn) donde la sustitución del metal central permite modular el comportamiento magnético para obtener materiales tanto ferri- como ferromagnéticos con valores de S_T variable y cuyas propiedades magnéticas se aúnan con la porosidad inherente al empaquetamiento de estas entidades. Como colofón, esta combinación de propiedades ha sido empleada para la captura activa de los fármacos ibuprofeno y naproxeno. Asimismo la respuesta de estos materiales frente a campos magnéticos externos permite cuantificar la masa adsorbida por estos compuestos en un claro ejemplo de materiales multifuncionales.